NASA Conference Publication 3227

Conference on Binary Optics

An Opportunity for Technical Exchange

19990604 053

Proceedings of a conference sponsored by
NASA, Office of Advanced Concepts and Technology;
NASA, George C. Marshall Space Flight Center;
U.S. Army Research Office;
USA MICOM Research, Development, and Engineering Center;
USA SSDC Sensors Directorate;
U.S. Army Night Vision and Electronic Sensors Directorate;
U.S. Army Test Measurement and Diagnostic Equipment Activity
held in Huntsville, Alabama
February 23–25, 1993

DISTRIBUTION STATEMENT A
Approved for Public Release
Distribution Unlimited

DTIC QUALITY INSPECTED 4

NASA Conference Publication 3227

Conference on Binary Optics

An Opportunity for Technical Exchange

Edited by
Helen J. Cole
NASA George C. Marshall Space Flight Center
Marshall Space Flight Center, Alabama, and
William C. Pittman
U.S. Army Missile Command
Redstone Arsenal, Alabama

Proceedings of a conference sponsored by
NASA, Office of Advanced Concepts and Technology;
NASA, George C. Marshall Space Flight Center;
U.S. Army Research Office;
USA MICOM Research, Development, and Engineering Center;
USA SSDC Sensors Directorate;
U.S. Army Night Vision and Electronic Sensors Directorate;
U.S. Army Test Measurement and Diagnostic Equipment Activity
held in Huntsville, Alabama
February 23–25, 1993

NASA
National Aeronautics and
Space Administration
Office of Management
Scientific and Technical
Information Program
1993

ACKNOWLEDGMENTS

We would like to acknowledge ERIM, Infrared Information Analysis Center of Ann Arbor, MI, and UWOHALI of Huntsville, AL, for their support in coordinating mailings and conference committee meetings and for their support in administering the agenda on the days of the conference. We would like to extend thanks to the Optical Society of America for service as a cooperating society through their contributions to planning and advertising of the conference.

FOREWORD

The first formal program designed to develop a diffractive optics technology based on microelectronic integrated-circuit technology was sponsored by the Defense Advanced Research Projects Agency at the Massachusetts Institute of Technology Lincoln Laboratory in 1985. This program was successful in launching a new diffractive optics technology of strong interest to industry, academia, and U.S. Government research organizations. During the course of this program, the term "binary optics" was introduced to describe diffractive micro-optical elements created using adapted VLSI fabrication techniques.

A recent search of technical data bases suggests that the available resources for binary optics technology transfer are limited. This conference was organized to promote an international exchange of technical information on the subject. An audience of 235 heard 25 presented papers and 7 invited lectures, including tutorials on special topics.

The keynote address focused on fabrication issues as the greatest challenge facing the future of binary optics with the most critical being the need for established quality control and replication methods. Other invited lectures confirmed the pivotal requirement for future manufacturing process development, and cautioned that technological contributions from small-to-mid size businesses may be thwarted by the high cost of fabrication equipment and infrastructure.

Binary optics is a promising technology for both NASA and the Army. It is well-suited to the space environment for which its potential size and weight reductions, and potential increases in ruggedness, performance, and survivability over standard optical components and holographic optical elements are of most interest. Some areas of application at NASA could include imaging and spectroscopic systems for astronomical and Earth observing missions, new reflective and refractive substrate materials, wavefront sensing for adaptive optical systems, and active optical systems for beam steering and combining.

Binary optics is capable of providing components and subsystems for military products as well. Overall Department of Defense (DOD) investments in photonics have been increasing and the DOD recognizes the major impact that photonics will have on U.S. Army programs. As such, binary optics has been identified as an element of the DOD Critical Technology in PHOTONICS. The most frequently mentioned areas of military application include optical data storage, communications, and sensors.

The U.S. Army Materiel Command, in a memorandum dated 19 Sep 1991, designated the U.S. Army Missile Command (MICOM) as the lead to develop the Photonics Manufacturing Technology (ManTech) Thrust Area for the Army; binary optics will be one of the key enabling technologies in this thrust. The Research, Development, and Engineering Center, as executive agent for MICOM, will work with other Federal laboratories and centers in order to carry out this mission assignment.

Binary optics is an enabling technology for space, military, and commercial products. When the art of optical fabrication makes the transition from a craft-base to a high-technology, manufacturing-base, as predicted, it will occur through merging binary optics with other photonics and microelectronics technologies.

Although optimistic projections have been made for binary optics, it is difficult to obtain an accurate picture of the investment level since binary optics is an enabling technology buried beneath

other programs. However, if the perceptions of many of the participants of this conference are correct, there is a ground swell in the making.

The steering committee would like to thank all the sponsors of this conference for their support as well as the speakers, session chairpeople, and the participants for their enthusiasm demonstrated in this contribution to the technology transfer process. Special thanks are due Ms. Rose Coleman, Mr. Ron Mitchell, and Ms. Colleen Richmond, Conference Coordinators, who guided the conference from its inception to a successful conclusion.

Helen Johnson Cole
William C. Pittman
For the Steering Committee

STEERING COMMITTEE

Co-Chairpersons

Helen Cole
NASA
Marshall Space Flight Center
Huntsville, AL

William Pittman
U.S. Army Missile Command
Redstone Arsenal, AL

Pete Black
U.S. Army Missile Command
Redstone Arsenal, AL

Steve Fawcett
NASA, Marshall Space Flight Center
Huntsville, AL

Tom Flournoy
U.S. Army TMDE Activity
Redstone Arsenal, AL

Patrick Kuykendall
U.S. Army TMDE Activity
Redstone Arsenal, AL

David Lanteigne
U.S. Army Missile Command
Redstone Arsenal, AL

Cassie Lofts
U.S. Army Missile Command
Redstone Arsenal, AL

George Sloan
U.S. Army Strategic Defense Command
Redstone Arsenal, AL

Bill Witherow
NASA, Marshall Space Flight Center
Huntsville, AL

Sam Wood
U.S. Army Missile Command
Redstone Arsenal, AL

PROGRAM COMMITTEE

Co-Chairpersons

Helen Cole
NASA
Marshall Space Flight Center
Huntsville, AL

William Pittman
U.S. Army Missile Command
Redstone Arsenal, AL

Alan Cox
Honeywell Systems and Research Center
Bloomington, MN

Steve Fawcett
NASA, Marshall Space Flight Center
Huntsville, AL

Thomas Gaylord
Georgia Tech
Atlanta, GA

Bobby Guenther
U.S. Army Research Office
Research Triangle Park, NY

Alan Kathman
Teledyne Brown Engineering
Huntsville, AL

David Lanteigne
U.S. Army Missile Command
Redstone Arsenal, AL

Donald Larson
NIST
Boulder, CO

Michael Morris
University of Rochester
Rochester, NY

Miles Scott
Teledyne Brown Engineering
Huntsville, AL

Dean Scribner
Naval Research Laboratory
Washington, DC

Anthony Tai
Environmental Research Institute of Michigan
Ann Arbor, MI

Pat Trotta
Texas Instruments, Inc.
Dallas, TX

Gary Wiese
Martin Marietta
Orlando, FL

Roger Witherington
Hughes Aircraft Company
El Segundo, CA

Andrew Yang
Advanced Research Projects Agency
Arlington, VA

TABLE OF CONTENTS

Page

KEYNOTE ADDRESS: MANUFACTURING THE KEY TO BINARY OPTICS
B.D. Guenther, Army Research Office, Research Triangle Park, NC 1

BINARY OPTICS: TRENDS AND LIMITATIONS*
M.W. Farn and W.B. Veldkamp, MIT Lincoln Lab., Lexington, MA 19

DIFFRACTIVE OPTICS: DESIGN, FABRICATION, AND APPLICATIONS*
G.M. Morris, University of Rochester, Rochester, NY 31

SESSION A: MODELING AND DESIGN
Chairpeople: Dave Lanteigne, Weapons Sciences Directorate, U.S. Army Missile Command, Redstone Arsenal, AL, and Steve Anderson, Hughes Aircraft Company, El Segundo, CA

REVIEW OF RIGOROUS COUPLED-WAVE ANALYSIS AND OF HOMOGENEOUS EFFECTIVE MEDIUM APPROXIMATIONS FOR HIGH SPATIAL-FREQUENCY SURFACE-RELIEF GRATINGS, E.N. Glytsis, D.L. Brundrett, and T.K. Gaylord, Georgia Institute of Technology, Atlanta, GA 61

SCALAR LIMITATIONS OF DIFFRACTIVE OPTICAL ELEMENTS, E.G. Johnson and D. Hochmuth, Teledyne Brown Engineering, Huntsville, AL, and M.G. Moharam and D. Pommet, University of Central Florida, Orlando, FL 77

SUBWAVELENGTH STRUCTURED SURFACES AND THEIR APPLICATIONS, D.H. Raguin and G.M. Morris, University of Rochester, Rochester, NY 87

DIFFRACTIVE OPTICAL ELEMENTS FOR GENERATING ARBITRARY LINE FOCI, J.N. Mait, D.W. Prather, J. van der Gracht, and T.J. Tayag, U.S. Army Research Laboratory, Adelphi, MD 99

FINITE DIFFERENCE TIME DOMAIN ANALYSIS OF CHIRPED DIELECTRIC GRATINGS, D.H. Hochmuth and E.G. Johnson, Teledyne Brown Engineering, Huntsville, AL 107

ASYMMETRIC THREE-BEAM BINARY OPTIC GRATING, A.D. Kathman, E.G. Johnson, and M.L. Scott, Teledyne Brown Engineering, Huntsville, AL 111

SCATTERING FROM BINARY OPTICS, D.W. Ricks, Naval Air Warfare Center, China Lake, CA 117

MATHEMATICAL MODELING FOR DIFFRACTIVE OPTICS, D. Dobson, University of Minnesota, Minneapolis, MN, and J.A. Cox, Honeywell Systems and Research Center, Bloomington, MN 135

*Indicates invited paper.

TABLE OF CONTENTS (Continued)

Page

FABRICATING BINARY OPTICS: AN OVERVIEW OF BINARY OPTICS PROCESS TECHNOLOGY,* M.B. Stern, MIT Lincoln Lab., Lexington, MA 153

SESSION B: FABRICATION
Chairpeople: John Davis, System Engineering and Production Directorate, U.S. Army Missile Command, Redstone Arsenal, AL, and Steve Fawcett, NASA, MSFC, Huntsville, AL

BINARY OPTICS AT HUGHES DANBURY OPTICAL SYSTEMS, J. Logue and M. Power, Hughes Danbury Optical Systems, Inc., Danbury, CT 167

FABRICATION TECHNIQUES FOR VERY FAST DIFFRACTIVE LENSES, A.M. Tai and J.C. Marron, Environmental Research Institute of Michigan, Ann Arbor, MI 179

LASER FIGURING FOR THE GENERATION OF ANALOG MICRO-OPTICS AND KINEFORM SURFACES, E.J. Gratrix, Hughes Danbury Optical Systems, Danbury, CT 187

DIFFRACTIVE OPTICS FABRICATED BY DIRECT WRITE METHODS WITH AN ELECTRON BEAM, B. Kress, D. Zaleta, W. Daschner, K. Urquhart, R. Stein, and S.H. Lee, University of California at San Diego, La Jolla, CA 195

PHASE HOLOGRAMS IN PMMA WITH PROXIMITY EFFECT CORRECTION, P.D. Maker and R.E. Muller, California Institute of Technology, Pasadena, CA 207

CURVED GRATING FABRICATION TECHNIQUES FOR CONCENTRIC-CIRCLE GRATING, SURFACE-EMITTING SEMICONDUCTOR LASERS, R.H. Jordan, O. King, G.W. Wicks, and D.G. Hall, University of Rochester, Rochester, NY; E.H. Anderson, IBM T.J. Watson Research Center, Yorktown Heights, NY, and Lawrence Berkeley Lab., Berkeley, CA; and M.J. Rooks, Cornell University, Ithaca, NY 223

MICRO-OPTICS TECHNOLOGY AND SENSOR SYSTEMS APPLICATIONS, G. Gal, B. Herman, W. Anderson, R. Whitney, and H. Morrow, Lockheed Missiles and Space Co., Palo Alto, CA 237

FABRICATION OF MICRO-OPTICAL DEVICES, W.W. Anderson, J. Marley, and G. Gal, Lockheed Missiles and Space Co., Palo Alto, CA; and D. Purdy, Phillips Components Limited, Southampton, Hampshire, UK 255

DIFFRACTIVE OPTICS IN ADVERSE ENVIRONMENTS, G.P. Behrmann, Army Research Lab., Adelphi, MD 271

*Indicated invited paper.

TABLE OF CONTENTS (Continued)

Page

LOW COST PATHS TO BINARY OPTICS, A. Nelson and L. Domash, Foster-Miller, Inc., Waltham, MA 283

THERMAL WEAPON SIGHT (TWS) AN/PAS-13 DIFFRACTIVE OPTICS DESIGNED FOR PRODUCIBILITY, J.S. Anderson and C.W. Chen, Hughes Aircraft Co., El Segundo, CA; and R.A. Spande, CECOM, Night Vision and Electronic Sensors Directorate, Ft. Belvoir, VA 303

SESSION C: APPLICATIONS I
Chairpeople: Paul Ashley, Weapons Sciences Directorate, MICOM, Redstone Arsenal, AL, and Alan Kathman, Teledyne Brown Engineering, Huntsville, AL

MEASUREMENTS OF MICROLENS PERFORMANCE, D. Shough, B. Herman, and G. Gal, Lockheed Missiles and Space Co., Palo Alto, CA 325

APPLICATIONS OF ADVANCED DIFFRACTIVE OPTICAL ELEMENTS, W.H. Welch, J.E. Morris, and M.R. Feldman, Digital Optics Corp., Charlotte, NC, and University of North Carolina, Charlotte, NC 341

LASER BEAM STEERING DEVICE, M.E. Motamedi, A.P. Andrews, and W.J. Gunning, Rockwell International Science Center, Thousand Oaks, CA 345

SURPHEX™: NEW DRY PHOTOPOLYMERS FOR REPLICATION OF SURFACE RELIEF DIFFRACTIVE OPTICS, F.P. Shvartsman, Du Pont Co., Wilmington, DE 359

PREDESIGN OF DIAMOND TURNED REFRACTIVE/DIFFRACTIVE ELEMENTS FOR IR OBJECTIVES,* M.J. Riedl, Optical Filter Corp., Keene, NH 369

OPTICAL SYSTEM STORAGE DESIGN WITH DIFFRACTIVE OPTICAL ELEMENTS,* R.K. Kostuk, University of Arizona, Tucson, AZ; and C.W. Haggans, 3M Co., Vadnais Heights, MN 387

SESSION D: APPLICATIONS II
Chairpeople: James Bilbro, Deputy Chief, Optical and RF Systems Division, NASA, MSFC, Huntsville, AL, and Paul Maker, Jet Propulsion Laboratory, Pasadena, CA

THEORY OF DISPERSIVE MICROLENSES, B. Herman and G. Gal, Lockheed Missiles and Space Co., Palo Alto, CA 395

COLOR SEPARATION GRATINGS, M.W. Farn, R.E. Knowlden, M.B. Stern, and W.B. Veldkamp, MIT Lincoln Lab., Lexington, MA 409

LIST OF ATTENDEES 423

*Indicates invited paper.

MANUFACTURING THE KEY TO BINARY OPTICS

DR. B. GUENTHER
ARMY RESEARCH OFFICE
RESEARCH TRIANGLE PARK, NC

Conf. on Binary Optics, 1993

Gratings

1786	First Grating David Rittenhouse
1821	Spectroscopy Joseph Fraunhofer
1882	Concave Grating H.A. Rowland
1910	Blazed Grating R.W. Wood

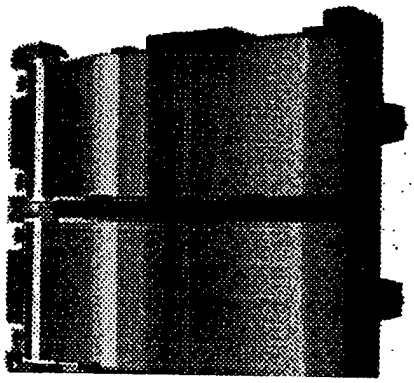

ARO

- American astronomer, David Rittenhouse, noticed diffraction from silk handkerchief and invented diffraction grating in 1786. He made no scientific measurements but did note red was bent more than blue.
- Joseph von Fraunhofer independently invented the diffraction grating in 1821 and used it to look at the sun's spectrum. He derived and verified the grating equation. He examined the effects of groove shape and position.
- In 1822 Sir John Barton, deputy controller of the London Mint patented the use of gratings in ornaments such as waistcoat buttons. This was the first commercial application of diffractive optics!
- H.A. Rowland of Johns Hopkins University invented concave gratings which allowed the spectrum to be focused into a sharp image. This enabled spectroscopy to extend into u.v. It enhanced accuracy of relative wavelength measurements.
- R.W. Wood developed a technique for controlling the distribution of light among the diffracted orders by controlling the shape of the grooves – **blazing**.

Grating Characteristics

- Fourier transform of grating structure displayed as angular spectrum
- Spectral sensitivity is an advantage
- No power
- Higher orders *"passed off"* (diffracted beyond 90°)
- Hard edges lead to many orders

ARO

- The spatial Fourier transform of the grating structure gives an angular spectrum. Because the ruled grating has hard edges, there are many high orders.
- Only a finite number of orders are observable because once the diffraction angle has reached 90° no orders are observable. The orders are said to be "passed off".
- The grating period is a constant thus the grating has no power. To focus light, the grating surface must be curved.
- For this optical component, dispersion is an advantage.

Grating Construction ☛

Grating Manufacture

- First observations with silk handkerchief
- First grating used hair to create apertures
- H.A. Rowland made first ruling engine
- R.W. Wood developed diamond tool for blazing
- Replication developed by J.V. White & W.A. Fraser

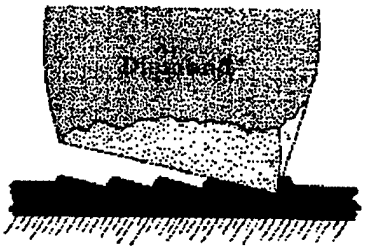

ARO

- The first grating was a fine silk handkerchief but in order to produce a more controlled condition, Rittenhouse made a grating of hairs spaced by two screws.
- Fraunhofer made his first transmission grating using wires held in screw threads and his first reflection grating by ruling grooves with a diamond point on a mirror surface. His best effort was a 12 mm wide grating with 9600 grooves.
- Rowland built a ruling engine in 1882 which was not the first but was the first **successful** device.
- John Hopkins University produced most of the accomplishments in grating technology up to the Second World War
  Wood developed blazed gratings
  Strong introduced the use of vacuum deposition of thin metal films for ruling.
- In **1915** Michelson suggested that the ruling engine be controlled by an interferometer and in **1955** the first use of an interferometer was made by Stroke of Johns Hopkins.
- Probably the most important development other than the ruling engine was the development by White and Fraser in 1949 of high quality replication.

Zone Plate

1871	First zone plate Lord Rayleigh
1898	Phase Zones R.W. Wood
1950	Connection to holography G.L. Rogers
1961	Application to x-rays A. Baez

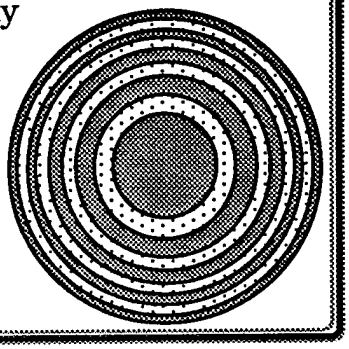

ARO

- The first zone plate with 15 zones was drawn by hand in 1871 by Lord Rayleigh.
- Lord Rayleigh suggested construction of a phase zone plate which was made by R.W.Wood in 1898.
- The connection between zone plates and holography brought a renewed interest in these optical elements.
- Ac curiosity until the ability to make zone plates using microlithography allowed the application of zone plates to x-ray optics. It is here that zone plates have found a real niche since there is little competition.
- The reason zone plates are seldom used can be found by examining their attributes.

Zone Plate Characteristics

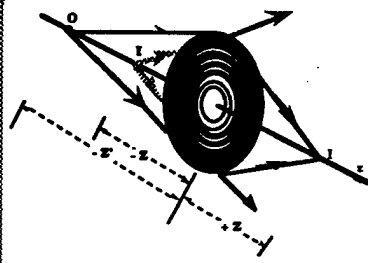

- Chirped grating with power
- Chromatic effects is handicap
- Resolution determined by grating period

- Fourier transform of grating structure displayed along optical axis
- All orders are observable yielding large amount of stray light

ARO

- The zone plate is made of concentric rings. The area of each of the rings is the same. The radii of the rings are proportional to the square root of the natural numbers.
- This construction results in a radial chirped grating. This gives the zone plate power allowing it to be used as a lens.
- The Fourier transform of this chirped grating is displayed along the optical axis of the zone plate. This distribution is viewed as foci of the zone plate.
- Because of the hard edges of the zone grating, an infinite number of foci appear along the optical axis. This leads to a lot of stray light.
- At best the zone plate will produce only a real and a virtual image.
- The dispersion of the zone plate is a handicap.

Zone Plate Manufacture

- Originally hand drawn
- Photographic reduction
- Ruling machine first used near turn of the Century
- Electron beam writing
- Blazed zone plates

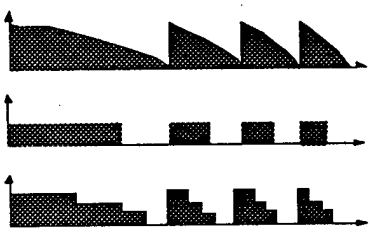

ARO

- Lord Rayleigh, in 1871, drew by hand the first zone plate which contained 15 zones alternately blackened.
- It was obvious to Rayleigh that the zone plate could be improved by replacing the darkened zones by transparent zones that simply reversed the phase. This was first done in 1898 by Robert Wood.
- Wood also developed a rotary ruling machine that allowed zone plates to be machined. He first used a wax substrate and a record needle.
- The microelectronic industry developed a number of techniques that allowed zone plates for the x-ray region to be produced.
- Photographic techniques have even been used to produce blazed zone plates with enhanced diffraction efficiency.

Holography

1927 A.A. Michelson suggested interferometry to make gratings

1949 Dennis Gabor invented holography

1962 E.N. Leith & J. Upatnïeks invented off axis holography

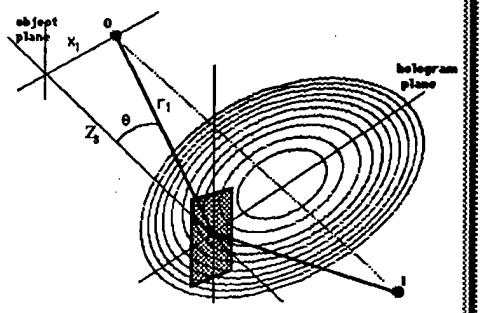

ARO

- In 1948 Dennis Gabor invented holography as a means of increasing the resolution of electron microscopy.
- The first suggestion of recording interference fringes to produce a diffractive optical component was by Michelson in 1927.
- The first gratings were made by J.M. Burch in 1960.
- Gabor's idea was not practical until the invention of the laser and the concept of off axis holography developed by Leith and Upatnieks in 1962.
- The view of the hologram as a segment of a zone plate was first suggested by Gabor and developed by G.L. Rogers in 1952.
- The zone plate analogy is a useful way of understanding the imaging properties of holography.

Holographic Aberration Correction

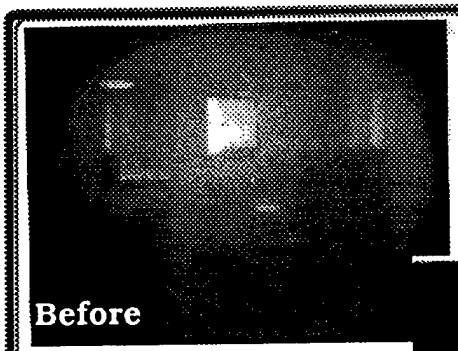

J. Upatnieks, A. Vander Lugt, and E. Leith "Correction of lens aberrations by means of holograms," *Applied Optics*, **5**, 589-593 , (1966)

ARO

- Even with all the difficulties, optical components have been produced.
- The first optical components as well as the first aberration correction of refractive components was done in 1966.
- Here a **before** photo is shown with a large amount of spherical aberration.
- The **after** photo demonstrates the removal of the spherical aberration by the use of a hologram.

Wavefront Generated Holograms

Advantages

- Sinusodial gratings
- Curved grooves
- Curved substrate
- Dynamic components with photorefractives

Problems

- Wavefront generation
- Control of groove shape and depth
- Materials
  - Stability during and after processing
  - Spectral and intensity sensitivity

- Holography allows sinusoidal grooves to be produced, eliminating higher orders in amplitude recordings.
- With photorefractive materials it is possible to consider dynamic diffractive elements.
- The substrate can have any shape.
- To generate a desired groove profile optically, Fourier synthesis techniques have been used. Here, in theory, a number of sinusoidal exposures are superimposed to generate the desired shape.
- Groove shape and depth has been very difficult to control.
- It is often hard to generate the desired wavefront so we have turned to the computer.

Computer Generated Hologram

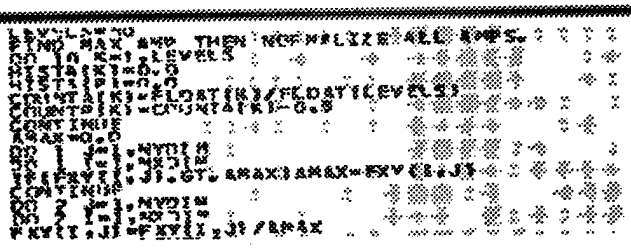

1966 Detour phase technique
A.W. Lohman

1969 Kinoform
L.B. Lesem

ARO

- Driven by the need to produce arbitrary waveforms. Computer generated holography was developed.
- The first CGH were produced using one bit computer plotters. The results of such a plotter are shown in the montage on this viewgraph.
- Kinoforms are computer generated holograms that modulate only the phase. This is done by using a gray scale film recorder. The master is reduced and bleached to convert the gray scale to optical path modulation.
- New fabrication technologies have been developed that provide seemly unlimited capability.

Fabrication

- **Diamond Turning**
- **Optical Recorders**
  - Dichromatic gelatin
  - Photoresist
  - Photopolymer
- **Electron Beam Recorders**
  - Wet etching
  - Plasma etching
  - Ion beam milling
  - Ion exchange
  - Implantation
  - Lift off

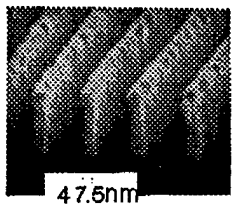

- Diamond turning utilizes the same technique as the grating ruling machines.
- Optical techniques use interferometry, beam writing, or imaging
- Dichromate provides 3000 l/mm resolution, low noise and high index modulation but it is sensitive to humidity. Dichromate undergoes shrinkage and swelling during processing.
- Photoresist has high resolution, 4000 l/mm but is most sensitive to uv. In visible, exposure can take minutes to hours.
- Photopolymers from Polaroid and DuPont have high index modulation (similar to dichromate). Volume changes are small.
- Electron beam lithography uses mask makers from microelectronics. The basic features are trapezoids which lead to errors in binary optics.
- Plasma etching yields 2500 l/mm but has high cost and takes hours.
- Anisotropic wet etching of silicon imposes restrictions on pattern size, groove curvature, spatial frequency variation, and reproducibility.
- Ion beam milling is slow and non-selective making it not useful to microelectronics but its properties are great for diffractive optics.
- Implantation, diffusion and ion exchange produces imbedded diffractive structures.

Fabrication Capabilities

	Machine	Feature Size μm	Space Bandwidth	Accuracy μm	Speed Pixel/sec
Single Beam Optical	Galvanometer	5	4×10^6	1	10^3
	Rotating Drum	5	1.6×10^7	1	10^4
	Translaton	1	10^{10}	0.5	10^6
	Rotating Disk	1	10^{10}	0.5	10^6
Parallel Optical	Imaging	5	10^8	1	10^4
	Interference	1	10^8	1	10^3
Electron Beam	Mask Maker	0.2	10^{10}	0.1	10^5
	Microscope	0.5	10^8	0.1	10^6
Mechanical	Lathe	0.2	10^{10}	0.1	10^6
	Milling	0.2	10^{10}	0.1	10^6

ARO

- Here are resolutions obtained from various commercial writing systems.
- Optical systems all have resolutions around 1 μm while electron beam has 0.2 μm.
- Optical systems can produce gray scale while electron beam devices cannot.
- Pattern generators designed for the microelectronics industry have problems currently with circularly symmetric patterns. They want to produce trapezoids all oriented in the same way.
- The use of patch by patch construction using interferometry has not been successfull.
- Major problem is all writing techniques are serial! These devices can produce masters but we need to be able to replicate to lower cost and increase speed of production.

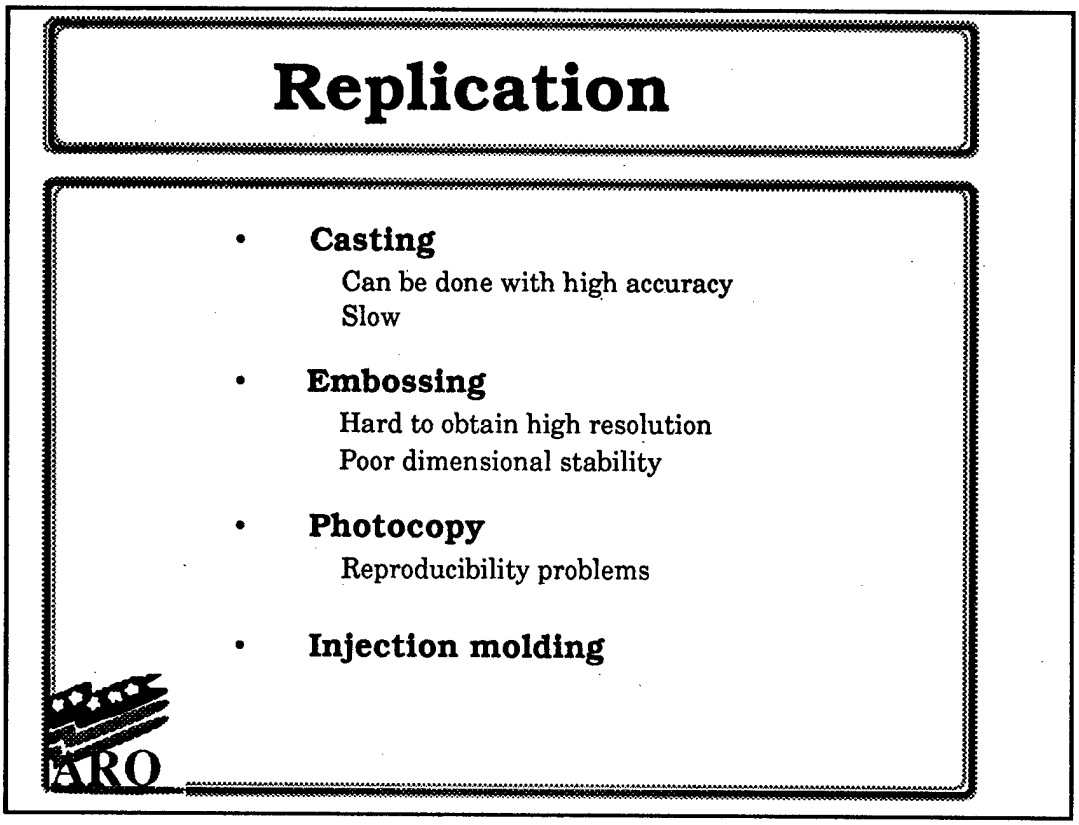

- Lord Rayleigh demonstrated at the turn of the century replication was possible by casting but it was not practical until 1949.
- A good release was needed so that the master was not destroyed during the replication process.
- The key to the wide spread use of gratings has been the development of replicating techniques and it will also be true for diffractive optics.
- If we are to use diffractive optics in transmission the substrate must be of good optical quality. This is not necessary in grating production.
- Casting using epoxy or sol gel can be done with extreme accuracy but it is slow.
- It is difficult to emboss extremely small diffractive structures and the plastics that are used in embossing have poor environmental stability.
- Holographic recording or copying is not very reproducible. It is hard to control the chemistry.
- Injection molding has been very successful for camera lenses but I am unaware of its use in diffractive optics.

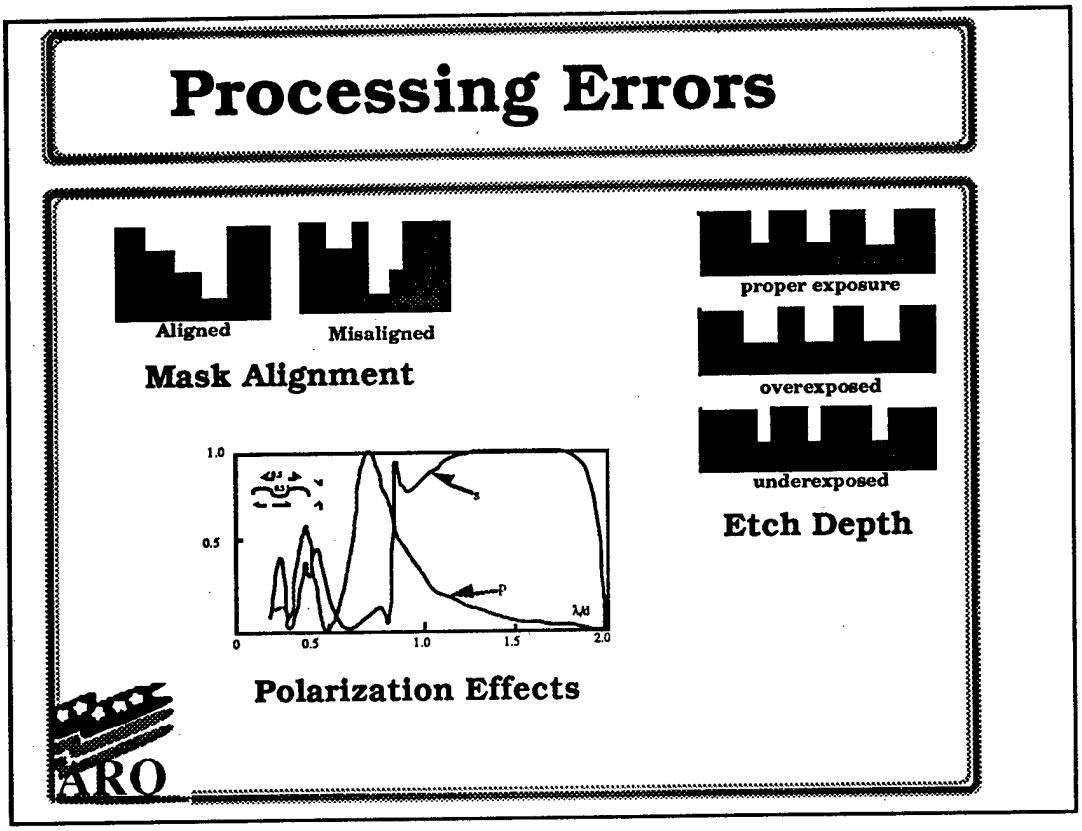

- Groove placement errors result in near scatter noise such as ghost and grass.
- Far scatter effects result from groove shape errors.
- The diffraction efficiency is very sensitive to groove shape. Ridge widths less than 0.01 of the minimum zone width are required.
- Image quality is not sensitive to groove shape and depth but noise due to scatter is.
- Sources of errors are control of development, mask alignment and material shrinkage.
- Polarization effects from processing errors that destroy circular symetry create form birefringence. This is theoretically understood but most lens designers encounter this type of birefringence only with improperly mounted components.

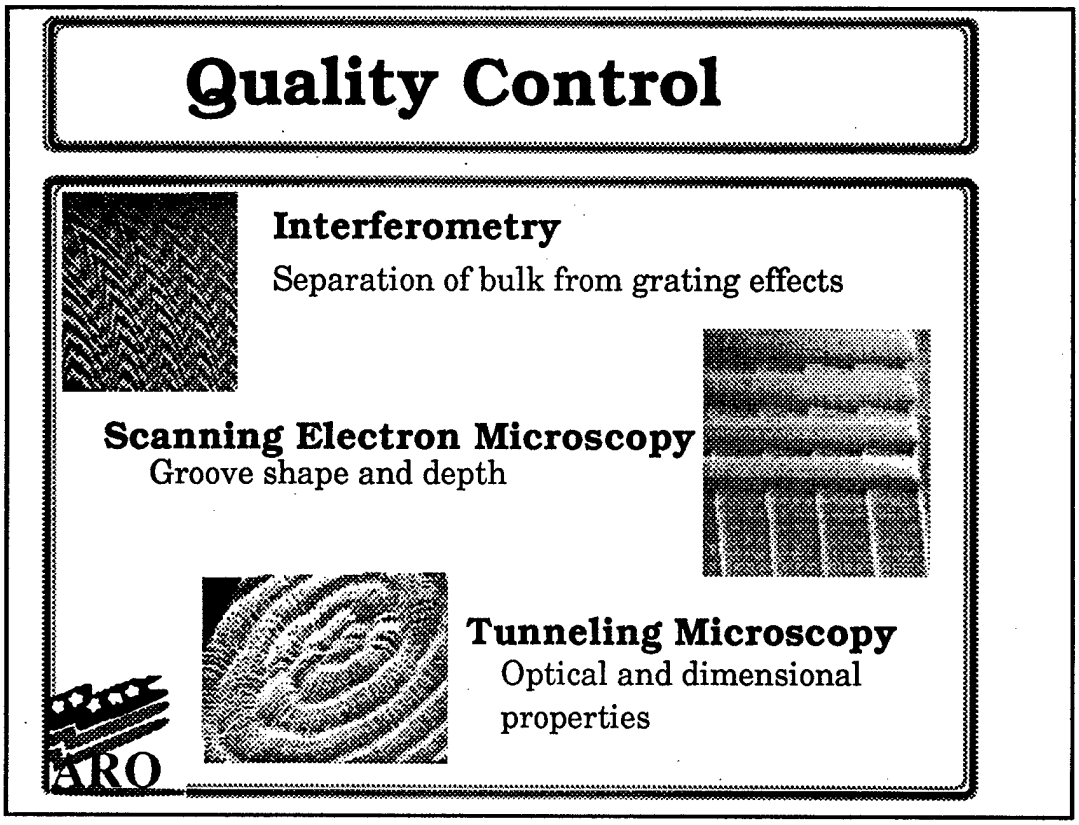

- In quality control we must be able to separate out the effects of the substrate from the diffractive elements so if there is a problem we can correct the offending element. It may require some intelligent application of interferometry to separate out the two contributions.
- Optical and mechanical methods for measuring groove profiles have resolution limitations. Scanning electron microscopes can be used but the techniques are invasive.
- Tunneling microscopes will provide noncontacting three dimensional measurements of the sample surface.
- Optical tunneling microscopes provide much more than simple groove profiles. By using Raman scattering, we can map out underlying stress fields.

Conclusions

- Theory is in good shape
- Tools for fabrication exist
- Replication needed for manufacturing
- Quality control needs development

- The theory has been developed since the mid 19 century and is in good shape.
- A wide range of fabrication tools exist. Many need to be modified to optomize for diffractive optics.
- If this technology is to find wide useage, replication must be developed.
- Quality control tools must also be developed.
- Neither of lthe needed developements appear to be unatainable. I expect to see diffractive loptics to become a widely used tool in optics systems design.

Binary Optics: Trends and Limitations

Michael W. Farn and Wilfrid B. Veldkamp
MIT/Lincoln Laboratory, HW45-108
244 Wood St., Lexington, MA 02173-9108

1. ABSTRACT

We describe the current state of binary optics, addressing both the technology and the industry (i.e., marketplace). With respect to the technology, the two dominant aspects are optical design methods and fabrication capabilities, with the optical design problem being limited by human innovation in the search for new applications and the fabrication issue being limited by the availability of resources required to improve fabrication capabilities. With respect to the industry, the current marketplace does not favor binary optics as a separate product line and so we expect that companies whose primary purpose is the production of binary optics will not represent the bulk of binary optics production. Rather, binary optics' more natural role is as an enabling technology - a technology which will directly result in a competitive advantage in a company's other business areas - and so we expect that the majority of binary optics will be produced for internal use.

2. INTRODUCTION

The goal of this paper is not technical. We assume the reader is familiar with the technology of binary optics (see the other papers in this proceedings) and our goal is to describe the current state of the binary optics field. More specifically, we intend to answer the following three questions:

- What is binary optics?
- What is the future potential of the technology?
- What are the factors limiting growth?

We will answer these questions both from a technical standpoint and also from an industry (i.e., marketplace) standpoint. Naturally, the answer to such questions must be somewhat subjective and the reader should recognize that our viewpoint is from a national laboratory whose goal is to cooperate with industry and government to develop this technology.

In answering these questions, we will use the following approach. In the remainder of this section, we will first develop a working definition for "binary optics" and then introduce some classification schemes for binary optics, in order to gain some insight into the field. In section 3, we will examine the current state of the binary optics technology, using one of the previously introduced classification schemes and in section 4, we will repeat this process for the industry as a whole. Finally, the last section will summarize the major points of this paper.

Conf. on Binary Optics, 1993

Table 1: Fields Related to Binary Optics.

Related Field	Why Is It Not Binary Optics?
Conventional Lenses	Conventional Fabrication
Holographic Optical Elements	Optical Fabrication, Volume Effect
Gradient Index Optics	Volume Effect
Optical Coatings	No Surface Relief
Non-linear Optics	Volume Effect, Active
Photorefractives	Volume Effect, Active
Liquid Crystal Displays	Active, Not Purely Surface Relief
Integrated Optics	Guided Wave Optics
Microelectronics	Not Optical, Active
Micromechanics	Not Optical, Active

2.1. Definition

What is binary optics? This basic question is not easily answered because there is no strict definition. Binary optics is a somewhat general term, invoking radically different images to different people. For example, to an optical designer, the meaning of binary optics is coupled to the application but that application may be any of the following: diffractive lenses for use in laser systems, aberration correction of wideband systems, null testing of aspheric elements, intraocular lenses, stereo vision systems, laser scanners, grating beamsplitters, read/write heads for optical data storage, custom diffusers, optical interconnects, laser cavity optics, beam shaping of lasers, laser diode collimation, fiber couplers, microlenses, anti-reflection surfaces, artificial index materials, artificial birefringent materials, etc. On the other hand, to a person involved with the fabrication aspect, binary optics may suggest the following activities: mask writing, photoresist exposure and development, analog exposure of resists, planarization of topology and tri-layer resists, mask alignment, dual-sided alignment, reactive ion etching, ion milling, wet chemical etching, laser chemical etching, laser ablation, laser writers, direct e-beam writers, chemical vapor deposition, liftoff deposition, metallization, sputtering, etc. These areas are all part of binary optics, yet they are so diverse that it is difficult to come up with an explicit definition which will fit them all. Therefore, we will not attempt this. Instead, we will define the field through descriptions and examples, an implicit definition of sorts.

As a first example, we consider closely related fields and ask why these fields are not considered part of binary optics. Table 1 lists a number of these fields and the differences between them and binary optics. Analyzing this list then yields the following distinguishing features:

- Surface Relief - The optical properties of binary optics are solely the result of the surface profile of the element. Volume effects are not significant, as with thick holograms, graded index optics or photorefractives. As a corollary, this property allows the possibility of inexpensive replication methods, such as embossing.

- VLSI-based Fabrication - Binary optics are manufactured using semiconductor fabrication technology. This allows the fabrication of elements with sub-wavelength precision and also the potentially simpler integration of optics and electronics.

- Free-space, Passive Optics - Binary optics are passive optical elements to be used in free-space applications. By free-space, we mean systems where a large number of modes are propagating (i.e., everything except guided wave systems).

Taken together, these characteristics provide a loose current definition of binary optics. As the field evolves, however, this definition will also change accordingly.

2.2. Classification Schemes

In order to further describe the field, this section considers different methods of classifying binary optics. In other words, we ask how can binary optics be subdivided.

One method of classification is by historical development. The evolution of binary optics over the past decade can be divided into three generations. The first generation focussed on elements with large features. Accordingly, the majority of applications were large individual elements (macro-optics) used for the residual aberration correction of conventional systems. This generation is now relatively mature and has been largely transferred to industry. Advancing fabrication techniques resulted in smaller feature sizes, thus spawning the second generation: microoptics and arrays of microoptics (especially microlenses). At present, this generation has progressed to the point of attracting much industry interest and activity but it is still far from mature. Further advances in fabrication and packaging are leading to the third generation, which will see the integration of optics and electronics/electro-optics. This generation is largely still in the laboratory - and only a few laboratories at that. However, this technology has a large commercial potential and as soon as it is clear how this potential may be realized, interest in this area will increase exponentially. Reviewing the history of binary optics shows that it is based on the evolution of fabrication capabilities. As fabrication capabilities increase, the technology progresses from generation to generation. The evolution of the fabrication technology is a natural one, but the resulting applications are not necessarily related. For example, compare the design of a FLIR telescope (first generation) with the design of integrated components for optical data storage systems (second or third generation). This is one reason why a definition of binary optics is so difficult.

Another way to classify binary optics is by application domain. Just running through the previously mentioned applications shows that binary optics can play a role in the areas of medicine, optical communications, data storage, entertainment, displays, electronic imaging, electro-optic warfare, photolithography equipment, surveillance and optical testing, to name a few. The good news is that binary optics can be used in many different domains. The bad news is that in each of these domains, binary optics is an enabling technology rather than the focus of an industry. For example, those working in electronic imaging might use binary optics to improve the performance of their systems, but they would not say that their field is binary optics. In short, there is not a separate application domain called binary optics.

Another method to classify binary optics is by the tasks required in the design and fabrication of binary optics. There are basically four tasks required. The first is the optical design of the element. The second is the translation of this optical design into a fabrication prescription (e.g., a set of masks or the commands to run a laserwriter). The third task is the actual fabrication of the element and the final task is the testing of the completed element. Of these tasks, optical design and fabrication are the dominant tasks. This approach is especially useful when discussing the technology of binary optics and we will follow it in section 3.

Analogously, we can use a similar method to discuss the current state of the industry. Specifically, we can classify organizations involved in binary optics according to their organizational goals, of which we have identified three possibilities. First, the organization could view binary optics as their major product line, with the goal being to profit from selling binary optics. Second, the organization's major business might not be binary optics, but the organization could use binary optics as an enabling technology to support their major product line. Third, and this is pertinent primarily for new technologies such as binary optics, the organization's goal could be research in binary optics. We will follow this classification scheme in section 4.

3. THE STATE OF THE TECHNOLOGY

In discussing the technology, it is useful to consider the classification of binary optics by task, with the emphasis on optical design and fabrication since these are the dominant technological areas:

- Optical Design - There is not one set of characteristics (other than omniscient) that would describe the ideal binary optics designer. This is because the application areas are extremely diverse and because the methods used to design the elements are also widely varying. In addition to designing elements, the designer is also often tasked with the more difficult problem of thinking up new applications.
- Translation - The translation of an optical design into a fabrication prescription is primarily a problem of software availability, optimized computer programming and efficient data management.
- Fabrication - On paper, fabrication appears straightforward. In reality, fabrication is very involved and there is a substantial learning curve, typically taking years to bring up a fabrication line from scratch. It is not uncommon for experts in microfabrication technology to have accumulated several decade's worth of knowledge and experience. In addition, fabrication requires capital and progress in fabrication is usually limited by the availability of resources - both financial and personnel.
- Testing - This is the tail end of optical design and therefore faces the same problems: diverse application areas and varying testing methods.

3.1. Optical Design

The task of optical design can be further subdivided according to which theory is used to model the binary optics element:

- Geometrical optics
- Scalar diffraction theory
- Vector diffraction theory for periodic structures
- General solution of Maxwell's equations

Of these areas, designs which require only geometrical optics are the most mature and this is the only area where commercial ray trace codes are commonly used. The most common example of this design type is the use of binary optics to correct the aberrations of conventional wideband imaging systems (e.g., a telescope). In this instance, a commercial ray trace code is used to design the system and the binary optics element is modelled using either the Sweatt model or the holographic optical element option in the ray trace code. The use of binary optics allows additional degrees of freedom in the design and a designer schooled in "classical" lens design principles would be the most adept at taking advantage of this. The resulting binary optics piece is typically a single element with large features. Since this type of application was among the earliest, it is also among the most mature, with some designs currently in production phases. The intraocular lens, a human lens replacement, is another design based on geometrical optics, except with the twist that the diffractive lens portion uses two foci (a phenomenon predicted by scalar theory). Another type of geometrical problem is the design of optics to incoherently couple as much energy as possible from a source (typically an array of LED's or lasers) to a sink (typically a fiber or detector). The design is based on tracing rays, but since the application is photon collection and not imaging, the usual ray trace codes are typically not used and the resulting design is often an array of microoptics, a far cry from an imaging system.

In the realm of scalar designs, the binary optics element is modelled using one of the scalar diffraction theories. The commercial ray trace codes are not applicable and the models are typically built on either matrix manipulation packages (e.g., IDL, MATLAB, etc.) or programming languages (e.g., C, Fortran, etc.), with the builder of these models having a background in Fourier optics and numerical methods (signal processing would not hurt either). A popular application is the design of grating beamsplitters (e.g., a grating which produces N uniform diffraction orders). There are several ways to solve this problem: the solution of non-linear equations (Dammann gratings), the use of an iterative phase retrieval method (e.g., Gerchberg-Saxton) or some form of search and/or optimization (e.g., Nelder-Mead or exhaustive search). The reader will note that these problems are substantially different from the geometrical design problems and so too is the background required to design this type of element. A second application example is the design of laser cavity optics, for example, to coherently couple lasers. Again, this design is based on Fourier optics and requires the knowledge of a physicist or Fourier optics.

In the realm of vector designs, the solution of Maxwell's equations for an arbitrary element is still too numerically expensive to solve for almost all cases of interest. Instead, we currently are limited to solving Maxwell's equations for periodic structures. The diffraction from gratings can be solved via a decomposition into space harmonics or a decomposition into the eigenmodes of the grating. In either case, the ideal person to analyze and design these elements would be a mathematician with

Table 2: Current State of Optical Design.

Design Domain	Maturity of Design Concepts
Geometrical Optics	Design concepts understood by industry.
Scalar Diffraction Theory	Design concepts understood by researchers.
Maxwell's Equations for Periodic Structures	Early design concepts being formulated.
General Maxwell's Equations	Analysis possible only for simple cases.

numerical methods background. Examples of applications in this regime would be anti-reflection coatings (artificial index materials) and artificially birefringent materials.

Table 2 summarizes the current status of optical design technology, with the left hand column listing the different design domains and the right hand column describing the maturity of each domain. As for future areas of interest, there are several. One obvious area is continued work in each of the areas in table 2. This will require the further development of theories (e.g., to build intuition) and the improvement of numerical methods (e.g., to efficiently solve Maxwell's equations for the general case). As the technology matures and moves onto the factory floor, another challenging area will be the solution of practical problems: manufacturing tolerances, handling procedures, quality control, etc. Yet a third domain of interest is the integration of binary optics with other technologies. For example, a monolithic compact disk head would require the common packaging of optics, sources and detectors. Finally, the biggest challenge facing the optical designer is the discovery of new applications. However, this is somewhat of a catch-22. You can't think of any new applications if you don't know what the capabilities of binary optics are, but you can't spend the time to learn about binary optics if you don't have a potential application.

3.2. Translation

After the optical design process is completed, the optical design must be translated to a fabrication prescription. For example, the mathematical description of an aberration corrector may be translated into a set of masks. There are a number of well-known ways to do this: following contours, bitmapping, sampling and interpolating, analytical solution, etc. However, there is not a single method which is appropriate for all cases and there is no commercially available software to accomplish these tasks. Therefore, everyone must learn and implement these translation algorithms themselves. The software that is available for VLSI layout is useful but it is designed for circuit layout and so is not exactly matched to the needs of binary optics. Specifically, the software does not implement any of the common translation algorithms, although it does allow the previewing of masks and can convert graphical layouts to common mask formats (e.g., MEBES, GDSII, etc.), and the software is expensive and includes unnecessary features (e.g., IC design rule checking). The translation task is primarily a computer task and is limited by computer performance, both in terms of speed and data volume. As computers become faster and can handle more data, the translation task will also become easier.

3.3. Fabrication

Fabrication is an extremely involved topic. A discussion of the different fabrication methods and their potential advantages and disadvantages is far beyond the scope of this paper (see Stern, "Fabrication of Binary Optics," elsewhere in this proceedings). Instead, we will examine the fabrication task by considering the characteristics of an ideal fabrication process:

- Accuracy - Fabricated elements should match their fabrication prescriptions. For optical components, the process must have sub-wavelength resolution in all three dimensions.
- Flexibility - The ideal fabrication system should be able to handle many types and size of substrates. It should also be able to handle shallow and deep features, regardless of aspect ratio.
- Reliability - The process should be both reliable (minimum downtime) and reproducible (infrequent calibration).
- Low cost - Of course, less cost is better.
- Speed - Naturally, fast turnaround is also desirable.

How does the current state of fabrication measure up to these ideal standards? Table 3 shows some "typical" numbers for three types of binary optics, with the accuracy and flexibility goals each subdivided into three criteria. The task considered is that of producing the very first element of a custom design (i.e., an initial master) and the figures are for fabrication processes requiring multiple masks, although we expect that comparable tasks using other fabrication processes will post comparable numbers. This type of task is the most expensive and time-consuming since we are at the most unfavorable point of the learning curve and do not consider the advantage of mass production techniques. Naturally, any following elements will be less problematic.

Simple elements are typically made by taking advantage of printing service bureaus, buying low-resolution photomasks, photoreducing plots made on large plotters or using some sort of laserwriter (e.g., a converted drum scanner). They are usually limited to binary elements, either amplitude or phase, since the writing of alignment marks requires higher resolution than is available and the repeated align and etch processes drive up the cost. A possible exception would be fabrication methods which rely on analog exposure of photopolymers. These methods may be able to produce low resolution multi-level elements while remaining in the simple category. The standard element represents what is normally seen on viewgraphs - a multilevel diffractive device utilizing an existing process. It is assumed that minimal process development is required although, at the minimum, new masks will be required. Finally, the exotic element has some aspect which requires considerable process development. This aspect could be unusually small feature sizes, new materials systems, large exposure areas or deep features.

Regarding future areas of interest, each of the desired characteristics (accuracy, flexibility, etc.) coupled with a specific fabrication method will result in a set of fabrication demands. For example,

Table 3: Current State of Fabrication.

	Simple Element	Standard Element	Exotic Element
Minimum Feature Size	10 μm	1 μm	0.3 μm
Feature Placement Accuracy	1 μm	0.2 μm	$< 0.1\mu$m
Levels (Vertical Resolution)	Binary	Typ. 8 or 16	Typ. to 64
Substrate Materials	Quartz	Quartz, Silicon	Many
Substrate Diameter	3 inch	4 inch	8 inch
Maximum Surface Relief	2 μm	2 μm	10 μm
Process Reliability	Guaranteed	Processes understood	New processes
Cost	\$100's to \$1000's	\$1000's to \$10,000's	\$10,000's to unlimited
Speed	Days to Weeks	Weeks to Months	Many Months

for systems based on multiple masks, the accuracy goal will require good mask-to-mask alignment and etch depth control; while for systems which rely on analog exposure of resists, accuracy will require good characterization and control of the resist exposure and development. The future task, then, is to improve the fabrication processes in order to meet these demands. Unfortunately, the nature of process development is usually arduous, unglamorous, time-consuming and money-intensive.

3.4. Testing

As a result of the various number of applications of binary optics, the testing of binary optics is also varied. In some cases, well-known test procedures can be directly applied to systems with binary optics components (e.g., the MTF testing of a telescope system with binary optics correctors). However, in many cases, new tests or variations of standard tests must be developed. For example, in the case of testing diffractive microlens arrays, one would want to measure the wavefront quality of individual microlenses, the diffraction efficiency of individual lenses and the uniformity of the entire array. These tests are commonly required but are not standard optical tests. As the technology progresses, we expect that tests of this sort will be identified, developed and then standardized.

4. THE STATE OF THE INDUSTRY

We now shift gears and consider the current state of the binary optics industry, focussing on marketplace issues rather than technical ones. In this discussion, we will use the classification of binary optics by organizational objective:

- Major Product - Some organizations view binary optics components as a major product line with the intent to profit from selling binary optics components. The current industry structure does not favor this approach and so we do not expect the bulk of the market to fall in this category.
- Enabling Technology - Some organizations use binary optics elements internally to improve

their other product lines. Since it is an enabling technology, we expect that binary optics will have its largest impact in roles of this type.

- Research - This early in the technology cycle, a fair number of organizations are involved in research in binary optics. However, the nature of the field results in some pitfalls of which researchers should be aware.

4.1. Binary Optics as a Major Product

There are a number of companies which are establishing binary optics as their major product line and there are several approaches to this end. Some companies have established standard products, while others offer custom fabrication services based on a number of fabrication technologies. Although such companies may be quite successful on a limited basis, we believe that the structure of the free marketplace (i.e., excluding grants and subsidies) does not favor the evolution of large dominant companies (such as Intel or Microsoft) for the following reasons.

First, high equipment costs and low component prices bias the industry against profitability. High volumes are necessary to offset capital costs. Fortunately, binary optics is amenable to mass production. However, the current technical emphasis, both in laboratories and in most companies, is not on mass production. A second obstacle is the fragmented market. A manufacturer cannot reach the many diverse application areas of binary optics with a single approach. Rather, each area must be targeted separately. This fragmented market encourages the development of niches, as is currently occurring, but discourages the development of large dominant companies. Thirdly, there are two major ways to gain competitive advantage: by differentiation and by cost. To date, there has been little differentiation among the companies in the binary optics industry so this suggests that most of the industry will compete on the basis of cost, which makes for an unprofitable industry. However, the industry is still young and it is possible that companies will differentiate themselves more as the industry matures. Finally, the possibility of backwards integration will limit the size of companies in the industry. Typically, company A will supply binary optics elements to larger company B, whose major business is not binary optics. If B decides that binary optics are crucial to their business interests, they will bring the binary optics technology in-house (i.e., backwards integration) either by acquiring A (not a bad fate for the owners of a small business) or by starting their own effort. In either case, the growth of A will be limited. Because of these industry characteristics, we believe that there will be small binary optics companies specializing in niche markets or consulting, but there will not be any large companies whose major product line is binary optics.

4.2. Binary Optics as an Enabling Technology

The majority of the market for binary optics will lie with organizations which use binary optics to give their other product lines a competitive edge. For example, a manufacturer of compact disk heads may significantly reduce the mass of his product by replacing a number of conventional components with a single binary optics element. That company is in the business of compact disk heads but has used binary optics to gain a competitive advantage. There are already many examples which fall in this category: the camcorder maker who uses microlenses to increase the

sensitivity of his products, the FLIR producer who uses binary optics to correct the aberrations of a telescope, the supplier of laser welding equipment who uses binary optics to shape the laser beam, etc.

However, the fact that binary optics is an enabling technology and not an organization's major product line has its own implications. First, the technology will not progress as quickly since it is not the focus of the company. The risk is that the company may later find itself at a competitive disadvantage because it lacks crucial binary optics technology. Small companies are especially vulnerable since their resources are more limited and they cannot spread the cost of technology development over several product lines or larger product volumes. One way to avoid this possibility without paying the full price for internal development is the cooperative establishment of consortia focussed on binary optics. Second, the fortunes of those working on binary optics technology will be determined by the fate of the major product line. The best binary optics person working in support of an ill-fated product will be ill-fated and his contributions may also be unappreciated. Third, much of the technology development will be proprietary, resulting in much reinventing the wheel (and the corresponding duplication of costs).

4.3. Research in Binary Optics

For organizations whose primary mission is research in binary optics, the current areas of interest are summarized in the technology section of this paper. Here, we point out some characteristics of the industry which affect the nature of research and research funding. First, in the current economic climate, research will be pulled by applications. It is difficult to secure research funding for the sake of technology development alone. Any research must have the promise of solving some problem. It is primarily the optical designer's or manager's task to make the match between binary optics and potential applications. However, although research is pulled by applications, it is the fabrication which makes the difference between paper research and real progress. After all, diffractive optics ideas have been around for a long time. It is the recent advances in fabrication which have spawned the binary optics industry. Therefore, we feel that most significant research must include fabrication. Having made this point, it should be noted that fabrication in a research environment cannot be expected to pay for itself. Previously, we argued that companies whose primary purpose is to turn a profit face significant market obstacles. It is unreasonable to expect research units, which are also constrained to always developing new ideas and prohibited from doing volume production, to do the same. Therefore, it should be expected that fabrication research in binary optics will have to be supported by grant money, usually from the government or from company internal funds.

5. SUMMARY

Table 4 summarizes the current state of the technology, with the two most important tasks being optical design and fabrication. In the area of optical design, we expect continued development of theories and numerical methods for designing elements in the scalar and vector diffraction regimes (modern optics designs). As binary optics moves into production, we also expect more emphasis on real world issues: manufacturing tolerances, packaging considerations, integration with electro-optics, etc. The primary limitation facing the optical designer is his creativity in thinking of new applications. In the area of fabrication, the trends follow the same lines as in the semiconductor

Table 4: Technology Trends and Limitations.

	Trends	Limitations
Optical Design	Modern Optics Designs, Manufacturing Issues	Human Innovation
Translation	Computers	Software Availability
Fabrication	Cheaper, Larger, Finer, Faster	Time and Money
Testing	Standardization	Cooperation

Table 5: Industry Trends and Limitations.

	Trends	Limitations
Major Product Line	Niche Markets, Consultants	Unfavorable Industry Structure
Enabling Technology	Bulk of the Market, Good Growth	Low Priority, Proprietary Efforts
Research	More Applications	Ideas and Funding

industry, pushing for ever smaller features, larger wafers, etc. As with the semiconductor industry, the major limitation to progress in fabrication is the time and money required to develop the technology.

Table 5 summarizes the current state of the industry. There are two major points. First, we believe that the structure of the industry does not favor organizations which view binary optics as their major product line. These organizations will be prevented from growing into large companies, although they could be quite successful in niche areas. Second, we believe the bulk of the market will be with organizations which view binary optics as an enabling technology and take advantage of binary optics to build a competitive edge in their other product lines.

Finally, we make the following two concluding remarks. First, we expect that binary optics has excellent future growth potential. It is a technology which has already been transferred to the manufacturing floor in some applications and we expect that it will become a significant component in many more applications in the future. However, the success of binary optics will be somewhat hidden since binary optics is undeniably an enabling technology. There will not be an array of successful binary optics products. Rather, there will be an array of products from diverse areas which will have used binary optics to improve their performance, reduce their weight, increase their reliability, etc. Second, the key to binary optics is the synergy between optical design and fabrication. Without fabrication, binary optics is no more than a collection of paper concepts missing the final link to reality. Without optical designs, binary optics is no more than a collection of geometrical patterns etched into a surface. In other words, the sale is made based on the merits of an optical design, but the payment is collected based on the fabrication of an element.

6. DISCLAIMER

The views expressed are those of the authors and do not represent the official policy or position of the U.S. Government or MIT/Lincoln Laboratory.

Diffractive Optics: Design, Fabrication, and Applications

G. Michael Morris

The Institute of Optics
University of Rocherster
Rochester, New York 14627

(716) 275-5140 TEL
(716) 271-1027 FAX

and

Rochester Photonics Corporation
330 Clay Road
Rochester, New York 14623

(716) 272-3010 TEL
(716) 272-9374 FAX

Conf. on Binary Optics, 1993

Diffractive (or Binary) Optics

Features

- Large aperture and lightweight elements
- Aspheric wavefront generation
- Achromatization of optical systems
- Reduction in weight and number of lenses
- Eliminates the need for exotic materials
- Synthesis of key research and development issues

  Extensive technological leveraging

  Replication methods for mass production

Diffractive (or Binary) Optics

Applications

Narrowband (Laser) Optics

Wide-field Imaging
Fourier Transform Lenses
Collimation & Beam Expansion
F-Theta Scan Lenses
Anamorphic (Cylindrical Elements)
Microlens arrays --Hartmann Sensors,
    Laser Diodes and Detector Arrays
Optical Interconnects
Null Optics for Interferometric Testing

Broadband Optical Systems

Hybrid Diffractive/Refractive Achromats
Beam Shaping for Diode Lasers
Bi-Focal Contact & Intraocular Lenses
Optical Data Storage
Head-up (HUD) and Head-Mounted (HMD)
    Displays
Aft-Imager Optics for NASA Sensors
Integrated Optics

Diffractive (or Binary) Optics

Applications (cont'd)

Sub-Wavelength Structured Surfaces

Anti-Reflection Structured (ARS) Surfaces
- Windows and Domes
- Low Observable (Stealth) Technology
- Detectors and Solar Cells

Polarization Components
- LInear Polarizers
- Waveplates (half-wave, quarter-wave)
- Retarders
- Beam Splitters

Narrowband Filters
- Static Filters (laser end mirrors)
- Tunable Filters (laser mode tuners, optical switches)
- Security Applications (Indentification -friend or foe)

Athermalization of Optical Systems

Diffractive Lenses

- Phase Function of Lens

$$\phi(r) = 2\pi (A r^2 + G r^4 + \ldots)$$

$r_m - r_{m-1} \cong 2\lambda F^{\#}$

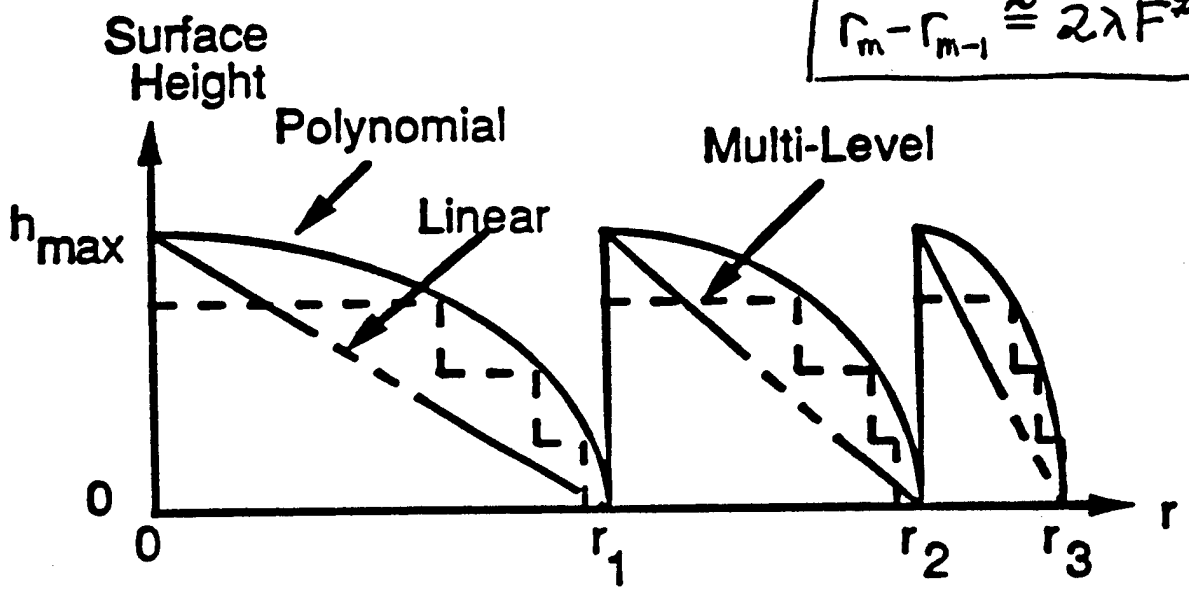

- Diffractive Zone Boundaries

r_m is the radius such that $\phi(r_m) = 2\pi m$

- Blaze Height

$$h_{max} = \frac{\lambda_0}{n(\lambda_0) - 1}$$

- Diffraction Efficiency (scalar diffraction theory)

Blaze	Peak Efficiency
Polynomial	100 %
Linear	99 %
16 level	98.7 %
8 level	95 %
4 level	81.1 %

Surface Relief Diffractive Optics

Advanced Designs Exist !

Fabrication of Surface Master

Photolithography

Multiple e-beam masks
(staircase blaze profile)

Diamond Turning

Linear and spherical blaze

Laser Writer System

Vary exposure to shape blaze profile

Replication Methods

Compression Molding

Cast and Cure Methods

(excellent temperature &
mechanical properties)

Binary Optics Lens
4-Level

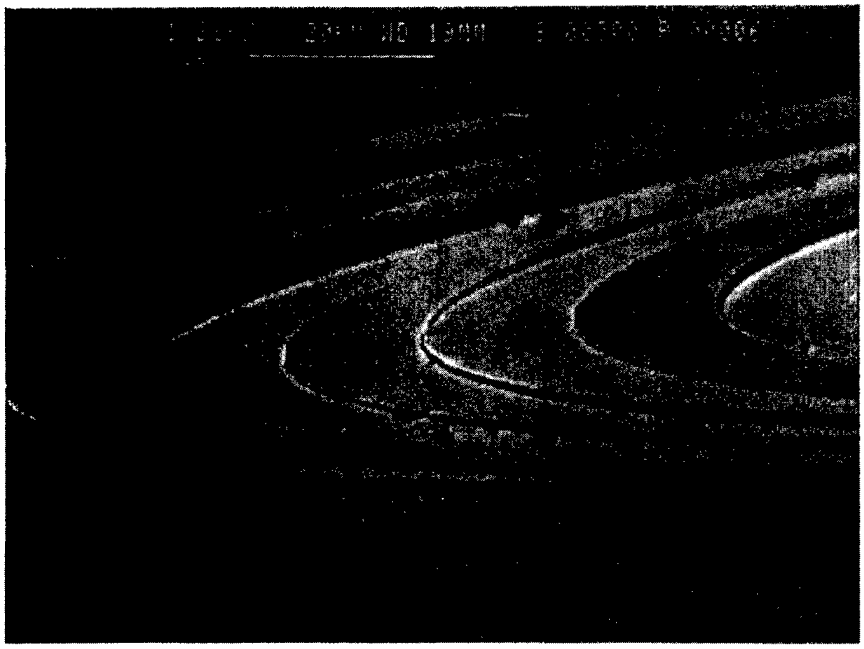

Etched Silicon Master

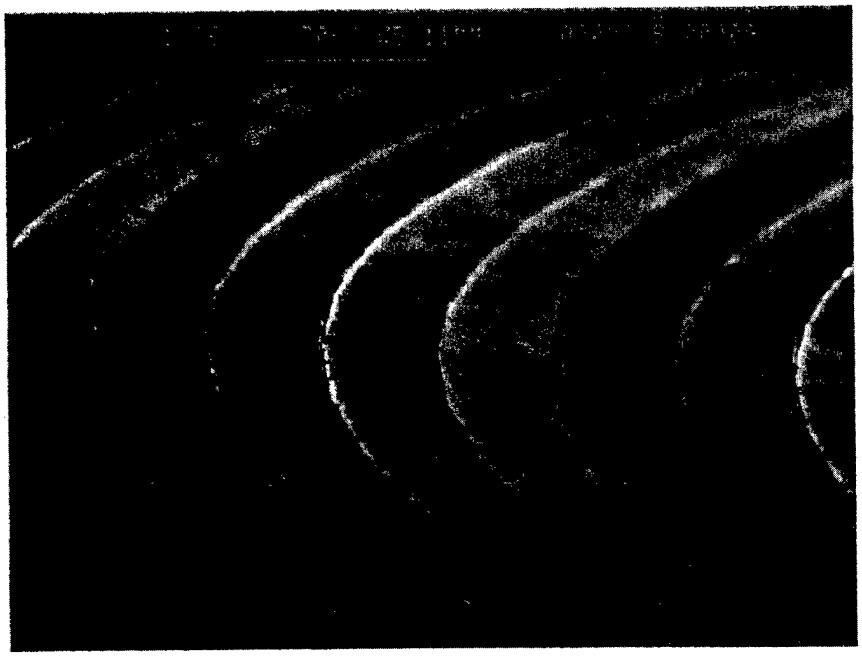

Electro-Formed Nickel Master

Blazed Diffractive Lens

F.L. = 75 mm, f/#3, λ_0 = 587.6 nm

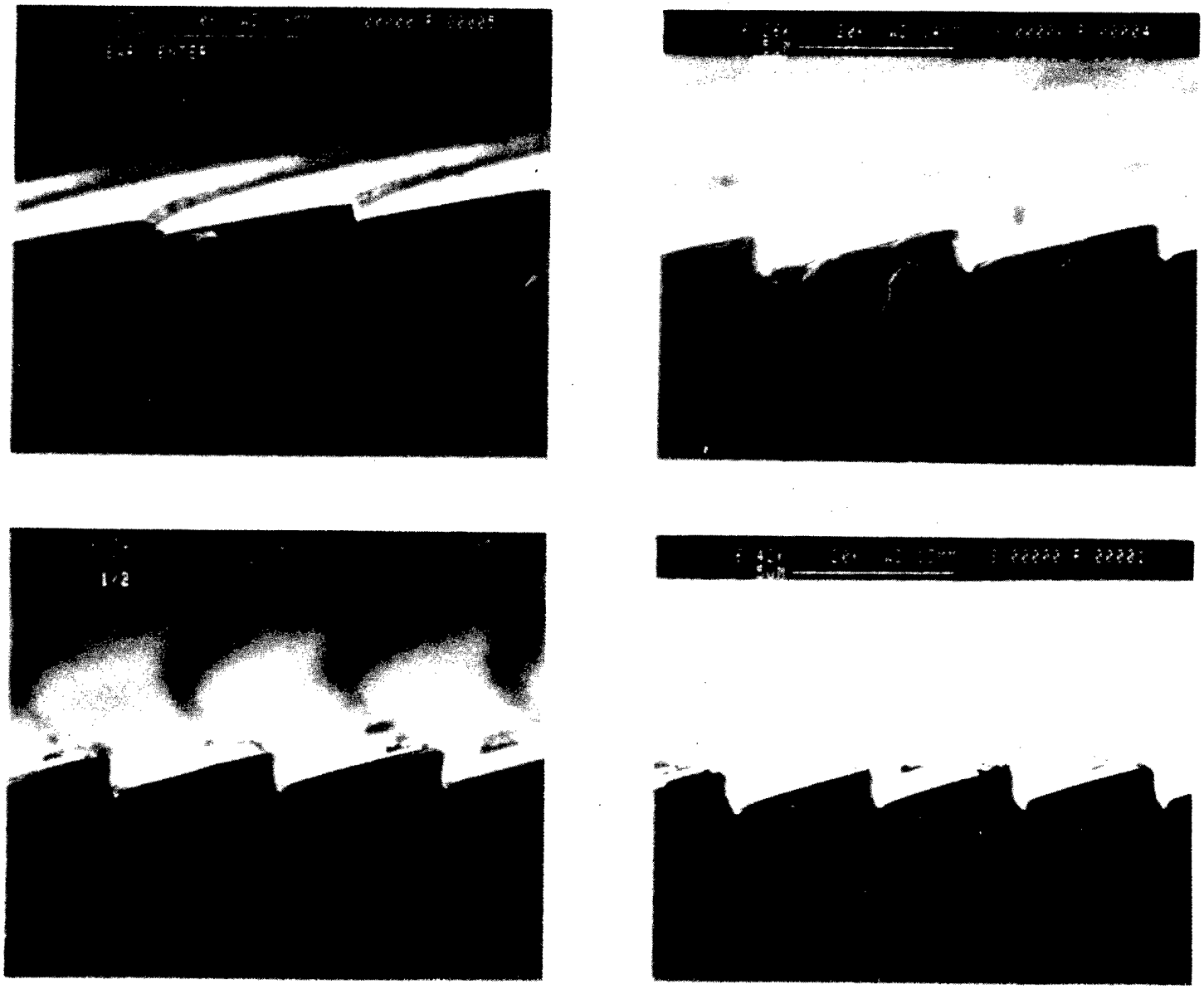

Laser Pattern Generator (Single-Point, X-Y)

Specifications

Wavelength	441.6 nm
Spot Size	0.7 - 10 μm
Pixel Spacing	0.25 - 5 μm
Edge Location Error	< 0.7 μm per 0.03 μm/inch
Part Size	4" x 4" x 0.5"
Write Time	3.1 hrs/100 sq. mm
Phase Levels	2 - 256
Substrate Curvature	< 3λ/inch
Photoresist Thickness	0.2 - 3 μm

Diffractive Landscape Lens

US Patent
#5,013,133

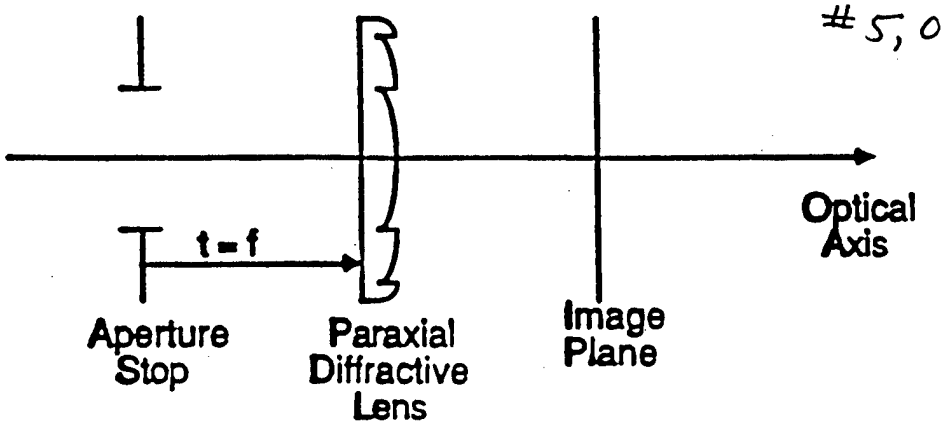

Modulation Transfer Functions

F/5.6 F = 50 mm λ_0 = 587.6 nm

Holographic

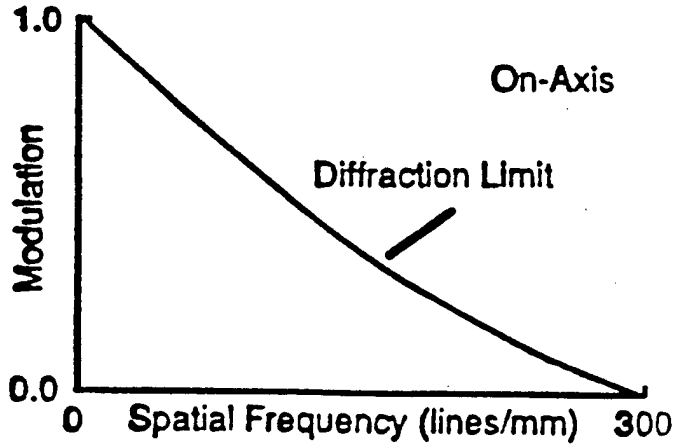

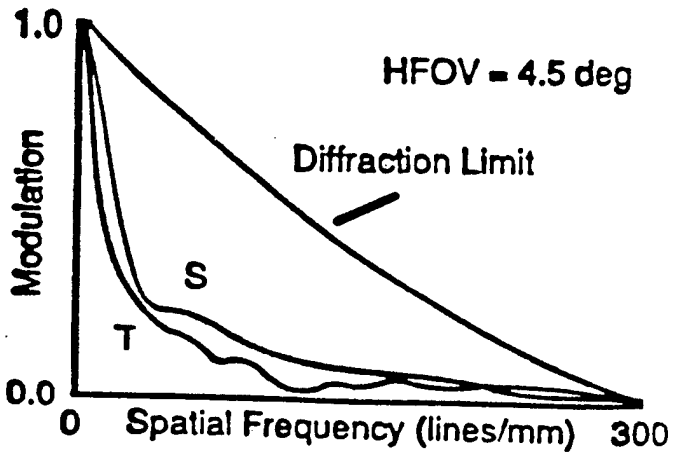

Diffractive Landscape

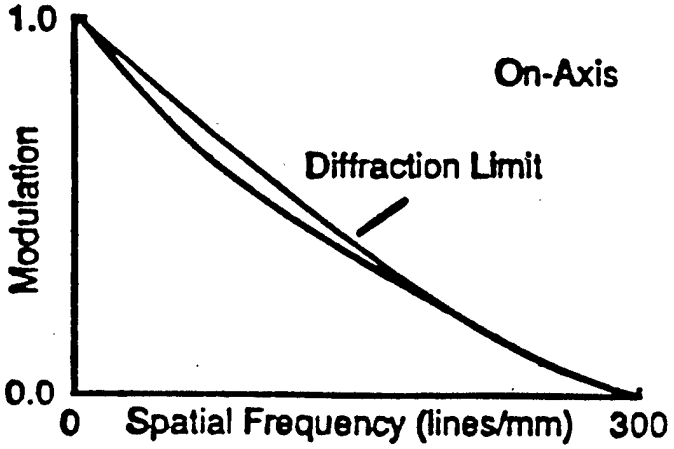

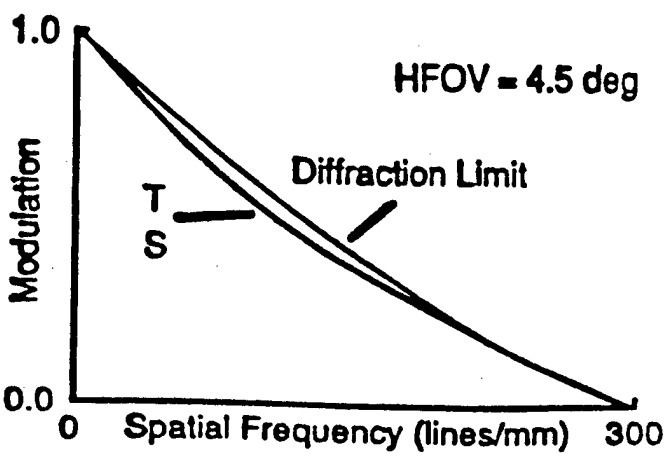

Achromatic Doublet

- Lens Powers

$$\phi_a = \frac{V_a}{V_a - V_b}\Phi$$

- Abbe numbers

$20 < V_{glass} < 90$

$V_{DOE} = -3.45$

- **Conventional Doublets**

crown $V_a = 60$

$\phi_a = 2.5\Phi$

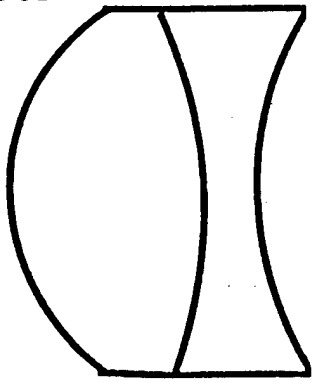

$V_b = 36$ flint

$\phi_b = -1.5\Phi$

- **Hybrid doublet**

crown $V_a = 60$

$\phi_a = 0.95\Phi$

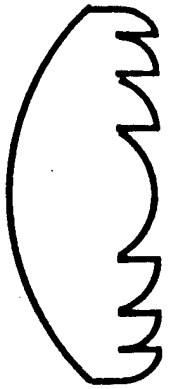

$V_b = -3.45$ DOE

$\phi_b = 0.05\Phi$

- Features of Hybrid Doublets
  - lower curvatures
  - lower F/#
  - lower weight
  - no need for exotic glasses

Application - Optical Data Storage

- General ODS element

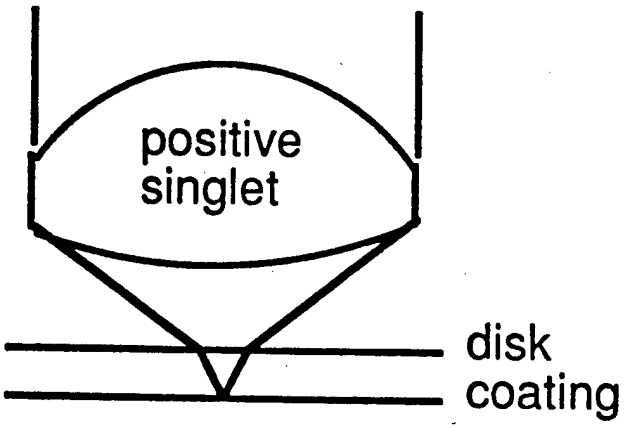

F / 0.9
f ≈ 3.0mm
HFOV = 1°
$\lambda_o = 0.780 \pm 0.01\mu m$
monochromatic

- Conventional Glass Doublet

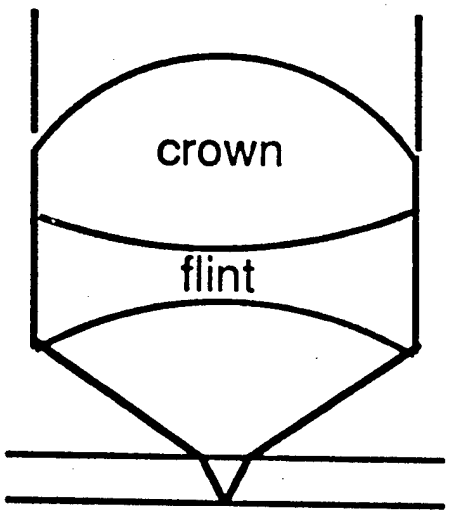

Conventional achromatic doublet
adds weight and size

- Hybrid Doublet

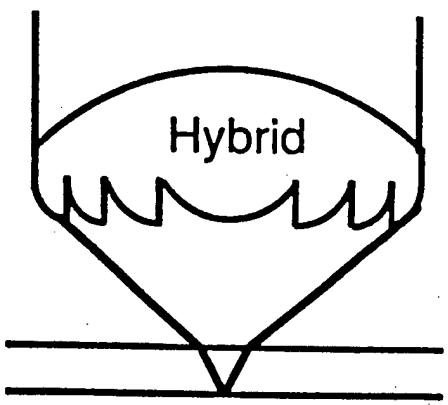

Hybrid lens reduces weight, and
helps correct other aberrations

Strehl Ratio vs Field Angle

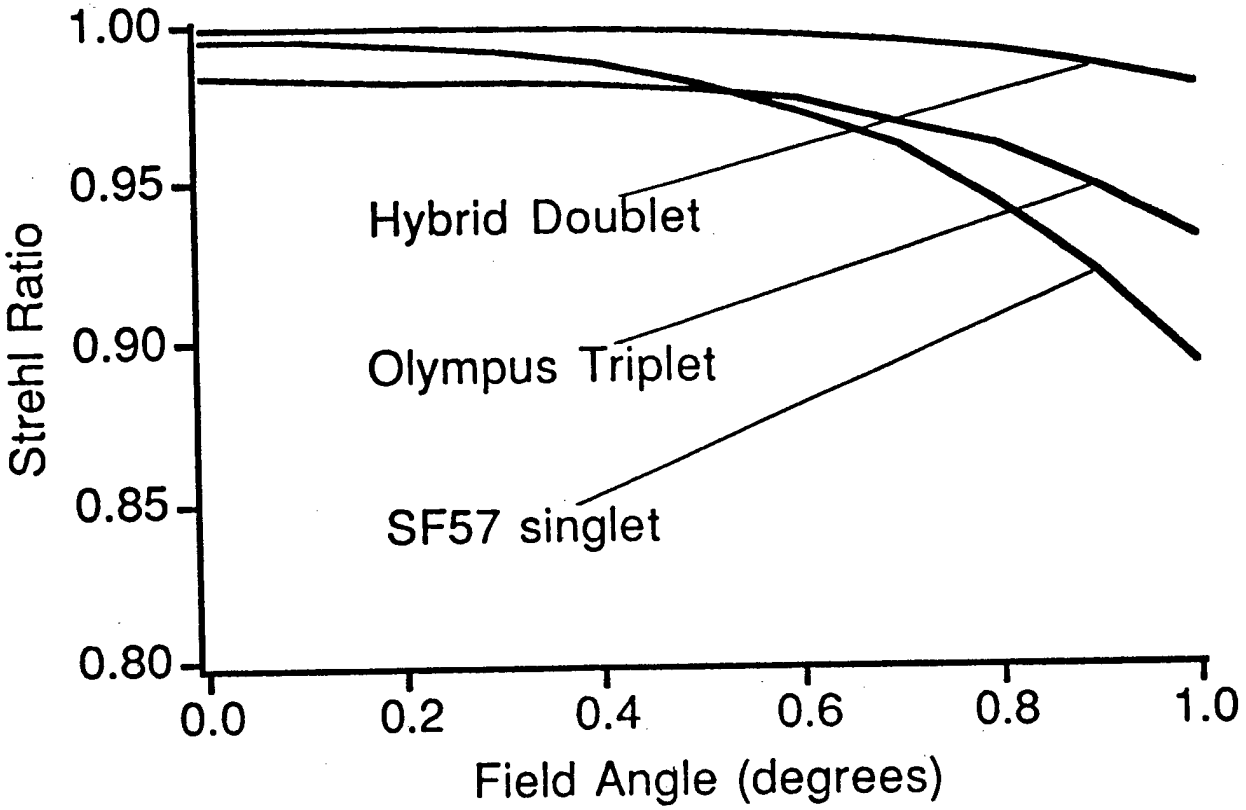

- Numerical Apertures:
  - Hybrid Doublet - 0.57
  - Olympus Triplet - 0.50
  - SF57 Singlet - 0.53

Waveguide Lenses

Mode-Index **Diffractive** **Achromatic Hybrid**

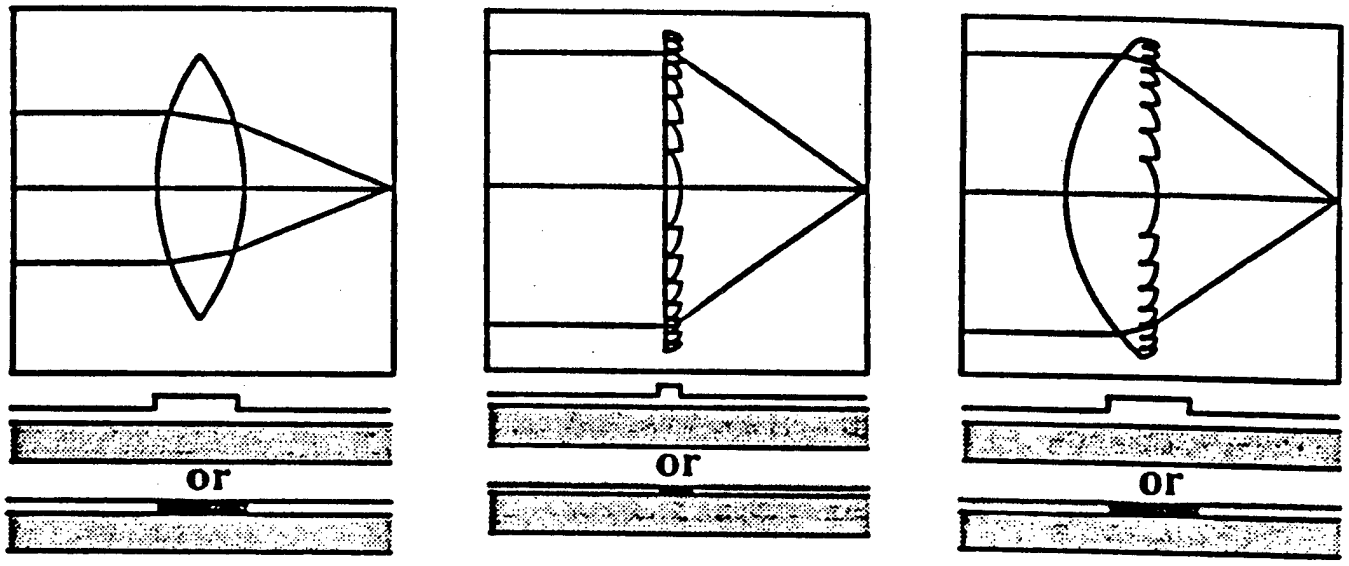

Longitudinal Chromatic Aberration

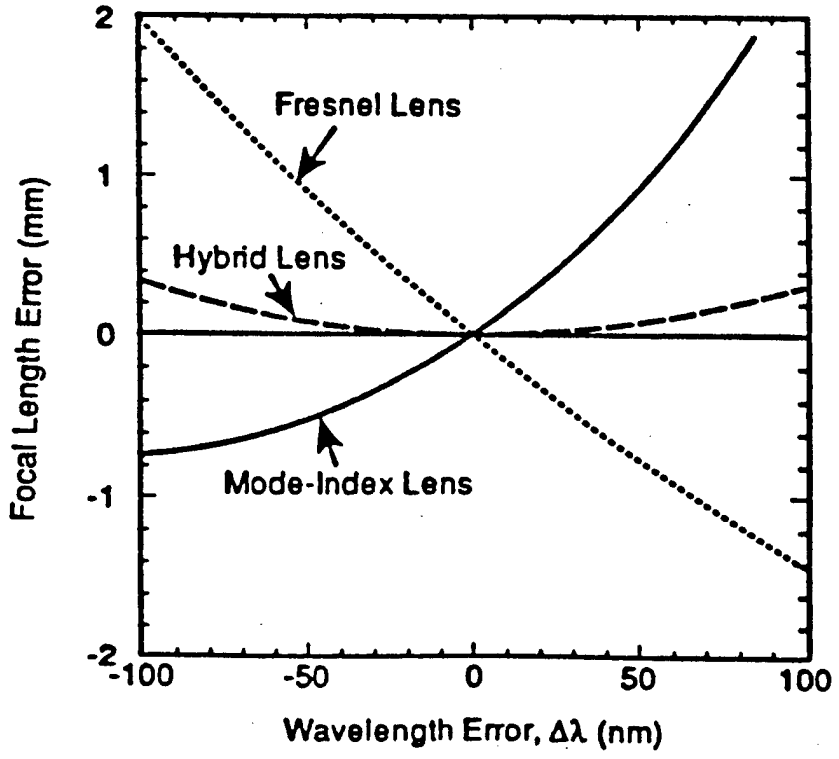

Waveguide Lens Comparison

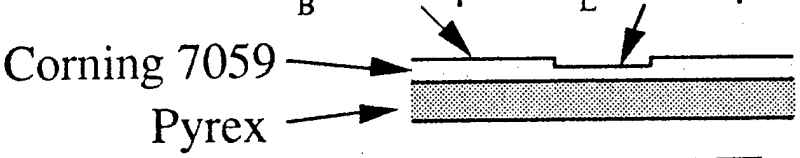

$N_B = 1.532, N_L = 1.497$
$\Delta N = -0.035$
focal length = 10mm, F/5

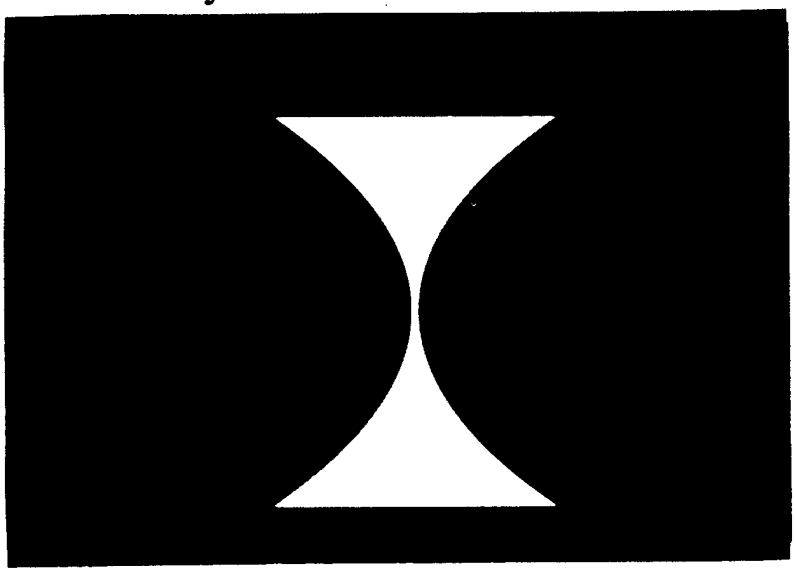

Mode-Index Lens

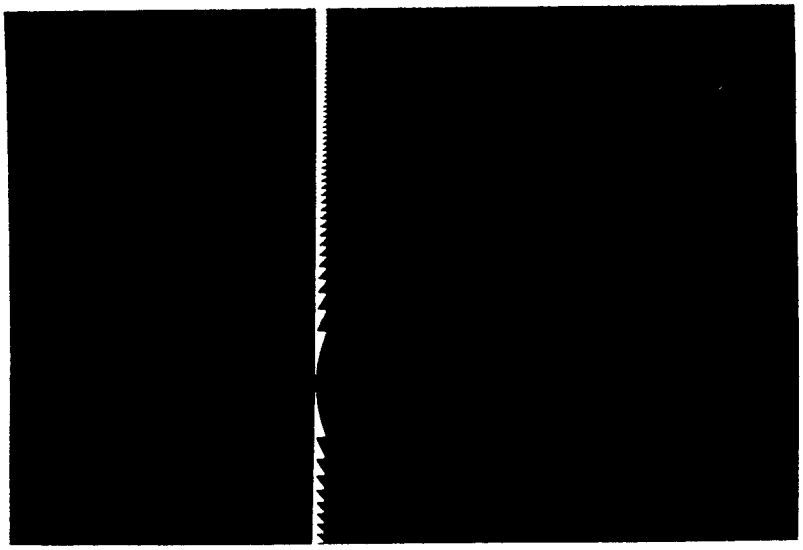

Diffractive Lens
h_0 = 17.5μm
zones = 54
smallest zone = 6.1μm

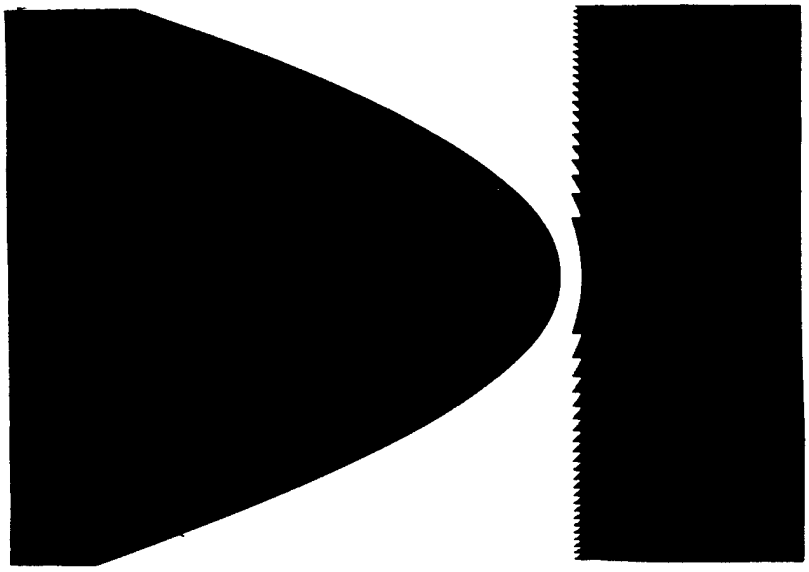

Hybrid Achromatic Lens
Mode-index surface
f_{mi} = 5.3mm
Diffractive surface
f_d = -11.5mm
h_0 = 17.5μm
zones = 47
smallest zone = 7.0μm

Waveguide Lens Performance Comparison

	Insertion Loss	Diffraction Efficiency
Mode-Index Lens	40%	—
Diffractive Lens	40%	70%
Hybrid Achromatic Lens	40%	70%

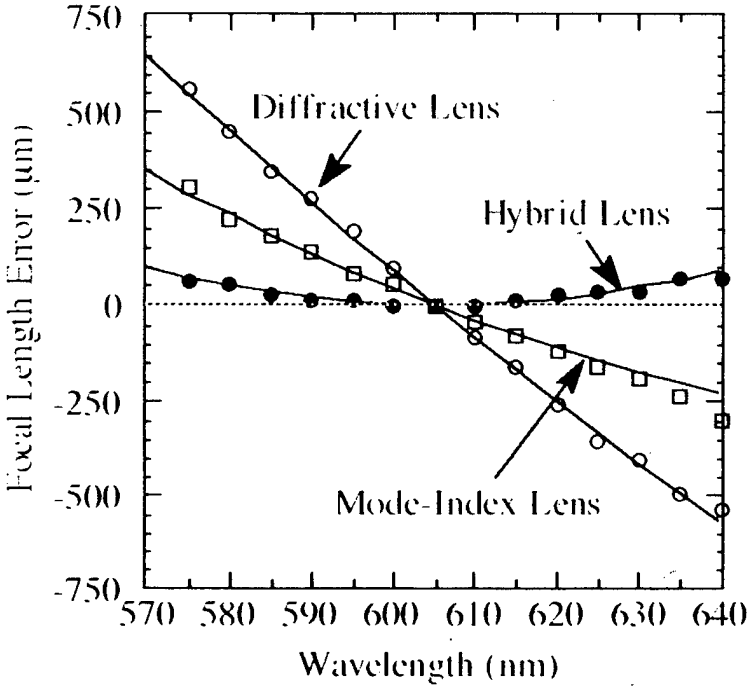

Wavelength Range for Strehl Ratio > 0.8

(Depth of focus = 44 μm)

Mode-Index: 11 nm
Diffractive: 5 nm
Hybrid: 49 nm

Diffractive Lens Imaging

- Undiffracted light forms background in image plane

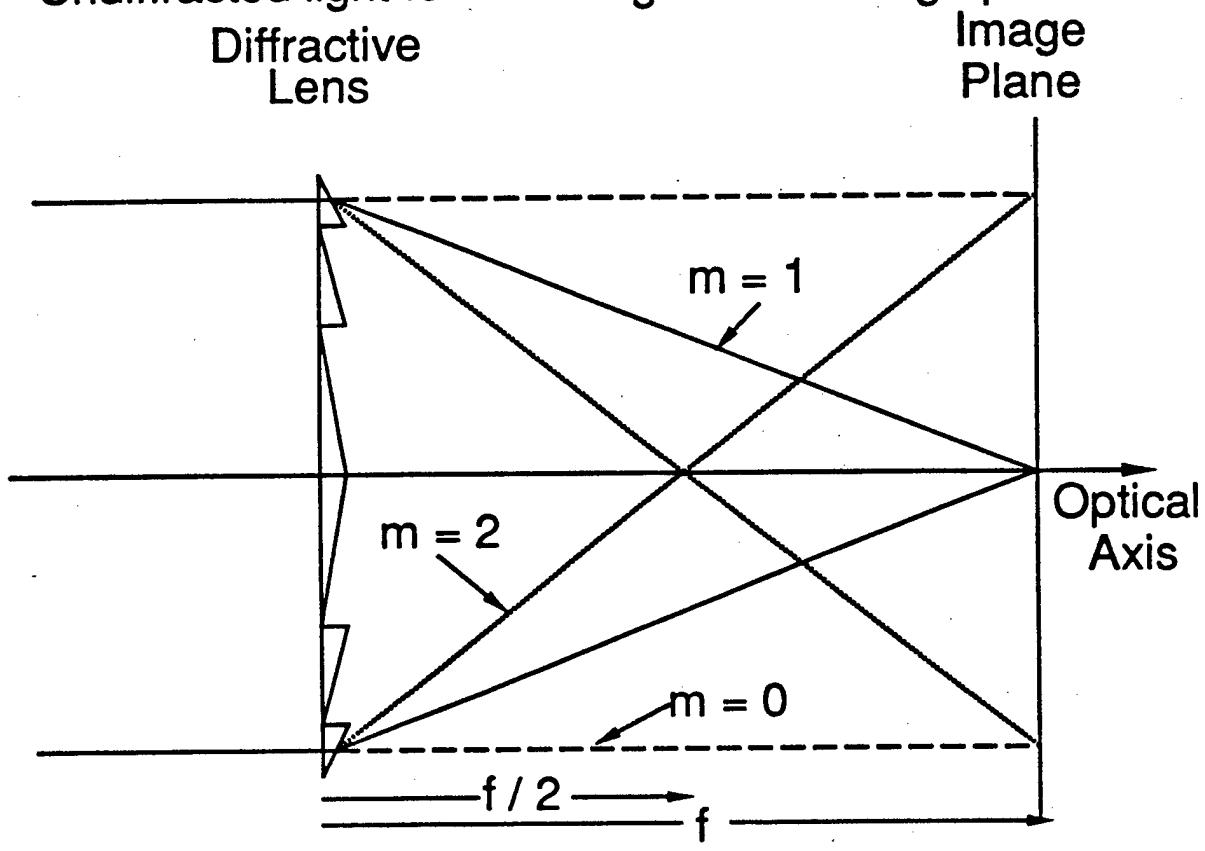

- Point Spread Function

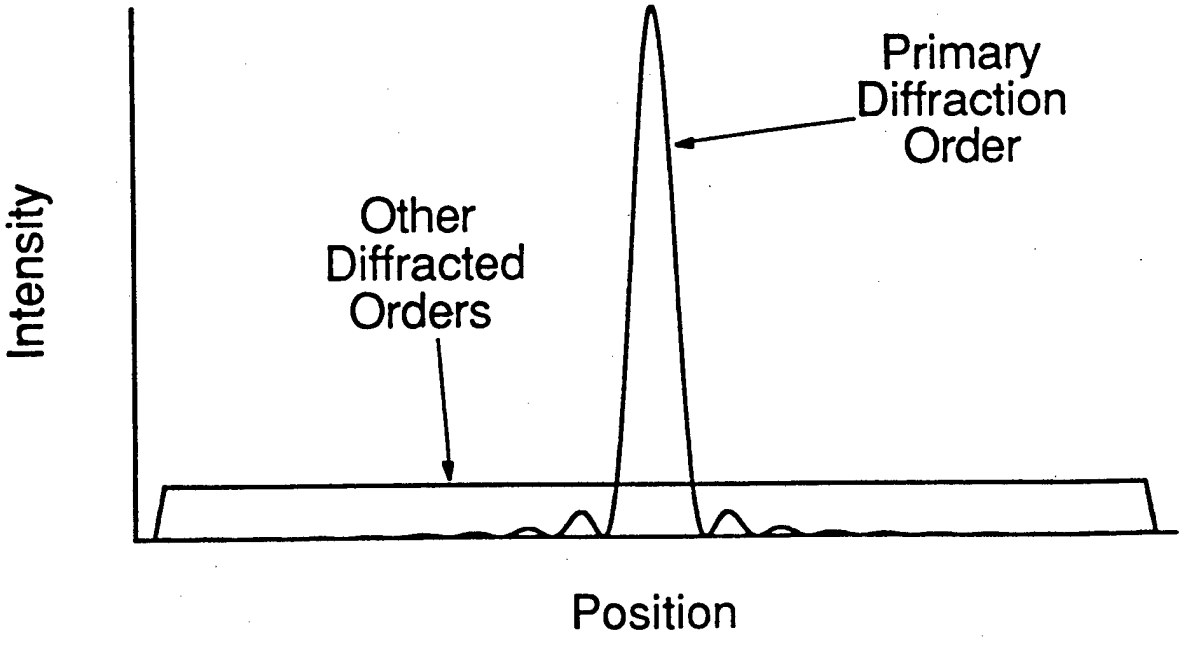

Diffraction Efficiency

- Analytic result for diffraction efficiency

$$\eta = \frac{\sin^2[\pi(\alpha - m)]}{[\pi(\alpha - m)]^2}$$

- Wavelength detuning parameter

$$\alpha(\lambda) = \frac{\lambda_0}{\lambda} \frac{n(\lambda) - 1}{n(\lambda_0) - 1}$$

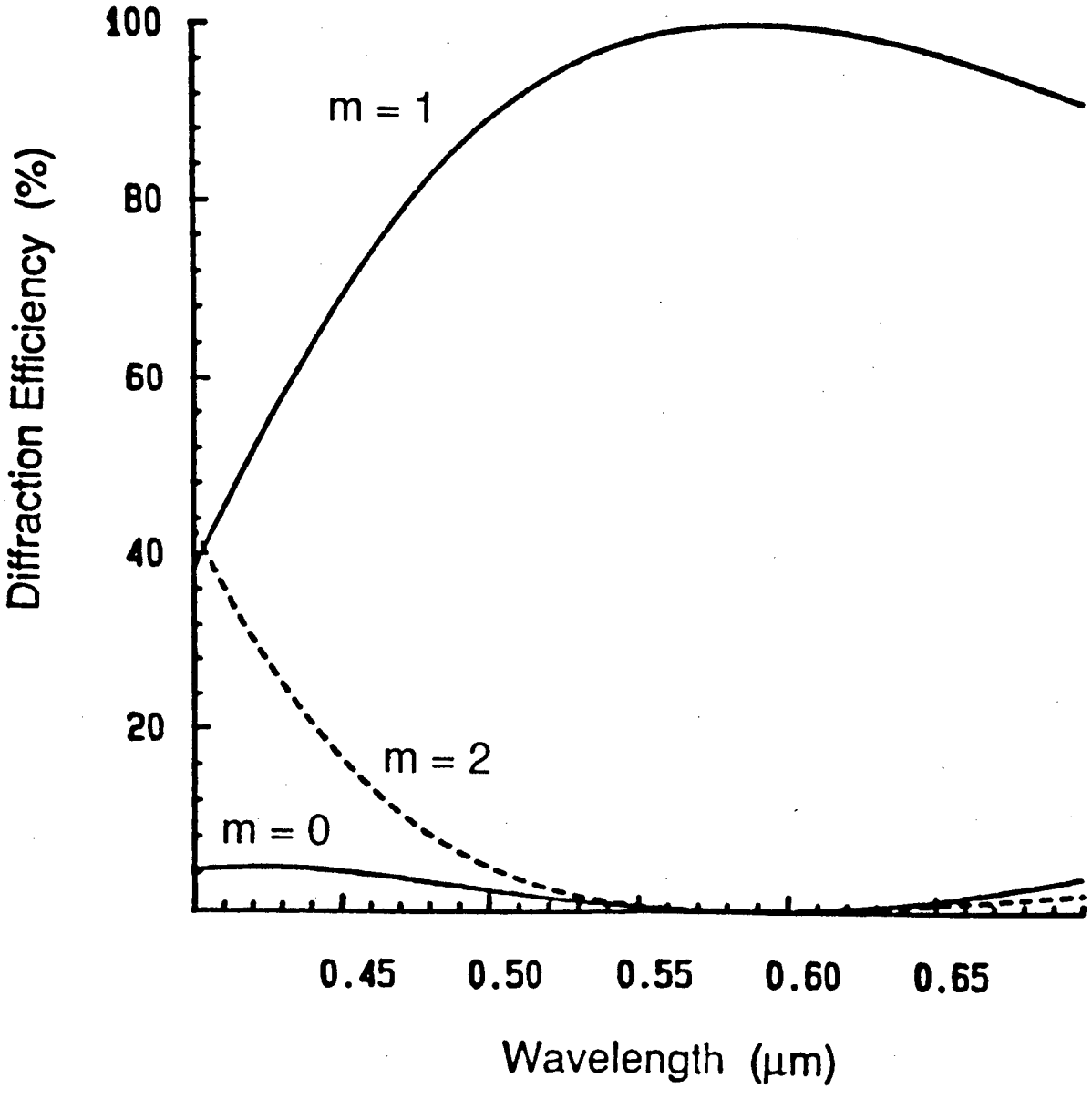

Polychromatic Examples

- $\lambda_0 = 0.55\ \mu m$ $\lambda_{min} = 0.4\ \mu m$ $\lambda_{max} = 0.7\ \mu m$
  $P = 8$ F/5.6 $\eta_{int,poly} = (0.95)(0.914) = 0.868$

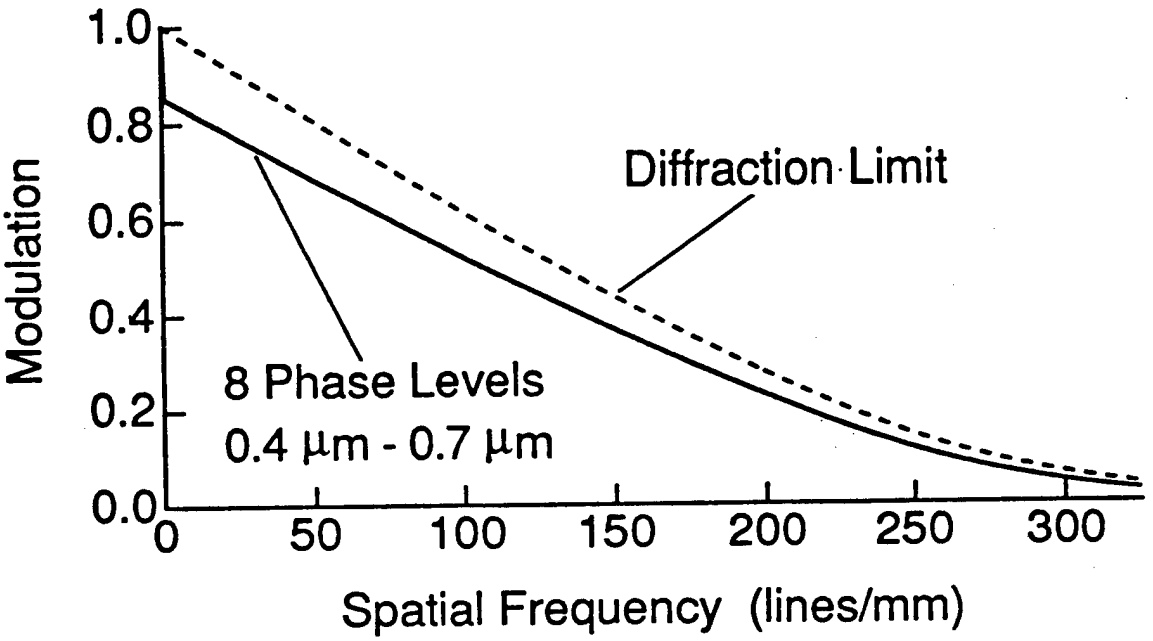

- $\lambda_0 = 10.0\ \mu m$ $\lambda_{min} = 8.0\ \mu m$ $\lambda_{max} = 12.0\ \mu m$
  Continuous profile F/2 $\eta_{int,poly} = 0.955$

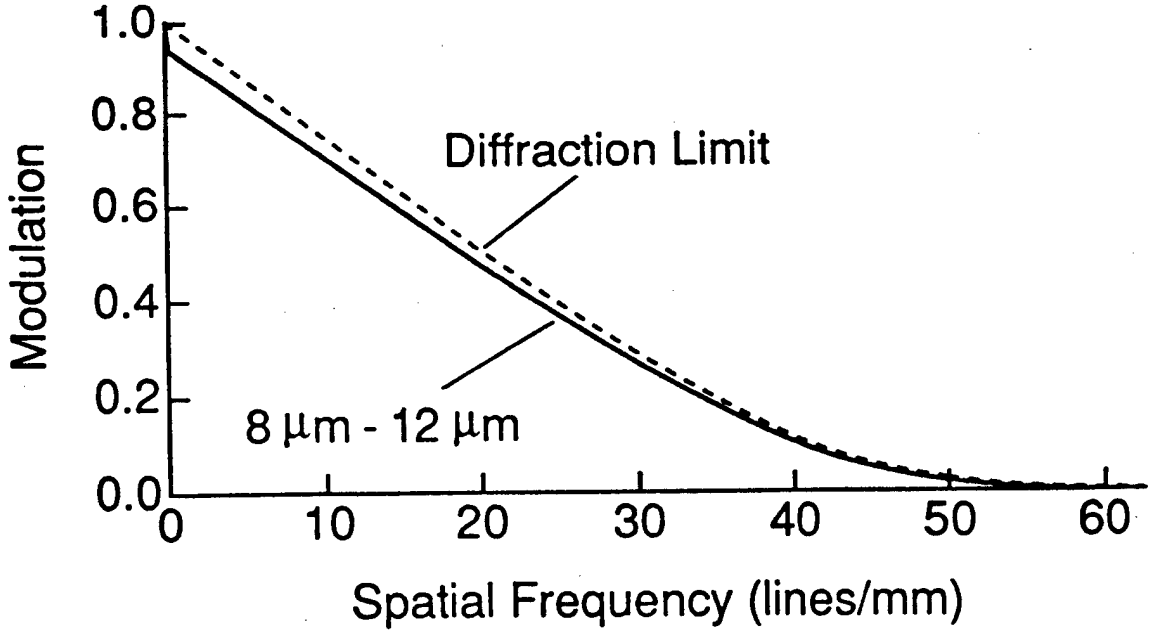

Synthesis of Phase Gratings From Known Fourier Modulus Data

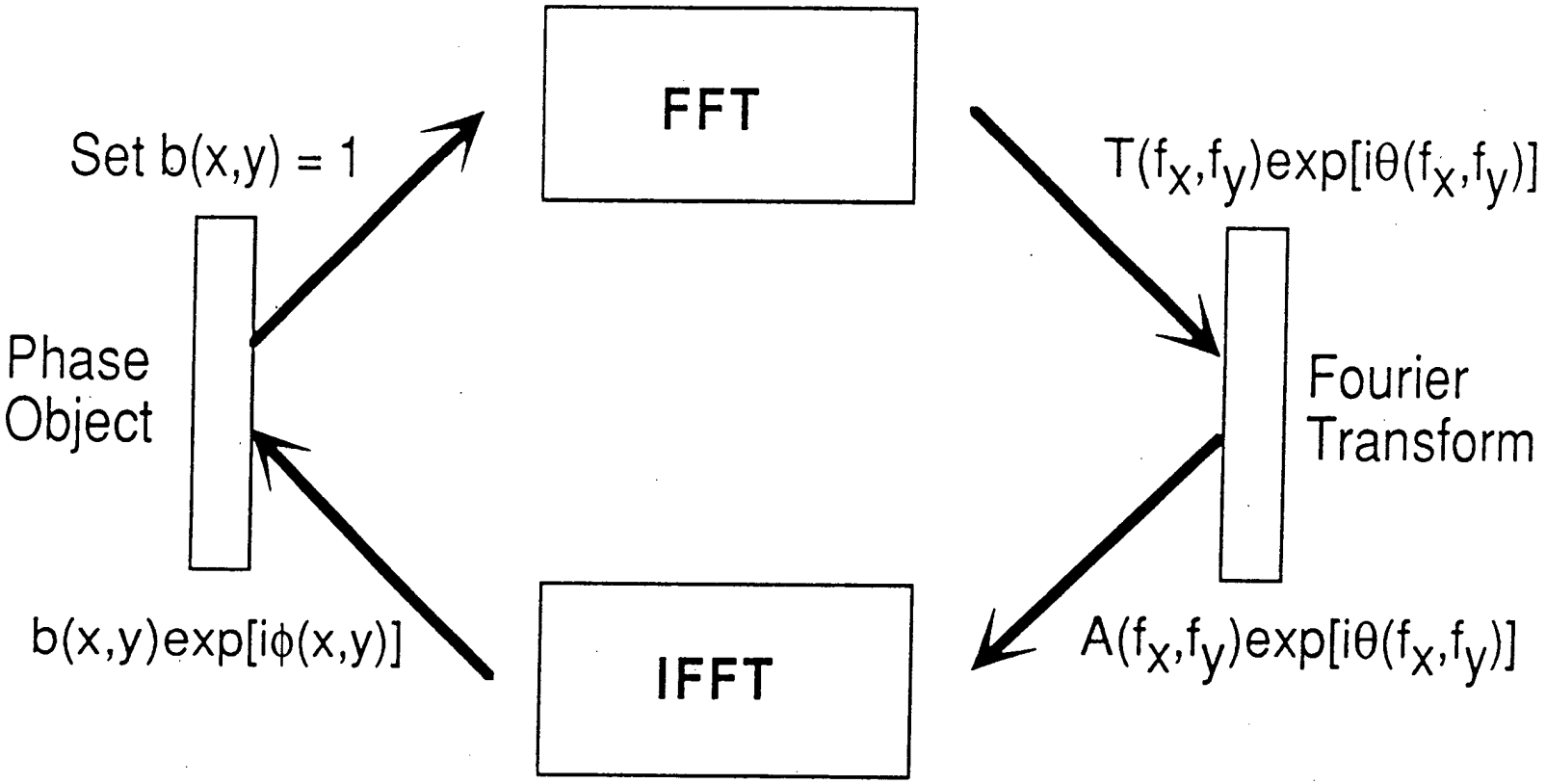

$A(f_x,f_y)$ = Desired Fourier Modulus

Phase Grating Synthesis

11 x 11 Array, Equal Intensity Diffracted Orders

Desired Fourier Modulus

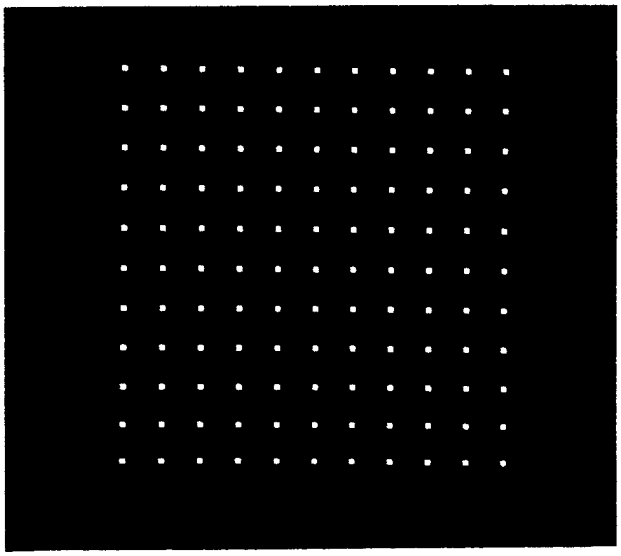

Phase Grating

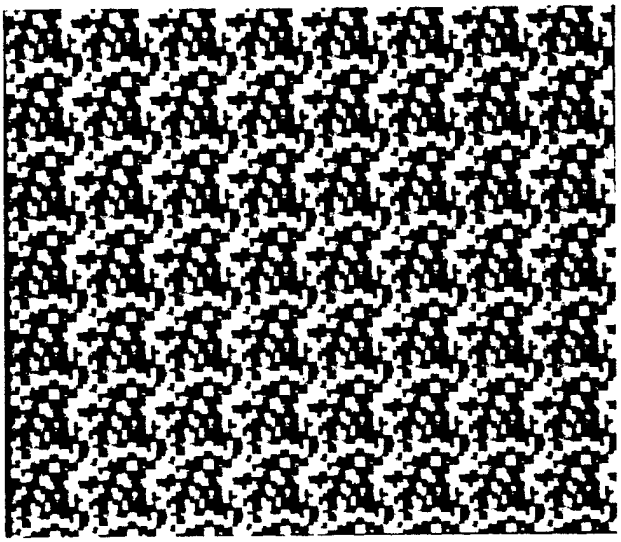

Reconstructed Fourier Modulus

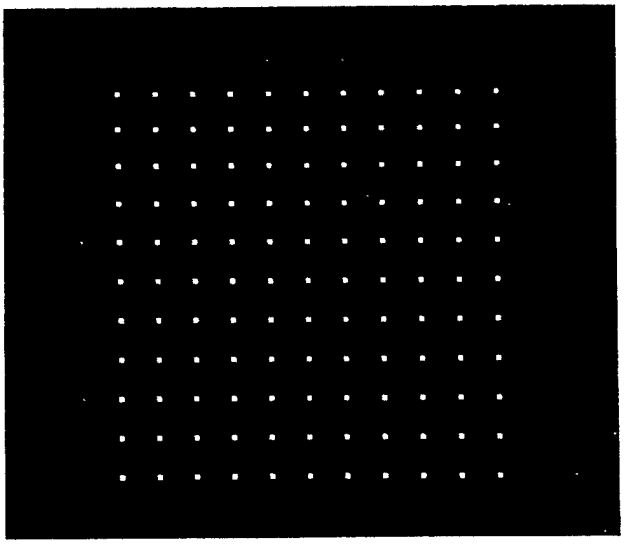

Phase Grating Synthesis

Triangular Array, Equal Intensity Diffracted Orders

Desired Fourier Modulus

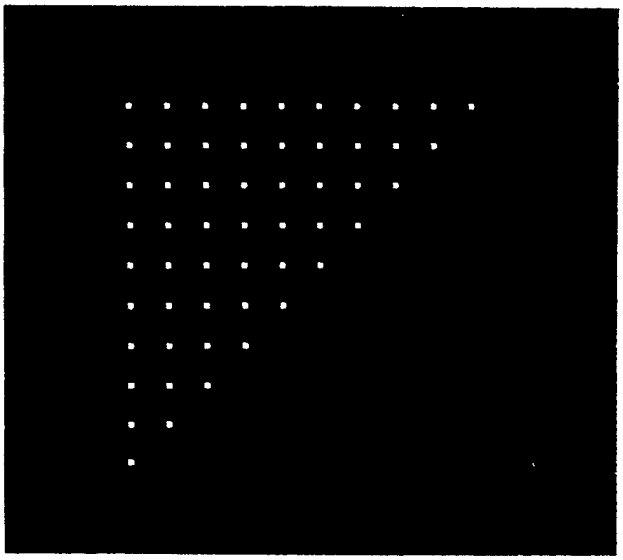

Phase Grating

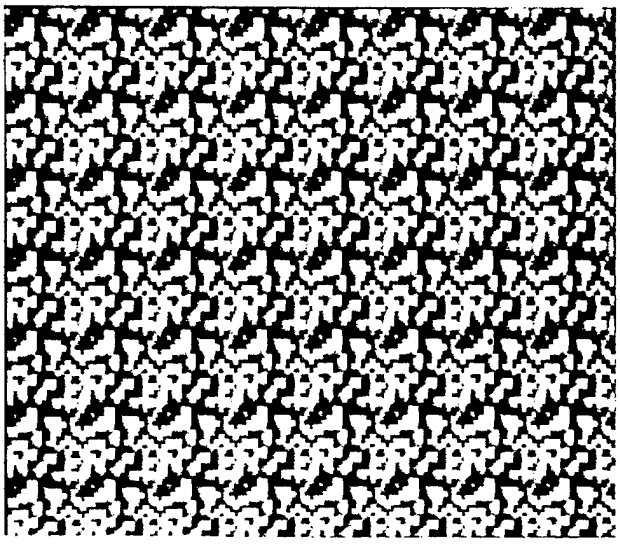

Reconstructed Fourier Modulus

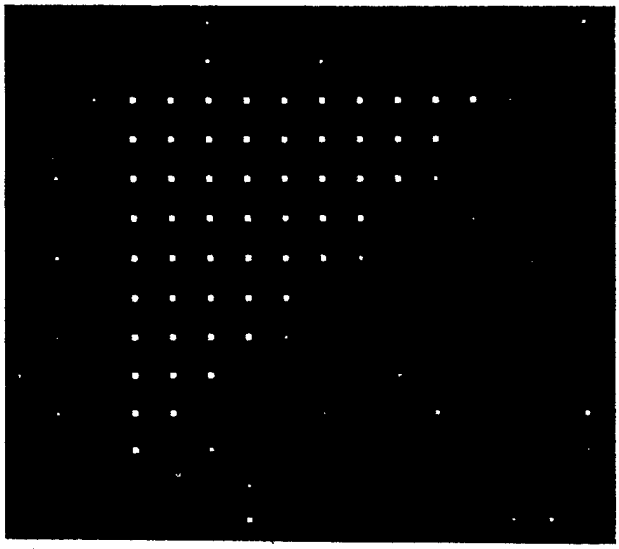

Sub-Wavelength Structured Surfaces

Concept

Use surface structure (small compared to the illumination wavelength) to *synthesize* an effective index of refraction

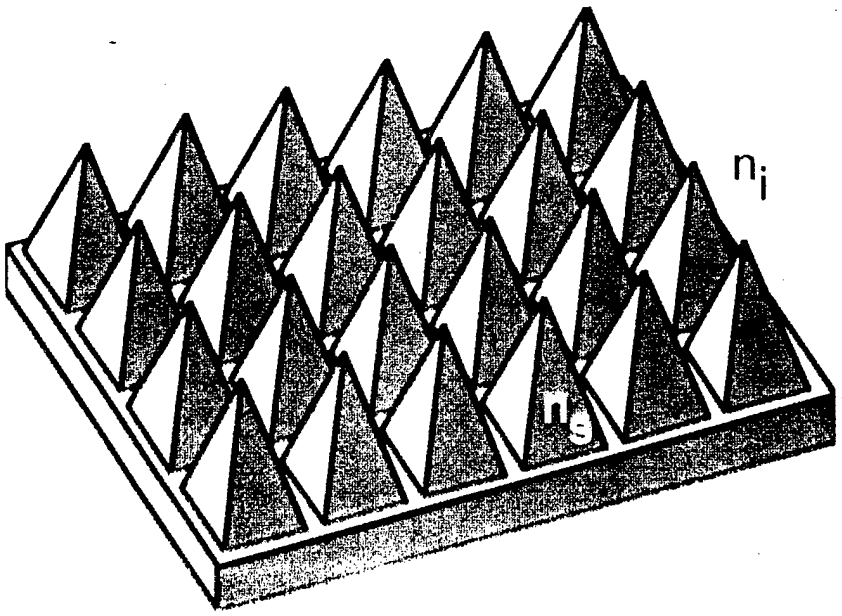

Approach

Effective Medium Theory
Rigorous Electromagnetic Theory
Tapered Transmission-Line Theory
Fabricate using Photolithographic Techniques

Features

Supression of Fresnel Reflections
Large Field-of-View and Spectral Bandwidth
Advantages over Thin Film Coatings
    No Cohesion Problems
Birefringent Surface

ARS Surfaces

- Require *ONLY* R_0 and T_0 non-evanescent

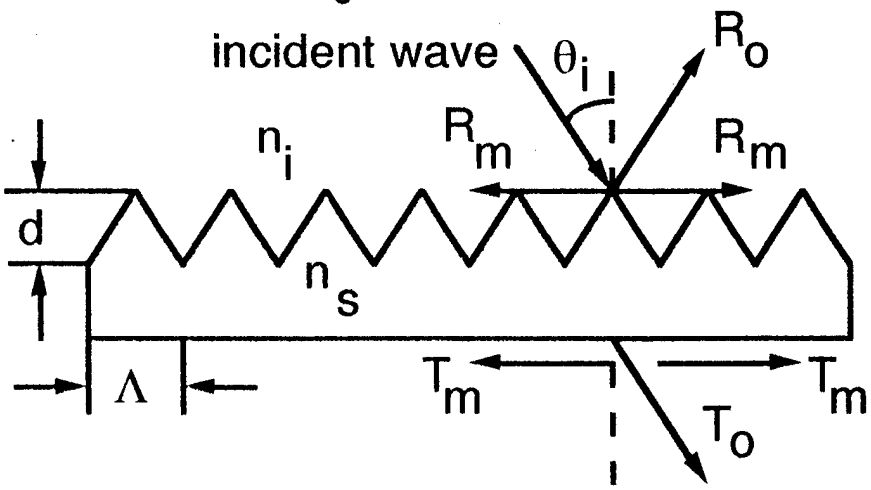

$$\frac{\Lambda}{\lambda} < \frac{1}{\text{Max}[n_i, n_s] + n_i \sin\theta_{max}}$$

- Period Λ smaller than wavelength λ

Effective Medium Theory (EMT)

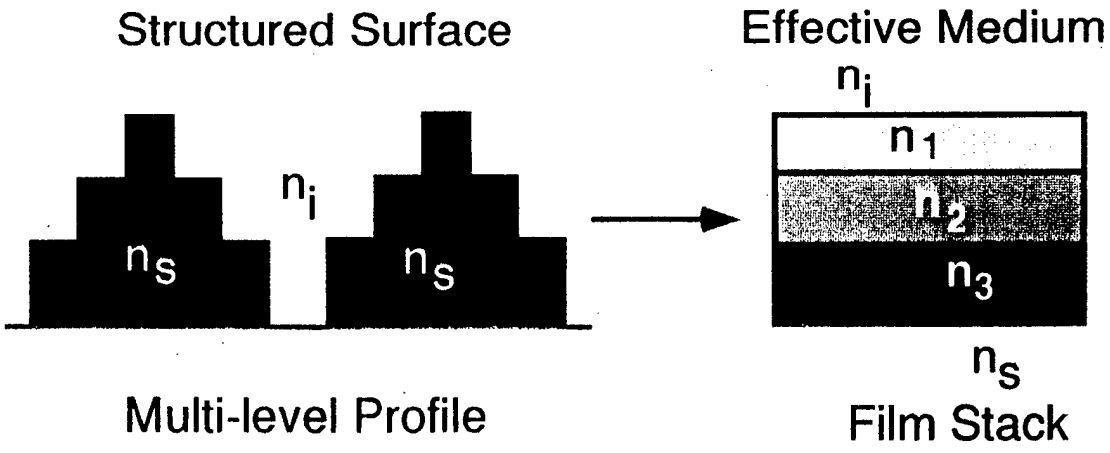

- Light averages optical properties of structured region

Angle of Incidence Sensitivity of GaAs 2-D Multilevel ARS Surfaces

- **Performance for randomly-polarized radiation**

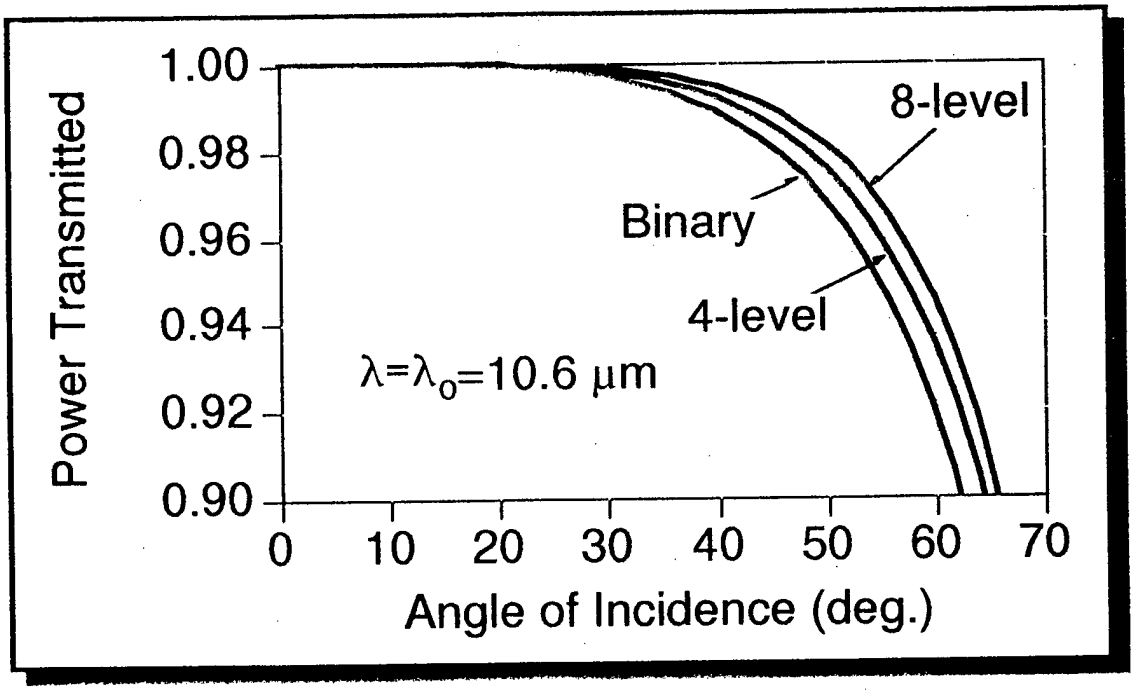

- **ARS Surface Parameters**

n_i=1, n_s=3.27, Λ_x=Λ_y=2.480μm		
Profile	Profile depth (μm)	Duty Cycle (%)
Binary	1.463	69.7
4-level	3.244	91.7
8-level	4.441	98.5

Spectral Sensitivity of GaAs 2-D Multi-level ARS Surfaces

- **4-level Pyramidal Profile**

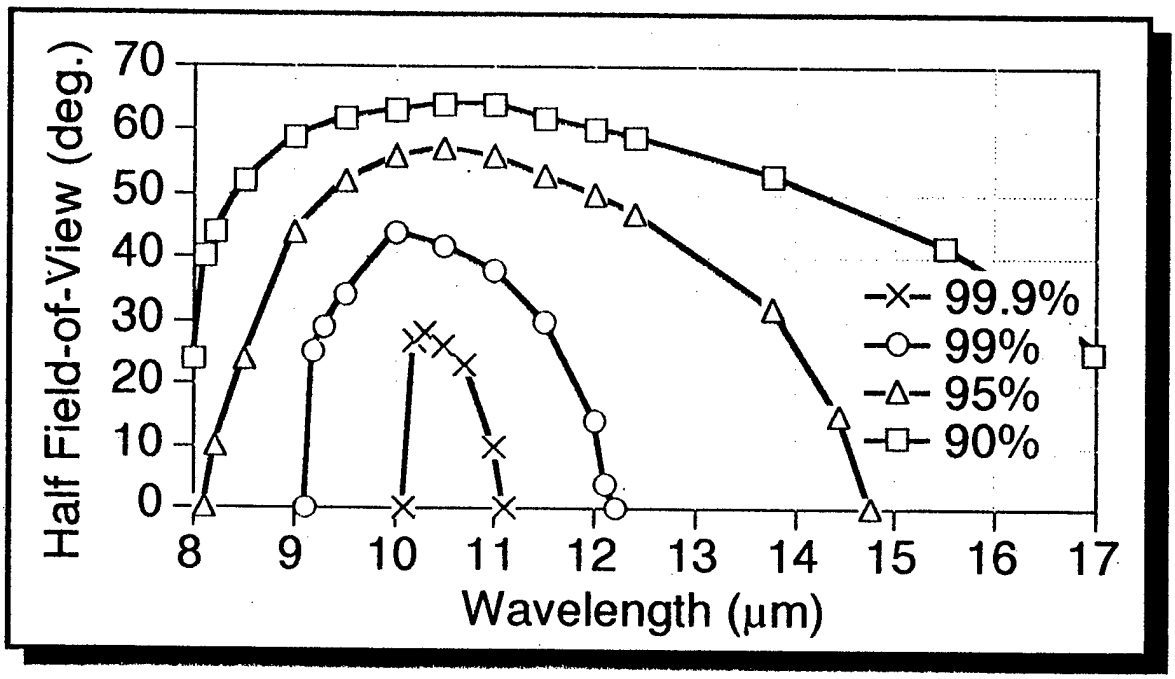

- **8-level Pyramidal Profile**

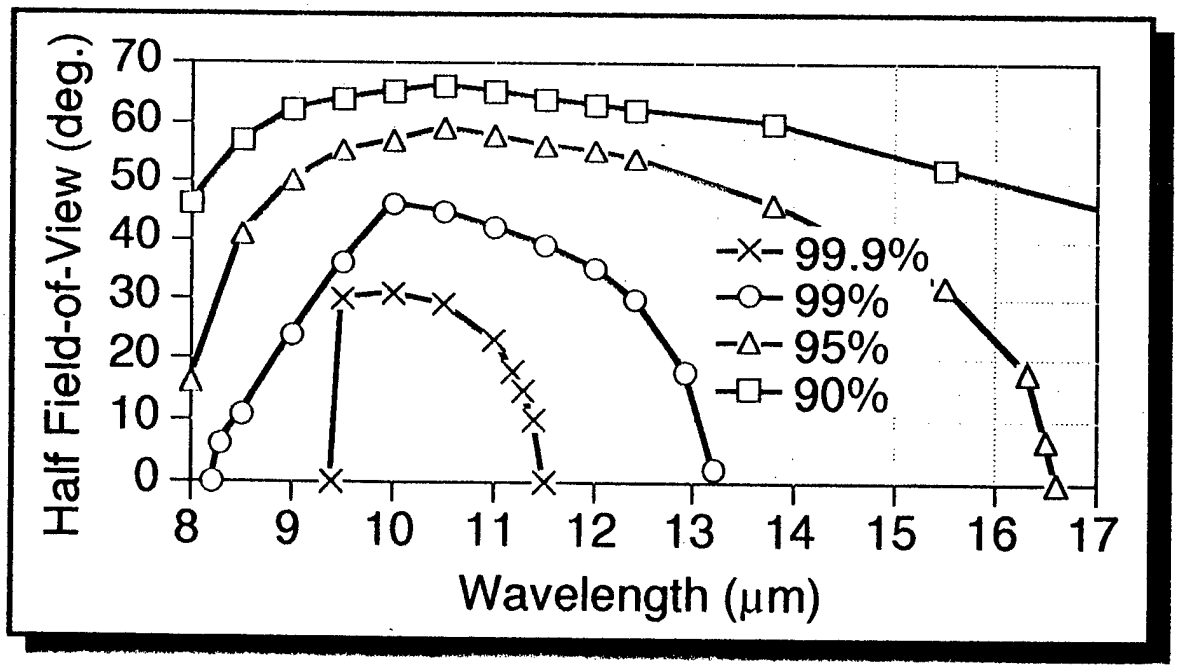

Experimental Work
2-D Binary ARS Surface for GaAs

- **Preliminary Results: CAIBE etched GaAs**

4.22k Magnification

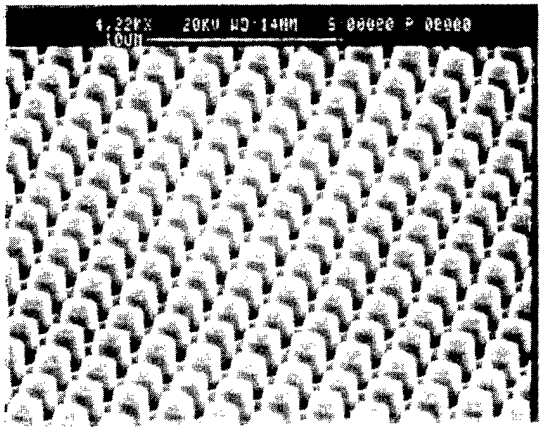

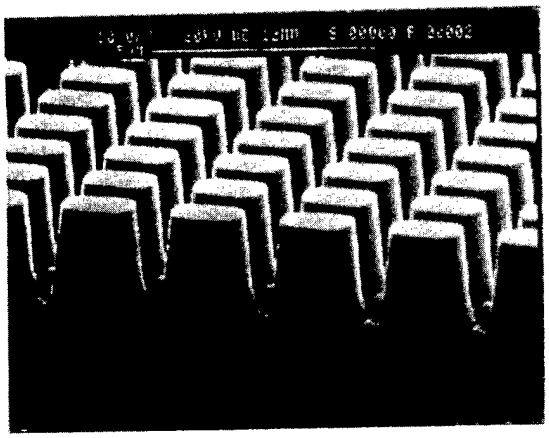

10.00k Magnification

16.50k Magnification

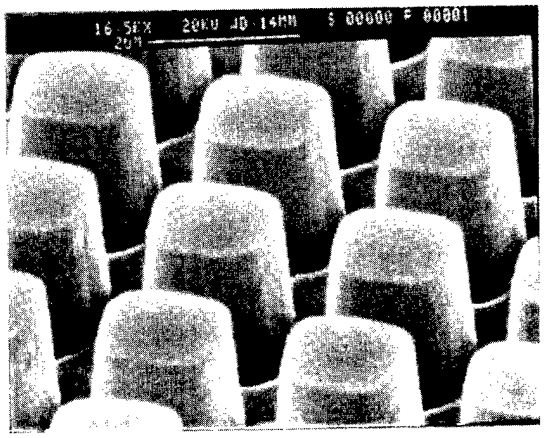

Surfaces Fabricated at Cornell's National Nanofabrication Facilities (NNF)

Polarization Components using Form Birefringence

- High-Frequency Surface-Relief Gratings

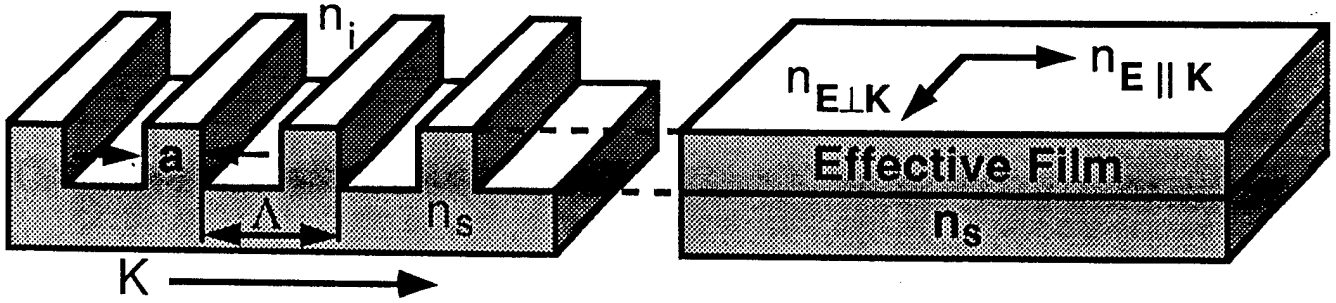

- Birefringence = $\Delta n = n_{E\perp K} - n_{E\parallel K}$
- Δn is a function of filling factor f

$$f = a/\Lambda$$

- Maximum Birefringence

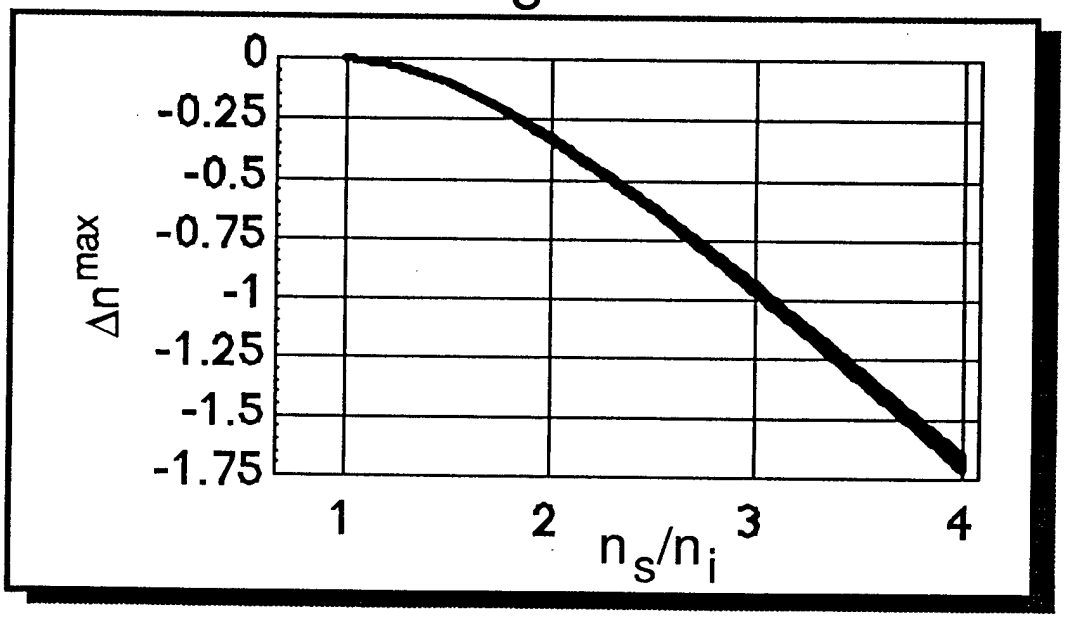

Resonance Structures

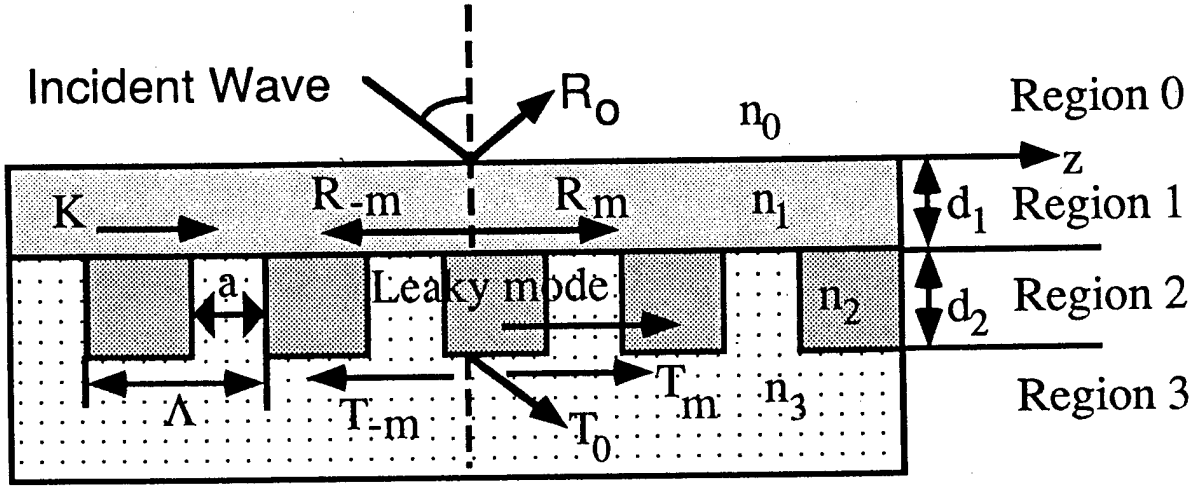

- Only Zeroth Orders Propagating ($\Lambda < \lambda$)
- Coupling occurs between incident wave and leaky wave
- Extremely narrrow FWHM possible.
- Example: FWHM of ~2Å

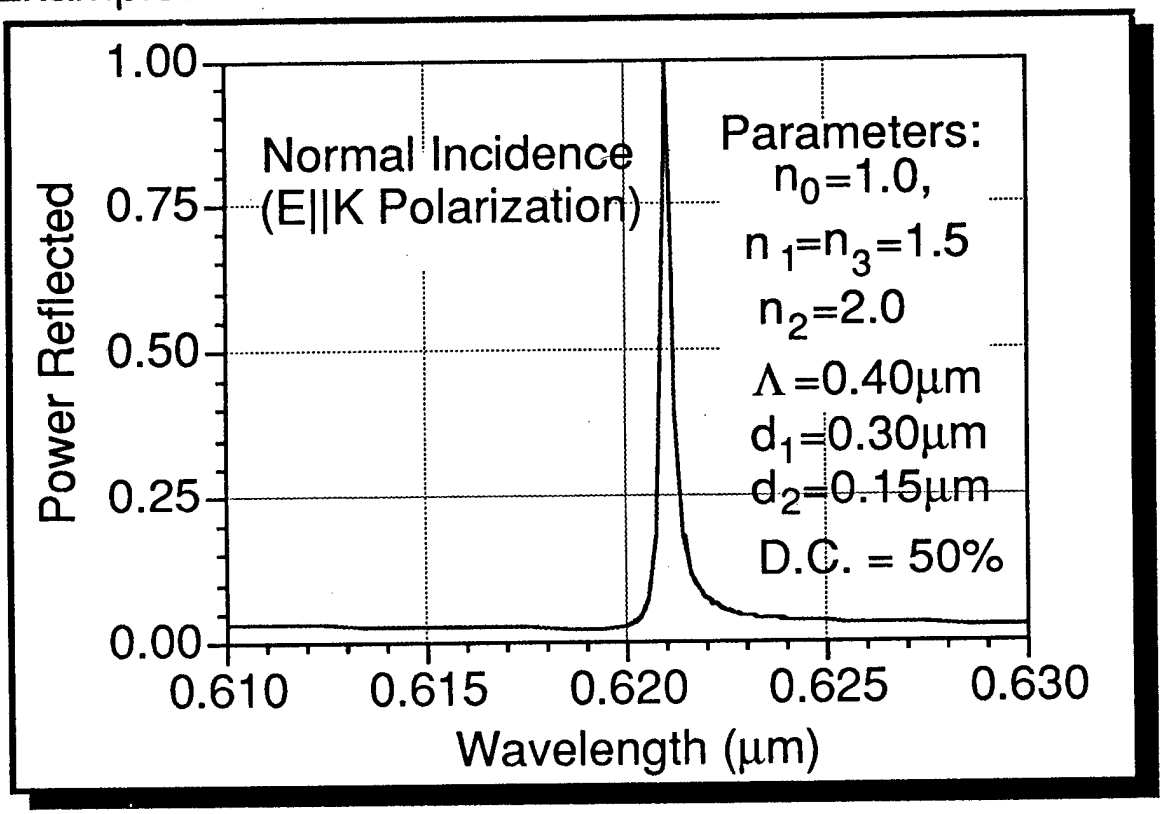

Future Directions in Diffractive Optics

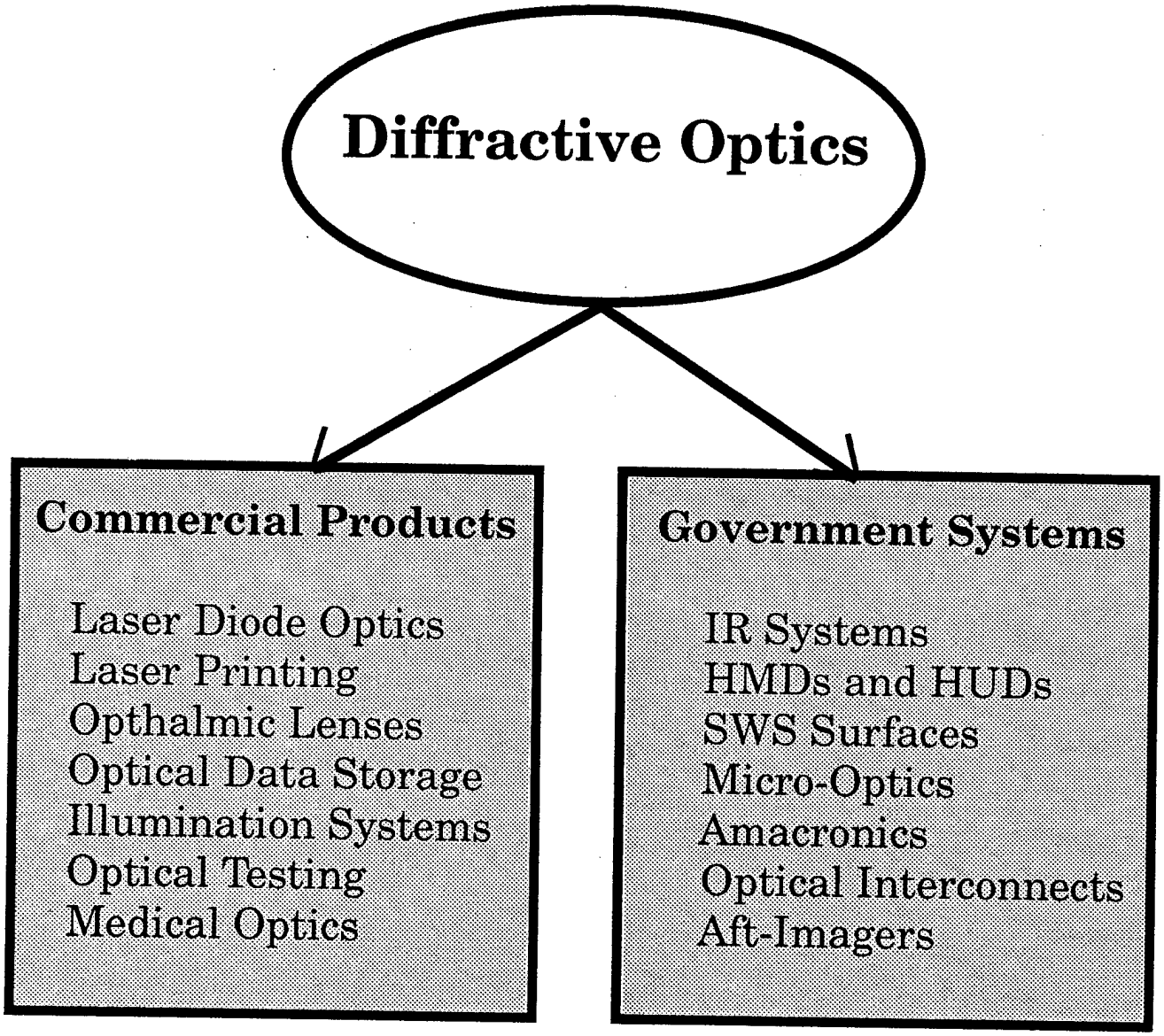

REVIEW OF RIGOROUS COUPLED-WAVE ANALYSIS AND OF HOMOGENEOUS EFFECTIVE MEDIUM APPROXIMATIONS FOR HIGH SPATIAL-FREQUENCY SURFACE-RELIEF GRATINGS

by

Elias N. Glytsis, David L. Brundrett, and Thomas K. Gaylord
School of Electrical Engineering and Microelectronics Research Center
Georgia Institute of Technology, Atlanta, Georgia 30332
Tel. No. (404) 894-8415 / (404) 894-2931

ABSTRACT

A review of the rigorous coupled-wave analysis as applied to the diffraction of electromagnetic waves by gratings is presented. The analysis is valid for any polarization, angle of incidence, and conical diffraction. Cascaded and/or multiplexed gratings as well as material anisotropy can be incorporated under the same formalism. Small period rectangular groove gratings can also be modeled using approximately equivalent uniaxial homogeneous layers (effective media). The ordinary and extraordinary refractive indices of these layers depend on the grating filling factor, the refractive indices of the substrate and superstrate, and the ratio of the freespace wavelength to grating period. Comparisons of the homogeneous effective medium approximations with the rigorous coupled-wave analysis are presented. Antireflection designs (single-layer or multilayer) using the effective medium models are presented and compared. These ultra-short period antireflection gratings can also be used to produce soft x-rays. Comparisons of the rigorous coupled-wave analysis with experimental results on soft x-ray generation by gratings are also included.

I. INTRODUCTION

The diffraction of electromagnetic waves by periodic structures continues to be of great practical importance owing to numerous applications in a variety of fields such as acousto-optics, integrated optics, spectroscopy, optical interconnects, binary optics, and quantum electronics. Furthermore, high spatial-frequency (small period compared to wavelength) surface-relief binary or multilevel stairstep diffraction gratings on dielectric or lossy substrates can behave as homogeneous uniaxial layer(s) for either polarization and angle of incidence. As a result these gratings can be used in applications such as in high-power lasers, antireflection surfaces, filters similar to thin-film coatings, wave plates, and polarization-selective mirrors.

In this paper a brief review of the rigorous coupled-wave analysis is presented along with the effective medium approximations for high spatial-frequency gratings. The analysis

is valid for any incident polarization and angle of incidence. The orientation of the plane of incidence can also be arbitrary (conical diffraction). The electric and magnetic fields in the grating region can be expanded in terms of spatial harmonics which must satisfy Maxwell's equations. The resulting set of first-order coupled differential equations can be solved simultaneously with the boundary conditions of the problem leading to the determination of all quantities of interest (diffracted fields, efficiencies). The review of the rigorous coupled-wave analysis is presented in sec. II.

In the small period limit, all diffracted orders except the zeroth orders are cutoff and the grating behaves like a slab of homogeneous uniaxial material (effective medium) with its optic axis parallel to the grating vector. The ordinary and the principal extraordinary indices of the slab depend on the grating filling factor (duty cycle), the refractive indices of the substrate and the surrounding medium, and the ratio of the freespace wavelength to period. These refractive indices can be determined by solving two transcendental equations (higher-order refractive indices). Approximate solutions of the transcendental equations define the second-order indices (second-order dependence on wavelength-to-period ratio), and first-order indices (no dependence on the wavelength-to-period ratio). The diffraction efficiencies using the effective medium models are compared with those obtained by the rigorous coupled-wave analysis for various diffraction geometries. The wavelength-to-period ratio necessary for the validity of each model is determined. The effective medium approximations are presented in sec. III.

Antireflection behavior can be obtained by appropriate combinations of the filling factor and the groove depth of the grating. Design procedures are presented using the higher-order, the second-order, and the first-order grating refractive indices and are compared. Multilevel stairstep gratings are also designed to perform like broadband antireflection filters (Butterwoth or Chebyshev). The design of antireflection gratings is described in sec. IV.

Finally, small period gratings can be used in conjunction with intense femtosecond laser pulses to produce sub-picosecond soft x-rays through the creation of a plasma grating. Antireflection grating design is needed to minimize the reflectance of these grating targets. The rigorous coupled-wave analysis was applied to analyze photolithographically produced SiO, Si, and SiN gratings with subwavelength periods. These results are presented in sec. V.

II. RIGOROUS COUPLED-WAVE ANALYSIS

Methods of grating diffraction analysis can be divided into two major categories, the integral methods,[1] and the differential methods.[1-7] The most common and accurate differential methods are coupled-wave approaches[2-5] and modal approaches.[6,7]

The general geometry of a grating structure along with an incident plane wave is shown in Fig. 1. This figure corresponds to a surface-relief type grating but it applies

to volume gratings too. The grating and the surrounding regions can be general anisotropic. The configuration in Fig. 1 corresponds to any general three-dimensional incidence and any allowable linear polarization. The electric and magnetic fields in the grating region(s) are expanded in terms of spatial harmonics $\vec{E} = \sum_i \vec{S}_i(z) \exp(-j\vec{\sigma}_i \cdot \vec{r})$ and $\vec{H} = (\epsilon_0/\mu_0)^{1/2} \sum_i \vec{U}_i(z) \exp(-j\vec{\sigma}_i \cdot \vec{r})$, where $\vec{\sigma}_i = \vec{k}_{inc} - i\vec{K}$ $(i = 0, \pm 1, \pm 2, \cdots)$, $\vec{S}_i$, $\vec{U}_i$ are the space harmonic amplitudes, $\vec{k}_{inc}$ is the incident wavevector (in the grating region), $\vec{K}$ is the grating vector, and ϵ_0, μ_0 are the permittivity and permeability of freespace, and ω is the angular frequency of the incident wave. The field expansions must satisfy Maxwell's curl equations in the grating region(s):

$$\begin{aligned} \vec{\nabla} \times \vec{E} &= -j\omega\vec{B} = j\omega\mu_0\tilde{\mu}(x,z)\vec{H}, \\ \vec{\nabla} \times \vec{H} &= \vec{J} + j\omega\vec{D} = [j\omega\epsilon_0\tilde{\varepsilon}(x,z) + \tilde{\sigma}(x,z)]\vec{E}, \end{aligned} \tag{1}$$

where $\tilde{\varepsilon}$, $\tilde{\mu}$, and $\tilde{\sigma}$ are the relative permittivity, relative permeability, and conductivity tensors of the grating regions and are periodic in the direction of the grating vector. More general equations can be written if constitutive relations of the form $\vec{D} = \tilde{\varepsilon}\vec{E} + \tilde{g}\vec{H}$ and $\vec{B} = \tilde{h}\vec{E} + \tilde{\mu}\vec{H}$ (for bianisotropic media) are used where $\tilde{g}$ and $\tilde{h}$ are the coupling tensors between $\vec{D}$ and $\vec{H}$, and $\vec{B}$ and $\vec{E}$. However, the most common and practical case in optics is when only the permittivity tensor is modulated. Using the spatial expansions of the fields into Eq. (1) an infinite set of linear coupled-wave differential equations is derived. If the infinite number of possible diffracted orders is truncated to a finite number m then the total number of coupled-wave equations becomes $6m$. Eliminating the components along the propagation direction (z in Fig. 1), the tangential components of the electric and magnetic fields can be expressed in the following compact matrix form[3-5]

$$d\tilde{V}/dz = j\tilde{A}\tilde{V}, \tag{2}$$

where $\tilde{V}$ is a $4m \times 1$ vector containing the tangential space harmonic components of the electric and magnetic fields and $\tilde{A}$ is a $4m \times 4m$ coupling matrix.[3-5] All special cases can be derived from the above general expression. For example if angle $\alpha = 0°$ (Fig. 1) and $\psi = 90°$, only the y-components of the electric field and the x-components of the magnetic field exist (TE polarization) and Eq. (2) reduces to a system of $2m$ equations. Similarly, Eq. (2) reduces to $2m$ equations in the case of $\alpha = 0°$ and $\psi = 0°$ (TM polarization). The above conclusions in these limiting cases are valid if isotropic or special orientation (with respect to the principal axes) anisotropic grating region(s) are considered. In general, for three-dimensional incidence (conical diffraction) the two orthogonal polarizations are coupled even in the isotropic case. Independently of the grating characteristics Eq. (2) can be solved in the form $\tilde{V} = \tilde{W} \exp(\tilde{\Lambda}z)\tilde{C}$, where $\tilde{W}$ and $\tilde{\Lambda}$ contain the eigenvectors and eigenvalues of the coupling matrix $\tilde{A}$, and $\tilde{C}$ contains $4m$ unknown constants.[2-4] Combining the previous field solutions with the known plane wave solutions in the regions external to the grating, a set of boundary conditions is formed. Solution of this set of conditions (a linear system of the form $Ax = b$) specifies all the unknown field coefficients.[3-5] Knowledge of the electric

and magnetic fields in any region of the problem determines all quantities of interest, such as the diffraction efficiencies. The same approach is valid for any type of volume or surface-relief grating of constant or varying modulation since they can represented as cascaded gratings.[5] The same formulation can be applied to multiplexed gratings.[5] The effective medium approximations for a high spatial-frequency surface-relief grating are presented in the next section.

III. HOMOGENEOUS EFFECTIVE MEDIUM APPROXIMATIONS

A high spatial-frequency surface-relief grating is characterized by a period Λ which is much smaller than the incident freespace wavelength λ_0. In this case all the diffracted orders except the zero forward-diffracted and the zero backward-diffracted orders are cutoff. This is shown schematically in Fig. 2a for a rectangular-groove grating in the case of conical diffraction geometry. A cross section of the grating is shown in Fig. 2b. The superstrate and substrate refractive indices are n_1 and n_3 respectively, while the filling factor of the grating is F. The grating vector is $\vec{K} = \hat{x}(2\pi/\Lambda)$ where $\hat{x}$ is the unit vector along the x direction.

In the case that $\lambda_0 \gg \Lambda$ it can be shown[8,9] that at normal incidence for TE polarization (electric field polarized perpendicular to the grating vector, $\vec{E} \perp \vec{K}$) there is an effective refractive index n_O defined, which is given by

$$n_O = [n_1^2(1-F) + n_3^2 F]^{1/2}. \tag{3}$$

For the orthogonal polarization (TM polarization or magnetic field perpendicular to the grating vector, $\vec{H} \perp \vec{K}$), the corresponding effective refractive index n_E is given by

$$n_E = [\frac{1-F}{n_1^2} + \frac{F}{n_3^2}]^{-1/2}. \tag{4}$$

In the general case of oblique incidence the high spatial-frequency grating is equivalent[10,11] to a uniaxial homogeneous slab with its optic axis oriented along the direction of the grating vector (x direction in this case), and ordinary and extraordinary refractive indices given by Eqs. (3) and (4) respectively or by the higher-order indices defined next. The thickness of the slab is equal to the groove depth d of the grating. The effective indices given by Eqs. (3) and (4) are the first-order indices and they are denoted by $(n_O^{(1)}, n_E^{(1)})$ in contrast to the second- and higher-order effective indices which are presented next.

Higher-order approximations of the effective ordinary and extraordinary indices have been found by Rytov.[12] These indices are given by the solutions of the following transcendental equations:

$$\begin{aligned}
&\sqrt{n_1^2 - n_O^2}\,\tan\left[\frac{\Lambda}{\lambda_0}\pi(1-F)\sqrt{n_1^2 - n_O^2}\right] = -\sqrt{n_3^2 - n_O^2}\,\tan\left[\frac{\Lambda}{\lambda_0}\pi F\sqrt{n_3^2 - n_O^2}\right], \\
&\frac{\sqrt{n_1^2 - n_E^2}}{n_1^2}\,\tan\left[\frac{\Lambda}{\lambda_0}\pi(1-F)\sqrt{n_1^2 - n_E^2}\right] = -\frac{\sqrt{n_3^2 - n_E^2}}{n_3^2}\,\tan\left[\frac{\Lambda}{\lambda_0}\pi F\sqrt{n_3^2 - n_E^2}\right].
\end{aligned} \tag{5}$$

The effective refractive indices which are solutions of the above equations are denoted as higher-order effective indices $(n_O^{(H)}, n_E^{(H)})$. Approximate solutions of Eqs. (5) with second-order dependence on the grating period to wavelength ratio, are characterized as second-order effective indices $(n_O^{(2)}, n_E^{(2)})$ and are given by

$$n_O^{(2)} = \left[(n_O^{(1)})^2 + \frac{1}{3}[\pi \frac{\Lambda}{\lambda_0} F(1-F)]^2 (n_3^2 - n_1^2)^2\right]^{1/2},$$
$$n_E^{(2)} = \left[(n_E^{(1)})^2 + \frac{1}{3}[\pi \frac{\Lambda}{\lambda_0} F(1-F)]^2 \left(\frac{1}{n_3^2} - \frac{1}{n_1^2}\right)^2 (n_E^{(1)})^6 (n_O^{(1)})^2\right]^{1/2}. \tag{6}$$

The higher- and second-order effective indices converge to the first-order incides when $(\Lambda/\lambda_0) \rightarrow 0$. The modeling of a high spatial-frequency surface-relief grating through a uniaxial homogeneous layer using the first-, second-, or higher-order effective indices constitutes the effective medium models that can approximate the grating behavior.

The dependence of the three different effective indices [Eqs. (3),(4), (5), and (6)] on the filling factor of the grating is shown in Fig. 3a for $\lambda_0/\Lambda = 5$ and for a silicon grating at $\lambda_0 = 1.5\,\mu$m in air ($n_1 = 1$, $n_3 = 3.5$). The dependence of the effective indices on λ_0/Λ is shown in Fig. 3b for $F = 0.5$. It is apparent that the three effective indices pairs differ substantially, especially for small λ_0/Λ ratios. For large ratios ($\lambda_0/\Lambda > 15$) the higher- and the second-order indices are essentially the same as the first-order effective indices.

The same uniaxial homogeneous slab model with ordinary and extraordinary indices given by the first-, second-, or higher-order effective indices can also be used in the more general case of the conical diffraction as long as all diffracted orders except the zero forward-diffracted (transmitted) order and the zero backward-diffracted (reflected) order are cutoff. To demonstrate the validity of the models for the conical diffraction case, a silicon grating of $F = 0.22$ and $d = 0.134\lambda_0$ is used at $\lambda_0 = 1.5\,\mu$m for a polar and azimuthal angles of incidence (Fig. 2) $\theta = \phi = 45$ deg and TE polarization. The zero-order backward-diffracted efficiency is shown in Fig. 4 using each of the three approximate models (using the first-, second- and higher-order effective indices) and using the rigorous coupled-wave analysis. It is observed that the second- and the higher-order models agree very well with the exact solution obtained with the rigorous coupled-wave analysis even for small λ_0/Λ ratios ($\simeq 2$). Consequently, these effective medium models can be used for the design of surface-relief gratings even with larger periods compared to the incident freespace wavelength. These models will be exploited next in order to design antireflection gratings on silicon substrates.

IV. ANTIREFLECTION GRATING DESIGNS

As was shown previously, high spatial-frequency gratings can be well approximated by homogeneous uniaxial layers with effective ordinary and extraordinary refractive indices which depend on the grating parameters, the incident wavelength and the refractive indices of the surrounding media. Thus, results from the thin layer designs can be used for the design of antireflection gratings. Antireflection grating designs on dielectrics, semiconductors

or metals, similar to thin film antireflection coatings designs, are well documented in the literature.[8,9,13-16]

The antireflection grating design procedure is analogous to the microwave wave-impedance matching technique. For a single layer antireflection coating (equivalent to a single-level rectangular groove grating) its thickness and refractive index are given by

$$d = \frac{\lambda_0}{4N_2}p, \qquad N_2 = \sqrt{N_1 N_3}, \tag{7}$$

where $p = 1, 3, 5, \cdots$, and N_1, N_2, N_3 are the effective indices that correspond to the wave impedance in the superstrate, the effective uniaxial layer, and the substrate. The N_2 is a function of the first-order, second-order, or higher-order refractive indices of the homogeneous uniaxial layer. Equations (7) can be solved either analytically (in the case that first-order effective indices are used) or numerically (in the case that second- or higher-order refractive indices are used) with respect to F and d. The solutions using the second- or the higher-order effective indices depend on the λ_0/Λ ratio. These designs can be greatly improved over the first-order designs which do not depend on λ_0/Λ ratio. Example antireflection designs of single-level rectangular-groove gratings are shown in Figs. 5. Specifically, the filling factor and the groove depth needed to suppress completely (according to the homogeneous layer approximation) the specular reflection are shown in Figs. 5a-b, and 5c as a function of the polar angle of incidence θ for four distinct cases of incident light of $\lambda_0 = 1.5\,\mu$m on silicon targets in air ($\phi = 0$ or 90 deg and for TE or TM incident polarization).

The same principles can be generalized to design broadband antireflection gratings similar to broadband antireflection thin film coatings[16]. These designs resemble the microwave Butterworth or Chebyshev transformers. The resulting grating is a multilevel stairstep grating as shown in Fig. 6. The detailed procedure is summarized in Ref. 16. An example design on silicon at $\lambda_0 = 1.5\,\mu$m is shown in Table I for a two- and a three-level maximally-flat (Butterworth) and equal-ripple (Chebyshev) filters using the first-order effective indices at normal incidence. The resulting reflectivity of these gratings is shown in Figs. 7a and 7b where the broadband antireflection response is apparent.

Antireflection grating designs can be obtained even for gratings with small λ_0/Λ ratio. In these cases the approximate effective medium models will not approximate the grating accurately. However, the designs obtained by the effective medium models can again be of significant value since they can serve as starting designs which can be improved by using the rigorous coupled-wave analysis and a simulated annealing type of algorithm.

V. ANTIREFLECTION GRATINGS FOR X-RAY EMISSION

Laser produced plasmas created by intense femtosecond laser pulses have been demonstrated to produce subpicosecond soft-x-rays.[17,18] The use of terawatt femtosecond lasers

permits the generation of more intense x-ray sources. However, increased target reflectivity at high fluence results in less efficient coupling. Grating targets can dramatically increase this coupling.[8] The rigorous coupled-wave analysis was applied to analyze photolithographically produced SiO, Si, and SiN diffraction surface-relief gratings with varying groove depths and filling factors and with periods of 240 or 300 nm. Good agreement between the experimental data and the calculated rigorous coupled-wave results was obtained (Figs. 8a and 8b). The plasma gratings are inhomogeneous due to the varying plasma temperature. However, the rigorous coupled-wave analysis can be applied since the plasma grating can be decomposed into a series of cascade homogeneous gratings. Specially designed antireflection gratings could potentially increase absorption resulting in an enhanced energy deposition, a hotter plasma, and consequently more intense x-ray emission.

VI. SUMMARY

A review of the rigorous coupled-wave analysis of grating diffraction was presented. The analysis is valid for both volume or surface-relief gratings and can incorporate lossy or anisotropic materials. The same formalism is also applicable to cascaded and/or multiplexed gratings. In addition, a review of the effective medium approximations as applied to small period surface-relief gratings was also presented. It was shown that high spatial-frequency gratings can be modeled as uniaxial homogeneous layers with their optic axis parallel to the grating vector. The ordinary and extraordinary indices of the layers depend on the grating parameters and the ratio of the grating period to the freespace wavelength. Three effective medium models were defined using first-, second-, and higher-order indices. It was demonstrated that the effective medium models are also valid in the case of conical diffraction. Applications of the first-order model to single-level and multilevel antireflection gratings were presented. Experimental comparisons of the rigorous coupled-wave analysis results on soft x-ray generating gratings were also included.

VII. REFERENCES

[1] R. Petit, Ed., *Electromagnetic Theory of Gratings*, Springer-Verlag, 62 (1980).

[2] H. Kogelnik, *Bell Syst. Tech. J.* **48**, 2909 (1969).

[3] M. G. Moharam and T. K. Gaylord, *J. Opt. Soc. Am.* **71**, 811 (1981).

[4] T. K. Gaylord and M. G. Moharam, *Proc. IEEE* **73**, 894 (1985).

[5] E. N. Glytsis and T. K. Gaylord, *J. Opt. Soc. Am. A* **7**, 1399 (1990).

[6] T. Tamir, H. C. Wang, and A. A. Oliner, *IEEE Trans. Microwave Theory Tech.* **MTT-12**, 323 (1964).

[7] R. S. Chu and J. A. Kong, *IEEE Trans. Microwave Theory Tech.* **MTT-25**, 18 (1977).

[8] Y. Ono, Y. Kimura, Y. Ohta, and N. Nishida, *Appl. Opt.* **26**, 1142 (1987).

[9] T. K. Gaylord, W. E. Baird, and M. G. Moharam, *Appl. Opt.* **25**, 4562 (1986).

[10] R. C. McPhedran, L. C. Botten, M. S. Craig, M. Neviere, and D. Maystre, *Opt. Acta*

29, 289 (1982).

[11] G. Bouchitte and R. Petit, Electromag. **5**, 17 (1985).

[12] S. M. Rytov, *Soviet Phys.* **JETP-2**, 466 (1956).

[13] T. K. Gaylord, E. N. Glytsis, and M. G. Moharam, *Appl. Opt.* **26**, 3123 (1987).

[14] E. N. Glytsis and T. K. Gaylord, *Appl. Opt.* **27**, 4288 (1988).

[15] T. K. Gaylord, E. N. Glytsis, M. G. Moharam, and W. E. Baird, *U. S. Patent No. 5,007,708* (1991).

[16] E. N. Glytsis and T. K. Gaylord, *Appl. Opt.* **31**, 4459 (1992).

[17] M. Murnane, H. Kapteyn, J. Bokor, W. Mansfield, R. Gnall, E. N. Glytsis, T. K. Gaylord, and R. Falcone, *OSA Topical Meeting on Short Wavelength Coherent Radiation*, Monterey, CA, April 1991.

[18] M. Murnane, H. Kapteyn, J. Bokor, W. Mansfield, E. N. Glytsis, and R. Falcone, *Appl. Phys. Lett.*, 1993 (accepted).

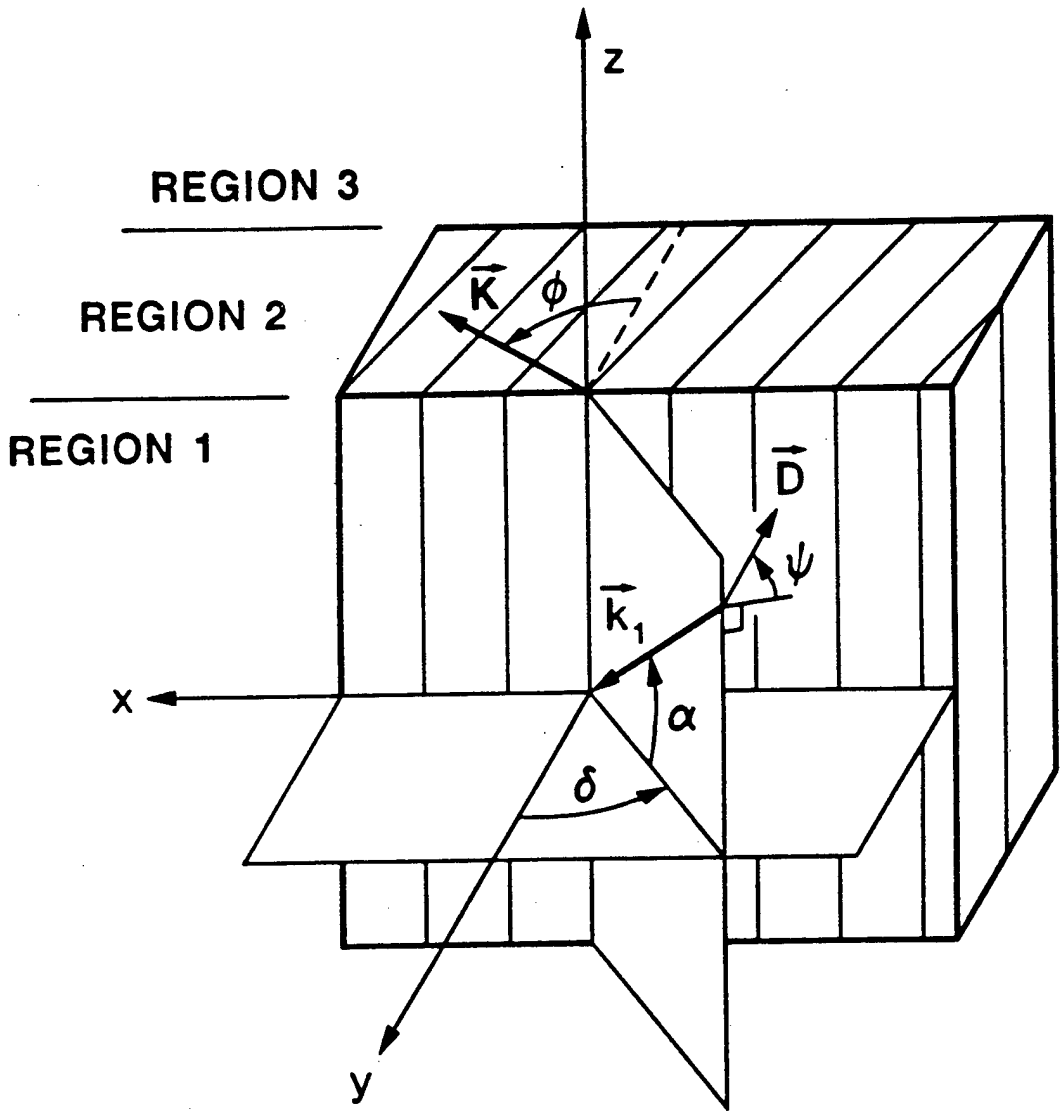

Fig. 1: The three-dimensional geometry of the grating structure and the incident plane wave. The angle of incidence is γ (in the plane of incidence). The angles α and δ are used to specify the incident wavevector in the xyz coordinates system. The angle ψ specifies the angular orientation of the incident polarization. An angle $\alpha = 0\,\text{deg}$ and $\psi = 90\,\text{deg}$ corresponds to TE polarization while an angle $\alpha = 0\,\text{deg}$ and $\psi = 0\,\text{deg}$ corresponds to TM polarization.

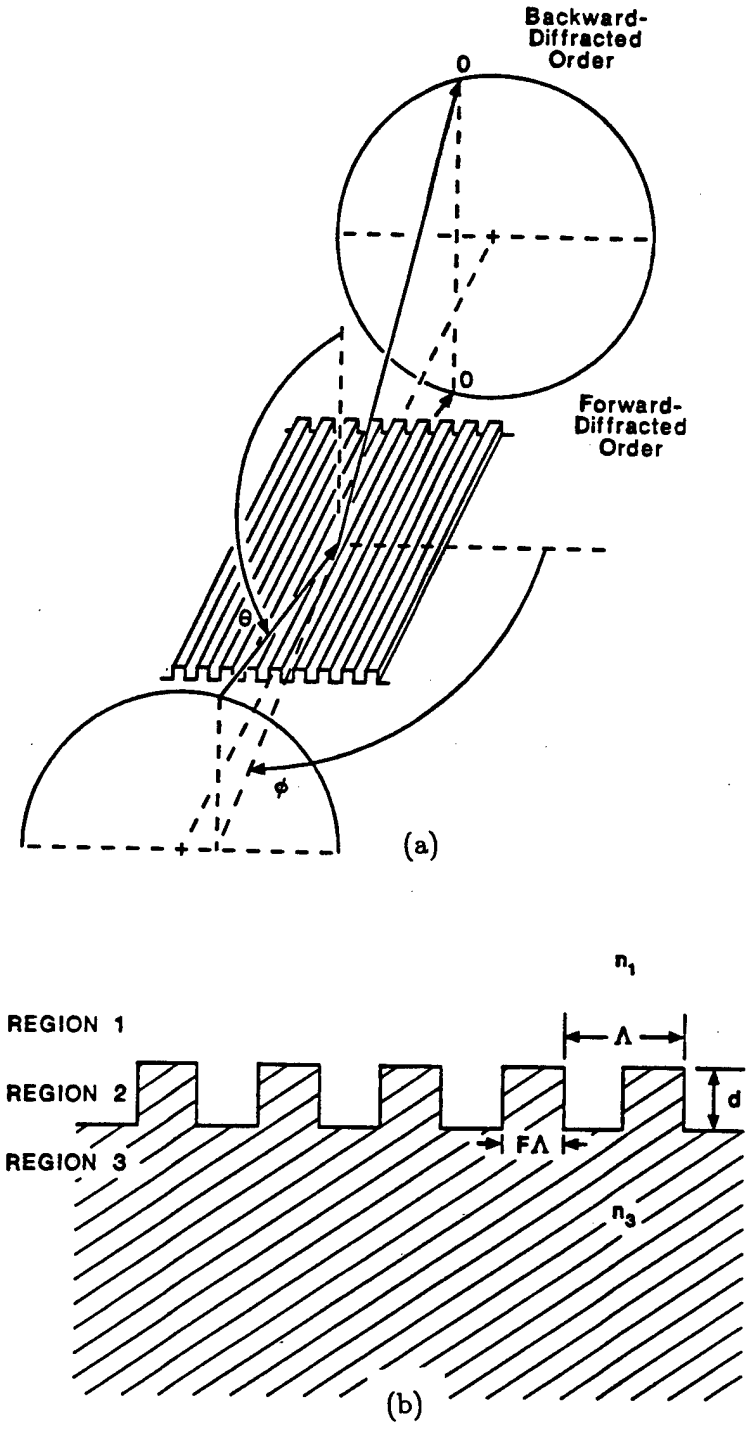

Fig. 2: (a) A high spatial-frequency ractangular groove surface-relief grating in the case of conical diffraction. Only the zero backward- and zero forward-diffracted orders are propagating as shown by their corresponding wavevectors. (b) A cross-sectional view of the rectangular groove high spatial-frequency grating.

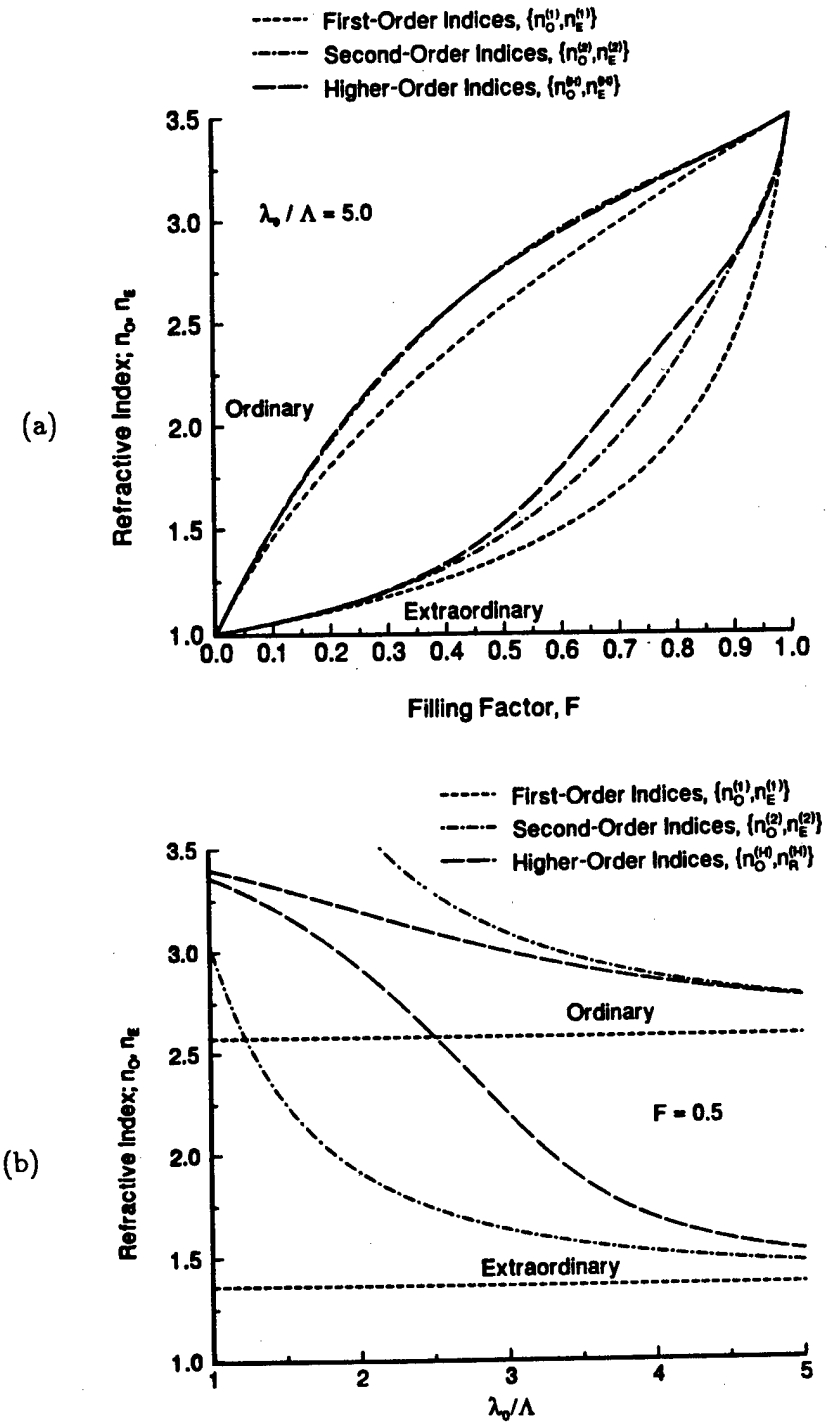

Fig. 3: (a) Dependence of the first-, second- and higher-order effective refractive indices (ordinary and extraordinary) on the filling factor of a rectangular groove grating for $\lambda_0/\Lambda = 3$. (b) Dependence of the first-, second- and higher-order effective refractive indices (ordinary and extraordinary) on the λ_0/Λ of a rectangular groove grating with $F = 0.5$.

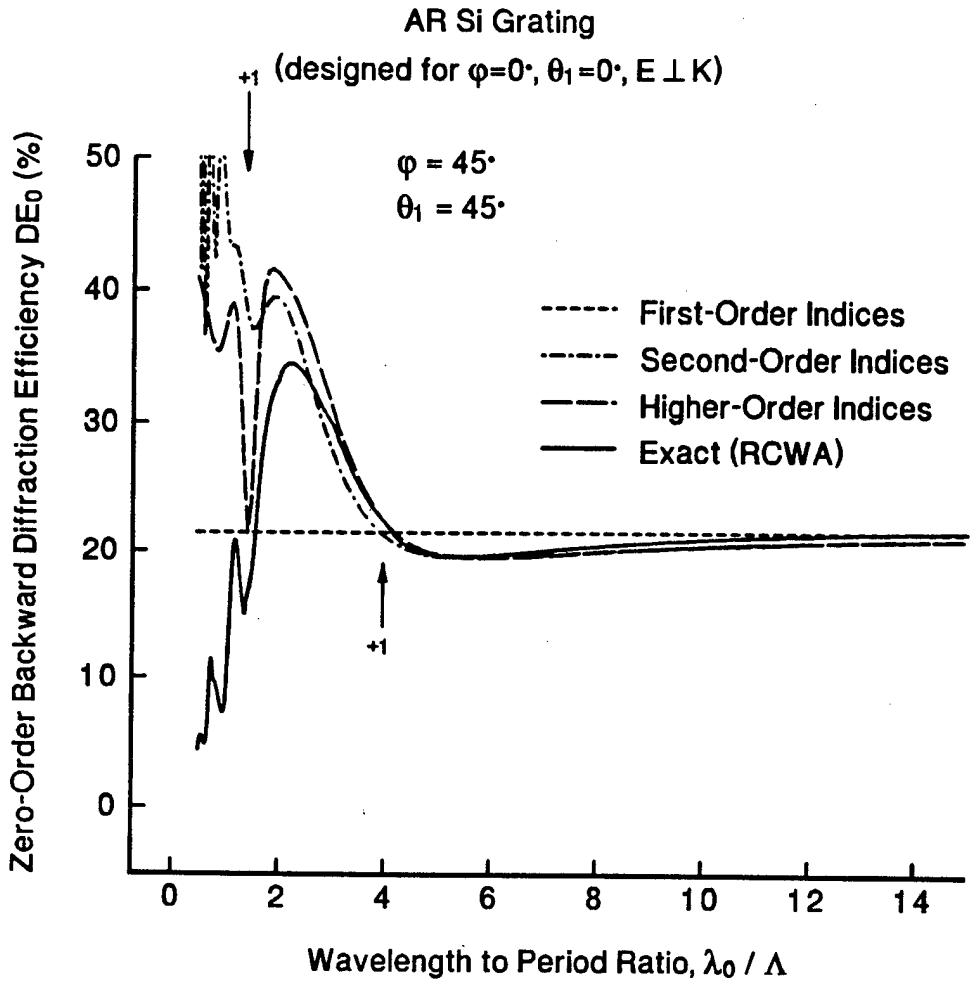

Fig. 4: The zero-order backward-diffracted efficiency of a silicon grating for $\lambda_0 = 1.5\,\mu$m in the conical diffraction case ($\phi = \theta = 45$ deg) as a function of λ_0/Λ. The results using the approximate models (with first-, second-, and higher-order indices) as well as the exact results using the rigorous coupled-wave analysis are shown.

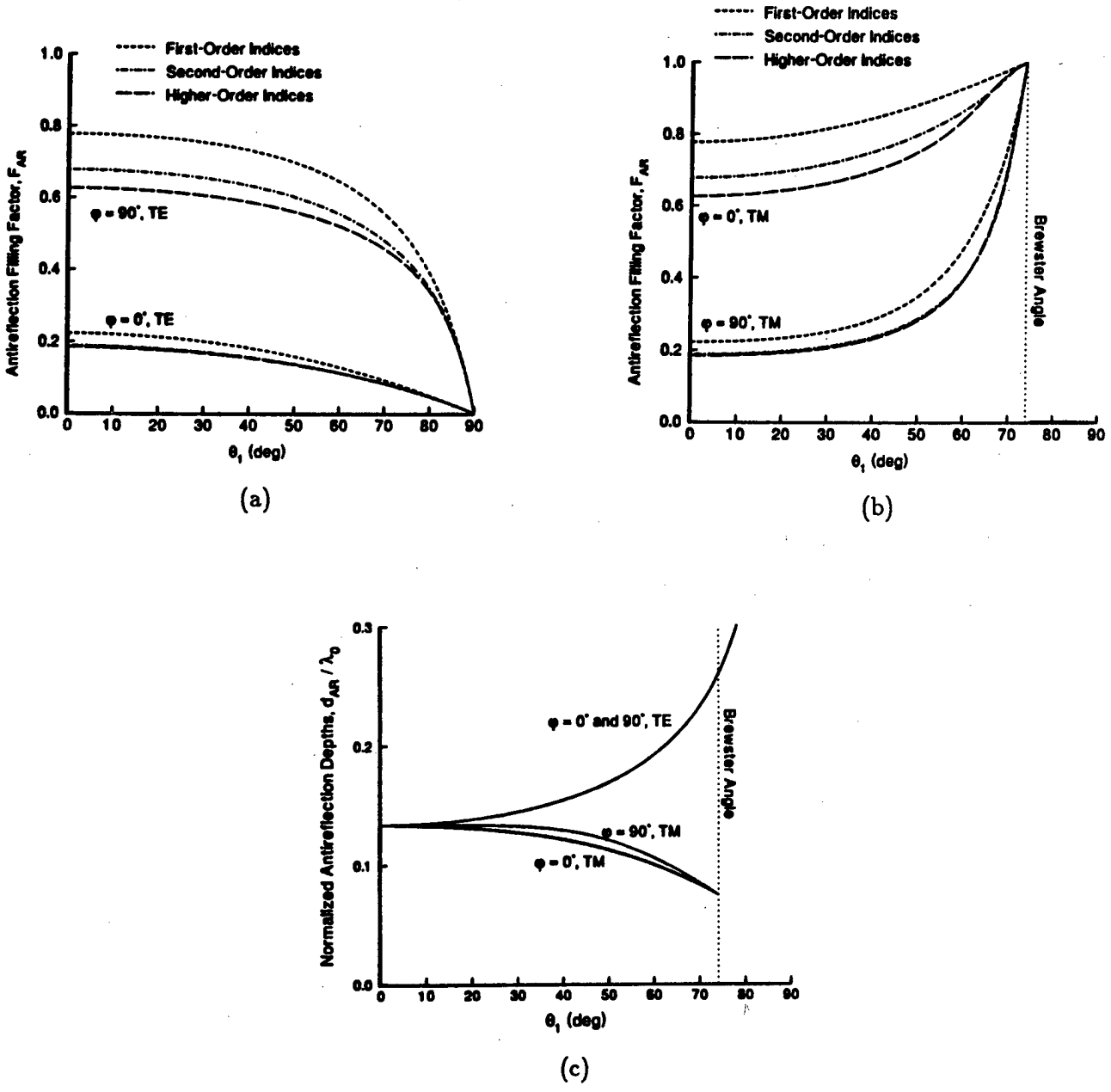

Fig. 5: The filling factor F of a rectangular groove surface-relief antireflection grating on silicon substrate at $\lambda_0 = 1.5\,\mu$m and at $\lambda_0/\Lambda = 3.0(?)$ as a function of the polar angle of incidence θ: (a) for $\phi = 0$ or 90 deg and TE incident polarization, and (b) for $\phi = 0$ or 90 deg and TM incident polarization. (c) The corresponding normalized groove depths ($/\lambda_0$) of the antireflection gratings for the same cases as in (a) and (b).

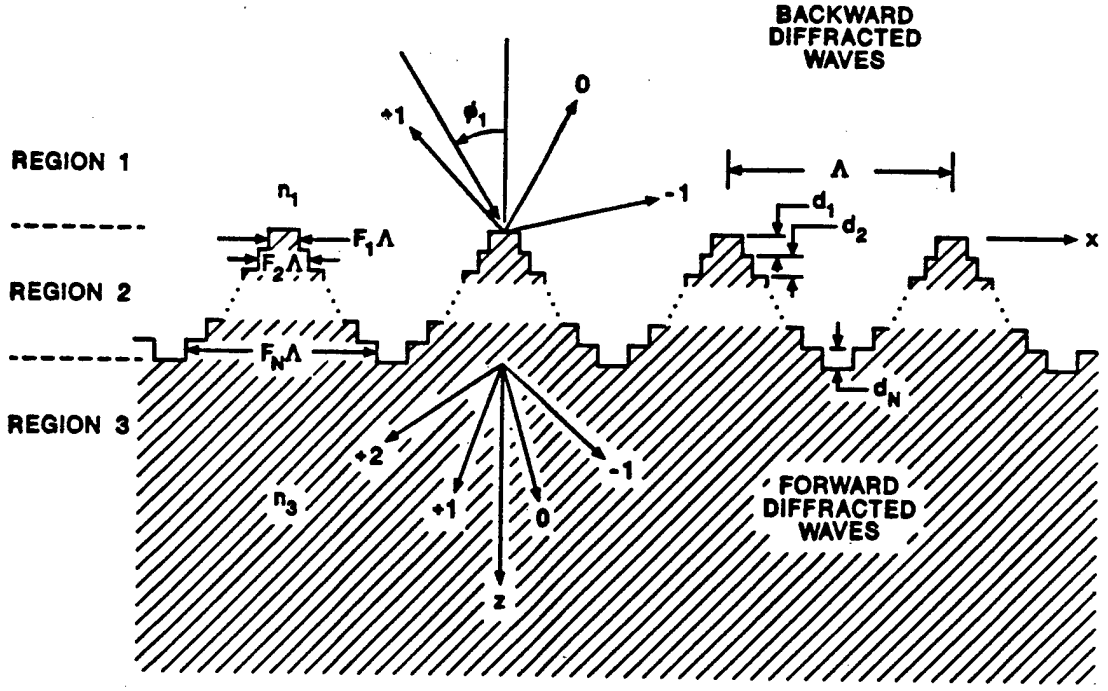

Fig. 6: Cross-sectional view of a multilevel (N-level) stairstep surface relief grating.

Table I: Grating Broadband Antireflection Surfaces on Silicon

Design parameters for grating quarter-wave (broadband antireflection surfaces) transformers for normal ($\phi_1 = 0°$) incidence on silicon ($n_3 = 3.5$) at center freespace wavelength $\lambda_0 = 1.5\mu$m. The filling factors F_{TE} (for TE polarization), F_{TM} (for TM polarization) and the groove depths d_i's, are summarized for two and three section maximally flat and equal-ripple transformers. Input region is air ($n_1 = 1.0$).

		Maximally-Flat			Equal-Ripple		
Levels	Layer						
N	i	d_i (μm)	F_{TE}	F_{TM}	d_i (μm)	F_{TE}	F_{TM}
2	1	0.2742	0.0774	0.5068	0.2821	0.0682	0.4727
	2	0.1465	0.4931	0.9226	0.1612	0.3923	0.8877
3	1	0.3206	0.0327	0.2928	0.3202	0.0330	0.2951
	2	0.2004	0.2222	0.7778	0.2139	0.1842	0.7345
	3	0.1253	0.7072	0.9673	0.1429	0.5229	0.9307

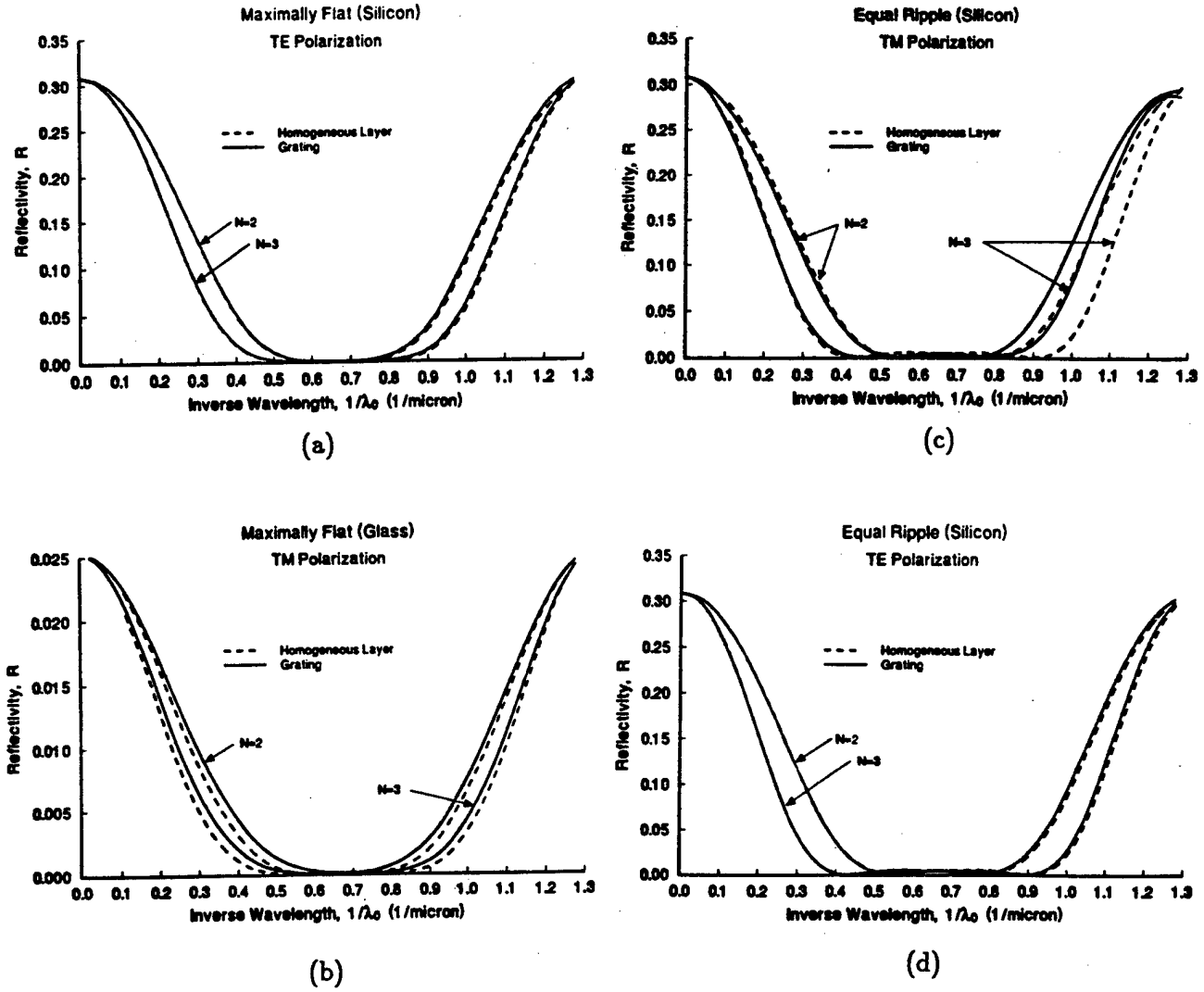

Fig. 7: Reflectivity R (zero-order backward-diffracted efficiency) of a silicon multilevel surface-relief maximally-flat antireflection grating for 2 or 3 levels as a function of the inverse wavelength at normal incidence. The solid curves represent the rigorous coupled-wave analysis results while the dashed lines represent the effective homogeneous layer whith first-order indices results; (a) for TE polarization and (b) for TM polarization. (c) and (d) the same results for an equal-ripple antireflection grating.

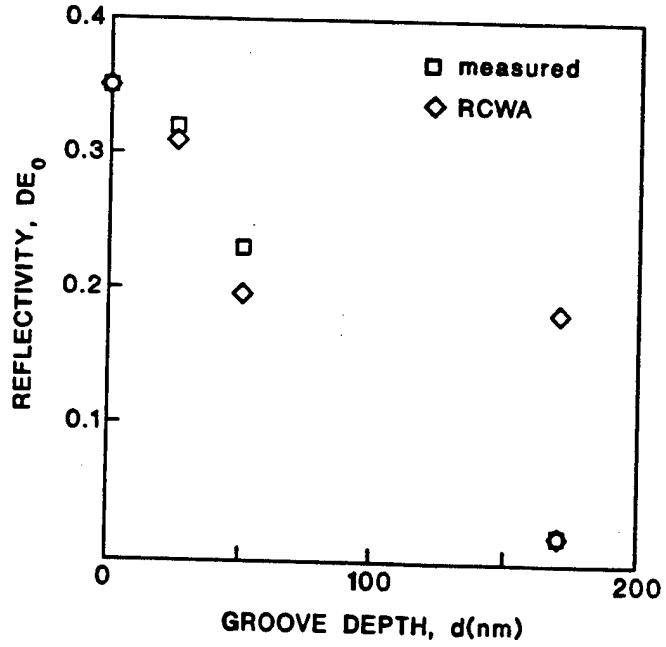

(a)

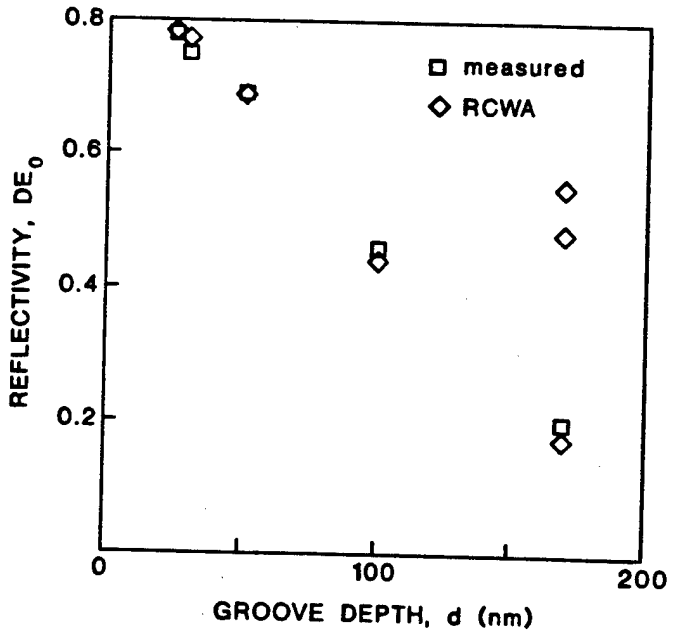

(b)

Fig. 8: Comparison of experimental and theoretical data (computed using the rigorous coupled-wave analysis) for different Si gratings using single or double cascaded gratings approximations. (a) Silicon gratings at room temperature, (b) silicon plasma gratings.

Scalar Limitations of Diffractive Optical Elements

Eric G. Johnson and Diane Hochmuth
Teledyne Brown Engineering
Sensor Systems Department
300 Sparkman Drive
Huntsville, Alabama 35807

M.G. Moharam and Drew Pommet
CREOL, University of Central Florida
Orlando, Florida

ABSTRACT

In this paper, scalar limitations of diffractive optic components are investigated using coupled wave analyses. Results are presented for linear phase gratings and fanout devices. In addition, a parametric curve is given which correlates feature size with scalar performance.

1. INTRODUCTION

Diffractive Optical Elements (DOE) are utilized in optical computing architectures, fiber optic systems, imaging cameras and numerous optoelectronic devices[1]. The major advantages are realized in coherent systems, due to the inherent chromatic behavior of these elements. Since DOE's are fabricated using standard photolithographic equipment, the feature sizes can be on the order of wavelengths. However, when the features are a few wavelengths, as is the case for fast microlens arrays, the scalar assumptions are no longer valid. To address this issue, exact electromagnetic modeling must be incorporated in the design process.

In this paper, the rigorous coupled wave formulation is implemented to determine where the separation is between the scalar theory and exact formulations. First, an analysis is presented for a discrete linear phase grating to demonstrate the polarization and coupling effects as a function of period size. Second, a Dammann fanout device is analyzed to demonstrate the effects on beam uniformity as a function of both polarization and period size. Third, an attempt is made to characterize the effect of feature sizes characteristic in multilevel structures.

2. THEORY

Diffractive optic components rely on phase perturbations in the transmitted wavefront to diffract the light. Quite often this is performed using 2π structures etched into a glass substrate using standard photolithographic techniques. Figure 1 illustrates a collapsed diffractive lens. This plate can be viewed as a series of zones diffracting energy into a prescribed diffraction order, as the zones move away from the center they become smaller since they are required to diffract energy through larger angles. Therefore, the smaller zones can be modeled as a dielectric grating since adjacent zone dimensions do not significantly change. For a multilevel diffractive optic, the -1 diffraction efficiency can be approximated using scalar diffraction theory as follows:

$$DE_{-1}=T^2\left(\frac{\sin\left(\frac{\pi}{N}\right)}{\left(\frac{\pi}{N}\right)}\right)^2 \qquad (1)$$

where, T represents the transmission coefficient squared and N is the number of phase levels used to approximate the profile. To determine the diffraction angle for a given zone, the grating equation is employed

$$\sin \theta_{-1} = \frac{\lambda}{(n)(\text{period})} \tag{2}$$

where λ is the wavelength and n is the index of refraction. The period is the zone size which is modeled as a grating unit cell. Another side effect of the small zones is that the scalar, or paraxial, assumptions associated with diffraction efficiencies are no longer valid and more robust techniques are required. Therefore, Maxwell's equations must be implemented to accurately model the polarization sensitivities and resonances present in small structures. Although numerous formulations exist under diverse titles, the majority require solutions to a system of differential or integral equations. The most common technique used for dielectric grating profiles is the coupled-mode approach, wherein a system of differential equations is solved[2]. The first step is to expand the fields in the incident and transmitted regions in terms of a common basis set representational of the floquet modes

$$\vec{E}_1(x,y) = \vec{E}_{inc}(x,y) + \sum_n \vec{R}_n e^{j(\alpha_n x + \beta_n^1 y)}$$

$$\vec{E}_2(x,y) = \sum_n \vec{T}_n e^{j(\alpha_n x + \beta_n^2 y)} \tag{3}$$

Since the modulated region is a multilayer structure of air/dielectric rectangles, it is expanded in the same basis set. This yields the following set of equations for the fields and modulated index:

$$E(x,y) = \sum_n E_n(y) e^{j\alpha_n x}$$

$$H(x,y) = \sum_n H_n(y) e^{j\alpha_n x}$$

$$\varepsilon(x,y) = \sum_m a_m(y) e^{j\alpha_m x}$$

$$\frac{1}{\varepsilon(x,y)} = \sum_m b_m(y) e^{j\alpha_m x} \tag{4}$$

operating on these field components with the curl equations, a set of coupled differential equations is formed for the modulated region

$$\frac{d}{dy}\begin{bmatrix} E_n \\ H_n \end{bmatrix} = \begin{bmatrix} A_{nm} & B_{nm} \\ C_{nm} & D_{nm} \end{bmatrix} \begin{bmatrix} E_m \\ H_m \end{bmatrix} \tag{5}$$

Then, an eigenvalue/vector computation is performed to derive the solution set for each sublayer.

$$E(x,y) = \sum_n \sum_m C_m W_{nm} e^{(\lambda_m y + j\alpha_n x)}$$

$$H(x,y) = \sum_n \sum_m C_m W_{nm} e^{(\lambda_m y + j\alpha_n x)} \tag{6}$$

After this is accomplished, the fields are matched to the incident and transmitted regions for computing the **Rn** and **Tn** coefficients. These are then used to compute the diffraction efficiencies and field values at any desired point.

3. NUMERICAL RESULTS

3.1 LINEAR PHASE GRATING

In order to determine where the scalar theory breaks down with a linear phase grating, a multistep grating was modeled using the coupled wave theory. Figure 2 illustrates an eight phase level structure with the polarizations defined as E and H, where E is parallel to the grooves and H is when the E lies in the plane of incidence. The computed diffraction efficiency for the -1 order is illustrated in Figure 3 as a function of period size and index of refraction. As can be expected for periods approximately a few wavelengths in size, scalar theory breaks down; whereas, for periods greater than 20 wavelengths the performance is close to scalar. Moreover, as the index is increased the scalar approximation is realized at smaller periods.

As was previously mentioned, the primary mechanism in the diffraction process is the phase modulation; therefore, to diffract the energy into the -1 order, the phase should be a stepwise linear approximation across the unit cell. To verify that the phase was linear after immediately passing through the profile, a scan of the phase was computed for both large and small period sizes. Figures 4 and 5 represent the results for both polarization states at period sizes of 2 and 20 wavelengths respectively. The small period demonstrated a complex phase profile for both E and H modes which signified a departure from scalar theory. In the 20 wavelength case, both polarizations demonstrated a well defined linear phase function close to the scalar approximation.

3.2 FANOUT DEVICES

Another area of interest is in fanout phase grating structures. Although numerous techniques exist for beam splitting, one of the most common is a Dammann grating as illustrated in Figure 6. Due to the thickness of the grating structure, the transmitted light assumes a 0 or π phase shift which is then used to diffract the light into a predetermined number of diffracted orders with uniform intensity[3]. However, as the number of desired spots is increased, so is the number of transition points in the grating profile. The increase in the number of transition points forces smaller features in the grating design which must be investigated using rigorous modeling techniques.

As an example, a five beam Dammann device was analyzed as a function of feature size. Figure 7 illustrates the unit cell which was designed in glass (n=1.5). This design was optimized using a steepest descent algorithm with scalar assumptions for a spot uniformity of less than 1% and an average DE of 14.9%. Uniformity is defined as follows:

$$\%\text{Unif} = 100\times\left(\frac{P_{max}- P_{min}}{P_{avg}}\right) \tag{7}$$

Figures 8 and 9 illustrate the spot uniformity and average DE as a function of period size for the 5 beam array. These results demonstrated polarization sensitivities and an unacceptable beam uniformity for period sizes up to 50 wavelengths. Therefore, to obtain acceptable performance out of a Dammann device, the period must be hundreds of wavelengths when there are small features.

3.3 FEATURE SIZE STUDY

Many concerns exist as to when scalar theory actually breaks down and how do you design around this phenomena. Additional studies have implicated that it is not the period size, but the actual feature size relative to a wavelength that causes the separation from scalar. In an attempt to verify this effect, numerous analyses were performed on a biphase-level structure

with alternate fill factors as illustrated in Figure 10. Seven fill factors were analyzed: 0.9375, 0.875, 0.75, 0.5, 0.25, 0.125, and 0.0625. Since most of the scattering occurs at the corners of the structure, only the E mode was analyzed with the coupled wave theory. The -1 order diffraction efficiency was compared to Fourier theory as a ratio. Figure 11 illustrates the result for an index of refrection of 1.5. The implications of these results signify extreme fluctuations in the DE as a function of feature size and as the index of refraction is increased, the effect is diminished.

4. CONCLUSIONS

In this study, the rigorous coupled wave approach was used to investigate the scalar limitations of diffractive optics. This analysis verified that coupling effects influence the diffraction efficiencies of the multistep phase gratings. Additionally, polarization sensitivities were observed for Dammann gratings with small features. Considering these findings, rigorous analyses must be performed when designing DOE's with feature sizes on the order of a wavelength. Areas of additional studies include the dispersive effects of multliphase structures, and angle of incidence effects. Further developments in the analytical tools are also required to adequately predicts the three-dimensional diffraction of microlens structures. Moreover, alternate formulations from the coupled mode approach are needed due to the increased ode coupling of a three-dimensional structure.

5. ACKNOWLEDGEMENTS

The authors would like to thank Anthony Cook, Jeff Howard and Jo Knight of Teledyne Brown Engineering for assisting in this effort. Also, Alan Kathman for his continual technical support and motivation.

6. REFERENCES

1. Alan Kathman and Eric Johnson, "Binary Optics; New Diffractive Elements for the Designer's Tool Kit. Photonics Spectra,, pp. 125-132, September 1992."

2. Moharam, M. and Gaylord, T. "Diffractive Analysis of a Surface Relief Grating," JOSA A. , Vol. 72, pp. 1385-1392, Oct. 1982.

3. Krackhardt. U. and Streibl, N. "Design of Dammann-Gratings for Array Generation," Optics Communications., Vol. 28, pp. 1267-1275, Dec. 1989.

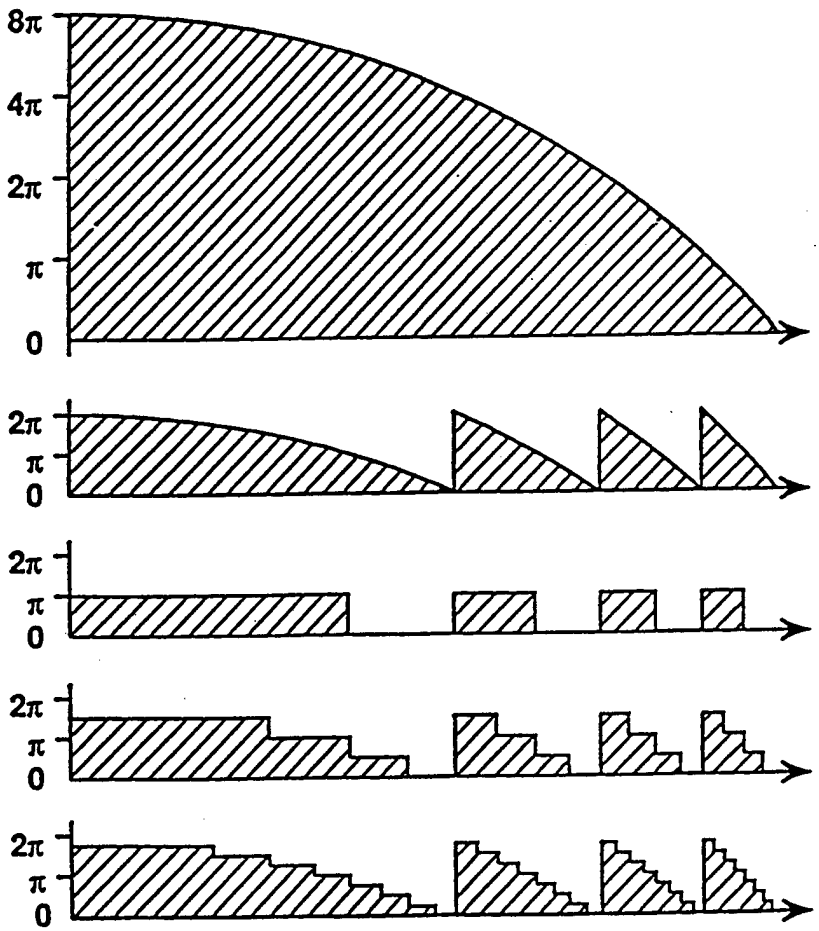

Figure 1. Diffractive collapsed-phase lens.

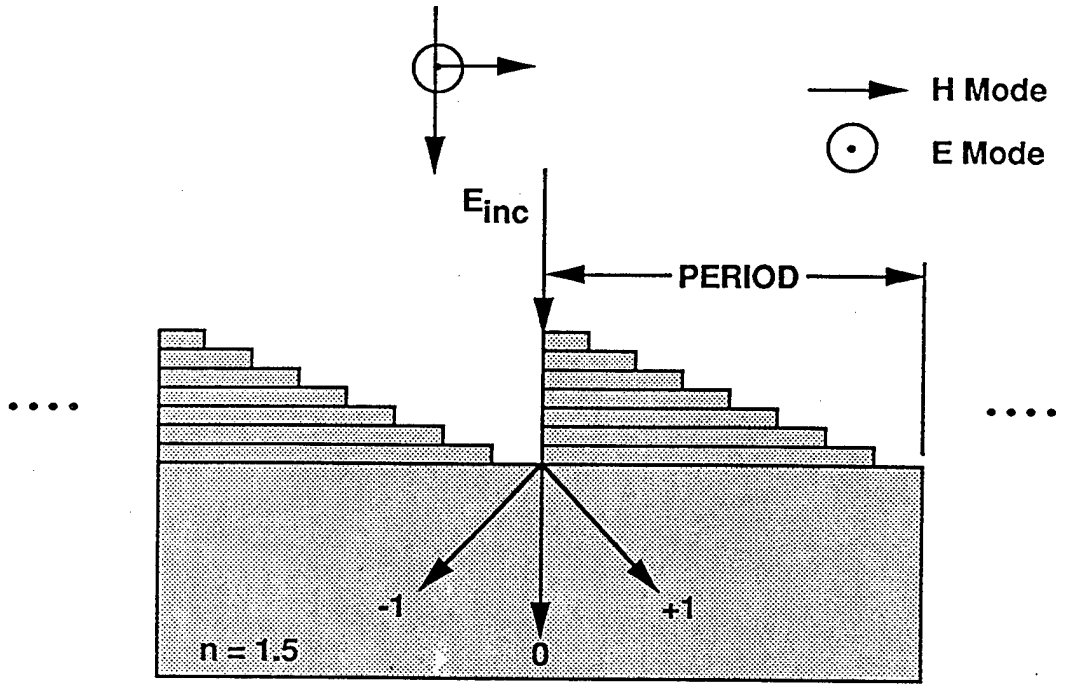

Figure 2. Linear phase grating geometry.

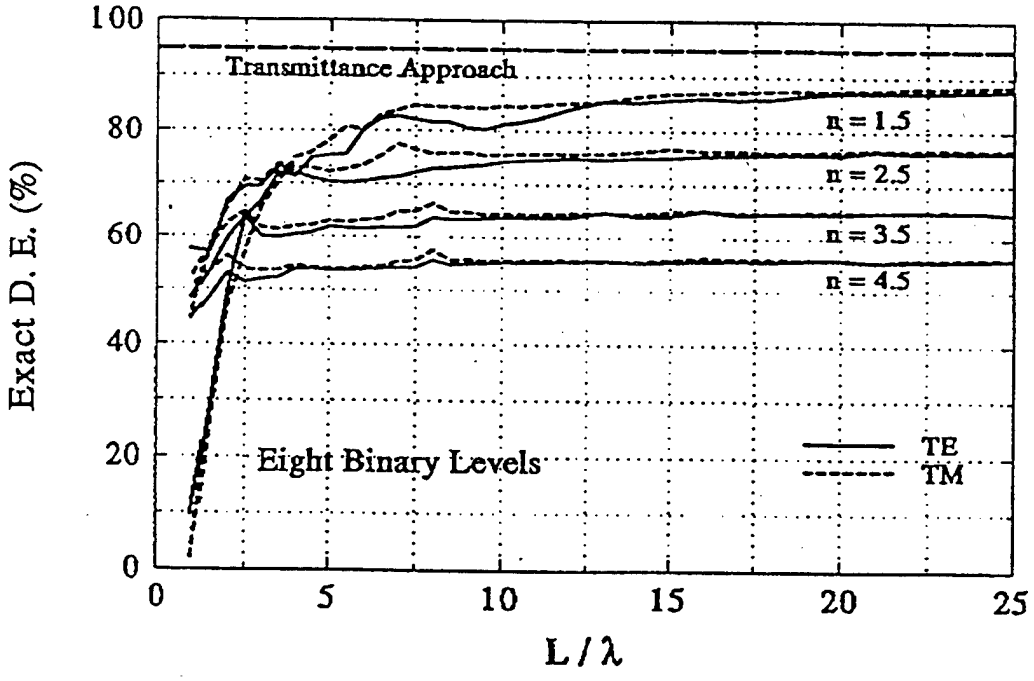

Figure 3. -1 DE comparison for an eight phase level grating.

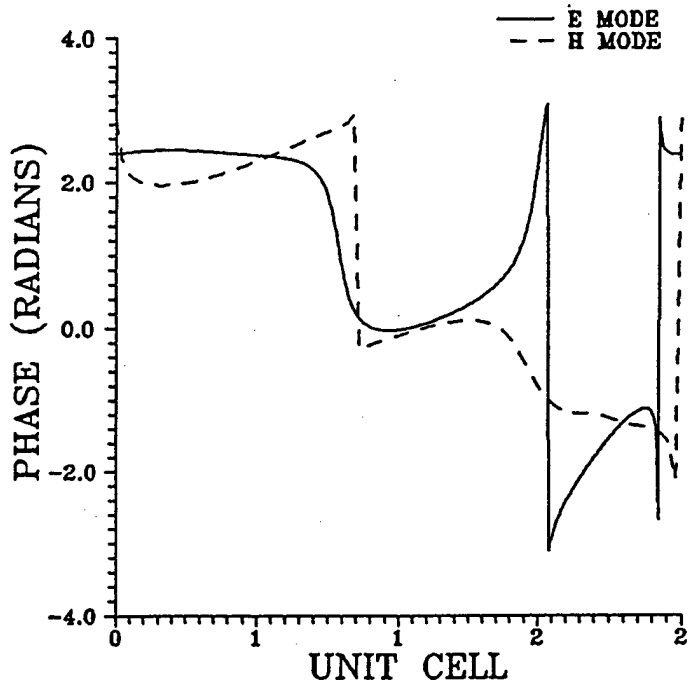

Figure 4. Eight level phase computation for two wavelength period.

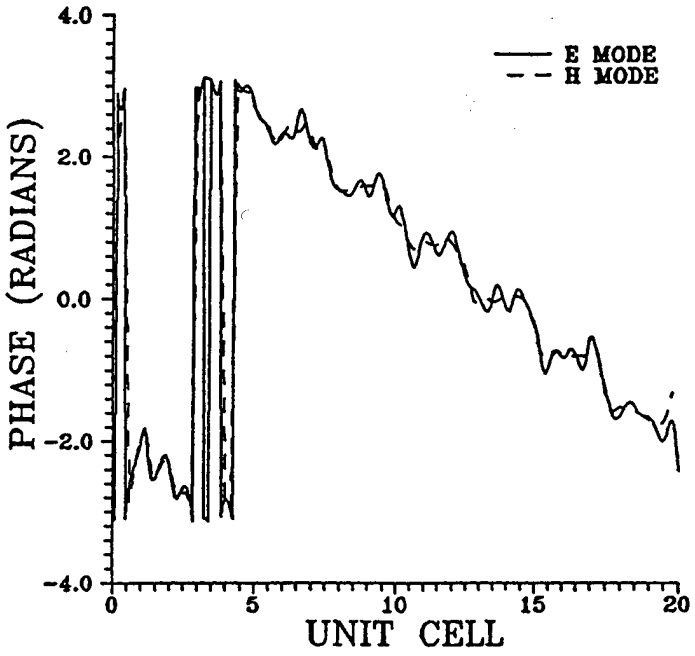

Figure 5. Eight level phase computation for twenty wavelength period.

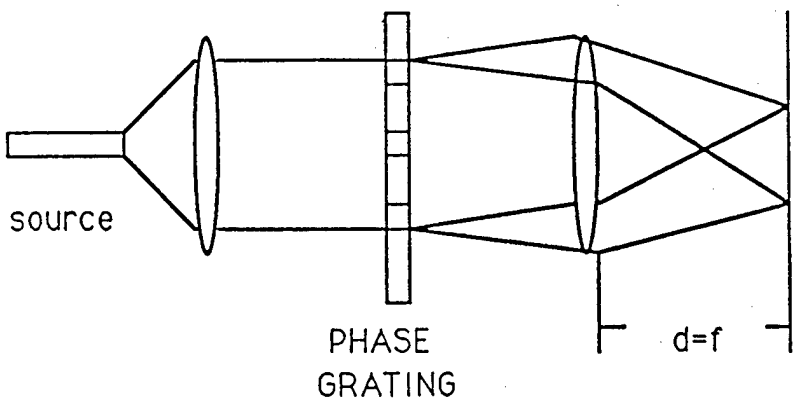

Figure 6. Optical implementation of a Dammann grating.

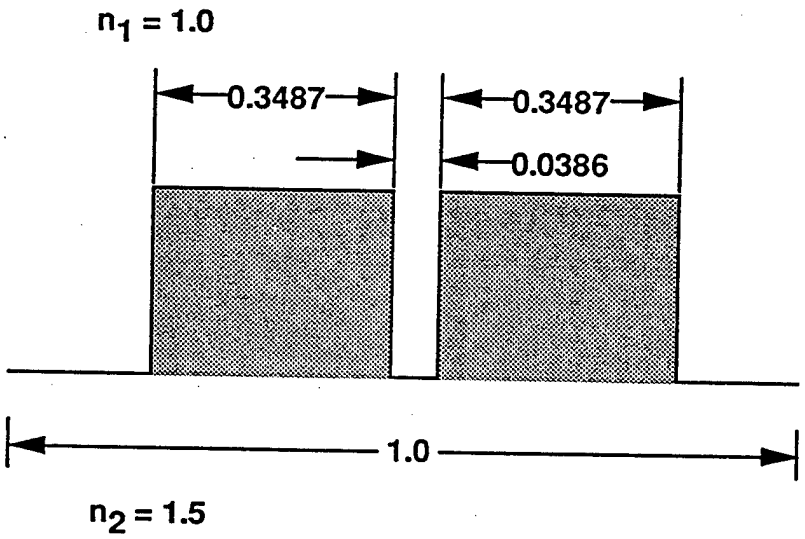

Figure 7. Dammann 5 beam unit cell.

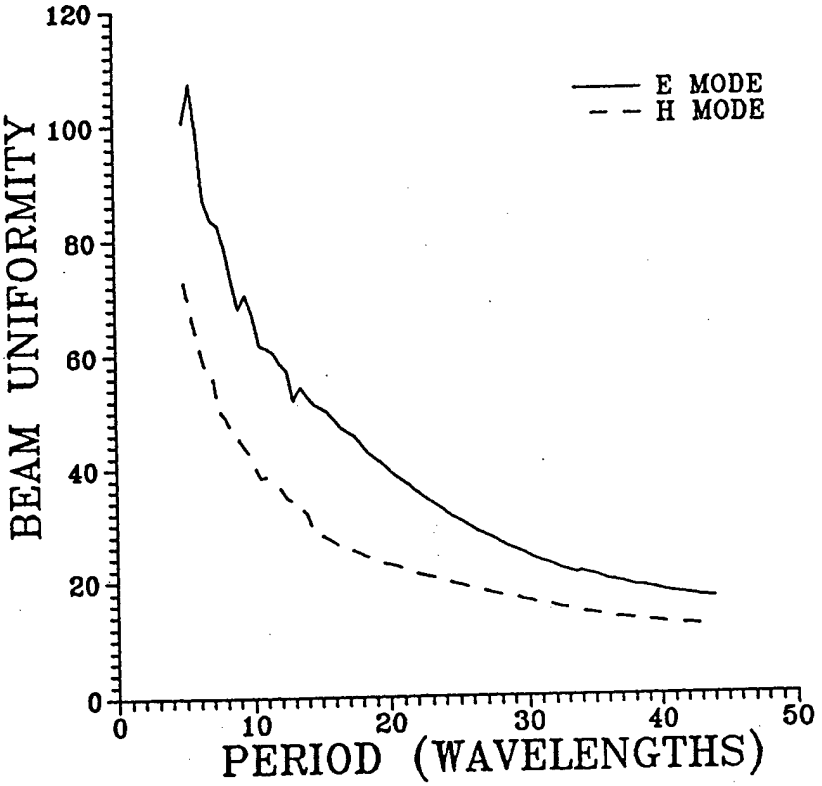

Figure 8. Computed beam uniformity for a 5 beam Dammann device.

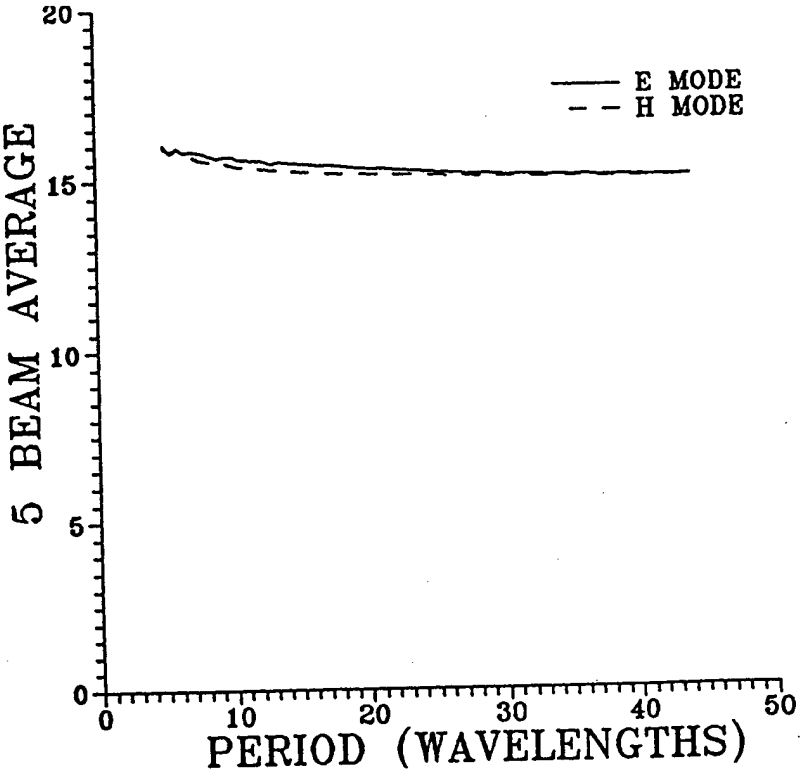

Figure 9. Computed average for a 5 beam Dammann device.

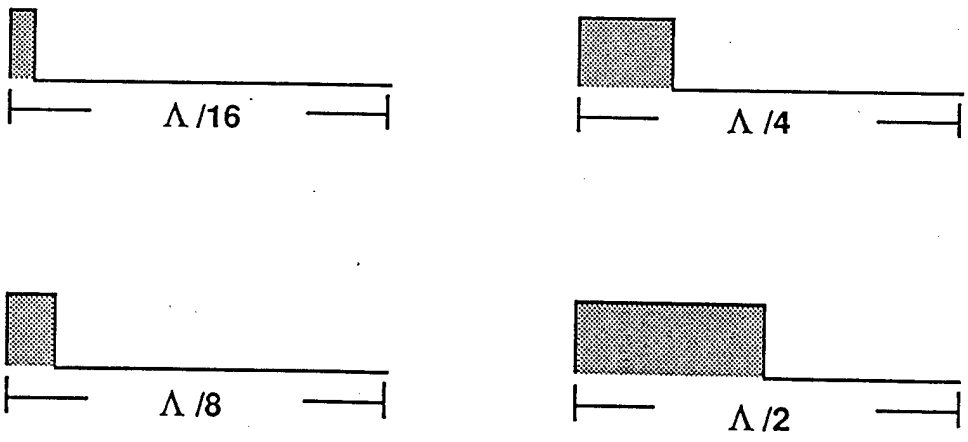

Figure 10. Fill factor geometry.

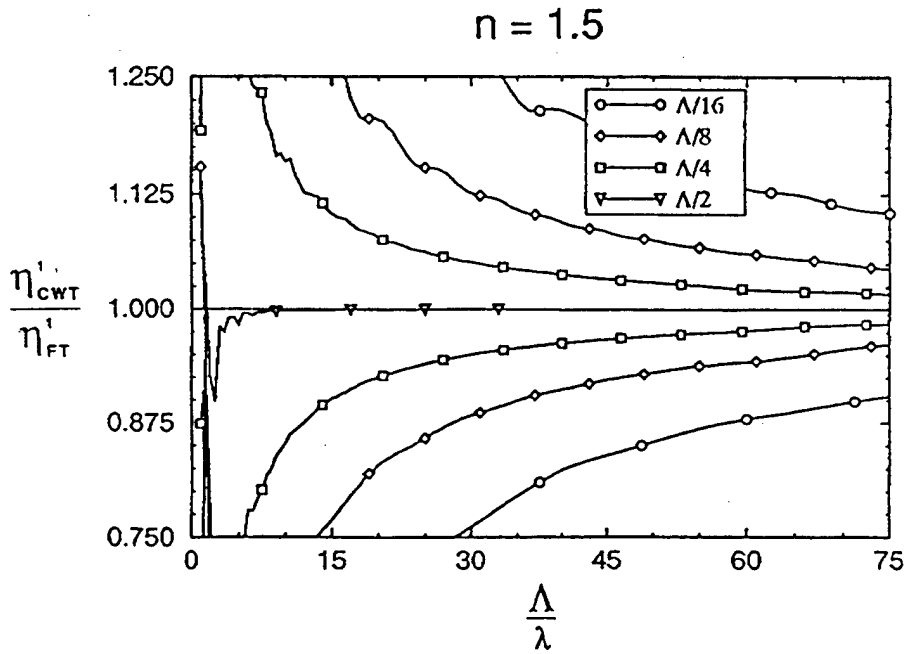

Figure 11. Exact and scalar comparisons for E mode as a function of feature size.
(fill factors > 0.5 are given in the lower half)

Subwavelength Structured Surfaces and their Applications

Daniel H. Raguin and G. Michael Morris

The Institute of Optics, University of Rochester, Rochester, NY 14627, (716) 275-8008

1. Introduction

The term subwavelength structured (SWS) surface describes any surface that contains a subwavelength-period grating or gratings, see Fig. 1. The grating may be of any type (e.g., surface-relief, phase, or amplitude) provided the period is sufficiently fine so that, unlike conventional gratings, no diffraction orders propagate other than the zeroth orders. Because of the fine periods involved, the fabrication of such surfaces for applications in the visible and infrared (IR) portions of spectral regime have only recently been considered. With refinements in holographic procedures and the push of the semiconductor industry for submicron lithography (both through optical and electron beam techniques), production of SWS surfaces is becoming increasingly viable.

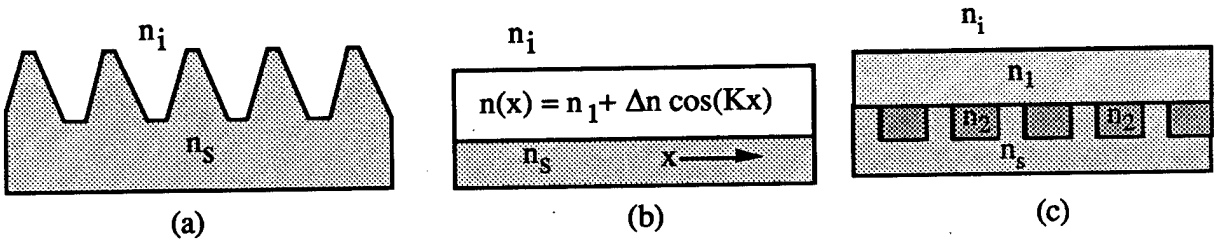

Fig. 1. Possible SWS surface geometries: (a) surface-relief profile, (b) phase grating, and (c) embedded surface-relief profile.

There are numerous applications for SWS surfaces: antireflection coatings, polarization components, narrow-band filters, and phase plates. As antireflection components, SWS surfaces are called antireflection structured (ARS) surfaces and have been studied extensively both theoretically and experimentally (see, for example, Refs. 1-7). Typically, ARS surfaces contain surface-relief gratings, see Fig. 1(a), which impedance match two media where one is a solid, and the other a gas, liquid, or solid. By structuring a surface with a subwavelength-period pattern (either through etching, embossing, or other techniques), one can synthesize an appropriate index of refraction distribution so that surface reflections are minimized. When designed properly, these structures can operate over large spectral bandwidths and fields of

view.[6] Because foreign materials are not being added to the substrate surface, problems commonly encountered in thin-film technology, such as cohesion and thermal expansion mismatches, are non-existent in the design of these structured surfaces. Although relatively new to mankind, ARS surfaces can be found on the cornea of certain night-flying moths.[8] The subwavelength structures of the moth's cornea reduce surface reflections which would otherwise betray the moth's position to its predators. The first scientists to investigate ARS surfaces for application in the visible or near-IR portion of the spectrum worked to replicate *moth-eye* surfaces (see, for example, Ref. 1). Only later were non-*moth-eye* profiles investigated.[2-7]

As polarization components, SWS surfaces may take any form diagrammed in Fig. 1. These surfaces operate on the fact that unlike in the scalar diffraction regime (where the surface period is large compared to the incident wavelength), when feature sizes are on the order of a wavelength, then, in general, radiation will react to the surface differently depending on the electric field's polarization orientation. SWS surfaces may be used to fabricate wire grid polarizers,[9] beam splitters,[10] waveplates and retarders,[11, 12] and polarizing mirrors.[13] SWS surfaces may be applied to any portion of the electromagnetic spectrum while conventional polarization devices must rely on the existence of a suitable birefringent material for the particular wavelength range of interest. Since the magnitude of the effective birefringence Δn (equal to $n_e - n_o$, where n_e and n_o are the structure's effective extraordinary and ordinary indices of refraction, respectively) can be quite large (e.g., for fused silica $\Delta n \approx -0.1$, for ZnSe $\Delta n \approx -0.65$, and for GaAs $\Delta n \approx -1.7$), the grating of a SWS surface need not be deeper than the wavelength of the incident radiation. Consequently, SWS surfaces are less bulky than conventional polarization devices and offer the possibility of replacing several conventional elements with a single structured one (e.g., beamsplitter waveplates or mirror waveplates).

A typical geometry of SWS surfaces for use as narrow-band filters is illustrated in Fig. 1(c). By filling the grooves of the grating with a material of index n_2 where n_2 is larger than n_1 or n_S, the structure can support the propagation of leaky waveguide modes. Coupling between the incident field and these leaky modes results in extremely sharp changes in the structure's spectral characteristics as a function of angle of incidence and wavelength. It is due to the highly selective coupling criterion of the waveguide mode that these structures can exhibit extremely narrow filter linewidths ($\Delta\lambda/\Lambda = 10^{-7}$).[14] Applications employing narrow-band filters are numerous. One field which can benefit tremendously from this new technology is the laser field. Laser end mirrors may be fabricated to reflect 100% of the incident radiation for a fixed wavelength. Since the narrow-band filter effects are polarization dependent, a laser with a SWS end mirror does not need any Brewster windows. Since the reflection spectra of these

SWS surfaces change remarkably as a function of incident angle, M. T. Gale has suggested utilizing these devices for security applications much in the same way that holograms are used on credit cards today.[15]

SWS surfaces may also be used as an alternative method of fabricating phase plates.[16, 17] By fabricating a binary SWS surfaces in which the duty cycle of the profile varies across the surface, any desired phasefront may be imparted onto the incoming radiation. Although the physical profile depth encountered by the radiation is the same at all points across the surface, due to the surface's changing filling factor, the optical path length accounted by the radiation will vary from point to point. By using a binary profile with subwavelength features, efficiencies may still be high (unlike binary profiles in the scalar regime) without resorting to a multi-mask fabrication process.

2. Analytic Approaches

To analyze SWS surfaces, the use of vector diffraction theory is required since due to the feature sizes involved, scalar diffraction theories are completely invalid. Both coupled-wave and modal approaches are valid (and equivalent) techniques for modeling radiation's interaction with SWS surfaces.[18] The vector analysis performed for the research presented takes advantage of the rigorous coupled-wave analysis (RCWA) proposed by Gaylord and Moharam.[18, 19]

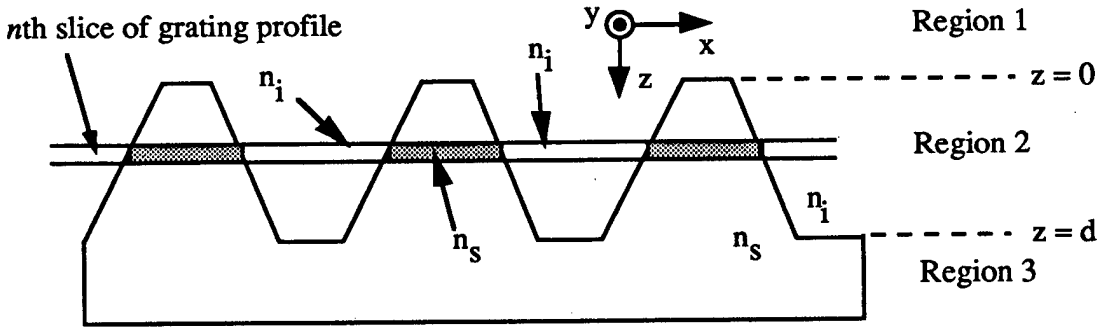

Fig. 2. Grating geometry. In rigorous coupled-wave analysis (RCWA), a grating with a continuous profile is approximated by an *N*-level profile where each layer or slice is analyzed as a thin grating.

RCWA approaches the problem by solving Maxwell's equations without making any assumptions regarding the profile period or depth. Grating profiles which vary as a function of depth, such as the continuous surface-relief profile diagrammed in Fig. 2, are approximated by *N* slices where in each slice, the optical parameters have no *z* dependence (a continuous surface-

relief profile is therefore represented as a multi-level profile). Provided that each slice is sufficiently thin, a grating which varies in z may be accurately modeled. Each slice of the grating region (Region 2) is treated as a thin grating and the fields within the slice expanded using the Floquet condition. These fields are substituted into the wave equation, resulting in an infinite set of second-order coupled-differential equations for the field space-harmonic amplitude. This set of equations is reduced to a doubly infinite set of first-order coupled-differential equations using a state-space representation. The space-harmonic amplitudes are extracted in terms of eigenvalues and eigenvectors of the resulting coefficient matrix. Maxwellian boundary conditions are then applied to the harmonic field amplitudes at each layer as well as at the boundaries of the incident medium (Region 1) and the substrate medium (Region 3). Reflection and transmission coefficients are obtained from the amplitudes of the propagating orders in Region 1 and Region 3, respectively.

Like most numerical techniques, RCWA, due to its intensive computational requirements, offers little opportunity for intuitive insight into the diffraction mechanisms. An alternative method for analyzing SWS surfaces is through effective medium theory (EMT). By relying on the fact that the structures have feature sizes smaller than the incident wavelength, an approximate description of the interaction of radiation with such structures can be obtained. The results are analytic and offer a great deal of insight towards the radiation's behavior.

Effective medium theories (EMTs) rely on the fact that when light interacts with periodic structures finer than its wavelength, it does not diffract, but instead reflects and transmits as if it is encountering a non-structured medium. EMTs describe the interaction of light with such subwavelength structures by representing regions of subwavelength heterogeneity in terms of a homogeneous material possessing a single set of effective optical constants: permittivity ε, permeability μ, and conductivity σ. This is sensible since no energy is lost to diffracted orders. All the energy is contained in the zeroth transmitted and zeroth reflected orders. The optical properties of the effective medium is governed by the specific structural intermixing between the incident and substrate material, but in general, the more substrate material present as compared to incident material in a given region, the closer that region's optical properties are to that of the substrate. In other words, when light interacts with subwavelength structures, it reacts to them as if it were encountering an effective medium whose optical properties are a weighted spatial average of the profile region's optical properties. For the specific case of a multi-level surface-relief profile, see Fig. 3(a), the effective medium will be a film stack where each layer of the film stack corresponds to a distinct level of the surface-relief profile. For a continuous profile, see Fig. 3(b), the effective medium will be a gradient film. Because the effective medium results from the weighted spatial averaging of the profile region's optical properties, the optical

properties of the effective medium must be bound by the properties of the incident medium and those of the substrate medium. Therefore, assuming $n_i < n_s$, in Fig. 3(a), $n_i < n_1 < n_2 < n_3 < n_s$, and in Fig. 3(b), $n_i \leq n(z) \leq n_s$.

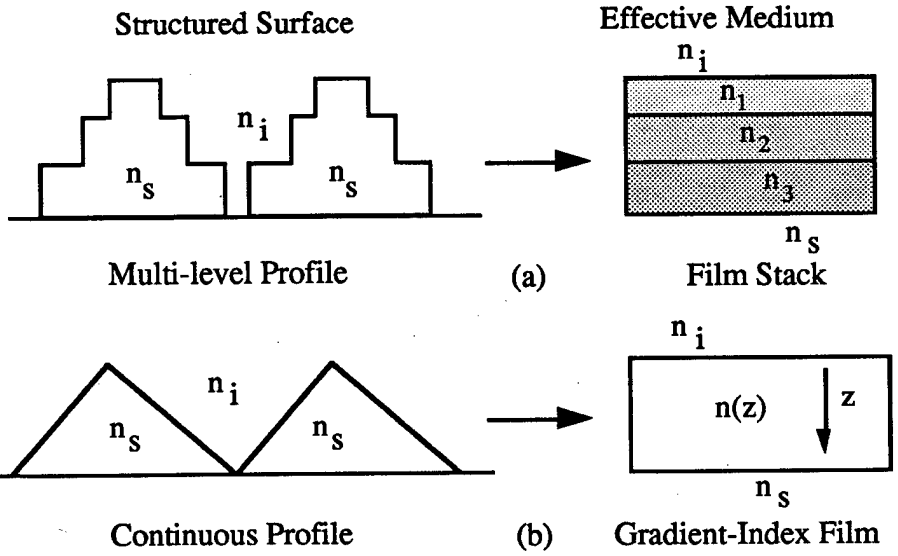

Fig. 3. Effective mediums: (a) for a multi-level surface profile the effective medium is a film stack, and (b) for a continuous surface profile the effective medium is a gradient-index film.

3. One-Dimensional Periodic Stratification and Effective Medium Theory

A one-dimensional (1-D) profile, see Fig. 4, is one of the more common profiles used by optical engineers. This profile may be fabricated through numerous techniques including optical and e-beam lithography, holography, and diamond ruling. Conventionally termed a linear diffraction grating, by making the period fine enough (or the incident wavelength large enough), these structures form one class of SWS surfaces. By determining the effective index of refraction at each depth z into the profile, the effective medium of the grating region is determined. Note that the effective index at a level $z = z_0$, is a function of the filling factor $f(z_0)$ at that level, where the filling factor describes the fraction of substrate material present in a period Λ, see Fig. 4(b).

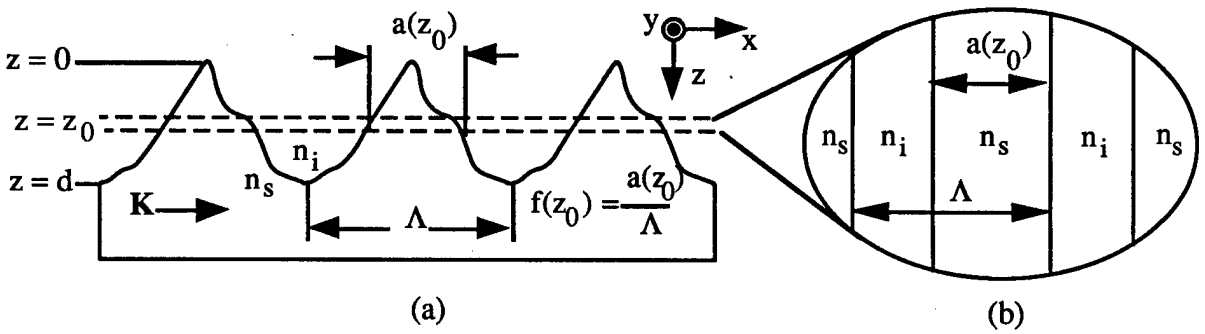

Fig. 4. General surface-relief SWS surface. In (a) the profile geometry is diagrammed, while in (b) the stratification present at a depth $z = z_0$ is illustrated. The filling factor at a depth z_0 is equal to $f(z_0) = a(z_0)/\Lambda$.

To describe 1-D ARS surfaces, previous authors have utilized zeroth-order EMT, see for example, Refs. 3 and 4. We have found that for most cases (particularly those in which the profile period is only several times smaller than the incident wavelength and/or in substrate materials whose permittivity is large compared to that of the incident medium's), the use of higher-order EMT produces more accurate results when compared to rigorous vector data.[6] The inaccuracy of zeroth-order EMT is due to the static approximations made in solving for the electromagnetic fields. These approximations result in expressions for the effective optical properties of a structure being independent of the incident wavelength λ and the period of the grating Λ. With the use of higher-order EMT, the dependence of the effective optical properties on λ and Λ is not neglected.

The higher-order EMT we use is based upon work by S. M. Rytov.[6, 20, 21] As is the case for zeroth-order EMT, higher order EMT predicts that the effective index of refraction for a 1-D SWS surface is dependent upon the orientation of the electric field **E** in relation to the grating vector **K**. The amount of birefringence, Δn, a 1-D SWS surface possesses may be defined as

$$\Delta n = n_{\mathbf{E}\|\mathbf{K}} - n_{\mathbf{E}\perp\mathbf{K}}. \tag{1}$$

4. Design of Waveplates using Form Birefringence

As may be noted in Section 3, a 1-D subwavelength stratification behaves as an effectively birefringent medium. Since this birefringence is the result of the form of the intermixing of two materials and not due to any molecular birefringence, this effect is termed form birefringence. Form birefringence thus enables the fabrication of polarization components,

such as waveplates, using isotropic materials. In Fig. 5 we diagram RCWA data for the spectral response of a ZnSe quarter-wave plate fabricated using a SWS binary profile.

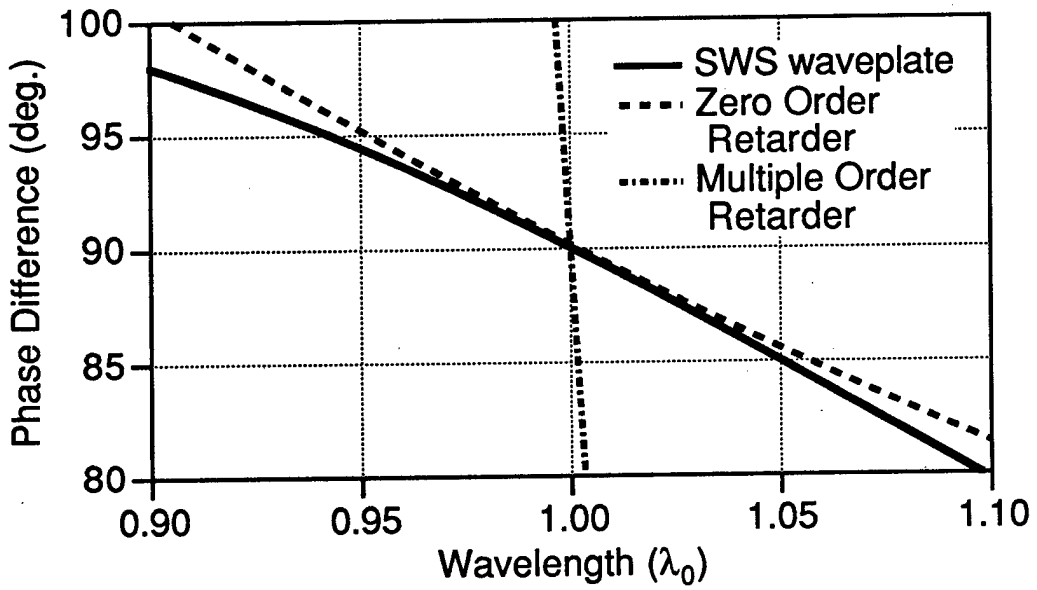

Fig. 5. Spectral performance of a SWS quarter-wave plate as compared to conventional zero-order and multiple-order wave plates.

Due to the large amount of effective birefringence for a ZnSe binary structure, the binary grating need not be very deep ($d = 0.455\lambda_0$) to achieve a quarter-wave retardance. For comparisons sake, the wavelength dependence of conventional waveplates, if they existed in the near-IR region of the spectrum, are included. Note that the spectral characteristics of a SWS waveplate is similar to that of a zero-order waveplate. This is not surprising since both devices impart a phase difference of exactly $\Delta\phi = \pi/2$ on the incident radiation. A multi-order waveplate, on the other hand, imparts a phase difference of $\Delta\phi = \pi/2 + m\pi$ (where m is an integer) and as a result, is highly wavelength sensitive. The period of the ZnSe waveplate is $\Lambda = 0.25\lambda_0$ which means that if the design wavelength λ_0 is scaled, so to must be the period and depth.

A disadvantage with binary profiles as waveplates is the Fresnel losses off the surface. For the case of the ZnSe waveplate illustrated in Fig. 5, roughly 10% of the incident radiation is being reflected. One method of reducing the reflection losses is through the use of a continuously profiled surfaces, which will act as an AR coating as well as a waveplate.[21] A continuous profile is able to suppress Fresnel reflections since the optical properties of its effective medium (a gradient film) gradually taper from the properties of the incident medium to

those of the substrate. Diagrammed in Fig. 6 is a triangular SWS profile along with its effective gradient medium.

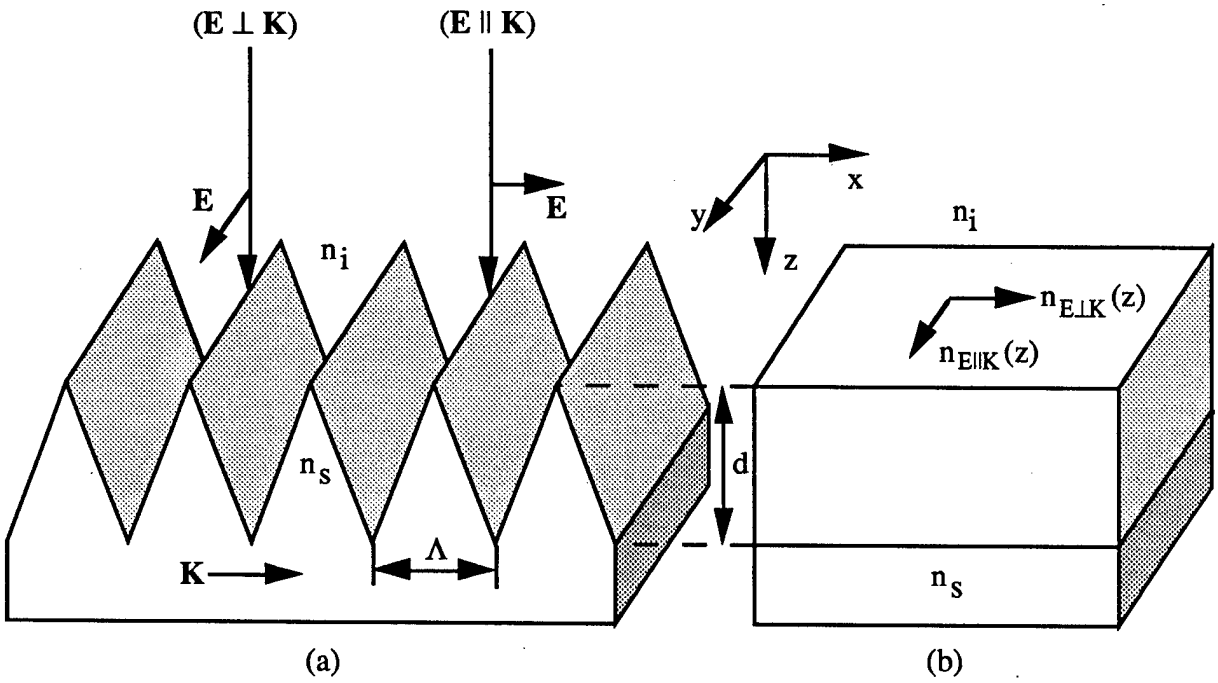

Fig. 6. Geometry of (a) a 1-D triangular SWS surface profile along with (b) its effective medium (a gradient film).

Although Fresnel reflections for both polarization states ($\mathbf{E} \perp \mathbf{K}$ and $\mathbf{E} \parallel \mathbf{K}$) may be suppressed by 1-D triangular profiles, each polarization state will travel a different optical path length and therefore accumulate a different amount of phase. In Fig. 7 we diagram the phase difference $\Delta\phi$ accumulated by the two orthogonal polarization states as a function of d, the depth of the triangular profile. Once the depth of the profile reaches $0.5\lambda_0$, less than 1.5% of the incident radiation is being reflected from the profile. One may note though that in order to achieve a quarter-wave retardance, the triangular profile must reach a depth of $0.65\lambda_0$ which is deeper than the depth of $0.46\lambda_0$ for the corresponding binary profile. The increase in depth for the triangular profile stems from the fact that the form birefringence of a structure is dependent upon the filling factor f, see Eqs. (1)-(6) of the stratification. For a binary profile, the filling factor does not vary with depth, and so can be at or near the filling factor f_0 which achieves maximum birefringence. For a continuous profile such as the triangular profile diagrammed in Fig. 6, the filling factor, and hence the effective birefringence Δn , changes with depth.

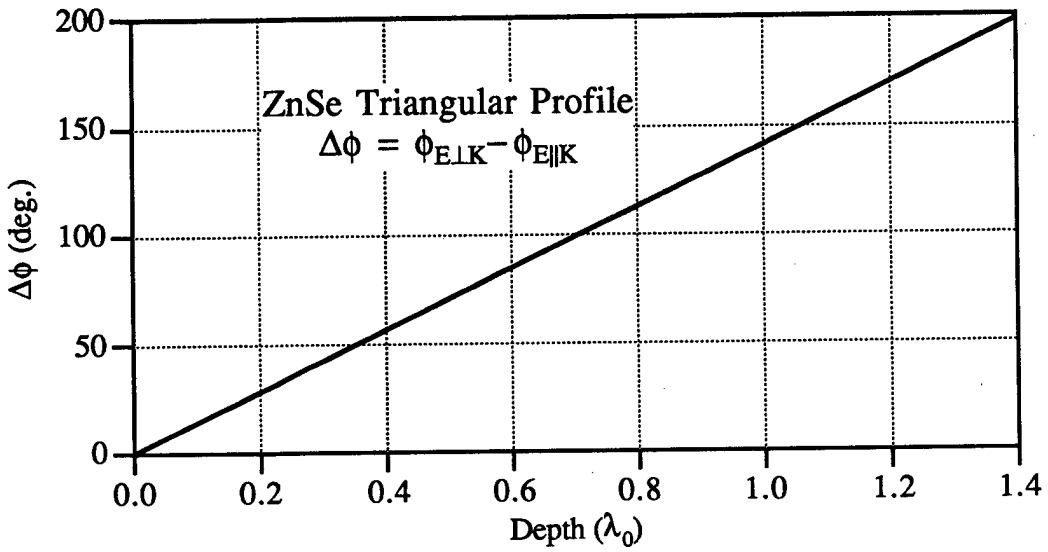

Fig. 7. Phase retardance $\Delta\phi$ accumulated by radiation encountering a triangular SWS profile as a function of profile depth *d*.

5. 2-D Binary Antireflection Structured Surfaces

For certain applications, birefringent behavior is not desired. One example in which isotropic behavior is preferred is the suppression of a surface's Fresnel reflections for randomly-polarized radiation. Since 1-D SWS surfaces are birefringent due to their surface asymmetry, by increasing the surface symmetry, more isotropic behavior is possible. Near-isotropic behavior may be achieved with a 2-D crossed grating structure.[Raguin, 1992 #21

In Fig. 8 an SEM photograph of a 2-D binary ARS surface is presented. This surface was fabricated on a three-inch silicon wafer using equipment at Cornell's National Nanofabrication Facility (NNF). Since the period of the grating is relatively large (2.45 μm in each direction), we were able to use optical lithography to pattern the substrate. Using optical lithography, the patterning of a three inch wafer takes relatively little time and through step and repeat procedures, larger surfaces may be patterned in under an hour. Etching of the pattern was achieved using reactive ion etching (RIE). These structures are designed to suppress surface reflections for 10.6 μm CO_2 radiation.

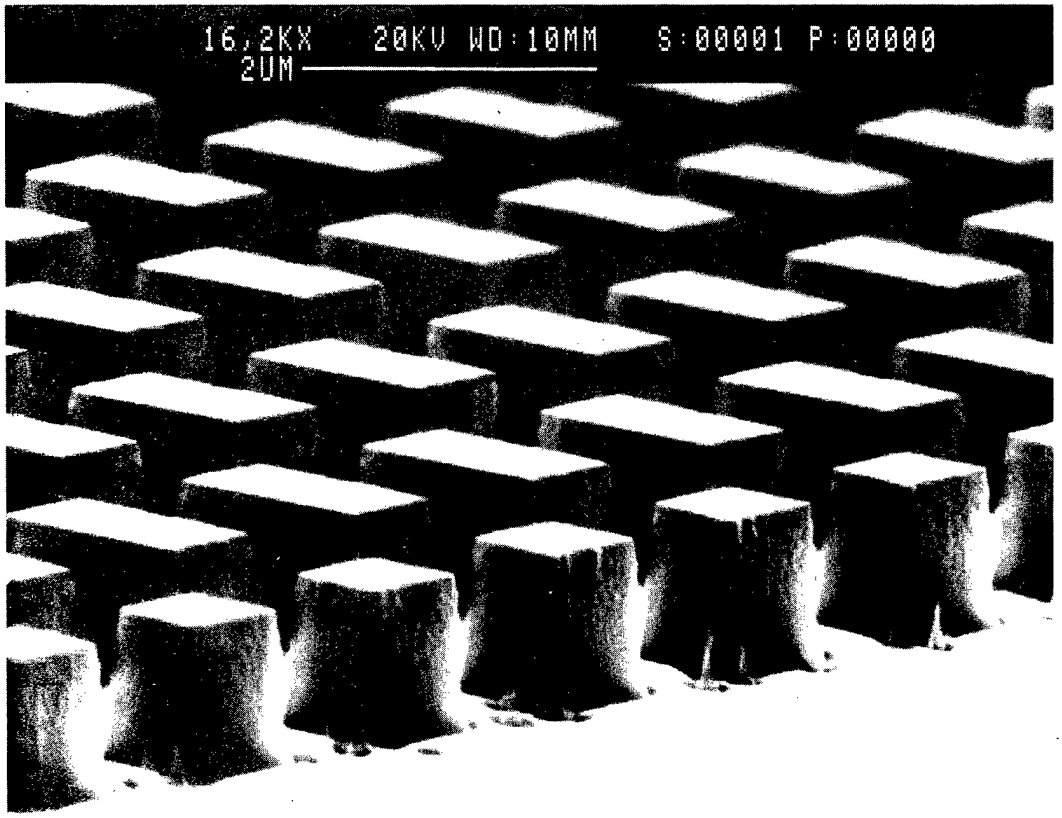

Fig. 8. Silicon 2-D binary ARS surface fabricated on a three-inch wafer.

References

1. S. J. Wilson and M. C. Hutley, "The optical properties of 'moth eye' antireflection surfaces," Opt. Acta **29**, 993-1009 (1982).

2. R. C. Enger and S. K. Case, "Optical elements with ultrahigh spatial-frequency surface corrugations," Appl. Opt. **22**, 3220-3228 (1983).

3. T. K. Gaylord, W. E. Baird and M. G. Moharam, "Zero-reflectivity high spatial-frequency rectangular-groove dielectric surface-relief gratings," Appl. Opt. **25**, 4562-4567 (1986).

4. Y. Ono, Y. Kimura, Y. Ohta and N. Nishada, "Antireflection effect in ultrahigh spatial-frequency holographic relief gratings," Appl. Opt. **26**, 1142-1146 (1987).

5. N. F. Hartman and T. K. Gaylord, "Anti-reflection gold surface-relief gratings: experimental characteristics," Appl. Opt. **27**, 3738-3743 (1988).

6. D. Raguin and G. M. Morris, "Antireflection structured surfaces for the infrared spectral region," accepted for publication in Applied Optics, July 1992.

7. M. E. Motamedi, W. H. Southwell and W. J. Gunning, "Antireflection surfaces in silicon using binary optics technology," Appl. Opt. **31**, 4371-4376 (1992).

8. C. G. Bernhard, "Structural and functional adaptation in a visual system," Endeavor **26**, 79-84 (1967).

9. P. Yeh, "A new optical model for wire grid polarizers," Opt. Commun. **26**, 289-292 (1978).

10. K. Shiraishi, T. Sato and S. Kawakami, "Experimental verification of a form-birefringent polarization splitter,," Appl. Phys. Lett. **58**, 211-212 (1991).

11. L. H. Cescato, E. Gluch and N. Streibl, "Holographic quarterwave plates," Appl. Opt. **29**, 3286-3290 (1990).

12. C. W. Haggans, L. Li, T. Fujita and R. K. Kostuk, "Lamellar gratings as polarization components for specularly reflected beams," submitted to the Journal of Modern Optics 1992.

13. E. N. Glytsis and T. K. Gaylord, "High-spatial-frequency binary and multilevel stairstep gratings: polarization-selective mirrors and broadband antireflection surfaces," Appl. Opt. **31**, 4459-4470 (1992).

14. R. Magnusson and S. S. Wang, "New principle for optical filters," Appl. Phys. Lett. **61**, 1022-1024 (1992).

15. M. T. Gale, K. Knop and R. Morf, "Zero-order diffractive microstructures for security applications," Optical Security and Anticounterfeiting Systems, SPIE **1210**, pp. 83-89 (1990).

16. M. W. Farn, "Binary gratings with increased efficiency," Appl. Opt. **31**, 4453-4458 (1992).

17. H. Haidner, P. Kipfer, W. Stork and N. Steibl, "Zero-order gratings used as an artificial distributed index medium," Optik **89**, 107-112 (1992).

18. T. K. Gaylord and M. G. Moharam, "Analysis and applications of optical diffraction by gratings," Proc. IEEE **73**, 894-937 (1985).

19. W. B. Veldkamp, G. J. Swanson, S. A. Gaither, C.-L. Chen and T. R. Osborne, "Binary optics: a diffraction analysis," MIT Lincoln Laboratory Project Report **ODT 20** (1989).

20. S. M. Rytov, "The electromagnetic properties of finely layered medium," Soviet Phys. JETP **2**, 466-475 (1956).

21. D. H. Raguin and G. M. Morris, "Analysis of antireflection structured surfaces with continuous one-dimensional surface profiles," accepted for publication in Applied Optics, Dec. 1992.

7. M. E. Motamedi, W. H. Southwell and W. J. Gunning, "Antireflection surfaces in silicon using binary optics technology," Appl. Opt. **31**, 4371-4376 (1992).

8. C. G. Bernhard, "Structural and functional adaptation in a visual system," Endeavor **26**, 79-84 (1967).

9. P. Yeh, "A new optical model for wire grid polarizers," Opt. Commun. **26**, 289-292 (1978).

10. K. Shiraishi, T. Sato and S. Kawakami, "Experimental verification of a form-birefringent polarization splitter,," Appl. Phys. Lett. **58**, 211-212 (1991).

11. L. H. Cescato, E. Gluch and N. Streibl, "Holographic quarterwave plates," Appl. Opt. **29**, 3286-3290 (1990).

12. C. W. Haggans, L. Li, T. Fujita and R. K. Kostuk, "Lamellar gratings as polarization components for specularly reflected beams," submitted to the Journal of Modern Optics 1992.

13. E. N. Glytsis and T. K. Gaylord, "High-spatial-frequency binary and multilevel stairstep gratings: polarization-selective mirrors and broadband antireflection surfaces," Appl. Opt. **31**, 4459-4470 (1992).

14. R. Magnusson and S. S. Wang, "New principle for optical filters," Appl. Phys. Lett. **61**, 1022-1024 (1992).

15. M. T. Gale, K. Knop and R. Morf, "Zero-order diffractive microstructures for security applications," Optical Security and Anticounterfeiting Systems, SPIE **1210**, pp. 83-89 (1990).

16. M. W. Farn, "Binary gratings with increased efficiency," Appl. Opt. **31**, 4453-4458 (1992).

17. H. Haidner, P. Kipfer, W. Stork and N. Steibl, "Zero-order gratings used as an artificial distributed index medium," Optik **89**, 107-112 (1992).

18. T. K. Gaylord and M. G. Moharam, "Analysis and applications of optical diffraction by gratings," Proc. IEEE **73**, 894-937 (1985).

19. W. B. Veldkamp, G. J. Swanson, S. A. Gaither, C.-L. Chen and T. R. Osborne, "Binary optics: a diffraction analysis," MIT Lincoln Laboratory Project Report **ODT 20** (1989).

20. S. M. Rytov, "The electromagnetic properties of finely layered medium," Soviet Phys. JETP **2**, 466-475 (1956).

21. D. H. Raguin and G. M. Morris, "Analysis of antireflection structured surfaces with continuous one-dimensional surface profiles," accepted for publication in Applied Optics, Dec. 1992.

Diffractive Optical Elements for Generating Arbitrary Line Foci

Joseph N. Mait, Dennis W. Prather, Joseph van der Gracht, and Tristan J. Tayag
U.S. Army Research Laboratory
AMSRL-SS-SF
2800 Powder Mill Road
Adelphi, Maryland 20783

1. Introduction

The key optical component in the architecture of the linearly variable magnification telescope shown in Fig. 1 is a conical lens. This architecture has application to Doppler radar processing and to wavelet processing. Unfortunately, the unique surface profile of a conical lens does not allow traditional grinding techniques to be used for fabrication and therefore its fabrication is considered custom. In addition to the requirement of custom fabrication, a refractive conical lens introduces phase aberrations that are intrinsic to its conic shape. Further, due to the large prismatic component of the lens, the variable magnification telescope architecture is off-axis.

To overcome the fabrication and application difficulties of a refractive lens, we consider the construction of a hybrid diffractive-refractive lens that has a phase profile given by

$$\phi(u,v) = \frac{2\pi}{\lambda}\,[f(v) - \sqrt{f^2(v) + u^2}], \tag{1}$$

where the focal length $f(v)$ is an arbitrary function of v and λ is the wavelength of illumination. The effect of such an arbitrary line foci element (ALFE) is to produce a focal line in three-dimensions whose shape along the axis of propagation follows that of the function $f(v)$. Cylindrical and conical lenses are the most common refractive elements that are capable of producing focal lines.

To generate the focal line $f(v)$ we consider a hybrid element that consists of a refractive element that generates the focal line $f_R(v)$ and a diffractive lens that generates the focal line $f_D(v)$:

$$\frac{1}{f_R(v)} + \frac{1}{f_D(v)} = \frac{1}{f(v)}. \tag{2}$$

If the refractive element is used to provide a constant optical power, $f_R(v) = f_R$, i.e., the refractive element is a cylindrical lens, constraints on the fabrication of the diffractive lens can be reduced. For example, an ALFE that varies in focal length from 160 mm to 240 mm over a 50 × 50 mm^2 aperture varies in f-number from 3.2 to 4.8. If f_R = 325 mm, the cylindrical lens is $f/6.5$ and the diffractive lens varies in f-number from 6.3 [$f(0)$ = 315 mm] to 18.35 [$f(50)$ = 917.5 mm], which is less difficult to fabricate than lower f-number lenses.

We now consider the design of a thin phase-only diffractive optical element (DOE) $P(u,v)$,

$$P(u,v) = \exp[j\phi_D(u,v)], \tag{3a}$$

that is capable of generating the focal line $f_D(v)$. A multi-level quantized phase-only DOE is assumed,

$$\phi_D(u,v) = \sum_{n=0}^{N}\sum_{m=0}^{M} \phi_{nm,L}\ \mathrm{rect}\left(\frac{u-u_n}{\Delta}, \frac{v-v_m}{\Delta}\right), \tag{3b}$$

where Δ is the minimum feature size of the pattern generator used to produce the binary masks and

$$\phi_{nm,L} \in [0, \frac{2\pi}{2^L}, 2\frac{2\pi}{2^L}, \ldots, (2^L-1)\frac{2\pi}{2^L}]. \tag{3c}$$

The resolution with which each phase pixel can be positioned is defined by the placement accuracy ϵ of the pattern generator, i.e., $u_n = \ell\epsilon$ and $v_n = k\epsilon$. The ability of $P(u,v)$ to generate a high-fidelity focal line $f_D(v)$ is limited by the minimum feature size Δ of the pattern generator, its placement accuracy ϵ, and the number of phase quantization levels 2^L. Design of the diffractive ALFE entails the determination of the parameters $\phi_{nm,L}$ and (u_n, v_n), from which L binary masks are produced.

We consider the design of a diffractive ALFE based on the sampling and quantization of $\phi_D(u,v)$ and experimental results from a binary-phase ALFE designed in this manner are presented. We also consider two alternative design approaches: a second approach based on sampling and quantization and an iterative approach that detemines the parameters by optimizing some design metric. The difficulties encountered in lens design and characterization of lens performance are addressed.

2. Deterministic Design

In the literature, the design of diffractive lenses implies the design of spherical lenses, which, by exploiting spherical symmetry, can be reduced from a two-dimensional problem to one that is one-dimensional. For diffractive ALFE design, symmetry properties can not be exploited to reduce the dimensionality of the design problem. Rather, dimensionality reduction is realized by noting that the phase function at every u-axis slice of the diffractive ALFE is a spatially scaled version of a one-dimensional lens:

$$\phi_D(u,v) = s(v)\ \phi_D[\frac{u}{s(v)}, 0], \tag{4a}$$

where $s(v)$ represents a normalized focal function,

$$s(v) = \frac{f_D(v)}{f_D(0)}. \tag{4b}$$

The even nature of the ALFE, i.e., $\phi_D(u,v) = \phi_D(-u,v)$, can be used to halve the number of design parameters.

Lens design is realized by quantizing lines of constant phase:

$$u_i(v) = \sqrt{\frac{\lambda\phi_i}{2\pi}\left[\frac{\lambda\phi_i}{2\pi} - 2f_D(v)\right]}, \tag{5a}$$

where

$$\phi_i = \frac{2\pi i}{2^L},\ i = [1, I]. \tag{5b}$$

The number of phase lines I to be quantized is dependent upon the minimum phase value obtained by $\phi_D(u,v)$:

$$I = \text{ROUND}\left[\frac{2^L}{2\pi}\min\{\phi_D(u,v)\}\right], \tag{5c}$$

where ROUND implies rounded to the nearest integer. The minimum phase is, in turn, related to the minimum f-number one-dimensional lens described by $\phi_D(u,v)$. If the DOE aperture is allowed to vary with $f(v)$ then the diffractive ALFE maintains a constant f-number and each lens has the same number of phase lines. However, to allow the aperture to vary represents an inefficient use of the overall aperture. On the other hand, a constant aperture generates variable f-number one-dimensional lenses and produces a focal line that has variable spot size and brightness. The tradeoff between aperture efficiency and focal line fidelity needs to be consider for each application. We assume that the aperture is constant and is defined by the aperture of the refractive cylindrical lens.

One method for implementing the design, referred to as the direct sampling (DS) method, is to ignore the effect of ϵ and quantize the lines $u_i(v)$ according to the minimum feature size Δ. For the DS method, L and Δ_x dictate the minimum f-number of the lens that can be designed and L dictates the lens

diffraction efficiency [1,2]. In effect, the DS method assumes that $\phi_D(u,v)$ is sampled on a regular Cartesian grid and is then quantized. The spacing of the grid is determined by the minimum feature size of the pattern generator used to produce the binary masks.

Figure 2(a) is the DS-generated binary mask for a conical lens that has a linear change in focal length from 300 mm to 480 mm over a 4×4 mm^2 aperture. The focal length increases in 3.6 mm increments over the aperture, thus, the ALFE consists of 50 one-dimensional lenses. The minimum feature size is 10 μm. The lens was fabricated on a Corning glass substrate that has an index of refraction $n = 1.53$ using a 1.8 μm layer of positive photoresist (Hoechst AZ 5214) and an Ar ion etch. The axial performance of the lens is represented in Figs. 2(b)-(d), which indicates that the focal length actually changes from approximately 220 mm to 350 mm.

Due to the varying axial behavior of the lens, it is difficult to characterize its performance. For a spherical lens, in most instances, it suffices to take a measure of the diffraction efficiency, the percentage of input light energy that is brought to focus. For an ALFE, the diffraction efficiency must be measured along the focal line:

$$\eta(y) = \int_{\mathbf{X}} |U[x,y;f(y)]|^2 \, dx \Big/ \int |U[x,y;f(y)]|^2 \, dx \tag{6}$$

where $\mathbf{X}$ is the width of the focal spot and $U(x,y;z)$ is the complex wave-amplitude field generated by $P(u,v)$ at an arbitrary distance z in the near-field,

$$U(x,y;z) = \frac{1}{j\lambda} \exp\left(j\frac{2\pi z}{\lambda}\right) \int\int_{\mathbf{A}} \exp\left[j\phi_D(u,v)\right] \exp\left\{j\frac{\pi}{\lambda z}\left[(u-x)^2 + (v-y)^2\right]\right\} du\, dv. \tag{7}$$

The area of the ALFE aperture is denoted by $\mathbf{A}$. To reduce the computational load in evaluating the three-dimensional function $U(x,y;z)$, if y-axis diffraction is ignored, Eq. (7) can be simplified

$$U[x,y;f(y)] = \frac{1}{j\lambda} \exp\left[j\frac{2\pi f(y)}{\lambda}\right] \int_{W_u} \exp\left[j\phi_D(u,y)\right] \exp\left[j\frac{\pi}{\lambda f(y)}(u-x)^2\right] du, \tag{8}$$

where W_u is the u-axis aperture of the ALFE. The diffraction efficiency along the focal line generated by the DS conical lens as determined using Eq. (8) is presented in Fig. 3.

Diffraction efficiency can be increased if the placement accuracy ϵ is not ignored. In other words, although the minimum feature size is fixed, the accuracy with which the lines of constant phase are quantized can be sampled on a finer grid determined by the placement accuracy. Fabrication of the masks, though, is still limited by the minimum feature size of the pattern generator. As represented in Fig. 4, to realize this finer quantization multiple exposures are used to generate the masks necessary for fabrication, but, because the masks are binary, multiple exposures do not affect mask transmission. This design technique is referred to as analytic quantization (AQ).

The distinction between DS- and AQ-designed ALFEs is evident in Fig. 5 and the increase in diffraction efficiency is represented in Fig. 6. The ALFE is characterized by a focal length change from 256 μm to 1040 μm in 19.6 μm increments (40 lenses) over a 80×80 μm^2 aperture. Minimum feature size is assumed to be 2 μm with a placement accuracy of 0.2 μm. The percent change in diffraction efficiency ranges from a minimum of zero to a high of 35% and is most notable for low f-number lenses, which have higher phase curvature than high f-number lenses. Note that the improvement in diffraction efficiency is reduced for those lenses that experience "edge effects" introduced by the minimum feature size limitation. Unfortunately, consideration of the placement accuracy during design increases by 100 the amount of data necessary for fabrication of a single mask. Thus, whereas the lens in Fig. 5(a) contains only 40×40 data points, the lens in Fig. 5(b) contains 400×400.

3. Iterative Design

Although performance characterization of an ALFE requires, in general, the evaluation of Eq. (7), the application to a variable magnification telescope allows us to characterize lens performance based on

telescope performance. For telescopic operation, the input and output are collimated, i.e., the input object is located at $-\infty$ and the output image is at $+\infty$, and the lenses are separated by a distance $d = f(0) + f(W_v)$, where W_v is the v-aperture of the lens. Thus, the image $i(x_i, y_i)$ of an input object $o(x_o, y_o)$ produced by the ALFE phase $\phi_D(u, v)$ is

$$\begin{aligned} i(x_i, y_i) &= \frac{-1}{\lambda^2 z} \exp\left[j\frac{2\pi(d+z)}{\lambda}\right] \exp\left[j\frac{\pi}{\lambda z}(x^2+y^2)\right] \int\int \exp\left[j\phi_D(-u,-v)\right] \\ &\times \left[\int\int_{\mathbf{A}} o(x_o, y_o) \exp\left[j\phi_D(x_o, y_o)\right] \exp\left\{j\frac{\pi}{\lambda d}\left[(x_o-u)^2+(y_o-v)^2\right]\right\} dx_o\, dy_o\right] \\ &\times \exp\left[\frac{2\pi}{\lambda z}(ux_i + vy_i)\right] du\, dv, \end{aligned} \tag{9}$$

where Fourier transformation is used to represent Fraunhofer diffraction to a distance z in the far-field. For a unit amplitude plane wave input, Fig. 7 represents simulated image reconstructions generated by Eq. (9) for a continuous phase zone plate lens and lenses designed using DS with phase quantization levels of 2, 4, and 8. No cylindrical lens was used and the diffractive lens has a focal change from 240 mm to 384 mm over a 3.2 mm aperture ($f/75$ to $f/120$). The smallest feature is 25 μm. Use of a cylindrical lens only changes the magnification and not the diffractive lens behavior. The magnification changes from 1.6 to 0.625 over the extent of the aperture.

It is apparent from Fig. 7 that a binary-phase DS conical lens is incapable of performing in the telescopic system. Diffractive artifacts are apparent even in the zone-plate image and it is interesting to note that more of the image is filled in as the number of phase quantization levels increases. The effect of variable magnification is also evident by the varying levels of image intensity; as the magnification increases, the intensity level decreases.

To account for the undesirable effects of deterministically designed lenses, it is possible to design $P(u, v)$ using iterative techniques to create a desired output image for a given input object. Because, from Eq. (9), the desired image $q(x_i, y_i)$ can be determined for a given input $o(x_o, y_o)$, it is possible to use iterative techniques, such as simulated annealing [2] and iterative Fourier transform algorithms [3], to determine $\phi_D(u, v)$ such that the error between $i(x_i, y_i)$ and $q(x_i, y_i)$ is a minimum. We will be investigating this technique in the future.

4. Conclusion

We have considered the design of a hybrid diffractive-refractive element that is capable of generating a focal line in space that has an arbitrarily specified shape. The element consists of a refractive cylindrical lens to provide optical power and a diffractive element for shaping the focal line. Although standard design and fabrication techniques have been applied to generate a diffractive conical lens, issues such as performance characterization and design for "improved" performance remain to be addressed more critically. Of utmost importance is data management to reduce design complexity, especially when placement accuracy is used as part of the design. These issues will be addressed in the future.

References

1. G. J. Swanson, *MIT Lincoln Laboratory Technical Report 854*, 14 August 1989.

2. W. H. Welch, J. E. Morris, and M. R. Feldman, "Iterative discrete on-axis encoding of radially symmetric computer generated holograms," submitted to Appl. Opt.

3. F. Wyrowski and O. Bryngdahl, Rep. Prog. Phys., 1481-1571 (1991).

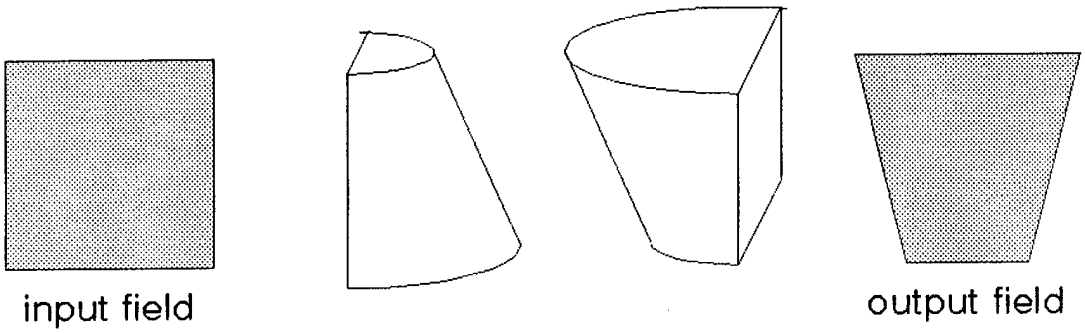

Figure 1. Linearly variable magnification telescope.

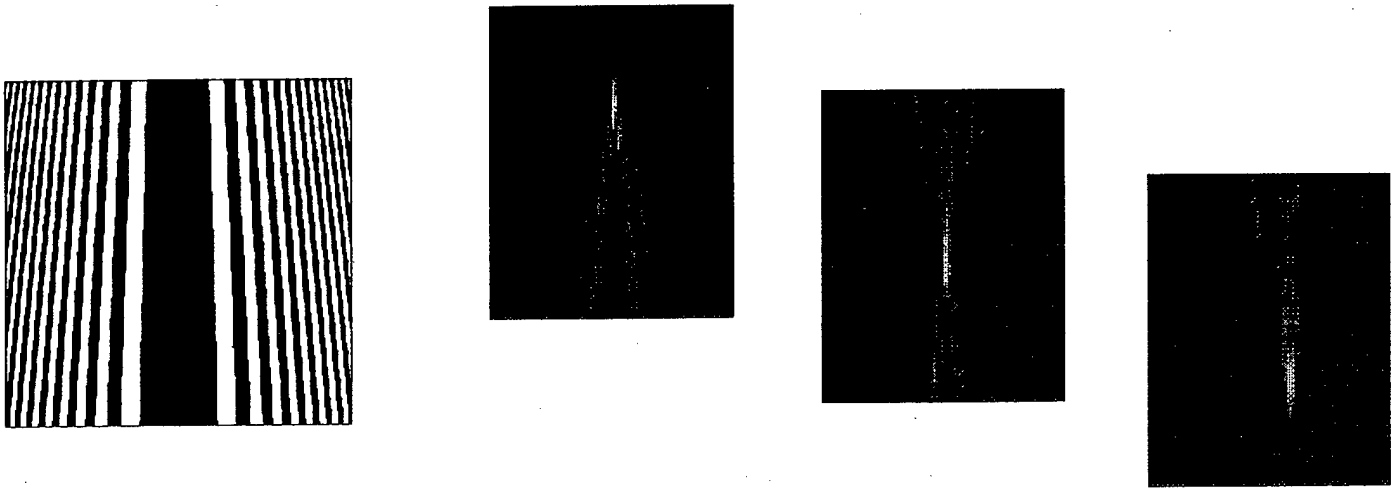

Figure 2. (a) Binary mask designed using DS method and used to fabricate binary-phase conical lens. Lens reconstructions at (b) ~220 mm, (c) intermediate distance, and (d) ~350 mm.

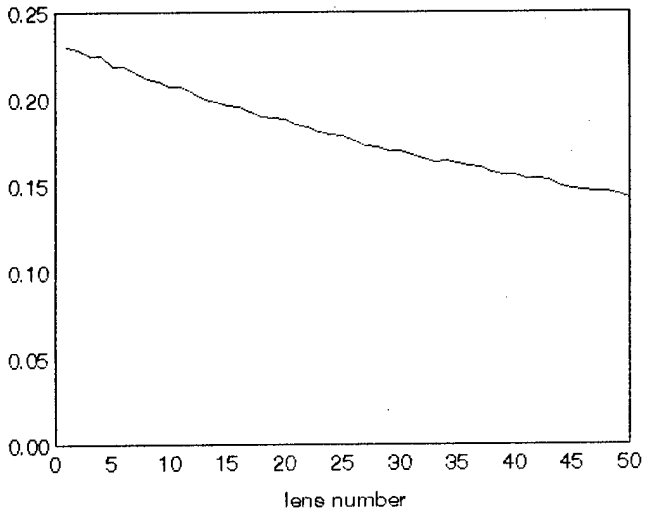

Figure 3. Calculated diffraction efficiency of DS designed binary-phase conical lens.

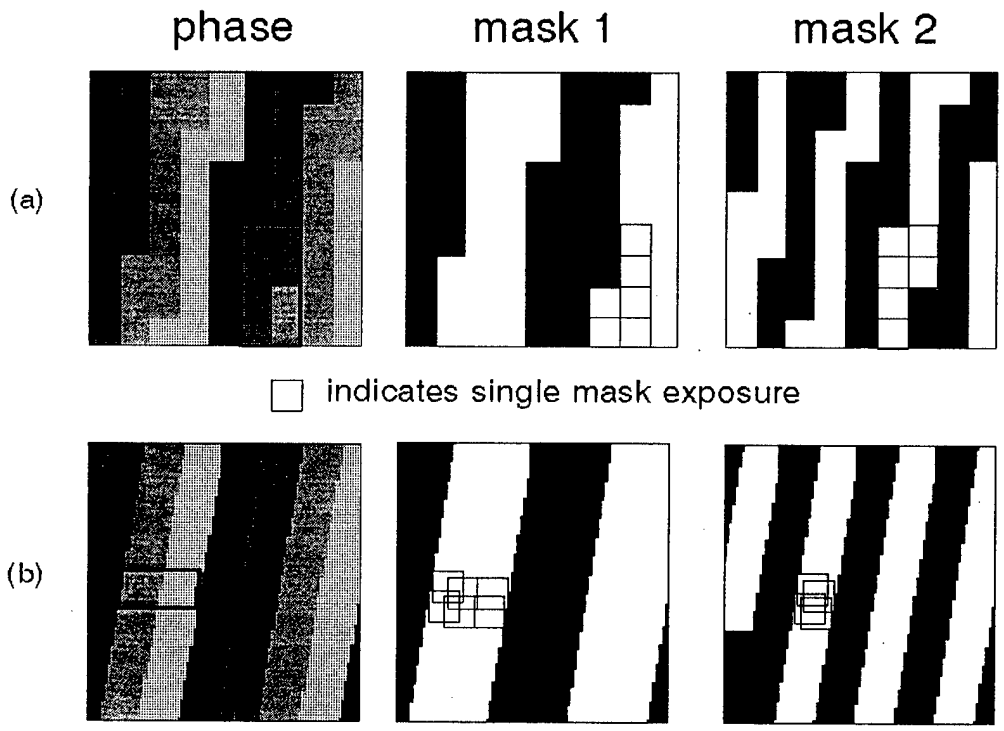

Figure 4. Distinction between (a) direct sampling and (b) analytic quantization design methods.

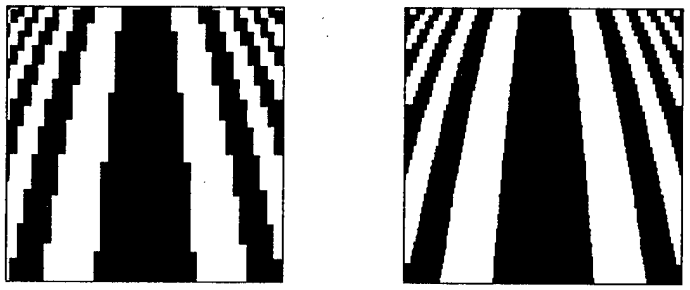

Figure 5. Conical lenses designed using (a) direct sampling and (b) analytic quantization.

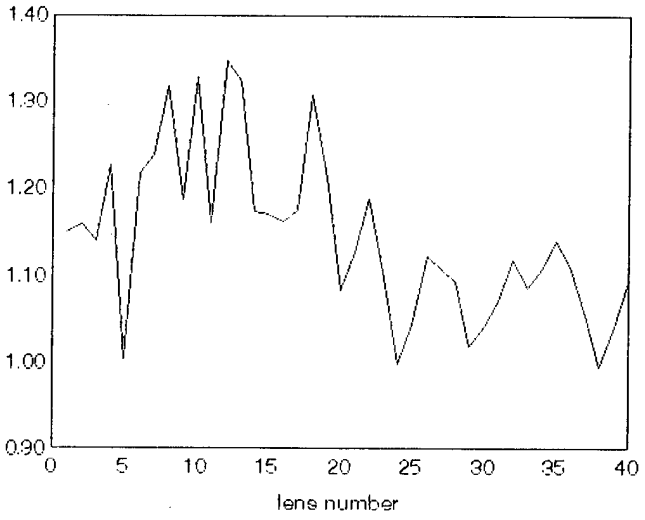

Figure 6. Gain in diffraction efficiency for AQ-designed lens of Fig. 5(b) over DS-designed lens of Fig. 5(a).

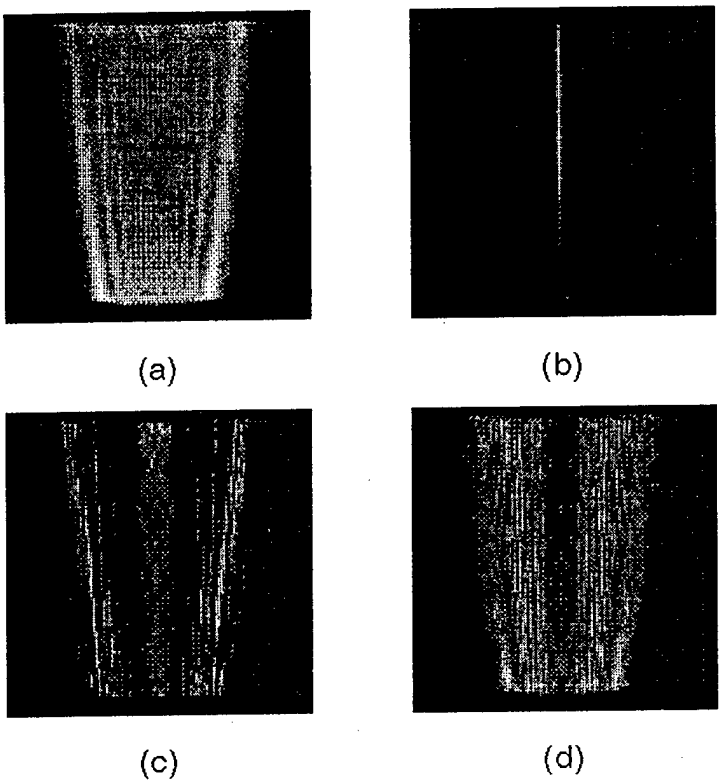

Figure 7. Simulated output image of phase-only conical lens illuminated by unit amplitude plane wave assuming: (a) continuous phase, (b) 2 phase levels, (c) 4 phase levels, and (d) 8 phase levels.

Finite Difference Time Domain Analysis of Chirped Dielectric Gratings

Diane H. Hochmuth and Eric G. Johnson

Teledyne Brown Engineering
300 Sparkman Drive
Huntsville, Alabama 35807-7007

Dielectric gratings have long been used for various applications at both optical and microwave frequencies; however, most of the optical applications were limited to performance regimes dictated by scalar theories and assumptions. Recently, with the development of finite difference time domain (FDTD) methods [1], both transient and steady-state solutions can be modeled to exploit the spectral filtering properties of chirped grating structures. In this paper, FDTD techniques are used to analyze various types of surface-relief structures including chirped dielectric gratings.

The FDTD method for solving Maxwell's time-dependent curl equations is accurate, computationally efficient, and straight-forward to implement. Since both time and space derivatives are employed, the propagation of an electromagnetic wave can be treated as an initial-value problem. Second-order central-difference approximations are applied to the space and time derivatives of the electric and magnetic fields providing a discretization of the fields in a volume of space, for a period of time. The solution to this system of equations is stepped through time thus simulating the propagation of the incident wave. If the simulation is continued until a steady-state is reached, an appropriate far-field transformation can be applied to the time-domain scattered fields to obtain reflected and transmitted powers. From this information, diffraction efficiencies can also be determined.

In analyzing the chirped structure, a mesh is applied only to the area immediately around the grating. The size of the mesh is then proportional to the electric size of the grating. Doing this, however, imposes an artificial boundary around the area of interest. An absorbing boundary condition must be applied along the artificial boundary so that the outgoing waves are absorbed as if the boundary were absent. Many such boundary conditions have been developed that give near-perfect absorption. In this analysis, the Mür absorbing boundary conditions are employed [2].

Several grating structures were analyzed using the FDTD method. First, the method was validated by comparing its results to that of the coupled-wave approach [3]. Two periods of a binary periodic grating were modeled in the center of an extended surface. The period was two wavelengths and the depth was one wavelength as measured in free space. The refractive index of the dielectric was 1.5. Both TE and TM polarizations were calculated. A comparison between the two methods is illustrated in Figures 1 and 2. Figure 1 shows the amplitude and phase for TE polarization calculated at the interface, and Figure 2 shows the same for TM polarization. In the FDTD analysis, the simulation was run until a steady-state was reached. At this point, the amplitude and phase were extracted from the complex field

values. The agreement is quite good. The FDTD results appear to be noisier due to the imperfect absorbing boundary conditions applied at the edges of the computation region.

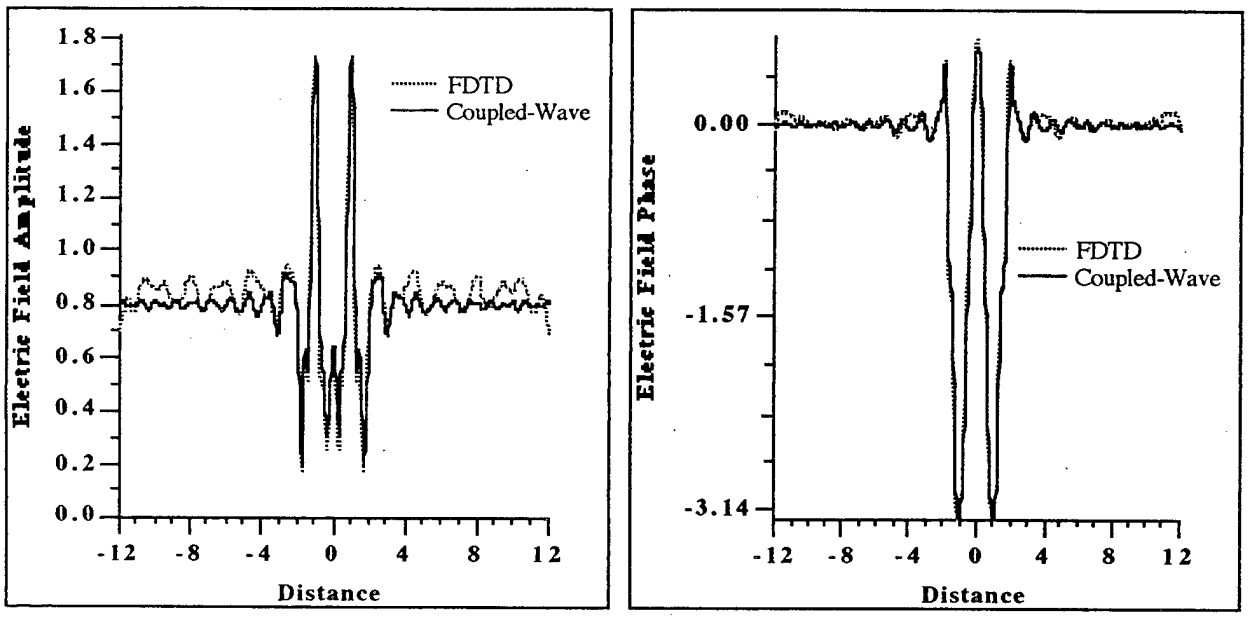

Figure 1. Comparison Between FDTD and Coupled-Wave, TE Case

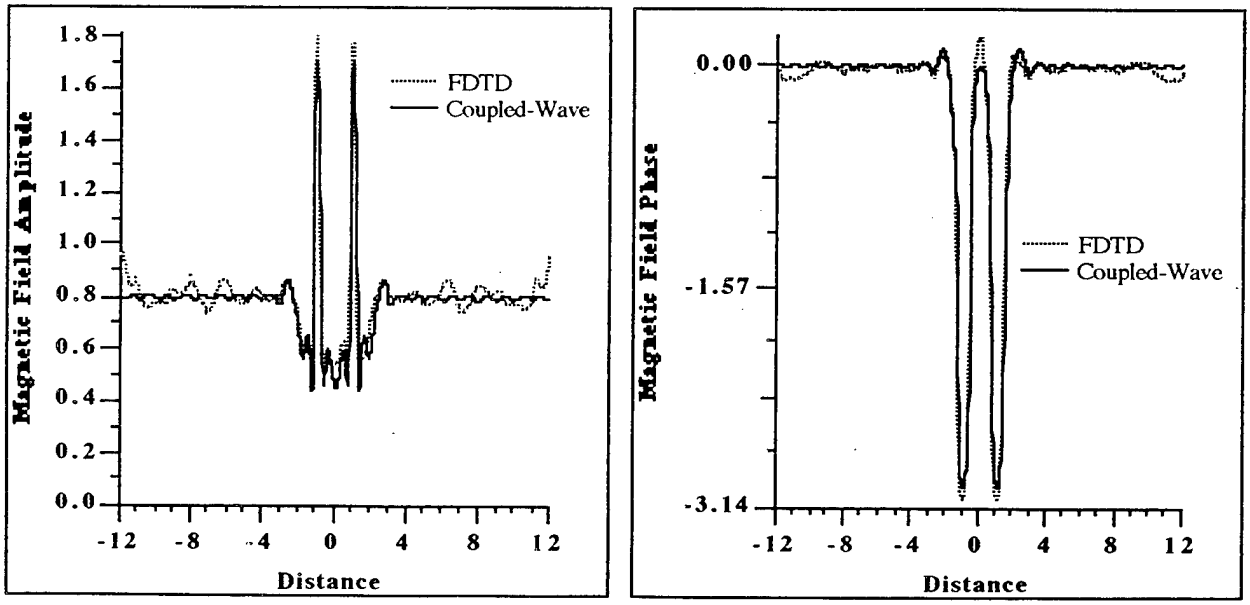

Figure 2. Comparison Between FDTD and Coupled-Wave, TM Case

Next, the number of periods was increased to demonstrate the effects of finite structures. In addition to the case mentioned above with two periods, four more cases were run with the maximum number of periods being ten. The far-field diffraction patterns were calculated by doing a fast Fourier transform on the amplitude and phase data. These results are shown in Figure 3. As would be expected, the zero-order decreases and the higher orders increase in intensity as the number of periods is increased. Figure 4 shows similar results from the same exercise performed on gratings with four phase levels. Just as a side note, the computation time required to analyze the four level gratings was no more than that for the binary gratings. This is a definite advantage of using this technique over the coupled-wave approach or the method of moments.

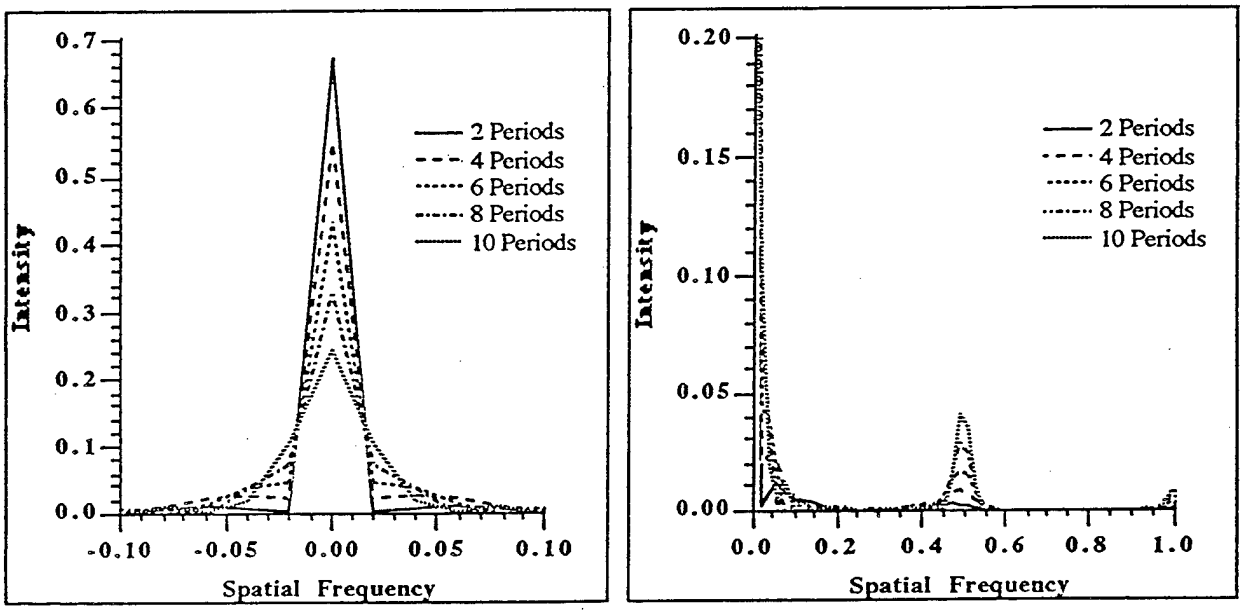

Figure 3. Far-Field Diffraction Pattern for Binary Grating

The final type of grating modeled was chirped gratings. The Fresnel zone equation

$$r_m = \sqrt{\frac{2mf\lambda}{n} + \left[\frac{m\lambda}{n}\right]^2}$$

where r_m = m-th zone radius
f = focal length
λ = free-space wavelength
n = dielectric refractive index

was used to determine the radii of the zones. If a large enough region is simulated, the focussing effect of the lens can be seen. Of equal interest is the behavior of the fields near the grating. A video of the time frames from this simulation shows this behavior as well as the focussing effect.

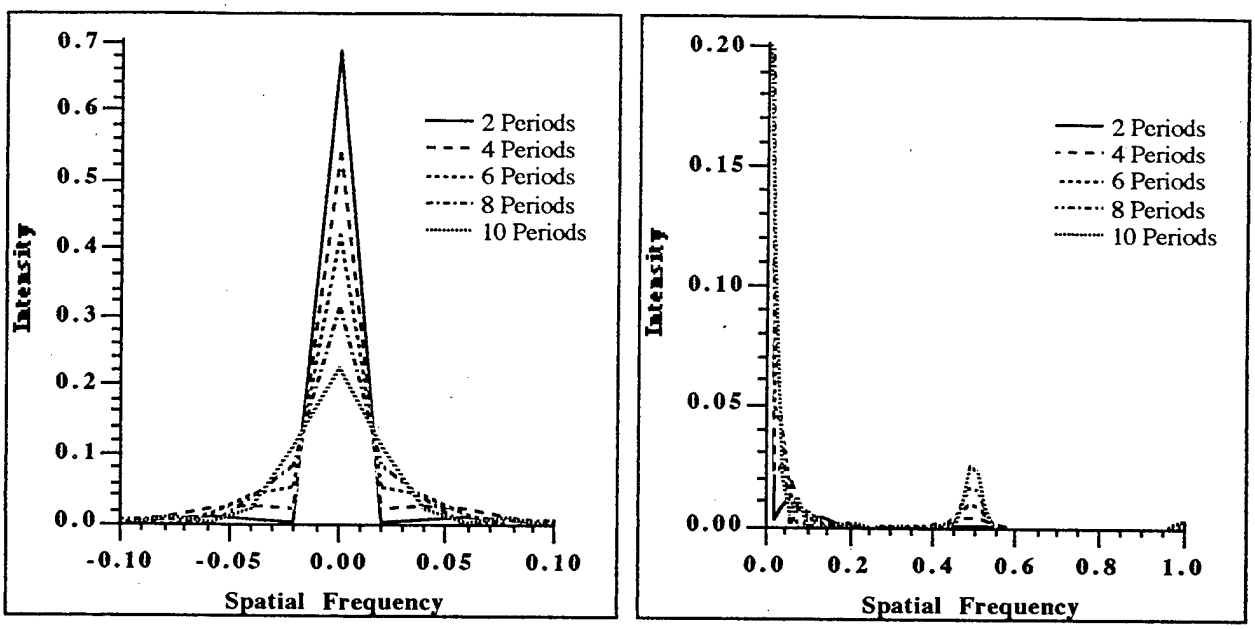

Figure 4. Far-Field Diffraction Pattern for Grating with Four Phase Levels

The finite difference time domain technique is well suited to analyzing finite grating structures. The results were seen to be very close to those achieved with the coupled-wave method. Also, since this method incorporates time, transient pulses can also be modeled.

References

[1] A. Taflove and M. E. Brodwin, "Numerical Solution of Steady-State Electromagnetic Scattering Problems Using the Time-Dependent Maxwell's Equations," *IEEE Trans. Microwave Theory Tech.*, vol. MTT-23, pp.623-630, Aug. 1975.

[2] G. Mür, "Absorbing Boundary Conditions for the Finite-Difference Approximation of the Time-Domain Electromagnetic-Field Equations," *IEEE Trans. Electromagn. Compat.*, vol. EMC-23, pp. 377-382, Nov. 1981.

[3] Moharam, M. G., and Gaylord, T. K., "Diffraction Analysis of Dielectric Surface-Relief Gratings," *JOSA*, Vol. 72, pp. 1385-1392, Oct. 1982.

Asymmetric Three-Beam Binary Optic Grating

A. D. Kathman, E. G. Johnson and M. L. Scott
Teledyne Brown Engineering
Huntsville, Alabama

Abstract

Binary and diffractive optical components are finding many applications in optical systems and integrated optical devices. A recent application required the development of a two-dimensional diffraction grating to perform an asymmetric, three-beam fanout. In this paper, techniques are presented for the design of arbitrary fanout grating devices. Modeling and optimization processes are demonstrate for the three-beam grating. The counter-intuitive results of the initial design are discussed, and experimental data verifying performance is presented.

Introduction

The growth in fabrication techniques using lasers and optical signal processing has produced a significant opportunity for innovation and the development of new optical devices.[1] Specialized gratings, designed to redirect light into specific diffraction orders, are finding many applications in optical interconnects, signal switching and interferometry. As the complexity of the fanout increases, particularly if the desired orders are asymmetric, the conventional design process becomes untenable and a non-deterministic optimization algorithm must be utilized.

A fanout device has been designed which produces three diffracted beams with equal power in each diffracted order, (see figure 1). The grating operates in transmission under normal incidence, directing light into three non-planar orders. The triangular geometry requires suppression of symmetric orders, increasing the mathematical complexity of the design effort. An attempt was made to design the grating in a deterministic manner using standard scalar diffraction theory, but yielded no solution. To overcome the limitations of our initial approach, a simulated annealing algorithm was used to produce a solution.

Approach

The fanout device produces three diffraction orders with equal power in each diffracted beam. The triangular geometry requires suppression of symmetric orders, which increases the mathematical complexity of the design effort. An analytic solution was attempted, but yielded no solution. The calculations did reveal that, due to the low angular deviation of the three beams, a scalar simulation code would provide accurate solutions, provided features in the grating structure were kept relatively large.

A simulated annealing algorithm was developed using a scalar simulation code to predict grating performance. A grating unit cell was defined as a 64 x 64 two-dimensional array of discrete phase values, thus the dimension of the problem was n = 4096. The irradiance in the central diffraction orders was calculated by coherent summation of the information in the discretely sampled unit cell. Irradiance targets were set to 0.33 for the 0,1, -1,-1 and 1,-1 orders with the remaining orders set to 0. The unit cell was initialized with random phase values prior to application of the annealing algorithm. During optimization, the convergence parameter or "cooling temperature" was decremented as a harmonic sequence. The cost function for the annealing algorithm was based

upon the mean squared error between the simulated irradiance values and the target values. Figure 2 outlines the logic flow for the simulated annealing algorithm. Designs were attempted with two, four, and eight discrete phase levels permitted in the grating. We found that the algorithm converges to the three desired orders very rapidly. Balancing the power in the orders, however, required a much greater fraction of the optimization time. The algorithm converged well for grating patterns of four or more phase levels; the asymmetric output required was not achievable using a binary phase grating. The results for the four level grating was counter-intuitive, but showed a simple repeated pattern (see figure 3).

Since the optimization was performed on an isosceles spot array, (orders 0,1, -1,-1 and 1,-1), a mapping was required to form the desired equilateral pattern. This was achieved by a linear scaling in x direction by a factor of 0.894. The scaled pattern, shown in figure 4, is the baseline design for the fanout device.

Evaluation of the pattern showed that it consists of two repeated shapes. The first is a hexagon with top and bottom sides concave, and the second is a bi-convex "football" shape. Each unit cell consists of four hexagons, each of a different phase level, and four footballs, also with different phase levels. The grating is constructed of these unit cells tiled into a tightly packed array.

The triangular output pattern suggests that shapes within the unit cell have edges at angles of 0°, 60° and 120°. In an effort to improve diffraction efficiency, the football shapes were replaced with small hexagons of similar shape and equal area. A simulation of this grating pattern demonstrated higher diffraction efficiency, but also a shift in the uniformity of the three beams. The size of the small hexagons was adjusted until irradiance in the beams was balanced. The result of this post optimization yielded an increase in diffraction efficiency from 77% to 79%, and only a slight change in the beam uniformity of less than 4% deviation. A signal to noise (SNR) value was calculated by comparing the irradiance in the weakest of the three beams to the irradiance in the highest undesired order present. The post optimization provided a boost in SNR from 8.4 to 11.2.

A second benefit of the modifications to the baseline design was a simplification in the mask patterns required to produce the optic. The two mask patterns required to produce the four level device were designed on Teledyne Brown Engineering's Computer-Generated Holography Workstation and are shown in figure 5. The patterns were written as a reticle at 5x and a step and repeat camera was used to create the masks. The fanout grating was fabricated in the binary optics processing lab at Teledyne Brown.

Test Results

Preliminary laboratory results have been completed on the three-beam fanout grating. To provide a simple measure of performance, the total laser power is measured and compared to the three diffracted beams. Figure 6 is a graphic depicting the percent power diffracted into each of the desired beams. A measure is also provided of the zero-order power. The undiffracted light provides a measure of processing errors encountered in the fabrication.

Analysis of the masks used to create the grating revealed dimensional inaccuracies resulting from processing errors. Sources of the errors involved the mask fabrication and subsequent replication. To better control etch depth and alignment across the large grating, (85 x 85 mm), a self masking technique was used. This procedure involves the use of a metal coating which must be chemically etched. Most of the dimensional errors have been traced to the photoresist exposure and the metal removal process used in the self masking procedure. The dimensional errors created difficulty in aligning the second mask to the first, resulting in errors of up to 0.5 microns. We are fabricating a second optic without this technique to assess the impact of self masking. This second three-beam grating, fabricated to better tolerances, will be subjected to more complete testing.

Conclusions

Optical fanout gratings of increasing sophistication are required for many current applications. As the complexity of the element increases the conventional design process becomes untenable and a non-deterministic optimization algorithm must be utilized. We have demonstrated a design approach using a simulated annealing algorithm to produce a baseline grating structure. This baseline can then be reviewed and further optimized by the system designer. Our initial design has been fabricated and experimental results demonstrate proof of principle.

Future work will include restructuring the merit function and the target values for the diffraction orders. We believe that this would allow the algorithm to converge more directly toward the solution designed during post optimization. Future work will also include the development and application of more advanced non-deterministic optimization algorithms, particularly genetic algorithms. Preliminary data suggests that as the dimension and complexity of the problem increase, genetic algorithms may achieve a global solution with reasonable rapid convergence.

The authors wish to acknowledge J. A. Teasley for her aid in the fabrication processing, B. R. Peters for his technical expertise in testing the grating and A. L. Cook for his assistance in interpreting the simulation results.

References

1. Alan Kathman and Eric Johnson,"Binary Optics: New Diffractive Elements for the Designer's Tool Kit". *Photonics Spectra*, pp. 125-132, September 1992.

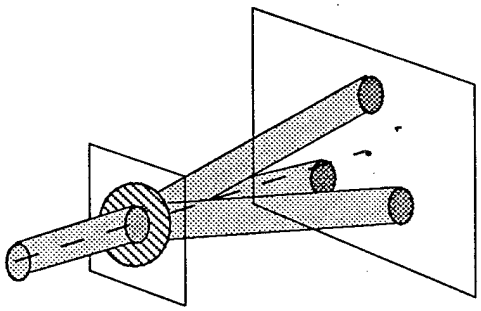

Figure 1. Functional performance of an asymmetric three-beam fanout grating.

```
Random Initialization;
T_initial = 1.0;
t = T_initial;
f1 = cost();
For ( i=0; i<MAX; i++) {
    perturb();
    f2 = cost();
    residue = f2 - f1;
    if ( residue < 0 ) {
        update();
        f1 = f2;
    } else {
        boltzman = exp(-residue/t);
        rnum = random(0., 1.);
        if ( rnum < boltzman ) {
            update();
            f1 = f2;
        }
    }
    t = T_initial / (1 + i );
}
```

Figure 2. Simulated Annealing algorithm for fanout grating optimization.

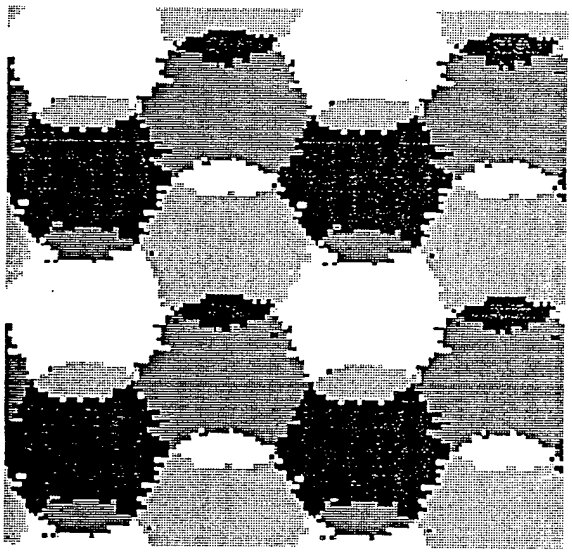

Figure 3. Four phase level pattern produced by simulated annealing.

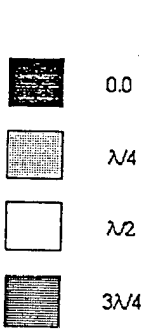

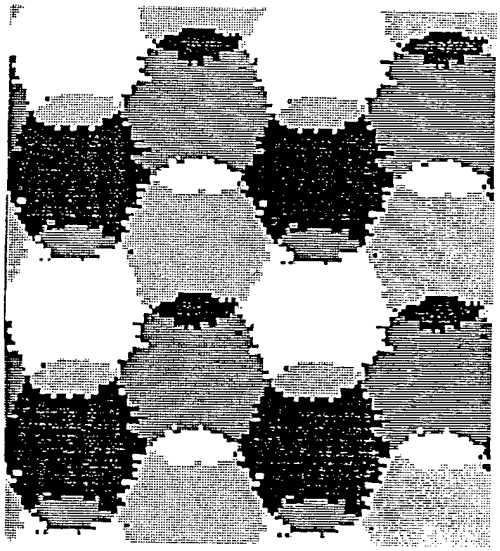

Figure 4. Scaled pattern necessary to produce equilateral triangle.

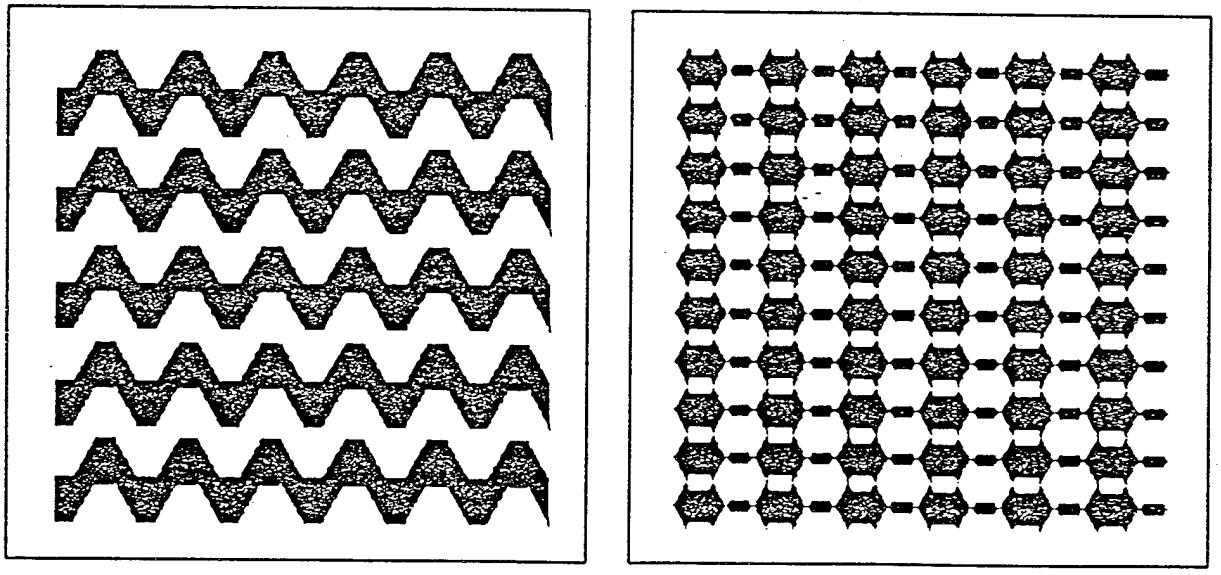

Figure 5. First and second layer mask reticles for three-beam grating fabrication.

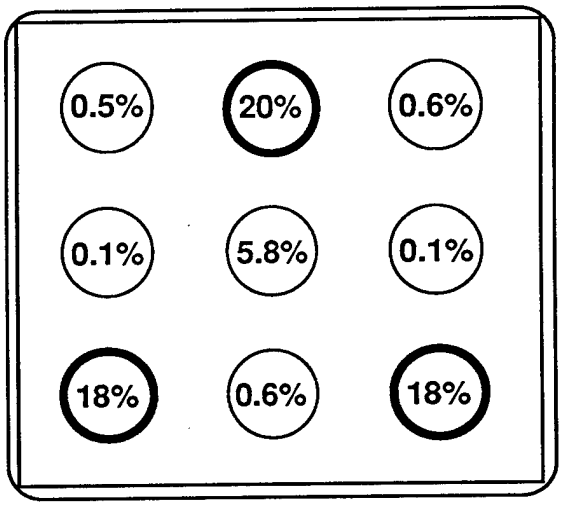

Figure 6. Preliminary experimental results showing the percentage of diffracted light in the nine lowest orders.

SCATTERING FROM BINARY OPTICS

February 1993

D. W. Ricks
Naval Air Warfare Center Weapons Division
China Lake, California, 93555

ABSTRACT

There are a number of sources of scattering in binary optics: etch depth errors, line edge errors, quantization errors, roughness, and the binary approximation to the ideal surface. These sources of scattering can be systematic (deterministic) or random. In this paper scattering formulas for both systematic and random errors are derived using Fourier optics. These formulas can be used to explain the results of scattering measurements and computer simulations.

1.0 INTRODUCTION

For a conventional optical element, such as a mirror, scattering comes from surface roughness or inhomogeneities of surface constants. These surface variations are usually random and are best treated by statistical analysis. In some cases the manufacturing method leads to periodic or quasi-periodic surface features. Single-point diamond turning is an example of a manufacturing process that leaves the surface with accidental periodic surface heights. In these cases the surface bears some resemblance to a diffraction grating and there will be distinct diffraction orders. A randomly rough surface can be regarded as the superposition of an infinite number of diffraction gratings, each with a different grating spacing and hence a different first order diffraction angle. If the *rms* roughness of the surface is much smaller than the wavelength of light, then only the first diffraction order is of any consequence.

In a binary optic the second and higher diffraction orders are important because the depth of the pattern is about one wavelength. In some cases these higher orders of diffraction are desirable, but in many cases anything except the first order can be considered "scattered" light. Scattering from binary optics will also come from the inevitable random surface roughness, just as it does from conventional optics. Binary optics calls for extremely precise positioning and control of etching to insure that each groove is the proper width and depth; errors of fabrication is another source of scattering. Errors of fabrication might be either systematic (deterministic) or random. We shall first consider systematic errors in section 2, and then random errors in section 3.

2.0 SYSTEMATIC ERRORS

Systematic errors, or deterministic errors, include: etch depth errors, line edge errors, mask alignment errors, quantization errors, and the shortcomings of an M-level binary optic approximation to the ideal continuous phase profile. We shall compare computer simulations to analytical formulas. The computer simulations were performed on a personal computer using the software tool Mathcad 2.5. Where possible these results are compared to the work of others.

2.1 GRATINGS

Several types of systematic errors have been investigated in the past in connection with diffraction gratings. When a groove position in the grating varies from the correct position, some energy will be scattered. *Periodic* variations result in the concentration of scattering into spurious diffraction orders called *ghosts*. Ghosts are common in ruled gratings because of periodic errors in turning screws and so forth. An approximate value of the intensity of such ghosts relative to the main diffracted order was given by Rowland in 1893. As presented by Hutley,[1]

$$I_{ghost}/I(m) = (\pi me/a)^2 \quad (1)$$

where m is the diffraction order, e is the maximum departure from the correct position, and a is the period of the grating. The location of the ghost will depend on the period of the error. As an example, if $e = 0.1\mu m$, $a = 1.0\mu m$, and $m = 1$, then the ghost intensity is approximately ten percent of the main diffraction order. We note in equation (1) that the ghost intensity is proportional to the square of the diffraction order. There should be no ghosts around the zero or central order. Random variations in the position of the grooves cause "grass," a broad spectrum of ghosts of random amplitudes in the plane of the diffraction orders. Scattering from surface roughness, on the other hand, has no preferred orientation and is just as intense out of the plane of incidence as in the plane of incidence.

The diffraction efficiency of a grating is the fraction of the incident energy that is diffracted into a particular order. If only one order is desired, then the diffraction efficiency is a measure of the total unscattered light. We consider a diffraction grating that consists of M steps per period. All step widths and heights are assumed equal. We use Fourier optics theory and assume that the grating pattern extends to infinity. With these assumptions it can be shown that the relative diffraction efficiency $\eta(p, M)$ of order p and with M levels is

$$\eta(p, M) = \{[\sin(\pi p/M)\sin(\pi p - \phi/2)]/[\pi p \sin(\pi p/M - \phi/2M)]\}^2 \quad (2)$$

where ϕ/M is the change in phase in each step.[2] We note that the highest efficiency for order p occurs when $\phi/2 = \pi p$. Equation (2) is often used for binary optics in general. The assumption is that in a small region of a binary optic the pattern is an approximation to a grating.

2.2 ETCH DEPTH ERRORS

The relative loss in diffraction efficiency with etch depth error can be obtained from equation (2). Let $\eta_{opt}(p,M)$ be the diffraction efficiency optimized for an order p and with M steps. Let ϵ be the relative etch depth error, then the phase is given by

$$\phi = 2\pi p(1 + \epsilon).$$

The diffraction efficiency is therefore given by

$$\eta(p, M) = \eta_{opt}(p, M)\{[\sin(p\epsilon\pi)]/[M \sin(p\epsilon\pi/M)]\}^2. \quad (3)$$

Figure (1) is a plot of the diffraction efficiency for Fresnel zone plate design FZP3A as a function of percent error in etch depth. Table 1 summarizes the design parameters for several Fresnel zone plates. The

TABLE 1. FRESNEL ZONE PLATE DESIGNS

Design	$\lambda(\mu m)$	Levels	T	f(mm)	f#	n	b(mm)
FZP1	0.6328	16	316	10	10	1.457	0.35
FZP2A	0.6328	4	79	10	10	1.457	0.35
FZP2B	0.6328	4	2005	254	10	1.457	∞
FZP3A	0.6328	2	40	10	10	1.457	∞
FZP3B	0.6328	2	40	10	10	1.457	0.35
FZP3C	0.6328	2	395	100	10	1.457	3.50
FZP4	10.6	16	19	10	10	4.0	0.35
FZP5	10	16	3360	152.4	3	4.0	∞
FZP6	10	16	300	12.7	1	4.0	∞
FZP7	10	8	1680	152.4	3	4.0	∞
FZP8	10	8	300	12.7	1	4.0	∞

data points were calculated using the approximate Rayleigh-Sommerfeld equation which for a circularly symmetric Fresnel zone plate, on axis, can be written as

$$U(0,0,z) = \Sigma_j (2\pi z/\lambda i)\, \phi_j \int_{aj}^{aj+1} r/(r^2 + z^2) \exp[ik(z^2 + r^2)^{1/2}]\, dr \qquad (4)$$

where,

$$a_j = [2fj\lambda/M + (\lambda j/M)^2]^{1/2} \qquad (5)$$

$$\phi_j = \exp\{-2\pi i[1 + e]\mathrm{mod}(j, M)/M\} \qquad (6)$$

and z is the distance from zone plate to observation point, f is the focal length, T is the maximum number of transition points $\{a_j\}$, M is the number of levels, and e is the fractional etch depth error. We define the function mod(j, M) as the remainder when j is divided by M. For this example the illuminating beam was assumed to be uniform, so the Gaussian beam radius b (at the $1/e^2$ points of intensity) is infinite.

For an etch depth error that is uniform across the surface we can use equation (3) for the far-field, paraxial case. In a 2-level Fresnel zone plate an etch depth error of e will alter the phase over half the surface of the optic (in the grooves only), so we use $e/2$ for the error term in equation (3). This curve, also shown in figure (1), matches the data very well. Data similar to figure (1) was shown by Cox, et. al.[3]

Uniform etch depth error is one type of systematic error that can occur in a binary optic. The etch depth can also vary across the binary optic; for example each etch depth may be 5 percent deeper than it should be near the center, gradually becoming 5 percent shallower near the edges. This might occur when the narrower grooves near the edges reduce the etching rate. We can model this type of error by writing

$$\phi_j = \exp\{-2\pi i[1 + e(1 - 2a_j/a_T)]\mathrm{mod}(j, M)/M\} \qquad (7)$$

for the phase term ϕ_j in equation (4). In computer simulations using the Huygens-Fresnel integral (the approximate Rayleigh-Sommerfeld equation), Goodman and Farn[4] found empirically that the diffraction efficiency of a Fresnel zone plate falls off as the square of the etch error. The effect of etch errors is only a weak function of the number of masks, and it is independent of the f-number and radius. They considered Fresnel zone plates with f-numbers $f/1$ and $f/3$ and radii of one and three inches.

Figure (2) shows results identical to Farn and Goodman's data for a 16-level and an 8-level Fresnel zone plate. The relative diffraction efficiency is the peak intensity (equations (4), (5) and (7)) divided by the product of the peak intensity of a perfect lens and the maximum efficiency of an M-level zone plate (equation (2)). Designs FZP5, FZP6, FZP7, and FZP8 from Table 1 are used in the calculations. The results do not depend on the f-number, and depend only slightly on the number of levels (hence on the number of masks in the fabrication process). Also shown in figure (2) are curves calculated from equation (3), where $\epsilon = 7/8\, e$ for an 8-level zone plate, and $\epsilon = 15/16\, e$ for a 16-level zone plate. The relative etch depth error ϵ appears to be the average systematic etch depth error along an axis of the Fresnel zone plate.

A systematic etch depth error decreasing from center to edge should shift the focal position. When the efficiency is calculated at the optimum focal position, then the diffraction efficiency decrease is not nearly as severe as calculated by Farn and Goodman in reference (4). The upper data points in figure (2) shows my calculations for diffraction efficiency at best focus (empirically determined). A good fit to the data is obtained by using equation (3) with $\epsilon = e/\sqrt{3}$, which is the *rms* value of the systematic etch depth error e along an axis of the Fresnel zone plate. At best focus it is found that the diffraction efficiency is essentially independent of the number of masks, the f-number, and the radius.

2.3 LINE EDGE ERRORS

One systematic line edge error would be a linear increase in the position of the transition points. We write the focal length f from equation (5) in terms of the jth transition point a_j, the wavelength λ, and the number of etch levels M,

$$f = a_j^2 M/2j\lambda - j\lambda/2M. \qquad (8)$$

A uniform expansion of the transition points $\{a_j\}$ by the factor B results in a new focal length f' given by

$$f' = B^2 a_j^2 M/2j\lambda - j\lambda/2M$$
$$= B^2 f + (B^2 - 1)\lambda j/2M. \quad (9)$$

In the paraxial case (i.e., when j is small) the second term of equation (9) can be ignored and the new focal length is just B^2 times the old focal length. In general the focal length depends on j, which means there is spherical aberration. The scattering in this case is a spreading of the energy around each diffraction order; and the larger the aperture, the larger the spreading.

Over- or under-exposure of the photoresist during the pattern transfer process can result in systematic line edge errors. Under-exposure results in the grooves being narrower than they should be. Farn and Goodman found that diffraction efficiency (defined as the Strehl ratio) of a Fresnel zone plate falls off linearly with the line edge error, the effect of line edge error is a strong function of the f-number, a weak function of the number of masks and is independent of radius.[4]

Cox et. al. measured the diffraction efficiency of an $f/10$ Fresnel zone plate in ten "zones" of equal area.[3] The first zone is the central portion of the zone plate, covering ten percent of the entire zone plate. Two zone plates were deliberately under-exposed so that the etched portions were 1.35 μm narrower than they should be. A plot of the measured local diffraction efficiency (fraction of power) is shown in figure (3) for the average of the two zone plates. Also shown is a plot of the calculated local diffraction efficiency in each of the ten "zones" as defined by Cox, et. al.

We expect the diffraction efficiency to decrease with increasing zone number since the error e becomes relatively more significant as the spacing decreases. In a 2-level zone plate a line edge error represents an area of the zone plate that does not contribute at all to the peak intensity. We therefore subtract the error fraction of a period from the efficiency. In a 2-level zone plate a period is every two transition points. In design FZP3A there are forty transition points, hence four transition points in each of ten "zones" as defined by Cox, et. al. If d_i is the average period in the ith "zone", or

$$d_i = (a_{4i+2} - a_{4i} + a_{4i+4} - a_{4i+2})/2, \quad (10)$$

then the local diffraction efficiency η_i is approximately given by

$$\eta_i(e) = (1 - e/d_i)\,[M/\pi \sin(\pi/M)]^2, \quad (11)$$

where e is the line edge error. When $e = 0$ equation (11) reduces to the standard formula for diffraction efficiency with no errors (equation (2)). To compare with the Cox data we use the value of $e = 1.35$ μm measured by Cox, and we find a good fit using equation (11), as shown in figure (3). The diffraction efficiency is seen in equation (11) to decrease linearly with line edge error and is a strong function of the f-number (the smaller the f-number, the smaller the value of d in the outer zones) as observed by Farn and Goodman.[4]

2.4 MASK ALIGNMENT ERRORS

The experimental and theoretical work of Cox[3,5] shows that a fixed lateral error, or a mask alignment error, leads to a fall off in diffraction efficiency that is more severe in the outer zones of the zone plate than near the center. In the outer zones a fixed error represents a greater percentage of the pattern and we expect it to cause the greater efficiency decrease. By measuring the local diffraction efficiency of a number of zone plates with design FZP2B, Cox found that the fall off in efficiency is approximately linear from zone to zone. I have plotted in figure (4) the diffraction efficiency in the outer most (i.e. 10th) zone as a function of the mask alignment error. The data points with a small alignment error represent typical fabrication errors, the large alignment error values were intentional. The straight line in figure (4) is given by

$$\eta_{10}(e) = (1 - e/\Delta a_{10,ave})\,[M/\pi \sin(\pi/M)]^2 \quad (12)$$

where $M = 4$ for this 4-level design, and $\Delta a_{10,ave} = 3.25\ \mu m$ is the mean separation of transition points in the tenth zone. The mean separation is much smaller than the average period used in equation (11). Cox concludes that mask alignment error is more significant than etch depth error or line edge error.

2.5 M-LEVEL APPROXIMATION ERRORS

A 100 percent efficient Fresnel zone plate would have a continuously curving profile. Equation (2) indicates that a 16-level binary optic approaches that level of efficiency. How is the energy distributed that is not diffracted into the first order? We know that in the absence of fabrication errors the energy goes into other diffraction orders which will have very low intensity at the first-order focal plane. To calculate the scattering we first reduce the diffraction "ringing," caused by the finite size of the Fresnel zone plate. The amount of energy outside of the central lobe can be minimized by assuming that the Fresnel zone plate is illuminated by a Gaussian beam that has low intensity at the edges of the aperture.

Figure (5) compares the intensity as a function of angle for a cylindrical Fresnel zone plates with 2-, 4-, and 16-levels. We are using designs FZP3B, FZP2A, and FZP1. The intensity is relative to the peak intensity I_p of a perfect lens with the same f-number. The data has been smoothed by averaging over sixteen successive data points. The first point plotted is the mean of the first sixteen computer generated data points, I_1 to I_{16}, divided by I_p. The second point plotted is the mean of I_2 to I_{17} divided by I_p, and so forth. There are 2048 data points for each curve, and the points are spaced at intervals of λ.

We notice in figure (5) that the intensity of the scattered light from the 2-level zone plate seems to drop to the intensity of the 4-level zone plate at about 5.7 degrees. This can be explained as follows. In the 1st-order focal plane the biggest visible difference between the 2-level scattering and the 4-level scattering will be the contribution of the 3rd-order energy. The diffraction efficiency equation (2) indicates that for a 2-level binary optic about 4.5 percent goes into the 3rd-order. The 4-level (and higher) binary optic has no energy in the 3rd-order.

The paraxial focus of the 3rd-order is at $f/3$, where f is the 1st-order focal length. Using geometrical optics the extreme ray from the edge of the zone plate which passes through the 3rd-order focus strikes the 1st-order focal plane at x_0' given by

$$x_0'/(f - f/3) = (f/2f^{\#})/(f/3) \tag{13}$$

where $f^{\#}$ is the 1st-order f-number of the zone plate. Hence

$$x_0' = f/f^{\#}. \tag{14}$$

This is the geometric edge of the 3rd-order diffraction in the 1st-order focal plane. As seen from the center of the zone plate this edge makes an angle θ', given by

$$\begin{aligned} \tan\theta' &= x_0'/f \\ &= 1/f^{\#}. \end{aligned} \tag{15}$$

For an $f/10$ zone plate $\theta' = 5.7$ degrees, in good agreement with our observation in figure (5).

3.0 RANDOM ERRORS

Random errors are processing errors that are statistical in nature. In this section we discuss some random errors that have been noted for gratings. We then derive a formula for random roughness for binary optics. We show that this formula can also be used to calculate the scattering from random etch depth errors and random line edge errors. We compare the formula to computer simulations of random fabrication errors. We use Dammann gratings and Fresnel zone plates as examples.

3.1 GRATINGS

From the theory of gratings a random change in form from groove to groove is called "accidental error of amplitude," and is a form of random error independent of grating order.[6] A random error in the position of the groove causes "grass," as mentioned previously. The proportion of the energy scattered into grass is given by[1]

$$\mathbf{I}_{grass}/\mathbf{I}(m) = (4\pi m e_{rms}/a)^2 \tag{16}$$

where e_{rms} is the *rms* error in groove position. According to this formula grass increases as the square of the diffraction order, the same as the intensity for ghosts.

3.2 RANDOM ROUGHNESS

We consider now the problem of a binary optic with slightly rough surfaces.[7] We shall consider the binary optic to behave like a grating and use the Fraunhofer diffraction formula. The illumination of the grating will be by a collimated laser beam of wavelength λ and beam radius b. The beam waist is at the grating. The field at the point (x_0, y_0, z) is given by (ignoring some unimportant phase terms)

$$\mathbf{U}(x_0, y_0, z) = 1/\lambda z \int_{-\infty}^{\infty}\int_{-\infty}^{\infty} \Sigma A_m \exp(2\pi i m x_1/a) \exp[ki\mathbf{h}(x_1, y_1)(n - 1)]$$
$$\exp[-ik(x_0x_1 + y_0y_1)/z] \exp[-(x_1^2 + y_1^2)/b^2]\, dx_1\, dy_1 \tag{17}$$

where $\Sigma A_m \exp(2\pi i m x_1/a)$ is the Fourier series of the field induced by the binary optic in the $(x_1, y_1, 0)$ plane, a is the grating period, n is the index of refraction of the grating material, and $\mathbf{h}$ is the roughness or surface height variation function. We multiply $\mathbf{U}(x_0, y_0, z)$ by its complex conjugate to obtain the intensity.

We next assume that the distribution of surface heights $\mathbf{h}$ is random with a Gaussian probability; therefore[8]

$$\langle \exp\{ki[\mathbf{h}(x_1, y_1) - \mathbf{h}(x_2, y_2)](n - 1)\}\rangle = \exp\{-[k(n - 1)\sigma]^2 [1 - \mathbf{R}(x_1 - x_2, y_1 - y_2)]\} \tag{18}$$

where $\langle\ \rangle$ denotes the average or expected value, σ is the *rms* surface roughness and $\mathbf{R}()$ is the autocorrelation function. If we assume that the surface roughness is small, $k\sigma << 1$, then

$$\exp\{-[k(n - 1)\sigma]^2 [1 - \mathbf{R}(x_1 - x_2, y_1 - y_2)]\} \approx 1 - [k(n - 1)\sigma]^2 [1 - \mathbf{R}(x_1 - x_2, y_1 - y_2)]. \tag{19}$$

Next, assume that the autocorrelation function is exponential,

$$\mathbf{R}(x_1 - x_2, y_1 - y_2) = \exp\{-[(x_1 - x_2)^2 + (y_1 - y_2)^2]^{1/2}/\tau\} \tag{20}$$

where τ is the correlation length. Recognizing that we now have the zero order Hankel Transform of the autocorrelation function we find that

$$\langle \mathbf{I}(x_0, y_0, z)\rangle = \langle \mathbf{I}_{rough}(x_0, y_0, z)\rangle + \langle \mathbf{I}_{smooth}(x_0, y_0, z)\rangle \tag{21}$$

where

$$\langle \mathbf{I}_{rough}(x_0, y_0, z)\rangle = [\pi\sigma\tau bk(n - 1)/\lambda z]^2 \Sigma|A_m|^2 \{1 + [(2\pi m/a - x_0k/z)^2 + (y_0k/z)^2]\tau^2\}^{-3/2}, \tag{22}$$

$$\langle \mathbf{I}_{smooth}(x_0, y_0, z)\rangle = (b^2\pi/\lambda z)^2 \{1 - [k(n - 1)\sigma]^2\} \Sigma|A_m|^2 \exp\{-2b^2\pi^2[(x_0/\lambda z - m/a)^2 + (y_0/\lambda z)^2]\}. \tag{23}$$

We can compare these results to the scattering formulas of others by rewriting this expression as the bidirectional transmission distribution function (BTDF). The sine of the specular angle $\theta_{2,m}$ in the mth order is given by

$$\sin\theta_{2,m} = \lambda m/a \tag{24}$$

and the sine of the scatter angle is, to the approximations we are using,

$$\sin\theta_s = x_0/z. \tag{25}$$

We define the spatial frequency p_m by

$$p_m \equiv k(\sin\theta_s - \sin\theta_{2,m}). \tag{26}$$

Along the axis, $y_0 = 0$, and we can write the BTDF using equation (22), and equations (24) to (26) by

$$\text{BTDF} = (2k^4/\pi)\,[\sigma\tau(n-1)/2]^2 \cos\theta_s\, \Sigma|A_m|^2\,/[1 + p_m{}^2\tau^2]^{3/2}. \tag{27}$$

The typical two-dimensional bidirectional *reflection* distribution function (BRDF) with an exponential autocorrelation function, for normal incidence is given by[9]

$$\text{BRDF} = (2k^4/\pi)\,(\sigma\tau)^2 \cos\theta_s\, F(\theta_s)\,/[1 + p_m{}^2\tau^2]^{3/2} \tag{28}$$

where $F(\theta_s)$ is approximately one for small angles, and is exactly one in some theories. Comparing equation (28) with equation (27) we see that one difference is the factor $[(n-1)/2]^2$. This difference exists because the phase change on reflection from surface features is proportional to twice the height of the feature, but in transmission the phase change is $(n-1)$. The second difference is the term $\Sigma|A_m|^2$. Evidently the existence of the grating replicates the scattering pattern around each diffraction order. The amplitude of the scattering is scaled by the amplitude of the diffraction order.

In a similar manner we can derive a formula for one-dimensional random roughness. We shall show that this formula can also predict the scattering from Dammann gratings with random etch depth and random line edge errors. In addition the formula will predict scattering for cylindrical Fresnel zone plates with random etch depth or line edge errors; the results agree well with the average of computer simulations. Equation (22) will predict scattering from circular Fresnel zone plates with random etch depth or line edge errors.

The one-dimensional random roughness formula is derived by assuming that the equations are independent of the y_1-axis. Instead of a zero order Hankel Transform of the two-dimensional autocorrelation function, we have the Fourier Transform of the one-dimensional autocorrelation function. The end result is

$$\langle \mathbf{I}(x_0, y_0, z)\rangle = \langle \mathbf{I}_{\text{rough}}(x_0, y_0, z)\rangle + \langle \mathbf{I}_{\text{smooth}}(x_0, y_0, z)\rangle \tag{29}$$

where

$$\langle \mathbf{I}_{\text{rough}}(x_0, y_0, z)\rangle = [k(n-1)\sigma/\lambda z]^2 b\tau\sqrt{(2\pi)}\Sigma|A_m|^2[1 + \tau^2(kx_0/z - 2\pi m/a)^2]^{-1} \tag{30}$$

$$\langle \mathbf{I}_{\text{smooth}}(x_0, y_0, z)\rangle = (b/\lambda z)^2\pi\{1 - [k(n-1)\sigma]^2\}\Sigma|A_m|^2\exp\{-2b^2\pi^2[x_0/\lambda z - m/a]^2\}. \tag{31}$$

We recall that σ is the *rms* roughness, τ is the correlation length, $k = 2\pi/\lambda$, b is the radius of the Gaussian beam, n is the refractive index of the substrate, a is the period of the grating, and $|A_m|^2$ (as it turns out) is the diffraction efficiency of the mth order.

3.3 ETCH DEPTH ERRORS

We now consider etch depth errors where the etch depth varies randomly from groove to groove. We can consider Dammann gratings and cylindrical Fresnel zone plates as one-dimensional rough surfaces. Circular Fresnel zone plates are two-dimensional.

3.3.1 DAMMANN GRATING

Dammann gratings are convenient to consider because they are simple two-level binary optics where the diffraction orders are spatially separated. We consider a number of designs, as shown in Table 2.

TABLE 2. DAMMANN GRATING DESIGNS

Design	Transition points $a_1(\mu m)$	$a_2(\mu m)$	depth $h(\mu m)$	period $a(\mu m)$	λ (μm)	Equal intensity (orders)
DG1	43.02	86.96	0.545	200	0.633	0, ±1, ±2, ±3
DG2	43.02	86.96	9.129	200	10.6	0, ±1, ±2, ±3
DG3	10.75	21.74	0.545	50	0.633	0, ±1, ±2, ±3
DG4	13.74	30.06	1.23	60.12	10.6	

Figure (6) shows the relative intensity of Dammann grating design DG1 with a random etch depth error. In addition to the values in Table 2, b = 4.5 mm, f = 1.82 m, and n = 1.45702, except for DG4 where b = 2.5 mm and n = 3.4178. The standard deviation of the error is δ = 0.01 μm. The intensity profile was calculated with four sets of random numbers and the results were averaged together. The results were also smoothed by averaging over sixteen data points, and normalized by dividing by the peak intensity in the error-free case. In figure (6) the zero diffraction order is at zero degrees, and the next four positive diffraction orders are also shown. The negative diffraction orders would be similar and are not plotted.

Also shown in figure (6) is a plot of equation (29). The correlation length τ we estimate to be approximately equal to the width of the etched portion of the Dammann grating. In this portion the correlation is unity, falling off to zero outside of the etched area. For design DG1 there are two etched portions per period; the width of each is 86.96 - 43.02 = 43.94, so we set τ = 44. The *rms* roughness σ is

$$\sigma = (\delta^2\tau/a + 0 + \delta^2\tau/a + 0)^{1/2}$$

$$= \delta\,(2\tau/a)^{1/2}. \tag{32}$$

In figure (7) the standard deviation of the etch error has been increased to δ = 0.1 μm. The average of four computer simulations using the Fresnel diffraction formula is shown together with the 1-D roughness equation (29). The value of τ is again 44 μm, and we use equation (31) to calculate the *rms* roughness. It appears to be a good fit. We see from equation (29), and it is confirmed in the computer simulations illustrated in figures (6) and (7), that the scattering is proportional to δ^2, since δ and σ are linearly related through equation (31). The diffraction efficiency can be given by equation (31), which indicates that for random etch depth errors with two etched surfaces per period, the diffraction efficiency decreases by

$$\eta = \eta_0\{1 - [k(n-1)\sigma]^2\}$$

$$= \eta_0\{1 - (2\tau/a)[k(n-1)\delta]^2\} \tag{33}$$

using equation (32). The efficiency with no errors is η_0, and is given by equation (2).

What effect does wavelength have on the scattering? Consider design DG2, which has the same transition points (hence the same pattern), but differs in the design wavelength and etch depth. The relative intensity profile is shown in figure (8), along with a plot of the one-dimensional scattering formula (29). Formula (29) agrees as well with computer simulations for the 10.6 μm wavelength as for the 0.6328 μm wavelength. The etch depth error has a standard deviation of 0.1 μm, the same as the error illustrated in figure (7), but the relative scattering is much less. This is in keeping with the prediction of equations (30) and (31) that the relative scattering is

$$\langle I_{rough}(x_0, y_0, z)\rangle / I_{peak} = [k(n-1)\sigma/\lambda z]^2 b\tau\sqrt{(2\pi)}\,\Sigma|A_m|^2[1 + \tau^2(kx_0/z - 2\pi m/a)^2]^{-1}/(b/\lambda z)^2\pi\,|A_{peak}|^2$$

$$= [k(n-1)\sigma]^2 \tau \sqrt{2}\, \Sigma |A_m/A_{peak}|^2 [b\sqrt{\pi} + b\sqrt{\pi}\,\tau^2 (kx_0/z - 2\pi m/a)^2]^{-1} \quad (34)$$

assuming there is not much overlap of energy between diffraction orders. We see from equation (34) that the relative scattering is proportional to $(k\sigma)^2$ and therefore proportional to $(\delta/\lambda)^2$, as we can also see by comparing figures (8) and (7).

3.3.2 CYLINDRICAL FRESNEL ZONE PLATES

Continuing with our examination of random etch depth errors, we now look at cylindrical Fresnel zone plates. This type of zone plate will show one-dimensional scattering characteristics. The cylindrical Fresnel zone plate creates a line focus (at $x_0 = 0$) for each diffraction order at a distance from the zone plate that depends on the diffraction order. We shall concern ourselves only with the scattering from roughness in the first diffraction order; in the 1st-order focal plane scattering from other diffraction orders is insignificant. The relative scatter intensity from roughness is therefore (using equation (34)),

$$<I_{rough}(x_0, y_0, z)>/I_{peak} = [k(n-1)\sigma]^2 \tau \sqrt{2}\, [b\sqrt{\pi} + b\sqrt{\pi}(\tau k x_0/z)^2]^{-1} \quad (35)$$

for the cylindrical Fresnel zone plate.

As before, the correlation length τ is the mean width of the etched portions;

$$\tau = \text{mean}\{a_{j+1} - a_j\} \quad (36)$$

which for design FZP1 gives $\tau = 1.58\ \mu$m. For the Fresnel zone plates all levels were assumed to have some etch depth error, so the mean is taken over all intervals. This also implies that $\sigma = \delta$. Figure (9) should be compared to figure (10) where the standard deviation of the etch depth error is $\delta = 0.1\ \mu$m and $\delta = 0.01\ \mu$m, respectively. The scattering drops two orders of magnitude with one order of magnitude decrease in the error. Again equation (35) provides a good prediction of the average value of the scattering at a particular angle. Equation (35) predicts that the scattering is proportional to σ^2, and $\sigma^2 = \delta^2$ in this case.

A 4-level Fresnel zone plate (FZP2A) shows behavior similar to the 16-level zone plates just considered. Figure (11) illustrates this case when the standard deviation of the etch depth error is $\delta = 0.1\ \mu$m. A plot of equation (35) is shown for comparison. Equation (36) gives $\tau = 6.33\ \mu$m; and $\sigma = \delta$. The random scattering in this case is less than the systematic error for angles greater than about three degrees; averaging is necessary to reveal the scattering. The gaps in the curve indicate where the average intensity with etch depth errors is less than the intensity without etch depth errors. Further averaging should make the relative scatter intensity converge to the plot of equation (35).

3.3.3 CIRCULAR FRESNEL ZONE PLATES

We now consider random etch depth errors in circular Fresnel zone plates. In this case we must use the two-dimensional roughness scattering formula, equation (21). For our purposes here we want the scatter intensity from the "rough" part divided by the peak intensity of the smooth part in the absence of roughness. Using equations (22) and (23) we find

$$<I_{rough}(x_0, y_0, z)>/I_{peak} = [k(n-1)\sigma\tau/b]^2\, [1 + (\tau k x_0/z)^2 + (\tau k y_0/z)^2]^{-3/2} \quad (37)$$

for the two-dimensional or circular Fresnel zone plate. The *rms* roughness σ will be, as before, equal to the standard deviation of the etch depth error, δ. The correlation length will again be given by equation (36).

The relative scattering for the circular Fresnel zone plate with design FZP1 is shown in figure (12). The relative scattering in the two-dimensional case is much less than the relative scattering in the one-dimensional case (figure (9)) for the same average etch depth error.

Design FZP1 also has much less relative scattering than design FZP4, shown in figure (13). What is the

reason for this? There are three terms in equation (37) which change from design FZP1 to FZP4; τ, λ, and n. The correlation length τ in turn is a function of the wavelength λ, the number of levels M, and the f-number $f^{\#}$. We now derive an approximate value for τ. If the f-number is not too small we can approximate the transition point a_j from equation (5) by using the paraxial approximation,

$$a_j^2 \approx 2\lambda fj/M.$$

Hence,

$$a_{j+1}^2 - a_j^2 \approx 2\lambda f/M$$

and therefore

$$a_{j+1} - a_j \approx 2\lambda f/(Ma_{j+1} + Ma_j).$$

We have then that

$$\tau = \text{mean}(a_{j+1} - a_j) \approx [2\lambda f/M]\ \text{mean}(1/[a_{j+1} + a_j]) = 2\lambda f/Ma_T$$

$$\tau \approx 4\lambda f^{\#}/M. \tag{38}$$

We see that the term $k\tau$ in equation (37) is approximately the same in both design FZP1 and FZP4, hence the difference in relative scattering levels is due solely to the difference in refractive index n of the two designs.

3.4 LINE EDGE ERRORS

We now examine the effects of random line edge error in Dammann gratings and Fresnel zone plates. The location of the line edge is made random by adding e_j to the transition point a_j, where e_j is a random number with mean of zero and standard deviation δ. Our random roughness formulas were derived under the assumption of a small random phase shift to the surface, but we will attempt to use these formulas for the random line edge errors.

A random line edge error could be regarded as a perturbation from the ideal pattern. The height of the perturbation is the step height, h. The *rms* roughness σ is then the square root of the average amount of height perturbation, or

$$\sigma = [m<w>h^2/a]^{1/2} \tag{39}$$

where m is the number of edges which vary from their proper positions in a period a, and $<w>$ is the mean width of the perturbations. For a uniform probability over either the interval $[0, \delta\sqrt{3}]$ or $[-\delta\sqrt{3}, 0]$,

$$<w> = \delta(\sqrt{3})/2 \tag{40}$$

and δ is the standard deviation of the error over that interval.

In the derivation of the *rms* roughness formula we assumed a two-sided exponential probability density function, $(1/2\tau)\exp(-|x|/\tau)$. Hence the standard deviation δ is related to the correlation length τ by

$$\delta = [(1/2\tau)\int_{-\infty}^{\infty} x^2 \exp(-|x|/\tau)\,dx]^{1/2}$$

$$= \tau\sqrt{2}. \tag{41}$$

With σ and τ now given by equations (39), and (41), we can compare the computer simulations of random line edge error to plots using the roughness formulas.

3.4.1 DAMMANN GRATINGS

We begin our examples of random line edge errors with the Dammann gratings. Figure (14) shows the relative intensity versus angle for Dammann grating DG1 with line edge error $\delta = 1\ \mu$m. A plot of the roughness formula (29) is also shown (it is almost constant at 10^{-4}). There are four edges per period in design DG1, so $m = 4$ in equation (39). The step height h is given in Table 2. The scattering predicted by equation (29) appears to be a little high compared to the computer simulation, possibly because the assumption made in the derivation that h is small compared to λ is not very good. Figure (15) shows the case for $\delta = 0.1\ \mu$m. Equation (30) correctly predicts an increase in scattering of magnitude 100 when δ is increased by a factor of 10. To see this in equation (30) we note that

$$\begin{aligned} \langle I_{rough}(x_0, y_0, z)\rangle &\propto \sigma^2 \tau \\ &\propto \langle w\rangle \tau \\ &\propto \delta^2 \end{aligned} \tag{42}$$

using equations (39), (40), and (41). When the period is decreased by a factor of four (design DG3), the scattering increases by a factor of four (not shown here). The scattering is proportional to σ^2 in equation (30), and therefore proportional to $1/a$, according to equation (39).

When the wavelength is increased, and the step height is increased proportionally (design DG2), the relative scattering intensity remains the same for random line edge errors. The roughness formula (34) predicts this since the relative scattering is proportional to $(\sigma k)^2$, which is proportional to $(h/\lambda)^2$ by equation (39).

Figure 16 is a comparison of the roughness formula with measured data. The design is the same as DG1 except the etch depth was (accidentally) 0.662 μm instead of 0.545 μm. This results in a reduction of the zero order about a factor of ten from the design value. Measurements using a WYKO profilometer indicate a *rms* roughness of about 0.43 nm, too little to explain the measured scattering. The random etch depth error was measured to be about 1.0 nm, which could account for some of the scattering. A random line edge error with standard deviation of 0.025 μm, when added to the etch depth error, gives a good approximation to the measured scattering. This level of random line edge error was too small to be measured with the WYKO, and is less than a typical manufacturing error.

Another comparison of measured data and the roughness formula is shown in figure (17) for design DG4. The *rms* roughness of the lands was about 1.0 nm, but the grooves had a slope giving an effective roughness of 27.6 nm. Since this slope was periodic we would expect a systematic error, rather than a random error. Plotting these values of etch depth roughness shows 1.0 nm accounts for only a small part of the measured scattering, and 27.6 nm predicts orders of magnitude more scattering than was measured. A line edge error with standard deviation of 0.03 μm agrees reasonably well with the scattering measurement.

3.4.2 CYLINDRICAL FRESNEL ZONE PLATES

We now consider random line edge errors in Fresnel zone plates. Figure (18) is a plot of the relative scatter intensity of a cylindrical zone plate, design FZP1. The systematic error part of a 16-level zone plate has been subtracted out. We add a random number e_i to each transition point a_i. To plot the roughness equation we use the same formulas for τ and σ as we did for Dammann gratings. We interpret equation (39) using $m = T$ for the number of transition points or edges in the half-width or radius a of the design. We could write

$$\sigma = h[\delta(\sqrt{3})T f^{\#}/f]^{1/2} \tag{43}$$

using equations (39) and (40). The relative scattering increases by a factor of 100 when the line edge errors increase by a factor of 10, as it does for Dammann gratings.

Design FZP2 has one fourth the transition points of design FZP1, but the step heights are four times

as high, since

$$h = \lambda/[(n - 1)M]. \tag{44}$$

Roughness is proportional to $h\sqrt{T}$, as we see from equation (43), so design FZP2 has twice the roughness of design FZP1, and therefore four times the scattering for the same random line edge error. Computer simulations confirm this prediction of the roughness formula.

There is less scattering from design FZP4 than design FZP1. It appears to be a result of differences in the factors λ, T, and n. The number of transition points T is reduced approximately in proportion to λ. The step height is increased in proportion to λ, but decreased in proportion to $(n - 1)$. We have from equations (30), (43), and (44)

$$\begin{aligned} I_{rough} &\propto [(n - 1)\sigma/\lambda]^2 \\ &\propto (n - 1)^2 h^2 T/\lambda^2 \\ &\propto (n - 1)^2 [\lambda/(n - 1)]^2 1/\lambda^3 \\ &\propto 1/\lambda. \end{aligned} \tag{45}$$

We see that the refractive index n doesn't really affect the scattering intensity for line edge errors, and the net result is that the scattering is inversely proportional to the wavelength. However, if one particular design were used at two wavelengths, then T and σ would be constant, and the scattering would be proportional to $1/\lambda^2$.

3.4.3 CIRCULAR FRESNEL ZONE PLATES

Lastly we consider designs FZP1 and FZP4 for random line edge errors in circular Fresnel zone plates. The intensity is found using random numbers e_j added to the transition points a_j. These results are compared to the roughness formula (37). As before, the correlation length is $\delta/\sqrt{2}$, and the *rms* roughness σ is the *rms* surface height with respect to the design step height. For a circular Fresnel zone plate

$$\begin{aligned} \sigma &= \{\Sigma_j[(a_j + \langle w \rangle)^2 - a_j^2](h/a_T)^2\}^{1/2} \\ &= (h/a_T)[T\langle w \rangle^2 + 2\langle w \rangle \Sigma_j a_j]^{1/2} \\ &= (h/a_T)[T\delta^2 3/4 + \delta\sqrt{3}\,\Sigma_j a_j]^{1/2}. \end{aligned} \tag{46}$$

Figure (19) shows that the relative intensity of the scatter is down six or seven orders of magnitude from the peak intensity, even for a fairly large line edge error of 1 μm standard deviation. As in the one-dimensional case, the roughness formula predicts a decrease in relative scattering proportional to $1/\lambda$ for optimized designs.

4.0 CONCLUSIONS

Using Fourier optics methods some formulas for scattering from binary optics have been developed. These formulas are similar to standard random roughness formulas used to predict scattering from smooth surfaces. The formulas are shown to agree reasonably well with computer simulations and actual measurements.

5.0 REFERENCES

1. M.C. Hutley, *Diffraction Gratings*, Academic Press, 1982.

2. G.J. Swanson, "Binary Optics Technology: Theoretical Limits on the Diffraction Efficiency of Multilevel Diffractive Optical Elements," Massachusetts Institute of Technology Lincoln Laboratory, Technical Report 914, 1 March 1991.

3. J.A. Cox, T. Werner, J. Lee, S. Nelson, B. Fritz, and J. Bergstrom, "Diffraction efficiency of binary optical elements," *Computer and Optically Formed Holographic Optics*, SPIE Proceedings Vol. 1211, pp. 116-124 (1990).

4. M.W. Farn, J.W. Goodman, "Effect of vlsi fabrication errors on kinoform efficiency," *Computer and Optically Formed Holographic Optics*, SPIE Proceedings Vol. 1211, pp. 125-136 (1990).

5. J.A. Cox, B. Fritz, and T. Werner, "Process error limitations on binary optics performance," *Computer and Optically Generated Holographic Optics (Fourth in a Series)*, SPIE Proceedings Vol. 1555, pp. 80-88 (1991).

6. C.M. Sparrow, "Theory of Imperfect Gratings," *Astrophysical Journal*, Vol. XLIX No. 2, March 1919.

7. This derivation was worked out with the help of Dr. Merle Elson and Larry Chizek. It was published in Larry's thesis "Near-Angle Scattering and Binary Optics," Naval Postgraduate School, December 1989. The results were given in D.W. Ricks and L.V. Chizek, "Light scattering from binary optics," *Computer and Optically Formed Holographic Optics*, Ivan Cindrich and Sing H. Lee, Editors, Proc. SPIE 1211, 24-37 (1990).

8. C.C. Sung and J.A. Holzer, "Scattering of Electromagnetic Waves from a Rough Surface," *Applied Physics Letters*, Vol. 28, No. 8, pp. 429-431, 1976.

9. E.L. Church, H.A. Jenkinson, and J.M Zavada, "Measurement of the finish of diamond-turned metal surfaces by differential light scattering," *Optical Engineering*, Vol. 16 No. 4, July-August 1977.

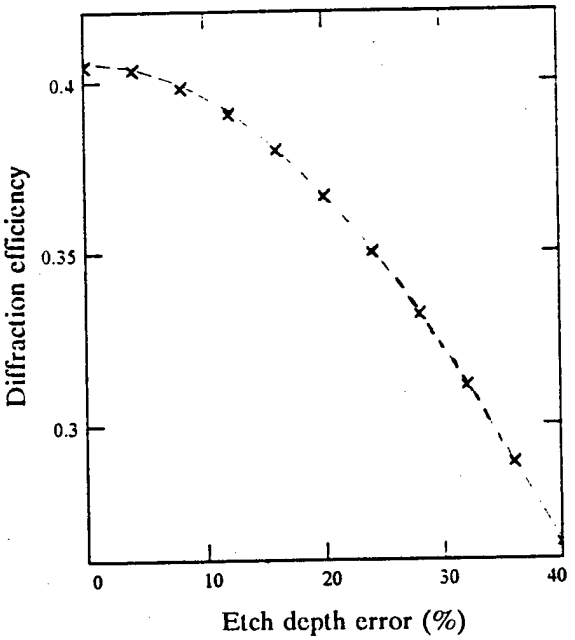

FIGURE 1. Diffraction efficiency versus uniform etch depth error (%), Fresnel zone plate (FZP3A). Computer simulation (X) compared to equation (3).

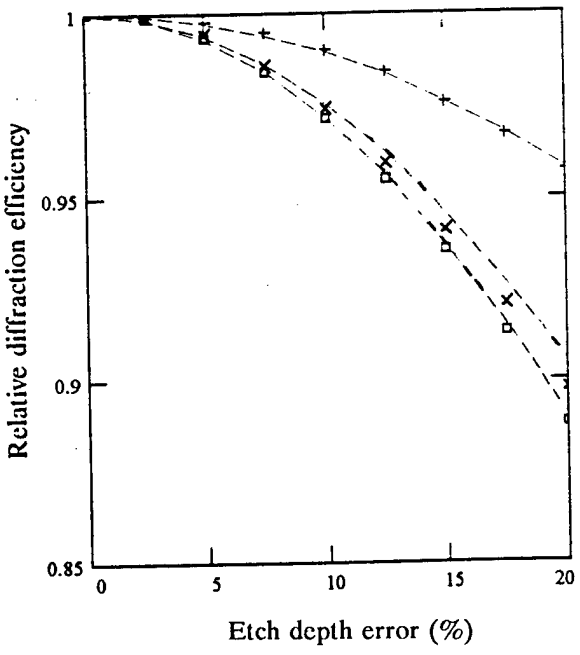

FIGURE 2. Relative diffraction efficiency versus systematic error (%). 16-level (0), 8-level (X), and best focus (+); compared to equation (3).

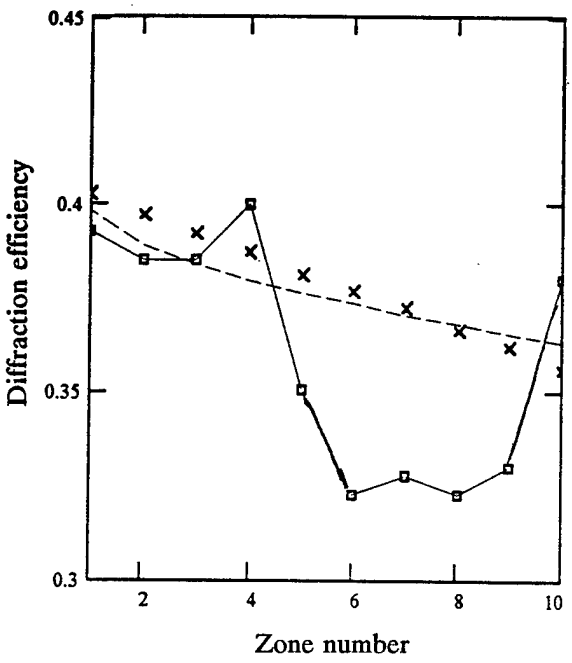

FIGURE 3. Diffraction efficiency versus zone number. Comparing Rayleigh-Sommerfeld (X), equation (11), and data (-0-0-) from ref. (3).

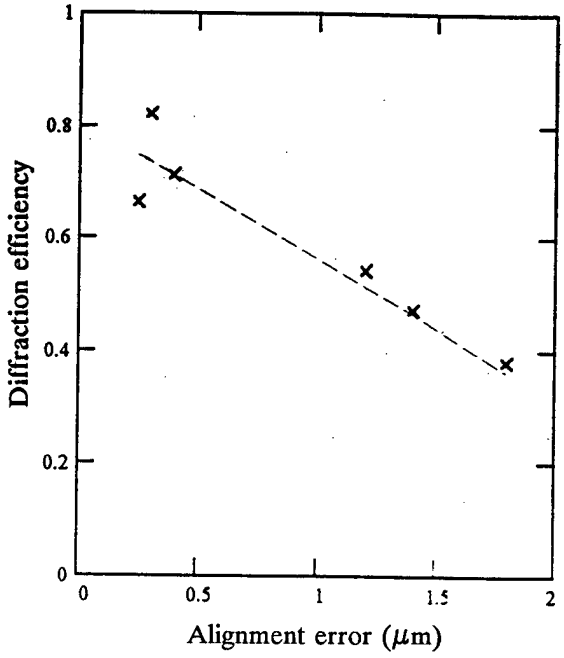

FIGURE 4. Diffraction efficiency in the outer zone versus mask alignment error (μm). Equation (12) compared to measured data (X) from ref. (5).

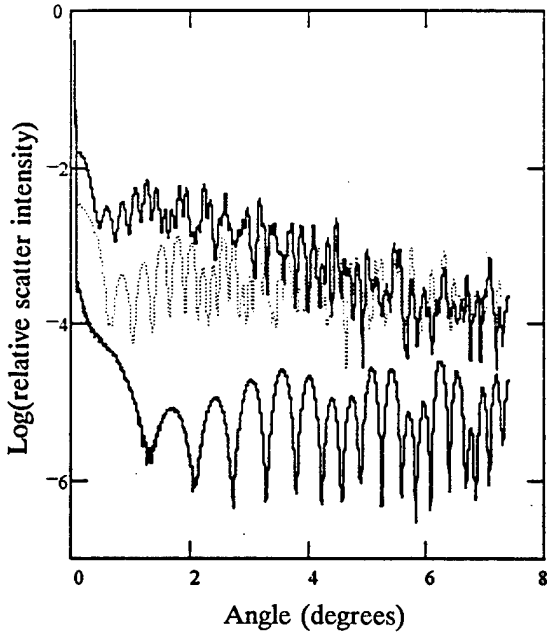

FIGURE 5. Relative scatter intensity versus scattering angle. Cylindrical Fresnel zone plate; 16-level (bottom), 4-level, and 2-level (top).

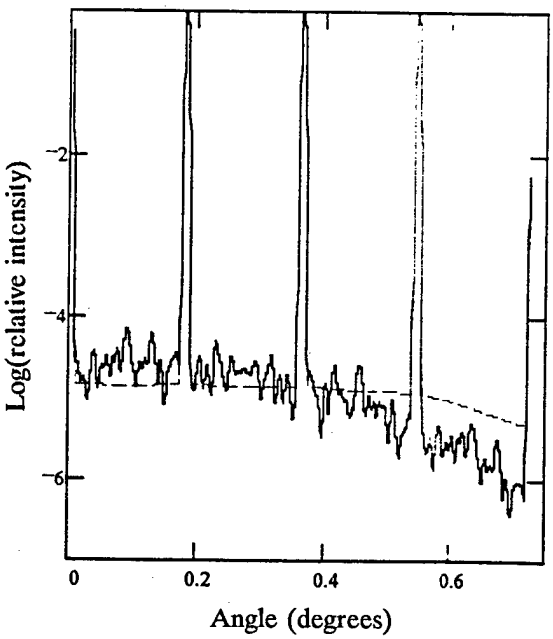

FIGURE 6. Relative intensity, Dammann grating (DG1). Etch depth error δ = 0.01 μm. Compared to 1-D roughness scattering formula.

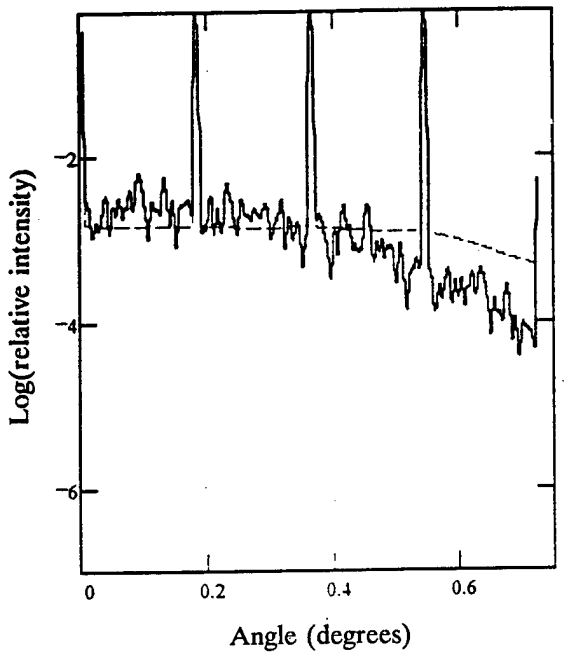

FIGURE 7. Relative intensity, Dammann grating (DG1). Etch depth error δ = 0.1 μm. Compared to 1-D roughness scattering formula.

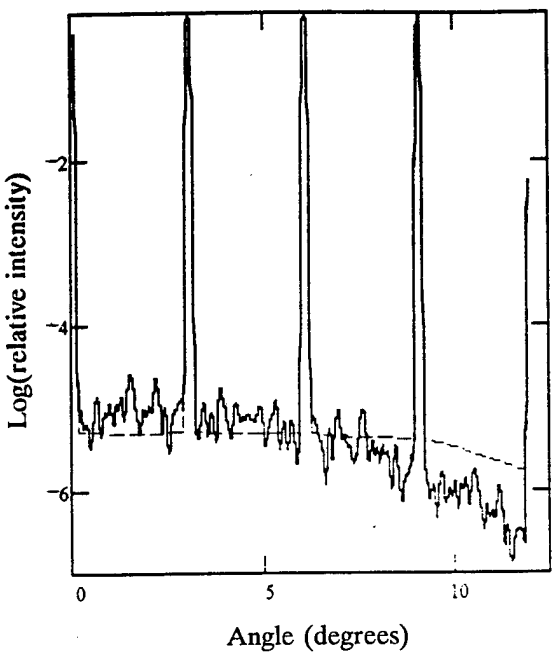

FIGURE 8. Relative intensity, Dammann grating (DG2). Etch depth error δ = 0.1 μm. Compared to 1-D roughness scattering formula.

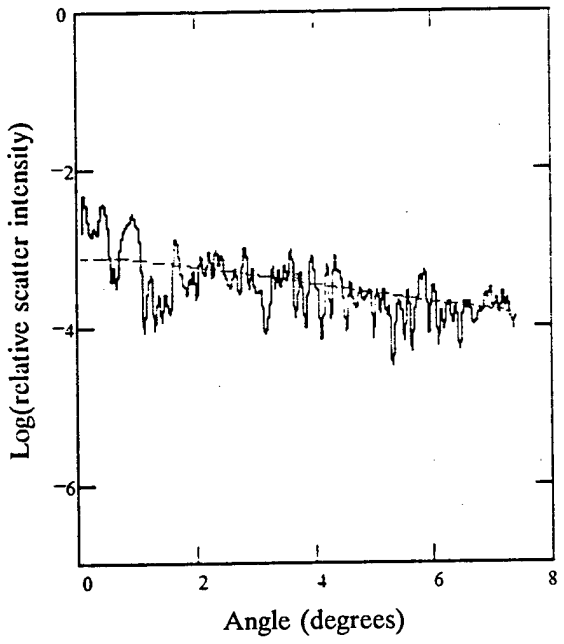

FIGURE 9. Relative scatter intensity, cylindrical Fresnel zone plate (FZP1). Etch depth error δ = 0.1 μm. Compared to 1-D scattering formula.

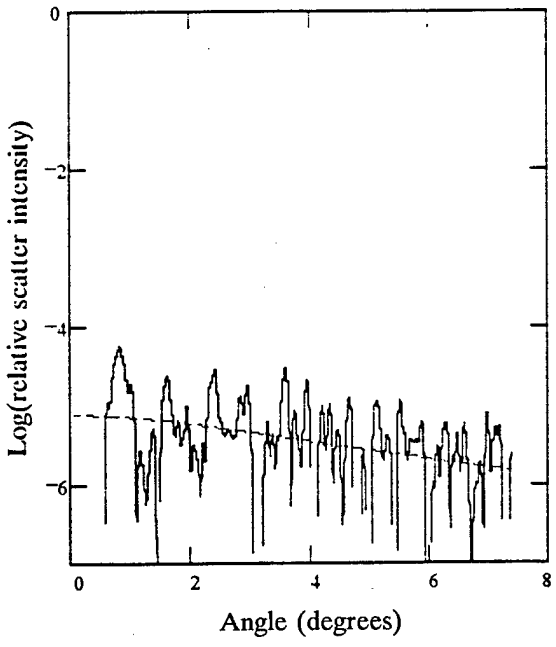

FIGURE 10. Relative scatter intensity, cylindrical Fresnel zone plate (FZP1). Etch depth error δ = 0.01 μm. Compared to 1-D scattering formula.

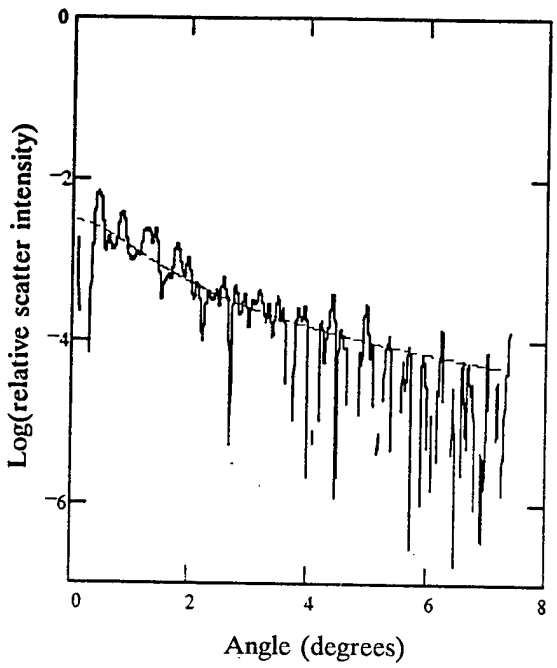

FIGURE 11. Relative scatter intensity, cylindrical Fresnel zone plate (FZP2A). Etch depth error δ = 0.1 μm. Compared to 1-D roughness scattering formula.

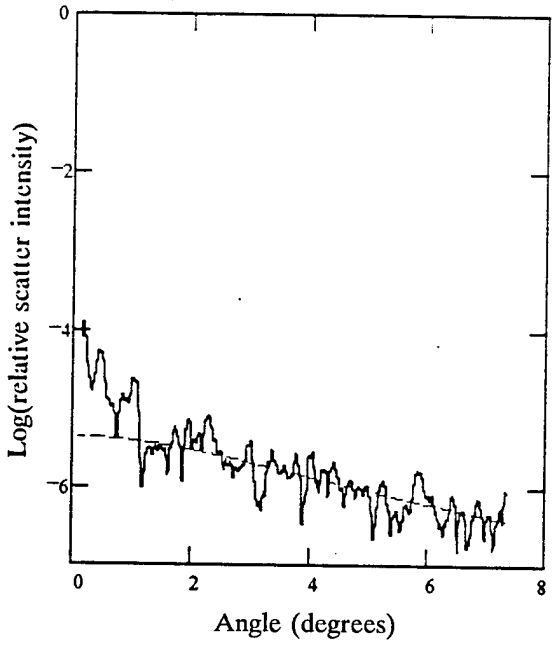

FIGURE 12. Relative scatter intensity, circular Fresnel zone plate (FZP1). Etch depth error δ = 0.1 μm. Compared to 2-D scattering formula.

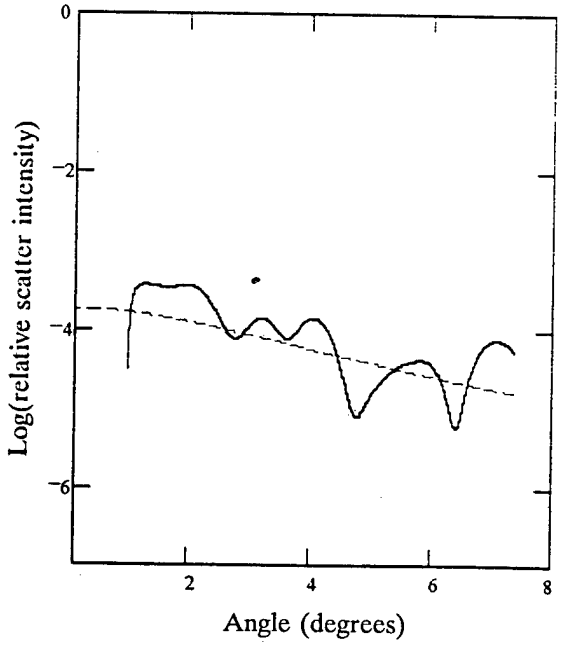

FIGURE 13. Relative scatter intensity, circular Fresnel zone plate (FZP4). Etch depth error δ = 0.1 μm. Compared to 2-D scattering formula.

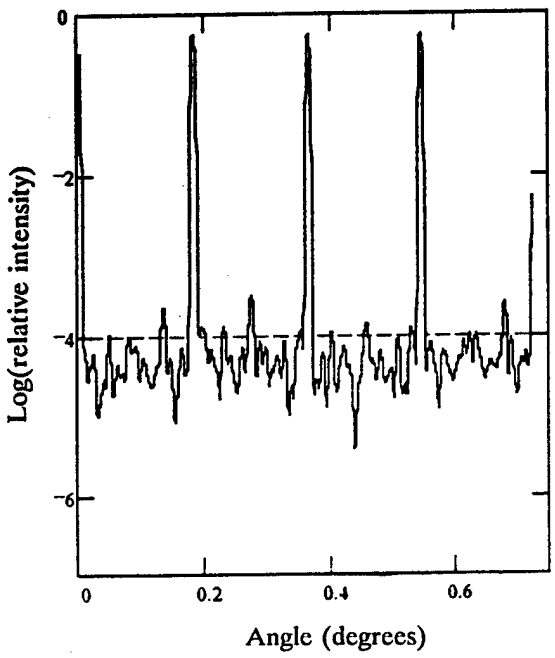

FIGURE 14. Relative intensity, Dammann grating (DG1). Line edge error δ = 1.0 μm. Compared to 1-D roughness scattering formula.

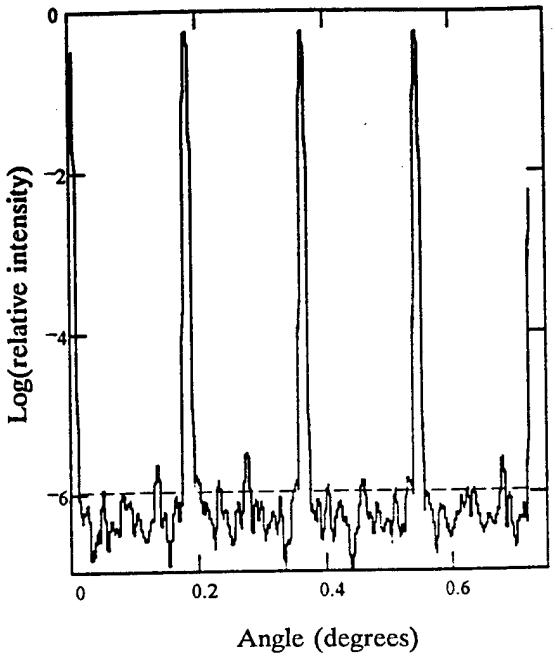

FIGURE 15. Relative intensity, Dammann grating (DG1). Line edge error δ = 0.1 μm. Compared to 1-D roughness scattering formula.

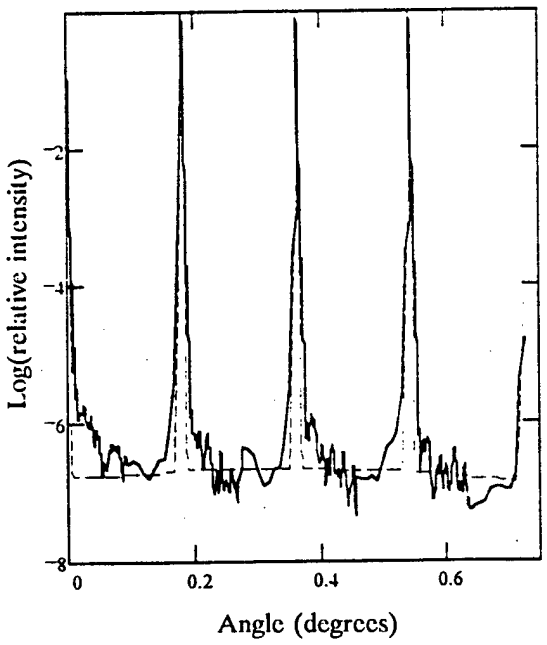

FIGURE 16. Measured relative intensity; compared to 1-D scatter formula with etch depth error δd = 1 nm, and line edge error δx = 25 nm.

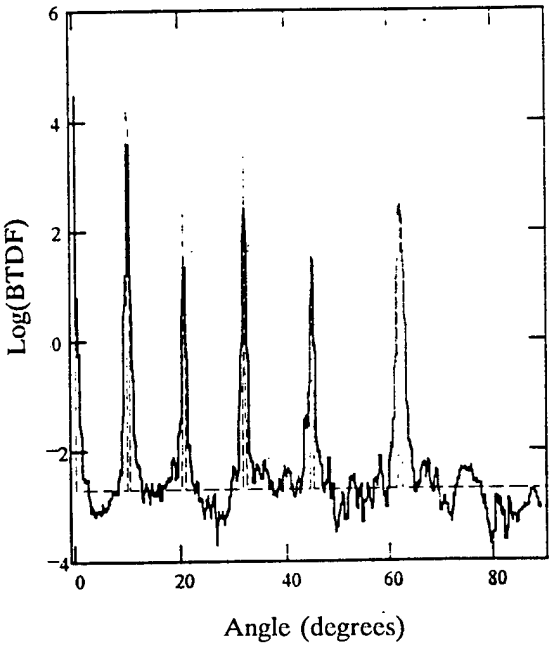

FIGURE 17. Measured BTDF compared to 1-D scatter formula with line edge error δ = 30 nm.

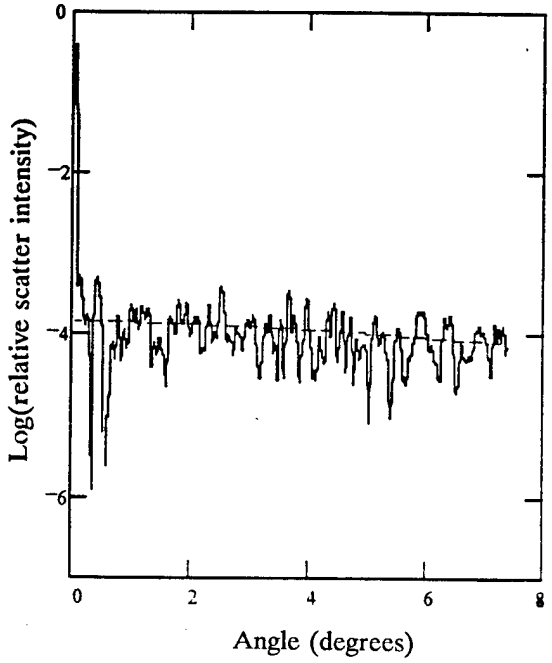

FIGURE 18. Relative scatter intensity, cylindrical Fresnel zone plate (FZP1). Line edge error δ = 1 μm. Compared to 1-D roughness scatter formula.

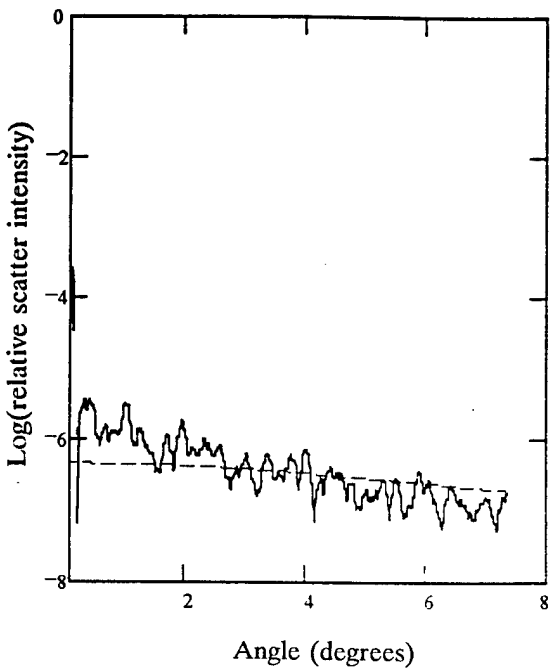

FIGURE 19. Relative scatter intensity, circular Fresnel zone plate (FZP1). Line edge error δ = 1 μm. Compared to 2-D scattering formula.

Mathematical Modeling for Diffractive Optics

David Dobson
School of Mathematics
University of Minnesota
Minneapolis, MN

J. Allen Cox
Honeywell Systems & Research Center
Bloomington, MN

Abstract

We consider a "diffractive optic" to be a biperiodic surface separating two half-spaces, each having constant constitutive parameters; within a unit cell of the periodic surface and across the transition zone between the two half-spaces, the constitutive parameters can be a continuous, complex-valued function. Mathematical models for diffractive optics have been developed, and implemented as numerical codes, both for the "direct" problem and for the "inverse" problem. In problems of the "direct" class, the diffractive optic is specified, and the full set of Maxwell's equations is cast in a variational form and solved numerically by a finite element approach. This approach is well-posed in the sense that existence and uniqueness of the solution can be proved and specific convergence conditions can be derived. An example of a metallic grating at a Wood anomaly is presented as a case where other approaches are known to have convergence problems. In problems of the "inverse" class, some information about the diffracted field (e.g., the far-field intensity) is given, and the problem is to find the periodic structure in some optimal sense. Two approaches are described: phase reconstruction in the far-field approximation; and relaxed optimal design based on the Helmholtz equation. Practical examples are discussed for each approach to the inverse problem, including array generators in the far-field case and antireflective structures for the relaxed optimal design.

Conf. on Binary Optics, 1993

Mathematical Modeling for Diffractive Optics

David Dobson
Institute for Mathematics and Its Applications
University of Minnesota
Minneapolis, MN

J. Allen Cox
Honeywell Systems&Research Center
Bloomington, MN

Outline

- Need
- Statement of Problem
- Overview of Approaches
- Examples

Mathematical Modeling for Diffractive Optics

Classes of Problems

- **The Direct Problem**

  Given the incident field and grating structure
  Predict the behavior of the outgoing fields
  Solve Maxwell's equations rigorously

- **The Inverse Problem**

  Given the incident field and the desired output field
  Calculate the optimum structure
  Model a scalar wave equation with simplifications

Definition of the Direct Problem

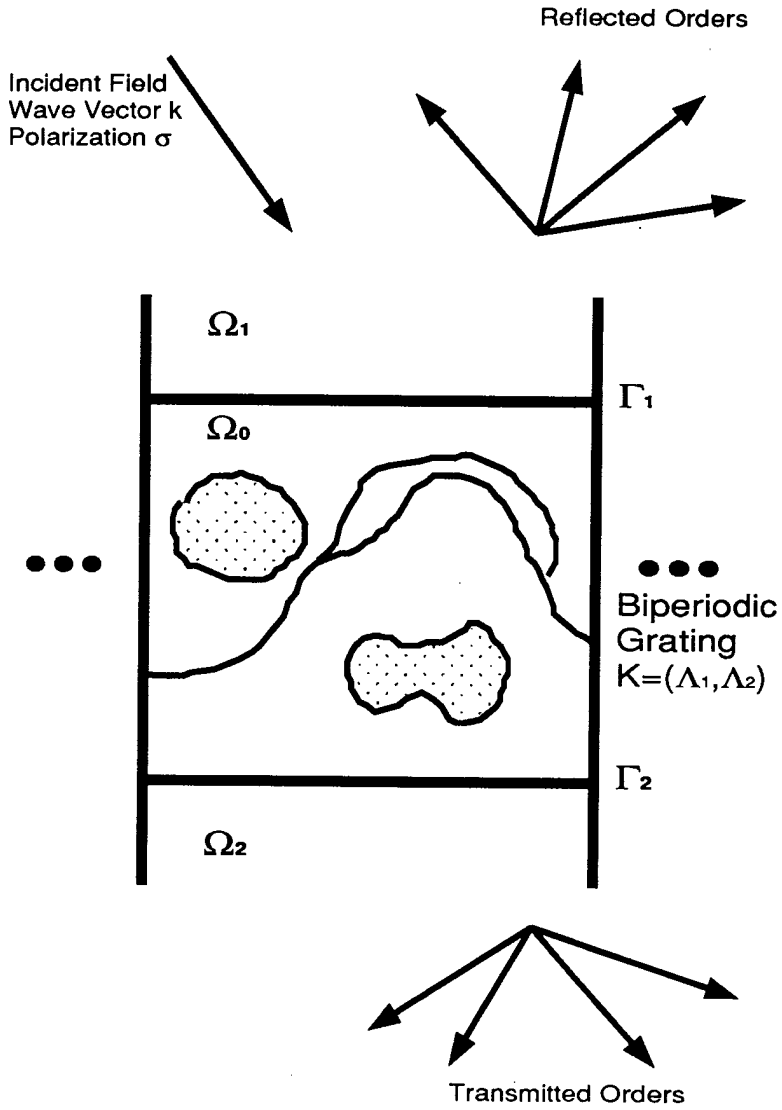

Time Harmonic, Source-free Maxwell's Eqs

$$\nabla \times E - i\omega H = 0$$

$$\nabla \times H + i\omega\varepsilon E = 0$$

$$\varepsilon \in L_\infty(\Omega_0) \quad \varepsilon = \varepsilon_1 \text{ in } \Omega_1 \quad \varepsilon = \varepsilon_2 \text{ in } \Omega_2$$

Find

Quasiperiodic Solutions with Bounded Outgoing Waves

Survey of Approaches to the Direct Problem

Approach	Comments
1. Integral Method	Discretized grating profile
2. Differential Method (coupled waves)	PDE embedded in infinite set of coupled linear eqs
3. Coupled Modes	Numerical implementation - truncate set of linear eqs - solve Ax = b
4. Variational Method	
5. Riemann-Hilbert Problem	
6. Analytic Continuation	Smooth grating profile Infinite Taylor series for Rayleigh coef. (recursion) Padé approximant sum of series

Mathematical Modeling for Diffractive Optics

Honeywell / IMA Program

The Direct Problem

1. Integral Method (Maxcoll)	Dobson & Friedman	Singly periodic grating Simple profile(graph)
2. Variational Method (Maxfelm)	Dobson	Biperiodic grating General profile
3. Analytic Continuation (TBD)	Bruno & Reitich	Biperiodic grating Simple profile(function)

The Inverse Problem

1. Phase Reconstruction (Phaseopt)	Dobson	Scalar field / Fraunhofer approx Nonperiodic structures Nonlinear least squares method
2. Relaxed Optimization (Profopt)	Dobson	Scalar field / Helmholtz eq Singly periodic grating Complex profile

Mathematical Modeling for Diffractive Optics

Examples

The Direct Problem

1. Reflective Polarization Beamsplitter
2. LIGA Grating
3. Mixed Index Biperiodic Grating

The Inverse Problem

1. Phase Reconstruction - Hypercube Beamsplitter
2. Relaxed Optimization - Angle Optimized Motheye Structure

Reflective Polarization Beamsplitter

$\lambda = 0.78\ \mu m$

$\theta = 45°$

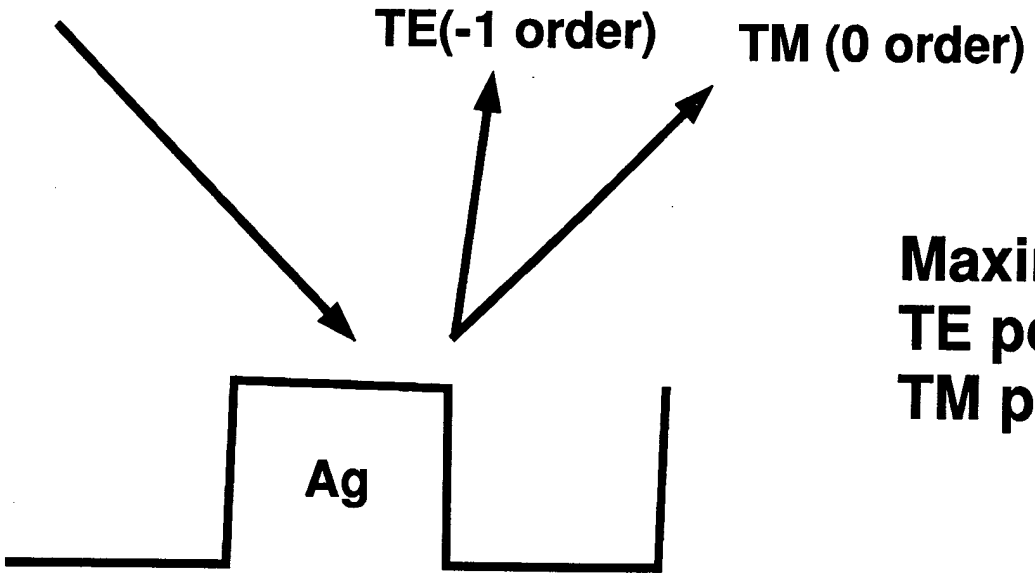

Maximize reflectivity
TE polarization (-1 order)
TM polarization (0 order)

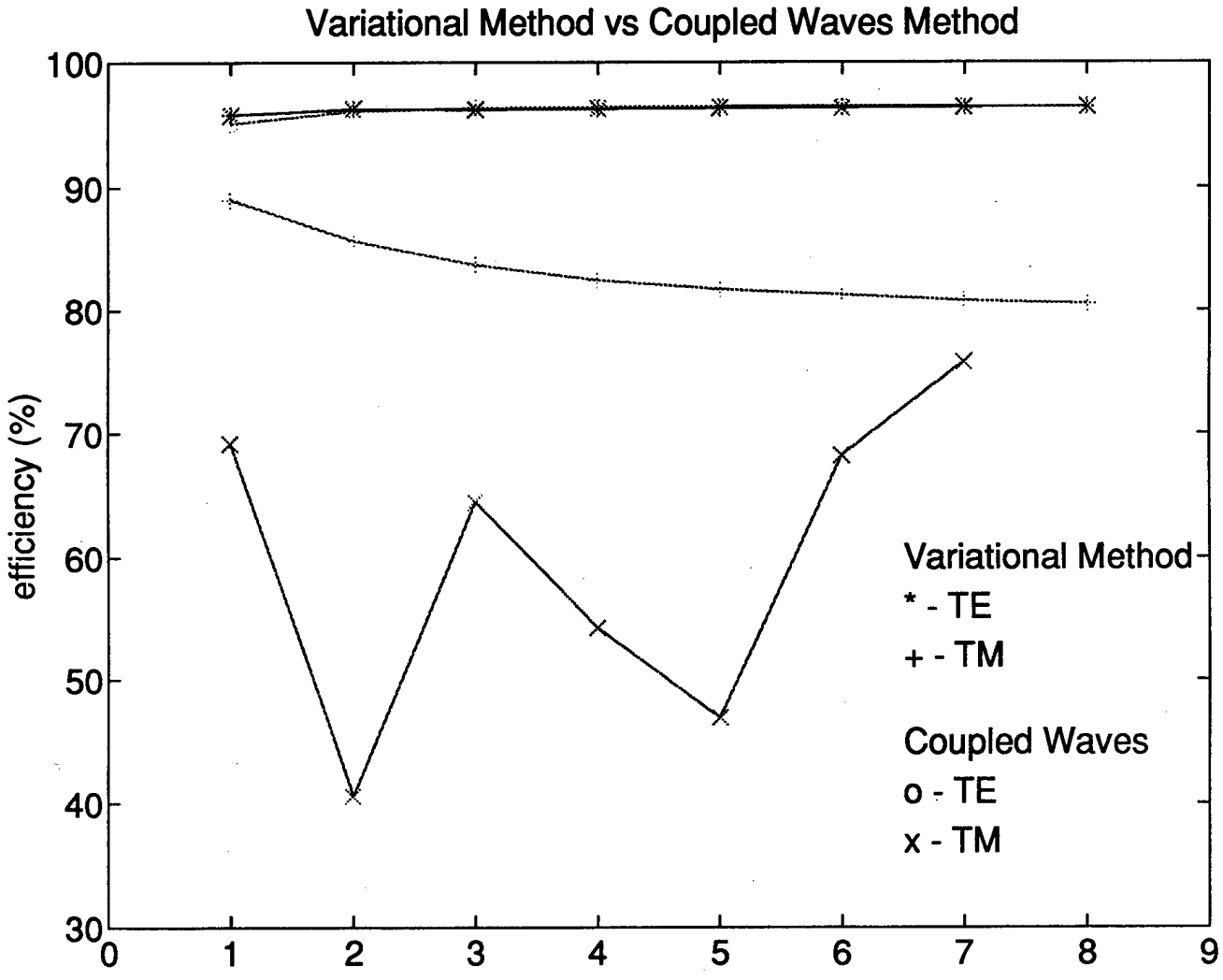
Variational Method vs Coupled Waves Method
efficiency (%)
100
90
80
70
60
50
40
30
0
1
2
3
4
5
6
7
8
9
Variational Method
* - TE
+ - TM
Coupled Waves
o - TE
x - TM

Variational Method (Maxfelm) Example

LIGA Grating

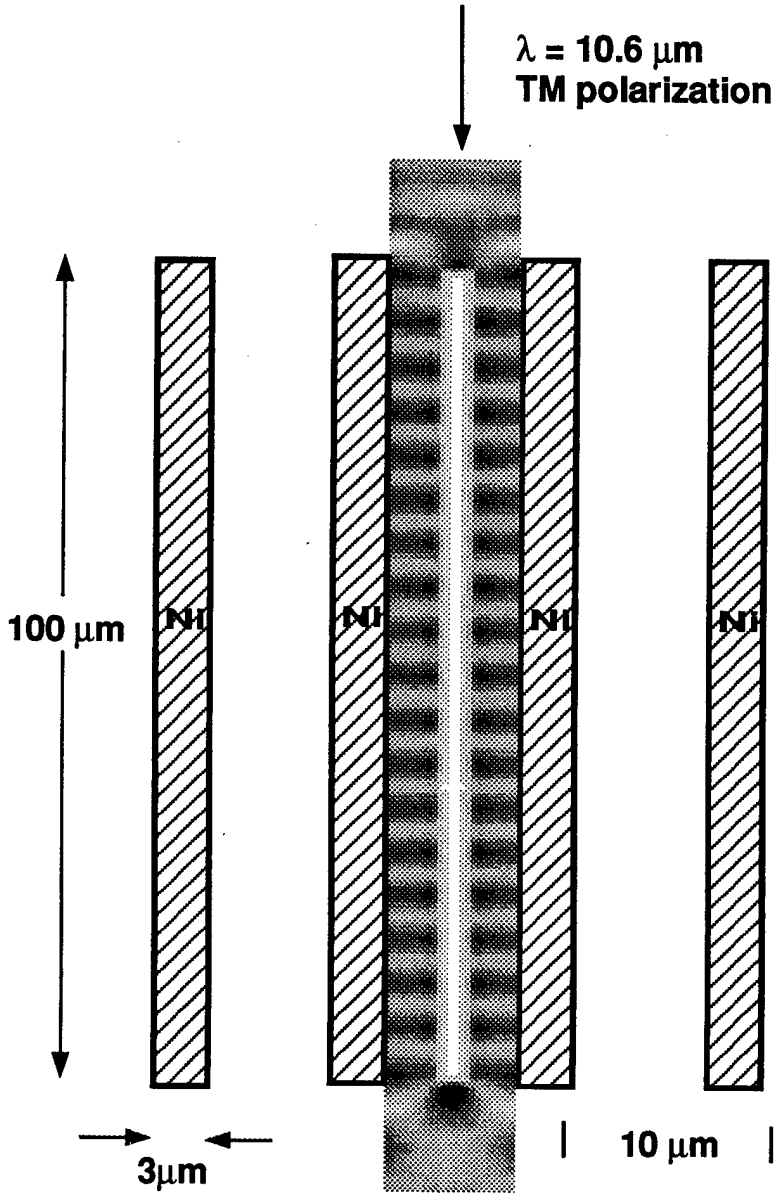

Variational Method (Maxfelm) Example

Mixed Index Biperiodic Grating

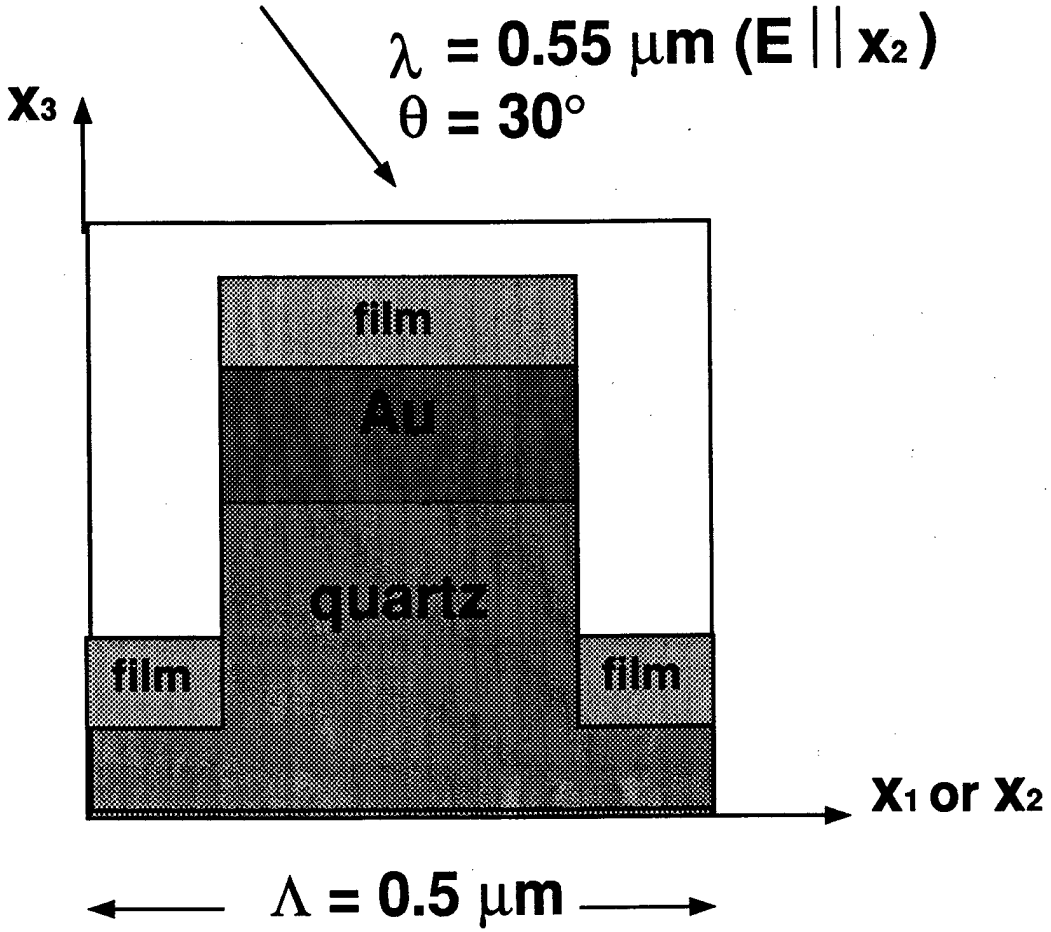

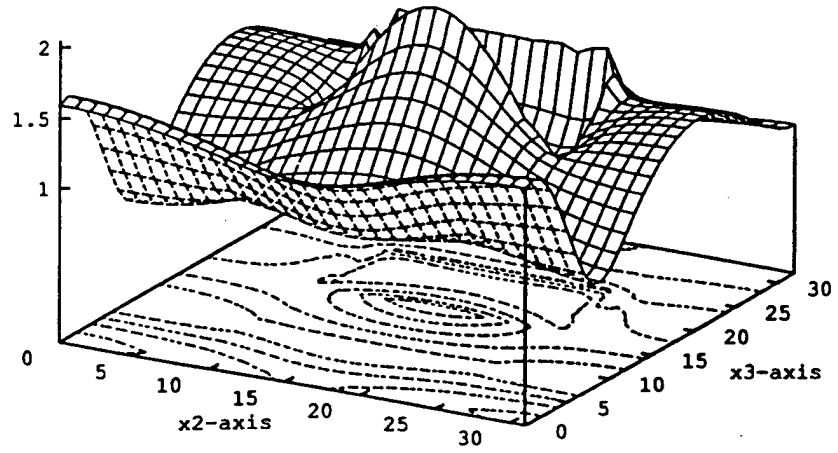

FIG. 2. *Cross-section of the amplitude $|H|$, taken through the metal region in the (x_2, x_3) plane.*

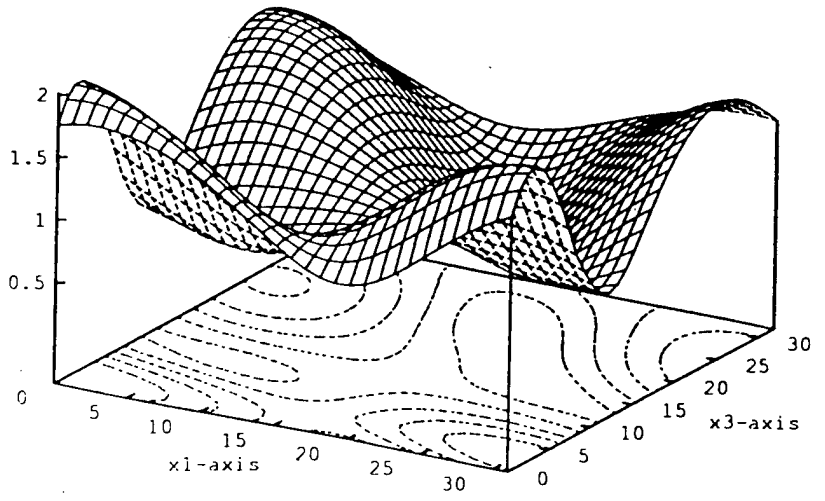

FIG. 3. *Cross-section of the amplitude $|H|$, taken through the non-absorbtive region in the (x_1, x_3) plane.*

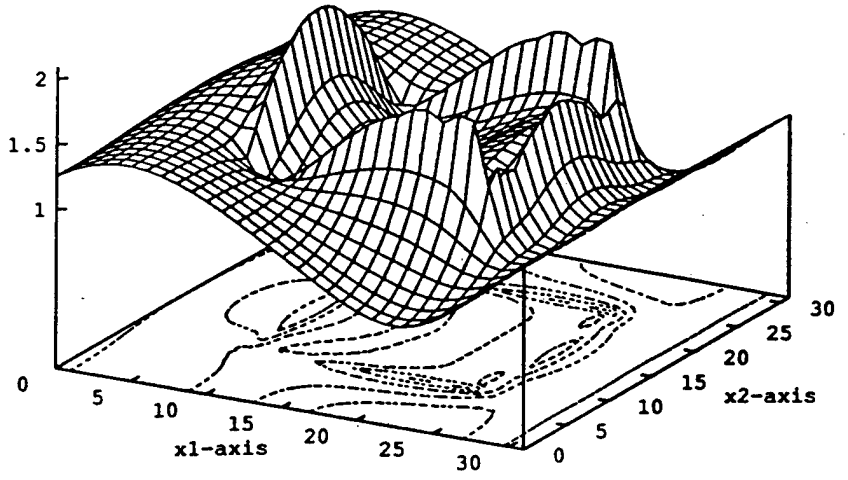

FIG. 4. *Cross-section of the amplitude $|H|$, taken through the metal region in the (x_1, x_2) plane.*

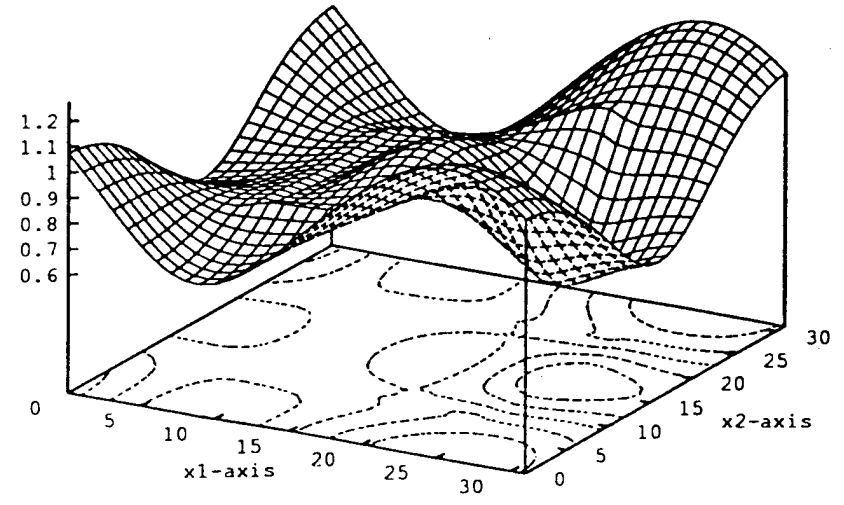

FIG. 5. *Cross-section of the amplitude $|H|$, taken below the metal region in the (x_1, x_2) plane.*

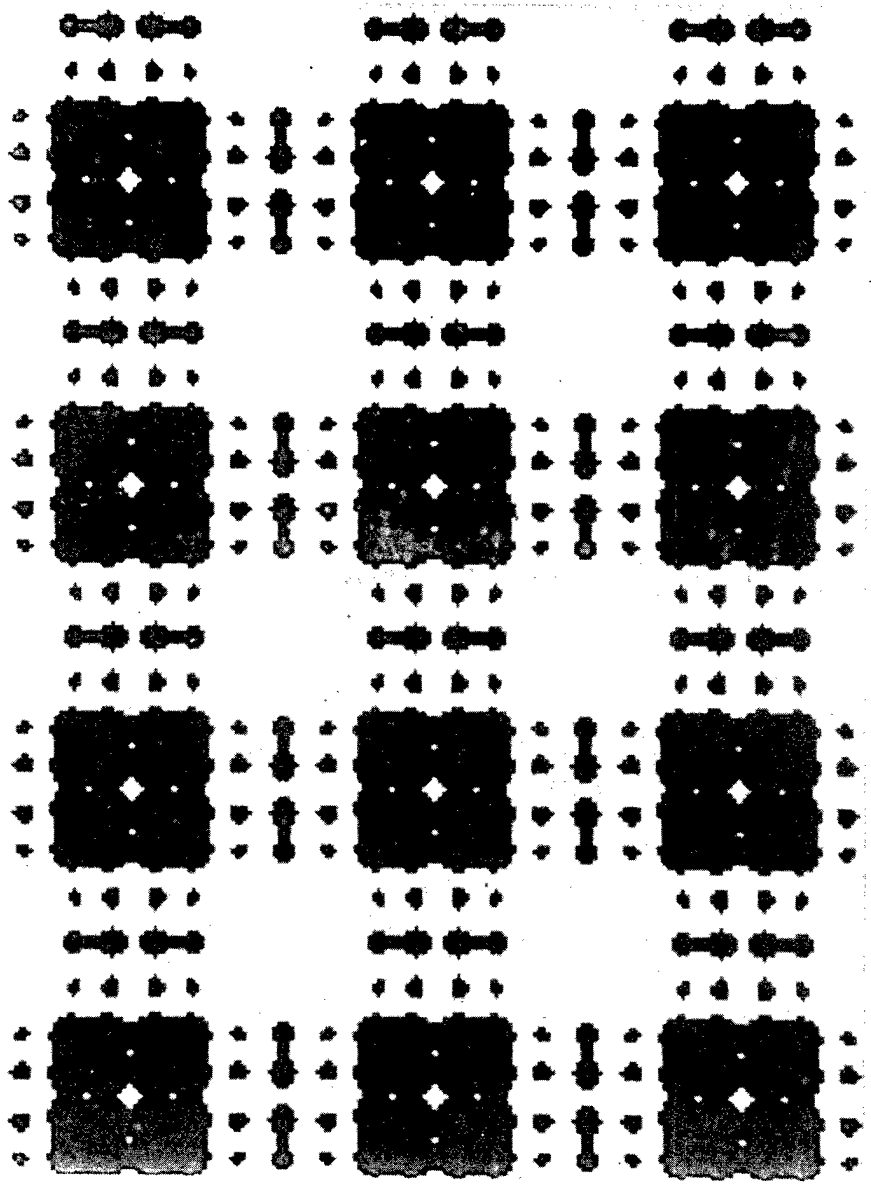

Dobson Method

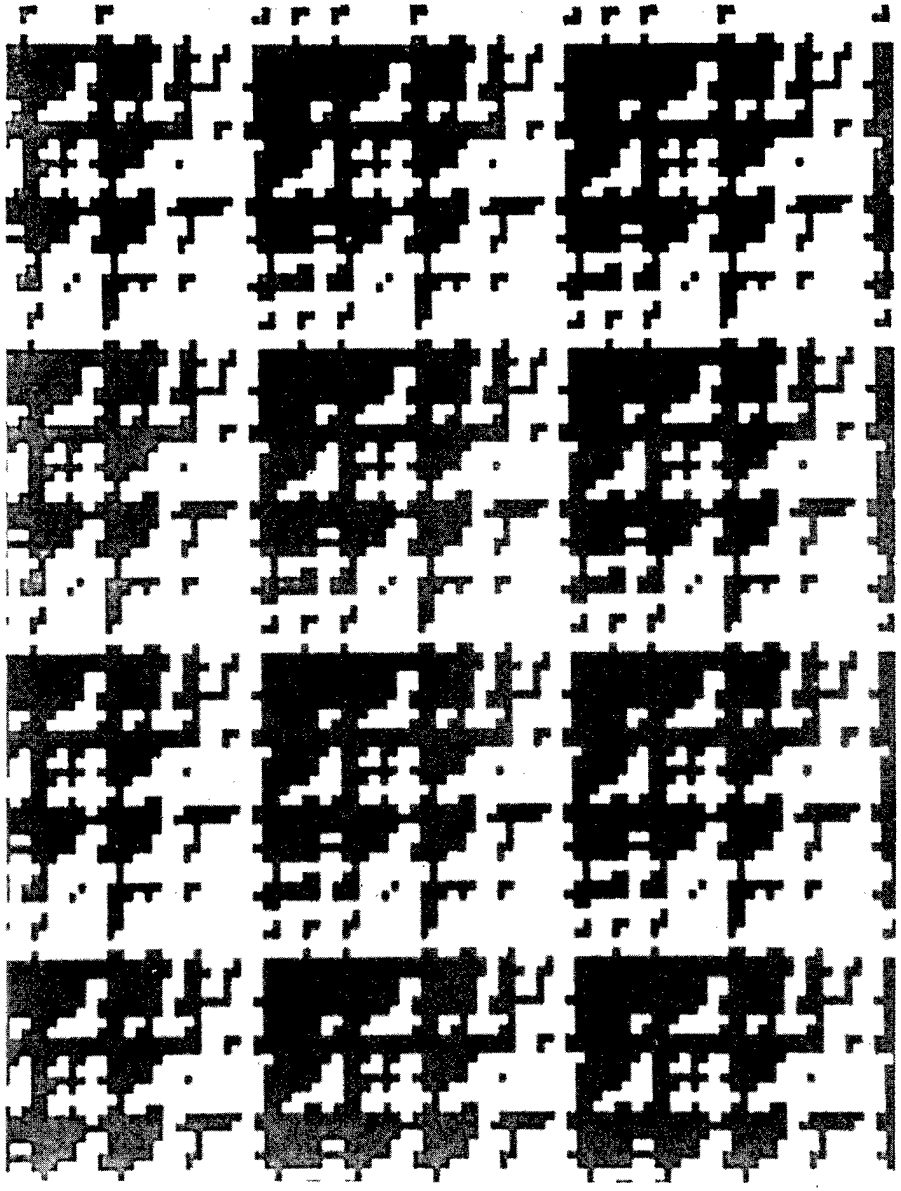

Gerchberg Saxton Method

Relaxed Optimization (Profopt) Example

Optimized Moth Eye Grating

$\theta = \pm 70°$

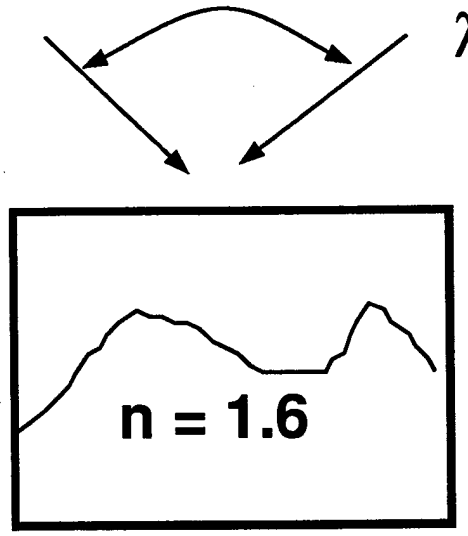

$\lambda = 1.0\ \mu m$

$\Lambda = 0.5\ \mu m$

Find structure of zero order grating to minimize reflectivity over range of incident angles

Relaxed Optimization (Profopt) Example

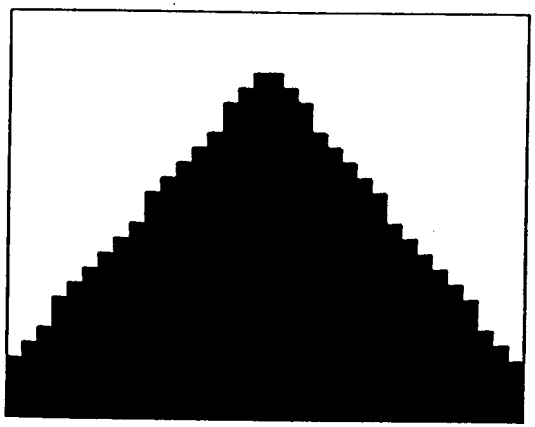

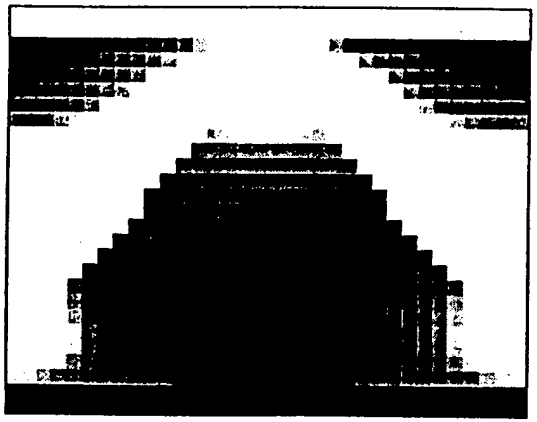

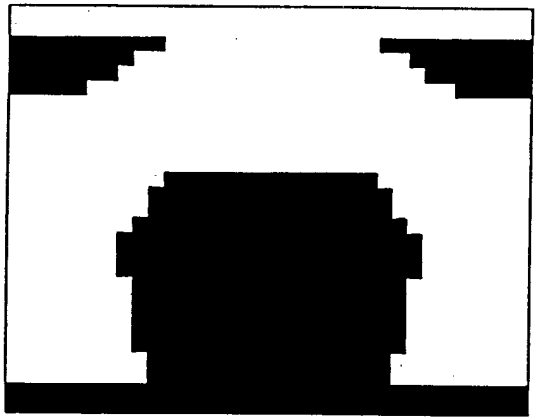

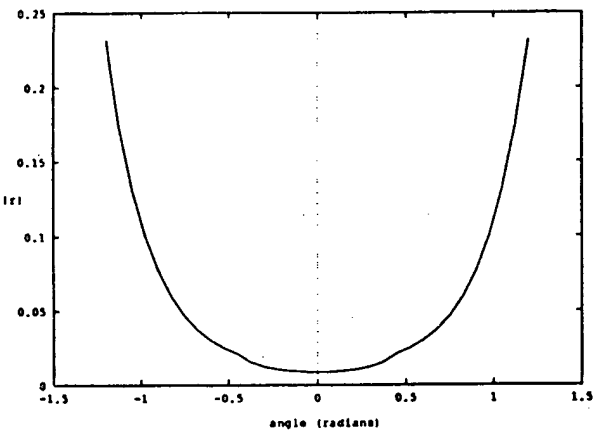

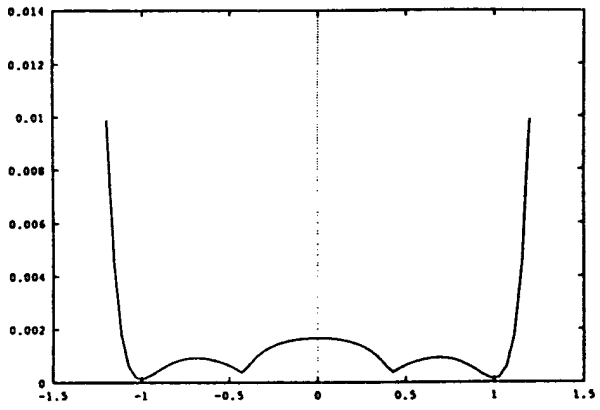

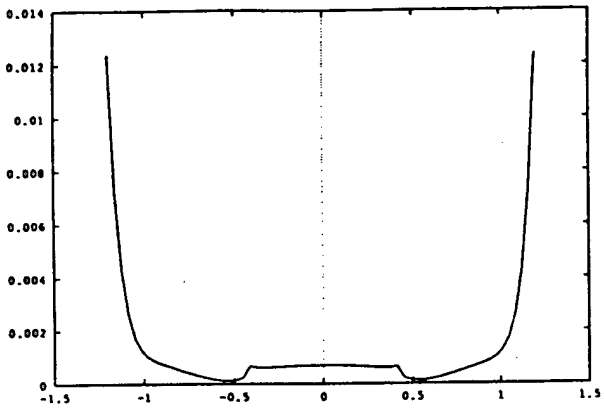

Mathematical Modeling for Diffractive Optics

Summary

The Direct Problem

Variational Approach with Finite Elements Method
- exhibits good convergence, numerical stability
- treats complicated biperiodic structures
- can be computationally intensive

Analytic Continuation Approach
- elegant solution
- limited domain of convergence and biperiodic structures
- computationally very fast

The Inverse Problem

Phase Reconstruction - comparable to other approaches

Relaxed Optimization - potential to identify new structures

Invited Paper

Fabricating Binary Optics: An Overview of Binary Optics Process Technology

Margaret B. Stern

MIT Lincoln Laboratory
244 Wood St , Lexington, MA 02173

ABSTRACT

A review of binary optics processing technology is presented. Pattern replication techniques have been optimized to generate high-quality efficient microoptics in visible and infrared materials. High resolution optical photolithography and precision alignment is used to fabricate maximally efficient fused silica diffractive microlenses at λ=633 nm. The degradation in optical efficiency of four-phase-level fused silica microlenses resulting from an intentional 0.35-μm translational error has been systematically measured as a function of lens speed (F/2 - F/60). Novel processes necessary for high sag refractive IR microoptics arrays, including deep anisotropic Si-etching, planarization of deep topography and multilayer resist techniques, are described. Initial results are presented for monolithic integration of photonic and microoptic systems.

1. INTRODUCTION

Optics systems in the twenty-first century will employ hybrid and integrated diffractive optical elements to effect lightweight, compact designs. This requires the optics industry to adopt a new manufacturing paradigm - i.e., to design the electro-optic system in totality, and to implement the new fabrication techniques necessary to make novel optical components. Binary optics technology adapts the zeitgeist of integrated circuit manufacturing technology, i.e., CADCAM optics tools and design packages coupled with sophisticated and mature VLSI microstructure fabrication techniques, to make both diffractive and refractive microoptics. By sharing a technology base with the microelectronics, photonics, and micromachining communities, manufacturing costs are reduced and integration of these technologies is simplified. From its inception, binary optics technology has been driven by the demand for fast broadband flat optics needed for low cost smart sensors. High functionality binary optical elements streamline the optical train and simplify system assembly.

In the past decade, binary optics technology has evolved through three generations: the first is characterized by slow diffractive macrooptics; the second by fast microlens arrays; and the third by integrated layers of microoptics and photonic devices. First generation binary optics elements have large periods (hundreds of microns); the second and third generations have submicron zone widths. The first generation hybrid diffractive-refractive technology, primarily used to correct aberrations in large-aperture refractive optics, has been adopted by many industrial, government, and defense organizations, as apparent from the papers presented at this conference. The second generation consists of fast microlens arrays comprised of large

numbers (>10^5) of identical elements used in such diverse applications as focal plane arrays, laser beam addition, Hartmann sensors, wavefront multiplexers, and beam-steering.[1-6] The ultimate potential of these microoptics arrays awaits the fruition of third generation binary optics technology - new "amacronic" architectures that integrate multiple planes of optics and electronics.[7]

Two major factors have contributed to the widespread success of binary optics technology: one - the flexibility made possible by the extensive use of preexisting microelectronics fabrication techniques, and two - the inherent reduced processing set, i.e., the binary coding of the fabrication steps which results in 2^M phase levels for M-mask layers.[1] To obtain high-quality optics, VLSI-techniques must be customized to meet the specific and distinct concerns of microoptics fabrication. For example, exacting control of etch depth and overlay tolerances are needed to achieve optimal efficiency[8], while novel "deep-structure" processing techniques are required to fabricate refractive microoptic arrays.[9]

This paper examines the pivotal role of fabrication in translating diverse optical designs into high-quality optics in a variety of materials. In particular, we evaluate how the alignment precision achieved during photolithography impacts the subsequent optical efficiency of diffractive microlenses.[8, 10] The effect of misalignment on optical efficiency is measured as a function of lens speed (F/2 to F/60) on 200-μm square fused silica microlenses at 633 nm.[11] Next, we describe the multilayer planarization/masking schemes and highly anisotropic Si reactive-ion etching (RIE) processes needed to manufacture high-bandwidth IR binary optics.[9] Finally, we present a nascent layered system - arrays of CdTe microlenses monolithically integrated with photodetectors on opposite sides of the same substrate.[5]

2. FABRICATION AND OPTICAL EFFICIENCY

Binary optics technology conjoins computer-generated optical phase profiles with VLSI photomask and processing technology to form planar surface relief structures that manipulate optical wavefronts.[1] Conventional binary optics processing, Figure 1, consists of several iterative steps of photolithographic patterning and phase-relief creation. The relief structures can be constructed by a variety of methods, including etching, deposition, and ion- or photon-induced structural changes in the refractive index or the volume. Dry etching techniques, in particular reactive ion etching (RIE), offer the greatest amount of flexibility and are used to manufacture the optics described below. Binary mask coding greatly reduces the number of process iterations required for highly efficient diffractive elements: only M process iterations result in an optic with 2^M phase steps.[1] Each of the M-steps creates a phase step of height $d = \lambda/(2^M(n-1))$, where λ is the design wavelength and n is the material index of refraction.

Standard VLSI techniques must be finessed to address the particular requirements of high-quality microoptics fabrication. The nested binary optics structures impose three critical restraints on the fabrication process: (1) to register the mask to the substrate pattern with 0% overlay tolerance; (2) to etch vertical sidewall profiles without lateral undercutting or erosion of the mask edge; and (3) to maintain precise control over the phase-step-heights, often to better

than 1%, for both shallow (≈ 10 nm) and deep (≈ 10 μm) structures. In addition, to achieve high fidelity pattern replication of curvilinear linewidths that can range from 0.5 μm to 50 μm on a single mask level, the bias in the photolithography process must be characterized and accommodated.[12] Failure to obtain positional and dimensional control results in phase-step-width errors, which appear as trenches and ridges in the etched structures. Phase-step-width and height errors can significantly reduce the optical efficiency.[13-15]

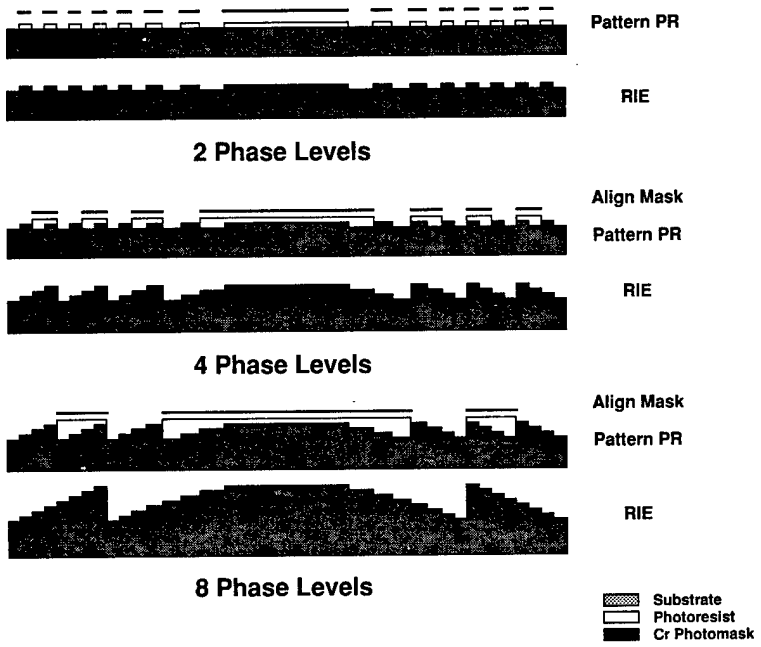

Figure 1: Fabrication steps for an eight-phase-level binary optics microlens. To maximize linewidth control, the mask layer with the smallest features is replicated first. The substrate is coated with photoresist, patterned photolithographically using a contact mask aligner, and then etched in an RIE system. Subsequent mask layers are carefully aligned to the patterned surface. This sequence is iterated until the desired number of phase levels is achieved. The binary coding scheme doubles the number of phase levels after each etch.

Practicality dictates that we establish criteria to determine where the incremental gain in optical performance justifies the required fabrication effort. We have undertaken a substantial effort at MIT Lincoln Laboratory to quantify the efficiency limits of diffractive binary-optic microlenses and to correlate losses in optical efficiency with specific fabrication errors. In particular, we have focused on the interrelation between alignment errors and microlens efficiency. The vehicle for these studies is the "Best Efficiency Array SeT" (BEAST), a fused silica microlens test set comprised of 10 different lenslets having 200 μm x 200 μm square

apertures and focal lengths between 0.17 and 14 mm at $\lambda = 633$ nm.[8] Test devices contain both isolated single lenslets and 10 x 10 microlens arrays distributed across a 1.2 cm x 1.8 cm area on a background grid of sixteen alignment patterns (Figure 4a). The fine verniers, shown in Figure 2, consist of a two-dimensional grid spanning a $\pm$ 0.5 μm graduated scale divided into 0.1 μm increments. The X and Y locations of the centered square can be read to $\pm$ 0.05 μm precision from these verniers. The vernier grid in Figure 2 indicates essentially "perfect" registration accuracy at this location.

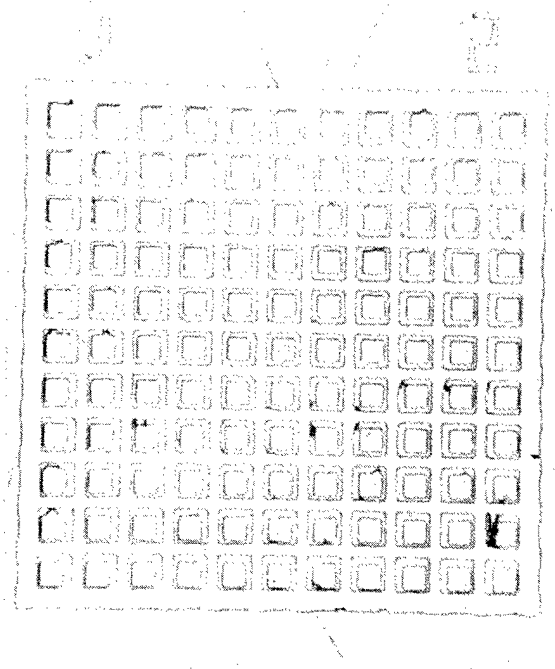

Figure 2: Example of a vernier grid pattern used to determine alignment accuracy. Results are shown for a level 2→3 alignment.

These verniers are used to determine the alignment accuracy both during the registration process (before photoresist exposure) and after the development of the photoresist pattern. We have achieved overlay registration to better than 0.1 μm over the two-square-centimeter area of the BEAST pattern by using these alignment marks.[8] The eight-phase-level F/6 fused silica microlens shown in Figure 3 is representative of the BEAST test set lenslets.

Benchmark optical efficiency measurements have been made on these diffractive quartz microlenses as a function of lens speed and then compared with predictions of direct electromagnetic calculations for 2-, 4- and 8- phase levels.[8,10] The first order diffraction efficiency is measured at $\lambda = 633$ nm using the "EtaMeter" system.[10] The EtaMeter, which exhibits low-noise and long-term stability, can measure relative efficiency with better than 0.001 precision and, with calibration, absolute efficiency accurate to 0.002.[10] For an eight-phase-level F/4.5 microlens having less than 0.1 μm misalignment error, we have measured an absolute efficiency of 0.85; this is, we believe, the highest efficiency reported to date for such a

fast, binary optics lens in the visible. This result corresponds to 96% of the predicted value for this lens and implies that net fabrication errors contributed only a 4% efficiency loss.

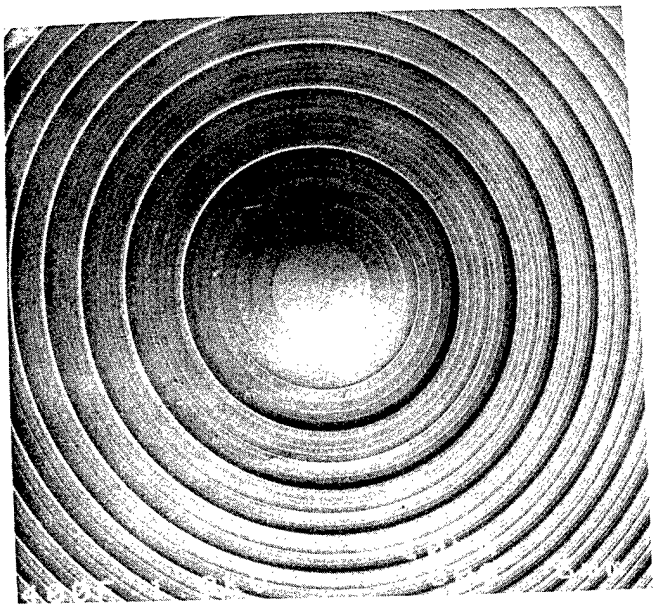

Figure 3: SEM of an eight-phase-level 200-μm square aperture F/6 fused silica microlens. The minimum zone width on level 3 is 0.8μm.

To quantify the impact of alignment errors on optical efficiency, we have intentionally introduced a 0.35-μm translational error between mask layers 1 and 2 in one set of four-phase level lenslets.[11] Optical efficiency measured for this "misaligned" set of microlenses are compared with a nominally identical, four-phase level, "well-aligned" set of microlenses. The alignment results are plotted in Figure 4 for both the well-aligned optic, QB2 (Fig. 4b) and the misaligned optic, QB3 (Fig. 4c). The average and standard deviation of the vernier readings at these sixteen sites, weighted equally, are 0.06 ± 0.03 (x), 0.1 ± 0.04 (y) for QB2; and -0.01 ± 0.17 (x), 0.38 ± 0.04 (y) for QB3.

It is apparent from the data plotted in Figure 5 that pattern registration has a significant effect on the absolute optical efficiencies of these two optics, measured as a function of the lens speed. The performance of the misaligned optic falls below the well-aligned optic at F/15; at F/6 the efficiency of the misaligned microlenses is 5% less than the well-aligned lenslets; and at F/2 the misaligned lenslets show a 10% decrease in efficiency below that of the well-aligned microlenses. A strong correlation exists between the sizeable efficiency losses displayed by the fast lenslets and the fraction of the zonewidth intercepted by the intentional misregistration. For example, 0.35 μm is only 3% of the minimum full zone for the F/60 lenslet, but is 25% of the minimum zonewidth for the F/2 microlens. Even the nominally well-aligned optic exhibits decreased efficiency for the fastest lenslets (F/2). Linewidth errors in the 0.5 μm outer zones of the fastest lenslets may contribute to the efficiency losses in both sets of microlenses. The etch depth errors recorded for these microlenses - 1-2% of the total phase-step-height - have negligible impact on the efficiency.

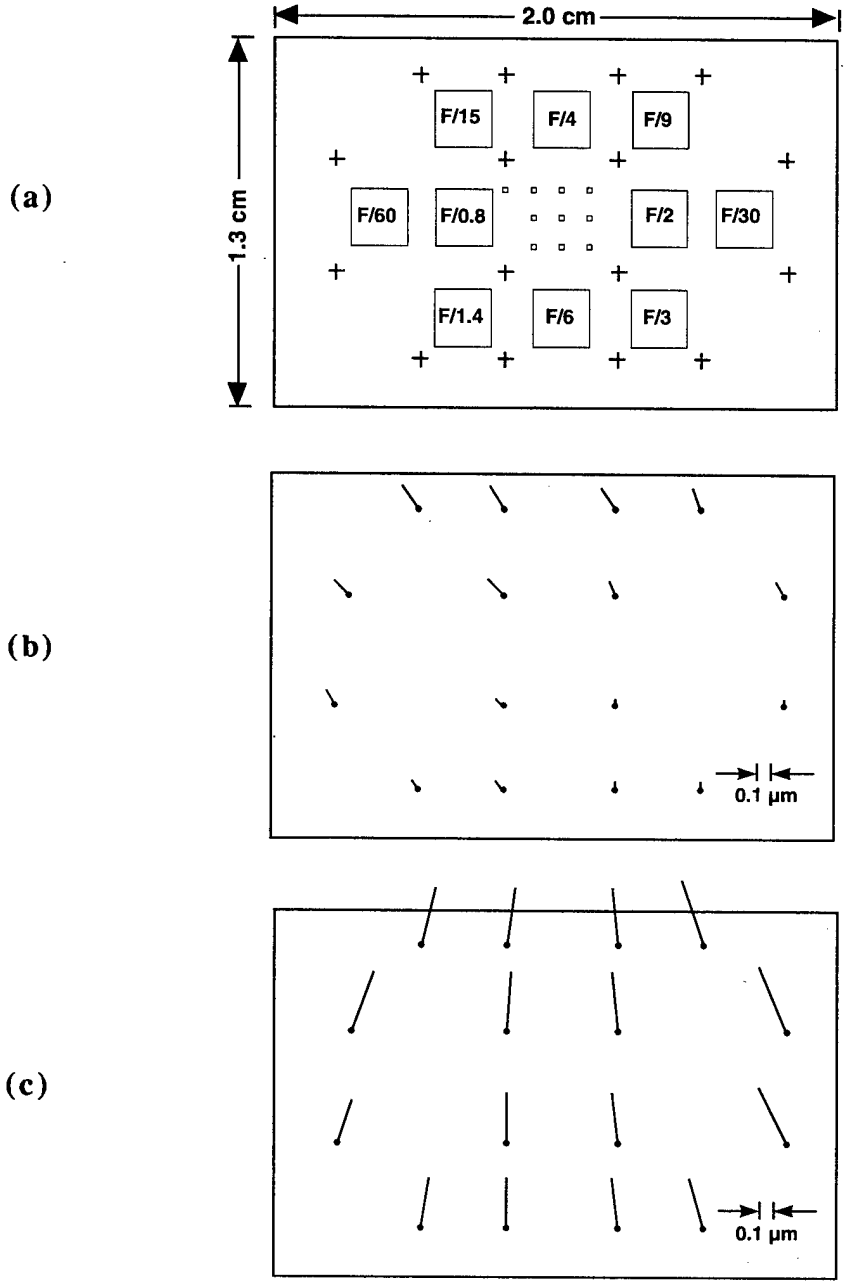

Figure 4: Comparison of mask layer 2→1 alignment results for a "well-aligned" and a "misaligned" optic at the 16 vernier sites. (a) Schematic of the BEAST mask layout showing the location of the verniers (crosses), 10x10 microlens arrays (large squares), and single lenslets (small squares). Alignment results for (b) BEAST sample QB2 ("well-aligned"); and (c) Beast sample QB3 ("misaligned"). Note the 0.1 μm scale marker for data plotted in (b) and (c).

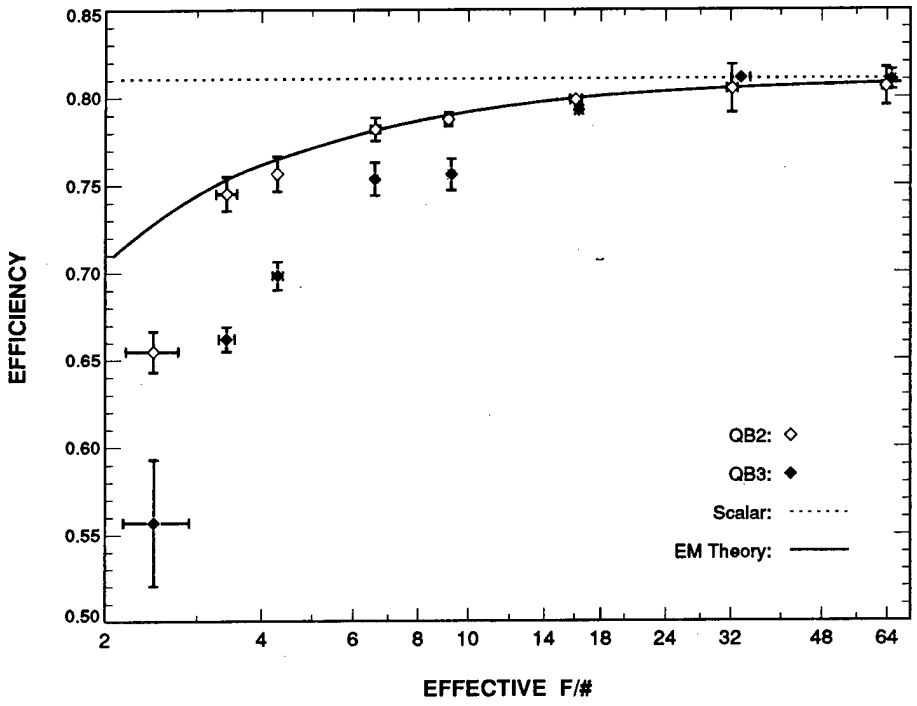

Figure 5: Optical efficiency of four-phase-level microlenses as a function of F/#. The open circles are the data from QB2 the ("well-aligned" sample); the solid circles are the data from QB3 (the intentionally misaligned sample). The dotted line is the scalar theory efficiency for four-phase levels (81%). The solid line is the predicted value from the full electromagnetic calculation.[12,13]

3. REFRACTIVE MICROOPTICS

3.1 Fabrication of infrared refractive microoptics

The demand for both visible and IR broadband microoptics has driven our development of fabrication capabilities necessary to create deep, high-resolution, three-dimensional structures. In particular, two refractive designs for the 8-12 μm bandwidth regime - a prototype sensor microlens with 14-μm sag and a color dispersive microoptic array with 7.5-μm sag - require deep anisotropic etching with precisely controlled phase-step heights. The desired refractive surface contour of the broadband IR microlens is approximated in a stepwise manner. In effect, we are eliminating the diffractive resets from the traditional binary optics phase-relief structure (i.e., one that has the appropriate phase-quantization for a particular efficiency) by a series of photolithography and deep-etching processes schematically outlined in Figure 6.

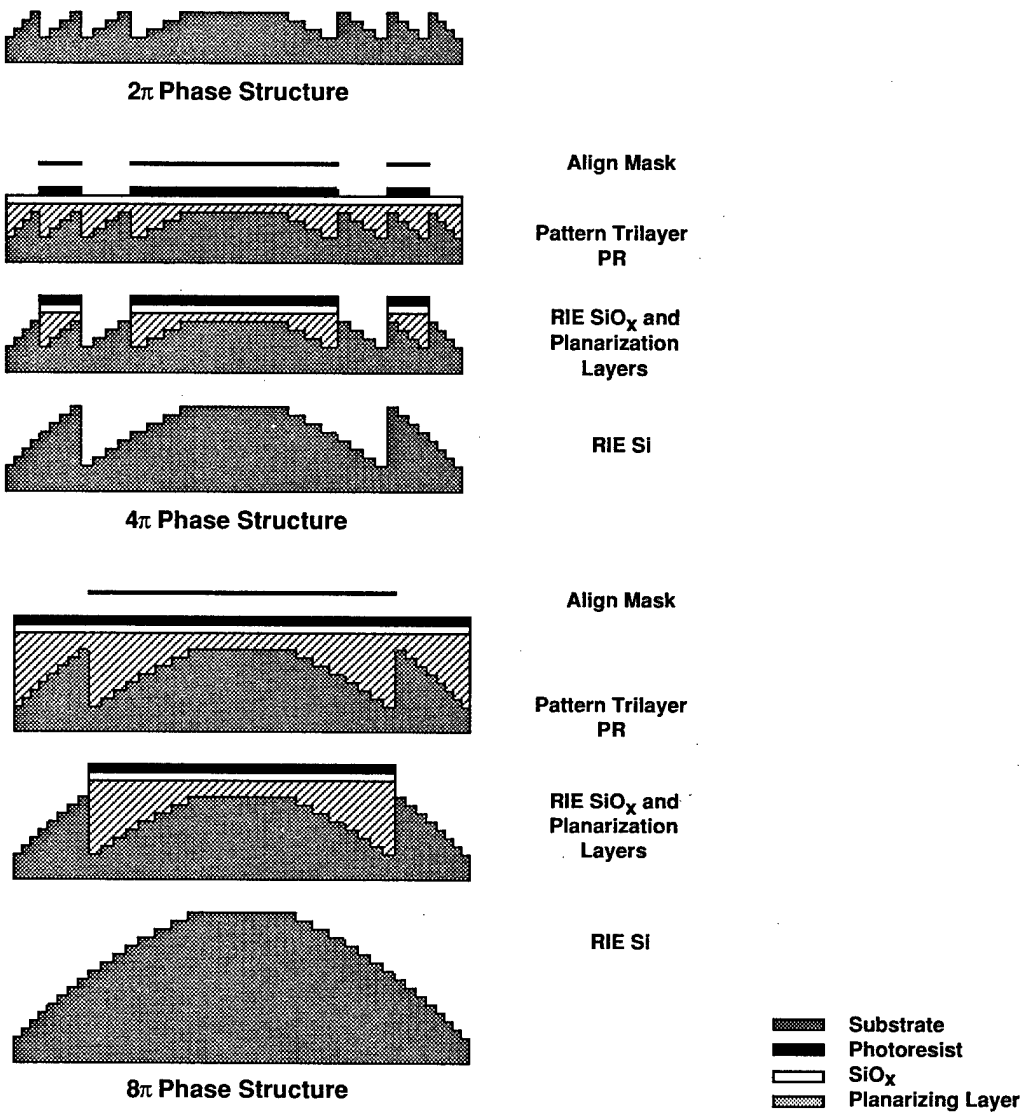

Figure 6: The sequence for fabricating refractive binary optics, consisting of iterated steps of photolithography, multilayer resist processing, and RIE. Assuming an initial stepped structure, multilayer resist techniques are required to complete the fabrication sequence. A thick polymer layer is used to planarize the steep topography. RIE is used to pattern both the intermediate SiO_x transfer layer and the planarization level. This forms the mask for the subsequent RIE of the silicon substrate. Each silicon RIE step doubles the previous etch depth, corresponding to sequential "2π", "4π", and "8π" total phase step heights.

To maintain the high fidelity pattern replication necessary for efficient binary optics structures, we must develop techniques to etch deep anisotropic profiles into the silicon substrate. By judicious choice of the plasma chemistry used in the RIE process, we can induce the in situ formation of a sidewall inhibition layer that prevents lateral undercut and enhances vertical profile control.[16,9] We have achieved vertical sidewalls without mask undercutting and with a 5:1 etch selectivity (ratio of Si:photoresist etching rates) by using an SF_6/O_2 gas mixture in a commercial RIE system (Semigroup TP1000).[9] Representative results for one-micron lines etched 8 μm deep in Si are shown in Figure 7. We observe no undercut of the photoresist mask, still present on these high aspect ratio vertical bars.

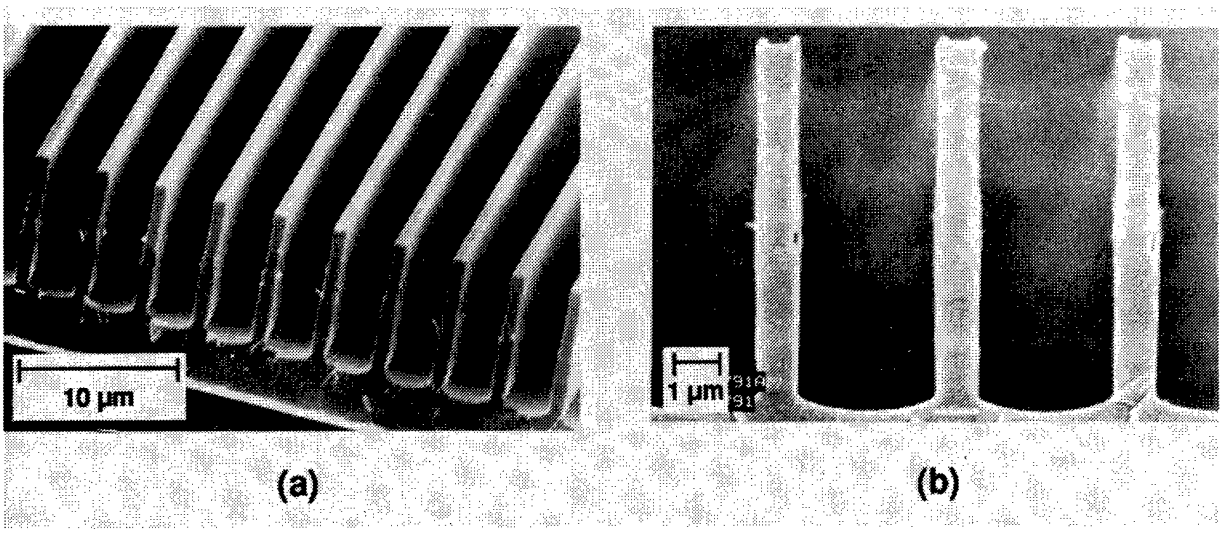

Figure 7: SEM micrographs of anisotropic features etched 8-μm deep in Si. (a) 3000x, (b) 9000x.

For such deep structures, a single layer of thin photoresist is insufficient to cover the existing substrate topography or to maintain reasonable linewidth acuity. Hence, we must resort to multilayer resist techniques for patterning subsequent levels as shown in Figure 6b and c.[9] The photoresist stencil in the imaging layer is first etched into the transfer layer, a thin film of SiO_x, in a CHF_3 plasma. This SiO_x mask is duplicated into the thick planarization layer by O_2 RIE, creating the final mask for the silicon substrate etch .

Assuming facile control of these individual processes, we now proceed to combine them to manufacture the desired broadband microoptics. The first example, displayed in Figure 8, is a prototype of a fully refractive Si microlens for an advanced satellite sensor and has a total etched depth of 14 μm. In an actual device, each of these two-micron steps would themselves be subdivided into quantized phase steps to produce an efficient microlens. In this particular

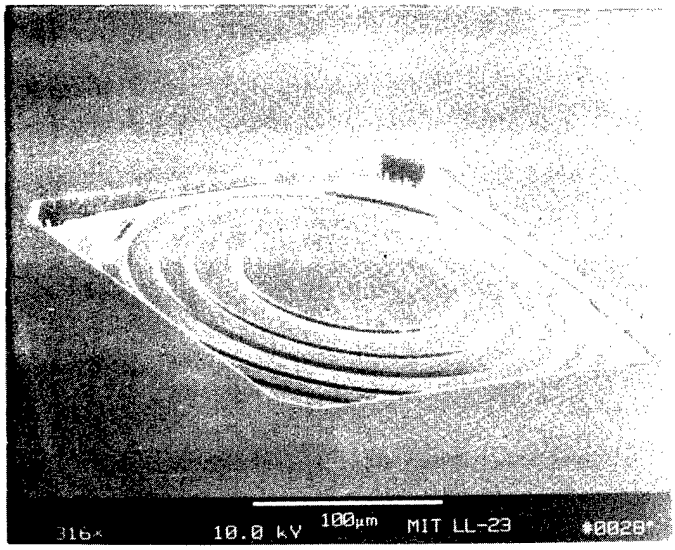

Figure 8: Eight-phase level 200 µm diameter refractive Si microlens with sag height of 14 µm.

demonstration, however, our motive is to establish the anisotropic deep etching and planarization capabilities required for broadband Si microoptics.

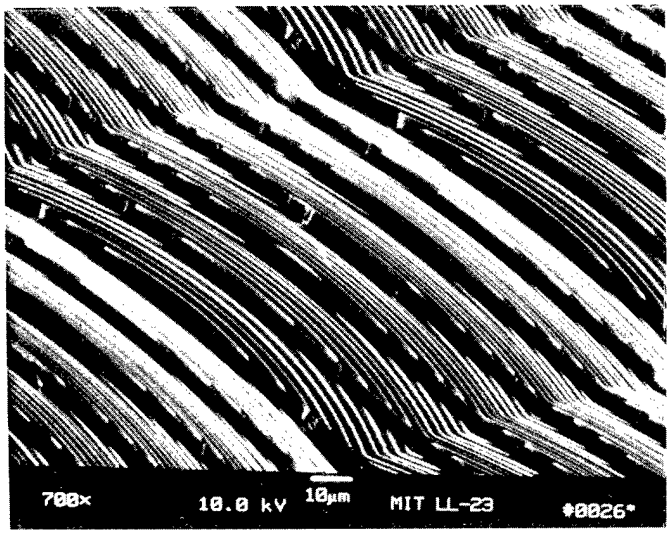

Figure 9: A 16-phase level color dispersing microlens array etched 7.5 µm deep. Shown is one pixel element from a 64 x 64 array.

The color dispersive microoptic, pictured in Figure 9, is a combination F/2 refractive microlens for focusing and 17 µm period diffraction grating for color separation. The total depth of this optic, made with four mask levels, is 7.5 µm. There are 64x64 identical pixel elements, each 100 µm x 100 µm square, in this array. The design and performance of this device are detailed elsewhere.[17]

4. LAYERED OPTICS

4.1 Integrated focal plane array optics

What is the future of binary optics technology development? High-quality microoptics will be integrated into layered systems. Such multilayered systems of optics and optics integrated with photonics and microelectronics will form the initial building blocks of amacronic focal plane arrays.[7] By exploiting the fill factor enhancement made possible by microlens arrays, photodetectors can be made smaller or spaced further apart; the newly available space can be filled with preprocessing circuitry. Monolithic integration of active and passive devices on the same substrate will eliminate difficult and time-consuming alignments between discrete planes of different devices.

Although major research and development efforts are required to realize amacronic focal planes that can combine detection with preprocessing capabilities, we have taken initial steps towards demonstrating dual-sided integration of optics and electronics. In a joint project with LORAL IRIS, we monolithically integrated focal plane arrays of microlenses with epitaxially grown HgCdTe photodetectors on opposite sides of a single CdTe substrate.[5] The microlens array pattern is registered to the HgCdTe photodetectors on the front side of the substrate to better than 2 μm, using our Karl Suss infrared backside mask aligner, and then etched into the backside of the substrate. Figure 10 shows the lensed substrate mounted to the carrier chip. Microlenses improved the detector quantum efficiency by a factor of 3.[5] In addition, by reducing the needed active detection area, the microlenses result in increased gamma radiation hardening.

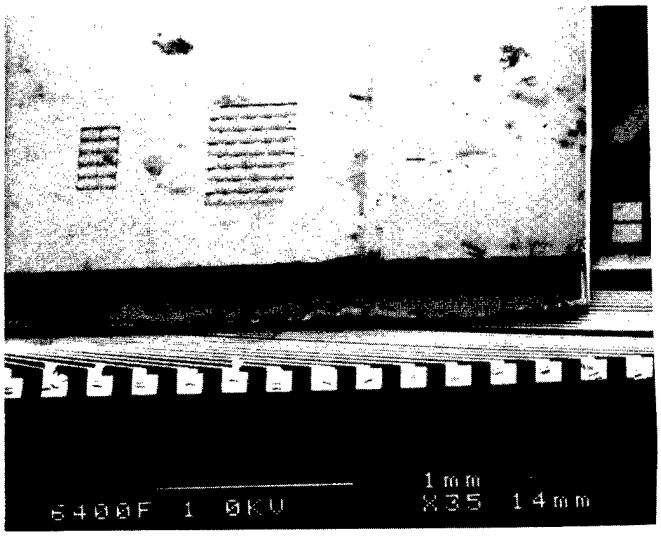

Figure 10: An SEM of monolithically integrated F/4 lenslets and HgCdTe photodetectors focal plane array.

5. CONCLUSION

Fabrication is the cornerstone for the realization of high-quality microoptics. We have highlighted details of the Binary Optics effort at MIT Lincoln Laboratory that lead to significant improvement in optical performance and to new microoptics capabilities. In particular, we have:

- recounted processing techniques used to fabricate benchmark quality, diffractive binary optics microlenses and presented measurements that clearly correlate efficiency loss with registration accuracy.

- described high-resolution Si RIE and multilayer resist processes developed to fabricate deep, three-dimensional, stepped optical structures. Fully refractive IR microoptics for applications in advanced sensors and color dispersive microoptics have been demonstrated.

- demonstrated monolithically integrated focal plane arrays of CdTe microlens and HgCdTe photodetectors - the initial step towards smart sensors.

Binary optics technology provides the base for a new class of smart, compact, low-cost sensors. In the future, system designers will integrate optics, electronics and photonics components to exponentially increase sensor processing capability. Implementation of these designs will be limited only by the creativity of microfabricators in inventing new techniques to fabricate them.

6. ACKNOWLEDGEMENTS

This work was sponsored by the Defense Advanced Research Projects Agency . We especially thank Wilfrid Veldkamp for his enthusiastic support of this work; Michael Holz, Theresa Jay, Mike Farn, and Bob Knowlden for technical contributions; Shirley Medeiros for fabrication assistance; and Walter Landoch for SEM work.

7. REFERENCES

1. W.B. Veldkamp and G.J. Swanson, "Developments in fabrication of binary optical elements", *SPIE Proc.* **437**, 54-59 (1983).

2. V.V. Wong and G.J. Swanson, "Binary optic interconnects: Design, fabrication and limits on implementation", *SPIE Proc.* **1544**, 123-133 (1991).

3. J.R. Leger, M. Holz, G.J. Swanson, and W. Veldkamp, "Coherent laser beam addition: An application of binary-optics technology", *Lincoln Lab. J.* **1**, 225-246 (1988); J.R. Leger, M.L. Scott, P. Bundman, and M.P. Griswold, "Astigmatic wavefront correction of a gain-guided laser diode array using anamorphic diffractive microlenses", *SPIE Proc.* **884**, 82-89 (1988); J. Leger, *Appl. Phys. Lett.* **56**, 4-6 (1990).

4. W. Goltsos and M. Holz, "Agile beam steering using binary optics microlens arrays", *Opt. Eng.* **29**, 1392-1397 (1990).

5. M.B. Stern, W.F. Delaney, M. Holz, K.P. Kunz, K.R. Maschhoff, and J. Welsch, "Binary optics microlens arrays in CdTe", Mat. Res. Soc. Symp. Proc. **216**, 107-112 (1991).

6. T.R. Jay, M.B. Stern,, and R. Knowlden, "Refractive microlens array fabrication parameters and their effect on optical performance", *SPIE Proc.* **1751**, 236-245 (1992).

7. W.B. Veldkamp, "Overview of microoptics: Past, present and future", *SPIE Proc.* **1544**, 287-299 (1991).

8. M.B. Stern, M. Holz, S. Medeiros and R.E. Knowlden, "Fabricating binary optics: Process variables critical to optical efficiency", *J. Vac. Sci. Technol.* **B9**, 3117-3121 (1991).

9. M.B.Stern and S.S. Medeiros, "Deep three-dimensional microstructure fabrication for IR binary optics", *J. Vac. Sci. Technol.* **B10**, 2520-2525 (1992).

10. M. Holz, M.B. Stern, S.S. Medeiros, and R.E. Knowlden, "Testing binary optics: Accurate high-precision efficiency measurements of microlens arrays in the visible", *SPIE Proc.* **1544**, 75-89 (1991).

11. Margaret B. Stern, Michael Holz, and Theresa R. Jay, "Fabricating binary optics in infrared and visible materials", *SPIE Proc.* **1751**, 85-95 (1992)

12. T.R. Jay, "Characterization of Shipley 1800 series Photoresist", MIT Lincoln Laboratory Project Report **BOP-2**, 25 October 1991.

13. J.A. Cox, T. Werner, J. Lee, S. Nelson, B. Fritz, and J. Bergstrom, "Diffraction efficiency of binary optical elements", *SPIE Proc.* **1211**, 116-124 (1990).

14. M.W. Farn and J.W. Goodman, "Effect of VLSI fabrication errors on kinoform efficiency", *SPIE Proc.* **1211**, 125-136 (1990).

15. G.J. Swanson, "Binary optics technology: Theoretical limits on the diffraction efficiency of multilevel diffractive optical elements", MIT Lincoln Lab. Tech. Rep. **914**, DTIC #AD-A-235404, March, 1991.

16. D.L. Flamm and V.M. Donnelly,"The design of plasma etchants", *Plasma Chem. Plasma Processing* **1**, 317-363 (1981).

17. M.W. Farn, private communication; Michael W. Farn, Margaret B. Stern, Wilfrid B. Veldkamp, and Shirley S. Medeiros, "Color Separation Using Binary Optics", submitted to *Optics Letters* (March, 1993).

BINARY OPTICS AT HUGHES DANBURY OPTICAL SYSTEMS

February 1993

James Logue and Michael Power
Hughes Danbury Optical Systems, Inc.
100 Wooster Heights Road
Danbury, CT, 06810

ABSTRACT

An overview of binary optics development at Hughes Danbury Optical Systems is presented. Design software used for mask design is presented. A brief discussion of fabrication follows. Two examples of actual projects are used to highlight the discussion: 1) a large aspheric lens and 2) a set of grating and lenslet arrays.

1.0 INTRODUCTION

Binary Optics components are fabricated to provide support to various programs at Hughes Danbury Optical Systems (HDOS). We have the capability to design and fabricate lenses, lens arrays, gratings, grating arrays, null correctors, and custom elements for special applications.

This paper will review the design and fabrication capability at HDOS. First, the software supporting mask design and the conversion of optic prescriptions into e-beam (MEBES) format for mask fabrication will be reviewed. Second, the fabrication of the binary optic from the e-beam masks will be covered. Lastly, two examples will be presented, highlighting the process flow we use to design and fabricate binary optics. The first example is a large aspheric lens and the second example is a set of grating and lens arrays.

Copyright© Hughes Danbury Optical Systems, Inc. 1993

2.0 SOFTWARE FOR MASK DESIGN

Software has been developed at HDOS to convert optical designs into e-beam (MEBES) data files.[1] Computer Aided Design (CAD) software (MicroStation PC) is used to design the mask set for a binary optic. This involves defining the placement of the MEBES files describing the optic and placement of alignment and fiducial marks. CAD data can be converted into MEBES format and vice-versa. Figure 1 shows the basic components and data flows of the binary optics design software. All of this software has been integrated to run on a 486-PC bases workstation.

The design conversion software is a set of FORTRAN subroutines and drivers that can be linked to customized interface subroutines which define the interface with an optic design. Two custom subroutine are required - one to compute the phase at a given position and one to set the design parameters for the phase equations in the first module. For example, a program to compute MEBES data for zone plates has a subroutine called PHASE(X,Y) to compute the phase of the zone plate at (X,Y) and a subroutine called DEFINE to set the wavelength and focal length of the zone plate for the user. These two custom subroutines, PHASE(X,Y) and DEFINE, are linked into the binary optics software library to create a program, ZONEMEBES, which generates MEBES files for zone plates.

We have developed custom interfaces with HDOS lens design software to support the generation of MEBES data for zone plates, aspheric lenses, gratings, Zernike surfaces, and b-spline surfaces. On one occasion, a special interface was developed to generate MEBES masks for a polar-log transform lens.[2]

Mask layout and design is done using CAD software. HDOS is currently using Intergraph's MicroStation PC. This program has multi-level design capability and supports cell libraries. We have created a cell library containing all of our standard alignment and calibration patterns. As shown in the following examples, this package helps us to rapidly design a complex mask set.

---

[1]. James Logue and Marilynn L. Chisholm, "General approaches to mask design for binary optics", Holographic Optics: Optically and Computer Generated, Ivan N. Cindrich, Sing H. Lee, Eds., Proc. SPIE 1052, 19-24 (1989).

[2]. David A. Zweig, Michael P. Power, Thomas J. McHugh, and James E. Logue, "Geometric transformations using binary optics", OSA Annual Meeting, 1989 Technical Digest Series, Vol. 18 (Optical Society of America, Washington, D.C., 1989).

The design laid out in MicroStation PC can be extracted by level and converted into MEBES format using the same conversion software described above to support generation of optical MEBES data. In this case, the custom subroutines are designed to extract and convert CAD commands into MEBES format.

MicroStation PC is also used to examine MEBES data and to generate check plots and blueprints. Conversion software has been developed to translate MEBES data into MicroStation CAD format. This allows us to capture and inspect MEBES data, either for checking MEBES data generated from optic prescriptions or for inspecting and capturing data provided to us in MEBES format.

Our binary optics design software and the CAD software run on a 486-PC based workstation with the following components.

- 9-track tape drive (1600/3200 BPI)
- hi-resolution VGA color monitor
- 660 MB hard drive
- HP LaserJet III printer
- Hughes network interface

3.0 BINARY OPTICS FABRICATION

In the fabrication area we use a basic set of equipment that is customized to handle the various substrate materials, sizes, and shapes which are defined by the design requirements of the particular optic being generated. Figure 2 shows the basic process flow using this equipment.

Cleanroom Class 10000	Laminar Hoods Class 1000, Chemical Hoods
Headway Spinner	Photoresist application on substrate
Cleanroom Ovens	Prebake/Postbake
Modified MJB3 Karl Suss Mask Aligner	Photolithographic Alignment/Exposure
Veeco 3" Ion Miller	Etching of the masked steps
Alpha-step; Dektak	Profilometers
Optical microscopes; SEM	Inspection

Over the years we have worked with a wide variety of materials.

crystal quartz	fused silica	BK7 BaF3	ZKN7	Ge	ZnSe ZnS
GaAs	Silicon	CdTe	Mica	dielectrics	etc.

Each material requires developing a particular process recipe that includes choice of photoresist, determination of etch rate, aspect ratios (resist/substrate), exposure/development latitudes (resist/substrate; linewidth/depth/area), special interface layers, jigs and fixturing, etc. We have done the bulk of our etching of binary optics using an ion miller which utilizes a neutral Ar^+ ion beam which generally eliminates the need to determine process chemistries as we change from one material to another. This is a multi-staged system capable of milling at multiple angles relative to normal. We also incorporate various in-situ monitoring schemes along with extensive use of profilometry to calibrate/control geometries of the etch process on each substrate.

4.0 EXAMPLE 1: LARGE ASPHERIC LENS

This section describes the design and fabrication of a large aspheric lens. The lens prescription is

$$f(r) = 3.38\ r - 3.36e\text{-}3\ r^3 + 1.40e\text{-}6\ r^5\ ,\ (r \text{ in mm})$$
$$r_{max} = 32.8 \text{ mm.}$$

Analysis of the phase equation above yields the minimum feature size and the estimated amount MEBES data required for each mask.

MASK #	MINIMUM FEATURE SIZE (MICRONS)	ESTIMATED DATA VOLUME (MB)
1	11.7	28
2	5.8	56
3	2.9	112
4	1.5	224

The data volumes are based on using a 0.2 micron address resolution for the MEBES data. This is sufficient to resolve the 1.5 micron lines on the fourth

mask. All four masks will be made using a 0.2 micron resolution to provide exact level-to-level alignment in the lens data.

The data volume required for this lens presented us with a problem. The maximum MEBES file size supported by our software is 64 MB.[3] This forced us to partition the lens data for the third and fourth masks as shown in Figure 3. This works well, as long as all quadrant data is explicitly generated by the aspheric lens conversion program. On our first attempt, in an attempt to save time, we used the aspheric conversion program to generate one quadrant of data (FILE 1). We asked the mask vendor to use MEBES utility software to generate the missing quadrants for the third mask by taking advantage of the axial symmetry of the lens data about its center. Unfortunately, the resulting mask contained minuscule roundoff errors which had been introduced by the utility software chosen by the mask vendor. After fabricating the lens, a shadow image was noticed in the image of the test system using the binary aspheric lens. This was traced back to an apparent phase shift in the fourth quadrant of the lens. We believe that this was due to roundoff errors in the data for FILE 4 for the third mask.

For all four MEBES masks, calibration and alignment marks were placed using MicroStation PC. These marks were used for mask-to-mask alignment, mask-to-substrate alignment, and feature size calibration. HDOS conversion software was used to extract the mask information from the CAD files and convert it into MEBES files for mask fabrication. Additionally, the mask layouts were printed out for use as specifications to the mask vendor (see Figure 4).

In keeping with the theme of pointing out some of the pitfalls we have encounter in designing and fabricating a wide variety of binary optics, we encountered a problem with double exposure of the resist in the center zones of this optic after the first level etch had defined the fresnel zones and the second mask was being exposed. This was caused by a reflection of the focused rays from the back surface of the optic. This led to the requirement of using a blocking layer between the resist and the optic to prevent this back reflection. We had used this particular scheme in the past to provide an enhanced image of the previously exposed layer for alignment purposes of the next mask, especially for very narrow linewidths or when the etch depth is very shallow, such that it is hard to see the original image through the subsequent mask or resist layer.

---

[3]. Actually MEBES files can be as large as 128 MB, but we have limited ourselves to 64 MB for now.

5.0 EXAMPLE 2: GRATING AND LENSLET ARRAYS

This section describes the design and fabrication of two lenslet arrays and a set of four grating arrays. All six arrays are hexagonal arrays on 5 mm centers. Each lenslet array contains 23 lenses, selected from three different aspheric lenses, each 5 mm in diameter, with the following prescriptions.

Ia: $f(r) = 92.8\ r - 2.87e\text{-}2\ r^3 + 1.52e\text{-}5\ r^5$, (r in mm)
Ib: $f(r) = 66.5\ r - 2.57e\text{-}2\ r^3 + 1.54e\text{-}5\ r^5$
II: $f(r) = 20.7\ r - 2.85e\text{-}3\ r^3 - 2.37e\text{-}6\ r^5$

The grating arrays consist of 12 or 17 gratings, all different, placed on the same hexagonal grid used for the lenslet array. Each grating array also contains four targets aligned to the type Ia and Ib lenses.

The main complication in this job was handling the many data files required. Including the lens data files, grating data files, and calibration/alignment data files, there were 67 data files to be placed on 6 MEBES masks (see Figures 5 and 6). MicroStation PC was used to design the mask layouts and insure mask-to-mask alignment for the lenslet arrays and lens-to-target/grating alignment between the lenslet and grating arrays. Additionally, the six grating and lenslet arrays were placed in pairs on three MEBES masks to optimize mask costs. Additional marks defining the cut lines for each array had to placed with the calibration and alignment marks. The convenience of using integrated software on a single workstation made this job relatively easy, since blueprints and checkplots could be generated at all stages of the design to insure that the masks would be correct on the first attempt.

In the fabrication of this set of optics, we encountered another problem due to material properties that sometimes present unique challenges when the system requirements call for changes in either the substrate material or the geometry (size, shape, thickness, etc.) of the particular optic. Here the rate of etching of the resist relative to the etch depth in the substrate was relatively high due in part to poor heat transfer from the substrate and to a minor extent to the substrate material makeup, which required extensive rework of the resist process; as the linewidth to depth ratios also varied widely over the total area of the arrays. This type of problem is overcome by maintaining an extensive set of resist recipes and continually updating resists and resist property definitions as new products emerge on the market. Over the years we have done extensive work in all types of device processing outside the realm of binary optics and have developed methodologies that are easily traded off against each other to solve problems that are encountered in the fabrication of binary optics.

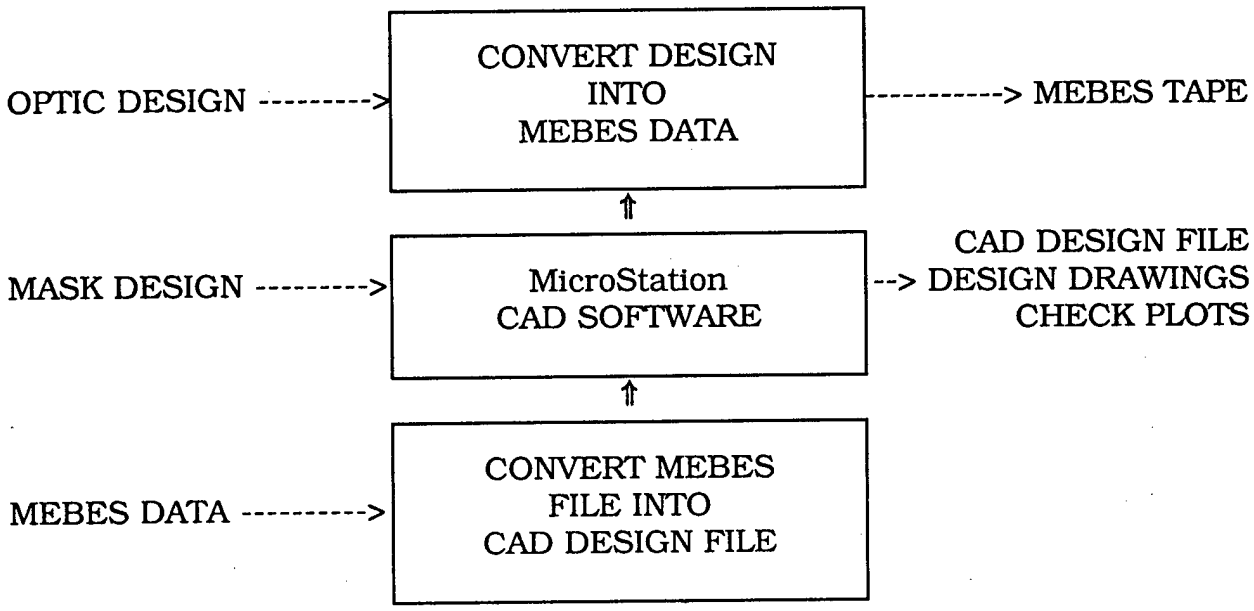

FIGURE 1. BINARY OPTICS MASK DESIGN SOFTWARE BLOCK DIAGRAM

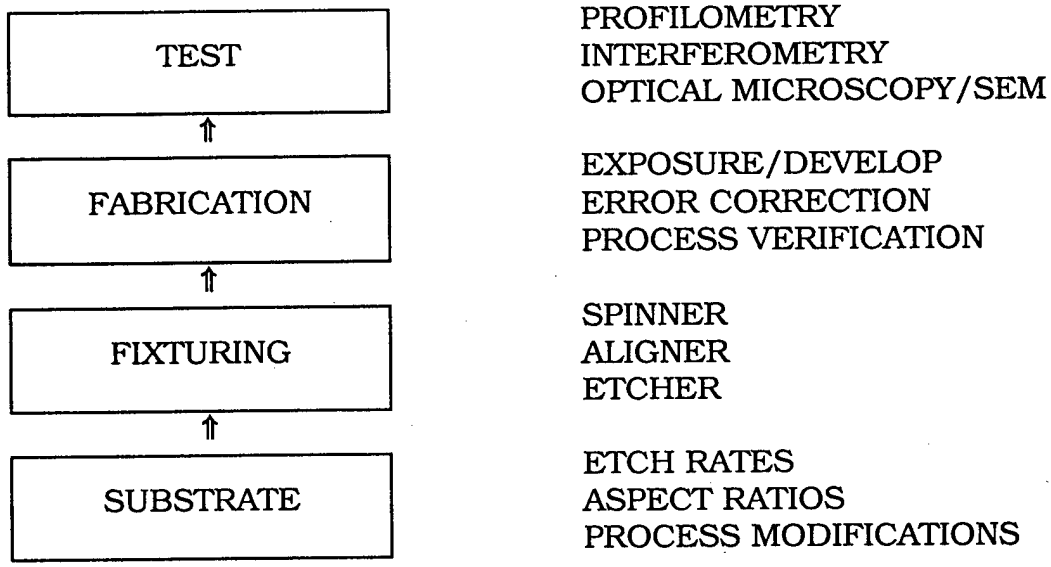

FIGURE 2. BASIC OPTIC FABRICATION PROCESS FLOW

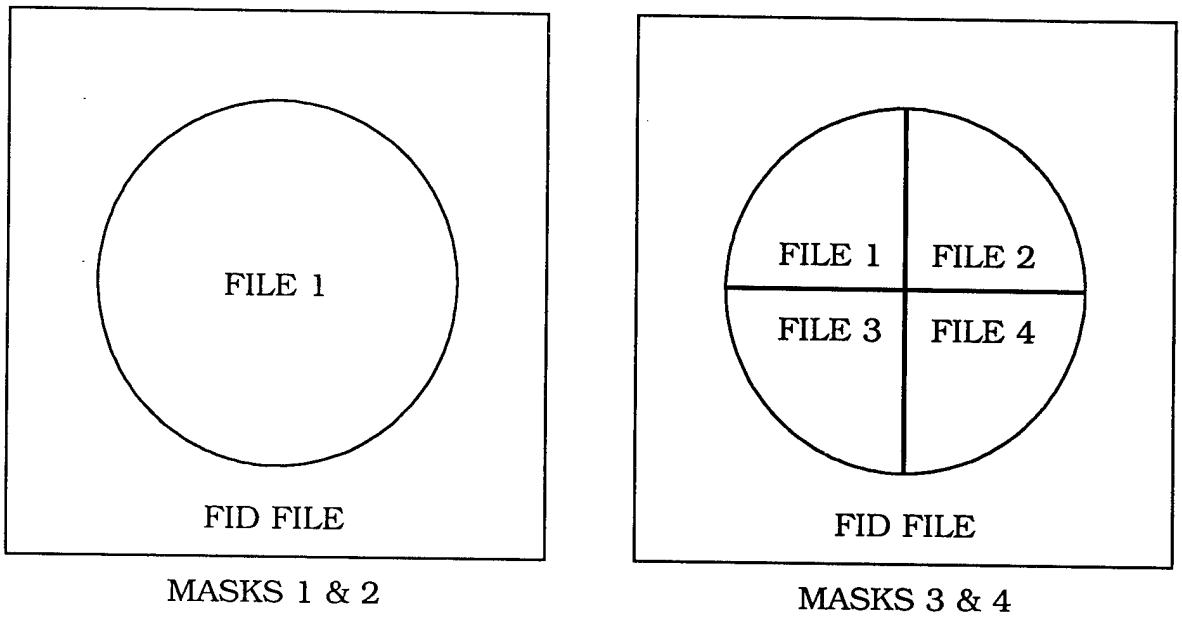

FIGURE 3. LARGE ASPHERIC LENS DATA PARTITIONS

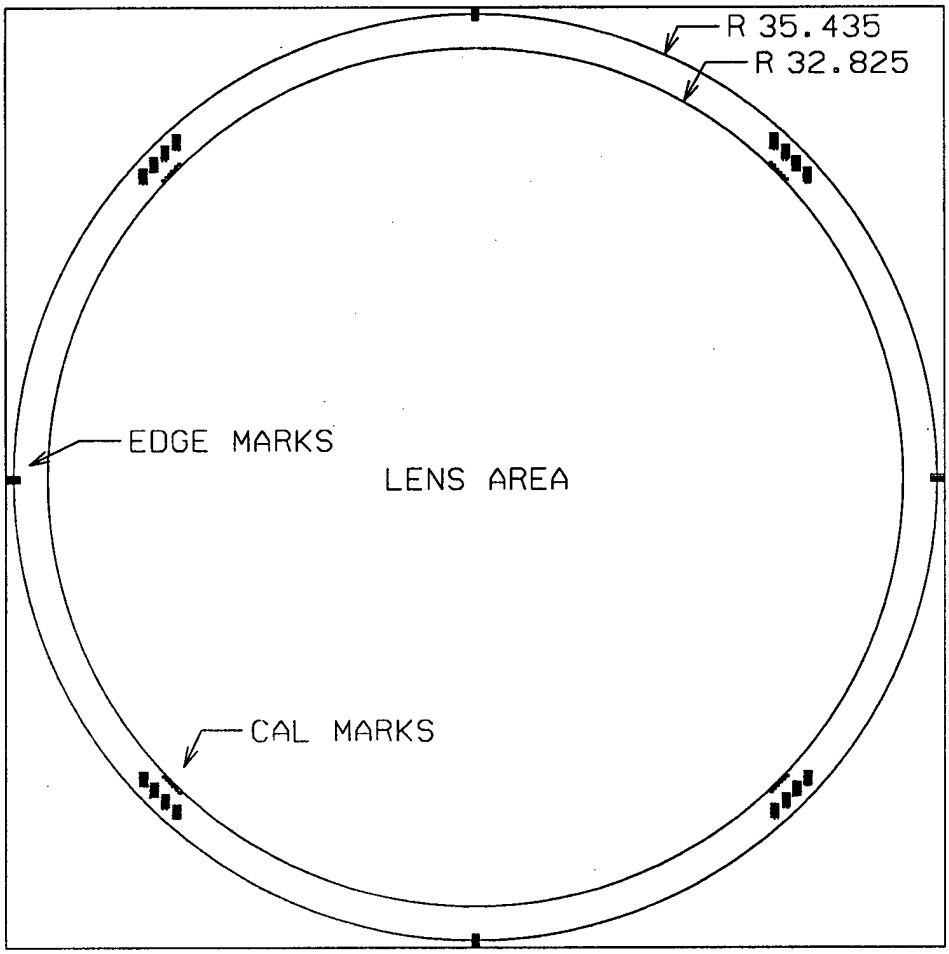

FIGURE 4. SAMPLE MASK LAYOUT FOR A LARGE ASPHERIC LENS

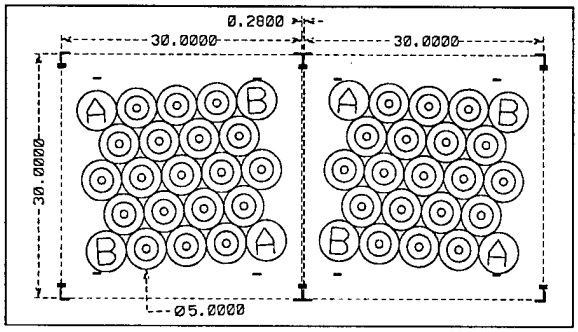

MASK 1

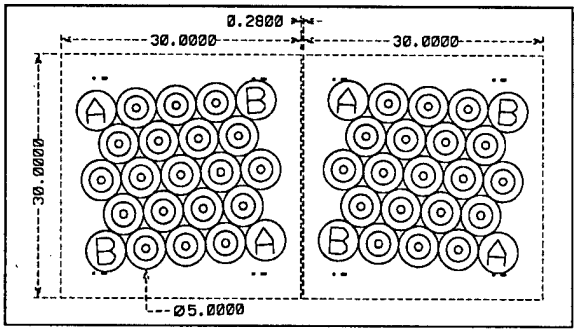

MASK 2

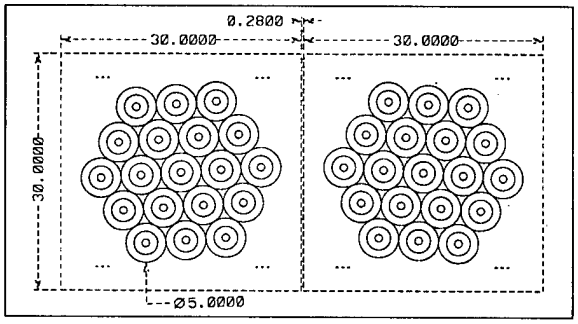

MASK 3

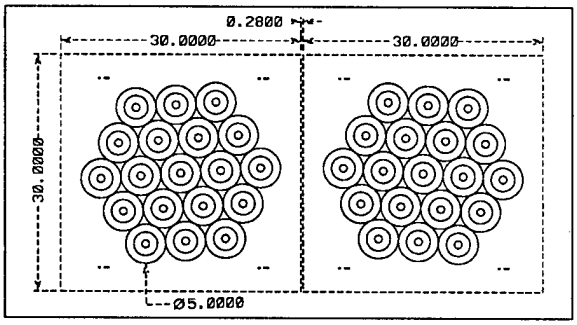

MASK 4

FIGURE 5. MASK LAYOUTS FOR LENSLET ARRAYS

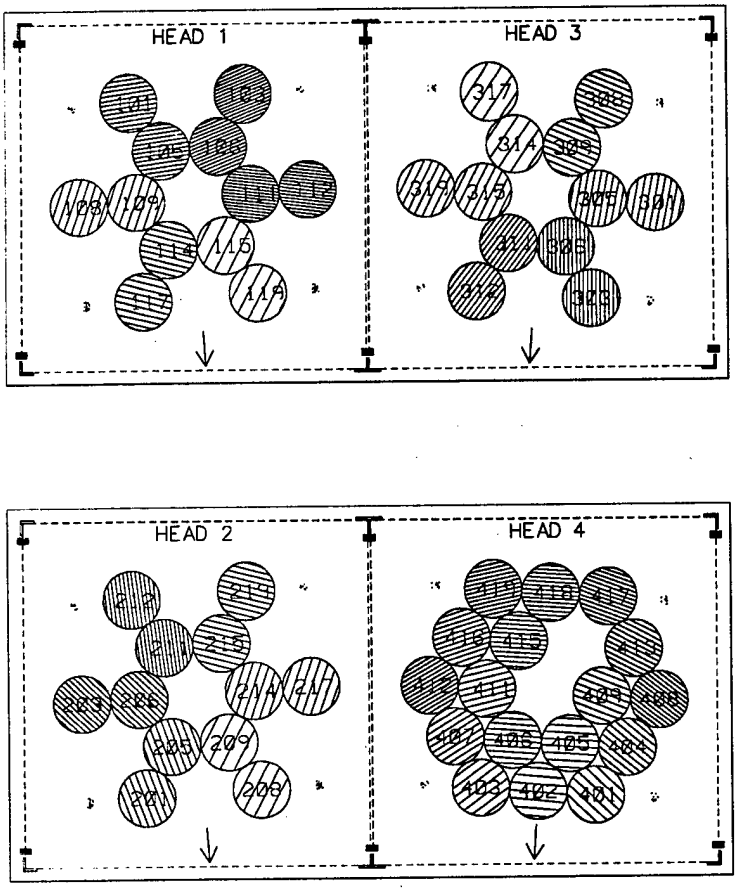

FIGURE 6. MASK LAYOUTS FOR GRATING ARRAYS

Fabrication Techniques for Very Fast Diffractive Lenses

Anthony M. Tai and Joseph C. Marron
Environmental Research Institute of Michigan
P.O. Box 134001
Ann Arbor, MI 48113-4001

Abstract

Aspheric lenses with arbitrary phase functions can be fabricated on thin light weight substrates via the binary optics fabrication technique. However, it is difficult and costly to fabricate a fast lens (f/number <1) for use at the shorter wavelengths. The pitch of the masks and the alignment accuracy must be very fine. For a large lens, the space-bandwidth product of the element can also become impractically large. In this paper, two alternate approaches for the fabrication of fast aspheric diffractive lenses are described. The first approach fabricates the diffractive lens interferometrically, utilizing a spherical wavefront to provide the optical power of the lens and a computer generated hologram to create the aspheric components. The second approach fabricates the aspheric diffractive lens in the form of a higher order kinoform which trades groove profile fidelity for coarser feature size. The design and implementation issues for these two fabrication techniques are discussed.

1.0 Introduction

The advantages offered by diffractive lenses are well known. A lens with an arbitrary aspheric phase function can be easily implemented on a thin and light weight substrate. However, if the lens is very fast (f/number <1) and the operating wavelength is short, the groove spacing at the edge of the lens becomes very narrow. For example, with a f/1 lens designed for 0.5μm operation, the zone or groove spacing at the edge is only 1.1μm. Fabricating the lens via the binary optics technique [1], the pitch of the binary masks for a 4-level lens will be about 0.25μm. In addition, the masks must be aligned with an accuracy much better than 0.25μm. If the size of the lens is also large (>25mm diameter), a substantial amount writing time with an electron beam machine will be required. Making the matter worse is the need to lower the beam intensity in order to achieve the fine pitch which further lengthen the writing time. Therefore, the fabrication of a large and fast diffractive lens with the binary optics technique is a very expensive proposition.

2.0 Computer-Originated-Hologram

To reduce the demand on the writer, optical interferometric recording can be combined with computer generated holography. Instead of generating the aspheric lens function directly as a computer generated diffractive optical element, the lens is fabricated

by interfering a spherical wavefront produced by a refractive lens (e.g. a microscope objective) with the aspheric wavefront produced by a computer generated hologram [2] as illustrated in Figure 1. Let the desired phase function of an aspheric lens with focal length f be $\theta_H(x,y)$, and

$$\theta_S(x,y) = \frac{2\pi}{\lambda}\left[f \sqrt{1+\frac{(x^2+y^2)}{f^2}} \right]$$

be the spherical phase function that matches the optical power of the aspheric lens. A holographic lens with the desired phase function is obtained by interfering the spherical wavefront with an aspheric wavefront having a phase function of $\theta_A(x,y)$ where $\theta_A(x,y) = \theta_S(x,y) - \theta_H(x,y)$.

To achieve high diffraction efficiency, the hologram has to be recorded in the form of an off-axis volume Bragg hologram [3]. Special design considerations must be taken to produce an on-axis lens with uniformly high diffraction efficiency across the entire lens.

An on-axis lens can be created by bonding two off-axis holographic lenses together which share a common reference beam as shown in Figure 2. The desired phase function of the lens is once again decomposed into spherical and aspherical components. The spherical component, $\theta_S(x,y)$, is recorded on the first hologram using a diverging spherical object wavefront and the aspheric component, $\theta_A(x,y) = \theta_H(x,y) - \theta_S(x,y)$, is recorded on the second hologram with an aspheric wavefront produced by a computer generated hologram.

In the example, the spherical phase function is placed in the first hologram and the aspherical phase function is put in the second. It does not have to be the case. The choice of the recording wavefronts is dependent on the operating geometry for which the lens is designed. To assure diffraction efficiencies that are uniformly high across the entire lens, the rays in the object wavefronts used to record the two holograms must match as closely as possible the ray directions of the input and output fields in the playback geometry. A wide angle diffractive lens had been fabricated using this approach [4]. The f/0.7 lens was designed to detect and determine the angle of arrival of 850nm laser radiation. The rms spot size and the diffraction efficiency of the diffractive lens were both uniform to within 10% over a field of view of 45° x 45°.

Using a microscope objective to provide the optical power, the slope of the remaining aspheric term will not be very steep. The computer generated hologram can be fabricated by a variety of writing machines, including the laser writer described in the following section.

2.0 Higher Order Kinoform

Kinoform [5] and Fresnel lens are both collapsed versions of a refractive lens. With a Fresnel lens, the optical path differences (OPDs) at the transitions between zones are many wavelength. The OPDs between zones can vary slightly and they are not exactly integer number of wavelengths. In other words, the zones of a Fresnel lens are not phased to produce diffraction limited performance. The optical path difference at the transitions between the zones of a kinoform, on the other hand, is exactly one wavelength. The angle of the first order diffraction of a kinoform matches the refraction angle of the wedge shape groove and a diffraction efficiency near 100% can be obtained.

A higher order kinoform resides between a Fresnel lens and a conventional, or first order, kinoform. The optical path difference between zones of an nth order kinoform is exactly equal to n wavelengths where n is an integer number greater than one. The zone spacing of an nth order kinoform is n times wider than its 1st order counterpart as illustrated in Figure 3. With a higher order kinoform, the angle of the nth order diffraction matches the refraction angle and a diffraction efficiency near 100% can also be achieved.

Higher order kinoforms are attractive because they can be fabricated very efficiently with a laser writer. A laser writer uses a focussed laser beam to expose a photo-sensitive recording material such as photographic film or photoresist. The scanning of the laser spot over the recording material can be accomplished by moving the recording material under the beam using a translator or a rotating drum, or by scanning the beam with a polygon, holographic or acousto-optics scanner. The spot size of a laser writer is typically >1μm which is much larger than available with e-beam writing machines. However, a laser writer is capable of postioning resolutions that are much finer than the spot size. In addition, they can provide gray scale writing capability with up to 8-bit of dynamic range.

To achieve high diffraction efficiency, the profile of the zones of a kinoform lens must be produced with high fidelity. It can be accomplished only if the spot size of the writing beam is smaller than the zone spacing. A 1st order kinoform with a zone spacing of 1μm, for example, cannot be fabricated with a laser writer whose spot size equals to or larger than 1μm. The laser writer, however, can be used to fabricate a higher order kinoform of the same lens function as illustrated in Figure 4. The laser writer cannot produce the sharp transition between zones but its effect on diffraction efficiency becomes less and less significant as n becomes larger. We should emphasize, however, that the fabrication of higher order kinoform does not reduce the resolution requirement in the positioning of the writing beam.

While using a larger n will place less demand on the spot size, it will also require a larger dynamic range, more linear recording and better control of the coating thickness. The rms phase error introduced should be < 1/8 of a wave to provide diffraction limited performance. As the zone becomes larger and higher, it will be increasingly more difficult to achieve the required profile fidelity.

In Figure 5, we show the normalized film thickness of a linear photoresist coating after processing as a function of exposure energy. The recording can be linearized by using a lookup table to adjust the exposure energy accordingly. Figure 6 shows the profilometer trace of linear grooves fabricated on a 5μm coating. They correspond to zones of a 5th order kinoform designed for 500nm operation. The rms phase error was less than 1/8th of a wave.

4.0 Concluding Remarks

It is difficult and expensive to fabricate a fast diffractive lens of appreciable size using the binary optics fabrication technique. We have described two alternate approaches that can be used to fabricate very fast diffractive lenses with arbitrary aspheric phase functions at much lower cost. The computer-originated hologram combines the strengths of optical holographic recording and computer generated hologram. The higher order kinoform trades profile fidelity for coarser feature size. Both approaches can be implemented using a laser writer with a spot size > 1μm. The use of laser writer is attractive for the following reasons. 1) Laser writers are much less expensive to acquire and operate than e-beam writing machines. 2) The spot size is independent of the laser power which allows very high writing speed by using a high power laser. 3) With gray scale writing capability and beam positioning resolution much finer than the spot size, a computer generated hologram can be written directly from its phase description without special coding or formatting. 4) By writing first onto a photographic film to form a gray scale mask, copies can be made on linear photoresist or other materials by simple contact printing.

The work reported in this paper was supported by ERIM Internal Research and Development funds.

References

1) G.J. Swanson and W.B. Veldkamp, "Binary Lenses for Use at 10.6 Microns," Opt. Eng. 24, 791 (1985).

2) R.C. Fairchild and J.R. Fienup, "Computer-Originated Aspheric Holographic Optical Elements," Opt. Eng. 21, 133 (1982).

3) H. Kogelnik, "Coupled Wave Theory for Thick Hologram Gratings," *Bell Syst. Tech. J.*, 48, 2909 (1969).

4) A. Tai, M. Eismann and B. Neagle, Holographic Lens for Wide Field of View Laser Communication Receiver," Final Technical Reprot to AF WRDC/AAAI-2, ERIM Report No. 213325-3-F, March 1990.

5) J.A. Jordan et al., "Kinoform Lenses," Appl. Opt., 9, 1883 (1970).

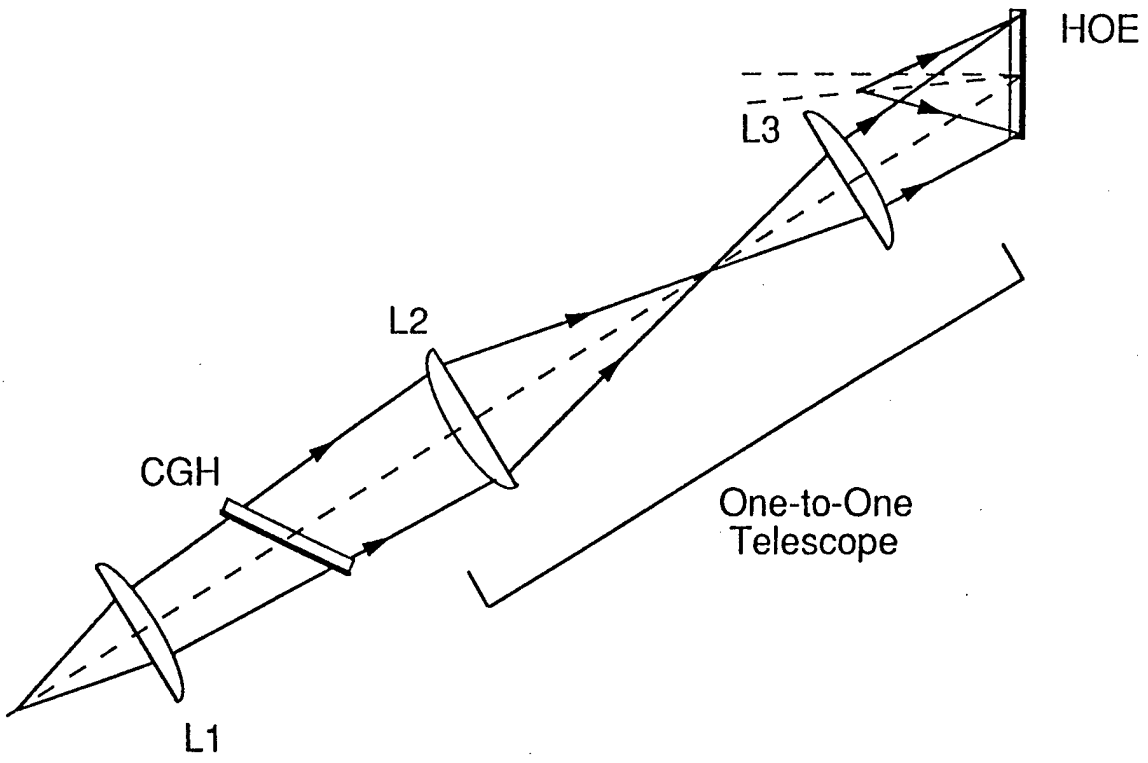

Figure 1. Fabrication of a computer-originated hologram.

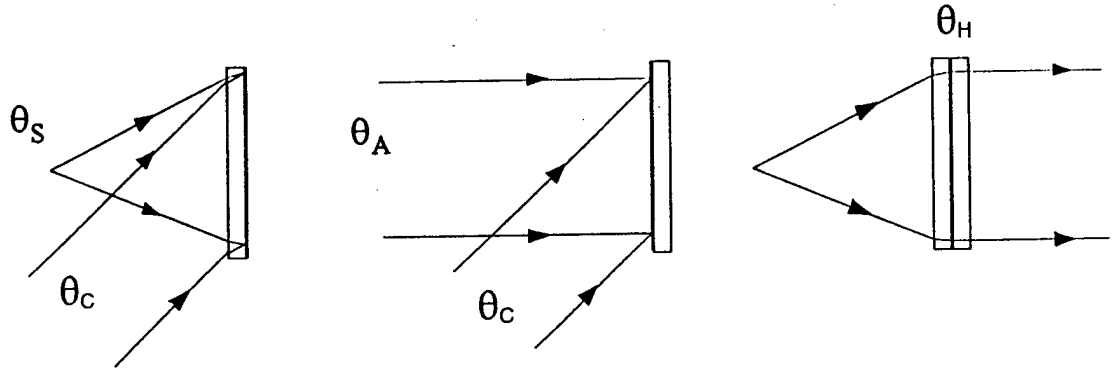

Desired phase function $\theta_H = \theta_S + \theta_A$

Figure 2. Fabrication of an on-axis lens by bonding two off-axis volume holograms

Higher order kinoforms

• OPD between zones: m waves

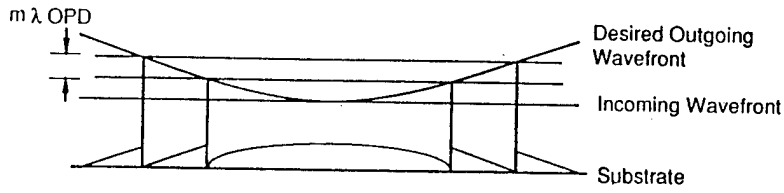

First order kinoform

• OPD between zones: 1 wave

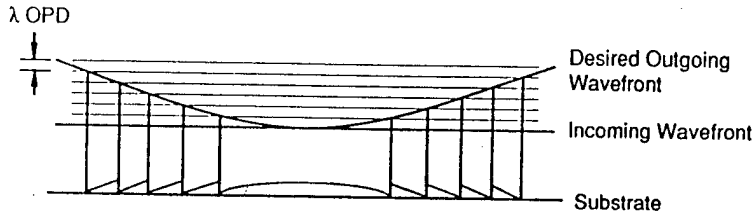

Figure 3. First order and higher order kinoforms

First order kinoform

• Small dynamic range and fine spot size

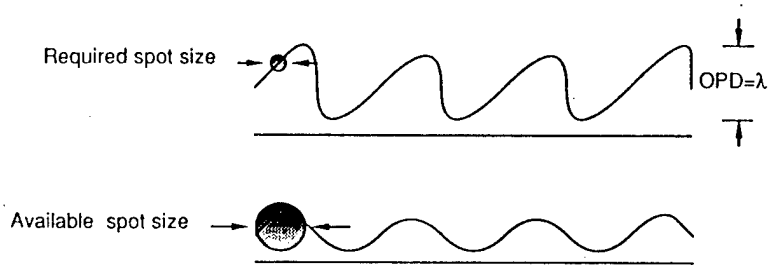

Higher order kinoform

• Large dynamic range and coarse spot size

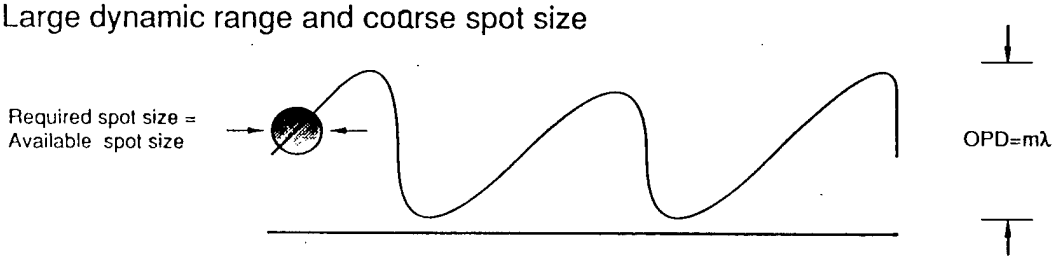

Figure 4. Fabricating kinoforms with a laser writer

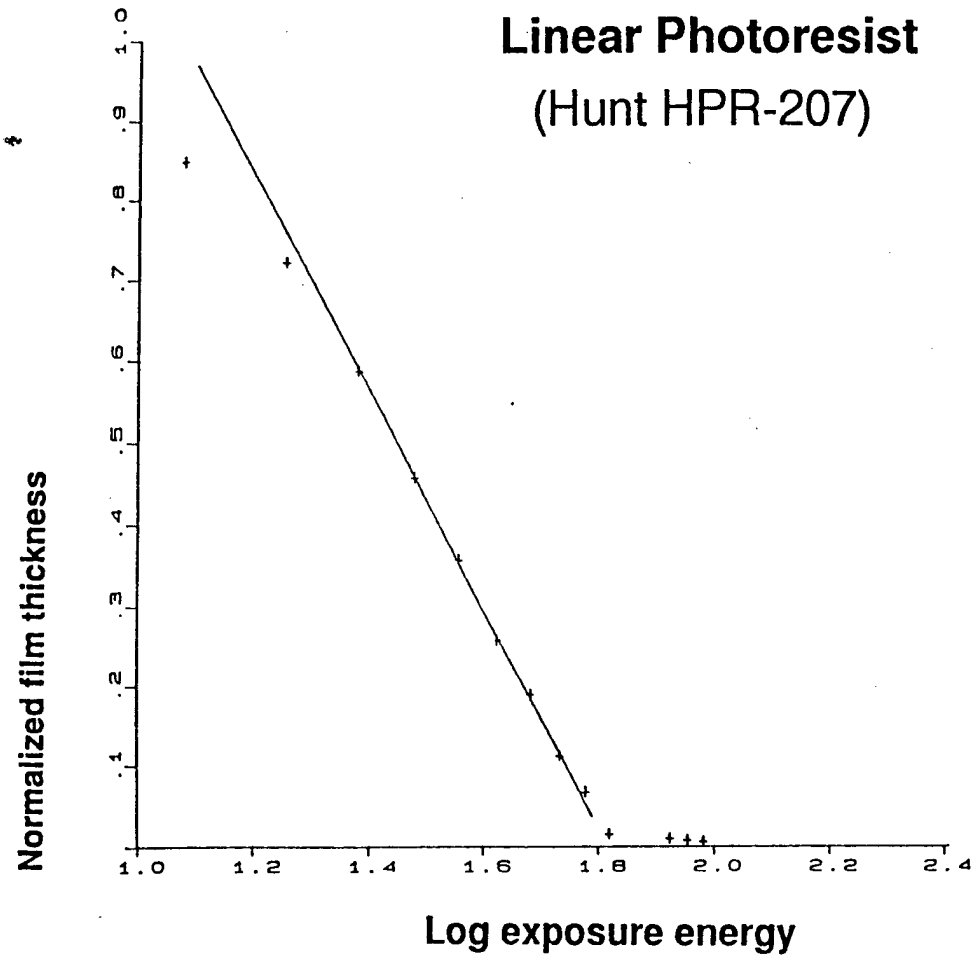

Figure 5. Normalized film thickness of photoresist after processing as a function of exposure energy

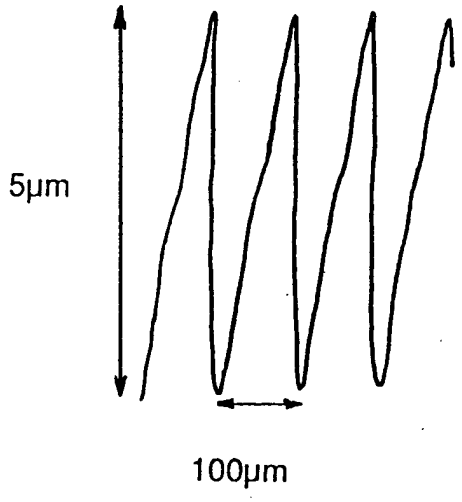

Figure 6. Profilometer trace of linear blaze fabricated on linear photoresist. (Corresponds to 5th order kinoform designed for 0.5μm operation)

LASER FIGURING FOR THE GENERATION OF ANALOG MICRO-OPTICS AND KINEFORM SURFACES

Edward J. Gratrix
Hughes Danbury Optical Systems
100 Wooster Heights Rd.
Danbury, CT 06810
(203) 797-6357

ABSTRACT

To date, there have been many techniques used to generate micro-optic structures in glass or other materials. Using methods common to the lithographic industry, the manufacturing technique known as "binary optics," has demonstrated the use of diffractive optics in a variety micro-optic applications. It is well established that diffractive structures have limited capability when applied in a design more suited for a refractive element. For applications that demand fast, highly efficient, broadband designs, we have developed a technique which uses laser figuring to generate the refractive micro-optical surface. This paper describes the technique used to fabricate refractive micro-optics. Recent results of micro-optics in CdZnTe focal planes are shown.

1.0 INTRODUCTION

Interest in the production of microlenses and microlens arrays has steadily increased with demand for improvements in detector arrays, optical processors, and laser diode systems. There are several techniques that are capable of generating microlenses in opto-electronic materials such as Si and CdZnTe. These include lithographically generated[1], melting[2] and gray-scale or half tone[3]. Each of these techniques has been found to have one or more limitations, such as; inadequate resolution, high scatter, inability to achieve high numerical aperture, inaccessibility to controlled aspherics or high efficiency.

The technique developed at HDOS involves the laser figuring of photoresist followed by a subsequent pattern transfer by ion milling[4]. This approach permits the

[1] G. J. Swanson, W. B. Veldkamp, "Binary Lenses for use at 10.6 Micrometers," *Opt. Eng.* **24**, 1985.
[2] Z. D. Popovic, et al, "Technique for Monolithic Fabrication of Microlens Arrays," *Appl. Opt.* **27**, 7, 1988.
[3] W. W. Anderson, et al, "Fabrication of Micro-Optical Devices" Conf. on Binary Optics, Huntsville, 1993.
[4] E. J. Gratrix, C. B. Zarowin, "Fabrication of Microlenses by Laser Assisted Chemical Etching (LACE)," *SPIE* **1544**, 238, 1991.

generation of accurate, highly efficient refractive micro-optics in materials suitable for implementation on detector arrays, optical processors, or laser diodes.

We will report on the recent progress of this technique in the fabrication of optical elements in photoresist, Si and CdZnTe. Specifically, results from the fabrication of 128 by 128 element arrays of microlenses in CdZnTe, will be shown. Extensions of this technique toward the computer figuring of the kineform diffractive surface will be evident.

2.0 MICRO-OPTICAL FIGURING

The technique we have developed is a microscopic, computer controlled exposure technique similar to the more macroscopic versions of plasma chemical figuring[5] and computer controlled polishing[6]. In each of these cases, the desired surface is generated by moving a tool, with a known footprint, over the surface while appropriately adjusting the amount of material removed. The tool in our approach is a laser spot, focused onto positive photoresist, with a footprint capable of addressing the spatial frequencies necessary to accurately figure a microlens. The laser spot is recorded by the photoresist for subsequent photodevelopment to yield the lens feature.

With knowledge of the shape of the laser spot, the photoresists response to the laser and an accurate description of the surface to be generated, we can calculate an intensity map[7]. The information from the intensity map, the lenslet location, and the footprint trajectory are coded into a computer. The entire array is exposed in a raster form with the appropriate intensity adjusted on-the-fly depending on the laser spots exact location. For arrays which have identical, symmetric lenslets, the range of calculations extends only over a single lenslet radius and is repeated as the spot enters the next region. Unique features can also be generated by solving for the various surface relief functions.

3.0 PHOTORESIST AS A MICROLENS

Photoresist lenses made by this microfiguring approach are shown in figure 1. This array was designed with 180 micron diameter, 200 micron square on center, lenses. The f-number of each lens was designed to range from infinity (flat), to f/1. For this, positive photoresist is coated onto a glass substrate and pre-baked. The array was then exposed by moving the substrate under a stationary laser position which varied in intensity. Finally, the array is completed by immersing the substrate in developer solution. The optical performance of this type of lens array was reported to be superior

---

[5] L. D. Bollinger, C. B. Zarowin, "Rapid, Non-Mechanical, Damage-free Figuring of Optical Surfaces Using Plasma Assisted Chemical Etching," *SPIE* **966**, 1988.

[6] R. A. Jones, "Modeling the Computer Controlled Polishing Process," Appl. Opt. **22** (15), 1983.

[7] C. B. Zarowin, "A Robust, Non-Iterative Computationally Efficient Modification of van Cittert Deconvolution," *JOSA*, in press.

to many other lens manufacturing techniques[8]. The interferogram in figure 2 demonstrates the optical surface generated in photoresist lenslets designed to be 200 micron on center, f/1.4, with a full fill-factor. Due to the high spatial frequency content of the laser spot, this technique can accurately figure over most of the available lenslet surface, which typically exceeds 95%. The fill factor is clearly demonstrated when the reference leg of the interferometer is positioned at the intersection of four adjacent lenslets, as shown in figure 3.

4.0 PATTERN TRANSFER

The use of photoresist as an optical medium is limited by the material transmission, index of refraction, and/or the robustness. There are a few techniques to eliminate photoresist as the final optical medium. One technique is to transfer the shape generated in the photoresist into the underlying substrate. This can be accomplished by either ion sputtering or chemical plasma etching. The basic principle behind this pattern transfer is to controllably erode the photoresist as well as the underlying substrate. While the erosion process may provide an additional mechanism to control the figure of the lenslets, it is not without limitations. In many cases the distortion of the microlens surface due to non-linearity in the pattern transfer process are not negligible[9].

For sputter erosion, or ion milling, the relative etch rate between photoresist and the substrate varies depending upon which materials are chosen, and at which angle the ions impinge. Ion milling, as a pattern transfer mechanism, has some limitations; the rates are slow (typically at hundreds of angstroms per minute) and the relative etch rates are low (typically between 1 : 1 to 5 : 1). For lens designed with a large sag it may take several hours of ion milling to complete the pattern transfer. However, since ion milling is accomplished at very high ion energies, it is a relatively robust technique when encountering defects, chemical impurities and processing changes. The inclusion of preferentially reactive species as the impinging source is termed reactive etching. This can extend the relative etch rate by several times however it still suffers the angular rate dependence described earlier.

Chemical plasma etching is strongly dependent upon the chemical composition of the materials and, to a lesser extent, the geometry of the surface to be generated[10]. One of the limitations to implementing a chemical plasma etch is that it is extremely difficult to find suitable etching conditions for materials which are not amorphous.

---

[8] P. de Groot, F. X. D'Amato, E. J. Gratrix, "Interferometric Evaluation of Lenslet Arrays for 2-D Phase-locked Laser Diode Sources," *SPIE* **1333,** 1990.

[9] C. B. Zarowin, "Comparison of the Smoothing and Shaping of Optics by PACE and Ion Milling," Appl. Opt., in press.

[10] C. B. Zarowin, "Relation Between the RF Discharge Parameters and Plasma Etch Rates, Selectivity, and Anisotropy," *J. Vac. Sci. Tech. A,* **2** (4), 1984.

G. M. Gallatin, C. B. Zarowin, "Unified Approach to the Temporal Evolution of a Surface Profile in Solid Etch and Deposition Processes," *J. Appl. Phys.* **65** (12), 1989.

Additionally, the chemical purity of the materials may locally interfere with the etch process causing micro-masking. Also, slight variations in the process parameters can cause large variations in the etch rates. However, there are conditions where with the correct materials and chemical plasma etching conditions, this approach can provide superior control over the relative etch rates and preservation of the initial photoresist figure.

4.1 ADJUSTMENTS TO THE FIGURE

The laser figuring approach presented here is amenable to correcting any distortions or errors associated with the pattern transfer mechanism. The optical designs which have been addressed have not needed significant amounts of lenslet sag, therefor, ion milling is an acceptable transfer method. It is possible to describe the evolution of the surface with knowledge of the transfer function due to ion milling, or any other transfer technique. This will allow us to predetermine the initial shape in photoresist which will generate the desired final lenslet figure after ion milling. We have measured the ion mill rate as a function of angle for different photoresists as well as optical materials such as Si, CdZnTe and SiO_2. With this data, We have been able to fabricate microlenses for numerous opto-electronic applications.

5.0 RESULTS

Figure 4 shows a scanning electron micrograph of a 10 by 10 array of lenslets etched into a silicon wafer. The design of these lenslets yielded f/1, parabolic lenses with 100 micron square lens aperture. Lenslet arrays of this type have been designed for optical improvements in Si detector arrays. Figures 5 and 6 show a region of a 132 by 132 element lens array in CdZnTe. These lenslets have a 60 micron square aperture, parabolic shape with a 100% fill-factor. Each lens was designed to work f/2, immersed, thus focusing light into a detector area located 120 microns below the lens. The array is designed to be aligned and etched into the backside of a thinned HgCdTe detector array to concentrate light into a reduced area detector.

ACKNOWLEDGMENTS

This work was funded by Hughes Danbury Optical Systems IR&D programs, as well as the PET program, which is in collaboration with Santa Barbara Research Center, funded by SDIO, and monitored by the U.S. Army Space and Strategic Defense Command. The author would like to thank Mike Power and Charlie Zarowin for their assistance and guidance.

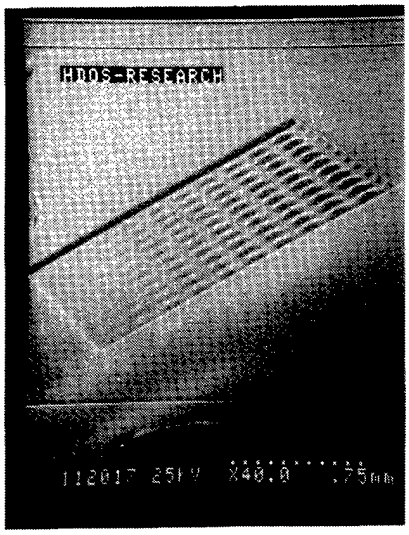

Figure 1.
This is an array designed with 180 micron diameter, 200 micron, square on center, lenses. The sag of each lens was designed to linearly range from a flat the to that of an f/1 lens.

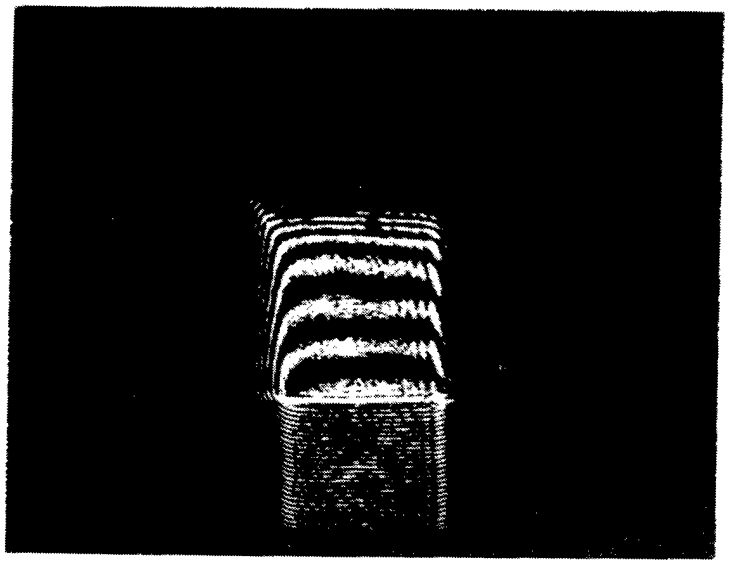

Figure 2.
Interferogram of a region of the array in figure 1 showing fringes from two adjacent lenslets.

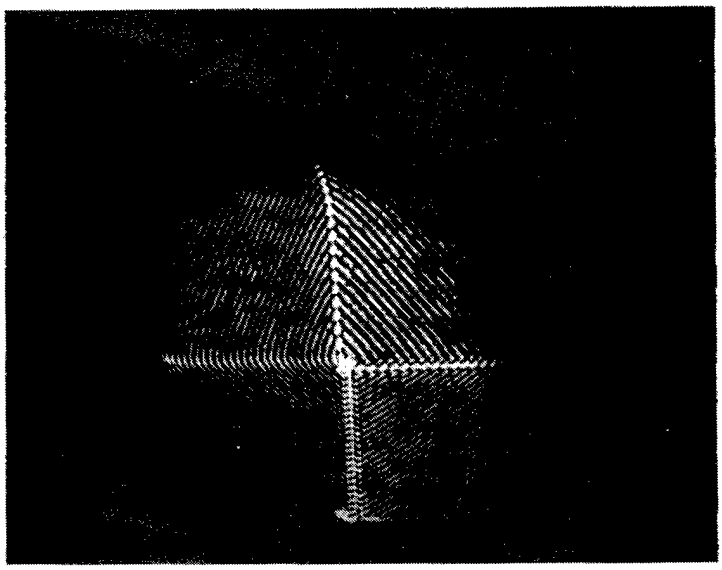

Figure 3.
Interferogram of a region of the lens array in figure 1. The reference leg is centered at the intersection of four adjacent lenses showing the fill factor achieved.

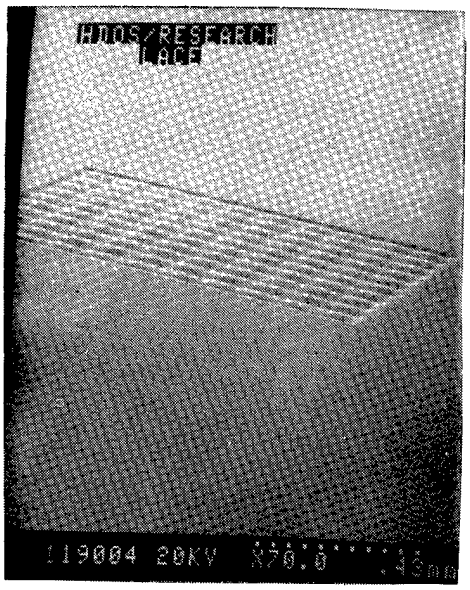

Figure 4.
This is a photomicrograph of a 10 by 10 array of f/1 microlenses, 100 micron on center, etched into a wafer of silicon.

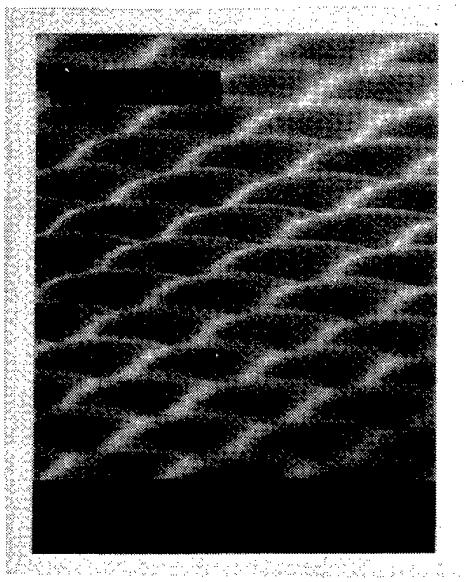

Figure 5.
This is a photomicrograph of a 132 by 132 array of 60 micron, f/2, microlenses etched into CdZnTe. The array is designed to concentrate light unto a reduced area detector located 120 microns behind the lenses.

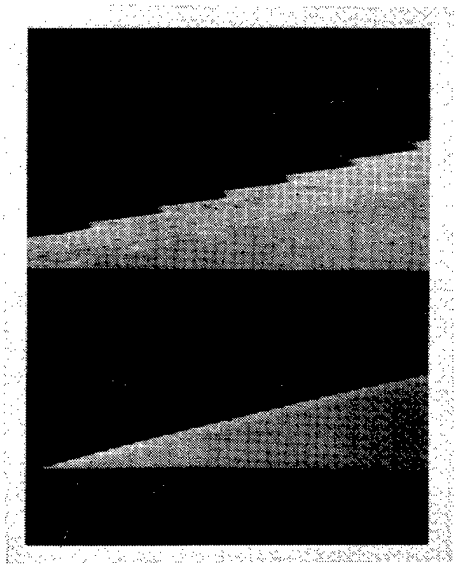

Figure 6.
This is a view of the edge elements of the array shown in figure 5.

Diffractive Optics Fabricated by Direct Write Methods with an Electron Beam.

Bernard Kress, David Zaleta, Walter Daschner, Kris Urquhart,
Robert Stein, Sing H. Lee.

Electrical and Computer Engineering Department
University of California at San Diego
La Jolla, Ca. 92093-0407
USA

1. Introduction.

State-of-the-art diffractive optics are fabricated using e-beam lithography and dry etching techniques to achieve multilevel phase elements with very high diffraction efficiencies. One of the major challenges encountered in fabricating diffractive optics is the small feature sizes required (e.g. for diffractive lenses with small f-number). It is not only the e-beam system which dictates the feature size limitations, but also the alignment systems (mask aligner) and the materials (e-beam and photo resists). In order to allow diffractive optics to be used in new optoelectronic systems, it is necessary not only to fabricate elements with small feature sizes but also to do so in an economical fashion. Since price of a multilevel diffractive optical element is closely related to the e-beam writing time and the number of etching steps, we need to decrease the writing time and etching steps without affecting the quality of the element. To do this one has to utilize the full potentials of the e-beam writing system.
In this paper, we will present 3 diffractive optics fabrication techniques which will reduce the number of process steps, the writing time and the overall fabrication time for multilevel phase diffractive optics.

2. Conventional fabrication technique.

Most multilevel phase surface relief structures are fabricated by utilizing n binary amplitude masks in n standard photolithography processes to achieve 2^n relief levels [1]. A standard photolithography process cycle for a single mask consists of the following steps ***(Fig.1)***:

1) Spin photo-resist on substrate
2) Place substrate in contact with chrome mask (or project mask pattern onto substrate), and illuminate with U-V radiation.
3) Process substrate to remove resist in exposed regions (for positive resist).
4) Place substrate in ion milling machine to create relief patterns.
5) Remove old resist.

Thus for a 16 phase level diffractive optics, 20 (=4x5) processing steps are required to complete the fabrication. Typically, this method allows fabrication of structures down to 1 micron (mainly limited by mask aligner type and the number of re-alignments required between masks). It is easy to see that this fabrication technique is very laborious and time consuming, and subject to many processing errors, which directly influence the cost of production. This is because this fabrication technique does not fully utilize the power and capabilities of the e-beam writing system.

3. Various improvements on the fabrication of multilevel relief structures using e-beam direct write techniques.

3.1) Direct write on e-beam resist.

In order to decrease the misregistrations between mask alignments, we have developed a fabrication technique which does not rely on amplitude masks. The different binary patterns are directly aligned and written on the e-beam resist on the substrate in the e-beam machine. Between each e-beam writing steps, a photolithographic and an etching step are involved (see ***Fig.2***). Since the e-beam machine is capable of automatically locking onto etched alignment marks and aligning the next pattern with respect to these marks, the alignment misregistrations errors are decreased to 0.1 micron. This allows the user to fabricate multilevel relief structures with features down to 0.5 micron. However, even though the misregistrations errors and the feature sizes are decreased, this method still requires long fabrication time because the substrate needs to be recoated with chrome and entered in the e-beam n times (for 2^n relief levels).

3.2) Direct write on e-beam sensitive photoresist

In order to cut down the processing time, we used a photoresist which is sensitive to electron beams (Hoechst AZ-5214-E photoresist) in place of the e-beam resist. ***Fig.3*** shows a comparison of the number of photolithographic processes used by each method. Since the photo resist can be exposed by the e-beam writer and then directly used in the etching process, the photolithographic steps between e-beam writing and ion milling are eliminated.

3.3) Direct write with various e-beam spot sizes.

To reduce the e-beam writing time, we have utilized a variable e-beam spot size to write fringes or shapes of different sizes. Since many diffractive optics patterns are composed of e-beam shapes whose sizes vary considerably over the aperture, these patterns can be

written more efficiently in time by increasing the spot size to write coarser features, and decreasing it to write finer features.
Although the e-beam has to run *n* different patterns for *n* spot sizes, the writing time can be decreased considerably if the partitioning between large and finer features is made in an efficient way. ***Fig. 4*** shows a spherical on-axis zone plate whose shapes have been partitioned into two different files to be written with two different spot sizes. Here, the first spot size is of 0.1 micron and the second of 0.2 micron. The gain in writing time is about 35%. The maximum spot size is limited by the maximum beam current (the larger the spot size, the higher the current): for a spot size of 0.1 micron, the beam current has to be set at least to 8 nA while for a spot size of 0.4 micron the beam current is only of 100 nA. More complex patterns can be further partitioned into more sub-patterns to be written with spot sizes ranging from 0.025 to 0.8 micron. However, the amount of time required to set the exact e-beam current for the intended spot size manually by the e-beam operator when using more than two spot sizes has also to be considered.

3.4) Direct write with various e-beam dosages on analog e-beam resist.

In order to significantly decrease the fabrication steps and to enable the fabrication of features down to 0.1 micron, we used a direct write method where the e-beam exposure on an analog resist varies over the desired pattern. This method requires a single e-beam run and a single etching process (with no photolithographic step) to fabricate a multilevel phase CGH. In standard e-beam lithography, an e-beam exposure contains enough electron dose in the exposed regions of the e-beam resist to fully clear the resist during the development process (for a positive e-beam resist). If the electron dose and/or the development process is reduced, it is possible for the e-beam resist to not fully develop. This is possible since the solubility of the resist in the developer varies with the electron dose, i.e. the higher the dose, the faster the resist dissolves in the developer. This allows different thickness control of e-beam resist simply by varying the electron dose. ***Fig.5*** shows the large decrease in fabrication steps when using this technique. The misregistration errors are decreased to the e-beam misregisration in field addressing, which is typically of 0.025 micron. Thus the fabrication of features down to 0.1 micron is only limited by the resist development, and no more by the alignment accuracy.
Two types of e-beam substrates have been used; one for reflection mode and one for transmissive mode diffractive optics. For reflection mode, a standard chrome on glass e-beam plate was used. For transmissive mode, an e-beam plate with an optically transparent layer of ITO (indium-tin-oxide) was used in place of the chrome. Two positive analog e-beam resists have been successfully used: EBR-9 (Toray) and PMMA (KTI 950K 9%). Since EBR-9 could not be coated thicker than approximately 500nm, its use was limited to reflection mode diffractive optics. PMMA was used for thicker layers (up to 2 microns thick), and was successfully applied to transmissive mode diffractive optics. The amounts of EBR-9 and PMMA resist removed by the developer are shown in ***Fig.6.***

4. Experimental results.

Several CGHs have been fabricated by using the different e-beam direct write methods described in this paper. Diffractive cylindrical and spherical lenses have been fabricated using the direct write on e-beam resist discussed in section 3.1 (see **Fig.7**). A set of linear gratings has been fabricated in analog e-beam sensitive photo resist as discussed in section 3.2, then etched successfully into glass (see **Fig.8**). A CGH for wavefront transformation is under fabrication using the various spot sizes method as discussed in section 3.3. Several arrays of CGHs have also been fabricated using the direct write on analog e-beam resist using 16 different e-beam dosages as discussed in section 3.4: **Fig.9** shows a 128 by 128 lenslet array of f/5 lenses with 50 microns diameter. **Fig.10** shows a diffractive lens out of the 2 by 2 array performing the space semi variant shuffle exchange optical interconnect. **Fig.11** shows a CGH out of the 64 by 64 CGH array performing the hypercube interconnection architecture; each CGH has been calculated by the Gerchberg-Saxton iterative algorithm [2]. Two optical reconstructions are shown when only one CGH out of the 64 by 64 CGHs is illuminated.

5. Conclusion.

We presented several new e-beam microlithographic fabrication techniques for the fabrication of multilevel surface relief phase structures for diffractive optics. These fabrication techniques have several advantages over the conventional fabrication technique described in *ref.1*. For example, the direct write on e-beam resist decreases significantly the misalignment errors which occur usually during the pattern transfers in the mask aligner, and decreases the minimum feature sizes allowed for fabrication. The e-beam sensitive photoresist contribute to reduction in processing time during the photolithography process, and the variation of the e-beam spot size decreases the overall e-beam writing time by writing the fractured patterns in a more efficient way. E-beam direct write on analog e-beam resist with various e-beam dosages can generate a sixteen phase level element in one exposure step and one processing step.

Acknowledgments

We would like to thank Jiao Fan and Peng Li for their contributions in the holographic pattern fracture and the e-beam data file preparation.

References.

[1] G.J.Swanson, *MIT technical Report* **854**, 17-24 (1989).

[2] R.W. Gerchberg and W.O.Saxton, *Optik* **35**, 237-246 (1972).

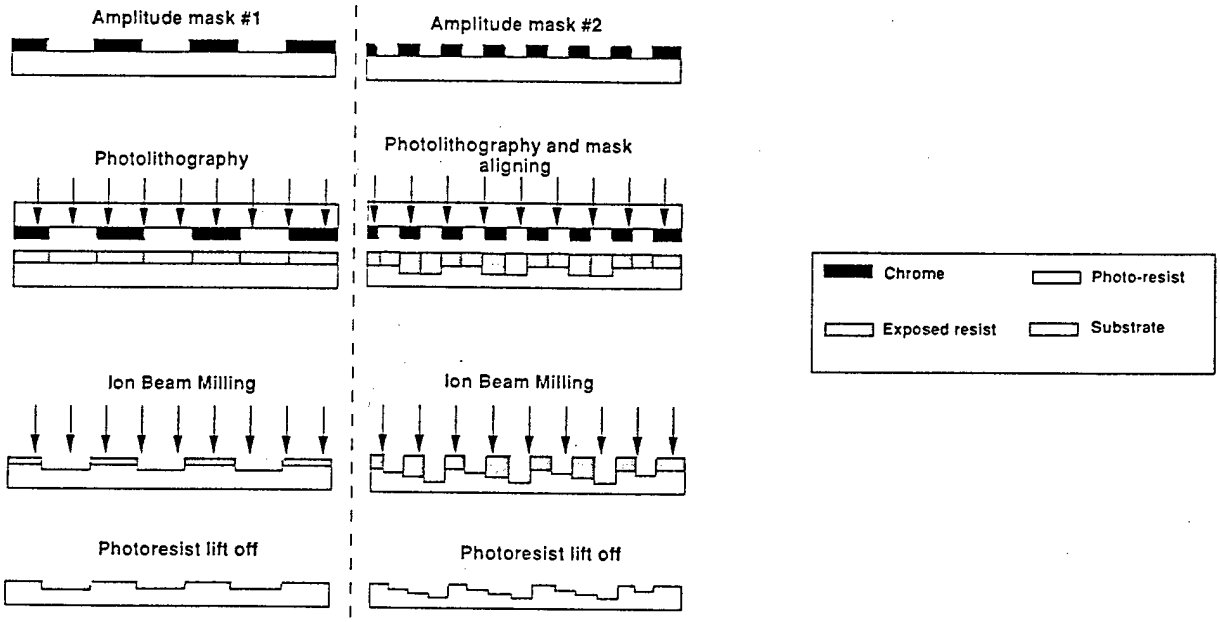

Fig.1) Conventional fabrication technique to produce multilevel relief phase structures.

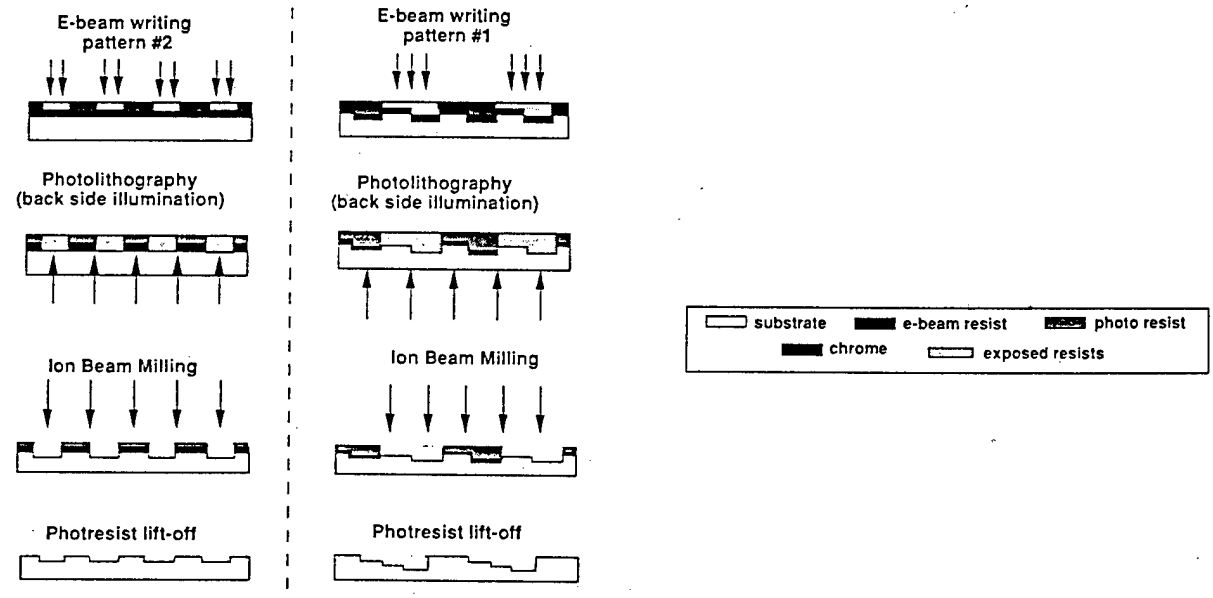

Fig.2) Direct write on e-beam resist, overcoming the need of using optical mask aligner. Pattern #2 is written first because it contains finer and shallower structures than pattern#1.

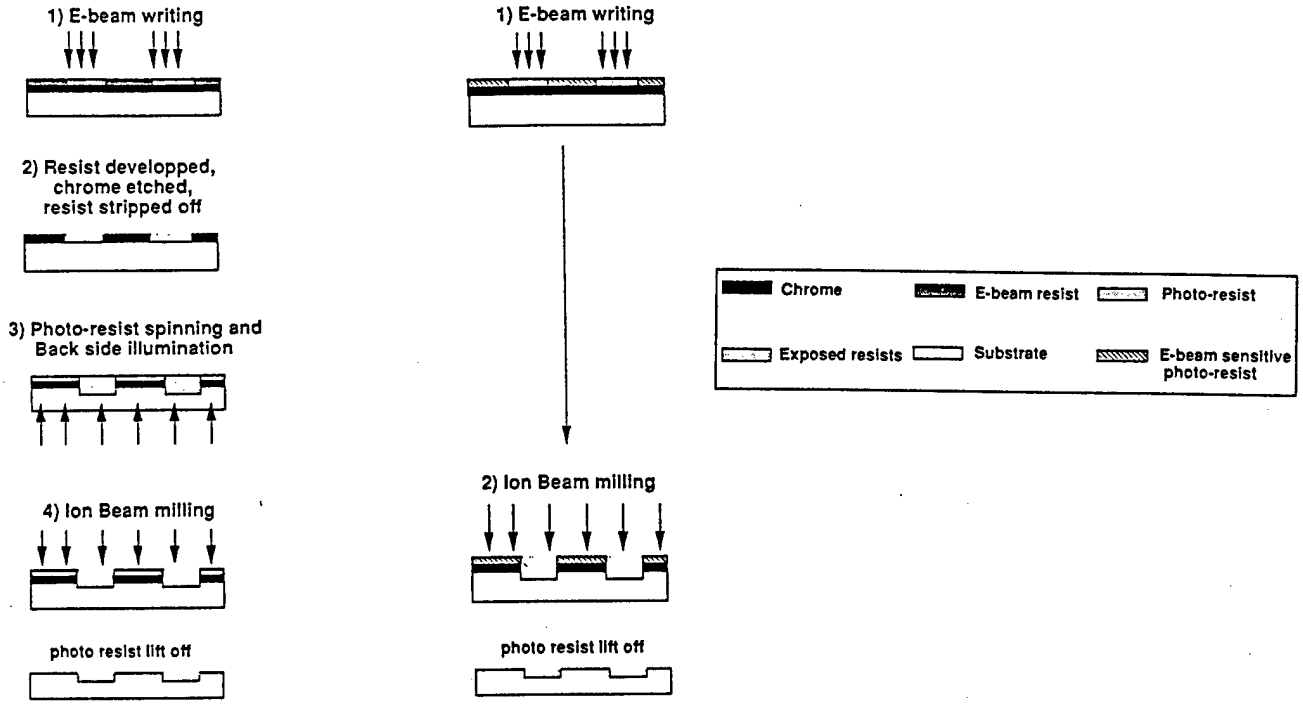

Fig.3) Comparison of processing steps (a) using regular e-beam resist, (b) using e-beam sensitive photoresist.

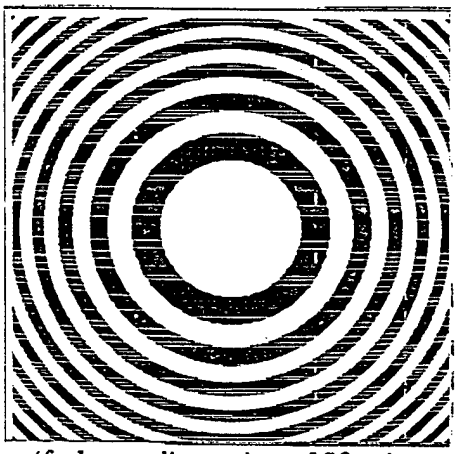

4.a) Original spherical lens (f=1mm, dimension=150 microns x 150 microns).

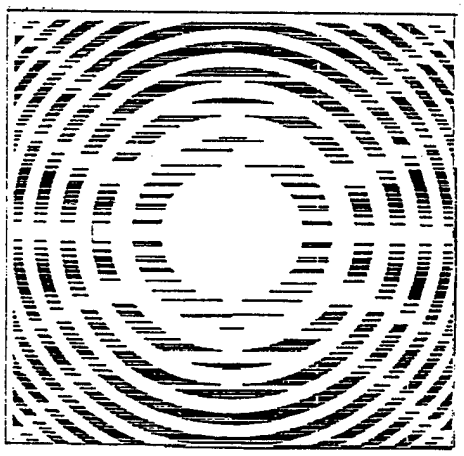

4.b) Fine shapes written with 0.1 micron spot size.

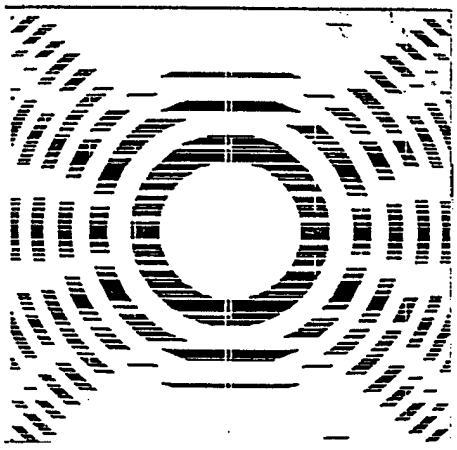

4.c) Coarse shapes written with 0.2 micron spot size.

Fig.4) Direct write with various e-beam spot sizes.

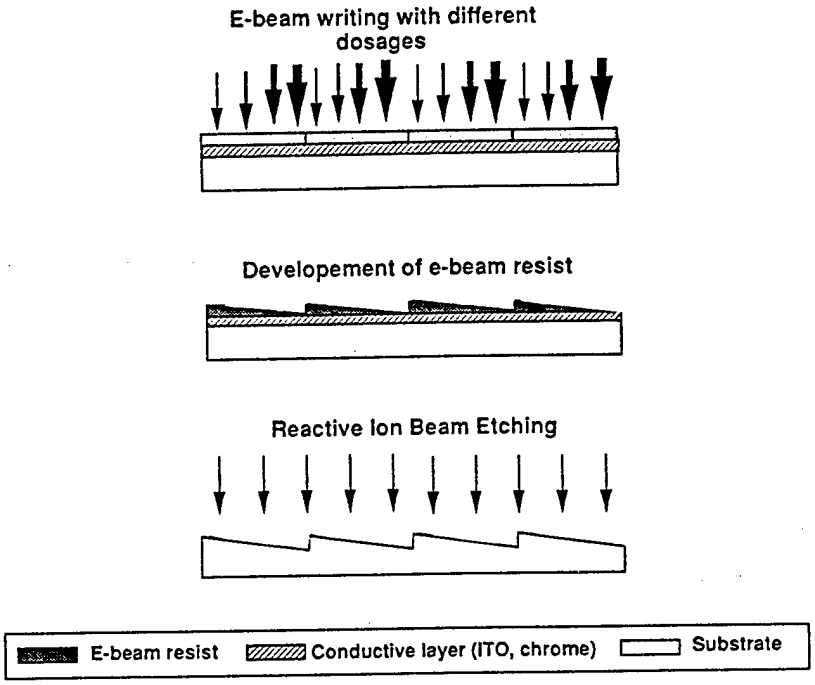

Fig.5) Direct write with various e-beam dosages on analog e-beam resist.

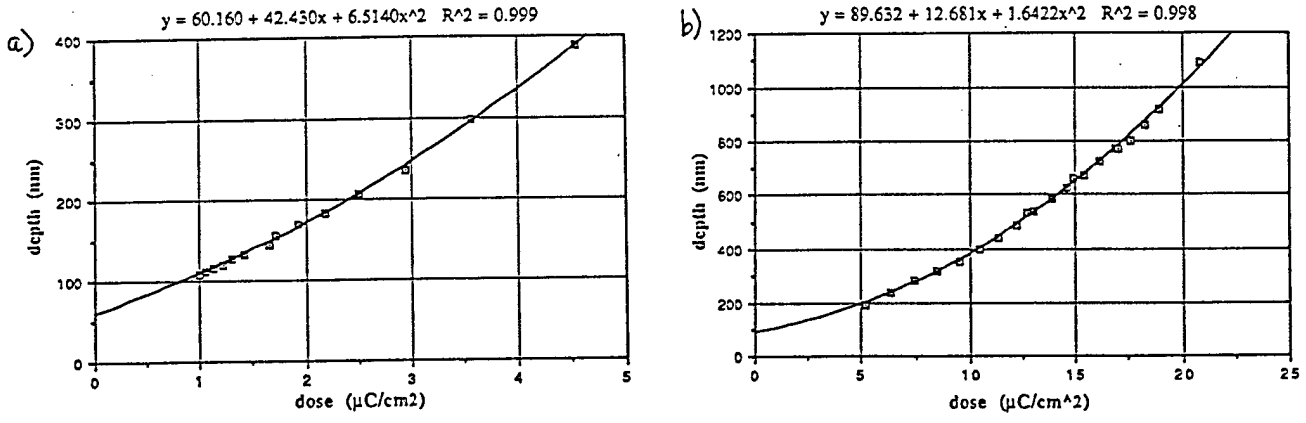

Fig.6) *Depth vs. electron dose for a): EBR-9 Torray resist, and for b): PMMA resist. Equation shows second order polynomial fit (correlation coefficient R).*

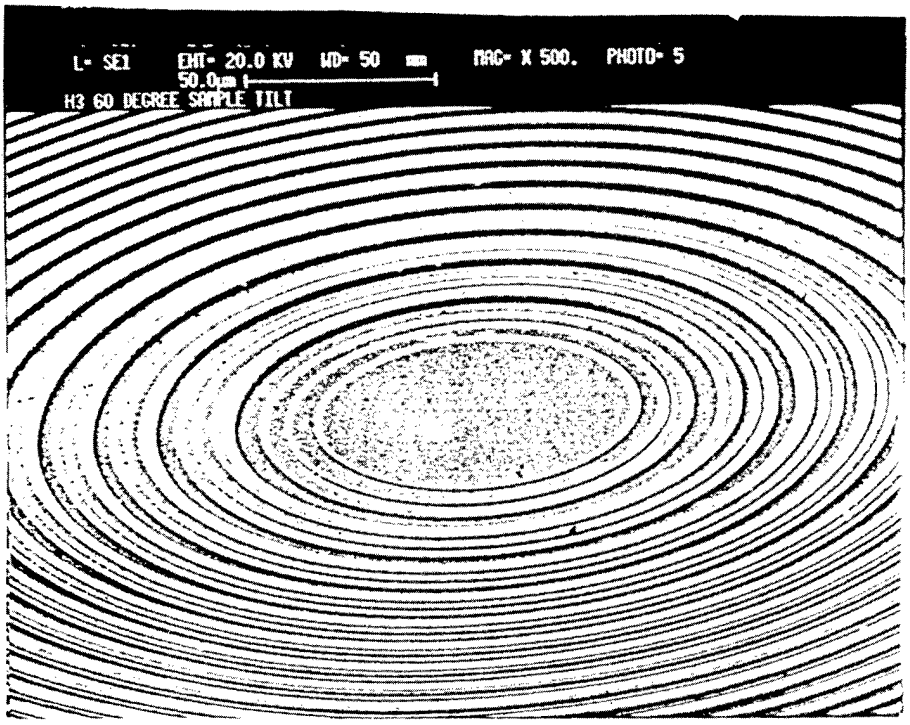

Fig.7) Four phase level f/1 diffractive lens fabricated by the direct write on e-beam resist, (method described in section 3.1).

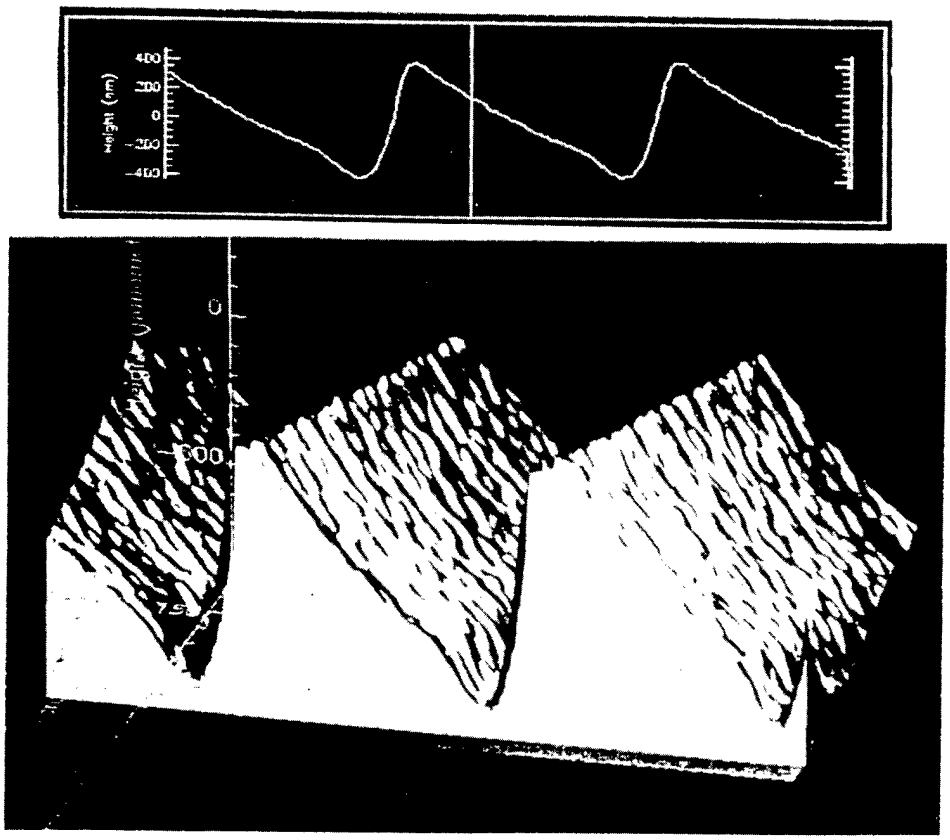

Fig.8) Linear grating of 60 microns period fabricated with the e-beam sensitive photoresist method (discussed in section 3.2) and etched into glass.

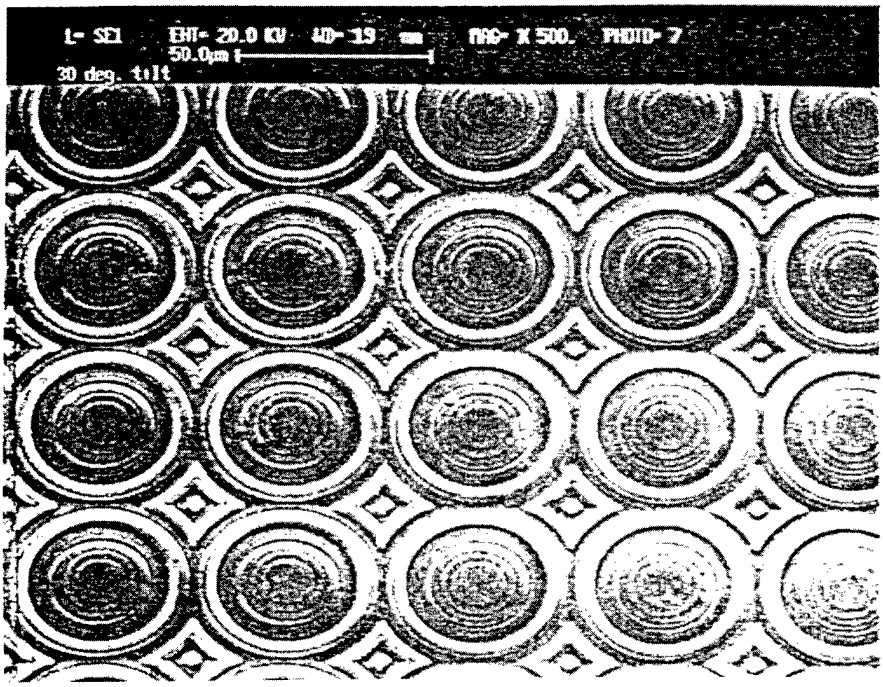

Fig.9) *SEM microphotograph of a 128 by 128 lenslet array (f/5, diameter: 50 microns) fabricated by direct write on analog e-beam resist using 16 different e-beam dosages.*

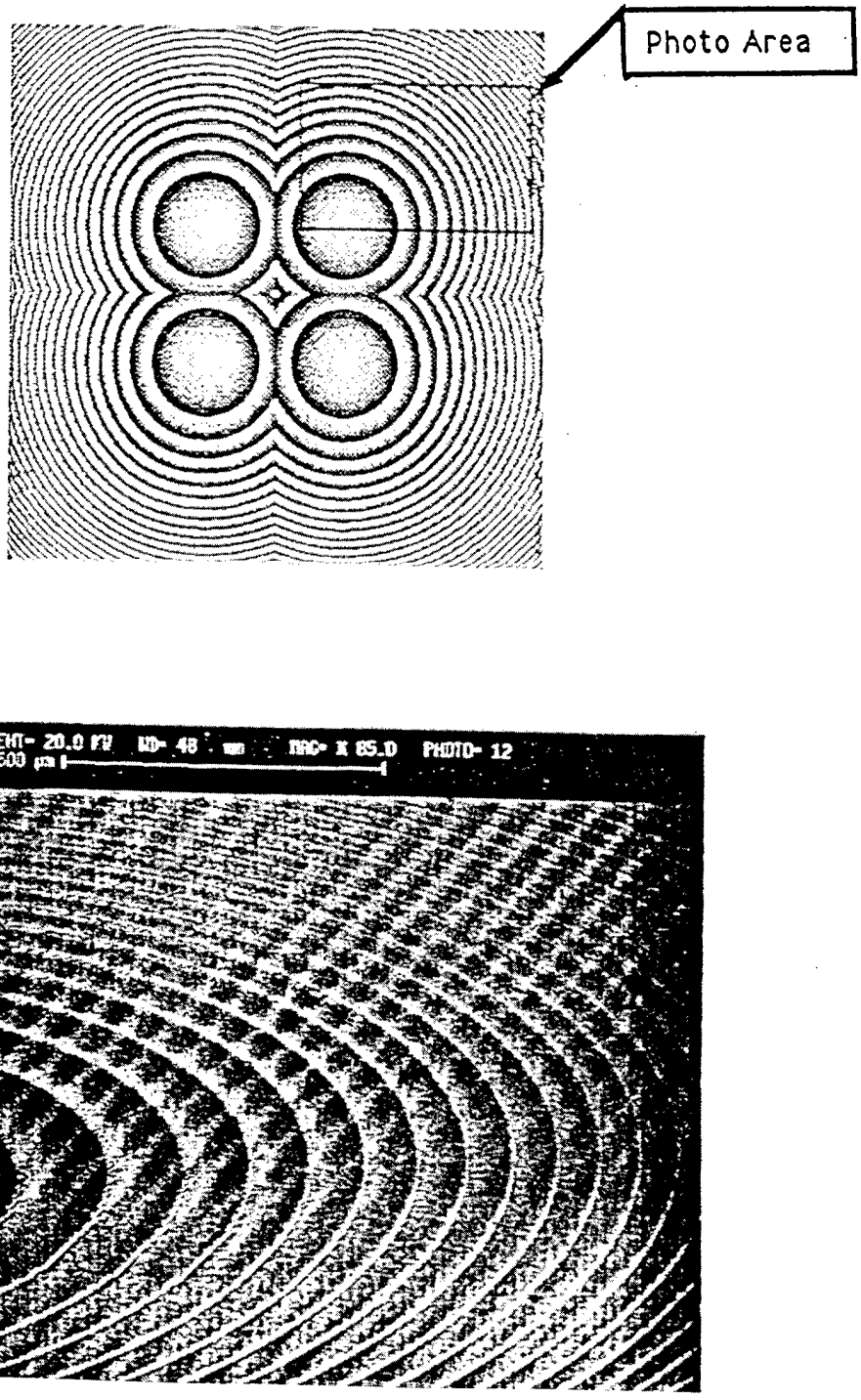

Fig.10) SEM microphotograph of a diffractive off-axis Fresnel zone plate out of a 2 by 2 space semi variant shuffle exchange interconnection architecture, fabricated by direct write on analog e-beam resist using 16 different e-beam dosages.

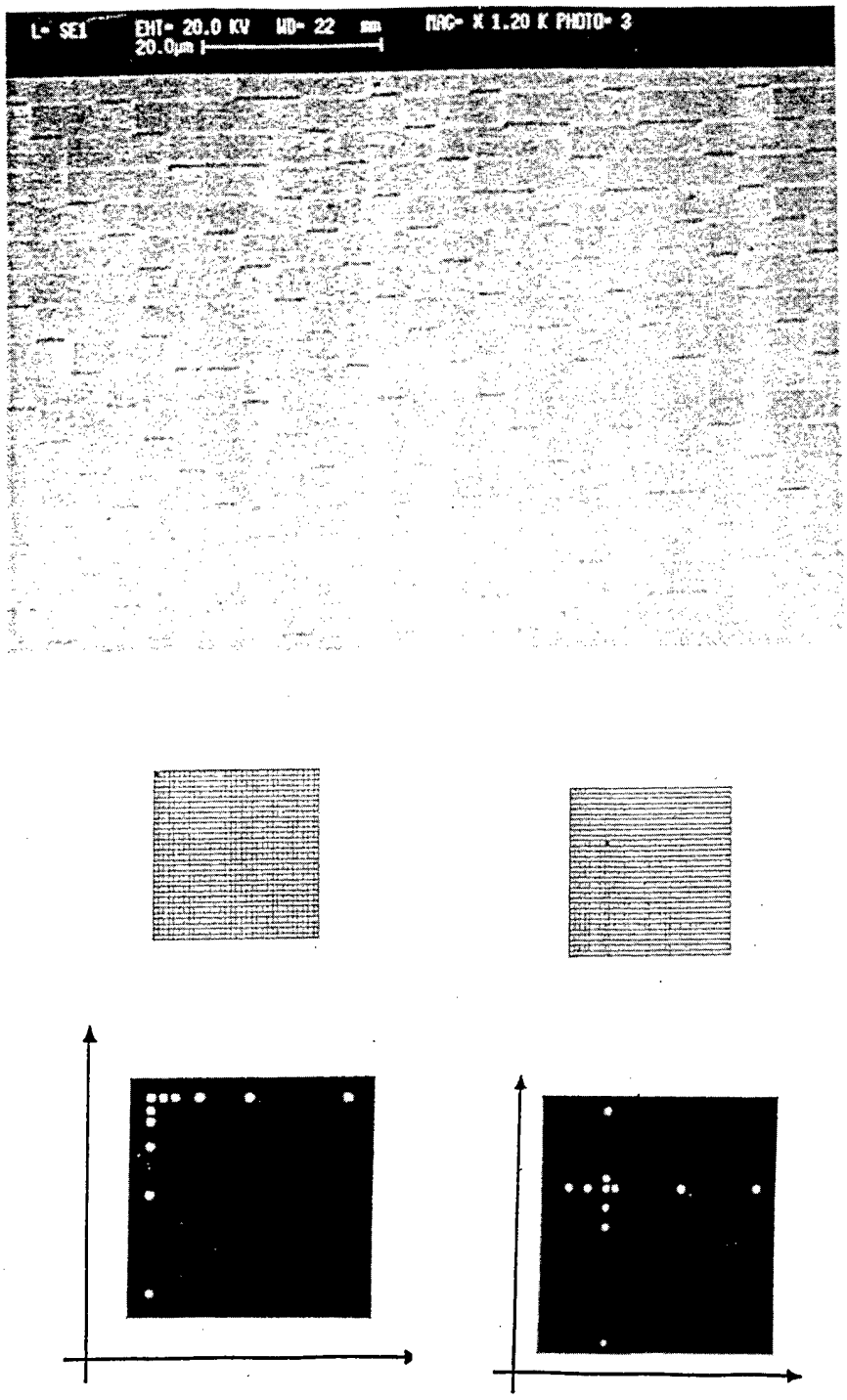

Fig.11) SEM microphotograph of a Fourier CGH out of a 64 by 64 array performing the hypercube interconnection architecture, fabricated by direct write on analog e-beam resist using 16 different e-beam dosages. The CGHs were calculated using the Gerchberg-Saxton iterative algorithm. Two optical reconstructions are shown when only one CGH out of the 64 by 64 array is illuminated.

PHASE HOLOGRAMS IN PMMA WITH PROXIMITY EFFECT CORRECTION

P.D. Maker and R.E. Muller
Center for Space Microelectronics Technology, Jet Propulsion Laboratory
California Institute of Technology, Pasadena, CA 91109

ABSTRACT

Complex computer generated phase holograms (CGPH's) have been fabricated in PMMA by partial e-beam exposure and subsequent partial development. The CGPH was encoded as a sequence of phase delay pixels and written by the JEOL JBX-5D2 E-beam lithography system, a different dose being assigned to each value of phase delay. Following carefully controlled partial development, the pattern appeared rendered in relief in the PMMA, which then acts as the phase-delay medium. The exposure dose was in the range 20-200 $\mu C/cm^2$, and very aggressive development in pure acetone led to low contrast. This enabled etch depth control to better than $\pm\lambda_{vis}/60$. That result was obtained by exposing isolated 50 μm square patches and measuring resist removal over the central area where the proximity effect dose was uniform and related only to the local exposure. For complex CGPH's with pixel size of the order of the e-beam proximity effect radius, the patterns must be corrected for the extra exposure caused by electrons scattered back up out of the substrate. This has been accomplished by deconvolving the two-dimensional dose deposition function with the desired dose pattern. The deposition function, which plays much the same role as an instrument response function, was carefully measured under the exact conditions used to expose the samples. The devices fabricated were designed with 16 equal phase steps per retardation cycle, were up to 1 cm square, and consisted of up to 100 million 0.3-2.0 μm square pixels. Data files were up to 500 MB long and exposure times ranged to tens of hours. A Fresnel phase lens was fabricated that had diffraction limited optical performance with better than 85% efficiency.

Conf. on Binary Optics, 1993

I. INTRODUCTION

Surface-contouring an E-Beam resist by controlling both the exposure dose and the development process was demonstrated by Fujita[1] et. al. in 1981. They designed, fabricated, and tested micro Fresnel-zone-plates, blazed gratings and Fresnel lenses in PMMA. The exposure method used involved scanning the E-Beam, in either straight lines or circles, with the dose adjusted to give the desired surface depth after development. This method produced somewhat irregular groove shapes, but efficiencies of 50% to 60%, with near-diffraction-limited performance were achieved. More recently Ekberg[2] et. al. reported on kinoform phase holograms. These were patterns comprising a 512x512 array of 10 μm square pixels, each with a unique E-Beam exposure dose calculated to give the appropriate etch depth upon development. Ten doses/depths were used. Diffraction efficiencies of 70% were reported. In an earlier paper[3], we reported upon the fabrication, physical, and optical characterization of kinoforms that encoded 16-level phase holograms and a Fresnel lens having a diffraction limited focal spot and 83% efficiency. At that time, only an approximate treatment of the E-beam proximity effect was used. The fabrication imperfections thus introduced caused significant performance degradation. In this paper, we report upon a technique for treating the proximity effect exactly and upon the performance of an off-axis Fresnel lens fabricated using the method. The lens had well shaped grooves with none of the peak-rounding and valley-filling that characterize the proximity problem, and its far-field pattern was very uniform. Near-diffraction limited focal spots were measured, and its overall efficiency was ~86%.

II. EXPERIMENT

High contrast (gamma) is a desirable property for photo- and e-beam-resists used for device patterning. With high gamma, large variations in exposure dose will have little effect on the pattern shapes as long as the exposure is above a critical level. Hence, the common resists and their development processes have been tailored in this direction. In the present application, however, unity contrast is desired. The developability of the resist would, ideally, be linearly related to the exposure dose. The early work reported by Fujita[1] employed PMMA as the resist with development temperature controlled at 10 °C, leading to very high contrast - small changes in exposure led to large changes in developability and etch depth. This certainly contributed to the roughness observed in the etch profiles. The present work began with a search for an appropriate e-beam resist process having near-unity contrast .

The first system tried was a Rohm and Haas Company experimental acid hardening positive resist tailored to have low contrast (ECX-1151). Initial experimentation revealed that after partial development, the remaining material was highly inhomogeneous, leading to unacceptable optical scattering.

Earlier work with PMMA had revealed no such problem - partial development simply removed a uniform layer of surface material. However, as noted above, PMMA is normally a very high gamma material. It is known however that contrast is governed by the development process and in particular, that aggressive development of slightly under exposed resist leads to decreased gamma. In a series of tests, it was found that by developing partially exposed PMMA in pure acetone (its usual solvent), contrast could be markedly reduced. Development time decreased drastically, however, to roughly 5-10 sec, and had to be controlled to ± 0.1 sec. This was accomplished using a Solitec resist spinner equipped with a

Tridak resist dispense head. Acetone was introduced onto a spinning sample (1000 rpm) through the Tridak head for durations controlled by a computer to tenths of a second. The development process was terminated abruptly by a powerful blast of nitrogen gas, again controlled by computer. A series of shorter and shorter development steps was used to achieve precise etch depths. This avoided the need for careful temperature control. Figure 1 illustrates typical exposure vs. development data.

Initially, film thickness was measured by channel fringe spectroscopy, wherein the interference fringes produced by light reflected from the top and bottom surfaces of a film are spectroscopically measured and analyzed. This was accomplished using the Leitz MPV-SP instrument. To measure PMMA films on glass, however, it was found necessary to deposit a thin film of aluminum on the substrate. Because the index of refraction of PMMA nearly matches that of glass, no usable interference fringes are produced by that interface. Etch depth data like that shown in Figure 1 were fit by a third-order polynomial, and that analytic expression was used to compute the dosage necessary to produce any desired etch depth. Further tests revealed that, within experimental error, etch depth was linearly related to development time.

A Digital Instruments Nanoscope III Scanning Probe Microscope (SPM) has recently been installed. Surface profiles at sub-wavelength resolution, as well as film etch depth, are conveniently measure using it. Further, actual devices can be examined directly as the SPM tip scans them without damage.

The proximity effect - exposure dose contributed by scattered electrons - plays a very important role in the present work. Much study has been given to the effect in the literature. It is found that typically 30% of the exposure dose at the center of a large uniformly exposed field can arise from electrons back-scattered from the substrate. For the present purposes, the spatial distribution of this proximity

effect dose can be modeled as a Gaussian[4] of the form

$$D_{prox}(\vec{r}) / Q_o = \frac{\eta}{\pi\alpha^2} \exp(-\vec{r}^2/\alpha^2)$$

where D_{prox} is the proximity dose intensity at distance r from a primary point dose Q_0 delivered at r = 0, η is the proximity factor, and α is the range of the Gaussian. The total dose arriving at point r due to a spatially varying, patterned primary dose D_{prim}, can be expressed as a convolution of an effective point spread function with that patterned dose, as:

$$D_{tot}(\vec{r}) = \iint d(\vec{r} - \vec{r}_o) \times D_{prim}(\vec{r}_o) \times PSF(\vec{r} - \vec{r}_o)$$

$$= D(\vec{r}) \otimes PSF(\vec{r})$$

where

$$PSF(\vec{r}) = \delta(\vec{r}) + \frac{\eta}{\pi\alpha^2} \exp(-\vec{r}^2/\alpha^2)$$

Both η and α depend strongly on substrate composition and geometry and upon the electron beam voltage. α is typically 2 to 5 μm. In the current work, we seek to control the absolute resist thickness to better than 60 nm and the relative thickness from pixel to pixel to better than 20 nm. This requires dose control at the percent level. Clearly, proximity effects must be taken into account. In an earlier paper[3] we reported on fabrication of Fresnel lens which treated the proximity dose problem only approximately. That lens displayed groove shapes that had rounded off tops and filled in trenches. It was at first suspected that the development procedure caused the problem. A series of experiments employing significantly different techniques convinced us that development was not causing the problem. The proximity effect can also cause such distortion in the groove shapes. At zone boundaries excess proximity dose from the heavily exposed valley regions overlaps into the lightly dosed areas, and vice-versa. In the present work, the proximity effect has been carefully measured, and corrections for it have been applied to the pattern.

Having calibrated the e-beam dose sensitivity of PMMA, direct measurement

of proximity parameters becomes possible. A square area many times larger than the range, α, of the effect is first exposed with a measured, heavy dose. After controlled development, the PMMA at the perimeter of the area is seen to be thinned in a characteristic way by the proximity dose. Integrating the above expression for geometry leads to the following expression for the decay of the proximity dose with distance from the edge of the exposed area:

$$D_{prox}(x) = \frac{\eta}{2} \times D_{prim} \times \mathrm{erfc}(x/\alpha)$$

where erfc(x) is the complimentary error function. Fig. 2 shows a fit of such data using the parameters $\alpha = 5.25$ microns and $\eta = 0.25$.

An exact solution for the proximity effect is possible in the present situation, which is not the case usually. In the usual application of e-beam lithographic practice, one desires that the resist be either fully developed or totally undeveloped. Since at the boundary of exposed areas, the proximity effect will always lead to exposure of the adjacent region, and negative dose is not possible, no exact solution is achievable. In the present case, every point in the pattern receives a finite primary dose (that might even include a bias value introduced to enable the correction). These doses can be adjusted both up and down to account for the proximity dose delivered from surrounding pixels. Several mathematical schemes are available to handle this correction. Deconvolution by Fourier transform represents a straightforward approach. If $\mathbf{P(r)}$ is the desired exposure pattern and $\boldsymbol{P}(\mathbf{k})$ its Fourier transform, and $\mathbf{PSF(r)}$ is the point spread function and $\boldsymbol{PSF}(\mathbf{k})$ its Fourier transform, then $\boldsymbol{Pc}(\mathbf{k})$, the Fourier transform of the desired function is:

$$\boldsymbol{Pc}(\mathbf{k}) = \boldsymbol{P}(\mathbf{k}) \,/\, \boldsymbol{PSF}(\mathbf{k}).$$

$\mathbf{Pc(r)}$ is then obtained by inverse transforming $\boldsymbol{Pc}(\mathbf{k})$. A carefully optimized two dimensional fast Fourier transform deconvolution program has been implemented on our VAX Station 3100 computer. It handles a 4K by 4K problem in five hours.

Indeed, it was found necessary to recess typical patterns by ~0.2 microns with bias dose to eliminate negative dose.

Consideration of the isotropic nature of the development/etching process being use here reveals that the risers separating adjacent lands etched to near-identical depths will be sloped at 45 degrees. Further, a shallow land adjacent to a very deep one will be etched laterally by an amount equal to its depth. Worse, a land half as deep as its neighbor will be etched laterally by half its depth. Noting that a transmission phase plate for use at the wavelength of the red helium neon laser must have groove depths of $\lambda/(n-1) = 1.29$ microns, it becomes apparent that the pixel size of kinoform-encoded CHG's must be larger than about one micron to avoid serious degradation at the hands of isotropic etching. Note that for patterns resembling uniform, curved gratings, as do those for simple lenses, the case of half-height risers, which leads to maximum lateral etching, does not arise as long as there are many pixels in the narrowest Fresnel zone.

The JEOL JBX-5D2 EBLS pattern data format requires sixteen bytes to specify a single elementary pattern unit, and cannot handle files longer than 512 MB. Thus a kinoform-encoded CGH can be no larger than 5K by 5K. To uniformly expose a 1 micron square pixel, an e-beam spot size of ~0.2 micron diameter should be used and it should increment between exposure doses by less than about 0.1 microns. The JBX-5D2 also has a maximum shutter speed of 0.5 microseconds. Since an area 0.1x0.1 microns square is exposed at each click, and a minimum dose of $20\mu C/cm^2$ is expected, the beam current must be limited to less than 3 na. Under these exposure conditions, one square cm can be exposed in ~15 hours.

Based upon the above considerations, an exposure pattern for an off-axis Fresnel lens 3 mm square, with 3751x3751 square pixels each 0.8 micron on a side, having a focal length of 38 millimeters, and with its center of curvature 2 mm from the lens center, was prepared. First, the requisit phase delay was calculated as a

floating point number for each pixel in a 4K by 4K array. These numbers were converted first to equivlent PMMA thickness to be removed and then to total electron dose, this based upon nonlinear calibration data like that show in Fig. 1. Next, the Fourier deconvolution proceedure was appled. The corrected dose pattern was then cropped to its central 3751 rows and columns eliminating wrap-around errors introduced by the FFT technique. A histogram of all the doses was assembled, and divided into 64 bins, equal numbers of pixels in each bin. This data set was then encoded in the format used by the JEOL EBLS. An algorithm was used that grouped adjacent pixels with identical exposure into larger rectangular patterns, thus achieving modest data compression. In place on the PDP 11/84 that controls the EBLS, this data set was some 125 MB long. Individual 3 mm square Fresnel lenses require 90 minutes to expose. Development time in pure acetone was 11 seconds.

This and like lenses have been fabricated and fully characterized both physically and optically. They were etched in 2 micron thick PMMA films on 1/10 wave BK7 glass optical flats. The PMMA was built up by 4 applications of 950K molecular weight polymer in 5% solution in chlorobenzene spun at 3000 rpm. Thorough baking (170 °C, 60 min.) between applications produced a uniform film - there was no evidence of vertical inhomogenity in the final results. A 100 Å layer of aluminum was applied over the PMMA prior to exposure to dissipate charge. This was stripped in mild alkali prior to development which proceeded as described above.

III. RESULTS

A. Physical Characterization

Figure 3 is a three-dimensional representation, produced by the SPM, of an area near the center of a characteristic Fresnel lenses. No evidence of field stitching or pattern overlap can be discerned. Even small errors of this sort produce dramatic effects as etch depth will be doubled in areas of pattern overlap. Individual phase steps can be seen. Note that the steepness of the vertical back walls is much enhanced in the Figure because of the difference in vertical and horizontal scales. In fact, the steepness recorded by the SPM is limited by its tip geometry. The instrument used to acquire the data for Figure 3 had is a pyramidal cone with an apex angle of ~114 degrees. SEM data and SPM data taken with ultra sharp tips, indicate that back wall steepness exceeded 60 deg. High resolution SPM topographic data indicate that the surface roughness of the partially developed PMMA was of the order of ±10 nm. Quantitative SPM profile data reveal flat ramps extending from valley to ridge with no sign of the rounding that plagued the earlier lenses.

B. Optical Characterization

A knife-edge test was performed to access the optical performance of the JPL-designed Fresnel lens. An expanded, collimated helium neon laser beam was focused by the lens, and a razor-blade knife edge was mechanically driven across the focal point, in the focal plane. Energy passing the knife edge was monitored by a photo diode detector. It was found that 86% of the incident light energy was focused (first diffraction order), <2% was redirected into high focusing orders, <1% was diffracted by the 'pixel grating', 1.6% passed through the lens undeviated (zeroth order), and about 10% of the incident radiation was scattered diffusely. An attempt was made to adjust the final etch depth to minimize the zeroth order energy. Figure 4 shows the intensity of the first order radiation as a function of knife edge position, plotted together with a curve derived by integrating the Airy function that indicates diffraction limited performance. The data points fit the predicted curve within

experimental limits. This result might be anticipated on the basis that the patterning precision of JEOL JBX-5DII lithography tool, ±50 nm, is essentially perfect on the scale of the Fresnel zone pitch and diameter.

IV. CONCLUSIONS

The results obtained indicate that direct write, partial exposure E-Beam lithography can produce excellent transmissive optical elements for use in the visible. Efforts are underway to reduce the diffuse scattering,, and it should be possible to produce devices with > 90% efficiency. Aspect ratio and side wall etching issues need study before pixel size can be reduced and focal lengths shortened. With the patterning positioning accuracy available, it is possible to overlay these phase patterns on a transmission mask, producing CGH's with controlled amplitude as well as phase. Work is also in progress in all of these areas.

ACKNOWLEDGMENTS

The research described in this paper was performed by the Center for Space Microelectronics Technology, Jet Propulsion Laboratory, California Institute of Technology, and was jointly sponsored by the Strategic Defense Initiative Organization / Innovative Science and Technology Office and the National Aeronautics and Space Administration / Office of Aeronautics and Space Technology.

FIGURE CAPTIONS

Fig. 1. PMMA exposure dose sensitivity using pure acetone as the developer at 21 ° C. The data were fit by a third order polynomial with a standard error of ±17 nm. This is equivalent to an optical phase shift, relative to air, of $\pm\lambda/75$.

Fig. 2. Fit of the experimentally measured proximity dose at the edge of a heavily exposed half-plane to the complementary error function.

Fig. 3. AFM topographic image of a section of a typical Fresnel phase lens rendered in 16 phase steps in PMMA by E-Beam lithography.

Fig. 4. Observed energy passed by a knife-edge scanned in the focal plane of the JPL-designed Fresnel phase lens. The calculated curve represents a diffraction limited focus. 83% of the energy incident on the lens passed through the focal spot, 14% was diffracted into higher orders, and 3% was unfocused.

REFERENCES

1 T. Fujita, H. Nishihara, and J. Koyama, Opt. Lett. **6**, 613 (1981). T. Fujita, H. Nishihara, and J. Koyama, Opt. Lett. **7**, 578 (1982).

2 M. Ekberg, M. Larsson, S. Hård, and B. Nilsson, Opt. Lett. **15**, 568 (1990).

3 P.D. Maker, and R.E. Muller, J. Vac. Sci. Technol. B **10**, 2516 (1992)

4 M. Gentili, L. Grella, A. Lucchesini, L. Luciana, L. Mastrogiacomo, and P. Musumeci, J. Vac. Sci. Technol. B **8**, 1867 (1990)

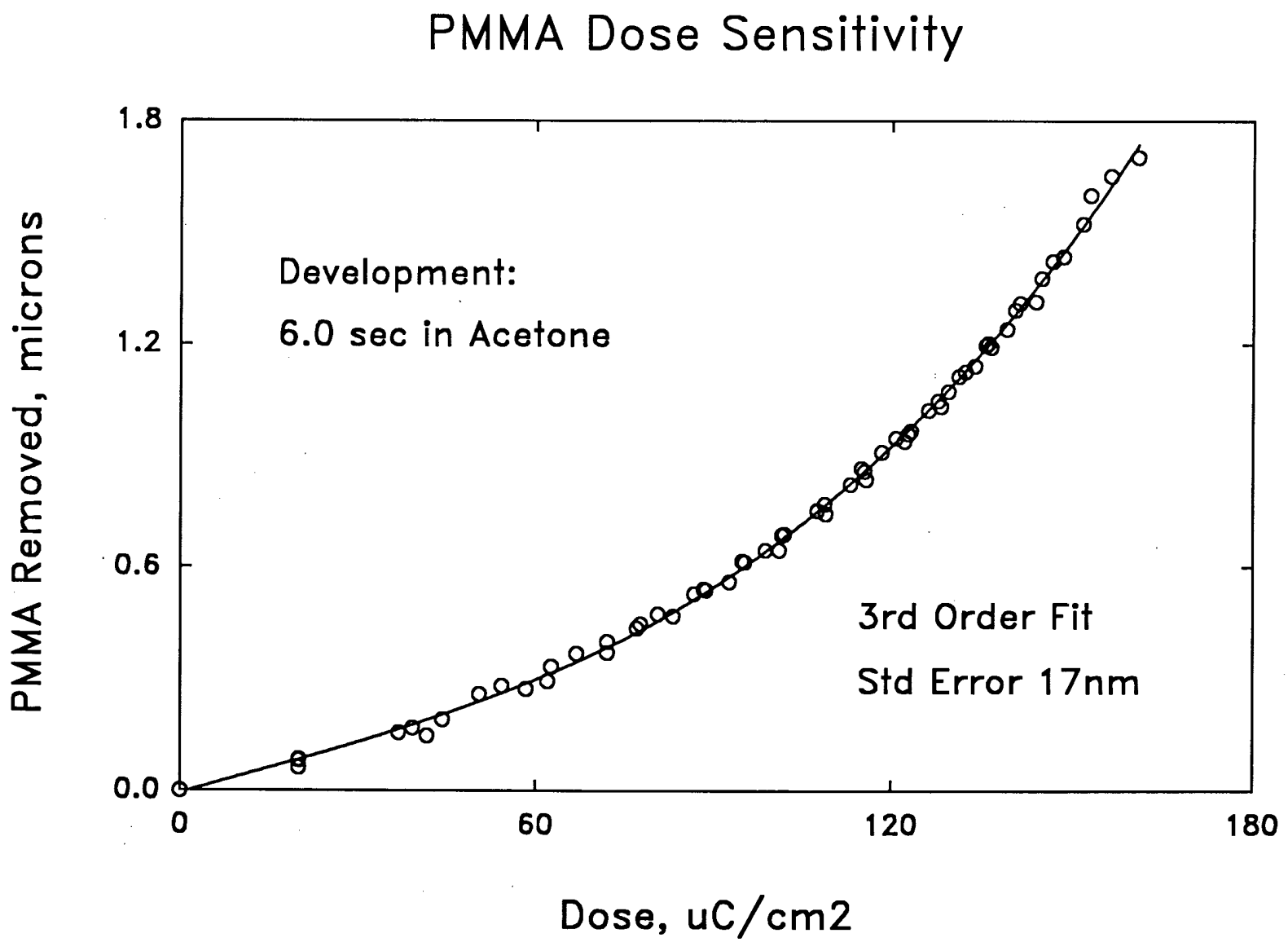
PMMA Dose Sensitivity
PMMA Removed, microns
1.8
1.2
0.6
0.0
0
60
120
180
Dose, uC/cm2
Development:
6.0 sec in Acetone
3rd Order Fit
Std Error 17nm

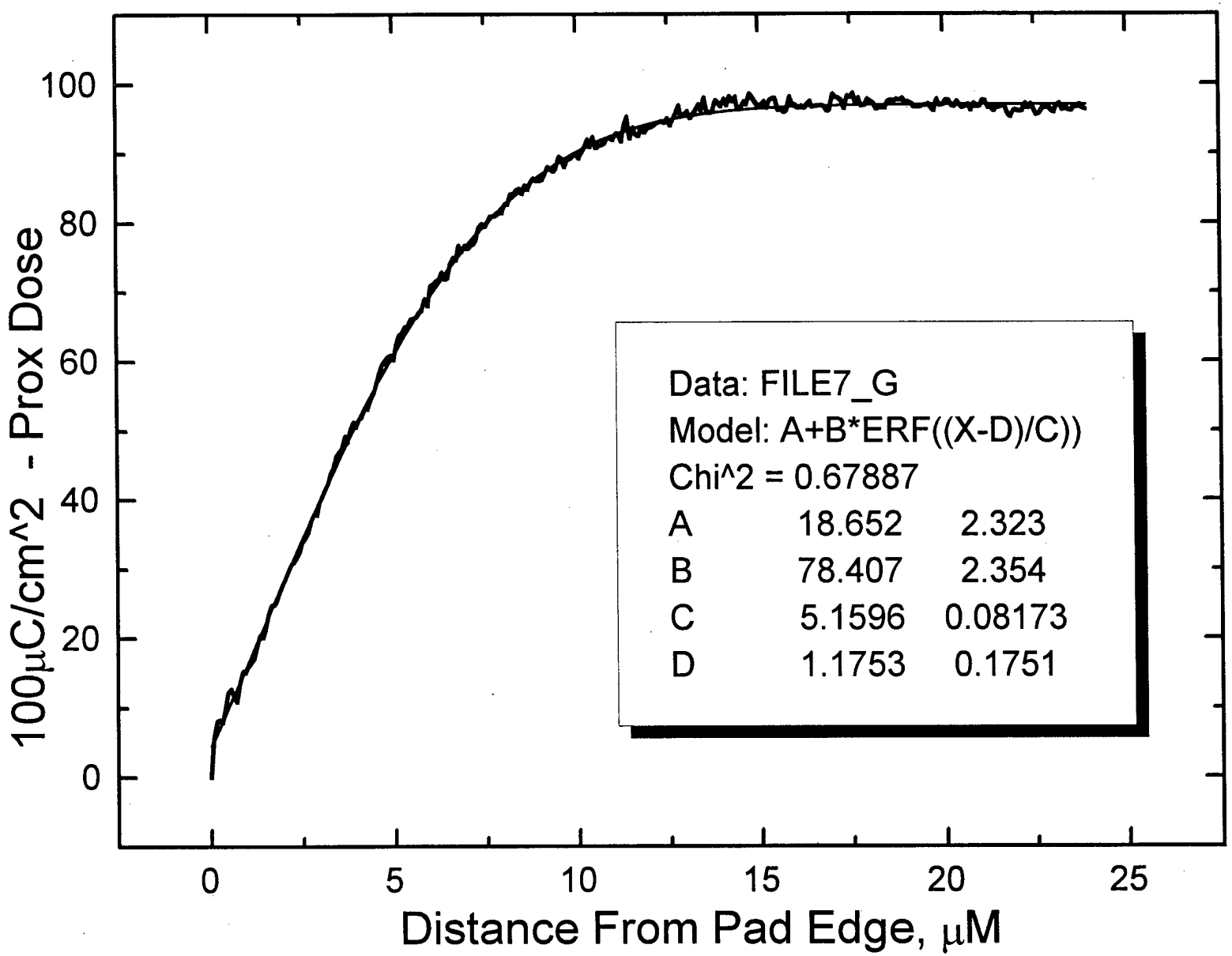
100
80
60
40
20
0
100μC/cm^2 - Prox Dose
0
5
10
15
20
25
Distance From Pad Edge, μM
Data: FILE7_G
Model: A+B*ERF((X-D)/C))
Chi^2 = 0.67887
A 18.652 2.323
B 78.407 2.354
C 5.1596 0.08173
D 1.1753 0.1751

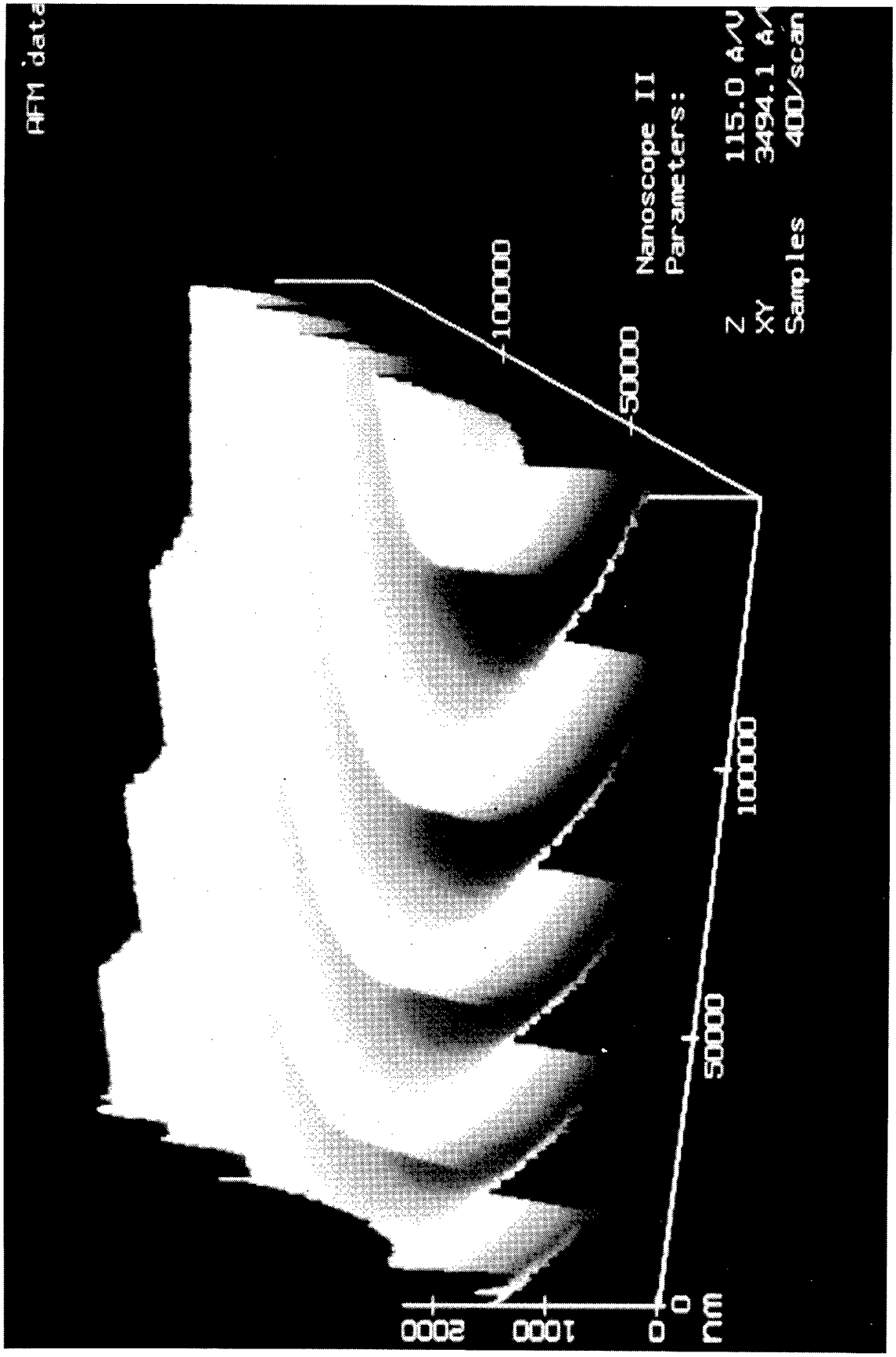
AFM data
Nanoscope II
Parameters:
Z 115.0 A/V
XY 3494.1 A/
Samples 400/scan
100000
50000
0
5000
10000
0
1000
2000
nm

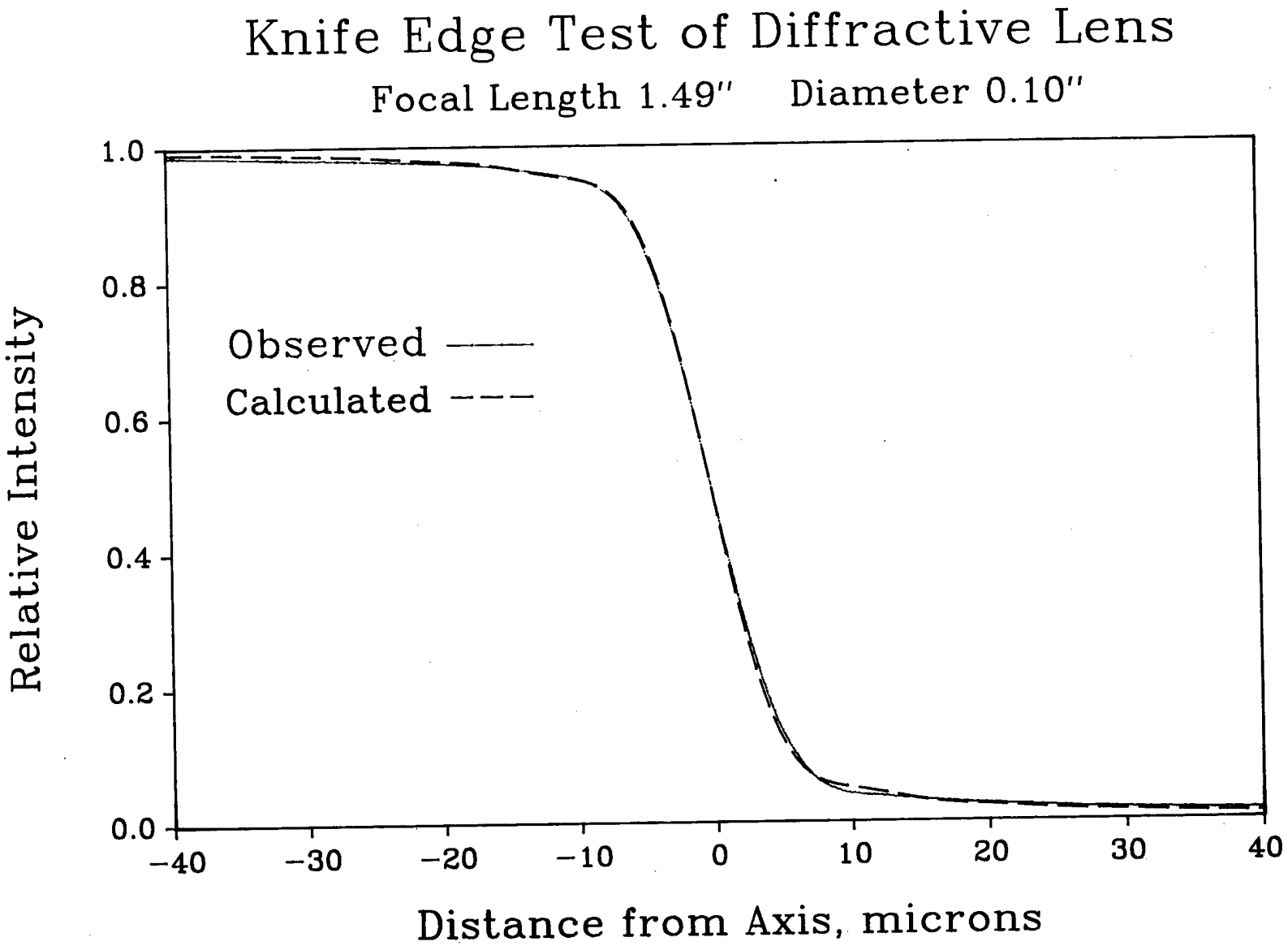
Knife Edge Test of Diffractive Lens
Focal Length 1.49" Diameter 0.10"
Relative Intensity
1.0
0.8
0.6
0.4
0.2
0.0
Observed
Calculated
−40
−30
−20
−10
0
10
20
30
40
Distance from Axis, microns

Curved Grating Fabrication Techniques for Concentric-Circle Grating, Surface-Emitting Semiconductor Lasers

Rebecca H. Jordan, Oliver King, Gary W. Wicks, Dennis G. Hall
The Institute of Optics, University of Rochester, Rochester NY 14627

Erik H. Anderson
IBM T. J. Watson Research Center, Yorktown Heights, NY 10598, and Lawrence Berkeley Laboratory, Berkeley, CA 94720

Michael J. Rooks
National Nanofabrication Facility, Cornell University, Ithaca NY 14853

Abstract

We describe the fabrication and operational characteristics of a novel, surface-emitting semiconductor laser that makes use of a concentric-circle grating to both define its resonant cavity and to provide surface emission. A properly fabricated circular grating causes the laser to operate in radially inward- and outward-going circular waves in the waveguide, thus introducing the circular symmetry needed for the laser to emit a beam with a circular cross-section. The basic circular-grating-resonator concept can be implemented in any materials system; an AlGaAs/GaAs graded-index, separate confinement heterostructure (GRINSCH), single-quantum-well (SQW) semiconductor laser, grown by molecular beam epitaxy (MBE), was used for the experiments discussed here. Each concentric-circle grating was fabricated on the surface of the AlGaAs/GaAs semiconductor laser. The circular pattern was first defined by electron-beam (e-beam) lithography in a layer of polymethylmethacrylate (PMMA) and subsequently etched into the semiconductor surface using chemically-assisted (chlorine) ion-beam etching (CAIBE).We consider issues that affect the fabrication and quality of the gratings. These issues include grating design requirements, data representation of the grating pattern, and e-beam scan method. We provide examples of how these techniques can be implemented and their impact on the resulting laser performance. A comparison is made of the results obtained using two fundamentally different electron-beam writing systems. Circular gratings with period $\Lambda = 0.25$ μm and overall diameters ranging from 80 μm to 500 μm were fabricated. We also report our successful demonstration of an optically pumped, concentric-circle grating, semiconductor laser that emits a beam with a far-field divergence angle that is less than one degree. The emission spectrum is quite narrow (less than 0.1 nm) and is centered at wavelength $\lambda = 0.8175$ μm.

I. Introduction

Curved grating structures have a considerable number of potentially interesting uses in the field of integrated optics, such as in-plane focusing elements, focusing input/output couplers, and various laser resonator designs employing curved gratings for feedback and surface emission. Although some of these applications have been proposed in the past, they have not gained general acceptance in large part because of the difficulty in fabricating such structures (1, 2). However, a surge of interest in the use of concentric circles as the grating elements in distributed feedback or distributed Bragg reflector laser structures (DFB and DBR) has occurred recently (3, 4, 5, 6, 7). A properly fabricated circular grating causes the laser to operate in radially inward- and outward-going circular waves in the waveguide, thus introducing the circular symmetry needed for the laser to emit with a circular cross-section. In this paper we report our successful demonstration of an optically pumped, concentric-circle grating, semiconductor laser (CCGSE) that emits a beam with a far-field divergence angle that is less than one

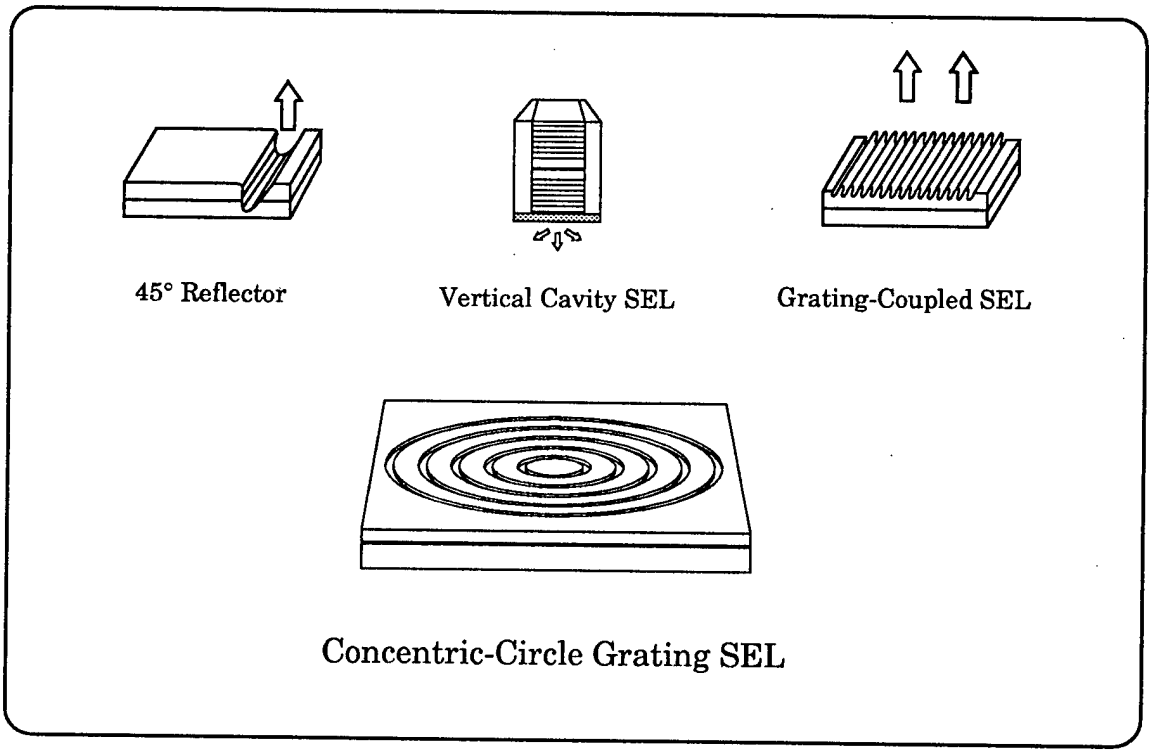

Figure 1. Types of surface-emitting lasers: (a) 45 degree reflector, (b) vertical-cavity surface-emitting laser, (c) grating-coupled surface-emitting laser, and (d) concentric-circle grating, surface-emitting semiconductor laser.

degree. The emission spectrum is quite narrow (less than 0.1 nm) and is centered at wavelength $\lambda = 0.8175$ μm. In addition to these features, other fabrication and performance advantages inherent in surface-emitting geometries, such as wafer-scale testing, are available for the CCGSE laser. The CCGSE lasers are particularly well suited for array operation. A large, phase-locked array of the devices could produce an exceptionally narrow, high power, single mode beam. Figure 1 shows schematics of several surface-emitting laser geometries: the 45 degree reflector, the vertical cavity surface-emitting laser, the grating coupled surface-emitting laser, and the CCGSE laser.

This paper focuses on the techniques employed to fabricate the grating element of our recently demonstrated concentric-circle grating surface-emitting semiconductor laser (8). We give particular attention to the use of electron-beam (e-beam) lithography for the definition of the grating rings, and consider how best to approach the problem of defining and writing features with circular symmetry in the Cartesian environment of an e-beam pattern generator.

II. Concentric-Circle Surface-Emitting Lasers

A schematic representation of the CCGSE laser is shown in Figure 2. The semiconductor material consisted of a graded-index, separate-confinement heterostructure (GRINSCH) quantum well laser structure. The undoped, molecular-beam-epitaxy (MBE) grown epi-layers consisted of a 1.5μm thick $Al_{0.85}Ga_{0.15}As$ lower cladding layer, a 0.3μm thick parabolically graded region with a 100Å thick quantum well, and a 0.25μm thick $Al_{0.85}Ga_{0.15}As$ upper cladding layer. The thin, high-aluminum-concentration upper clad allows for efficient continuous-wave (cw) optical pumping with the 5145Å line of an Argon-ion laser as well as a strong coupling between the grating and the TE_0 guided mode. In this structure a circular grating comprised of concentric rings is used to define the resonator cavity. The grating serves both to provide feedback to the cavity waveguide modes, which propagate inwardly and outwardly along the radial direction, and to couple these guided modes to radiation modes propagating normal to the surface of the waveguide. The resulting emission from a properly operating laser has the form of a narrowly diverging beam with circular cross-section and narrow wavelength spectrum.

All the gratings shown in this paper were written by either the JEOL JBX-5DII e-beam system at the National Nanofabrication Facility at Cornell University, or an IBM Vector Scan 6 (VS-6) system equipped with a real-time polar-to-rectangular coordinate conversion system (9). In each case the patterns were written in a 1500Å thick layer of polymethylmethacrylate (PMMA) resist. The

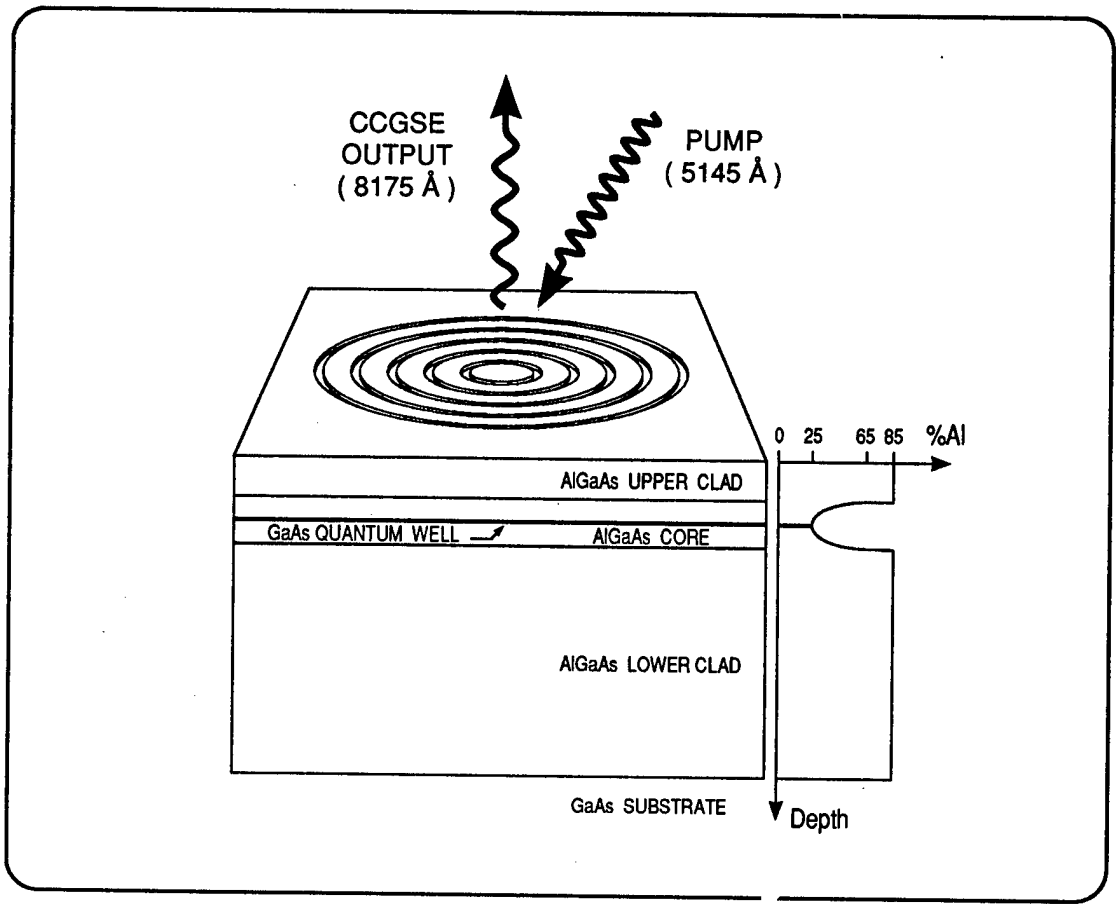

Figure 2. Schematic drawing of the concentric-circle grating, surface-emitting semiconductor laser, showing the AlGaAs/GaAs epitaxial layer structure. The circular grating etched into the AlGaAs/GaAs laser structure provides cavity feedback and coupling for surface emission. Pump power is provided by a cw Argon-ion laser operating at 5145Å.

resulting developed pattern was etched into the underlying semiconductor laser material using chemically assisted ion-beam etching (CAIBE) with chlorine as the reactive species (10). The etched depth of the gratings varied from 800 Å to as deep as 3500 Å. A 3500 Å deep grating is shown in Figure 3.

In order to characterize the performance of the completed lasers the substrate was lapped to a thickness of 100μm, soldered to a gold-plated alumina substrate, and mounted in a dewar held at 77° K. The lasers were then excited by a continuous-wave Argon-ion laser pump beam. The laser's near- and far-field patterns were monitored with a silicon CCD camera and the spectrum was collected by a 0.75 meter spectrometer and photomultiplier tube.

The requirements for such a grating present a considerable fabrication challenge. To provide optimum feedback, the period Λ of the grating must be 0.25 μm, and the grating must posssess a 1:3 peak-to-trough ratio (25% duty-cycle, where a grating trough representing the "on" state). While the precise value of the peak-to-trough ratio is not crucial, the relative variation of this ratio within a completed grating is crucial. Even slight variations in the ratio with respect to the grating's azimuthal angle will destroy the circular nature of the lasing modes (11). Not only must the linewidth variation be held to under one percent, the grating lines must maintain this required phase relationship over a circular field having a diameter of at least 100 μm.

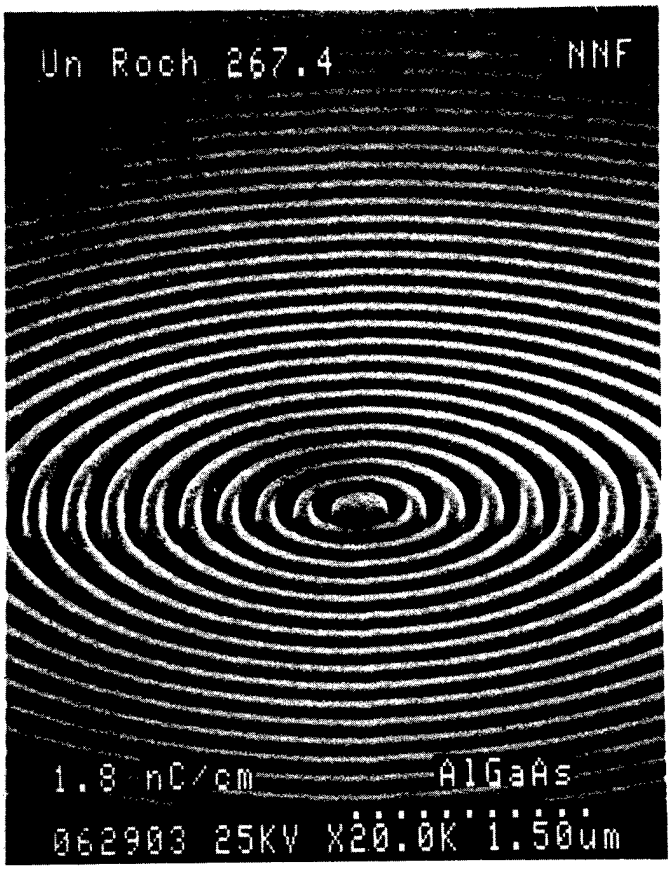

Figure 3. Scanning electron micrographs of a 0.25μm period concentric-circle grating. The grating has been etched to a depth of 3500Å using chemically assisted ion-beam etching.

Although it might seem initially that holographic exposure techniques are a reasonable alternative to e-beam lithography, in practice this is a difficult approach. To produce a holographic pattern consisting of equally spaced rings with roughly constant amplitude and fringe visibility, a plane wave and a conical wave must be interfered (mixed). Two methods for forming conical waves present themselves(12, 13), but the cone angle necessary to achieve the period required for this application is so severe as to preclude the use of conventional optics. It should be pointed out that while methods for producing straight line gratings ordinarily rely on a large spatial separation of the interfering beams to achieve large interference angles and, hence,

appropriately small periodicities, this separation is not easily achieved in two dimensions.

III. Grating Data Representation

A primary consideration in the problem of writing curved line structures by e-beam lithography is the question of how best to describe curved features with an XY (Cartesian) digital-to-analog converter (DAC) pattern generator. We consider three

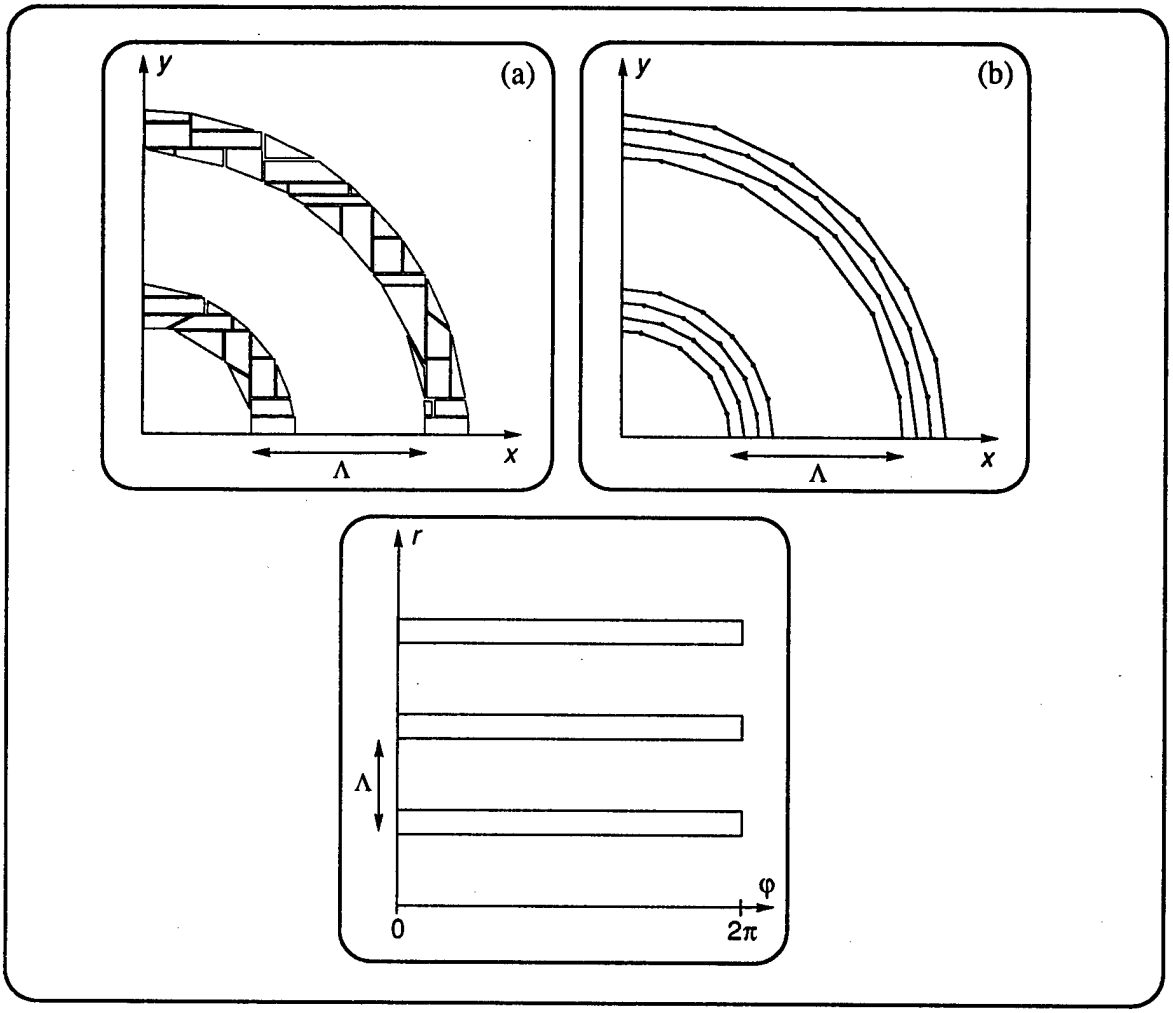

Figure 4. Examples of the three approaches for data representation of the curved gratings. (a) An example of the JEOL fractured-polygon representation of an arc segment. (b) A portion of a circular grating as represented by single-pass-line segments in the JEOL system. The endpoints of each line segment are staggered with respect to those of its neighbors in order to more closely approximate a circle. (c) The radius versus angle (r vs θ) polar data representation used by the IBM Vector Scan 6 e-beam machine.

possibilities here, two of which have been implemented on the JEOL machine and the other on the IBM VS-6.

The least workable of these solutions makes use of a fractured polygon representation of curved line segments, as implemented on the JEOL machine. Here, a best fit of rectangles and triangles is made to the ideal arc segment. An example is shown in Figure 4(a). This technique, however, leads to two unacceptable difficulties. The first arises from the problem of accurately exposing small features with dimensions approaching the 25 Å grid of pixels to which the beam is addressed. The resulting developed rings tend to have scalloped edges and, hence, local variations in linewidth. Of equal concern is the very large amount of data generated using this scheme. The disk space required grows with the square of the number of rings generated, and easily becomes unwieldy.

A second method used with the JEOL machine utilizes rings comprised of many single-pass-line segments as demonstrated in Figure 4(b). For these gratings, four single-pass-line rings were used to approximate a single grating period. The length of each line segment was determined by setting a maximum allowed radial deviation of the segment, or chord, from the ideal circle. In order to more closely approximate a circle rather than a many-sided polygon, the starting position of each single-pass-line segment was shifted in relation to its neighboring line-segment circles. Additionally, in an effort to eliminate any angular correlations, the starting

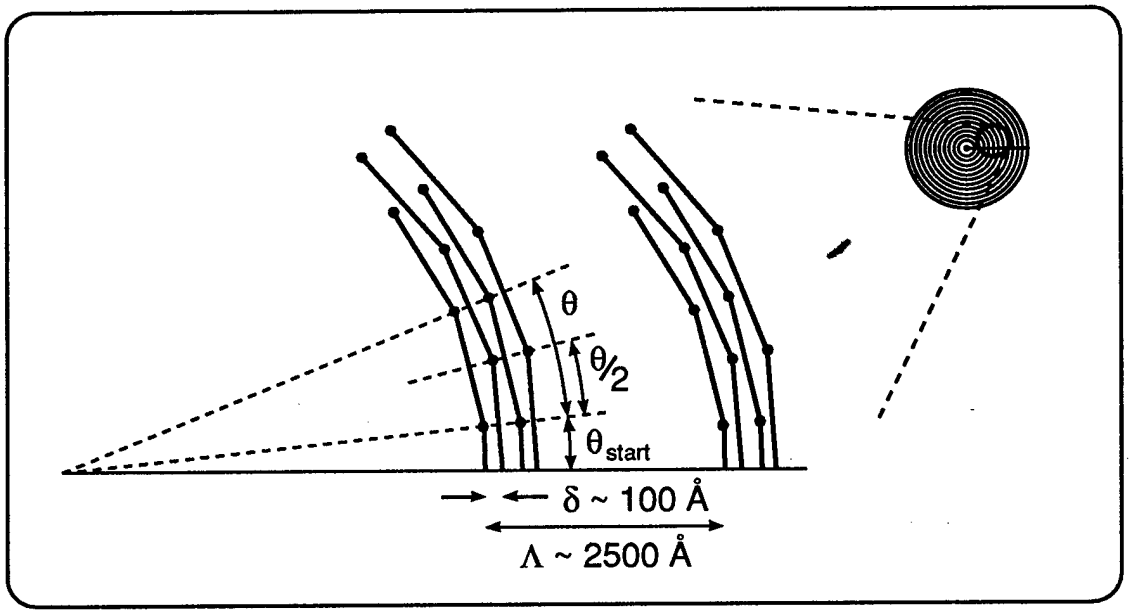

Figure 5. An enhanced detail of the JEOL single-pass line technique, showing the staggered onset of the single pass lines with respect angular location.

position of each group of four rings that define a grating period is shifted in angle by some small, random amount. This is shown in greater detail in Figure 5. When using the single-pass-line technique, particular care must be taken to specify the correct dose. Although the ring data is specified in terms of line segments, exposures are actually performed by mapping the line, in a pixel-wise fashion, onto a Cartesian grid. As a result, the exposed points along a 45° line, for example, are therefore more widely spaced than those of a line at 0°. In order to correctly expose lines which deviate from the Cartesian coordinate axes by an angle θ, a $1/\cos(\theta)$ dose correction must be applied in order to compensate for the corresponding geometrical increase in the inter-pixel spacing along the line. JEOL has provided us with a customized exposure program which allows the user to assign dose corrections as a function of angle.

Of the pattern generation techniques attempted on the JEOL, the use of angular dose corrections has shown the most promise for generating circular lasing modes, as shown in Figure 6(a). However, to date the JEOL still has not produced devices with true circular lasing modes. Without the customized JEOL software, the patterning system will separate the pattern into 9° wedges. Each wedge will have a slightly different duty cycle, or peak-to-trough ratio, and the laser will operate with one independent linear mode corresponding to each wedge. As an example, Figure 6(b) shows lasing along the four radial directions with the smallest

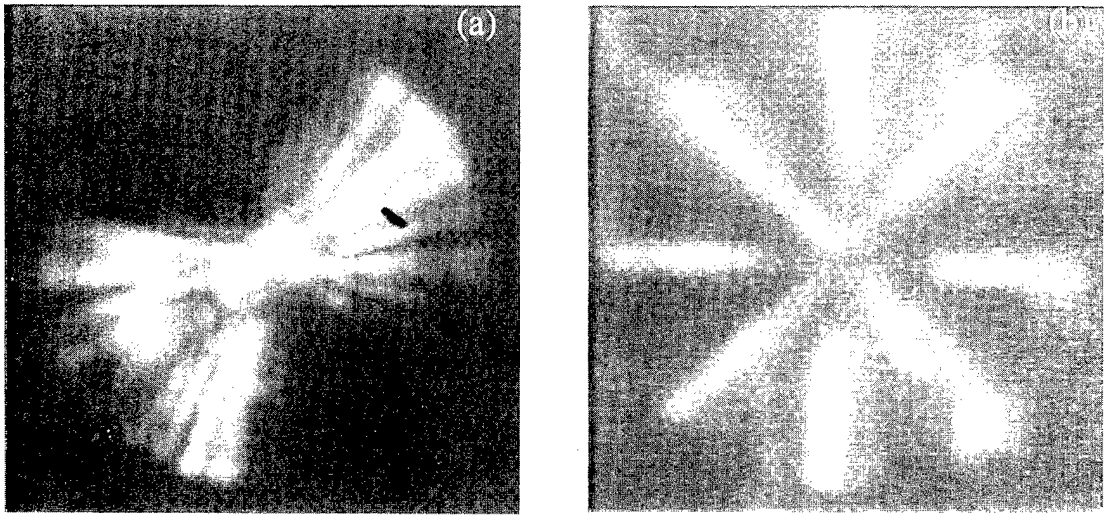

Figure 6. (a) An image of the near-field of a 160μm diameter laser defined by the JEOL system using a single field with a $1/\cos(\theta)$ dose correction applied. (b) A 240μm diameter laser with the default angular dose correction applied. The laser operates in several independent linear modes.

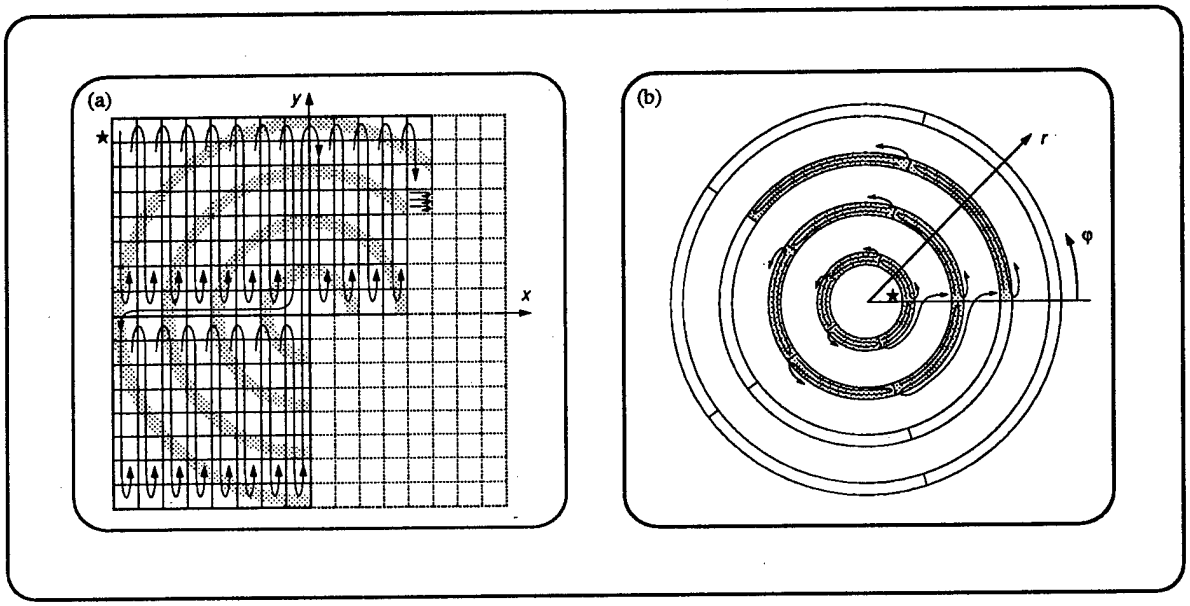

Figure 7. A drawing of the two types of scan format. (a) The rectangular, raster-scan format used by the JEOL e-beam machine, and (b) the polar scan format used by the IBM Vector-Scan 6 e-beam machine.

line-to-space ratios. Unfortunately, the additional information required to ensure the correct exposure and eliminate as much angular correlation in the pattern as possible results in file sizes which approach those generated by the fractured polygon technique.

A more practical approach to this problem has been implemented on an IBM VS-6 machine equipped with a real-time polar-to-rectangular coordinate conversion system. This system makes good use of the inherent angular symmetry in circular structures. Here, the pattern file specifies radius as a function of angle. A representation of this is shown in Figure 4(c). This information is then converted to Cartesian coordinates in real time utilizing hardware sine- and cosine-lookup tables. For this method, no exposure correction is needed to maintain a fixed linewidth since the line dose determined for the polar representation is preserved during the coordinate transformation. The use of the VS-6 system allows for a significant reduction in the size of the stored data set in comparison to the JEOL representations. For example, a 300 period, 150μm diameter grating requires 14 megabytes of disk storage if using the JEOL system, whereas the VS-6 system format occupies only 278 kilobytes. Additionally, there is a corresponding decrease in the length and complexity of the pre-exposure computing tasks.

IV. Scan Format

Another issue critical to the successful fabrication of CCGSE lasers is the choice of scan format. In the case of the JEOL machine, the grating pattern is segmented into rectangular fields and sub-fields for exposure. The grating is then written sub-field by sub-field within a given field. At the completion of each field the sample stage is moved to the next field, and so on. An example of this raster-scan technique is shown in Figure 7(a). A worst case example of the results of this technique is shown in Figure 8. Figure 8 shows the near-field of a 160 μm diameter laser consisting of 80 μm × 80 μm fields filled by 10 μm × 10 μm sub-fields. Clearly, there are significant errors in the phase and/or linewidth of the grating at the boundaries between both fields and sub-fields, as evidenced by the local variations in the intensity of the emitted radiation. The hardware involved in scanning this pattern includes an interferometrically controlled stage, a set of DACs used for deflection to a sub-field within a field, and a second set of DACs used for deflection within the sub-field. We attribute the grating errors to an imperfect match between these components due to inaccuracies in calibration as well as any drift incurred during the time interval required to expose a given field/ sub-field.

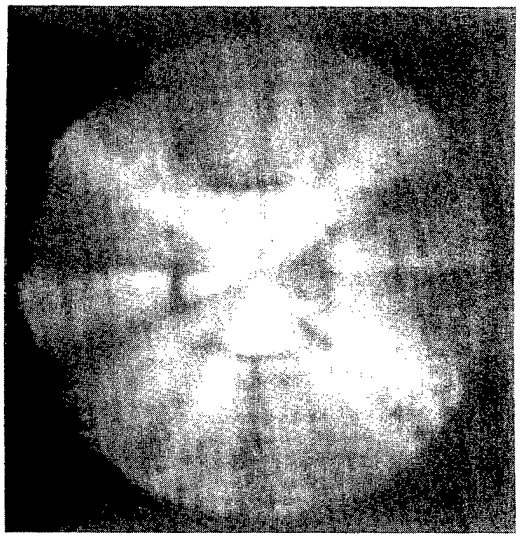

Figure 8. An image of the near-field of a 240 μm diameter laser having significant field (80 μm × 80 μm) and sub-field (10 μm × 10 μm) stitching errors. This grating was written by the JEOL machine using the single-pass line technique.

In comparison, the VS-6 machine scans the grating in a polar, rather than rectangular, fashion, as shown in Figure 7(b). Again, two sets of DACs are used, the first of which addresses the beam to the neighborhood of the next shape to be filled (in this case, an arc-segment), while the second performs the fill. The order of exposure is different, however, as abutting arc-segments making up a ring are written sequentially and each ring is completed before moving to the next period. As a result, there is a diminished likelihood of introducing abrupt local errors in the phase or linewidth. The near- and far-field radiation patterns of a laser made using this method are shown in Figure 9. This 150μm diameter grating was written in a single field, one ring at a time, beginning with the center ring of the grating. The

near-field emission is circular with no apparent local non-uniformities, indicating lasing in the desired, lowest order circular modes. In the far-field, a narrowly diverging (< 1 degree), circular beam results. This laser's radiation spectrum, centered on 8175 Å, had width less than 0.1 nm.

V. Conclusions

The problem of writing sub-micron period curved gratings is sufficiently difficult that producing patterns of the quality necessary for applications such as CCGSE lasers requires hardware and software designed with such applications in mind. When writing large, complex structures, it may not be practical to store the data required to completely specify the pattern in a Cartesian representation. Other techniques, such as using real-time hardware coordinate conversions or dedicated fast processors to calculate coordinates in real time, are viable alternatives. Additionally, care must be taken to design exposure hardware that can scan reasonably large fields with sufficiently low distortion, and with sufficient resolution and stability. If these criteria are met, as they are in the IBM VS-6, it is possible to fabricate a CCGSE laser which oscillates in circular modes and produces a good quality, narrowly diverging, circular beam with a relatively narrow wavelength spectrum. This CCGSE semiconductor laser is a very tough test for the fabrication technology, since the grating itself determines the lowest threshold mode in which the laser will oscillate. A grating that does not meeting the exacting fabrication requirements does not just reduce lasing efficiency, it changes fundamentally the way the laser operates.

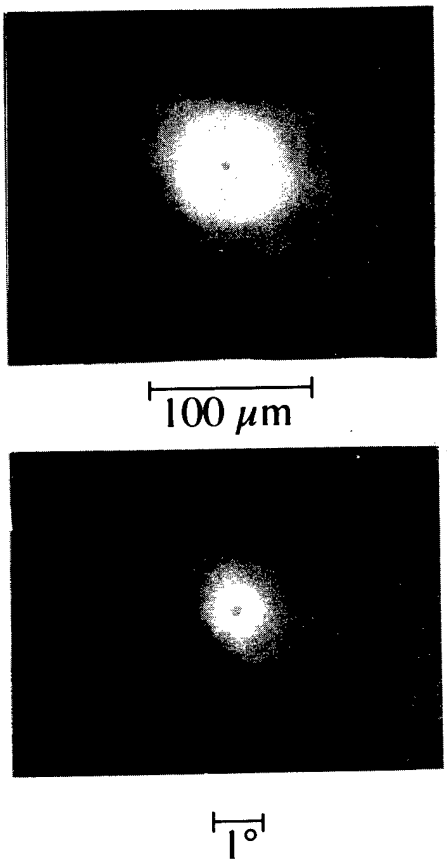

Figure 9. (a) Top. An image of the near-field of a 150 μm diameter laser written by the IBM VS-6 machine. Note the uniform, circular nature of the emission. (b) Bottom. The resulting beam profile in the far-field. The beam divergence angle is less than 1°.

This research was supported by the National Science Foundation (Grant ECS-9112973), the U. S. Army Research Office (Durham, NC), and the New York Center for Advanced Optical Technology. E. H. Anderson acknowledges the support

of the U. S. Department of Energy (DE-ACO3-76SF00098), and R. Jordan acknowledges the support of the IBM Almaden Research Center. Grating fabrication was performed in part at the IBM T. J. Watson Research Center, and in part at the National Nanofabrication Facility. The National Nanofabrication Facility is supported by the National Science Foundation (Grant ECS-8619049), Cornell University, and industrial affiliates. The authors acknowledge the assistance of Michael Koch, University of Rochester, and artwork of Turan Erdogan, AT&T Bell Labs.

References

1. P. K. Tien, *Optics Letters* **1**, 64 (1977).

2. G. I. Hatakosi, H. Fujoma, K. Goto, *Applied Optics* **23**, 1749 (1984).

3. T. Erdogan, D. Hall, *Journal of Applied Physics* **68**, 1435-1444 (1990).

4. T. Erdogan, D. G. Hall, *IEEE Journal of Quantum Electronics* **28**, (1991).

5. R. M. Schimpe, US Patent No. 4,743,083, (1988).

6. C. Wu, T. Makino, J. Glinski, R. Maciejko, S. I. Najafi, *Journal of Lightwave Technology* **9**, 1264-1277 (1991).

7. X. H. Zheng, *Electronics Letters* **25**, 1311-12 (1989).

8. T. Erdogan, et al., *Applied Physics Letters* , (1992).

9. D. Kern, et al., *Proceedings of the SPIE* **447**, 204 (1984).

10. R. C. Tiberio, et al., *Journal of Vacuum Science and Technology B* **9**, 2842 (1991).

11. T. Erdogan, et al., *Applied Physics Letters* **60**, 1773-1775 (1992).

12. Q. S. Ru, N. Ohyama, T. Honda, J. Tsujiuchi, *Optics Communications* **67**, 195-188 (1988).

13. M. V. Perez, C. Gomez-Reino, J. M. Cuadrado, *Optica Acta* **33**, 1161-1176 (1986).

MICRO-OPTICS TECHNOLOGY AND SENSOR SYSTEMS APPLICATIONS

G. Gal, B. Herman, W. Anderson, R. Whitney, and H. Morrow
Lockheed Palo Alto Research Laboratory
3251 Hanover Street
Palo Alto, CA 94304

ABSTRACT

The current generation of electro-optical sensors utilizing refractive and reflective optical elements require sophisticated, complex, and expensive designs. Advanced-technology-based electro-optical sensors of minimum size and weight require miniaturization of optical, electrical, and mechanical devices with an increasing trend toward integration of various components. Micro-optics technology has the potential in a number of areas to simplify optical design with improved performance. This includes internally cooled apertures, hybrid optical design, microlenses, dispersive multicolor microlenses, active dither, electronically controlled optical beam steer, and microscopic integration of micro-optics, detectors, and signal processing layers. This paper describes our approach to the development of micro-optics technology with our main emphasis for sensors applications.

1.0 INTRODUCTION

The current generation of electro-optical sensors, with refractive and reflective optical elements, requires sophisticated designs which are complex and expensive. The system complexity, which drives the cost, is a combination of optical design, focal-plane design, processor design, etc. A technology breakthrough in any of these areas would significantly reduce the cost and enhance the performance of these sensors.

The area of micro-optics technology (MOT) has potential for a breakthrough in a number of areas. In micro-optics technology, micro-optical components are fabricated through a variety of means, including photolithographic methods for multilevel and analog lenses. In binary optics, elements are fabricated using a series of binary masks. This is a proven technology for elements which operate in the infrared over a small wavelength band, but is infeasible for use over a wide wavelength band or shorter wavelengths because of the large number of mask sets required or

too-small feature sizes on the masks. Micro-optics fabrication for elements operating under the latter conditions will require the development of a new etching technology utilizing grayscale masks. (One grayscale mask can replace several binary masks.)

On a macroscopic scale, hybrid lenses using diffractive structures superimposed on refractive optical elements can achromatize and/or aspherize the optical train and improve optical performance with few optical elements. On a microscopic scale, layered microscale integration will combine microlens layers with analog signal processing elements to produce Photonic-Z plane technology, which can enormously enhance optical and signal processing capability. A new systems design application is an agile beam steering (ABS) unit used for laser scanning and also as part of an inexpensive sensor design for smart weapons. A properly designed microlens array with additional dispersion effects will allow multicolor focal-plane arrays (FPAs). Simultaneous multicolor operation for an advanced FPA has the potential for realtime temperature discrimination. We have initiated an R&DD effort for micro-optics technology development and focused on the most important system applications as outlined in Figures 1 and 2.

In this paper, we will discuss our approach to micro-optics technology development and discuss several novel applications of micro-optics to sensors. We will not address system design issues associated with advanced technology based sensors, but will focus on the applicability of micro-optical elements and their benefits to the sensor.

2.0 MICRO-OPTICS TECHNOLOGY DEVELOPMENT

There are several options available for micro-optics that can be used in system applications. They fall into three broad categories: refractive, diffractive, and hybrid elements. Design and fabrication also affect the resulting elements. Elements can be designed either as Fresnel or non-Fresnel, and can be fabricated either as multilevel or analog (smooth).

Refractive elements are the type ordinarily associated with optics and work by redirecting light by refraction at media interfaces. Refractive lenses are typically spheric surfaces with aspheric corrections to mitigate aberration effects.

Diffractive elements redirect light by creating phase differences in the optical field using diffractive structures. At a single wavelength, diffractive elements can be designed which perform identically to refractive elements. Over a wavelength band, however, diffractive elements introduce chromatic effects due to the fact that the optical path differences created by their structure are wavelength dependent. These can be used to advantage to create dispersive elements (as, for example, in the familiar diffraction grating) when information contained in a wavelength band is important.

Hybrid elements are refractive elements with diffractive structures etched onto their surfaces to perform specified functions. For example, material dispersion has a wavelength dependence opposite to that of diffractive dispersion. By etching a diffractive structure onto a refractive microlens, it is possible to make these effects negate each other, allowing chromatic correction by use of a single hybrid element (using a single material) instead of a multiple refractive element (using different materials). This leads to a concomitant savings of weight and cost of the optics.

Fresnel elements are elements whose thicknesses have been reduced modulo a material thickness equivalent to a change of 2π in the optical phase. A 2π phase change is unseen by the optical wave so that the Fresnel element acts the same as the non-Fresnel element upon which it is based. Because the optical path length through the material is wavelength dependent, the 2π

phase changes can only occur at a selected ("design") wavelength and its harmonics. At all other wavelengths the Fresnel element introduces chromatic aberrations. Thus the Fresnel element is ideally suited only for monochromatic light.

In the fabrication of micro-optics by photolithographic techniques, a standard method is to etch the element surface into a substrate using a series of masks made up of opaque and transparent regions. The regions are designed to give a multilevel approximation to the element surface. A set of M masks yields 2^M levels and the resulting elements have acquired the name "binary optics." The multilevel structure reduces the efficiency of the elements, although for Fresnel elements, fabrication using three masks yields 95% efficiency.[1] New techniques are being proposed to fabricate more efficient elements. One of these, grayscale fabrication, has been pioneered by Lockheed in conjunction with Philips of England and will be discussed below. In grayscale fabrication, only a single mask is used to fabricate an analog element.

The different options and types of micro-optical elements are shown in Figure 3.

2.1 TECHNOLOGY DEVELOPMENT OBJECTIVES

The Lockheed Research & Development Division (R&DD) has a continuing multiyear independent research program for the development of micro-optics technology. The long-term objectives of the program are to develop optical design methodology and computer-aided design tools for diffractive/refractive micro-optical elements, designed and fabricated either as analog elements or with multilevel approximations; to implement photolithographic fabrication technology for producing optical elements on different substrates as required for various research areas; and to evaluate these optical elements or subassemblies in the laboratory.

Micro-optics technology has potential applications in a vast number of areas. Our current efforts are focused on eventual integration of micro-optics devices to achieve the full integration required for an advanced technology sensor. Our technology approach is broken down into four main tasks. These are (1) Analysis and Computer Software Development, (2) Fabrication Process Development, (3) Laboratory Evaluation of Micro-Optical Elements, and (4) System Applications of Micro-Optic Devices.

2.2 ANALYSIS AND COMPUTER SOFTWARE DEVELOPMENT

Because of the large variety of options and types of micro-optics, it has been necessary to develop generic methods and tools to analyze different elements. A sampling of different kinds of elements we have had under consideration is shown in Figure 4.

Our analytical methods are based upon the scalar wave theory of physical optics.[2] These methods are applicable to all elements where polarization is unimportant (as is the case for most of the elements shown in Figure 4). We have developed analytic techniques for dealing with analog and multilevel elements, designed as either Fresnel or non-Fresnel. These techniques are a great help in paramaterizing the performance of an element. For example, if an element is characterized by a certain set of parameters, its corresponding Fresnel element will introduce one additional parameter, the ratio of the design wavelength to the radiation wavelength. Constructing a figure of

1. Swanson, G. J., "Binary Optics Technology: Theory and Design of Multilevel Diffractive Optical Elements," *Lincoln Lab. Tech. Rep. 854*, Aug 1989.
2. Goodman, J. W., *Introduction to Fourier Optics*, McGraw Hill, New York, 1968.

merit comparing the Fresnel element performance to the non-Fresnel element performance is a straightforward matter. This figure of merit can be plotted in parameter space and the result can be used to determine when the chromatic effects introduced by the Fresnel element become too severe. This approach can save an enormous amount of time over an alternative approach where the performance of the Fresnel element is calculated numerically over a range of parameters to determine a "best" performance. An example of the analytic approach applied to the dispersive microlens is given in Reference 3.

In addition to analytical tools, we have developed a host of computer codes to treat wavefront propagation through micro-optical elements. These codes are used when more detail is needed than can be obtained from simple analytical models. For example, integration of micro-optics on a focal plane requires knowledge of how much light falls on a proposed detector layout. This is most easily calculated using numerical codes. Another example is when one has to deal with more complex topologies (such as hexagonal or skewed elements) where analytic methods are too cumbersome to be useful.

More sophisticated codes are also used in the optical design of some micro-optics concepts. For example, the concept of an agile beam steering unit is shown in the lower left corner of Figure 4. Here, a pair of microlenses are displaced relative to each other. This causes a deflection of a beam of light traveling through the lens pair. The deflection is dependent upon the size of the displacement, so as one lens is scanned behind the other, the beam also scans up and down. In a first-order approximation, the scan can be paramaterized by the displacement and the diameter and f-number of the lenses. To incorporate this concept into a real-world application, system-defined requirements must be met (e.g., no vignetting, minimization of aberrations in the optical train). This can only be done using computer codes. As an example, this concept was extended to develop the two-dual-sided-element, agile-beam-steering unit cell shown in Figure 5. This unit cell is capable of scanning over a $\pm 20°$ field of regard without vignetting. The work was performed using the Lockheed OPTIMA ray tracing code.

We have also developed codes to determine micro-optical elements that modify a wavefront to give a desired phase or intensity distribution. Types of elements that fall into this category are shown in the last two columns of Figure 4. The programs operate by iterating back and forth between the element and a focal plane, applying constraints until the desired distribution is reached. The resulting "phase plates" can be used, for example, for wavefront aberration correction or for beam shaping. An example of a phase plate that is used as a spot-array generator is given in Figure 6.

Finally, we have developed a set of codes for generating the binary mask sets needed for the photolithographic fabrication process. The codes generate the required masks for any specified micro-optical element surface and are flexible enough to handle any number of masks along with a specified mask feature size.

2.3 FABRICATION PROCESS DEVELOPMENT

In the past few years, new developments in semiconductor industry process technology have made it feasible to generate diffractive and refractive micro-optic components. These process technologies are submicron photolithography and large-scale dry etching.

---

3. Herman, B. and G. Gal, "Theory of Dispersive Microlenses," Conference on Binary Optics, Huntsville, AL, Feb 1993.

In Reference 4 we reported the progress and research programs for micro optics fabrication at Lockheed and Philips U.K., hence only a summary is given here.

For multilevel elements, the etching must produce vertical side walls well registered with mask features (i.e., no undercutting or shadowing) or some lens area is lost. The etching must also produce smooth surfaces at the bottom of the etched area. Finally, the etch rate (or, equivalently, etch depths) must be reproducible for a production process. The two technologies that satisfy these requirements are reactive ion etching (RIE) and ion beam milling.

In RIE, ions produced in a plasma discharge react with a substrate material to form a volatile compound which is then removed from the system. The RIE process is highly anisotropic so that vertical side walls are obtained at the multilevel steps.

In ion beam milling, a collimated, uniform beam of inert ions, extracted from a plasma discharge, bombards the surface of a substrate. The momentum transferred by these ions breaks the bonds of the substrate surface atoms. Material not protected by a mask is selectively etched away. Etch features down to 0.2 μm and with aspect ratios of 5:1 can be achieved.

We have fabricated Fresnel microlens arrays for operation at a wavelength of 10.6 μm in both Si and CdTe substrate materials using binary masks. Both RIE and ion beam milling technologies were utilized. The optical performance of the lenses was measured to be diffraction limited. Sections of the eight-level Si and CdTe arrays with a 100-μm pixels are shown in Figure 7.

Two approaches are available for continuous curved surface micro-optics element fabrication. Both rely on the differential milling rate of photoresist and substrate material. In both approaches, only one photolithographic step is required so that problems of multiple mask registrations are avoided. The thickness profile of the photoresist is controlled in one case by the surface tension of isolated circles of photoresist during a controlled bake and in the second case by "half-tone grayscale" exposure control of the photoresist pattern.

In the first case, photoresist patterns with diameters in the range of 60 to 250 μm are delineated by conventional photolithographic techniques. They are then baked at a temperature higher than the glass-transition point of photoresist so that spherical contours are generated by the effect of surface tension on the photoresist surface. Then the substrate is subject to Ar ion-beam milling. During the milling, the spherical mask contour is transferred to the substrate surface. While this technique is effective and straightforward, it is severely limited in that only spherical (and closely related) shapes are possible. In particular, it is not possible to incorporate diffractive structure superposed on the basic refractive optical shape, as required for dispersive microlenses.

The second option is the half-tone grayscale approach. The desired thickness profile is modeled by a related submicron half-tone photoresist exposure pattern. The photoresist exposure and development process is adjusted so that a smooth contoured photoresist mask is produced with (almost) completely controlled topography. Differential milling of photoresist and substrate is again used to transfer the contour to the substrate.

Grayscale fabrication technology is essential for the fabrication of non-Fresnel analog dispersive microlenses. This type of microlens is ideally suited for multicolor focal planes, and is currently under research and development in our laboratory.[3] An example of a microlens designed to operate in the LWIR spectral region is shown in Figure 8.

---

4. Anderson, W., J. Marley, D. Purdy, and G. Gal, "Fabrication of Micro-Optical Devices," Conference on Binary Optics, Huntsville, AL, Feb 1993.

The analog microlens was fabricated in silicon. Figure 8 indicates the criticality of the grayscale single mask technology to generate smooth surface with vertical steps. The dispersive microlens array is currently under experimental performance evaluation.[5]

A third area for fabrication technology development is that of microchannel fabrication. Microchannel fabrication is necessary when cooling channels must be introduced to a micro-optic component so that the component can be kept at a required operating temperature. A variety of technologies are available for microchannel fabrication. Technology choice is determined by required channel dimensions. The technologies are: plasma or dry etching (appropriate for depths less than ~20 μm), anisotropic wet etching (appropriate for depths of 10 to 1000 μm with depth to width ratios 10:1 or greater), laser machining (appropriate for widths greater than 25 μm), and precision wafer sawing (appropriate for widths greater than 175 μm).

An example of microchannels fabricated in silicon using a hot KOH etch is shown in Figure 9. There is the order of 100:1 etch rate difference between the weakly bonded $<110>$ planes and the strongly bonded $<111>$ planes. By aligning the channel direction along the $<\bar{1}21>$ direction of a $<110>$ oriented wafer, the channel walls will be the weakly etched $<111>$ planes. The 100:1 directional etch ratios require alignments to the order of 0.1°. The microchannels were etched into one silicon substrate and another silicon substrate was fusion bonded to the top of the etched substrate to close off the microchannels.

More details of the fabrication process technology we have developed at Lockheed can be found in Reference 4.

2.4 LABORATORY EVALUATION

LMSC R&DD has built up facilities over the years for testing different types of microlenses. The experimental setup, shown in Figure 10, provides a direct measure of the point-spread function (PSF) of any individual microlens or a microlens array. The basic idea is to illuminate a microlens array with a collimated beam, magnify the PSF onto a detector, and record and control the experiment using a computer.

The light source is a laser operating at the appropriate wavelength. The source is chopped at 1 kHz by a mechanical chopper. The laser sources provide large amounts of power, allowing the measurement in detail of the wings of the PSF that might interfere with neighboring lenslets. The dynamic range can be more than six orders of magnitude. For wideband testing, the lasers will be replaced by a blackbody source and spectral filters.

An all-reflecting microscope objective magnifies and relays the PSF to an appropriate detector (e.g., a Si photodiode). The objective provides a standoff distance of 8 mm between the plane of focus and the front of the microscope. Varying the separation of the objective and detector changes the magnification and the effective area covered by the square area of the detector. The output of the detector is preamplified and sent to a lock-in amplifier. Synchronous detection reduces the background noise.

The output of the lock-in amplifier is measured by an analog-to-digital converter located in a computer. The same computer controls motor-driven xyz translation stages that position the microlens array. By moving the array, the detector sees different portions of the microlens PSF. A

5. Shough, D., B. Herman, and G. Gal, "Measurements of Microlens Performance," Conference on Binary Optics, Huntsville, AL, Feb 1993.

program on the computer scans the transverse position of the array, pauses until the output of the lock-in amplifier has had time to stabilize, measures the voltage output, and then steps to the next scan position.

The PSF of an isolated CdTe Fresnel lens shown on Figure 7 has been measured at LMSC using a 10.6 μm CO_2 laser, and the result is shown on Figure 10b. This measurement is to be compared to the theoretical PSD, which has been convolved with the 16-μm detector size. The difference between the measured and theoretical results is hardly distinguishable.

Due to the multicolor nature of the next generation of micro-optics, we are adding the capability to vary the wavelength at which we test the lenses. Our laboratory has been updated to multicolor capability with the inclusion of lead-salt lasers operating at 8, 10 12, and 14 μm. Lasers are also available for testing in the 3- to 5-μm MWIR region. More details about our laboratory setup can be found in Reference 5.

3.0 SENSOR SYSTEMS APPLICATIONS

The next generation of multispectral seekers may include the capability of realtime, on-board color discrimination, along with other smart-pixel, on-focal-plane processing capabilities that will enhance data throughput. Neural-network-technology-based analog circuits for acquisition, centroiding, nonuniformity correction, tracking, and image motion compensation are potential candidates for smart-pixel-integrated analog-signal-processing designs for semi-autonomous sensors. Opto-electronic signal processors for these seekers will consist of different layered components, each performing specific tasks. The design goal for these seekers is to produce compact, lightweight designs with optimal performance. Feed-forward/backward closed control loops may also be included in the Z-layered integration. The monolithic integrated sensor system may be designed for strategic, tactical and/or commercial applications such as smart robotic sensors.

3.1 INTERNALLY COOLED MICROLENS ARRAY APERTURE

The first component for the monolithic integrated system may be the internally cooled aperture of the seeker, which may be enhanced with a built-in step/stare capability to address a large field of regard (FOR). This aperture will function as an internally cooled protective window for endoatmospheric encounters. For exoatmospheric missions, the system would operate in the longer wavelength region; hence, it is desirable to cool the aperture to reduce background noise due to the optics thermal self-emission. For a generic research and development effort we have addressed the optical design issues of an internally cooled microlens array aperture. The use of microlens arrays allows some volume of the window to be optically inactive. This will allow for the inclusion of microcooling channels through which heat can be removed.

Development of an internally cooled microlens array aperture[6] requires the use of innovative technologies and novel optical designs. Technology areas include micro-optics and cooling channel fabrication, cooling systems, and opto-mechanical integration. Novel optical designs are required to meet thermal, FOR, size, and weight requirements.

There are two basic conceptual aperture design options. These fall into the categories of staring arrays and agile beam steer scanners (phased arrays).

---

6. Gal, G., B. Herman, H. Morrow, W. Anderson, I. Hsu, and D. Stubbs, "Seeker Multispectral Atmospheric Technology (SMART) Window Development," *AIAA-92-2804*, AIAA SDIO Annual Interceptor Technology Conference, Huntsville, AL, May 1992.

The staring array shown in Figure 11 is limited in its FOR by the fixed field of view (FOV) of the microlenses. The FOR can be increased either by the maneuver of the sensor orientation, which may not be feasible for many applications, or by scanning. We have studied an innovative design option that will include an agile beam steering unit to achieve the required FOR using an optomechanical step/stare device which includes a feed backward control subsystem design.

The idea of using microlens arrays as the basis for an ABS unit has been presented by Goltsos and Holz.[7] Our implementation uses a different design layout (Figure 12). Shifting one of the arrays allows the angle of the incident light to vary, thus extending the FOR. The angle shifts obtained are proportional to the microlens sizes, not the aperture size, so that a large range of angles can be obtained using only micromovements. In our conceptual design, we have achieved scanning over a range of $\pm 20°$. Microlens arrays in the ABS again allow for microcooling channels.

Our choice of implementing an ABS in the window to increase the FOR posed fundamental design problems which have never been addressed before. First, we designed a unit cell train in the optical layout. Upon successful completion of the unit cell design, our effort focused on the assembly of unit cell trains into a 2-D aperture array and the multiaperture effect on the transmitted wavefront and image quality.

The afocal design of the unit cell train will allow either a transmitter or receiver mode of operation and was approached from two different directions: (1) Unbiased unit cell train design for high performance shown in Figure 5. The approach was to discover the best design form for a cell train which met the imaging requirements one step at a time, gradually increasing the angular requirements of the design. (2) Large look angle bias (LAB) required for sloped surfaces. A 3×3 element array segment of the aperture is shown in Figure 12. The approach was to quickly generate all the angular requirements and then gradually improve the imaging performance.

The purpose for approaching the cell train design in this manner was so that the best ideas from the different approaches could be combined in a final design. We have concluded that the unit cell design option shown on Figure 5 will provide a better performance. The design included a detailed thermalization trade study and the cooling provided through the microchannel were sufficient to to yield excellent thermal performance.

Phased array issues are important because a wavefront entering a microlens array obliquely will be stepped upon its exit. If the steps are an integral number of wavelengths apart, the reconstructed image will suffer no detrimental effects from this stepping. For a given wavelength, this condition will occur only at selected angles (eigenangles). Over a spectral band, this stepping will introduce aberrations even at the eigenangles because the steps are wavelength dependent.

Phased array issues for imaging were addressed by developing computer tools to perform numerical optical experiments. The current state of the tools is such that we can analyze arrays as large as 9×9 (81 cells) either monochromatically or polychromatically. The only limits on the number of wavelengths and array sizes we can treat are those imposed by computer memory and time constraints.

A high-performance cell-train with -1 magnification has been successfully designed. This two-element form has a $40°$ full FOR and room for cooling channels. It scans without a trace of vignetting. The image is diffraction limited over a $4°$ field and over the full FOR. The LAB of this

7. Goltsos, W. and M. Holz, "Agile Beam Steering Using Binary Optics Microlens Arrays," *Optical Engineering*, Vol. 29, No. 11, pp. 1392-1397, Nov 1990.

design is zero. It has also been set in arrays up to 9 × 9 for mosaic wavefront image formation investigations. The polychromatic PSF in the MWIR for the 9 × 9 array in the unscanned position is also shown in Figure 12. The polychromatic performance proved to be inadequate and additional micro-optical elements are required for chromatic phase correction A detailed design study is currently underway and preliminary results indicate that the phase corrector subassembly can be successfully implemented.

Several important design lessons were learned while designing the ABS. The scan element must move in an arc to maintain wavefront collimation. The internal focus should be inside the first element to give the best wavefront performance. All four surfaces need high-order aspherics; the outer surfaces on the pupils required 8th order polynomial correction.

We have achieved a 55° LAB with ±20° FOR scan. The −1 magnification cell train required three elements. Several of the surfaces were toric aspheres. At 55°, the output beam is parallel to the input beam.

3.2 LASER BEAM DIRECTOR

If we confine ourselves to monochromatic light, then perfect reconstruction of a stepped wavefront can be obtained at the eigenangles which are determined by the grating equation. By scanning with an ABS unit, a discrete set of (two-dimensional) eigenangles can be addressed. This concept can be used as the basis of a laser beam director. The unit cell of an monochromatic afocal design is given on Figure 13a with the calculated point-spread function shown in Figure 13b which is based on a 9 × 9 elements microlens multiaperture ensemble.

3.3 INTEGRATED FOCAL PLANE

Several advanced technology sensor development programs currently under development at Lockheed identified the need to research innovative methods to achieve high-performance integrated focal planes. The utilization of a microlens-integrated detector has several potential benefits. MOT has been identified as a key technology to achieve the severe performance requirements derived from systems engineering flowdown studies.

Microlenses integrated with the detectors shown in Figure 14 will focus the incident energy onto each detector which can be significantly smaller than the pixel area. This has several benefits, including increased R_0A with subsequent lower thermal noise (thus increased sensitivity), smaller detector volume that will minimize the gamma susceptibility, and a relatively large available chip real estate area for other planar devices, such as multiple detectors for inband multicolor separation or for analog signal-processing devices. The use of a microlens also will allow near 100% fill factor to be maintained while allowing the readout under each detector to take full advantage of the total pixel area. The design may be a hybrid with an indium bump (Figure 15) or monolithically integrated MQW detectors where the available area may utilize readout electronics directly integrated with the substrate.

3.3.1 Focal Plane Array Microlens Hybrid

The FPA microlens hybrid concept is illustrated in Figure 15 which shows three layers of hybrid assembly. The backside illuminated detector arrays are initially built using conventional techniques. The substrates are thinned to the required thickness defined by system design and the microlens array is then fabricated by conventional photolithographic procedures. Fresnel-type

microlenses were produced by binary fabrication processes on a CdTe substrate. The fabrication processes were pioneered by Lockheed R&DD in the initial phase of the Long-Wavelength Advanced Technology Seeker (LATS) program. A Fresnel-type microlens fabricated with a three-mask (eight-level) binary method is shown in Figure 16. A technology transfer agreement with LORAL for integrated detector development is currently underway. The hexagonal pixel topology is required from the system optimization point of view and is being implemented by LORAL on the focal plane to be delivered to the LATS program.

3.3.2 Inband Multicolor Detector Focal Plane (Dispersive Microlens)

Conceptual design studies for an advanced technology compact and lightweight sensor concluded that an integrated solid state solution to measure target spectral signatures is one of the most important potential methods for realtime technique in discrimination among various targets. Such an advanced sensor system requires an optical design that allows a simultaneous spectrally narrowband signal detection. Several techniques have been investigated in system engineering studies and one of the most technically innovative concepts relies on the dispersive microlens concept.[8]

The incident wideband wavefront contains temperature information about the targets and it is desirable to separate the wideband information to narrower subbands while maintaining perfect spatial and temporal registration. A successfully implemented optical design for the sensor would eliminate the need for extensive additional computational signal processing.

Micro-optics technology offers a potential solution through use of the dispersive microlens. We have been investigating a novel concept which may be implemented by superimposing the microlenses with a diffraction grating in each unit cell to cause the colors in the signal to be separated by the detector. The optical blur spot is stretched along an optical axis perpendicular to the superimposed grating direction. The dispersive patterns can be integrated into a combined surface fabricated as one surface utilizing photolithographic methods.

The dispersive microlens can be designed as either a Fresnel or non-Fresnel type. We are developing these two basic design options with both binary and our analog grayscale photolithography utilizing differential ion milling techniques.

The two basic concepts are shown in Figure 17: a dispersive Fresnel design (Figure 17a) and a dispersive non-Fresnel (analog) design (Figure 17b). Amber Engineering is assisting LMSC with the readout electronics for the Fresnel design option and we are jointly developing the non-Fresnel design and grayscale photolithography with Philips U.K. Computer-simulated unit cells for these two design are given in Figure 18 and fabricated test pixels for these two options are shown in Figure 19.

4.0 SUMMARY

We have discussed our current approach to micro-optics technology at Lockheed R&DD and outlined many of the system applications we have considered for advanced technology seekers. Micro-optics technology has a vast potential for making seeker components lighter, more compact, and more effective. It does this in three ways. The first is by combining bulky trains of optical elements into single elements through the use of hybrid optics (e.g., aberration correction).

8. Gal, G., "Dispersive Microlens," under patent application, 1992.

The second is by introducing novel designs to achieve results previously obtained with macro-optics (e.g., beam steering/scanning). The third is by integrating micro-optical components with signal-processing elements to enhance information processing (e.g., multicolor focal planes).

Our efforts in micro-optics technology development cover all aspects of the technology, including development of analytic methods and computer codes, new fabrication techniques (e.g., fabrication in CdTe, grayscale technology), and laboratory testing. The general technology we have developed can be applied not only to the evolution of advanced seekers, but also to an entire range of areas, including optical communications, microlasers, and optical computing.

ACKNOWLEDGMENTS

This work was funded by Lockheed Internal Research (IRAD) programs as well as projects performed under U.S. Army Strategic Defense Command contracts. The authors would like to acknowledge Ron Calhoun of ASDC/KEW Directorate for his leadership and support. We also thank Don R. Purdy of Philips Infrared Components (U.K.); without his dedicated effort, the grayscale fabrication technology would be a dream only.

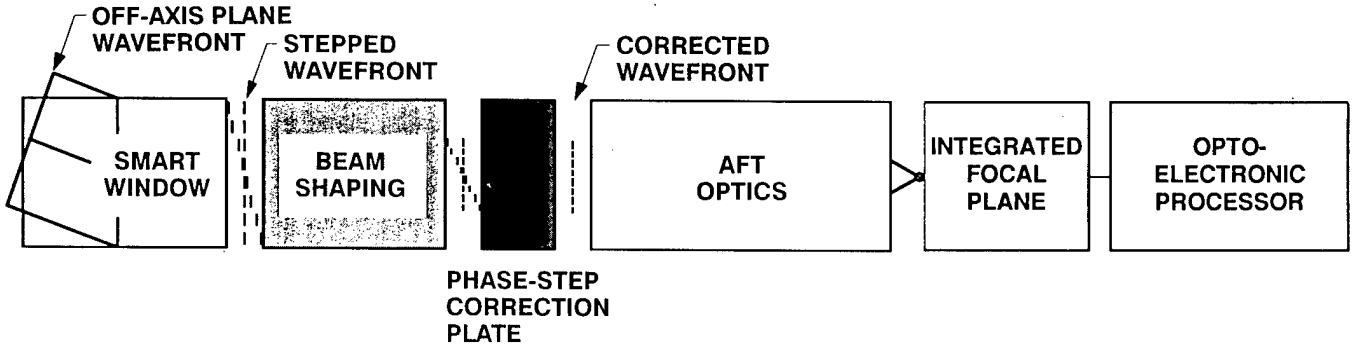

FIGURE 1. BLOCK DIAGRAM FOR A GENERIC PHOTONIC-Z TECHNOLOGY SMART SENSOR.

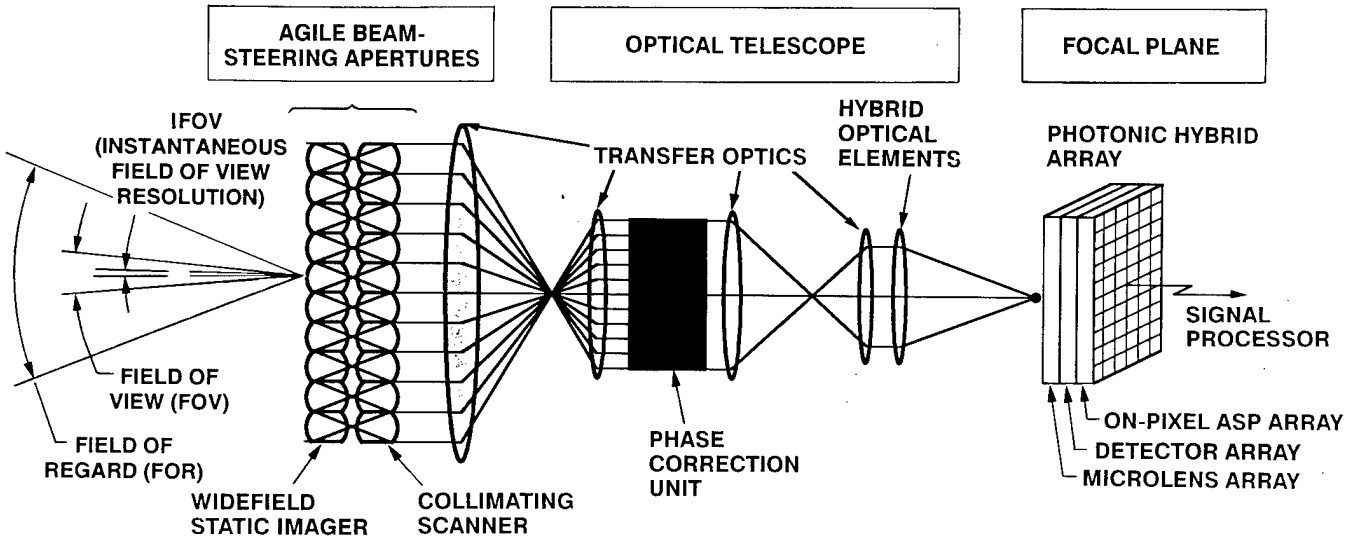

FIGURE 2. MONOLITHIC INTEGRATION WITH MICRO-OPTICS TECHNOLOGY.

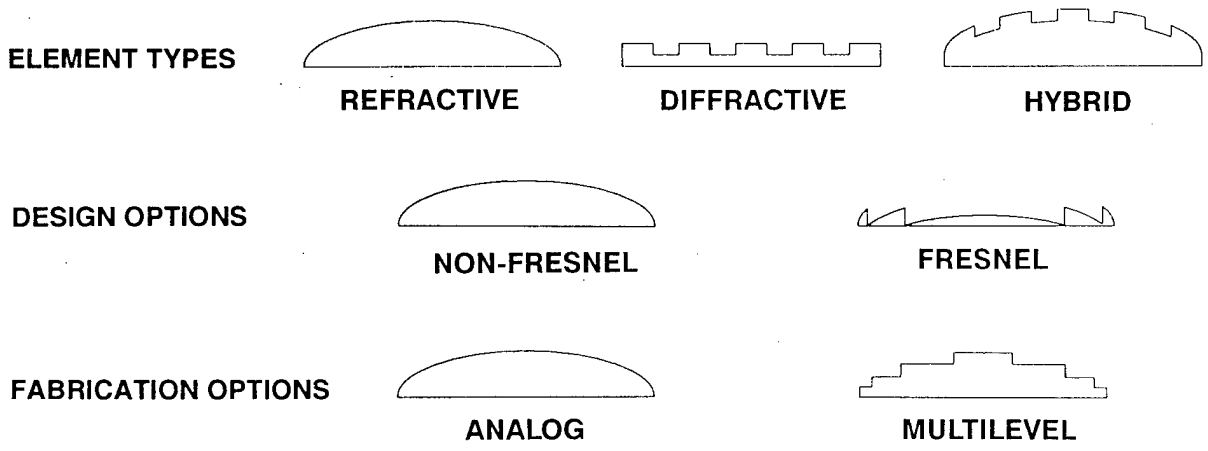

FIGURE 3. DIFFERENT MICRO-OPTICS OPTIONS (REFRACTIVE, DIFFRACTIVE, HYBRID) AND TYPES (NON-FRESNEL/FRESNEL, ANALOG/MULTILEVEL).

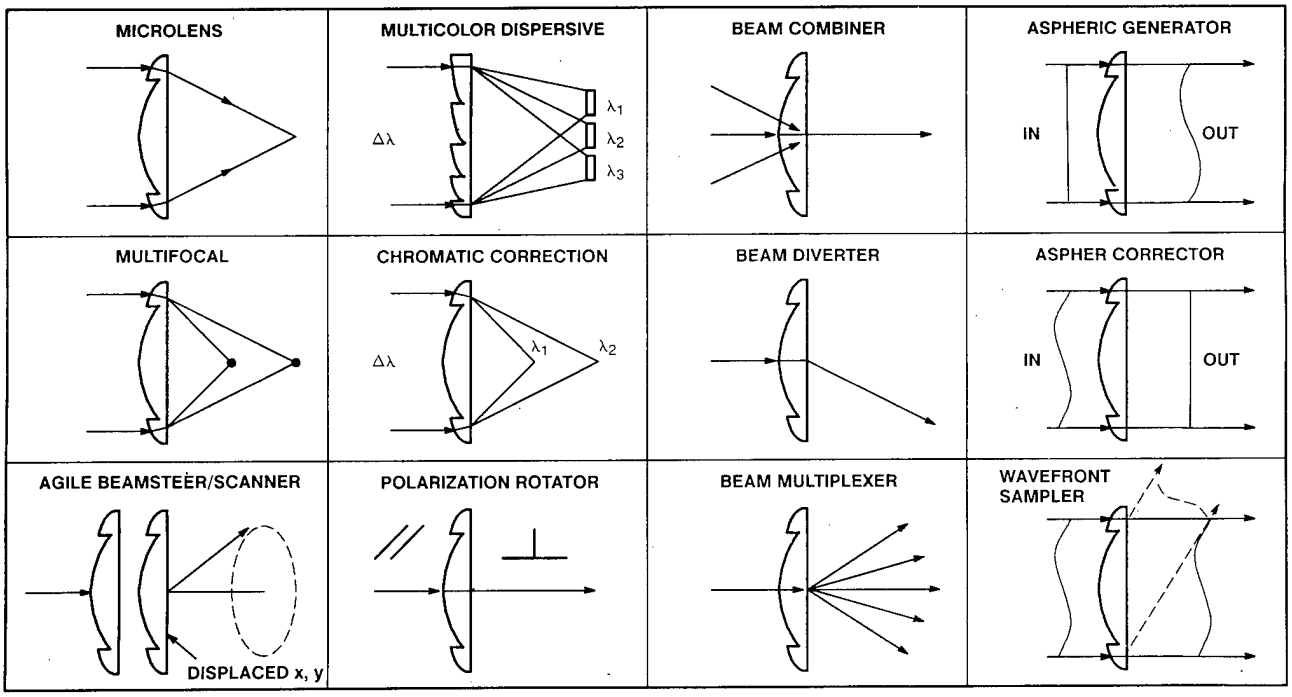

FIGURE 4. EXAMPLES OF MICRO-OPTICAL COMPONENTS.

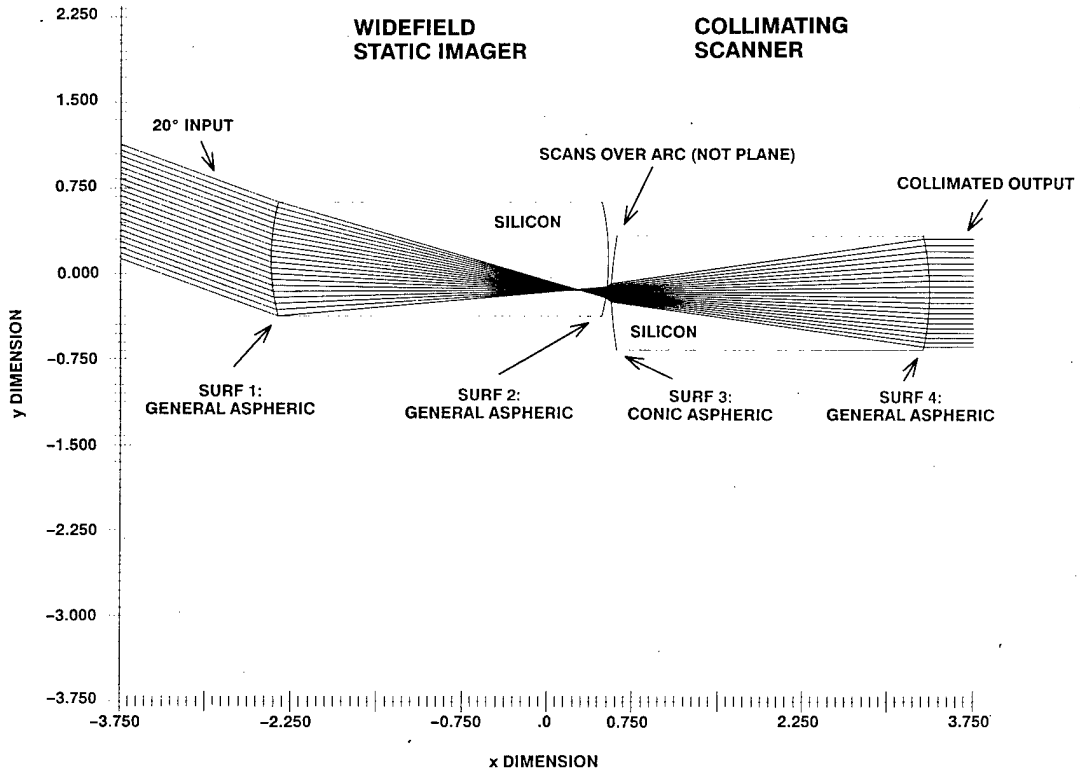

FIGURE 5. MICRO-OPTICS TWO-ELEMENT −1 MAGNIFICATION UNIT CELL TRAIN DESIGN EXAMPLE FOR AGILE BEAM STEERING. Collimating scanner is at the +20° scan position.

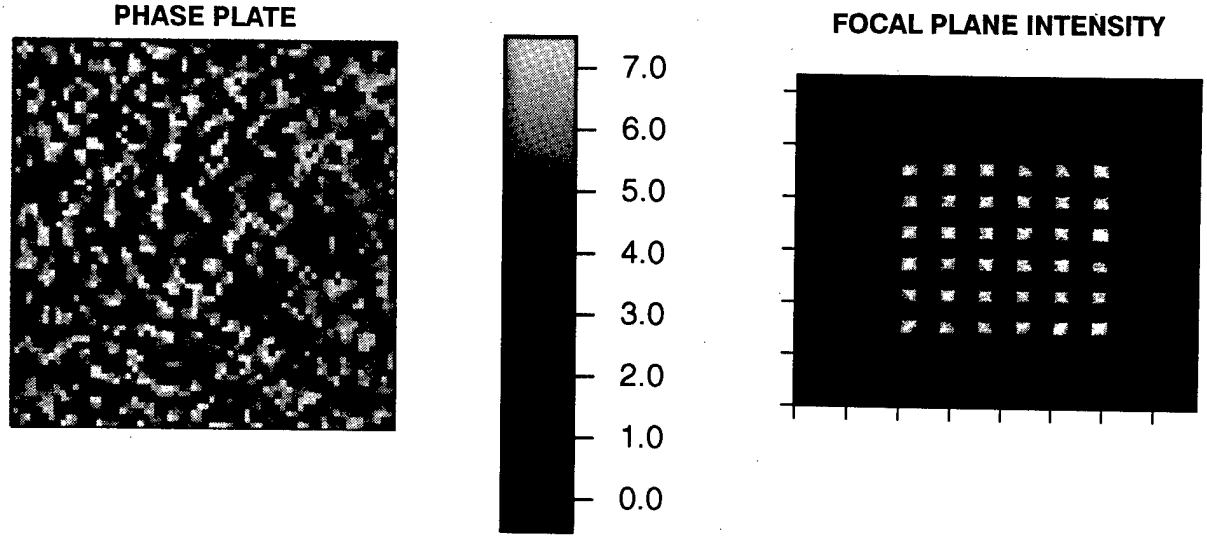

FIGURE 6. A 6 × 6 SPOT ARRAY PHASE PLATE GENERATOR AND THE RESULTING INTENSITY DISTRIBUTION.

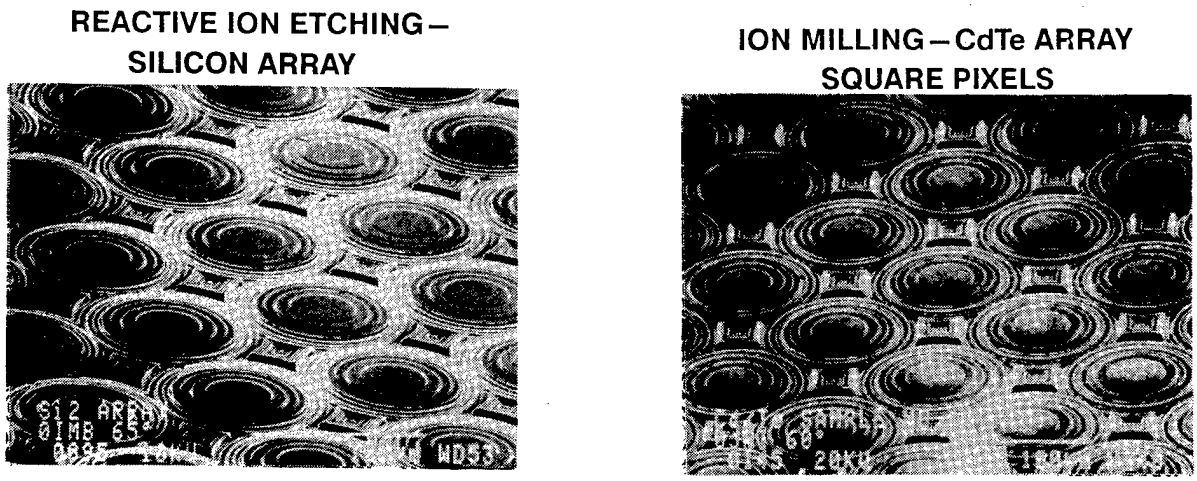

FIGURE 7. EXAMPLES OF THREE-MASK, EIGHT-LEVEL MULTILEVEL FRESNEL MICROLENSES OPERATING IN THE LWIR WAVEBAND REGION.

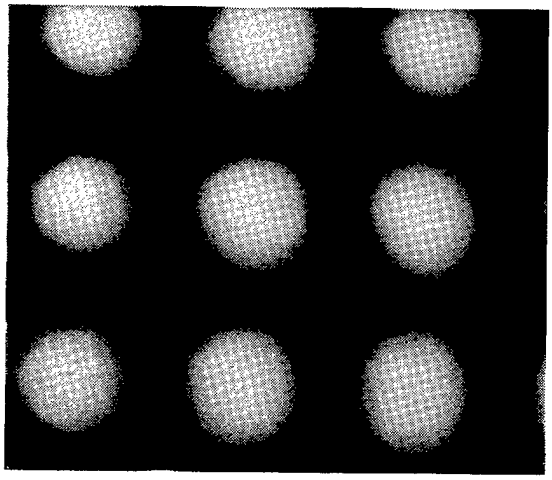

FIGURE 8. MICROLENS FABRICATED WITH THE GRAYSCALE PROCESS.

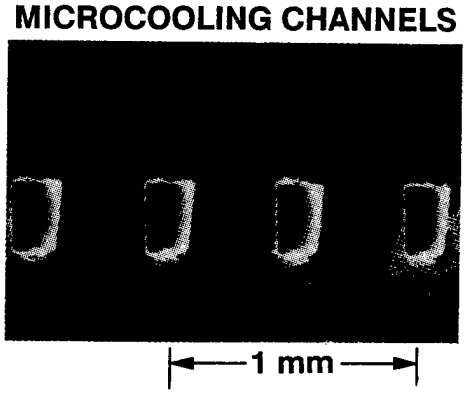

FIGURE 9. EXAMPLE FOR MICROCHANNEL FABRICATED WITH A HOT KOH ETCH IN Si.

Top part of channel is closed by fusion bonding to a separate Si wafer.

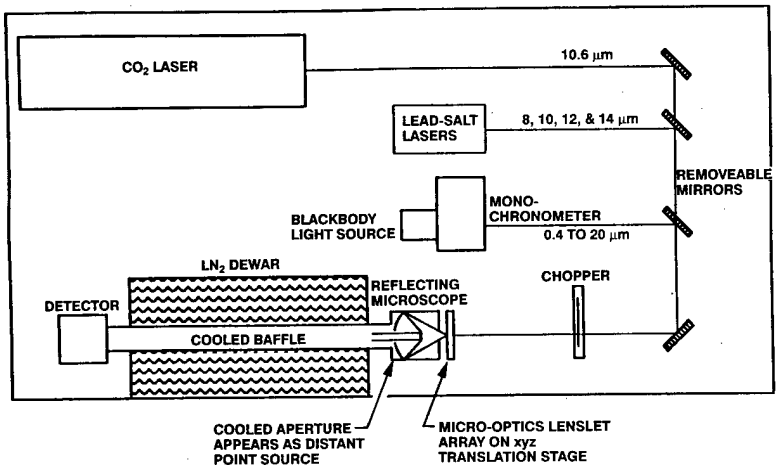

a. OPTICAL BENCH LAYOUT

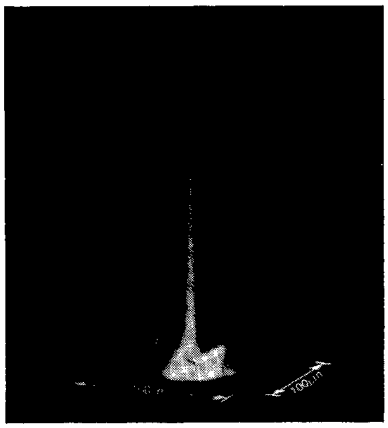

b. MEASURED PSD FOR A SINGLE MICROLENS SHOWN IN FIG. 7

FIGURE 10. MICROLENS PERFORMANCE TEST.

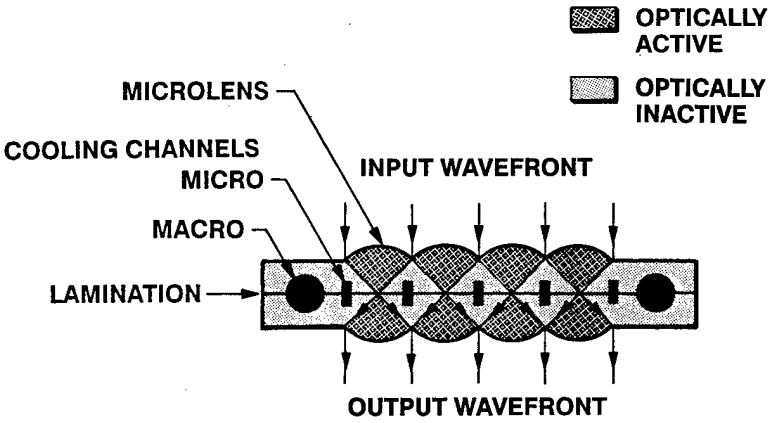

FIGURE 11. USE OF MICROLENS ARRAY AT THE APERTURE CREATES OPTICALLY INACTIVE VOLUME FOR MICROCHANNELS FOR INTERNAL COOLING.

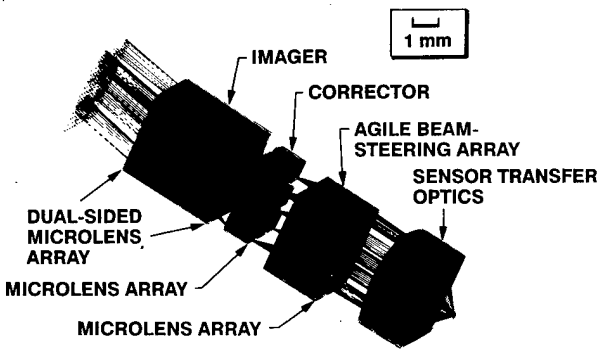

a. 3 × 3 ELEMENT SEGMENT OF THE ABS UNIT

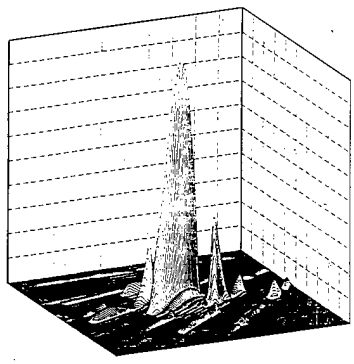

b. UNCORRECTED POINT-SPREAD FUNCTION FOR A 9 × 9 ELEMENT SEGMENT AT THE UNSCANNED POSITION

FIGURE 12. DESIGN EXAMPLE FOR A POLYCHROMATIC PHASED-ARRAY WINDOW OPERATING IN THE MWIR WAVEBAND REGION.

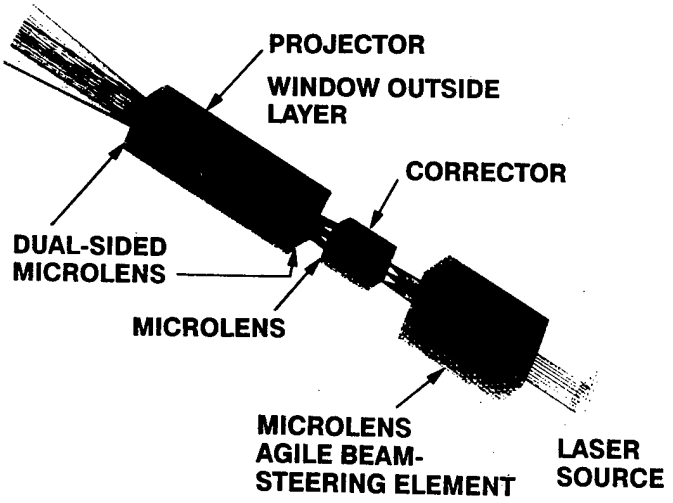

a. UNIT CELL OF A LASER BEAM DIRECTOR

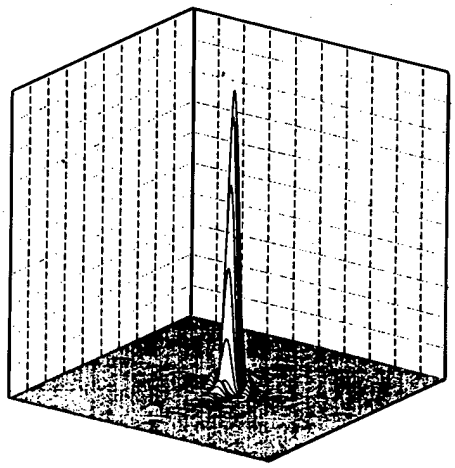

b. POINT-SPREAD FUNCTION OF A 9 × 9 ELEMENT PHASED-ARRAY APERTURE AT EIGENANGLE SCANNED POSITION

FIGURE 13. EXAMPLE FOR A MONOCHROMATIC ABS DESIGN.

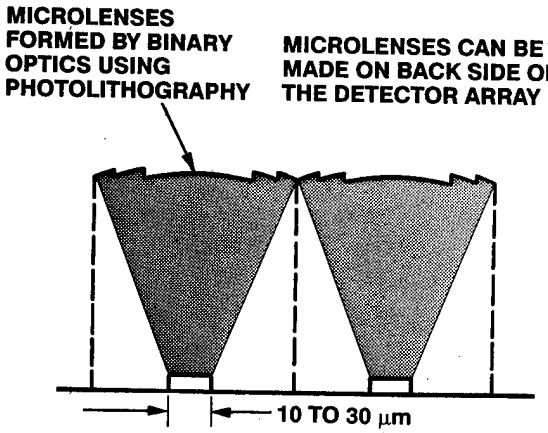

FIGURE 14. CONCEPT OF MICROLENS INTEGRATED WITH A DETECTOR.

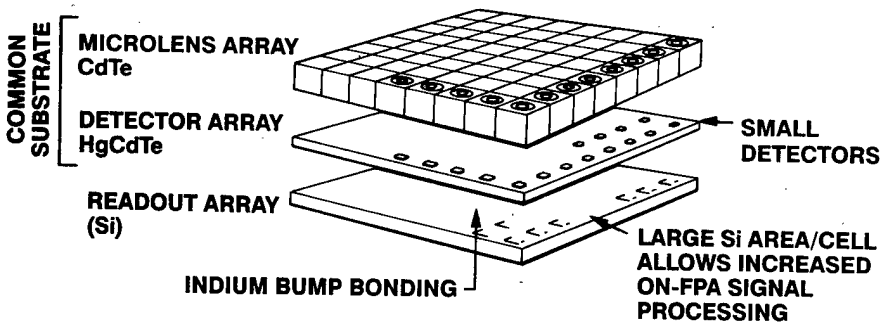

FIGURE 15. PHOTONIC HYBRID ARRAY FOR LWIR HIGH-PERFORMANCE FOCAL PLANE.

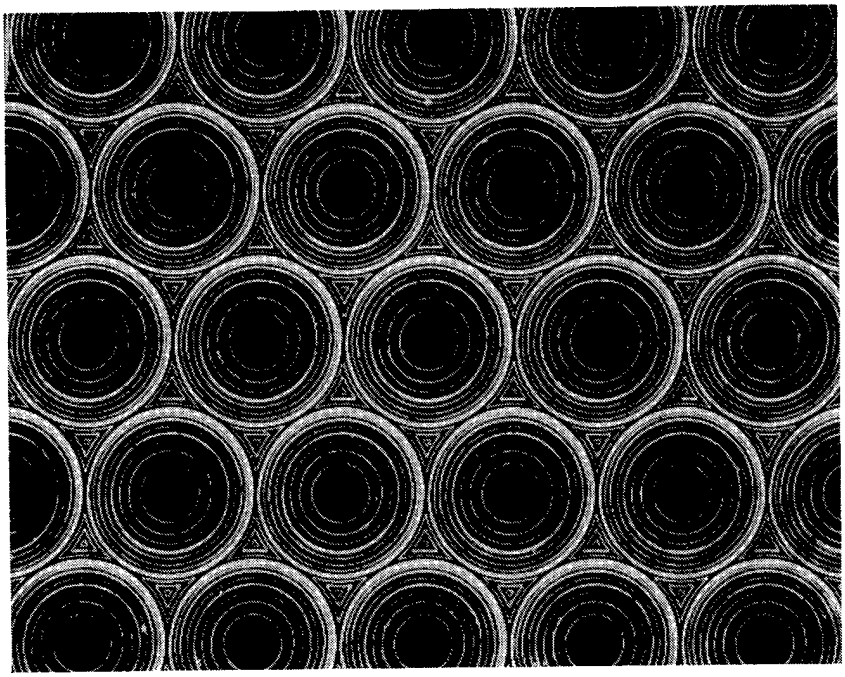

FIGURE 16. CdTe MICROLENS ARRAY WITH HEXAGONAL PIXEL LAYOUT FOR LWIR OPERATION.

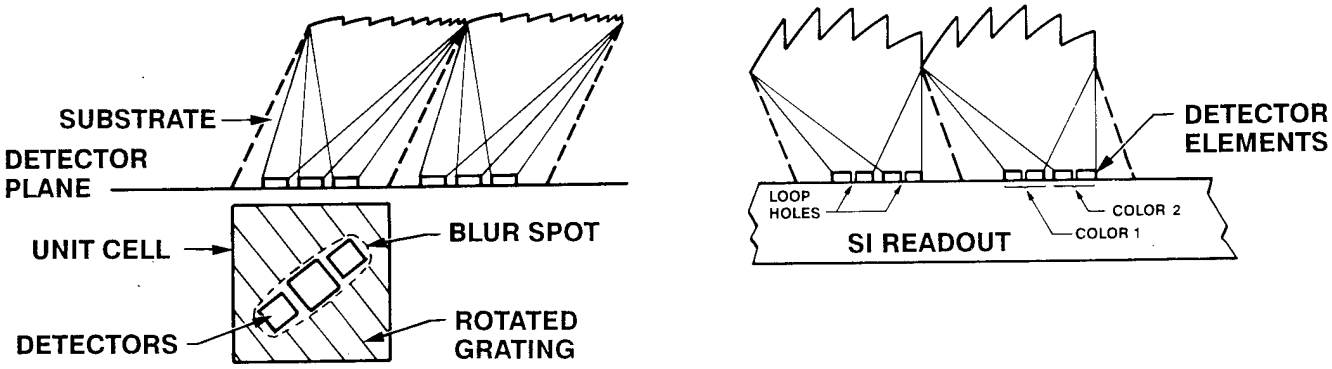

a. DISPERSIVE DIFFRACTIVE

b. DISPERSIVE REFRACTIVE

FIGURE 17. DISPERSIVE MICROLENS CONCEPT.

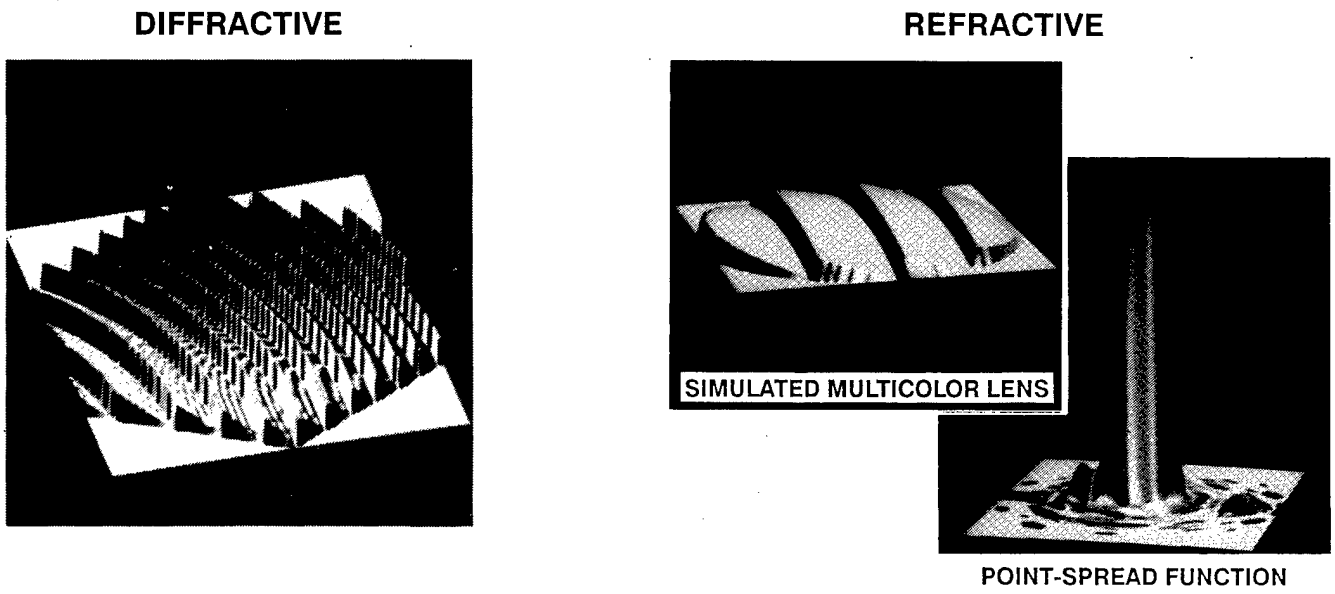

FIGURE 18. SIMULATION OF DISPERSIVE MICROLENSES AND PREDICTED OUTPUT.

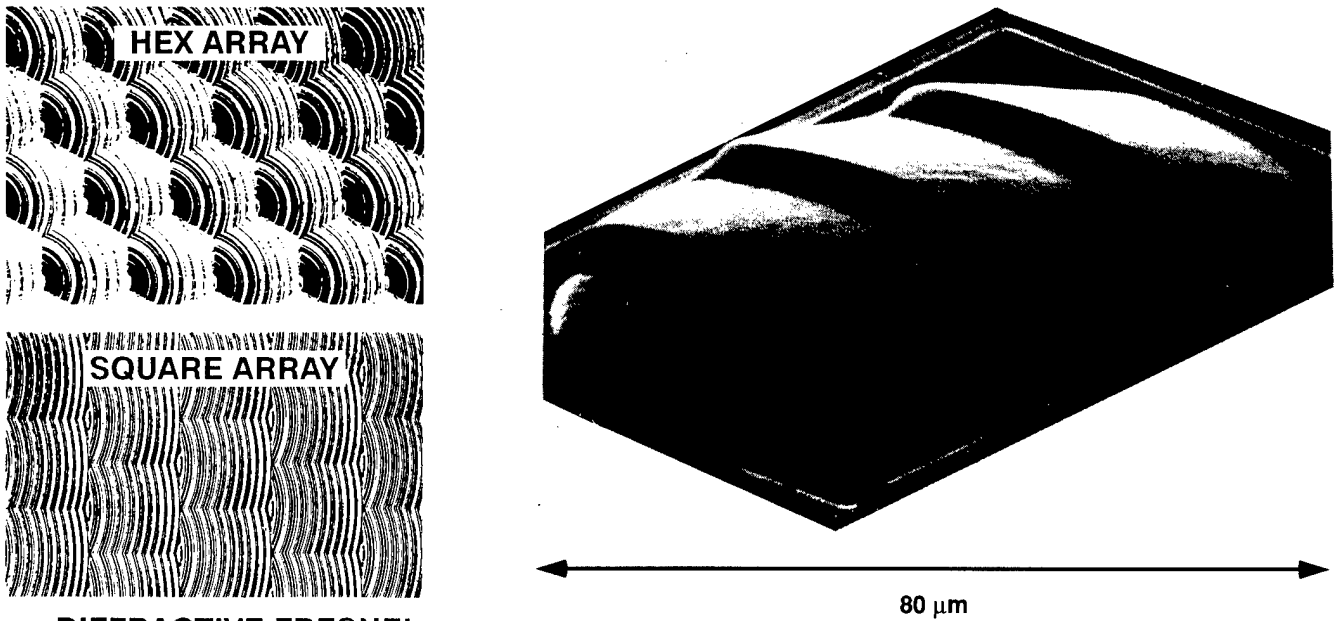

a. DIFFRACTIVE FRESNEL TYPE WITH BINARY METHODS

b. REFRACTIVE TYPE WITH GRAYSCALE MASK

FIGURE 19. FABRICATED DISPERSIVE MICROLENSES.

FABRICATION OF MICRO-OPTICAL DEVICES

W. W. Anderson, J. Marley, and G. Gal
Lockheed Palo Alto Research Laboratory
3251 Hanover Street, Palo Alto, California 94304
and
D. Purdy
Philips Infrared Defense Components
Philips Components Limited
Southampton, Hampshire, SO9 7QG

ABSTRACT

We have fabricated a variety of micro-optic components including Fresnel and non-Fresnel lenses, off-axis and dispersive lenses with binary stepped contours and analog contours. Process details for all lens designs fabricated are given including multistep photolithography for binary fabrication and grayscale mask photolithography for analog fabrication. Reactive ion etching and ion beam milling are described for the binary fabrication process, while ion beam milling was used for the analog fabrication process. Examples of micro-optic components fabricated in both Si and CdTe substrates are given.

1.0 INTRODUCTION

We differentiate between two fabrication options for micro-optical components as binary and analog. Within each of these fabrication options, the components may be designed as Fresnel or non-Fresnel. These distinctions are illustrated in Figure 1. The discrete jumps in the Fresnel elements correspond to changes of 2π in phase. The thickness of Fresnel elements is $\lambda/(n - 1)$, independent of element type, where n is the refractive index of the substrate material and λ is the design wavelength. The limited thickness of Fresnel elements relaxes the requirement of deep etching, but the Fresnel elements suffer from chromatic aberration.

The binary fabrication process derives its name from the sequence of process steps indicated in Figure 2 wherein a set of m photomasking and etching steps results in 2^m distinct levels. The photolithographic masks are either transparent or opaque. The analog fabrication process derives its name from the continuous curvature of the fabricated component which, in turn, derives its shape from the (almost) continuous grayscale optical density of a single photomask and the exposure/development process of positive photoresist.

The binary fabrication technology was originally described by d'Auaria et al.[1] Limitations of this technology include limitations on photolithographically definable feature size, accuracy of multiple masking step alignments, anisotropy of etching processes and maximum etching depths available. Several of these issues have been addressed in the past few years.[2]

An early version of analog fabrication of microlenses was described by Wada.[3] Baking a small circular positive photoresist layer above the glass transition temperature was found to produce a spherical contour of the photoresist dot by the action of surface tension. The spherical contour was reproduced in the substrate by ion milling. This technique was limited to special shapes. In a positive photoresist system, the exposed areas become more soluble than the unexposed regions. By a grayscale exposure, the percentage of photoresist remaining after development is a function of exposure. Thus, ion milling of a substrate after exposure through a grayscale mask will replicate the photoresist profile in the substrate. Limitations of this technology include limitations on grayscale mask characteristics, differential etching characteristics of photoresist and substrate, and maximum etching depths available.

Both fabrication technologies require photolithography followed by anisotropic etching via reactive ion etching (RIE) or ion beam milling. The chemistry of RIE is quite substrate specific and so tends to be limited to the binary fabrication process wherein we wish to etch the substrate only and leave the masking layer intact. Ion milling, on the other hand, is a purely physical phenomenon in which the incoming ions are energetic enough to sputter material from the surface of the wafer. Thus the masking layer will be etched at a rate proportional to the substrate etching rate. Etching characteristics of both processes tend to be machine specific but once a machine is properly calibrated, the results are quite reproducible both with respect to depth versus time and anisotropy of etch.

A number of optical functions can be realized by properly designed and fabricated micro-optical components, as described in our companion papers.[4-6] In this paper, we will describe our experience with the fabrication of a variety of micro-optics lenses by both analog and binary fabrication technologies.

2.0 BINARY FABRICATION

In this section, we describe the fabrication of simple microlens arrays for operation at a wavelength of 10.6 μm in both Si and CdTe substrate materials. In addition we will describe preliminary results on the fabrication of wideband and dispersive microlenses in CdTe. Two anisotropic etching technologies were utilized, RIE and ion beam milling. In addition, two separate masking sequences were used, fine-to-coarse and coarse-to-fine. The optical performance of the lenses is described in Reference 6.

---

1. d'Auaria, L., J. P. Huignard, A. M. Roy, and E. Spitz "Photolithographic Fabrication of Thin Film Lenses," *Opt. Commun.*, Vol. 5, 1972, pp. 232-235.
2. Stern, M. B., and S. S. Medeiros, "Deep Three-Dimensional Microstructure Fabrication for Infrared Binary Optics," *J. Vac. Sci. Technol.*, Vol. B 10, 1992, p. 2520.
3. Wada, O., "Ion-Beam Etching of InP and Its Application to the Fabrication of High Radiance InGaAsP/InP Light Emitting Diodes," *J. Electrochem. Soc.*, Vol. 131, 1984, p. 2372.
4. Gal, G., et al., "Micro-Optics Technology for Sensor System Applications," Conference on Binary Optics, Huntsville, AL, 1993.
5. Herman, B., and G. Gal, "Theory of Dispersive Microlenses," Conference on Binary Optics, Huntsville, AL, 1993.
6. Shough, D., B. Herman, and G. Gal, "Measurements of Microlens Performance," Conference on Binary Optics, Huntsville, AL, 1993.

The simple lens array mask consisted of a 16 × 16 lens array at the center of the mask, lens doublets widely spaced along orthogonal axes centered on the array, and single lenses sparsely populating the rest of the 12 mm × 12 mm mask area. The singlets and doublets were for diagnostic purposes such as individual lens point-spread-function (PSF) measurement, nearest neighbor crosstalk determination, and large area uniformity evaluation. (A non-negligible consideration was the cost of a fully populated, e.g., 128 × 128 array, set of lens array masks.) In addition to the three-level mask set (which provided eight distinct phase steps modulo 2π), a light-blocking metallization mask was utilized to isolate the individual lens elements and arrays.

The master masks were 1X electron-beam generated using a 0.1-μm spot size. The substrate material was 4 × 4 × 0.6-in. quartz coated with antireflective chrome. Minimum feature size was 0.5 μm. For this work, working plates were made from the masters. If feature sizes smaller than 0.5 μm were required, the quartz master plates would be used due to their low expansion coefficient and superior ultraviolet transmission characteristics. Each individual lens was 100 μm × 100 μm. Since the same mask set was used for Si and CdTe, the Si lens was designed to have a focal length of 525 μm and the CdTe lens to have a focal length of 420 μm.

2.1 BINARY ETCHING

Anisotropic etching to depths of $\lambda/8(n-1)$ to $\lambda/2(n-1)$ is required. Uniformity of etching on the order of $\lambda/20$ is required over the entire lens array area. A step-wise approximation to a smooth profile may be fabricated by a multiple-step, binary-etching process as shown in Figure 2 for a positive photoresist. The anisotropic etching depths progress from $\lambda/8(n-1)$ to $\lambda/2(n-1)$ for the fine-to-coarse sequence shown in Figure 2. The same final profile could, in principle, be obtained by reversing the sequence to a coarse-to-fine order. In either sequence, multiple step lithographic processing will result in photoresist surface texturing the order of $\lambda/2(n-1)$, which may degrade the photolithographic resolution attainable.

The etching must produce vertical side walls well registered with mask features (i.e., no undercutting or shadowing) or some lens area is lost. The etching must also produce smooth surfaces at the bottom of the etched area. Finally, the etch rate (or equivalently, etch depths) must be reproducible for a production process. The two technologies that satisfy these requirements are RIE and ion beam milling.

In RIE, ions produced in a plasma discharge react with a substrate material to form a volatile compound which is then removed from the system. The RIE process is highly anisotropic so that vertical side walls are obtained at the phase steps.

In ion beam milling, a collimated, uniform beam of inert ions, extracted from a plasma discharge, bombards the surface of a substrate. The momentum transferred by these ions breaks the bonds of the substrate surface atoms. Material not protected by a mask is selectively etched away. Etch features down to 0.2 μm and with aspect ratios of 5:1 can be achieved.

The chemistry of RIE for Si is well established so we used this technology for fabrication of Si components. The chemistry of CdTe is both more complex (a binary compound) and more primitive (limited level of developmental effort vis à vis Si) than that of Si, so the physical process of ion beam milling was used for the fabrication of CdTe components.

2.2 Si MICROLENS FABRICATION

Si substrate material specifications were: double-side optical-grade surfaces, <100> orientation (for RIE etching properties), 500 to 550-μm thickness (to place lens focal point near

opposite surface when illuminated from lens side), and resistivity $>10\ \Omega$-cm (to minimize free carrier absorption at 10.6 μm). The substrates were cleaned by soaking in a H_2SO_4/H_2O_2 bath at 120°C to remove organic residues. They were then immersed in a rinse tank of DI water until the water resistivity recovered to $>10\ M\Omega$.

The Si micro-lenses were fabricated in a fine-to-coarse feature sequence as shown in Figure 2. A 2-μm-thick photoresist layer was an adequate etch mask for the first etch step of 550 nm. However, transfer masks of 250 and 500 nm CVD-deposited oxide were required for the second and third etching steps.

RIE was performed in a Plasma Therm 700 wafer/batch system using a Cl-based chemistry of $SiCl_4$:BCl_3:Cl_2 introduced into the etch chamber at 35:5:5-sccm flow rates. With a chamber base pressure of 20 mTorr, the Si etch rate was $\approx$46 nm/min. The Si to oxide selectivity etch rate was 10:1 which determined the choice of the transfer mask oxide thicknesses mentioned above. The etch time for the fine feature mask did not polymerize the photoresist so it was easily stripped after etching. However, it was necessary to remove the photoresist from the oxide transfer masks prior to etching since the required longer etch times polymerized the photoresist making it difficult to remove.

In Figure 3 we show a low magnification scanning electron microscope (SEM) micrograph of the 16 $\times$ 16 array of Si microlenses to provide a qualitative indication of the uniformity achieved over the array. Note that individual lenses are of Fresnel type and are 100-μm $\times$ 100-μm squares. The principal defects are isolated photoresist fragments. In Figure 4 we show a higher magnification SEM micrograph of the array at a 65° angle to reveal the depth profile. Of particular note are the 2π phase steps near the lens corners and the various characteristics of the edges associated with multiple masking and etching steps as indicated in Figure 2.

The 2π phase step is shown in the higher magnification SEM of Figure 5. Note the stratigraphic marks of the $\lambda/8$, $\lambda/4$, and $\lambda/2$ etching steps and their order in the 2π phase step wall. From Figure 2e we see that this wall was formed by first, the shallow $\lambda/8$ etch step, then the $\lambda/4$ etch step and finally the $\lambda/2$ etch step and, from Figure 2d, that there were two alignment steps after the initial shallow etch step. The other double alignment edge indicated in Figure 2d can result in rather distinct features associated with slight mask misalignment problems as shown in Figure 6a. If the subsequent masking steps for an edge are offset as indicated in Figure 6b, then trenching of the double alignment edge between levels 3 and 4 of Figure 2e and of the single alignment edge between levels 1 and 2 of Figure 2e are as predicted in Figure 6c and observed in Figure 6a.

2.3 CdTe MICROLENS FABRICATION

New low-temperature lithographic and ion milling process schedules were developed in order to be compatible with future dual-sided, integrated HgCdTe focal plane array processing. Samples of CdTe 1.5 $\times$ 1.5 cm were polished to an optical finish on both sides with 0.1-μm alumina abrasive to a flatness of less than three fringes. The samples were lapped to a thickness of 425 μm. They were mounted on 5-cm polished sapphire substrates with paraffin and Turcowax-5580. This technique is intended to provide sample support throughout the entire fabrication procedure without remounting after each resist process. Ion milling of CdTe was accomplished using 500 V argon ions at a current density of 0.31 ma/cm^2 in a Technics Model 20 ion mill equipped with a cooled sample stage. Up to three samples could be pressure mounted against the water-cooled sample substrate holder which was positioned at an angle of 25° to the ion beam and rotated at 4 rpm. The sample temperature was monitored during milling using temperature-sensitive decals and maintained at a temperature below 80°C. These parameters resulted in a milling rate of 55 nm/min for CdTe.

Developed positive photoresist was used as the ion milling mask. Etch selectivity toward photoresist improves with increasing resist baking temperature. Since we limited our maximum process temperature to 80°C, the resist milling occurs at about 15 nm/min or an etch selectivity of about 3.7:1, CdTe to resist. In our standard process, the photoresist is baked at 120°C which results in an ion milling rate of about 10 nm/min or a selectivity ratio of about 5.5:1. A higher selectivity allows the use of a thinner resist schedule which, in turn, permits a more accurate pattern transfer. However, the lower selectivity does not seem to have had an adverse effect on our pattern replication. The lower process temperature results in easier resist stripping and less chance of resist distortion. Separate calibration runs were performed before each lens milling run. Milling depths were generally within $\pm 5\%$ of the target value, i.e., within $\lambda/20$.

In Figure 7 we show SEM photomicrographs of a CdTe broadband microlens array fabricated with the same set of masks used for the Si microlens array shown in Figures 3 through 6. (Figure 7 is directly comparable with Figure 4 for the Si array.) Gross quality of this array is comparable to that of the Si array. Higher magnification SEM micrographs reveal distinct differences in the wall features between RIE fabrication of Si and ion beam milling of CdTe. Trenching and redeposition during ion milling are well known[7] and both are evident in the higher resolution SEM micrographs of the fracture cross section in Figure 8. Overall fabrication defects of < 1 μm ($\lambda/10$) did not affect optical performance significantly This lens produced near theoretical diffraction limited performance as described in Reference 6.

A set of nine microlens designs, including various combinations of pixel shapes and dispersive lenses of various orders and grating orientations, was developed and fabricated as a research test wafer to demonstrate the power of binary-fabricated micro-optics. Some of the lenses and arrays as fabricated by ion milling of CdTe are shown in Figures 9 and 10. The photomasks were divided into nine zones, one for each lens type. Each zone was partially populated with single lenses, doublets, 2 × 2 arrays, 4 × 4 arrays, and some special diagnostic arrays dependent on the particular lens design in each zone.

The dispersive lens mask set is a 1 × E-beam generated master mask set, consisting of three layers for lens generation and a fourth layer for reflective metallization of areas outside the lenses. The patterns were written with a 0.1-μm E-beam spot size which resulted in a minimum resolvable feature size of 0.4 to 0.5 μm. Submicron resolution was required on mask layer 3 since several lens types contained features as small as 0.8 μm.

The small feature size required that we use the E-beam generated master masks for our contact photolithography process. The mask vendor was unable to print low defect chrome copies of the finest geometries contained on mask layer 3 because of too-small feature sizes. Results to date suggest that mask damage occurring from contact between mask and substrate is not currently a significant factor. Successful submicron feature resolution may be improved with better and more reproducible mask-to-substrate contact. This can usually be achieved by initially mounting the sample as flat as possible on the sapphire substrate carrier. An added advantage could be obtained by printing images with conformable masks. Near-perfect contact is easier to achieve if either the mask or the substrate is able to conform to the opposite member. Since the sapphire substrate is purposely chosen for its stiffness to minimize CdTe fracture, the mask must be the flexible element.

All the dispersive microlens fabrication has used AZ 5214-E positive resist since the AZ 5200 series product has submicron resolution capability and offers near-vertical profiles to give

7. Glöersen, P. G., "Ion-Beam Etching," *J. Vac. Sci. Technol.*, Vol. 12, 1975, p. 12.

accurate pattern transfer in ion beam etching applications. It also has high thermal stability to maintain resist profile quality in severe process environments. The smallest geometries are printed first on a completely planar surface so depth of field is not an issue. Also, no alignment is required on the first mask. Resist thickness is 1 to 1.5 μm. Layer 2 is also aligned under rather favorable conditions. The first milling step resulted in 0.75-μm-deep features in the CdTe surface and is the next most favorable surface for applying a thin, uniform resist layer for patterning the second layer using 1.5 μm of photoresist. After milling the second pattern the total surface topography is about 2.25 μm at the deepest feature which makes uniform resist coating and exposure of the third layer much more difficult. Line width narrowing due to over exposure of the top of narrow features as well as underexposure of the resist-covered trenches may result in broadening of the deepest features. Linewidth variations may also occur due to any layer-to-layer misalignment.

Successful printing of mask layer 3 on small samples of CdTe was anticipated to offer a very challenging process sequence, especially since the mask vendor was unable to fabricate chrome mask copies on ultraflat quartz plates under ideal conditions. However, the smallest features, namely 0.8-μm lines and spaces were successfully printed and developed on both CdTe and Si. The most difficult process steps have involved obtaining accurate mask registration over all nine zones simultaneously. Excessive resist reworking has often been required on some of the CdTe samples. This may be due in part to lack of flatness either on the sample surfaces or due to the mounting process on the sapphire wafers. We have found that repeated remasking can cause extensive sample damage by fracturing the finest features at the edges of lens arrays.

3.0 ANALOG FABRICATION

The analog fabrication of arbitrary topographies relies on the process characteristics of positive photoresists and the anisotropic etching characteristics of the ion milling process.

Positive resists contain a photosensitive dissolution inhibitor, an alkaline-soluble base polymer, and a solvent. The dissolution inhibitor prevents the base polymer from dissolving in the alkaline developer. After exposure to light, the dissolution inhibitor concentration is reduced in selected areas, leading to an increased solubility. The relevant characterization of the resist is a "characteristic curve," as shown in Figure 11, giving the percentage of resist remaining after development as a function of exposure. By exposing the photoresist through a grayscale mask[8] such that the maximum exposure is less than the threshold exposure, Eo, the quantity of photoresist remaining after development will be a one-to-one analog of the optical density of the mask. Obviously, the characteristic curve must be used to determine the optical density of the mask for a desired residual photoresist thickness.

Ion milling and rf-sputter etching have the capability of quite faithfully reproducing in relief in a substrate a pattern formed in photoresist on the substrate surface. Ion milling machines have been developed which allow control of incident ion beam angle, ion beam energy, and current density (or flux density if the beam has been neutralized). In Figure 12, if the etch rate of the resist is R_1 and the etch rate of the substrate is R_2, then the total thickness of material removed is

$$\Delta(x) + \mu(x) = \Delta(x) + (t - \Delta(x)/R_1)R_2$$

8. Gal, G., "Method and Apparatus for Fabricating Microlens," under patent application, 1992.

as long as the etch time is sufficiently long to remove all of the photoresist, i.e., $t > \Delta(x)_{max}/R_1$. The final substrate profile is then given by

$$h(x) = \Delta(x)/k + H - R_2 t$$

where k is the relative etch rate of resist and substrate, $k = R_1/R_2$. Since photoresist typically mills at a rate of 20 nm/min and semiconductors at a rate of 40 nm/min, the relative milling rate, $k \approx 0.5 < 1$, and the milled topography will be an amplified version of the residual photoresist topography as indicated in Figure 12.

The fabrication of nonspherical surfaces such as a refractive/dispersive optic by standard techniques, such as the reflow of photoresist, have limited scope for further development. Consequently, it was necessary to develop a more flexible process. The adapted technique depends upon the exposure of a positive resist through a specially designed grayscale mask which was used to, in effect, photosculpt the surface relief pattern. Such a technique enables aspheric lens to be fabricated in a high-density matrix and is ideally suited to nonsymmetrical surfaces, such as the dispersive micro-optic. Modern electron beam mask writing systems can now achieve detail fine enough to enable half-tone-type images to be generated at a pixel size of 1-μm or less. The number of grayscales available from our mask design was 256. Current Philips designs contain nearly 1000 grayscale levels. This enables three-dimensional surfaces to be created with submicron accuracy and facilitates the production of the combined refractive/dispersive surface. This process eliminates the mask registration problem associated with binary fabrication and the too-small feature sizes required on multiple mask sets for an optic operating at short wavelengths (e.g., in the visible).

The first mask manufactured using this principle was a linear scale of stepped values used to calibrate the sensitivity of the resist and the resultant depth of exposure achieved for each gray level in the mask. Using this calibration for exposure depth versus gray value, a mask was produced where the contours of the refractive/dispersive optical design were encoded into gray values at each spatial coordinate of pixel steps in the x and y directions. The resultant mask was used on a 10:1 stepper to expose a resist layer of suitable thickness. Development of the resist revealed an array of lens images which were ready to be transferred into the supporting substrate. The thickness of this substrate matched the focal length of the optical design and, after transfer of the resist image, the optic needed no further work to complete it.

The transfer of the resist image uses ion beam milling where all the parameters were controlled in such a way that the resist is made to erode at the same rate as the underlying substrate in an anisotropic fashion, i.e., $k = 1$ from the discussion above. Two SEM views of the finished lens are shown in Figure 13. Note the smooth contour of the analog surface vis à vis the highly textured surfaces of the binary-fabricated lenses shown in Figures 9 and 10.

The optical components were fabricated and tested by Philips for their ability to disperse infrared radiation from a 500 K blackbody. Detection of the position of the dispersed radiation was made by comparing the spectral response curves taken from each element in a linear array of small detectors spaced at 20-μm pitch. The optical elements were mounted in contact with this detector array. The pitch between the optical elements was 85 μm and, therefore, the resultant vernier effect enabled the dispersion effect to be evaluated in some detail. The cutoff wavelength of the array was 12 μm at 77 K and a shift of peak sensitivity from 8 to 12 μm was observed over a linear distance of about 50 μm on the focal plane.

4.0 SUMMARY

We have described the fabrication of a number of micro-optic components, both Fresnel and non-Fresnel, broadband and dispersive, by binary and analog techniques. The advantages and disadvantages of the various fabrication technologies are summarized in Table 1 where + indicates a preferred advantage, + + indicates a significant advantage, - indicates a difficulty, and -- indicates a significant difficulty.

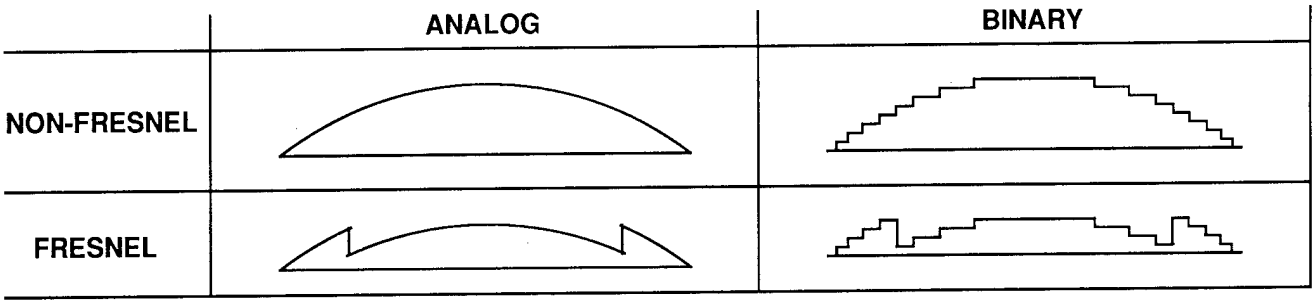

FIGURE 1. MICRO-OPTIC COMPONENT DESIGN AND FABRICATION OPTIONS.

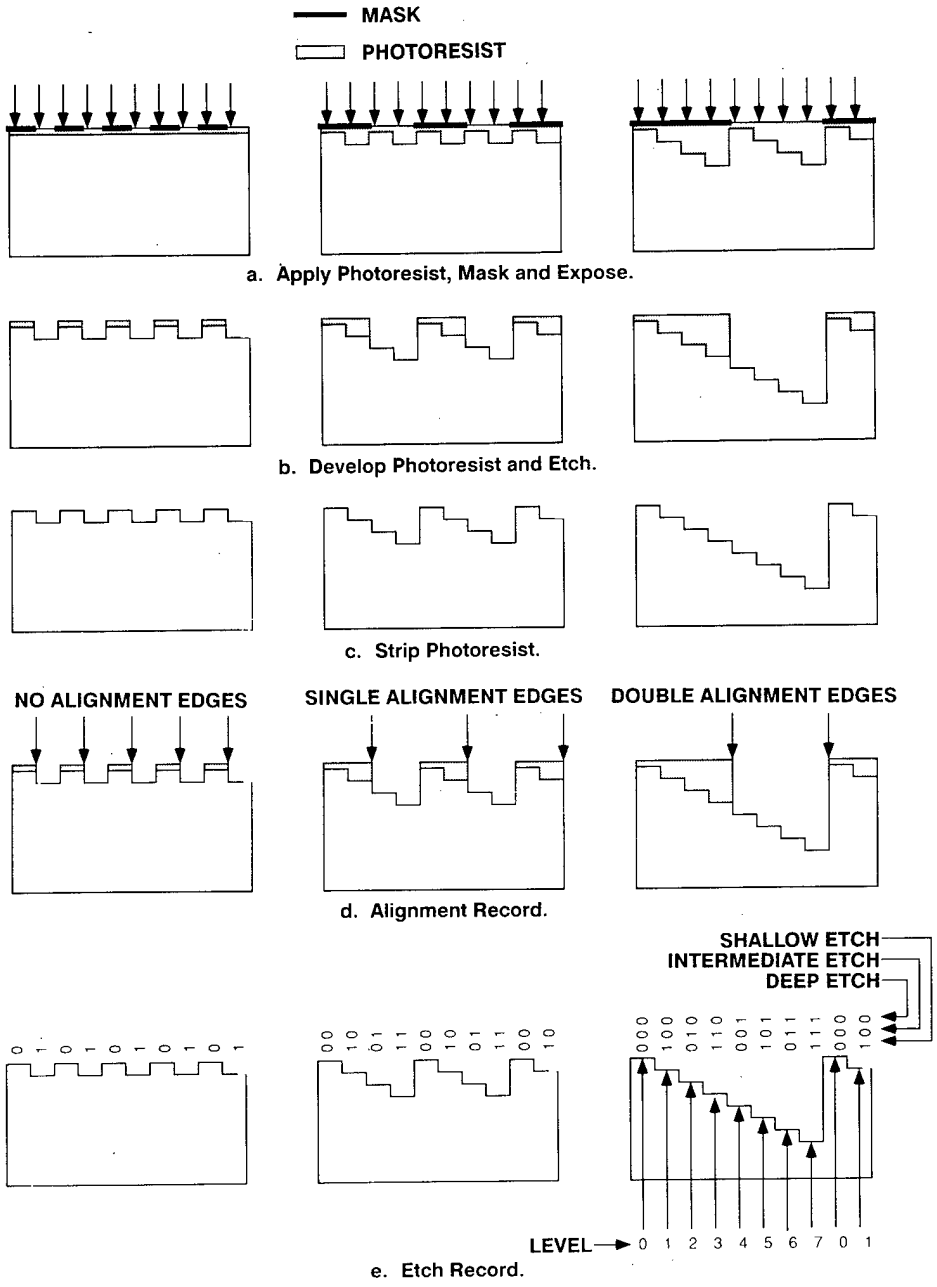

FIGURE 2. BINARY MICRO-OPTIC FABRICATION SEQUENCE.

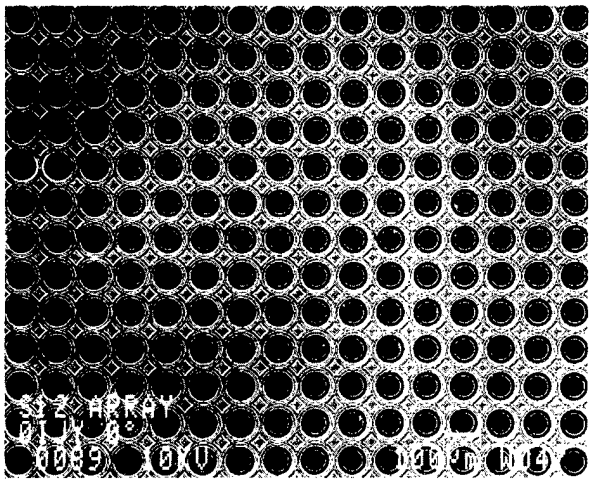

FIGURE 3. SEM MICROGRAPH OF 16 × 16 ARRAY OF Si MICROLENSES FABRICATED BY REACTIVE ION ETCHING.

FIGURE 4. SEM MICROGRAPH OF Si MICROLENS ARRAY AT 65° ANGLE. Note 2π phase step at individual lens corners.

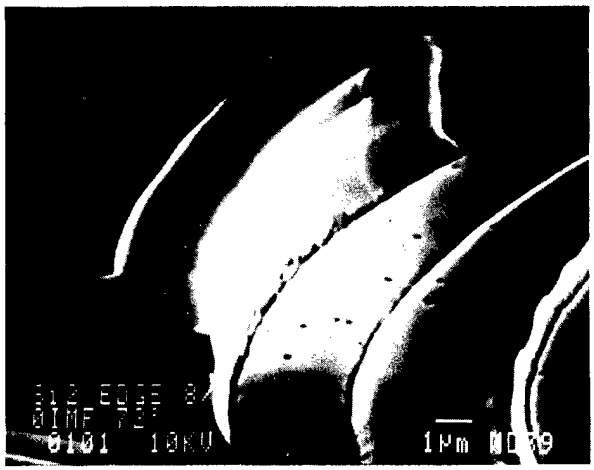

FIGURE 5. SEM MICROGRAPH OF 2π PHASE STEP. Note stratigraphic marks of $\lambda/8$, $\lambda/4$ and $\lambda/2$ etching steps in 2π wall.

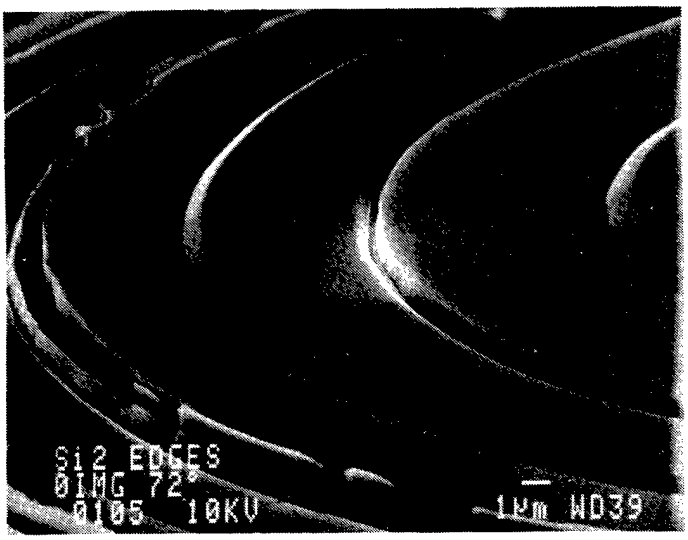

a. SEM Micrograph of Multiple Step Alignments and Etching.

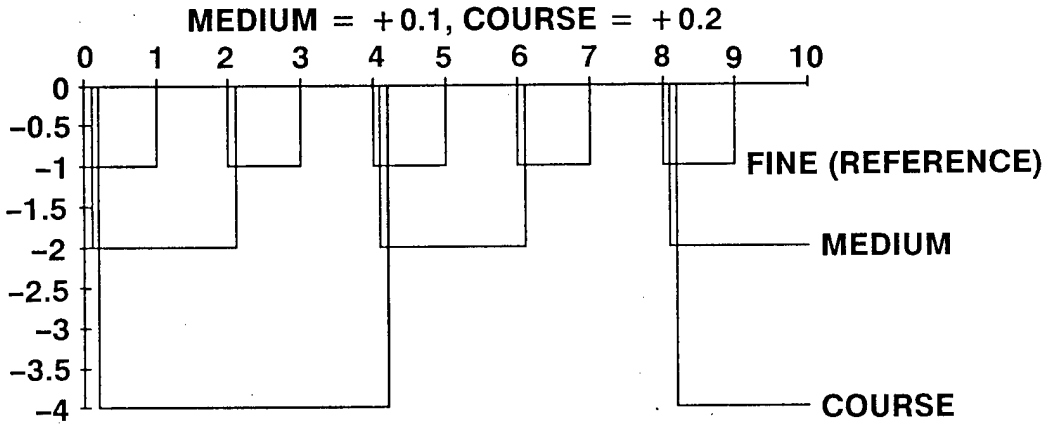

b. Relative Mask Alignments.

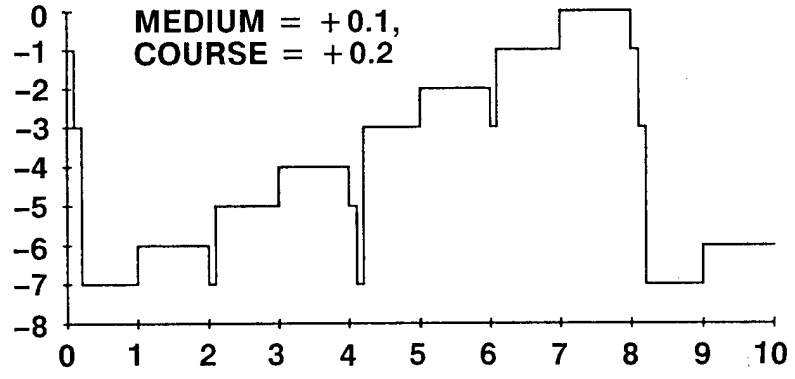

c. Resultant Etching Profile.

FIGURE 6. EFFECTS OF MISALIGNMENT IN MULTIPLE STEP BINARY MASKING OPERATIONS.

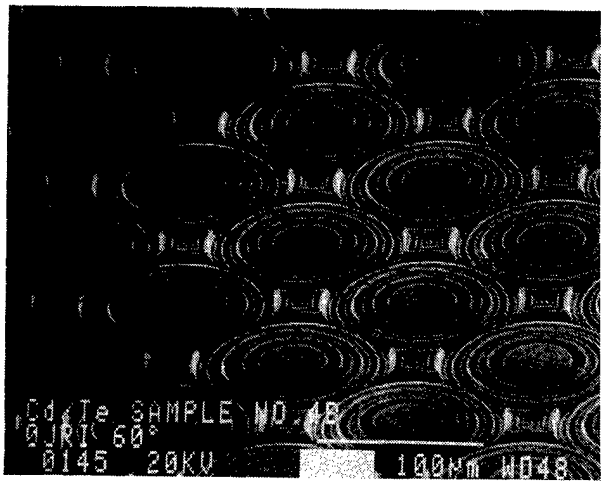

FIGURE 7. SEM MICROGRAPH OF CdTe MICROLENS ARRAY AT 65° ANGLE. Note 2π phase step at individual lens corners.

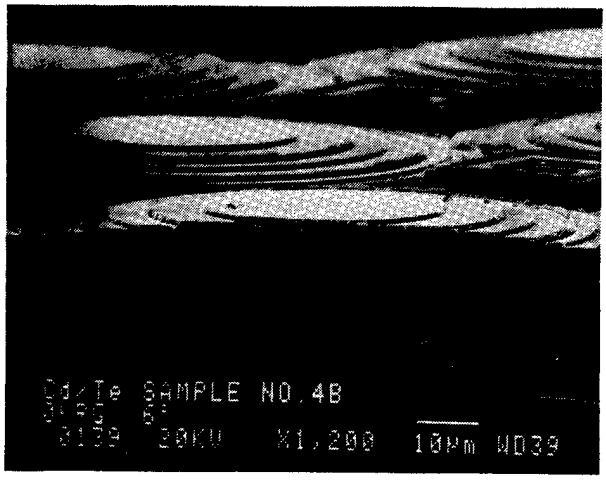

a. SEM Micrograph of CdTe Microlens Fracture Cross Section.

b. Detail of Ion Beam Etched Wall.

FIGURE 8. CHARACTERISTICS OF BINARY PHASE STEPS IN WALLS OF CdTe MICROLENS FABRICATED BY ION BEAM MILLING.

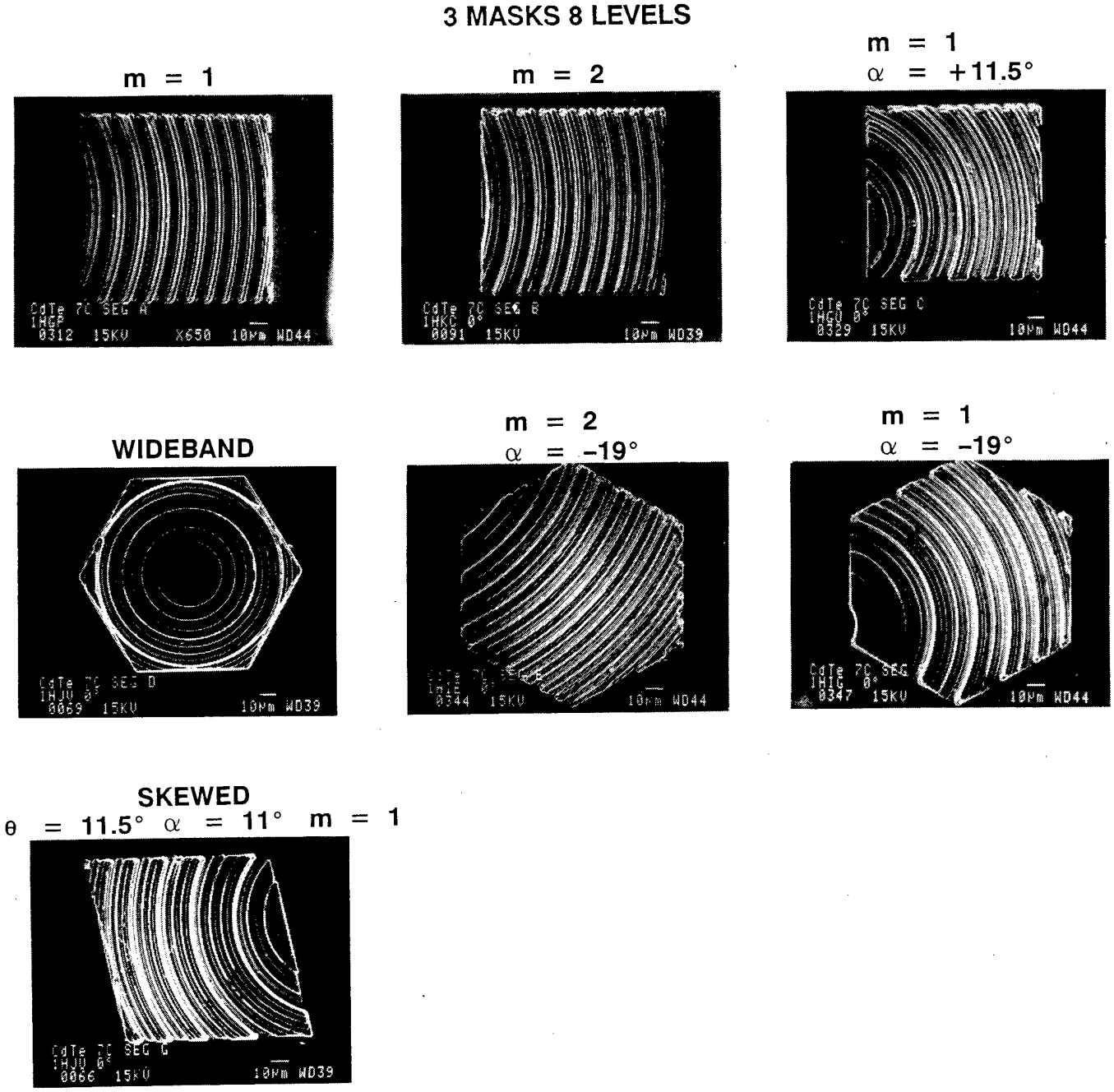

FIGURE 9. EXAMPLES OF BINARY FABRICATED WIDEBAND AND DISPERSIVE MICROLENSES FORMED IN CdTe.

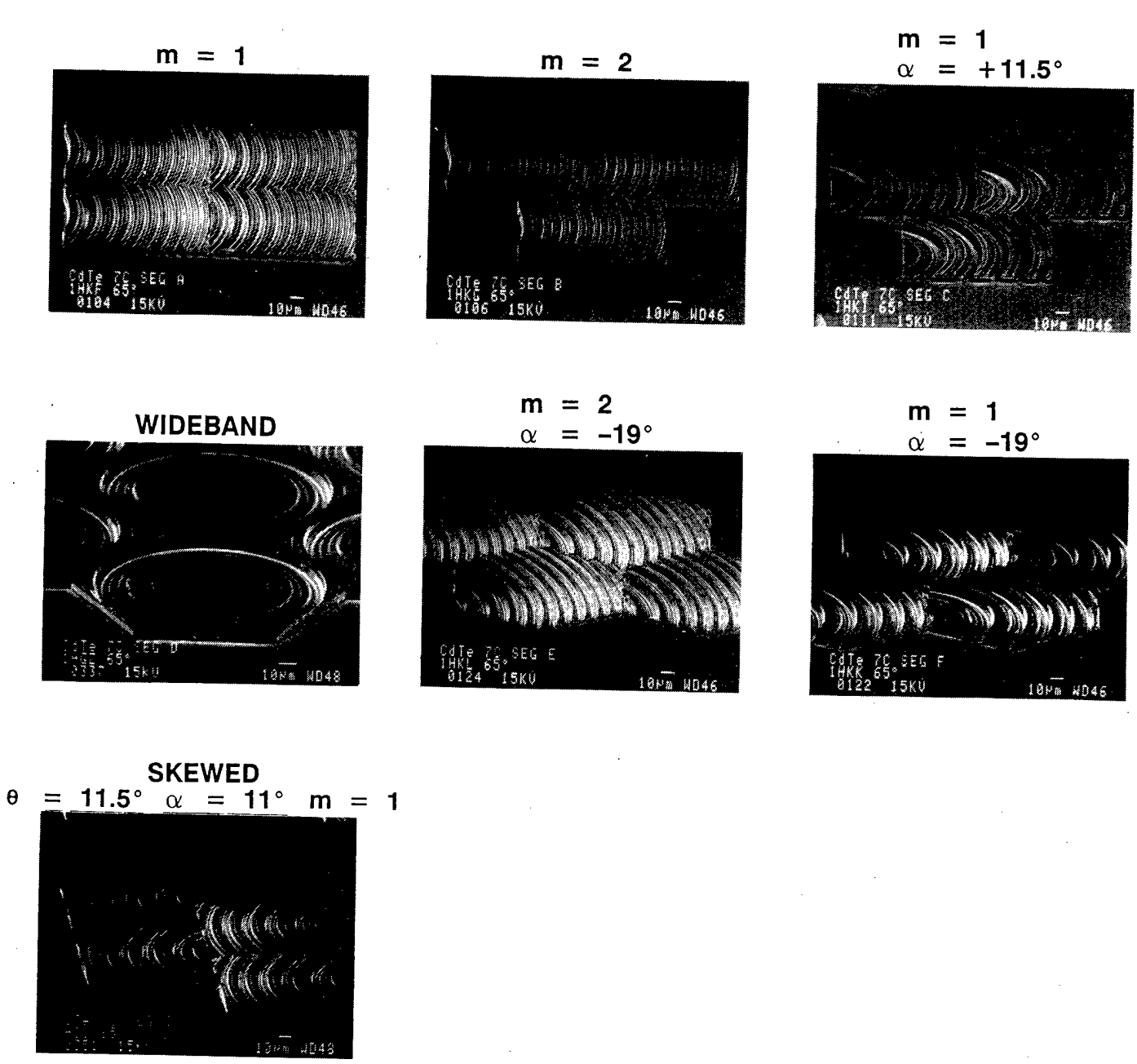

FIGURE 10. ARRAYED WIDEBAND AND DISPERSIVE MICROLENSES IN CdTe.

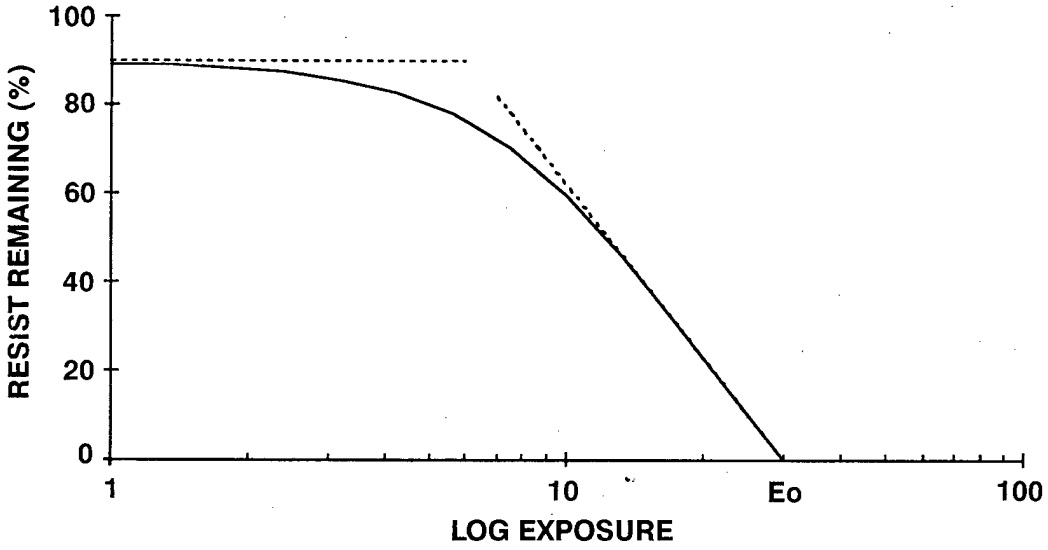

FIGURE 11. CHARACTERISTIC CURVE FOR A POSITIVE RESIST.

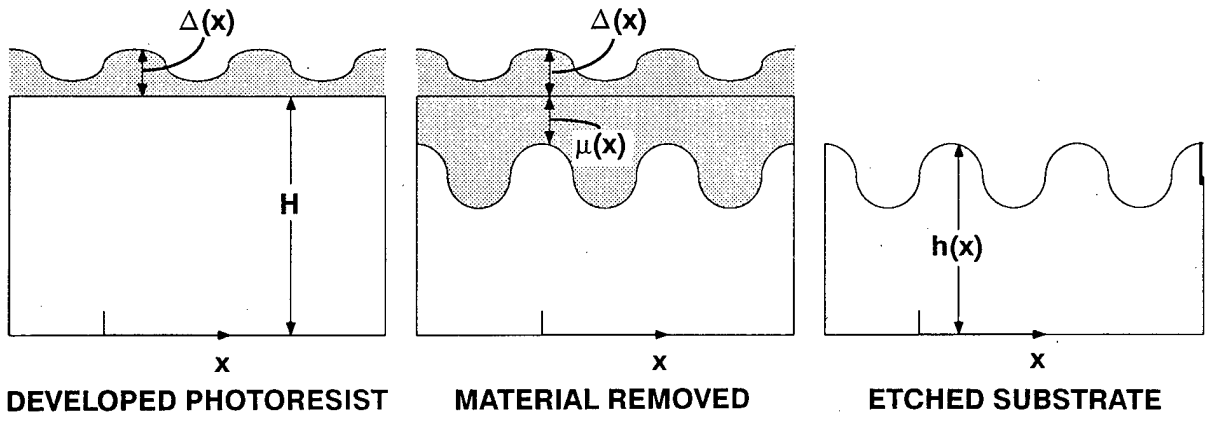

FIGURE 12. PHOTORESIST TOPOGRAPHICAL PATTERN TRANSFER BY ION MILLING.

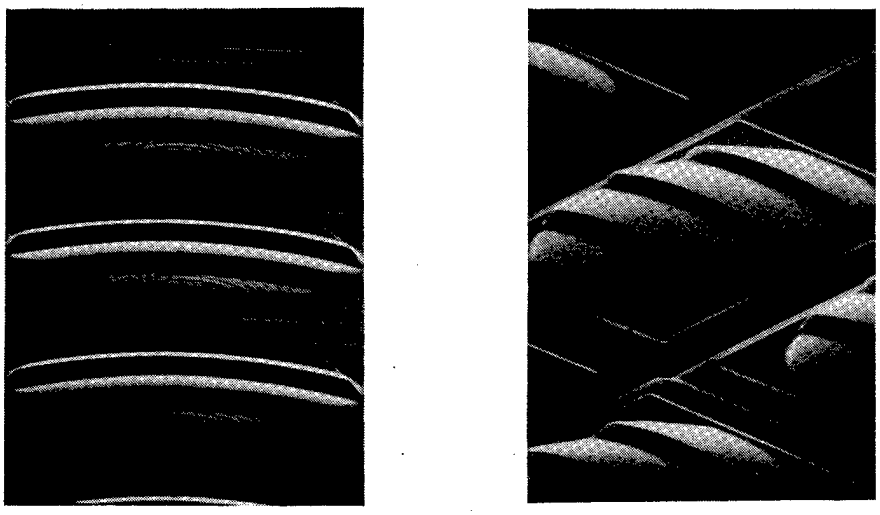

FIGURE 13. TWO SEM VIEWS OF ANALOG FABRICATED DISPERSIVE MICROLENS.

Diffractive Optics in Adverse Environments

February 24, 1993

Gregory P. Behrmann
Army Research Laboratory
AMSRL-SS-SF
2800 Powder Mill Road
Adelphi, MD 20783
(301) 394-3800

Abstract

An investigation at the Army Research Laboratory is in progress to characterize DOE performance in mil-spec environments. One of the most significant environmental influences is temperature. An analysis of a diffractive lens is presented in which optical performance is described as a function of temperature. In particular, we review the thermal dependence of focal length and diffraction efficiency. It is shown that the change in these parameters is independent of lens shape and relates only to material properties. Athermalized hybrid refractive/diffractive designs are discussed.

1.0 Introduction

For military and aerospace applications, temperature is one of the more important environmental influences. Typical military specifications can require a system to operate over a temperature range of -30°C to 50°C. In fact, it is not uncommon for commercial products to operate over a significant temperature range. Sometimes, the combination of changes in dimension and index can affect the optical performance of a system.[1]

To date, the effects of temperature on DOEs have received little attention.[2,3] Recently, several researchers[4,5,6,7] have independently examined the relationship among temperature, material properties, and optical performance.

In this paper, we will describe focal length as a function of temperature and describe the temperature dependence of diffraction efficiency. We will show how an athermalized lens can be designed by combining refractive and diffractive surfaces and discuss its limitations. In addition, we will present a new design that is both athermal and achromatic. Finally, we will end with some concluding remarks.

---

[1] D. S. Grey, "Athermalization of Optical Systems," JOSA 38 (1948), p. 542.

[2] A. McKay and J. White, "Effects of Simulated Space Environments on Dichromated Gelatin Holograms," SPIE Proc. 1044 (1989), pp. 269-275.

[3] M. Tanigami, S. Ogata, S. Aoyama, T. Yamashita, and K. Imanaka, "Low-Wavefront Aberration and High Temperature Stability Molded Micro Fresnel Lens," IEEE Photonics Tech. Lett. 1 (1989), pp. 384-385.

[4] J. Jahns, Y. H. Lee, C. A. Burrus Jr., and J. Jewell, "Optical Interconnects Using Top-Surface-Emitting Microlasers and Planar Optics," Appl. Opt. 31, (1992), pp. 592-597.

[5] 5. C. Londono, W. T. Plummer, and P. P. Clark, "Athermalization with Diffractive Optics," Diffractive Optics: Design, Fabrication, and Applications 1992, Techical Digest Series 9 (OSA, Washington D.C., 1992), p. 7.

[6] G. P. Behrmann and J. P. Bowen, "Thermal Effects in Diffractive Lenses," Diffractive Optics: Design, Fabrication, and Applications 1992, Techical Digest Series 9 (OSA, Washington D.C., 1992), p. 8-10.

[7] G. P. Behrmann and J. P. Bowen, "The Influence of Temperature on Diffractive Lens Performance," accepted for publication in Applied Optics.

2.0 Opto-thermal Expansion Coefficient

The opto-thermal expansion coefficient for a refractive lens, $x_{f,r}$, as defined by Jamieson,[8] relates the change in focal length to a change in temperature. This coefficient is a measure of a system's sensivity to temperature. In this section we examine the opto-thermal expansion coefficient for both the refractive and diffractive lens.

The opto-thermal expansion coefficient for a thin refractive lens, $x_{f,r}$ is given by

$$x_{f,r} = \frac{1}{f}\frac{df}{dT} = \alpha_g - \frac{1}{n - n_o}(\frac{dn}{dT} - n\frac{dn_o}{dT}), \tag{1}$$

where α_g is the coefficient of thermal expansion of the lens, n is the refractive index of the lens, and n_o is the refractive index of the image space. Note that the opto-thermal expansion coefficient is independent of the shape of the lens and is dependent only on material properties. Since $x_{f,r}$ is normalized by f it can be used to calculate the change in focal length by

$$\Delta f = f x_{f,r} \Delta T. \tag{2}$$

For a more complex system, the opto-thermal expansion coefficient is a function of the thermal properties of all lenses and spaces. To evaluate the effects of temperature, it is necessary to determine the opto-thermal expansion coefficient for the entire system.

In analyzing systems that include diffractive lenses it is useful to have a similar expression. With an opto-thermal expansion coefficient for a diffractive lens, $x_{f,d}$, the techniques that have been developed to evaluate and athermalize refractive systems can be applied.

In the paraxial region, the focal length of a diffractive lens can be expressed as a function of the zone radius:

$$f = \frac{n_o r_m^2}{2m\lambda_o}, m = 1, 2, 3, ... \tag{3}$$

As the temperature changes, the zone spacing will expand and contract. The zone radius, r_m, can, to the first order, be expressed as

$$r_m(T) = r_m(1 + \alpha_g \Delta T). \tag{4}$$

Additionally, the index of the image space will change with temperature by

$$n_o(T) = n_o + \frac{dn_o}{dT}\Delta T. \tag{5}$$

By incorporating Eqs. 4-5, the opto-thermal expansion coefficient for a diffractive lens can be expressed as

$$x_{f,d} = 2\alpha_g + \frac{1}{n_o}\frac{dn_o}{dT}. \tag{6}$$

See References 4 or 7 for a more complete derivation.

Note that the change in focal length of a diffractive lens is only a function of α_g and index changes of the image space. It is not a function of temperature-induced changes in the refractive index of the lens material. This is a fundamental difference between the thermal behavior of

[8] T. H. Jamieson, "Thermal Effects in Optical Systems," Opt. Engr.20 (1981), pp. 156-160.

refractive and diffractive lenses. Table 1 shows the relevant parameters and the opto-thermal expansion coefficients for several optical materials.

Opto-thermal expansion coefficients can be used by a designer to athermalize a system. One way in which this is achieved is by matching the opto-thermal expansion coefficient of the lens system to the coefficient of thermal expansion of the mounting material so that the change in image position corresponds to the change in position of the focal plane. See Fig. 1.

Because $x_{f,r}$ for a refractive singlet and $x_{f,d}$ for a diffractive singlet made of the same material can be different, it is theoretically possible to design an athermalized hybrid refractive/diffractive element. Such an element has a refractive power due to the curvature of the surfaces and a diffractive power due to surface-relief structure. This is pictorially represented in Fig. 2. The practical limitations on such designs are discussed in the Sec. 4.0.

3.0 Diffraction Efficiency

Diffraction efficiency is also an important consideration for systems. In this section we examine the temperature-dependent parameters that are associated with diffraction efficiency and present an analysis that determines the effect of temperature.

To attain a diffraction efficiency of 100 percent, a continuous-phase profile must have a blaze height given by

$$h = \frac{\lambda_o}{n - n_o}, \tag{7}$$

where λ_o is the design wavelength, n is the index of refraction of the lens material and n_o is the index of the image space. A temperature change will cause the blaze height to change. An incorrect blaze height will reduce the diffraction efficiency. Additionally, the index of both the lens material and the image space will change with temperature, influencing the diffraction efficiency.

For a relative error, ϵ, in the blaze height, Swanson[9] has shown from scalar diffraction theory that the first order diffraction efficiency, η_1, is

$$\eta_1 = [\frac{\sin(\pi\epsilon)}{\pi\epsilon}]^2. \tag{8}$$

By examining the index and physical expansion effects separately, a desired height, h_d, and an actual height, h_a, can be defined. Considering only the changes in index, h_d can be thought of as a desired height that would be required to maintain maximum diffraction efficiency:

$$h_d = \frac{\lambda_o}{[n + (\frac{dn}{dT})\Delta T] - [n_o + \frac{dn_o}{dT}\Delta T]}. \tag{9}$$

The actual height, h_a, is associated with the physical expansion of the lens material with a temperature change. It can be expressed as

$$h_a = h(1 + \alpha_g \Delta T). \tag{10}$$

Therefore, the true error, δ, after a temperature change is

$$\delta = h_a - h_d. \tag{11}$$

[9]G. J. Swanson, "Binary Optics Technology: The Theory and Design of Mulit-Level Diffractive Optical Elements," MIT Lincoln Laboratory Tech. Rep. 854 (1989).

The relative error, ϵ, in Eq. (10) is

$$\epsilon = \frac{|\delta|}{h_d}. \tag{12}$$

If we consider optical systems that operate in air, we have found that, for most materials, the change in diffraction efficiency due to temperature effects is negligible. This is true even for plastics which have both a high α_g and dn/dT.

For example, acrylic has a coefficient of thermal expansion of $65.5 \times 10^{-6o}C^{-1}$ and a dn/dT of $-125 \times 10^{-6o}C^{-1}$. If the temperature of a diffractive lens made of acrylic is increased by 30^oC, ϵ would be 0.0056 and the change in diffraction efficiency would be less than 0.1 percent.

4.0 Design Examples

In the following section, we show how opto-thermal expansion data can be used to design hybrid athermalized lens systems. Here we restrict our analysis to the case of an athermalized doublet and an athermalized/achromatized triplet . For systems containing more elements or airspaces, the same methodology applies.

The total power of a lens, ϕ_t, imersed in air, can be expressed as

$$\phi_t = \frac{1}{f_t} \tag{13}$$

where f_t is the focal length of the lens. It follows that for a k-element lens, ϕ_t can be determined by

$$\phi_t = \phi_1 + \phi_2 + ... + \phi_k. \tag{14}$$

In Eq. 14, ϕ_1 is the power of the first lens, and ϕ_2 is the power of the second lens and so on.

An opto-thermal expansion coefficient for the lens, $x_{f,t}$, is given by

$$x_{f,t} = f_t\phi_1 x_{f1} + f_t\phi_2 x_{f2} + ... + f_t\phi_k x_{fk}. \tag{15}$$

In Eq. 15, x_{f1}, x_{f2}, and x_{fk} are the corresponding opto-thermal expansion coefficients of the individual lens elements.

Consider lenses made from polycarbonate. This material offers several advantages: it is inexpensive, lightweight, and easy to shape. However, for the refractive case, polycarbonate has an extremely high opto-thermal expansion coefficient ($245 \times 10^{-6o}C^{-1}$). This can be attributed to its large coefficient of thermal expansion and its large dn/dT. For the diffractive case, the opto-thermal expansion coefficient is also quite large ($130 \times 10^{-6o}C^{-1}$). Therefore, polycarbonate lenses are difficult to incorporate in optical systems that must operate over wide temperature ranges.

If it were necessary to athermalize a polycarbonate lens, a hybrid doublet could be designed to meet this requirement. Consider an $f/5$ doublet with a focal length of 100 mm operating at λ_o equal to 632.8 nm. By using Eqs. 14 and 15, we can select powers in the refractive surface and diffractive surface such that the net opto-thermal expansion coefficient matches the mounting material. For an aluminum mount, Table 2 shows the coefficients and calculated powers required for athermalization.

As a basis of comparison, it is appropriate to compare the performance of the athermalized hybrid to an all refractive singlet made from polycarbonate mounted in aluminum.

The thermal performance of a refractive singlet is shown in Fig. 3. It is assumed that the system is perfectly aligned at 20^oC. If focal length and detector position are plotted as a function

of temperature, it is seen that when the system is heated to $50°C$, the distance between detector and focal length is 0.67 mm. This seperation is more than 20 times the tolerable depth of focus for diffraction limited performance.

On the other hand, Fig. 4 is a plot of focal length and detector position for the athermalized hybrid. For a first-order approximation of material properties, the distance between the two remains the same.

This athermalization technique is similar to one used to achromatize refractive and diffractive surfaces.[10] In achromatization, power is distributed in the refractive and diffractive surfaces based on the relative dispersions of the lens materials. Typically, the dispersion of a lens material is measured by its Abbe number, V. Therefore, an achromatized lens with a real object should meet the following condition:

$$0 = \frac{\phi_1}{V_1} + \frac{\phi_2}{V_2} + ... + \frac{\phi_k}{V_k}. \tag{16}$$

For the refractive surface, the Abbe number of polycarbonate is 30. The diffractive surface has an Abbe number of -3.45. Note that in the athermalized hybrid, the refractive power is negative and the diffractive power is positive. Therefore, the conditions of Eq. 16 are not satisfied and chromatic aberrations must be addressed.

For diffraction limited performance, the refractive singlet has a bandwidth of $\pm$ 2.94 nm, and the athermalized doublet has an equivalent bandwidth of $\pm$ 0.1 nm. Thus, the chromatic aberrations are more severe in the athermalized hybrid element. For polycarbonate, this athermalization technique may only be useful for monochromatic applications.

Estelle[11] has examined the requirements for simultaneously athermalizing and achromatizing refractive lens systems. For the most part, a three-material triplet is required. With three materials, one can use Eqs. 14-16 to set up a system of 3 equations and 3 unknowns in which to solve for the necessary power in each element. Other aberrations, for example spherical aberration, can be reduced by solving for the optimal bending of the lens elements. Estelle studied a family of triplet solutions consisting of two plastics and one glass element. In the following, due to the unique dispersive and thermal behavior of the diffractive lens, we examine the possibility of replacing one of the three materials with a diffractive surface. See Fig. 5.

Assume now that it were necesssary to design an $f/5$, 100 mm focal length lens mounted in aluminum. In this case, the lens must be achromatized over the visible range. If we use BK-7 and polycarbonate, both inexpensive materials, an element can be designed that has the mass and volume of a doublet but the performance of triplets discussed by Estelle. Table 3 shows the calculated powers for a solution with the glass element in front and the diffractive surface on the back. Note that the diffractive surface is relatively weak and would therefore be easier to fabricate. Additionally, the powers in the refractive components are manufacturable. In fact, similar levels of performance can be attained in IR lenses.[12] Infrared materials exhibit large changes in index with temperature. Traditionally it has been difficult to athermalize such systems.

[10]T. Stone and N. George, "Hybrid diffractive-refractive lenses and achromats," Applied Optics, 27, (1988) pp. 2960-2971.

[11]L. R. Estelle, "Third-Order Theory of Thermally Controlled Plastic and Glass Triplets," SPIE Proceedings, 237, (1980) pp. 392-401.

[12]G. Behrmann, "Color Correction in Athermalized Hybrid Lenses," to be presented at OSA Topical Meeting, Design for Photonics, March 22, 1993.

5.0 Conclusions

We have performed an analysis of thermal effects and their influence on the performance of diffractive lenses. Formulas describing the change in first-order properties have been presented. These expressions are useful for designing systems that must operate over wide temperature ranges.

The opto-thermal expansion coefficient for a diffractive lens has been derived. It is different from its refractive counterpart in that the focal length of a diffractive lens is not dependent on temperature-induced changes in refractive index of the lens material. An analysis of the change in diffraction efficiency due to temperature was performed. We have found for systems operating in air that the changes are insignificant.

A design technique was presented that shows how refractive and diffractive surfaces can be used together to produce hybrids with desirable thermal behavior. For a single hybrid, the amount of chromatic aberration will usually be increased if the athermal conditions are imposed. It was also shown that a diffractive surface can be used to significantly reduce the mass and volume of all-refractive triplet solutions that are both athermal and achromatic.

Material	n	α	dn/dT	$x_{f,r}$	$x_{f,d}$
λ = 546.1 nm					
FK52	1.487	14.4	-7.8	27.64	27.89
PSK2	1.571	6.4	1.5	1.28	11.89
BK7	1.519	7.1	1.7	0.98	13.89
K10	1.503	6.5	3.0	-2.17	12.09
BaF9	1.646	6.5	4.0	-2.00	12.09
F5	1.607	8.0	3.5	-0.17	15.09
LaFN2	1.748	8.2	0.7	5.14	15.49
SF11	1.792	6.1	11.4	-10.35	11.29
Acrylic	1.495	67.9	-105	227.40	134.89
Polycarb.	1.585	65.5	-107	245.80	130.04
λ= 10 μm					
ZnS	2.199	6.9	50	-36.45	12.91
ZnSe	2.401	7.7	48	-28.09	14.51
Ge	4.003	6.1	390	-124.95	11.31
KRS-5	2.370	58	-234	290.0	115.11

Table 1: Opto-Thermal and Thermal Properties of Various Lens Materials

α, dn/dT, $x_{f,r}$ and $x_{f,d}$ in ppm/°C

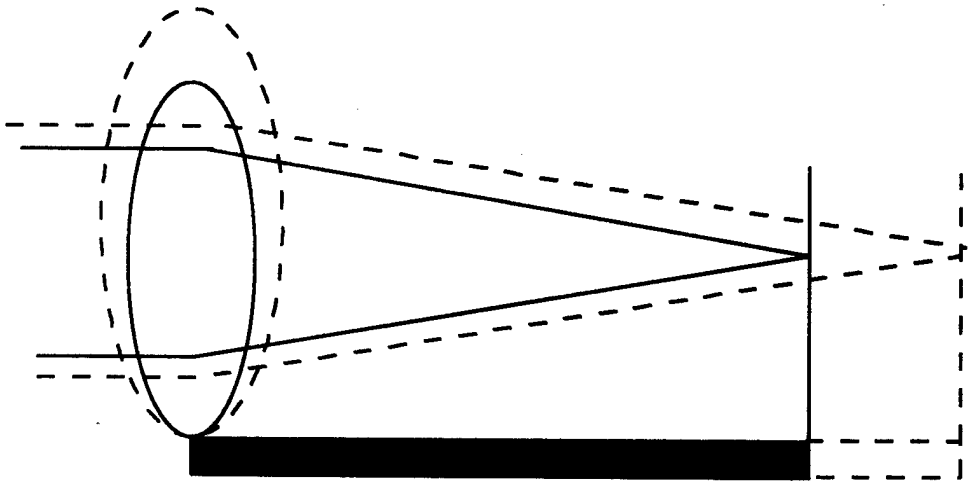

Fig. 1 Athermalized Lens System

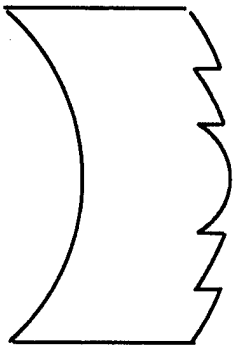

Fig. 2 Athermalized Hybrid Lens

α_{mount}	$x_{f,r}$	ϕ_r	$x_{f,d}$	ϕ_d
23 ppm/°C	246 ppm/°C	-0.0092	130 ppm/°C	0.0192

Table 2 Coefficients, Refractive and Diffractive Power for 100 mm focal length hybrid polycarbonate lens, athermalized to aluminum.

Polycarbonate Singlet

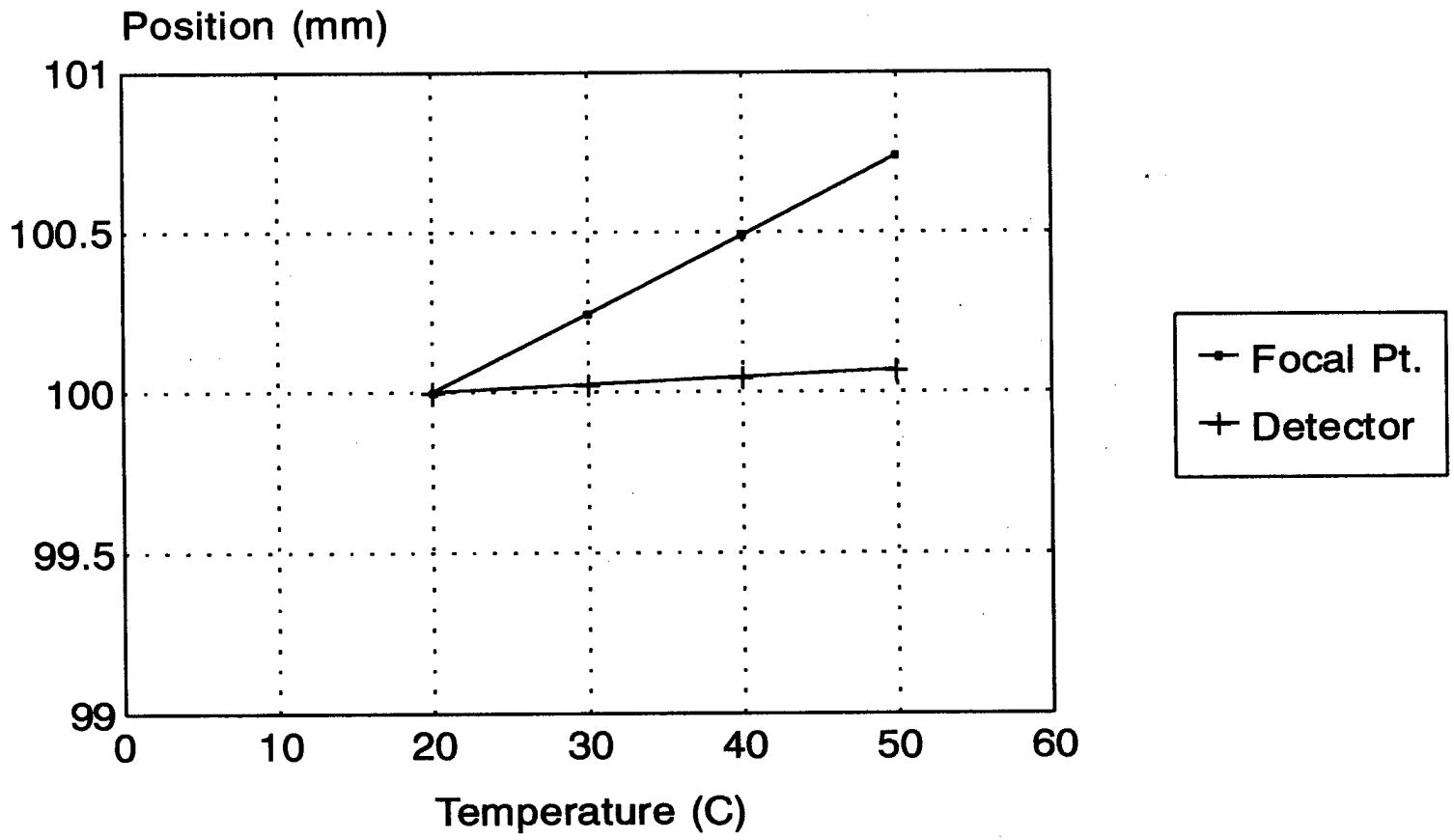

Fig. 3 Focal Point and Detector Position for 100 mm focal length, all-refractive, polycarbonate lens,aluminum mount.

Athermalized Hybrid Polycarbonate Lens

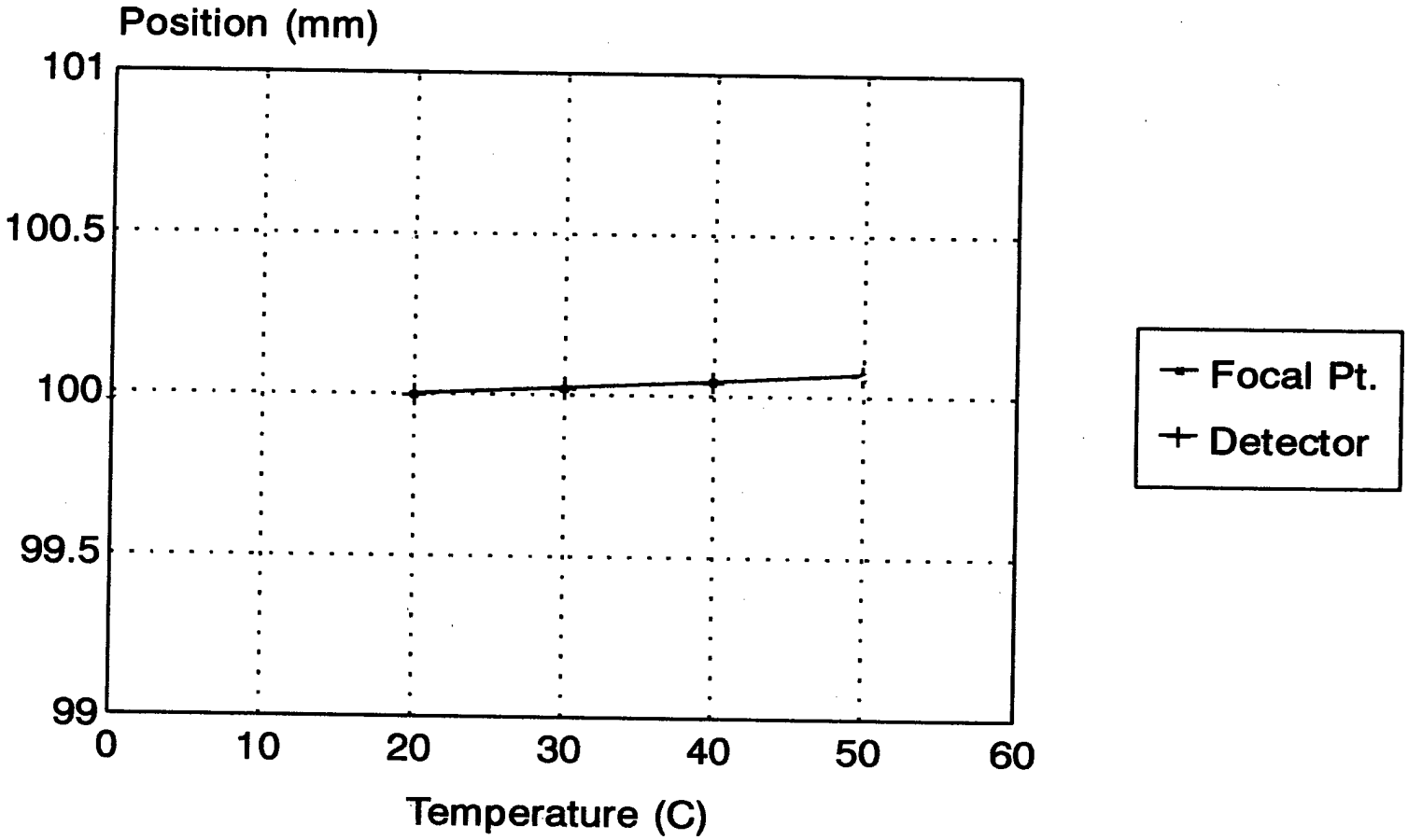

Fig. 4 Focal Point and Detector Position for 100 mm focal length, athermalized hybrid, polycarbonate lens, aluminum mount (the two lines are superimposed).

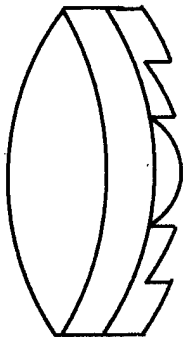

Fig. 5 Athermal/Achromatic Hybrid Lens

Mat'l	x_f	V	ϕ
BK-7	0.98 ppm/°C	64.2	0.0088
Polycarb.	246 ppm/°C	30.0	0.0006
DOE	130 ppm/°C	-3.45	0.0006

Table 3 Athermal/Achromatic Hybrid Lens, 100 mm focal length, athermalized to aluminum.

Low Cost Paths to Binary Optics

February, 1993

Arthur Nelson and Lawrence Domash
Foster-Miller, Inc.
Waltham, MA 02154

ABSTRACT

Application of binary optics has been limited to a few major laboratories because of the the limited availability of fabrication facilities such as e-beam machines and the lack of standardized design software. Foster-Miller has attempted to identify low cost approaches to medium-resolution binary optics using readily available computer and fabrication tools, primarily for the use of students and experimenters in optical computing. An early version of our system, MacBEEP, made use of an optimized laser film recorder from the commercial typesetting industry with 10 μm resolution. This report is an update on our current efforts to design and build a second generation MacBEEP, which aims at 1 μm resolution and multiple phase levels. Trials included a low cost scanning electron microscope in microlithography mode, and alternative laser inscribers or photomask generators. Our current software approach is based on Mathematica and PostScript compatibility.

1. Introduction: The need for more widely available binary optics

It is widely agreed in the binary optics community that in spite of many successful applications and demonstrations the technology has been slow to be utilized in industrial and scientific optics due to the requirement for highly specialized fabrication facilities unavailable outside of a few major laboratories. The microlithographic, multimask methods from the electronics industry shown to yield highest performance represent a capital investment of many millions of dollars. Until very recently, few commercial services were available to offer design and fabrication capabilities. In any case, multimask fabrication is too costly for many research budgets.

Fortunately, not every optical designer or researcher experimenting with binary optics needs state of the art submicron e-beam, multimask fabrication with optimum diffraction efficiency. In many cases, optical computing researchers, students and engineers testing new ideas would be adequately supported if they had access to moderate resolution elements, provided they could obtain them easily and quickly, at reasonable cost, and use design software they already have or can easily obtain. This approach is particularly appropriate for non-lens applications such as Dammann or interconnect gratings, Gerchberg-Saxton kinoforms, beam combiners or other elements required in optics research.

Foster-Miller designed the original MacBEEP (Macintosh-based, Binary Elements Encoding Phase) desktop manufacturing system around personal computers and a widely accessible laser film recorder from the publishing industry (Linotronic) with 10 μm resolution and two level output processible into phase elements. PostScript compatibility assured that a wide range of existing personal computer CAD software could be

combined to design elements and create files. Although the first MacBEEP system had strict limitations of modest resolution and low diffraction efficiency, it has proven useful at its installation in the Naval Surface Warfare Center in support of optical processing research. Other users around the country have been able to apply the processing and software methods developed for MacBEEP to generate their own binary phase elements using Linotronic machines available in their local communities at printing service bureaus.

This paper is a status report on our continuing development program for a second generation MacBEEP, in which our goal is to develop methods for multiphase levels with 1 μm resolution, incorporating designs generated from any PostScript compatible source such as Mathematica. In evaluating the best way to pursue this, we have evaluated low cost e-beam methods and are presently studying laser direct write methods.

In comparing the facility we plan with existing fabrication laboratories, it is important to understand the fundamental tradeoffs that are involved between system cost, diffractive performance, and range of applications. Our preferred approach will incorporate a 0.5-1 μm resolution laser microlithography system originally developed for the production of microwave integrated circuits. It employs acousto-optic modulators to accurately control both the position and intensity of the laser beam for exposing photoresist. The capital cost of the exposure system as such is less than $100K. We expect to be able to expose multilevel resist patterns (up to 8 levels) through exposure/dose control. This should yield reasonably high diffraction efficiency (95% for a simple grating) with relatively low fabrication complexity. In comparison, presently the most advanced fabrication facilities rely on electron beam machines to expose e-beam resist to an accuracy of 0.1 μm. E-beam laboratories also require that software definitions be provided in file formats used by the microelectronics industry, such as MEBUS.

The advantages of the electron beam process will remain very high resolution (0.1 μm or better) and superior (up to 99%) diffraction efficiency. This level of performance can probably not be matched by any laser direct write approach. By accepting somewhat reduced performance adequate for many concept demonstration purposes, our goal is to offer fabrication services for approximately $500-1000 per element. The tradeoffs are a reduction in maximum theoretical diffraction efficiency from 99% to 95% and a projected maximum resolution in production on the order of 1.0 μm, as opposed to the 0.1 μm achievable with electron beam techniques. Multimask methods will remain the path of choice for highest performance applications and creation of embossing master elements. But as illustrated in Figure 1, there is an enormous gap between the performance and cost range of e-beam systems and the original MacBEEP. A capability for 1 μm features with 4-8 phase levels in resist or glass substrates would be valuable for proving the value of many proposed designs before investing in e-beam elements. Users also emphasize the need to use readily available commercial scientific or CAD software; computations in standard computational environments such as Mathematica and graphics files in PostScript format are a highly desirable standard.

In Section 2, we briefly review the original MacBEEP program and its capabilities. This is followed in Section 3 with a report on our evaluation of a relatively low cost scanning electron microscope (SEM) in a microlithography mode to replace the less widely available e-beam machine for creating binary optic elements for optical interconnects. In Section 4, we describe our work in progress to develop MacBEEP II.

2. Review of MacBEEP I

MacBEEP originated when we discovered that PostScript (1), the industry standard page description computer language for desktop publishing, could be used to efficiently encode holographic patterns (2). PostScript describes patterns in a universal file format which is interpreted by each compatible output device at its own limit of resolution. Thus files representing holographic or diffractive patterns can be proofed on paper at 80 μm resolution using PostScript-compatible office laser printers and then used to produce film output at 10 μm resolution using PostScript-compatible laser typesetters such as the Linotronic made by Linotype-Hell AG. One of the techniques we demonstrated for PostScript, a language designed for typesetting, is the creation of a "diffractive font" in which the "characters" are a set of Fresnel zone plates, line gratings, or other patches of fringe patterns which can be tiled together by a word processor. This approach to diffractive optics could probably be accomplished from any PC, but we chose the Macintosh because it was optimized for the PostScript compatible graphics environment and allowed effortless interchange of graphics files from program to program through universal "cut and paste" operations, performing different operations as the data was passed between different graphical or scientific Macintosh programs. This meant that a suite of commercial software applications could often be combined to carry out functions which otherwise would require writing new programs. The personal computer selected was the Macintosh IIx, supplemented by a 50 Mhz 68030 hardware accelerator board to speed up numerical processing. A frame grabbing board and CCD camera or document scanner adds image input capabilities to the host computer. Foster-Miller developed the software keystone for the system, also named "MacBEEP". MacBEEP incorporated modules from the source code of a basic image processing and frame grabbing program created at the National Institute of Health (Image 1.4) and added powerful Fourier transform and related capabilities. Most important, MacBEEP contains algorithms to optimize printing of files on PostScript printers, for which precision control of pixel placement proved important in holographic applications. MacBEEP software capabilities include computation of up to 512 X 512, 32 bit forward and inverse fast Fourier transforms in about 150 seconds; input images may be bitmaps or analytic patterns from a variety of sources. MacBEEP also has facilities for exchanging large 32 bit files with Mathematica, and offers precise software control of the Linotronic at the pixel level, particularly with regard to scaling, pixel boundaries, page placement and tiling of patterns.

Our chosen output device was the Linotronic 300 Imagesetter, a 2540 pixel per inch HeNe laser-based laser film recorder manufactured in Germany by Linotype AG; other PostScript compatible devices of similar resolution are also available. Our program included purchasing a Linotronic (cost approximately $70K) and optimizing the internal hardware, adjusting it to expose special films and other techniques which require access to a dedicated machine. However, many of our results can be duplicated simply by outputting PostScript files to any standard service-bureau Linotronic, available in most communities for charges on the order of $10-20 per page of film, containing up to 20,000 X 25,000 binary pixels.

2.1 Processing Alternatives

We investigated various alternative methods of converting binary amplitude films produced by the Linotronic to binary phase elements. The methods we tried included bleached film, contact printing to photoresist, contact printing to a photopolymer, etched glass, and 5X photoreduction. As a standard against which to evaluate the results, we had an outside vendor fabricate a submicron resolution binary phase

Dammann grating by traditional means of e-beam lithography, and used this as a reference master in optical reconstruction tests to compare the performance of various lower cost approaches.

Bleaching. Bleaching is the simplest technique to convert amplitude to phase and yielded our best results. While standard high contrast Linotronic graphic arts film can be bleached, we obtained better results by loading a Linotronic with the holographic film Agfa 10E75. A photomicrograph of a bleached 10E75 film exposed directly in the Linotronic is shown in Figure 6a. Figure 6b shows an optical reconstruction with the DC spot almost eliminated and indicates a successful exposure.

Photoresist. Photoresists, typically used as acid resists for photolithography, are also convenient media for binary optical elements formed by UV contact printing from Linotronic masks. A photomicrograph of a photoresist plate is shown in Figure 2.

Photopolymer. Photopolymers such as Polaroid DMP-128 are high resolution phase recording materials primarily used for holography. Modulation of the film's index of refraction results from variations in porosity which are proportional to the local light intensity during exposure; diffraction efficiency has been reported to exceed 80% (3). A Dammann grating binary amplitude mask produced on Linotronic film was the source for contact printing onto the DMP-128. Phase of exposed areas depended on the size of the area, exposure and processing variables.

Etched glass. Photoresist-coated glass plates which have been exposed and developed may also be further processed with an etching step. In this case, the photoresist pattern, which remains after development, serves as an acid resist. For standard glass plates, a dilute solution of aqueous hydrofluoric acid is used to etch away exposed portions of the glass to a predetermined depth. There is a tendency to introduce some optical noise due to micro-pitting and nonuniform etching. Depth of etch is process and materials sensitive, so that optimization of the phase modulation requires repeated trials.

Photoreduction. Photoreduction has been used as a method to produce computer holograms since the 1960's, when wall-sized plotter output was reduced in a sequence of camera steps. Multistep photoreduction introduces distortions and inhomogenities, however. In our experiments, Linotronic films with 20μm features provided excellent masters for single-step photoreduction. In our trials, an outside vendor used a step-and-repeat system to produce 5X reductions of Linotronic film output providing nominal 4 μm features with better than 0.8 μm resolution at a cost of appoximately $250 per sample. The standard mask used as a source for electronics industry photoreduction is chromium on a glass plate but we found that a typical photoreduction apparatus can also accommodate the film transparency masks produced on the Linotronic 300. Restrictions on distortion and depth of field of the lenses used necessitate that the input aperture for the photoreducer be small; in our case 12 mm X 12 mm, yielding 2.4 mm X 2.4 mm after reduction or 600 X 600 pixels. Larger fields are routinely reduced by precision step and repeat. In our tests, photoresist-coated chrome-on-glass plates were exposed in the photoreduction output plane, and the plates were developed and etched to generate a finished chrome pattern on the glass to make a high resolution binary amplitude object.

In summary, bleaching of holographic film loaded and exposed directly in the Linotronic yields satisfactory binary phase objects at 10 μm resolution provided the researcher has direct access to the Linotronic; otherwise, an extra step of contact printing may be used. To achieve 2-4 μm features defined with submicron resolution,

Linotronic films are excellent masters for photoreduction through standard services available at moderate prices in the microelectronics industry.

2.2 Applications

MacBEEP outputs have been shown to be suitable for many different applications. As examples, we demonstrated zone plates, Fourier plane filters, Dammann gratings, detour phase holograms, line gratings, 3D holograms, and various binary elements incorporating random phase, error diffusion, or band pass filtering.

Binary phase Dammann gratings may be designed to produce holographic reconstructions consisting of 2D arrays of equal intensity focussed laser spots or beamlets, and are of interest for optical interconnects, laser beam combining, and photoreproduction. One half period of a Dammann grating is typically described by a "basic cell," which is rotated and translated to build up a complete grating (Figure 3). In our studies, we created the basic cells in Mathematica and imported the patterns to MacBeep, where rotations and translations of the basic cells could be easily accomplished.

The quality of a Dammann grating may be conveniently quantified since a perfect binary phase sample yields equal intensity among all the reconstructed beamlets and no extra DC spot. Thus they provide a good standard test to compare the performance versus cost for different processing alternatives. Several processing methods were applied to the pattern of Figure 4, designed to produce a 9 X 9 array of equal intensity beamlets assuming a π binary phase step. The optical reconstructions were generated with a 35 cm Fourier transform lens and digitally imaged by a CCD camera.

The simplest process yields binary amplitude film; the Dammann grating was printed on Linotronic standard film at 10 μm per pixel (ie, one printer pixel for each grating pixel). A 100X photomicrograph of the film is shown in Figure 5a. Since this sample was binary in amplitude, the reconstruction (Figure 5b) displays a large DC spot at the center, but the other beamlets show appoximately equal intensities (Figure 5c). If the DC spot may be ignored, this binary amplitude element might be useful for many purposes; the materials cost to produce such a film would be less than $20 at a typical laser typesetting service bureau.

To make a binary phase version, we produced the sample of Figure 6a by the bleaching of Agfa 10E75 exposed directly in the Linotronic, as described earlier. The optical reconstruction and densitometry traces show excellent equality of intensity peaks (Figures 6b,c). Materials cost for this approach is on the order of $50 per sample, but the cooperation of the Linotronic operator or service is required. In the absence of such cooperation, an additional step of contact printing the Linotronic film onto 10E75 would be necessary using a parallel exposer.

A reference master Dammann grating was produced for comparison purposes by an outside vendor according to our specifications based on a mathematical definition. The pattern and features were identical to those produced on Linotronic film in our laboratory, but the vendor used e-beam exposure and plasma-etching to produce a glass element with 0.5 μm resolution and a highly uniform phase step, at a cost of $3000 and a turnaround time of two months. The pattern edges of this sample are much sharper than those of the Linotronic films. For many experimental purposes however, the MacBEEP film based elements were remarkably competitive in performance at about 1/300 the cost.

2.3 Detour-phase Filters for Optical Correlators.

Development of the MacBeep system included the creation of several custom Mathematica-language routines (known as "packages"). One of these packages calculates the Brown-Lohmann detour-phase encoding for a complex-valued array (4). Mathematica was used in conjunction with MacBeep to calculate the detour phase hologram of a sample pattern consisting of a 3 x 3 matrix of apertures, of which the central aperture was 50% transmissive, as shown in Figure 7. An enlarged view of the resulting detour phase hologram is shown in Figure 8. This hologram consists of 64 X 64 detour-phase cells, each cell containing 16 X 16 pixels, for a total of 1024 X 1024 physical pixels. Phase and amplitude of the Fourier transform of the original image are each quantized in 8 levels. The detour phase hologram was produced on Linotronic binary amplitude transparency film at 20 microns per pixel. The Fourier optical reconstruction is shown in Figure 9. For comparison with the detour phase encoding, a 512 X 512 binary Fourier filter computed simply as the binarized real part of the FFT was computed from the original pattern (Figure 10) and produced as a binary amplitude film, also with 20 μm pixels; the reconstruction from this reference filter is shown in Figure 11.

Finally, the detour phase encoded filter was photoreduced 5X by an outside vendor as a chrome-on-glass element with an effective mapping of 4 X 4 μm for each of the original 1024 X 1024 hologram pixels; a 100X photomicrograph of the photoreduction is shown in Figure 12. The improvement in reconstruction quality due to the photoreduction step is evident in Figure 13, where the 50% gray of the central cell is accurately reproduced. Here again, the use of MacBEEP to create masks for photoreduction yielded excellent results. Figure 14 shows a test of the optical performance of the photoreduced detour phase hologram used in the filter plane of a 4f optical correlator constructed using 35 cm focal length Fourier lenses.

2.5 Summary of MacBEEP I

The Linotronic is the highest resolution output device which is available virtually everywhere. The MacBEEP system was successful within its narrow goal, to explore the optimum use of such equipment. Good quality bleached phase elements can be obtained if access to a dedicated unit permits loading the Linotronic with holographic film. Film outputs also make excellent masks for photoreduction. The system may be used to produce useful binary optics for a variety of experimental, developmental and proof-of-concept applications. However, an order of magnitude improvement in feature size is needed to greatly expand the range of applications.

3. Low Cost E-beam Lithography Using a Scanning Electron Microscope

The next phase of our program aimed at increasing the resolution while maintaining the low cost philosophy. One major effort was to evaluate a low cost alternative to e-beam methods.

Very high resolution binary optic elements are generally produced using traditional microelectronics electron beam systems (e-beams). We evaluated the possibility that a scanning electron microscope (SEM) can be used in a microlithography mode as a replacement for the much less common and more expensive e-beam machines. Precision control of the electron beam in the SEM offers extremely high resolution (0.05 μm), higher than that usually obtained with microelectronics e-beam systems. The e-beam system employs a larger current and therefore has faster writing speed, but this is not a significant advantage for fabricating prototype or small numbers of diffractive elements.

SEMs typically cost less than 1/10 as much as e-beam systems and are much more widely available to the scientific community.

To test the suitability of the SEM for this application, we fabricated and tested several 7x7 Dammann gratings. The original procedure for fabricating the Dammann grating is illustrated in Figure 15. Starting with a flat SiO_2 substrate, an AlF_3 coating is evaporated on the glass with a thickness chosen to yield a precise π phase step for light passing through the AlF_3 relative to air. Following the coating with AlF_3, the substrate is spin coated with e-beam resist, and the Dammann pattern is written in the resist with an SEM. The resist is then developed, and the Dammann pattern is then fabricated in the AlF_3 using appropriate etchants.

The SEM can expose a 1 mm^2 area with little geometric distortion, but beyond those dimensions, rounding of rectangles may occur due to the excessive deflection of the electron beam. With the SEM the substrate is not translated under the electron beam. Larger areas may possibly be fabricated in the future with the addition of corrections in the software to compensate for the beam deflection. Estimating that a minimum of 10 grating cycles were necessary, we specified a 10 x 10 cell pattern to be written in 1 mm^2. Thus each cell was about 100 microns wide, and individual rectangles in a cell were as small as 5 μm. The software and electronics interface to drive the SEM from a PC was developed by J.C. Nabity Lithography (Bozeman, MT) and sent to the University of Oregon for use on their SEM.

Several samples were exposed at the University of Oregon using PMMA on the fused silica directly. Figure 16 shows a photograph at 400X. The pattern appears to have excellent definition at this magnification and the diffraction pattern indicates excellent construction and edge resolution. Subsequent measurements were made on the e-beam resist pattern, as opposed to the pattern etched in the substrate or AlF_3. Figure 17 is a printed copy of the image as captured on the computer by the CCD camera using the HeNe laser. The image is further analyzed quantitatively in Figure 18, where intensity traces have been taken for several "lines" of the grating pattern. Additional diffracted orders at reduced intensity are, of course, also visible beyond the original 7x7 array. In order to suppress these additional orders, multistep grating levels are required. The bright central spot due to the undiffracted beam results from poor control of the phase depth, and this processing step still requires improvement.

3.1 Summary of SEM approach

Demonstration that the SEM can be used in a very high resolution microlithography mode was successful, although considerable effort would be necessary to optimize the process. The PC driving arrangement permits controlling the SEM beam to render virtually any pattern which can be designed in standard CAD software. However, the system is not designed to write a field larger than about 1 mm on a side. Within the program goals of reduced costs, the SEM is of limited value because the costs of the remainder of the processing cycle were not affected and in some respects may be increased. Low cost electron beam recording as such does not help with multimask fabrication to achieve high diffraction efficiency through multiple phase levels. Because the beam current is low, direct write e-beam methods such as those recently reported by UCSD (5) would be more difficult using the SEM. We concluded that overall the SEM was not the best alternative for low cost binary optics.

4. Laser Direct Write and Current Plan for MacBEEP II

Our current program for extension of MacBEEP performance has two major thrusts: improvement in resolution from the 10 μm range to 1.0 μm and fabrication of 4-8 phase levels. Our discussions with users indicate that a facility offering 1 μm resolution with eight phase levels (95% diffraction efficiency) would meet many needs.

Based on a total assessment of performance goals, user needs, equipment costs and processing alternatives, the plan we are currently pursuing employs a laser microlithography system to write multilevel patterns directly in photoresist with a single pass exposure at approximately 1 μm resolution. The laser system employs acousto-optic modulators for intensity control and positioning of the laser beam over 0.1 mm dimensions. Laser interferometric control of air-bearing mechanical stages are used to translate the substrate over larger dimensions. The local acousto-optic writing ability yields faster writing speed (100 mm/s) compared with mechanical translation alone. A block diagram of a laser system with 1 μm resolution available from Newport Electro-optic Systems is shown in Figure 19.

Capability to fabricate multilevel diffractive elements is key requirement for the MacBEEP II system. Simple two-level phase gratings offer only 41% diffraction efficiency, while four levels increases the 81%, and eight levels to 95%. In the direct write approach, a variable intensity laser beam exposes a multilevel resist pattern directly, and the subsequent pattern is anisotropically etched using ion milling or reactive ion etching into the substrate (Figure 20).

Previous reported efforts (6,7) have shown the ability to perform direct multilevel writing with photoresist, although primarily with slower mechanical systems. Figure 21 shows the dependence of photoresist relief depth with energy from reference (6). Using an optical energy bias (pre-exposure) on the resist, it is possible to have nearly linear etch depth with optical exposure energy. However, the difference in etch rates between the resist and the substrate will likely require adjustments in the linearity of the resist step structure to obtain a linear stepped pattern in the substrate.

5. Software compatibility

Constructing a fabrication facility for diffractive optics is not sufficient to guarantee easy access to outside users. The biggest barrier to effective use of the system continues to be the myriad of incompatible software systems and specialized file formats being used by researchers to design and specify diffractive optics. To date, there exists no accepted standard software environment in which to design and specify diffractive masks for a wide range of applications. Also, there is no standard file interface to carry the design into a driver for the inscribing engine. A distinction must be made between lens designs, as for example generated by Code V and other programs which are beginning to incorporate diffractive capabilities, and non-lens applications. Our approach is biased towards non-lens uses.

In addition to input universality in terms of design, there must be provision for output universality as well, to interface with a laser writing engine. This means that the patterns defined by the CAD or scientific design software must be prepared into files which are set up to drive the desired mask fabricating engine via the electronics which move the laser beams (via acousto-optic cells) and computer controlled stage. It also implies capabilities for manipulation of the output as graphics. This requirement is similar to the need faced by the desktop publishing industry which led to the definition of PostScript, which has since become a standard of computer graphics hardcopy; in

fact we believe that PostScript is probably also a viable format to describe laser recorded holograms.

5.1 Mathematica as a Software Standard

While there is no universal and complete solution for this problem, we believe that standardizing on Mathematica as a software environment goes some distance to the goal.

Mathematica, a complete environment for computation offered by Wolfram Research Corp. is rapidly being accepted worldwide as a standard environment for all sorts of scientific computation and graphics. It incorporates capabilities (compiler, 2D FFT, statistics) which could only be duplicated in a special diffractive optics application at the cost of many manyears of work, runs on almost every computer platform in common use by scientists (PC, Mac, Unix workstations, VAX, supercomputers) and is constantly being upgraded and expanded. Mathematica has recently been extended specifically to make the import and export of code and files from other applications more manageable. Also, the computational kernel can be operated remotely on a networked supercomputer without any change in software to accelerate computationally intensive problems, such as optimization routines or iterative diffractive optics algorithms (for example, simulated annealing). Several of the potential users who contacted us specifically mentioned that computations of phase profiles had been carried out in Mathematica. Also, Mathematica has flexible capabilities for graphical output centered around the PostScript file format.

Figure 22 shows an example of PostScript graphics created in Mathematica. If it were possible to send this for "printing" not just to an office laser printer or publishing system, but rather to our laser incribing engine with micrometer resolution and multiple phase levels in each pixel, a very large variety of diffractive optical concepts could be produced quickly and with low cost.

To demonstrate this and accomplish the first practical examples, we plan to develop a body of Mathematica routines and "packages" (a term for modules of related routines) to implement a full system of desktop diffractive optics. These Mathematica templates can then be distributed to outside users as vehicles for their designs. Resulting PostScript files for fabrication would then be sent or downloaded to the Foster-Miller laboratory to produce physical realizations.

Mathematical Version 2, recently released by Wolfram, has new features which make it sufficiently mature to become an environment for diffractive optics. These include a 2D FFT command, and a compiler to speed execution of programs. Another key feature is that the kernel performing basic computation is separate from the user interface front end, which differs from computer platform to platform. This means not only that different computer systems can easily share development efforts, but also that the kernel can, for example, run on a remote Cray over a network from a front end on a desktop PC. Thus local development by a graduate student in a home office is no barrier to very high speed execution over a supercomputer network.

Wolfram Research Corp. has recently released a communications standard called Mathlink, along with supporting software which promises to interconnect a wide variety of software languages with Mathematica. MathLink provides the format and software for the translation of functions, strings, symbols, messages and real, complex and integer numbers between external programs and Mathematica. This gives the tools to integrate other software with Mathematica operationally without rewriting code.

5.2 PostScript Language

In the past, file formats of diffractive optical patterns have often been cast into MEBUS or other forms suitable for driving microelectronics e-beam machines. However, e-beam software formats are by nature very poorly adapted to diffractive patterns; for example, their primitive graphic shapes are restricted to rectangles. Our early MacBEEP research showed that PostScript, although also not designed for scientific optics, was in fact much better adapted because the graphical primitives were Bezier curves with natural similarities to fringe patterns. Figure 22 showed a PostScript graphic created in Mathematica which, if converted to a physical representation at a micrometer fabrication scale so that gray scale mapped to phase, could be used directly as a diffractive element. All graphics generated by Mathematica are automatically encoded in PostScript format. Our existing MacBEEP software incorporates a number of optimizations relating PostScript to diffractive optics design. Tiling, scaling, distortion, pixel mapping and precision page placement are all functions which are conveniently defined within PostScript and are therefore accessible within Mathematica as well as within MacBEEP. Pixel mapping refers to the exact number of output device pixels which are to be used to represent an original pattern pixel.

A full PostScript driver for the laser inscription system will ultimately be required. This would permit any PostScript file to be output on the system automatically, including not only diffractive optics but other graphical files or even word processing documents, if desired. This requires an integration of the electronic control interface for the laser writer and stage control engines, and the design of a Mac compatible hardware board which incorporates the driver including a PostScript interpreter

6. Summary and Conclusions

Foster-Miller's binary optics program has different goals than most other laboratories. Our development of a relatively low cost, easy-to-access system is complementary rather than competitive with traditional multimask e-beam facilities. Whereas the e-beam approach is not likely to be replaced for state of the art diffractive performance, there appears to be a need for an alternative, lower resolution method which can provide rapid turn around and ease of use for a broader community of users. Ultimately, our goal is to offer a process for designing and making diffractive elements which is as easy to access as a publishing service bureau.

7. Acknowledgements

The work reported here was supported by the U.S. Navy SBIR program, managed through the Naval Surface Weapons Center, and by the US Army SBIR program, managed by the Center for Night Vision and Electro-Optics. We wish to express our appreciation for the encouragement and guidance of Nick Caviris, Scott Spence, and Robert Spande.

8. References

1. PostScript is a product of Adobe Systems, Inc.

2. L. Domash and P. Levin, Computer Holographic Elements Using PostScript Laser Printers, Topical Meeting on Optical Computing, Technical Digest Vol 9, Optical Society of America, Salt Lake City, 1989. Also: P. Levin and L. Domash,

MacBEEP: A Desktop System for Binary Optics, Proc. First Topical Mtg. Diffractive Optics, OSA, New Orleans, April, 1992.

3. R. Ingwall and M. Troll, Mechanism of hologram formation in DMP-128 Photopolymer, Opt. Eng. 28, p586, 1989.

4. Brown and Lohmann, Applied Optics, v.5, p. 967, (1966).

5. Urquhart, Stein and Lee, Computer generated holograms fabricated by direct write of positive e-beam resist, Opt. Lett. 18, p.308, 1993.

6. Andersson, Ekberg, Hard, Jacobsson, Larsson and Nilsson, Simple photomask multilevel kinoforms in quartz and photoresist: manufacture and evaluation, Appl. Opt. 29, p.4259, 1990.

7. Gale, Lang, Raynor, Schutz and Prongue, Fabrication of kinoform structures for optical computing, Appl. Opt. 31, p.5712, 1992.

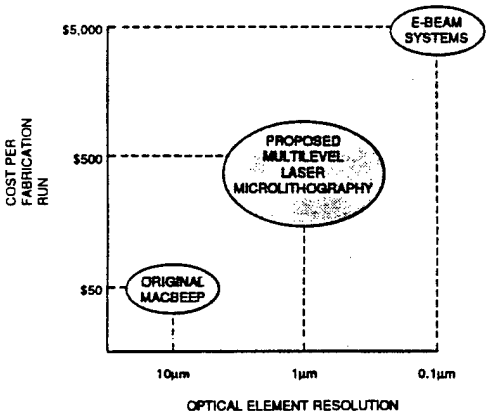

Fig 1. Comparative cost of several methods of diffractive optics fabrication.

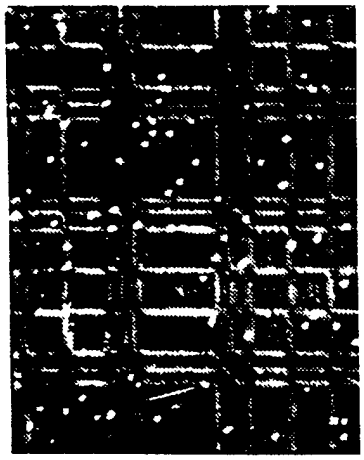

Fig 2. MacBEEP film transparency contact printed onto photoresist. (100X photomicrograph of Dammann grating.)

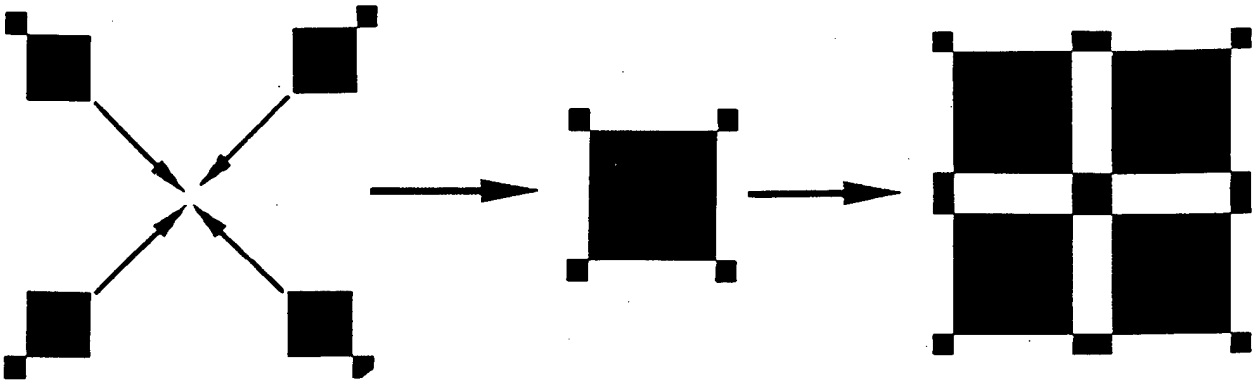

Fig 3. A Dammann grating is composed of basic cells.

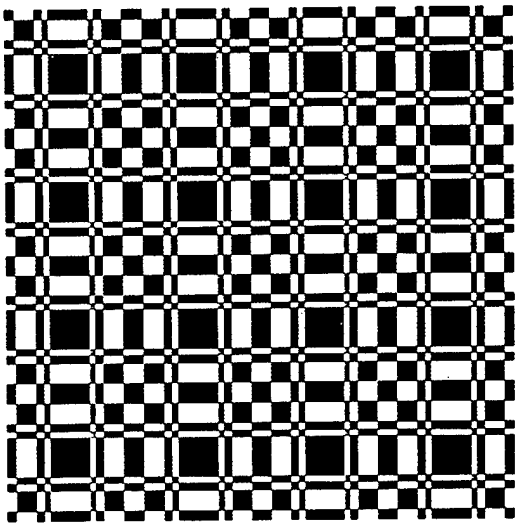

Fig 4. Binary Dammann grating pattern computed in Mathematica and MacBEEP.

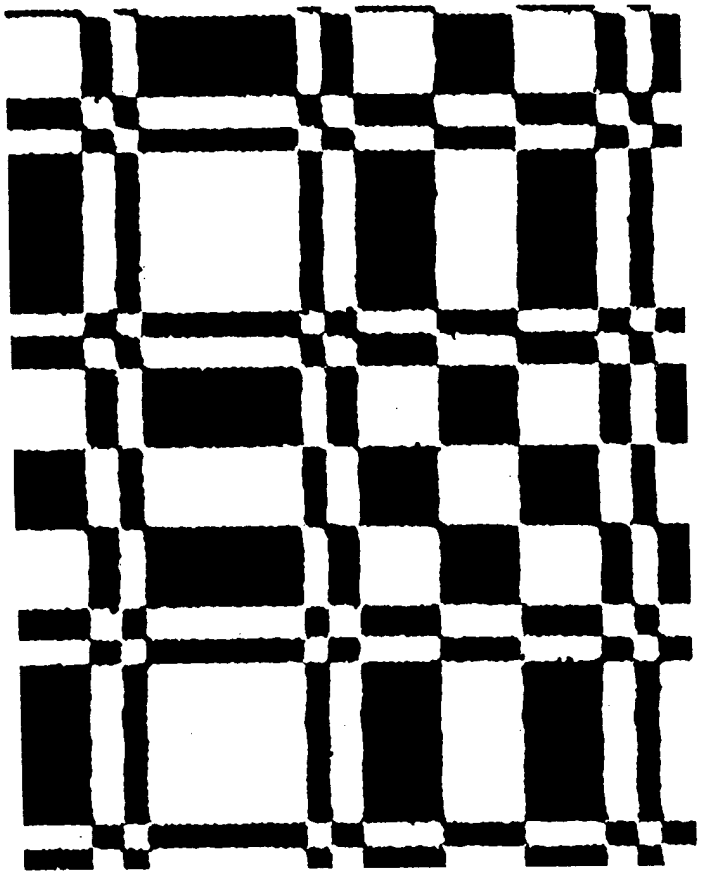

Fig 5(a). 100X photomicrograph of binary amplitude Linotronic film output: no further processing.

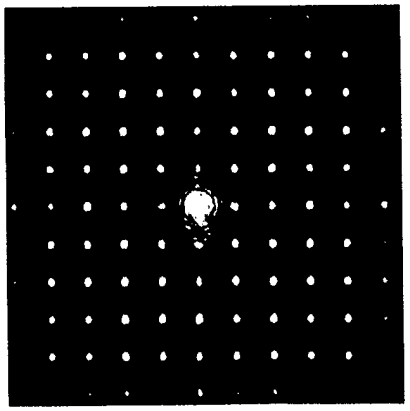

Fig 5(b). Optical reconstruction. DC spot is characteristic of binary amplitude grating. Materials cost <$10.

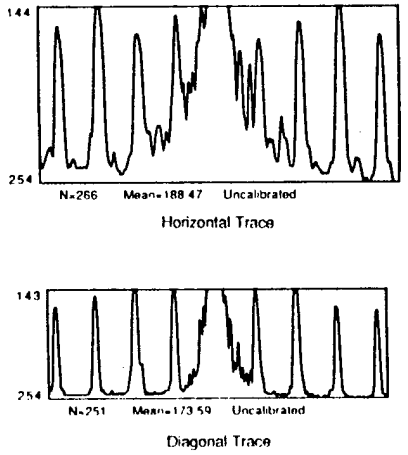

Fig 5(c).

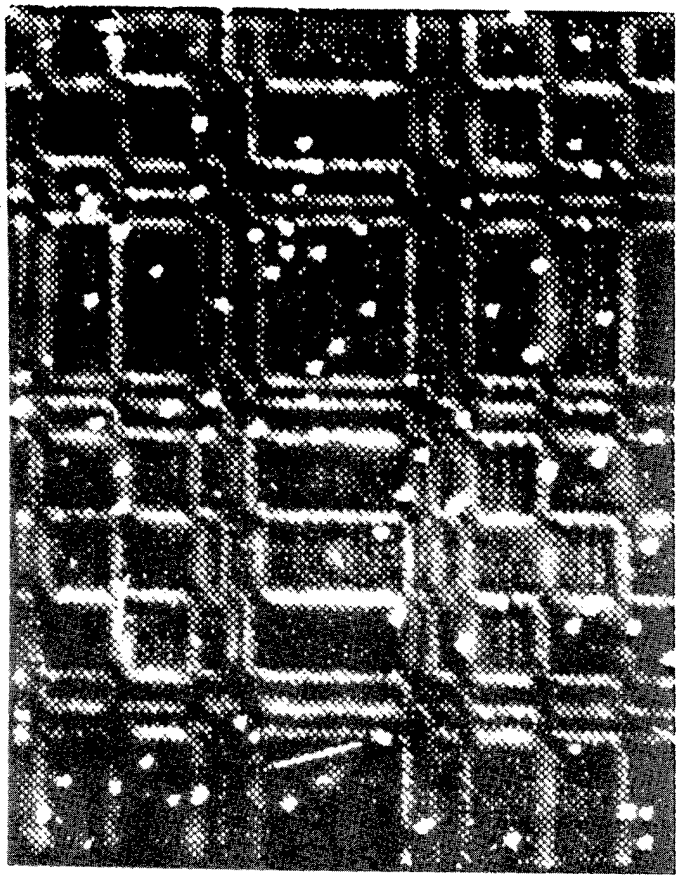

Fig 6(a) 100X photomicrograph of binary phase element produced by bleaching Linotronic film output.

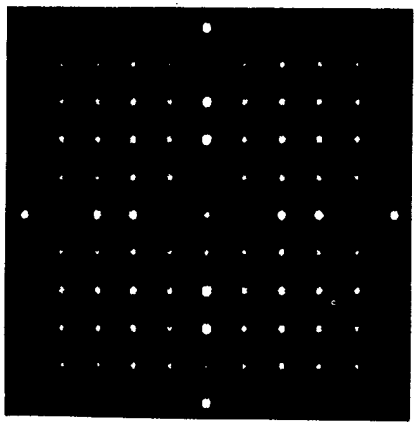

Fig 6(b). Optical reconstruction: Material cost <$150.

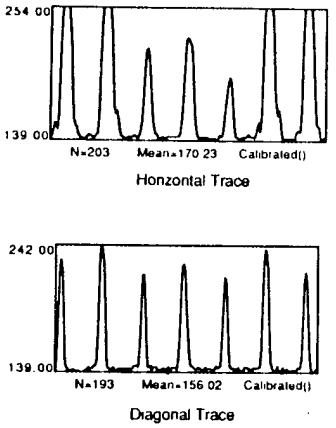

Fig 6(c)

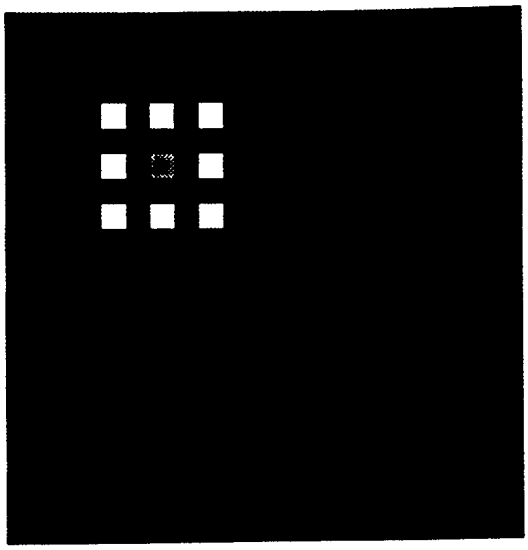

Fig 7. 3x3 matrix of apertures.

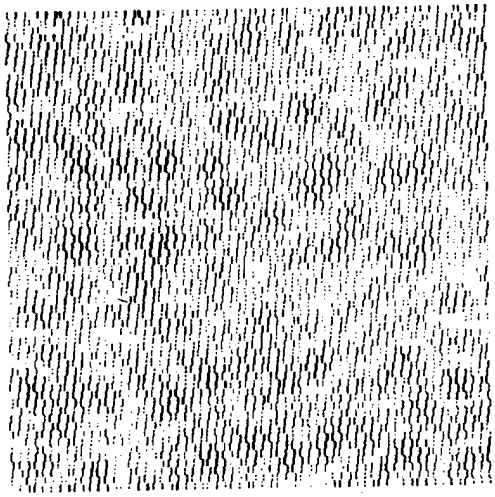

Fig 8. Detour-phase encoding using a combination of MacBEEP and Mathematica.

Fig 9. Optical reconstruction from the detour phase encoding.

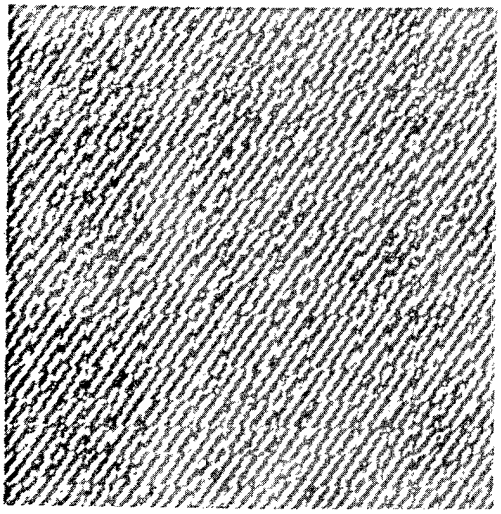

Fig. 10. Binarized Re(FFT) (512x512) using MacBEEP.

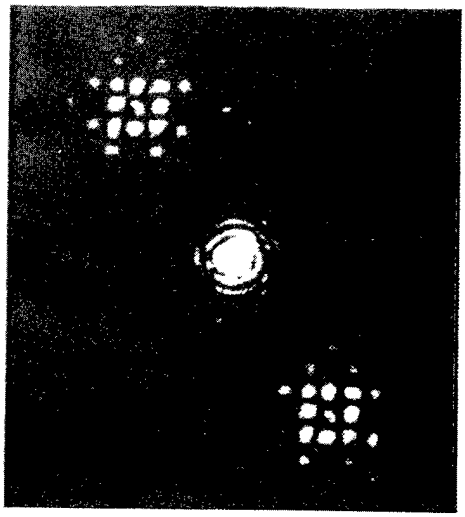

Fig 11. Optical reconstruction from the binarized Re(FFT).

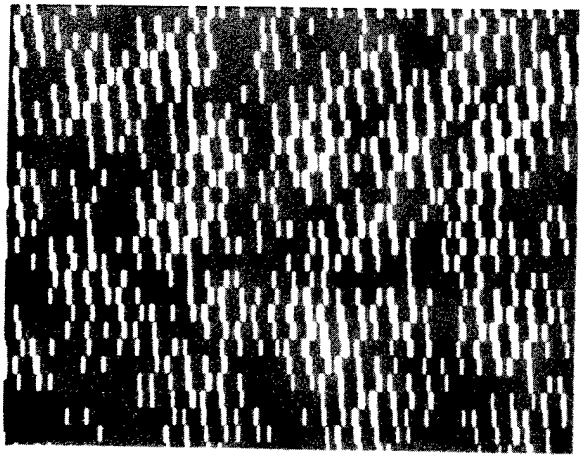

Fig. 12. Photomicrograph of higher quality element achieved by 5x photoreduction of Linotronic film output.

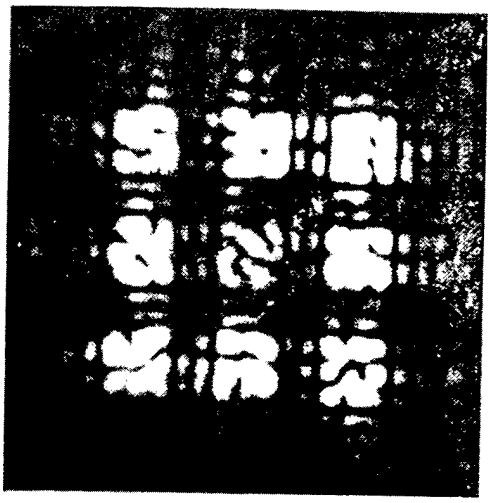

Fig. 13. Optical reconstruction from the photoreduced detour-phase filter.

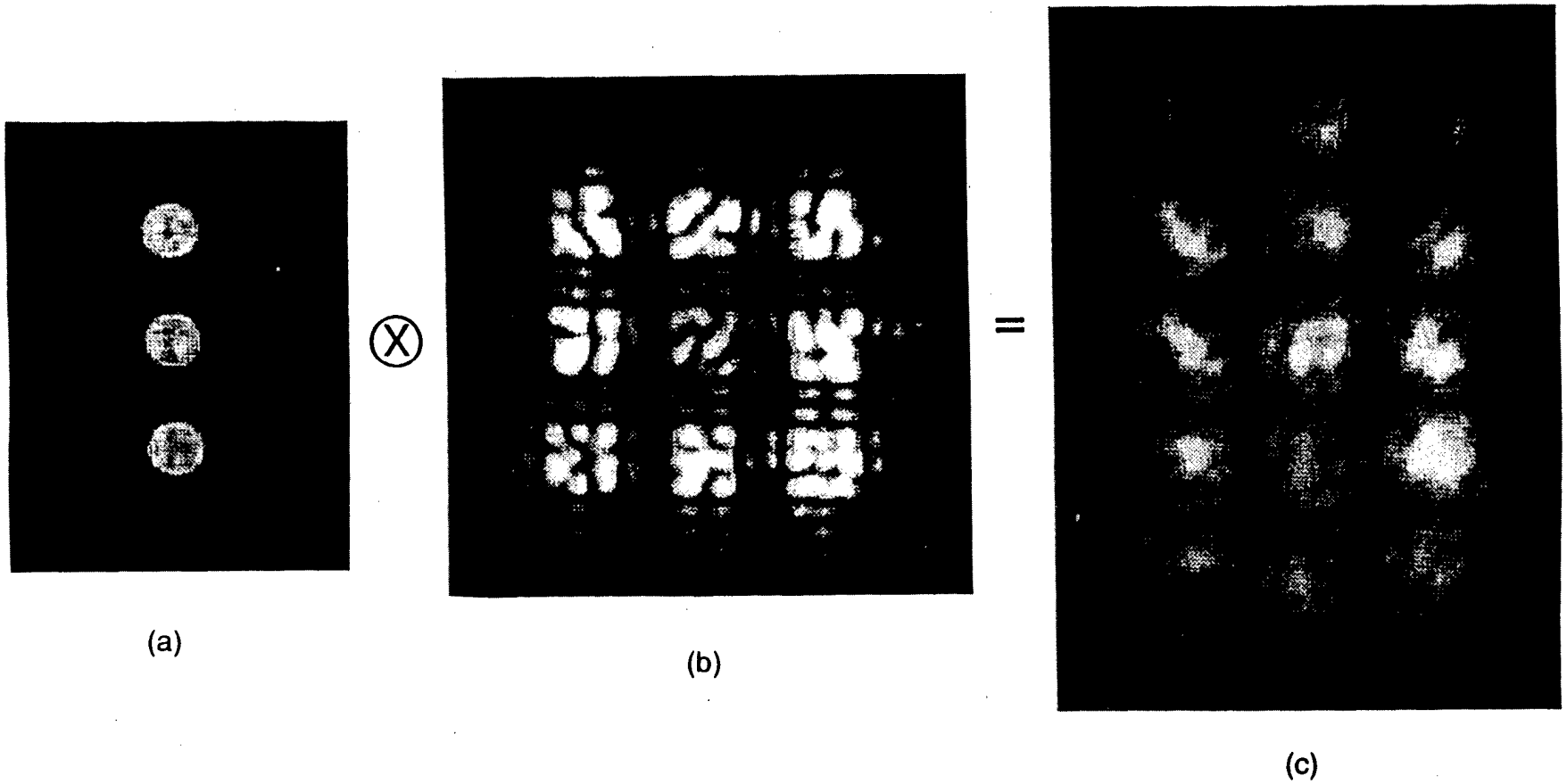

Fig. 14. Correlation of input pattern with photoreduced detour phase filter. (a) input pattern, (b) optical reconstruction from the photoreduced detour-phase filter, (c) CCD image of the correlation plane.

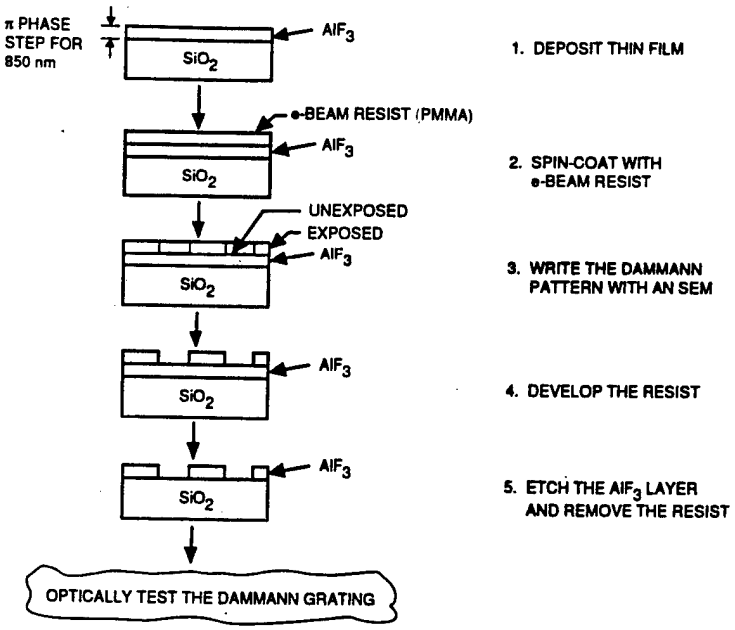

Fig. 15. Fabrication of Dammann grating using SEM.

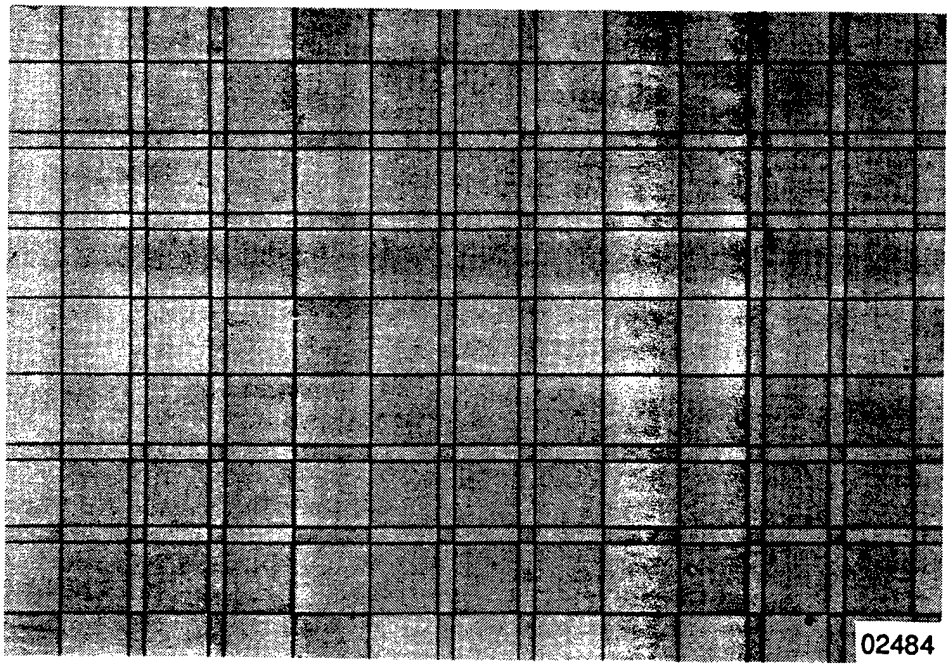

Fig. 16. 200X photomicrograph of SEM-exposed Dammann grating.

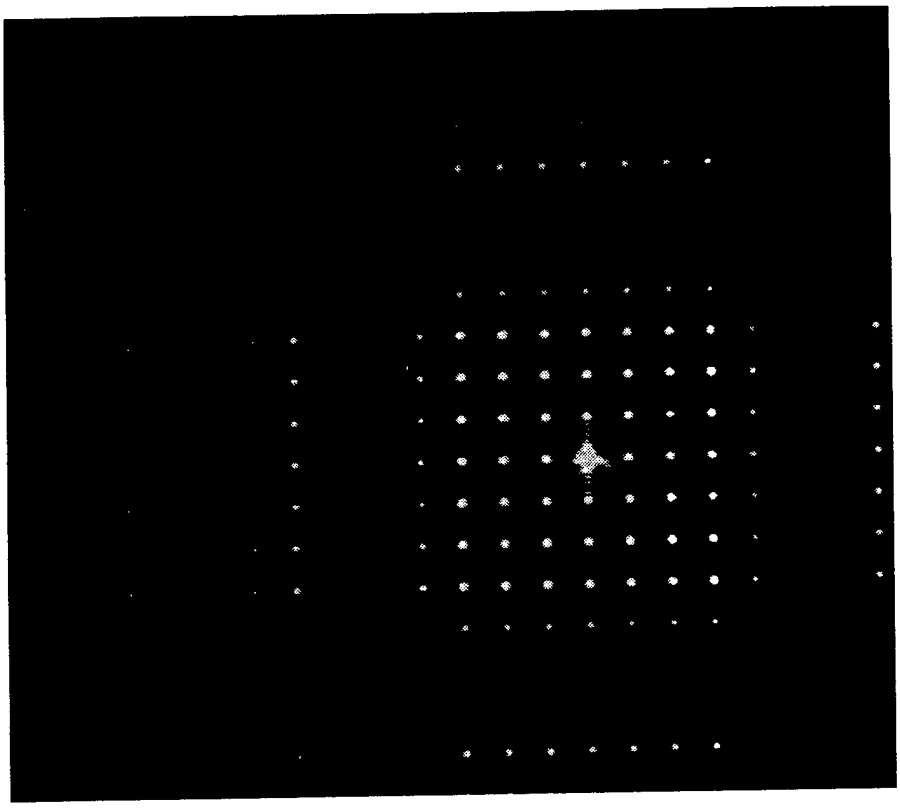

Fig. 17. Optical reconstruction from the SEM fabricated Dammann grating.

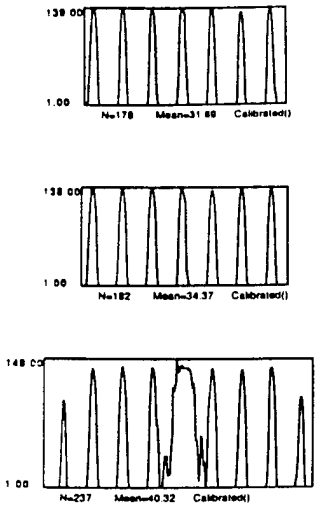

Fig. 18. Optical intensity traces from Figure 17.

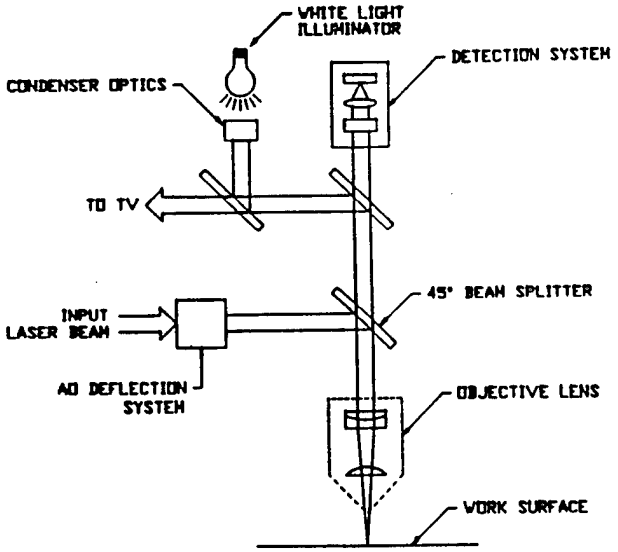

Fig. 19. Direct write laser microlithography from NEOS Corporation.

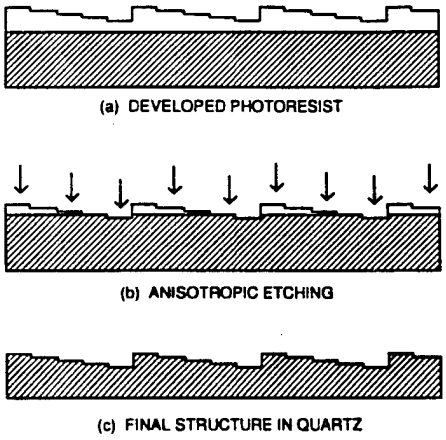

Fig. 20. Etching photoresist pattern in substrate.

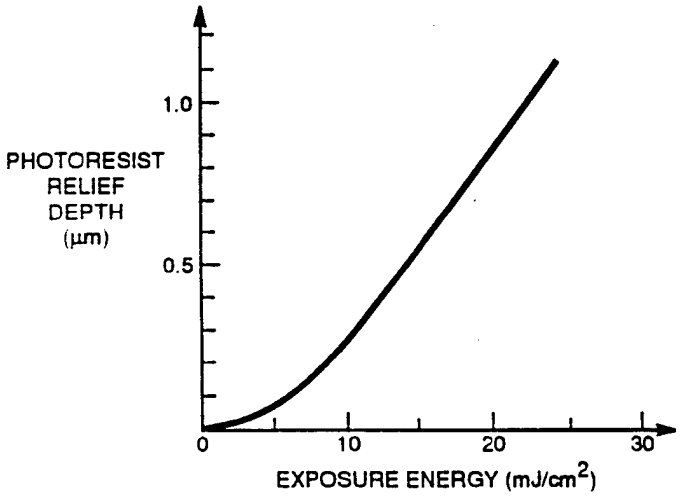

Fig. 21. Photoresist relief depth versus exposure energy from reference 6.

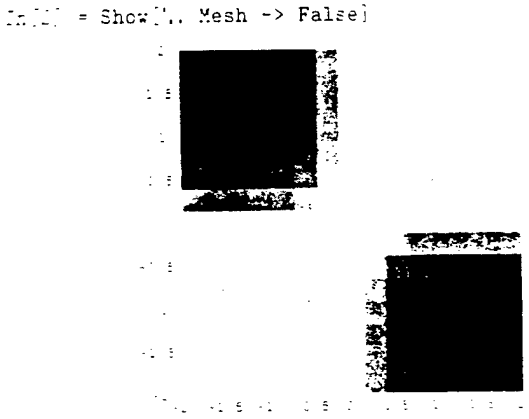

Fig. 22. Example of PostScript graphics created in Mathematica.

THERMAL WEAPON SIGHT (TWS) AN/PAS-13* DIFFRACTIVE OPTICS DESIGNED FOR PRODUCIBILITY

February 1993

J. Steven Anderson
Chungte W. Chen
Hughes Aircraft Company
Electro-Optical Systems
El Segundo, CA 90245

Robert A. Spande
CECOM, Night Vision and Electric Sensors Directorate
Lasers and Photonics Division
Fort Belvoir, VA 22060-5677

Abstract

The Thermal Weapons Sight (TWS) program is a manportable 3 – 5 micrometer forward-looking-infrared (FLIR) rifle sight. The manportable nature requires that the optics modules be lightweight, low cost and compact while maximizing performance. These objectives were met with diffractive optics. TWS promises to be the first FLIR sensor to incorporate kinoform surfaces in full scale production.

1.0 INTRODUCTION

TWS is a mid-infrared thermal sensing sight being developed for the Army by Hughes Aircraft Company. The program is managed by the U.S. Army Project Manager for Night Vision and Electro-optics (PMNVEO) with technical support provided by CECOM, Night Vision and Electronic Sensors Directorate (NVESD). The technology for this program is based on the use of thermoelectrically cooled second generation PV-HgCdTe MWIR focal plane arrays. The sight will be either hand held or mounted on manportable weaponry (Figure 1). As such, the sight is required to be compact and lightweight. In addition, the battlefield mission requires that the sight provides high optical resolution. The use of diffractive optics has emerged as a powerful design tool which has aided in meeting these criteria.[1] The application of diffractive surfaces to the TWS optical designs has resulted in an overall reduction in lens count while improving performance and lowering cost.

* This work was performed in connection with CECOM contract No. DAAB07-91-K254.

1 "Optical Element Employing Aspherical & Binary Grating Optical Surfaces." Chungte W. Chen, US Patent: 5,044,706

The TWS program calls for an initial production option up to 6,200 units and is the first large-scale military production program to incorporate diffractive optics into its infrared optics.

The TWS sensor is designed for varying mission scenarios (Figure 2). It can be used as a wide-field-of-view (WFOV) sensor in the Basic Sensor mode without any telescope attachments or with 1 or 3 interchangeable telescopes. The 2× telescope provides the Light Weapon Thermal Sight (LWTS) configuration for lighter weapons in near field engagements. The Medium Weapon Thermal Sight (MWTS) telescope is dual-field-of-view (DFOV) with a 3.3× narrow-field-of-view (NFOV) and a 2× WFOV for mid-range situations. The Heavy Weapon Thermal Sight (HWTS) is intended for long-range operation with a 10× NFOV and a 3.3× WFOV.

The TWS infrared sensor contains a mosaic array of detectors which paints the scene by scanning the image across it. The infrared optics are composed of a re-imaging imager and the 3 application specific telescopes. The visual train paints the display image by scanning a line image of an LED array across the image plane of the eyepiece. (Figure 3.)

2.0 THE USE OF DIFFRACTIVE OPTICS

Figure 4 illustrates how diffractive optical elements (DOE) can provide chromatic correction to an optical system. A conventional lens ***without*** a diffractive surface will focus light of differing wavelengths at different points due to the inherent dispersion of the lens substrate material. By adding the diffractive surface, the dispersion of the substrate material can be compensated for and the differing wavelengths of light will focus at a common point. Conventional broad wavelength band optical designs employ two or more lens materials with different powers and dispersion characteristics to balance the chromatic aberrations. This would generally results in a greater number of lenses in the design to provide chromatic correction than that required for the basic geometrical correction. With the simple addition of a diffractive surface, the color correction can b e accomplished with the minimum number of lenses.

The diffractive elements used on TWS are surface-relief circularly symmetric gratings with very high diffraction efficiency. This is created by reducing a continuous phase profile (Figure 5-a) into discrete 2π increments located along a common surface (Figure 5-b). This analog type of surface relief profile is commonly known as a kinoform and is theoretically capable of achieving 100 percent diffraction efficiency at its functional wavelength. The TWS kinoform surface relief profiles are formed by single-point precision diamond machining methods.

3.0 THE TWS DIFFRACTIVE DESIGNS

A diffractive optic was used in each of the TWS IR optical designs for simplification and/or to improve its performance. Table 1 compares the modulation transfer function (MTF) of the diffractive designs against the conventional. In general, the MTF of the diffractive design out-performs its conventional counterpart.

The utilization of a diffractive optic element reduced the number of optical lens elements required in the IR imager from 5 to 3 (Figure 6). As an added benefit, the overall MTF was improved, the distortion was cut in half and the sensitivity of the lenses to positional tolerances was reduced. The geometrical aberration (H-TanU) curves of the conventional and diffractive imager are shown in Figure 7 and Figure 8 respectively. The top, middle and bottom curves in each are the H-TanU curves corresponding to the full field, 70 percent field and on-axis, respectively. Note that the diffractive design demonstrates much better chromatic as well as higher order aberration correction.

The design principles for the TWS re-imaging imager that consists of refractive optical elements and DOE are:

1. The primary lateral color, secondary lateral color, and coma are self-corrected through the symmetry principle, wherein the front and rear groups are symmetric with respect to the intermediate image plane.
2. The axial color of the entire system is corrected by a DOE in the second group. This DOE also corrects the high-order chromatic aberrations, such as spherochromatism and chromatic coma. Because this DOE is positive, it contributes to the overall system power, unlike a classical flint glass. Using the DOE for chromatic aberration significantly reduces the intrinsic aberrations of each element and, therefore, that of the entire optical system.
3. The spherical aberration and coma of the front and rear groups are corrected by using an aspherical surface or by bending the lenses.
4. The astigmatism is corrected by placing the lens elements in the proper positions with adequate optical power distribution.
5. The DOE and germanium significantly reduce the field curvature, as compared to the conventional equivalent.

Likewise, the incorporation of a diffractive surface in the LWTS telescope design eliminated one lens element while improving performance (Figure 9). This is attributed to the germanium-DOE, which has similar dispersion characteristics to a silicon lens but with a higher index of refraction. Therefore, the low-order, high-order aberrations and field curvature are significantly reduced. The objective portion of this design is also more compact.

Unlike the IR imager and the LWTS telescope, the number of optical elements remained the same in the MWTS diffractive NFOV and WFOV telescope designs (Figure 10) but performance benefits were achieve. The significant improvement in the MWTS image quality is also attributed to the germanium-DOE element, as described for the LWTS case. The MWTS NFOV diffractive design, on average, picked up 15 absolute MTF points over the conventional design! The MWTS WFOV also made gains.

For the HWTS telescope (Figure 11), replacing the CaF_2 objective secondary with a diffractive ZnS lens element allowed the Si objective primary to be simplified from an asphere to a sphere. The combination of ZnS and a DOE creates an Abbe number about the same as that of the CaF_2 lens. Indeed, the combination of ZnS and a DOE has optical characteristics even better than the CaF_2 lens, such as higher index of refraction to reduce aberrations with a tunable Abbe number for better chromatic aberration correction. This permitted the Si objective to be fabricated with less costly conventional polishing. The difference between precision diamond machining the ZnS kinoform rather than the Si objective results in an overall cost savings. Si is difficult to diamond machine and tool wear is significant due to its inherent hardness. For equivalent 1.0 inch diameter parts, more than 30 ZnS lenses can be diamond machined without replacing the tool compared to only 1 Si lens. Thus, ZnS provides significant savings in tooling. In addition, the predicted MTF performance is enhanced especially for the WFOV. (See Table 1.)

4.0 HARDWARE EXAMPLES

Figure 12 describes the first prototype imager used to validate the performance of precision diamond machined diffractive designs for TWS-type applications.[2] The kinoform element required a14 2π zones (Figure 12a). Figure 12b shows these zones as fabricated on the lens. The success of achieving the required analog pattern is exhibited in the profilometer trace of the surface (Figure 12c).

Another kinoform example can be easily seen on the second lens of the HWTS telescope. The zones on this ZnS piece are quite evident in the cutaway view of the telescope (Figure 13).

2 "The Use of Diffractive Optical Element in 3 – 5 Micrometer Optical System," Chungte W. Chen, J. Steven Anderson, presented at IRIS Specialty Group on Passive Sensors, February 1992

5.0 TWS TEST DATA

Preliminary MTF tests have been conducted on the first optical modules produced in the development production prove-out (DPPO) phase of the TWS program. Tables 2 – 5 compare the MTF test data of each module against the nominal design value and the predicted performance due to manufacturing tolerances. Note that some of the variations in MTF test values may be related to the test accuracy. (The better MTF stations are only accurate to 3 percent.) However, the trend of all tested values match closely with the predicted performance. These results verify with multiple cases that the diffractive optic model predictions are accurate.

6.0 CONCLUSION

The use of diffractive optics has been successful in achieving the optical design goals. TWS boasts optical systems that are lighter, more compact, and lower cost than their conventional counterparts while attaining significant performance gains. The technology of precision diamond machining kinoforms has now been realized. The Thermal Weapons Sight is blazing a vivid path in the deployment of diffractive IR optical sights.

Figure 1: THERMAL WEAPON SIGHT (AN/PAS-13). ***The TWS, shown here in its LWTS configuration, is lightweight in all configurations for manportable mobility.***

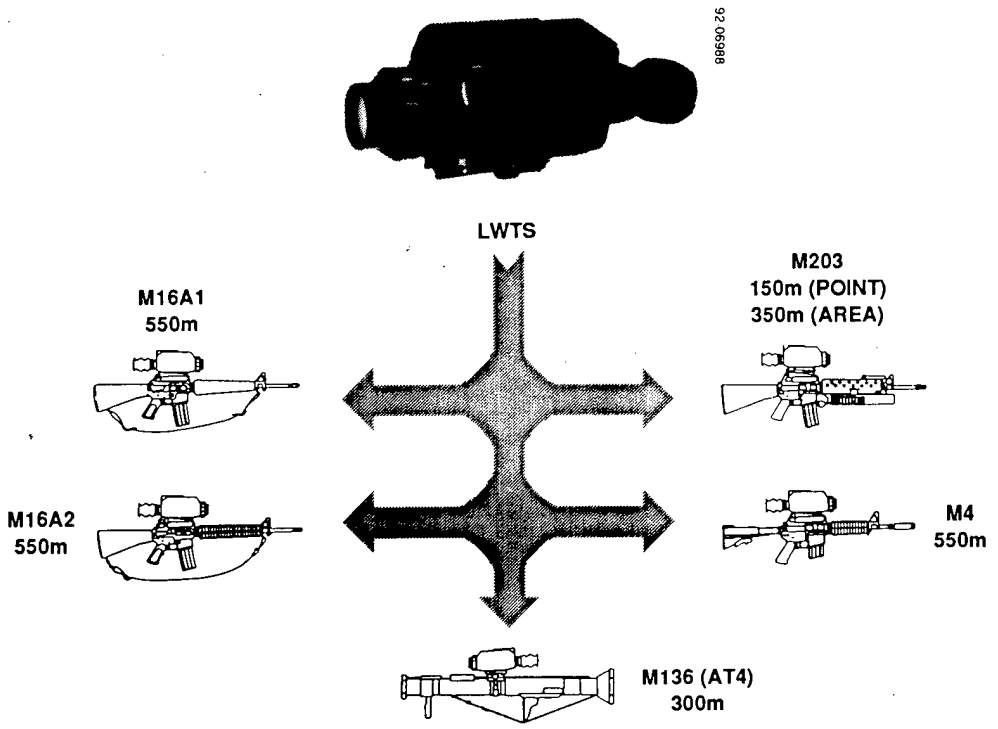

(a) LWTS

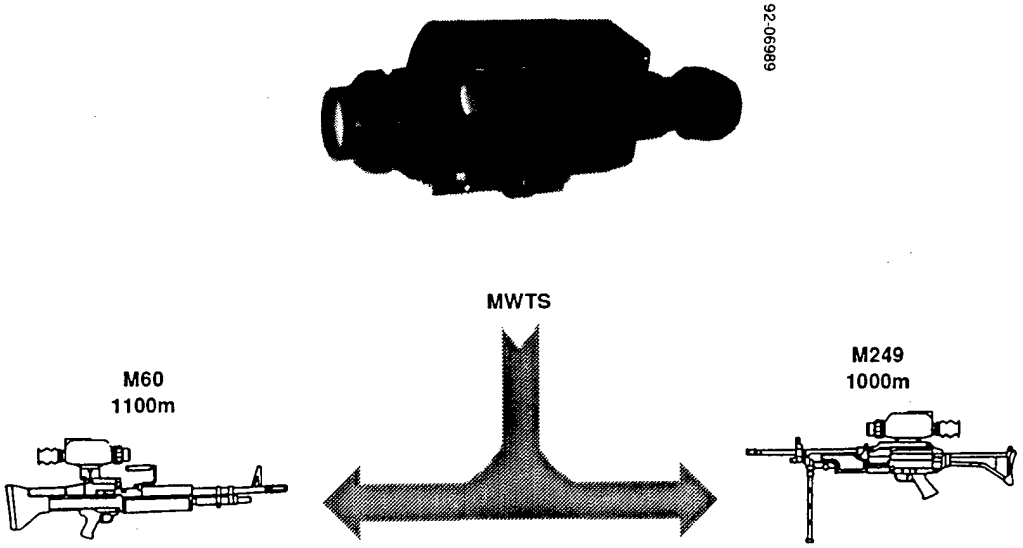

(b) MWTS

Figure 2: TWS WEAPON APPLICATIONS. *The TWS is designed to meet all thermal imaging needs of the Infantry squad. A full complement of mounting brackets and electronic reticles are available for a wide variety of weapons.*

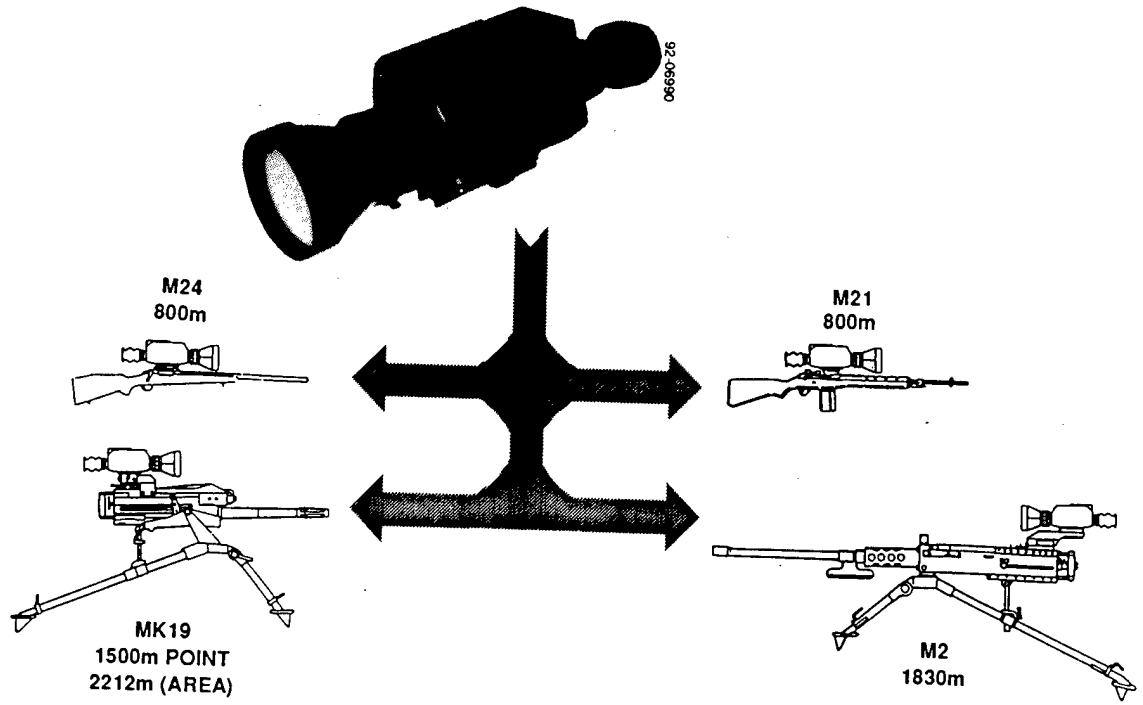

(c) HWTS

Figure 2: TWS WEAPON APPLICATIONS *(Continued).*

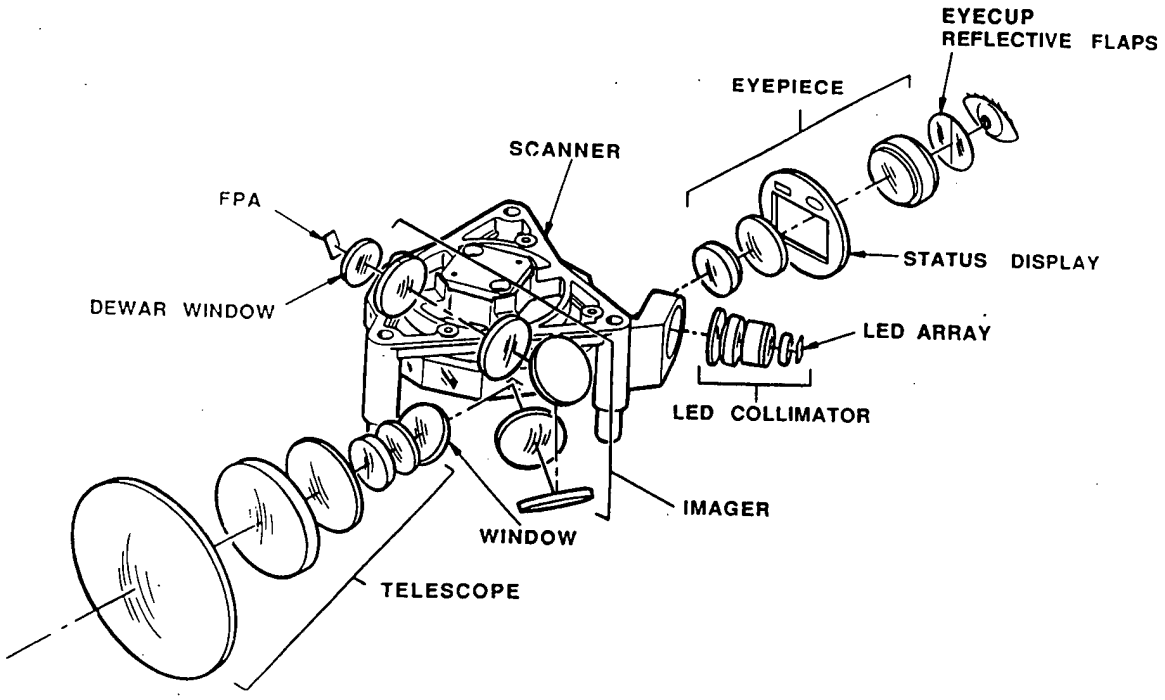

Figure 3: TWS OPTICAL DESIGN. *Different facets of the same polygon wheel are used for both the IR and visible scans.*

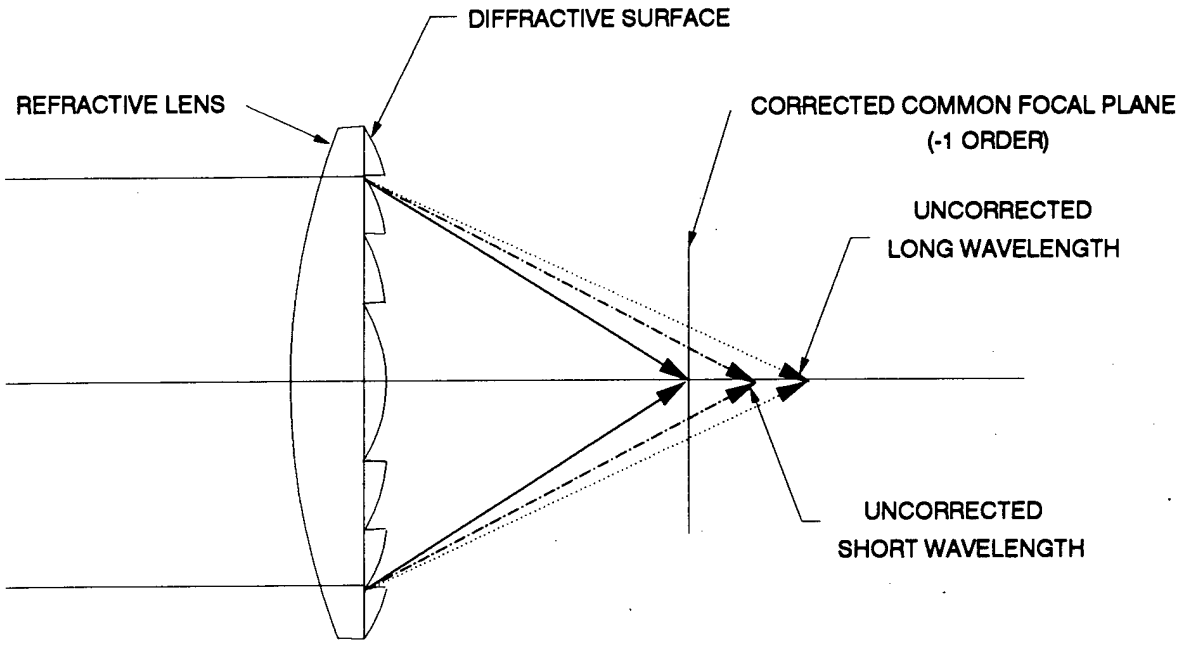

Figure 4: DIFFRACTIVE COLOR CORRECTION. *The diffractive surface creates a common focus for the short and long spectral wavelengths.*

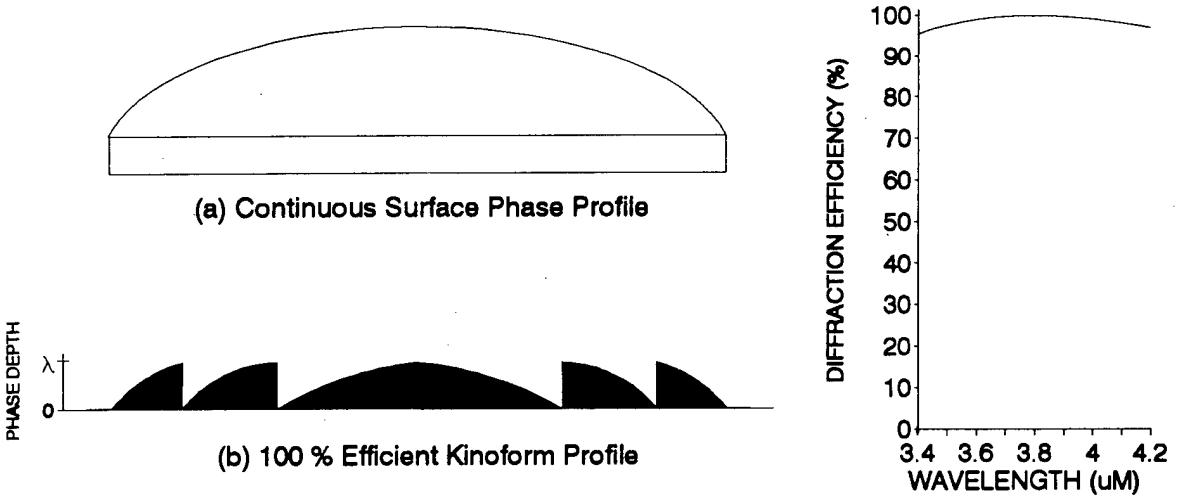

Figure 5: KINOFORM SURFACE RELIEF PROFILE. *Diffractive surfaces are the reduction of continuous surface phase profiles into 2π increments. Diffraction efficiency peaks at the reference wavelength.*

TABLE 1.

MTF COMPARISON BETWEEN CONVENTIONAL DESIGN AND DIFFRACTIVE DESIGN

	IMAGER		HWTS WFOV		HWTS NFOV		MWTS WFOV		MWTS NFOV		LWTS	
FIELD	C	D	C	D	C	D	C	D	C	D	C	D
0.25 VER	.79	.78	.73	.80	.73	.73	.75	.79	.62	.80	.71	.71
0.25 HOR	.77	.74	.60	.77	.64	.68	.72	.75	.56	.73	.64	.69
0.75 VER	.71	.72	.60	.77	.76	.80	.74	.79	.61	.65	.62	.61
0.75 HOR	.63	.75	.43	.70	.39	.47	.69	.64	.36	.56	.49	.71

C: CONVENTIONAL DESIGN, **D:** DIFFRACTIVE DESIGN **MTF** AT 23.3 LP/MM

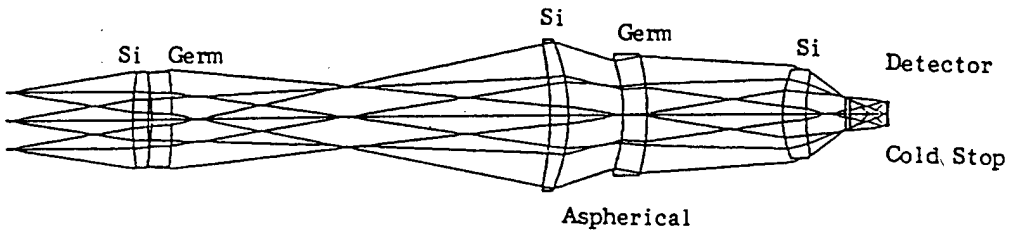

(a) Conventional Design

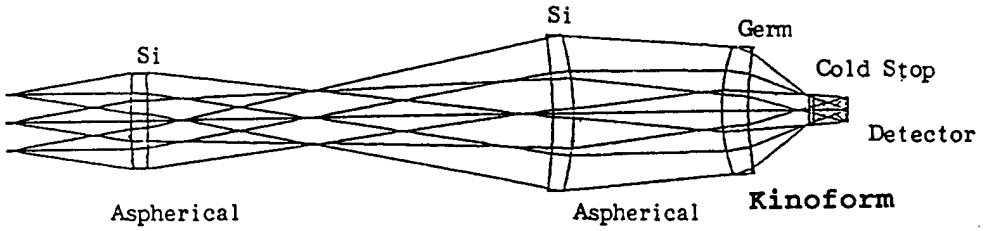

(b) Diffractive Design

Figure 6: TWS DIFFRACTIVE IR IMAGER. ***Diffractive optics create a 40 percent reduction in lens count, cut distortion in half and relax fabrication tolerances.***

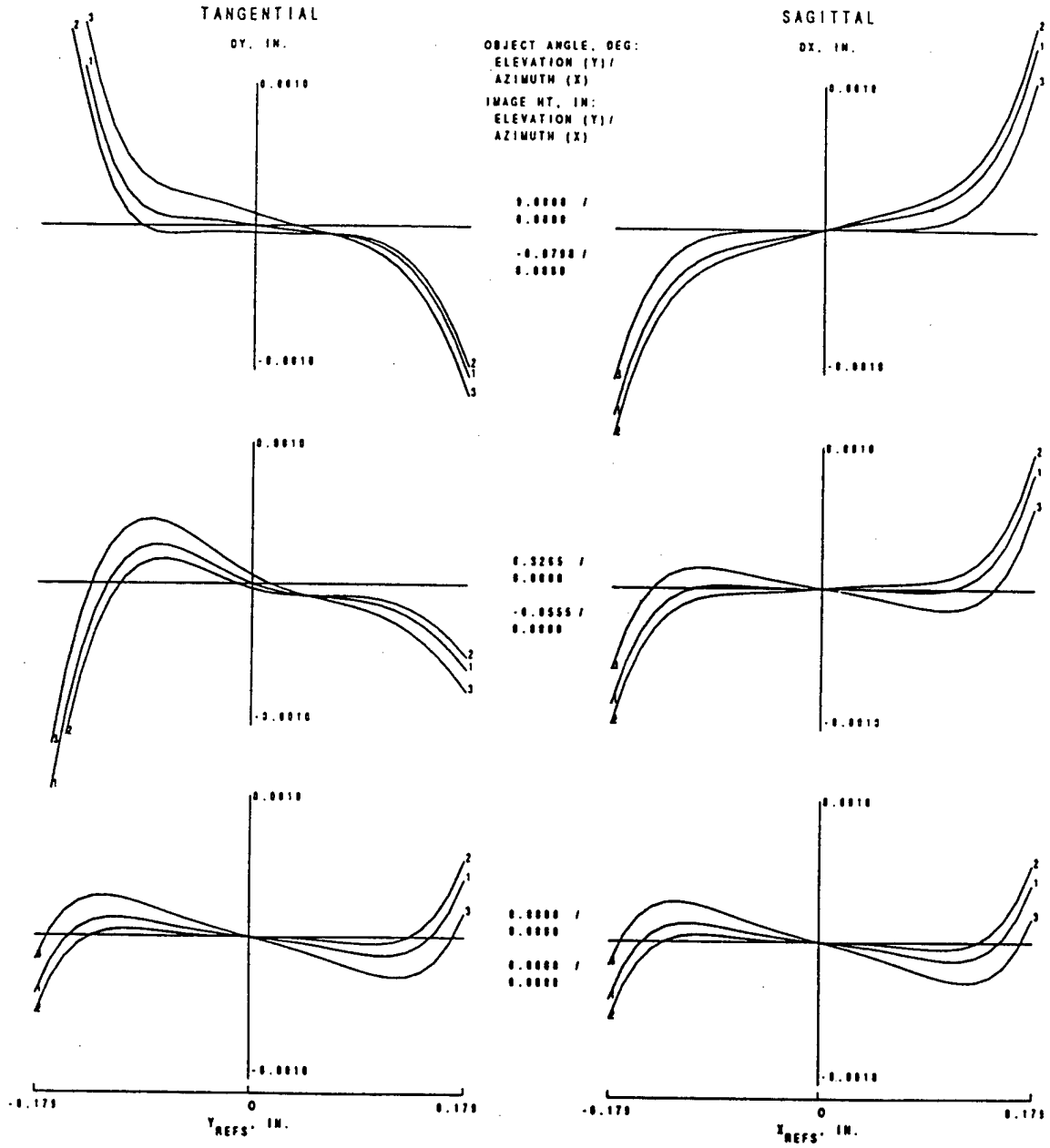

Figure 7: CONVENTIONAL IMAGER PERFORMANCE. ***The H-TanU curves of the conventional imager exhibit chromatic aberration.***

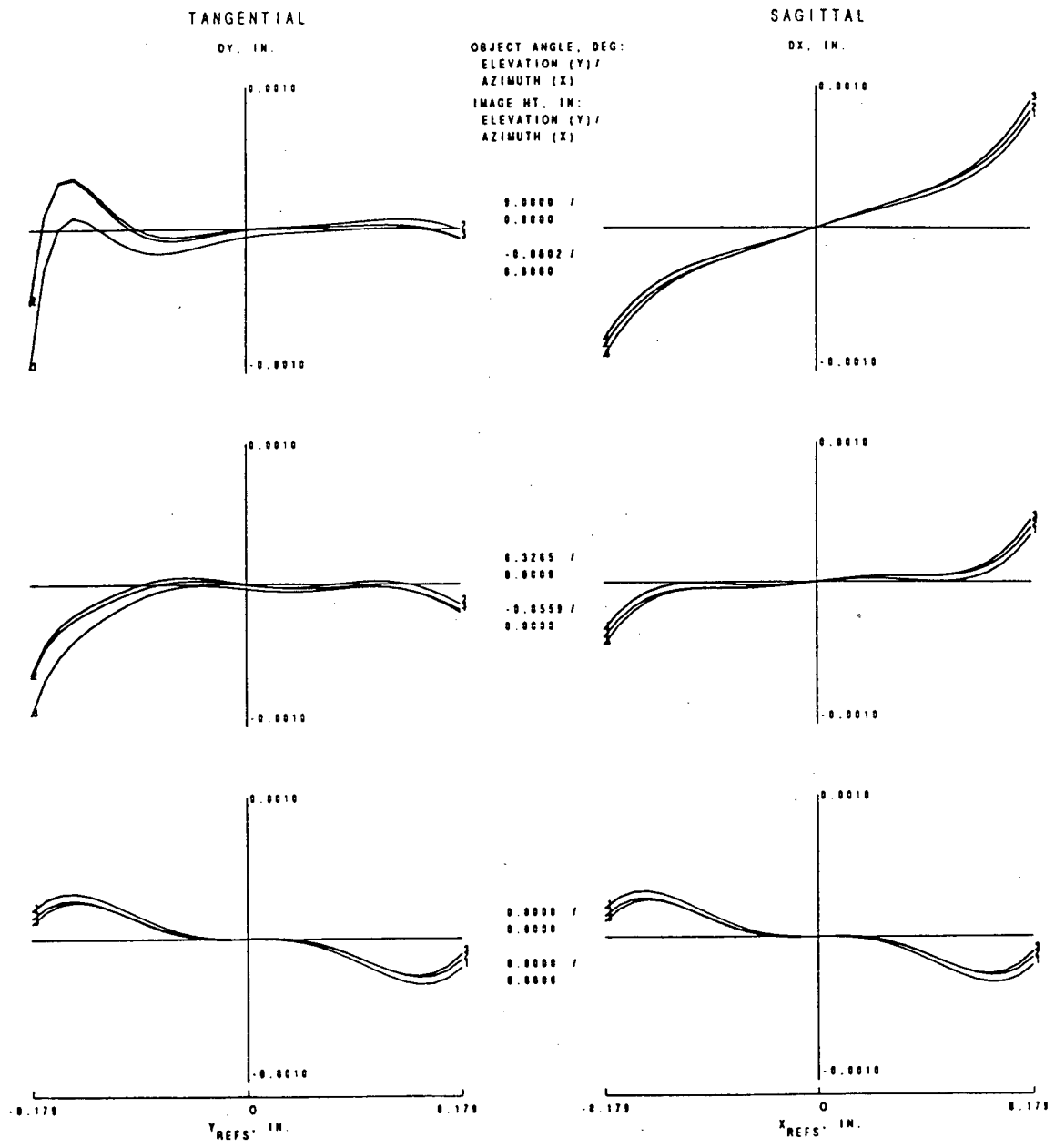

Figure 8: **DIFFRACTIVE IMAGER PERFORMANCE.** *The diffractive imager chromatic aberrations are well corrected and the geometrical aberrations are less than the conventional design.*

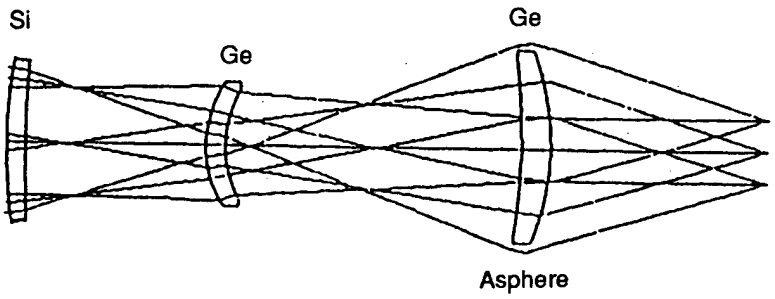

(a) Conventional design

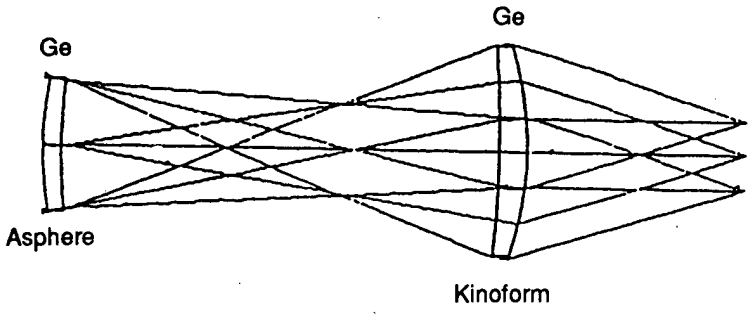

(b) Diffractive Design

Figure 9: LWTS DIFFRACTIVE TELESCOPE. ***The LWTS diffractive telescope has 33 percent fewer lenses and is more compact.***

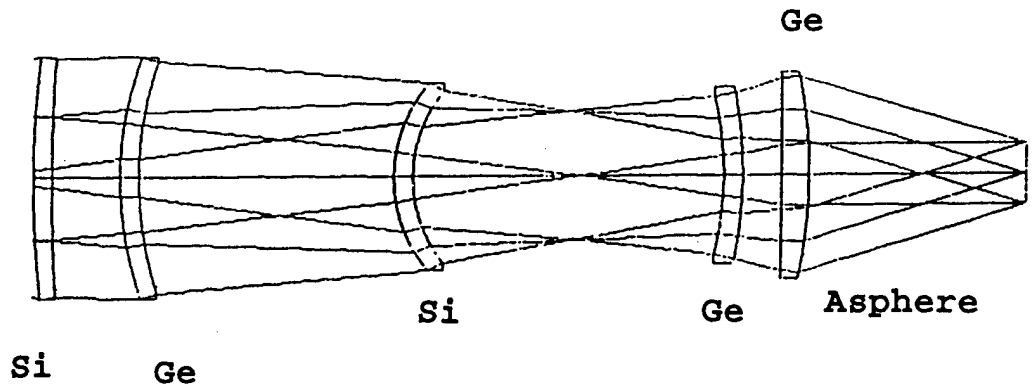

(a) Conventional Design (WFOV View)

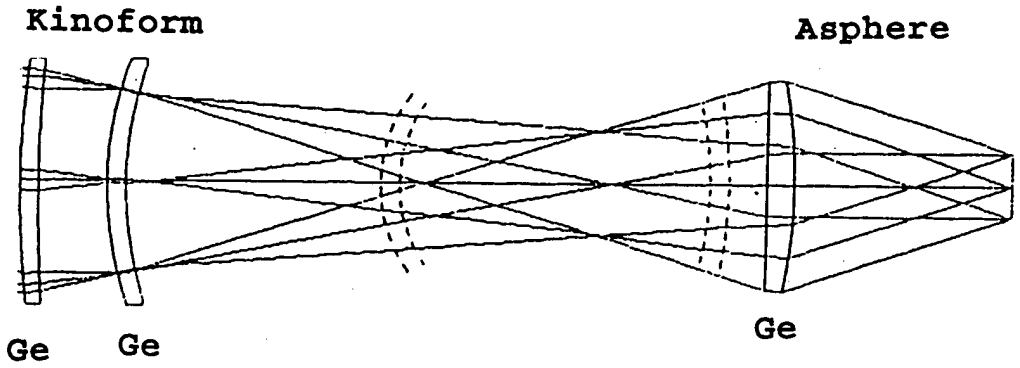

(b) Diffractive Design (NFOV View)

Figure 10: MWTS DIFFRACTIVE TELESCOPE. ***The MWTS diffractive telescope provides substantial MTF improvement through better chromatic correction.***

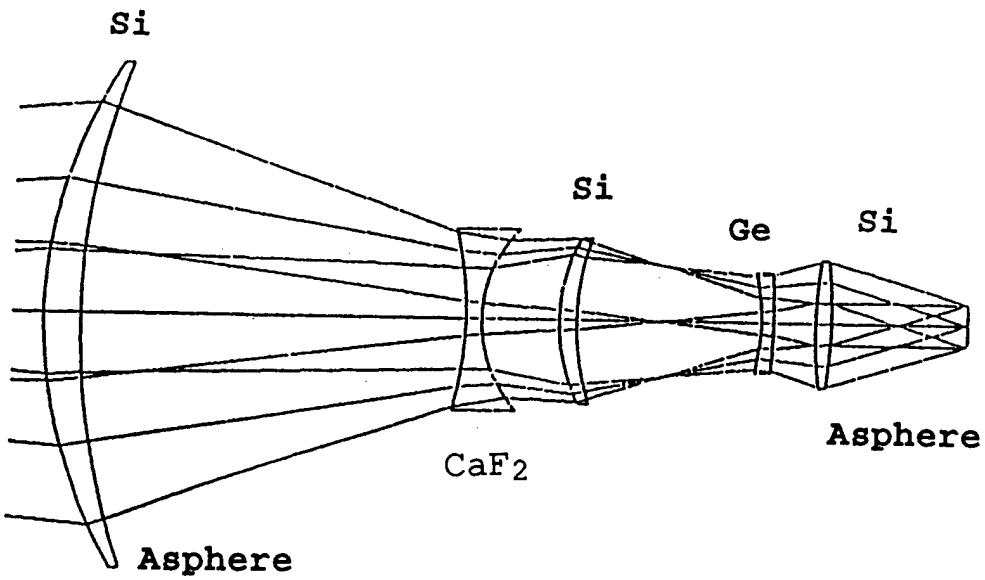

(a) Conventional Design

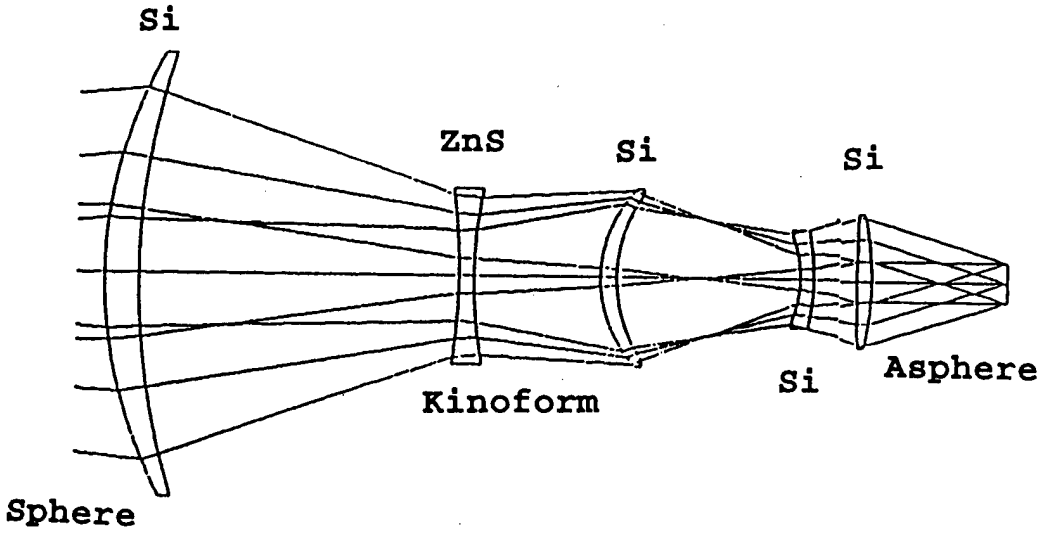

(b) Diffractive Design

Figure 11: HWTS DIFFRACTIVE TELESCOPE. ***The HWTS diffractive telescope provides enhanced producibility and imagery.***

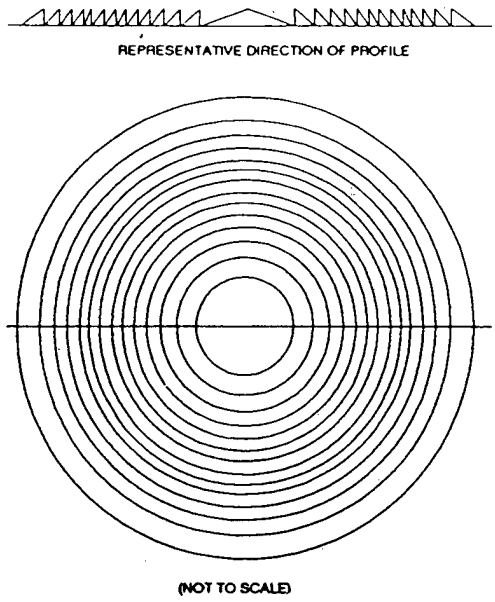

a. Diffractive imager 2Π zones (14)

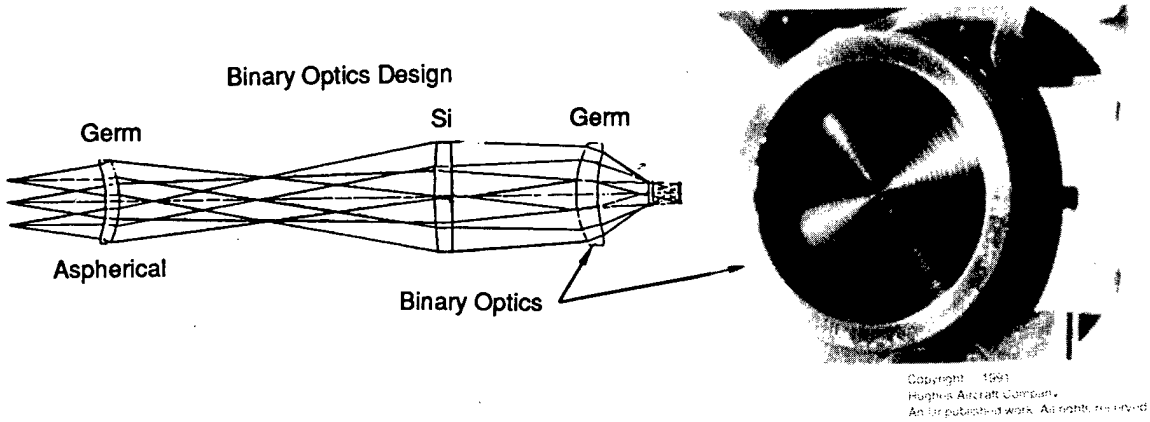

b. Kinoform Surface

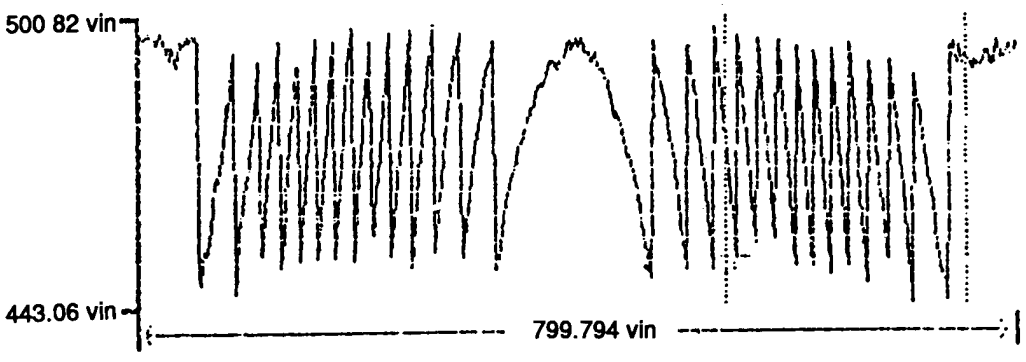

b. Kinoform Profile Measurement

Figure 12: TWS PROTOTYPE IR IMAGER. ***The diffractive lens is composed of 14 precision diamond machined zones with a depth of 1.28 micrometers.***

Figure 13: HWTS DIFFRACTIVE TELESCOPE. *The ZnS kinoform on the second lens of the telescope can be seen in this cut-away view.*

TABLE 2. SUMMARY OF MTF DATA FOR IR IMAGER

FIELD	DESIGN	DESIGN & TOLERANCES	TEST RESULTS
On-Axis	0.83	0.79	0.82
0.5 Elevation	0.80	0.79	0.80

Spatial Frequency 0.296 lp/mrad
Vertical Bar Reponse

TABLE 3. SUMMARY OF MTF DATA FOR LWTS TELESCOPE

FIELD	DESIGN	DESIGN & TOLERANCES	TEST RESULTS
On-Axis	0.72	0.69	0.72
0.5 Elevation	0.73	0.7	0.68
0.5 Azimuth	0.74	0.71	0.73

Spatial Frequency 0.6 lp/mrad
Vertical Bar Reponse

TABLE 4. SUMMARY OF MTF DATA FOR MWTS TELESCOPE

FIELD	DESIGN	DESIGN & TOLERANCES	TEST RESULTS
On-Axis	0.83	0.82	0.83
0.5 Elevation	0.83	0.82	0.79
0.5 Azimuth	0.7	0.68	0.66

WIDE FIELD OF VIEW

Spatial Frequency 0.6 lp/mrad
Vertical Bar Reponse

FIELD	DESIGN	DESIGN & TOLERANCES	TEST RESULTS
On-Axis	0.82	0.8	0.81
0.5 Elevation	0.81	0.79	0.82
0.5 Azimuth	0.78	0.76	0.71

NARROW FIELD OF VIEW

Spatial Frequency: 1.0 lp/mrad
Vertical Bar Response

TABLE 5. SUMMARY OF MTF DATA FOR HWTS TELESCOPE

FIELD	DESIGN	DESIGN & TOLERANCES	TEST RESULTS
On-Axis	0.74	0.71	0.74
0.5 Elevation	0.75	0.73	0.67
0.5 Azimuth	0.59	0.56	0.63

WIDE FIELD OF VIEW

Spatial Frequency 1.0 lp/mrad
Vertical Bar Reponse

FIELD	DESIGN	DESIGN & TOLERANCES	TEST RESULTS
On-Axis	0.81	0.72	0.72
0.5 Elevation	0.81	0.72	0.71
0.5 Azimuth	0.71	0.63	0.67

NARROW FIELD OF VIEW

Spatial Frequency: 1.0 lp/mrad
Vertical Bar Response

MEASUREMENTS OF MICROLENS PERFORMANCE

D. Shough, B. Herman, and G. Gal
Lockheed Palo Alto Research Laboratory
3251 Hanover Street, Palo Alto, California 94304

ABSTRACT

We present results of laboratory evaluations of several microlens types that have been designed and fabricated at the Lockheed Research and Development Division. The microlenses include wideband and dispersive types, in isolation and in arrays, and fabricated with binary or grayscale methods. Different lens pixel geometries are considered, including square, hexagonal, and skewed microlenses. We describe our micro-optics laboratory testbed which has been designed for the evaluation of individual lenslets or 2D arrays at selected spectral wavelengths. Measurement capabilities include focal length, point-spread functions, wavefront quality, and modulation transfer functions. Our present effort focuses on the results of point spread function measurements and their comparison with design predictions.

1.0 INTRODUCTION

The Lockheed Research & Development Division (R&DD) has an ongoing effort in the research and development of micro-optics technology. The effort encompasses research and development of innovative micro-optics elements for systems applications that require the design, fabrication, and optical performance evaluation of microlenses and microlens arrays. The purpose of this paper is to report the establishment of a micro-optics metrology laboratory and to describe some of the techniques and equipment that have been developed specifically for the study of microlenses, both as individual elements and as arrays.

Testing microlenses is in principle no different than testing any other optical element. The same parameters need to be measured and the techniques required are the familiar methods utilized in any conventional optical testbed. However, in many cases the measurement of microlenses presents practical problems because of the size of the elements. Microlenses of interest to us have diameters between 50 μm and a few millimeters and have speeds between f/1 and f/10.

On an individual basis as well as for arrays, measurements that are of interest are: the focal length; point-spread function (PSF); wavefront quality; modulation transfer function (MTF); micro-

lens surface quality, shape, and radius; transmission efficiencies; and wavefront properties. For testing a microlens array, we must include dropouts and uniformity across the array. This is especially important for integrated devices such as focal plane arrays.

Internally cooled apertures and agile beam steering (ABS) units[1] require the utilization of a special grouping of array lenses to produce combined pairs defined by Gabor as superlenses.[2] These lenslet arrays have interesting optical properties and it is necessary to measure their MTF and subsequent image formation properties. Detailed optical performance evaluation is our long-term objective.

2.0 MICRO-OPTICS TESTBED

We have established a laboratory dedicated to testing micro-optics. Table 1 outlines our test capabilities for single microlenses and/or microlens arrays.

Testing an individual microlens allows detailed measurements of its properties. This is very important in order to verify the design and fabrication of microlenses. The side lobes of the PSF, which might cause cross-talk in adjacent pixels of a focal plane array, can be measured, or the ripple in the wavefront quality, which might cause severe image degradation can be examined. The main problems are providing enough power through the small size of a single microlens and magnifying the image to a reasonable size.

For some applications, such as integrated focal planes, each lens in the array must be tested to ensure that manufacturing problems did not cause one or more microlenses to drop out or to be substandard. Testing every microlens in a 100 by 100 array requires 1 week if each lens takes only 1 min. This precludes the detailed testing that we do for individual microlenses.

These optical measurements may be performed according to a test plan at a variety of wavelengths from various sources:

- CO_2 laser at 10.6 μm
- Lead-salt lasers at 8, 10, 12, and 14 μm. Other lead-salt lasers from 3.3 to 20 μm can easily be added
- Blackbody source with monochromator adjustable from 0.4 μm to 20 μm
- HeNe laser at 3.39 μm
- HeNe laser at 1.52 μm
- Solid state lasers from 0.7 to 1.6 μm

3.0 POINT-SPREAD FUNCTION (PSF) MEASUREMENT

The PSF is the image of a point source formed by a lens. Measurement of the PSF provides a detailed examination of the performance of a fabricated lens. The basis for our measurements of

1. Gal, G., et al. "Micro-Optics Technology and Sensor System Applications," Conference on Binary Optics, Huntsville, AL, 1993.
2. Hutley, M. C., and R. F. Stevens, "The Formation of Integral Images by Afocal Pairs of Lens Arrays ("Superlenses")," *Microlens Arrays*, M. C. Hutley, Ed., IOP Short Meeting Series No. 30, Institute of Physics, Vol. 199, IOP Publishing, Ltd., UK.

the PSF (Figure 1) is to place the microlens array on a computer-controlled XYZ translation stage and to examine the intensity from individual microlenses. The PSF is magnified by a microscope objective onto a detector. The system is flexible, accurate, and extendible.

3.1 CO_2 LASER SOURCE

All measurements presented in this paper use a 10 W CO_2 laser operating at 10.6 μm. A rotating polarization attenuator prevents thermal damage to the optics. A quartz window acts as a dichroic beam splitter, allowing us to coalign a visible HeNe laser for alignment purposes. The laser beam passes through a mechanical chopper and two apertures before striking the lens array. The illuminated area of the array is a 0.5-in.-diameter circle.

The CO_2 laser produces a nearly collimated beam and has more than enough power for the desired measurements. Because of the small size of the microlenses, the collimation requirements for the incident beam are very lax. To have less than one-quarter wave peak-to-peak error across a microlens, the radius of the wavefront should be greater than 5 mm, i.e., the wavefront appears collimated if the beam focus is at least 5 mm away from the microlens. Even then the effect of using a slightly diverging beam is to test the microlenses at an incorrect magnification.

3.2 LEAD-SALT LASERS

For testing dispersive microlenses[3] (which simultaneously focus and disperse light in a wavelength band), it is necessary to vary the spectral wavelength. We are in the process of adding four lead-salt lasers that operate at 8, 10, 12, and 14 μm to our set-up. All four lasers are mounted within one LN_2 dewar. To switch between lasers, we are installing a kinematic base that allows easy and repeatable repositioning of the dewar in four different positions corresponding to the lasers. We switch between the CO_2 and the lead-salt lasers by removing a mirror mounted on another kinematic base.

The lead-salt lasers emit approximately 1 mW of power from an area of 10 by 20 μm. This produces a beam with a large divergence and low power through the microlenses. Therefore, we must collimate the beam in order to increase the amount of power through the microlenses.

When switching between lasers, we do not expect perfect alignment of the sources, which will cause an apparent shift in the position of the PSF. We calibrate for this effect by first testing a microlens that does not have any dispersion (and, hence, does not deflect the focused spot).

3.3 MAGNIFICATION OF THE PSF

The output of the microlenses is collected by an Ealing all-reflecting microscope objective. The numerical aperture of the 36X objective is 0.50. It has a central obscuration of 12.5%, a field of view of 500 μm, and a focal length of 5.2 mm. The working distance for an unmodified objective is 8.0 mm. The light baffles in an unmodified Ealing objective (Figure 2) proved to be unusable for our purposes because the baffles let light pass straight through the objective to the image plane. We added a new stop to eliminate this effect. The exact size and position for the new stop was determined by trial and error.

The resolution of an ideal microscope objective with no central obstruction and with a numerical aperture of 0.5 is 26 μm. The effect of the obstruction on the PSF is to decrease the total power and to increase the power outside the central lobe. The radial distribution of power becomes

3. Herman, B., and G. Gal, "Theory of Dispersive Microlenses," Conference on Binary Optics, Huntsville, AL, 1993.

$$I(r) = \pi P_t\left(\frac{D}{2\lambda f}\right)^2\left|\frac{2J_1\left(\frac{\pi Dr}{\lambda f}\right)}{\left(\frac{\pi Dr}{\lambda f}\right)} - \frac{d^2}{D^2}\frac{2J_1\left(\frac{\pi dr}{\lambda f}\right)}{\left(\frac{\pi dr}{\lambda f}\right)}\right|^2$$

which is basically the difference between Airy patterns caused by the unobstructed objective and the obscuration. The last term is the contribution of the obscuration. The shape change is shown in Figure 3, with the obscured objective shown in black and the equivalent, unobscured objective shown in gray. The measured PSF out of the detector is the convolution of the PSF of the microlens, the PSF of the microscope objective, and the response of the detector.

In our current setup, the distance from the objective to the detector is 82 cm. Adding 4 cm for the separation of the principal plane and the objective shoulder gives an image distance of 86 cm. This produces a magnification of 160 for the 36X objective.

3.4 DETECTION

All data presented in this paper were taken using a HgCdTe detector cooled in a LN_2 dewar. The detector area is 1 mm by 1 mm. The microscope objective is used at 160X magnification; this corresponds to 6.25 μm at the plane of the PSF.

The light source is mechanically chopped at 1 kHz. The output of the detector is fed through a preamplifier specifically matched to the detector. The preamplifier output is fed to a lock-in amplifier which is read by the computer.

The range of the detector/preamplifier/lock-in amplifier extends from 3.3 pW to 0.4 μW, a dynamic range of over 5 decades. This allows detailed examination of the light outside the central diffraction lobe. The disadvantage to this setup is the long time required to complete a scan. A 101 by 101 2D scan or a 21 by 21 by 21 3D scan using a time delay of 1 s between readings requires 3 h.

Some scans require overnight runs with the result that the detector's LN_2 dewar warms up. This causes loss of all data until the dewar is refilled. Similarly, the power output of the CO_2 laser drifts over a range of 25 to 1. We are adding a second detector whose purpose is to monitor the output power. Future data will include corrections for these power fluctuations.

3.5 PSF, CONVOLUTION, AND SCANNING

The microlenses we have tested produce PSFs with diameters of 33 μm. This is magnified 160 times by the microscope objective and imaged onto the plane of the detector. At the detector, the magnified PSF diameter is 5.3 mm. The detector integrates the intensity over its 1 mm by 1 mm surface area to measure the power level.

To measure the spatial distribution of the PSF of the microlens, either the detector and microscope objective or the microlens must be moved. Either motion is approximately equivalent and moving just the microlens is far easier. The microlens array is mounted on a set of computer controlled Klinger XYZ translation stages with a resolution of 0.1 μm over a range of 50 mm. Maximum speed is 400 μm/s.

The measured value out of the detector is the convolution of the PSF of the microlenses, the PSF of the microscope objective, and the area or PSF of the detector divided by system magnification (160).

$$p(x,y) = l(x,y) \otimes\otimes m(x,y) \otimes\otimes d\left(\frac{x}{m}, \frac{y}{m}\right)'$$

$$= l(x,y) \otimes\otimes s(x,y)$$

where l, m, and d are the PSFs from the micro-optic lens, the microscope objective, and the detector, respectively, and $\otimes\otimes$ is a two-dimensional convolution. We are trying to measure l, the spatial distribution of the microlens PSF. This can be done by decorrelating l from the system response s.[4] In the Fourier transform frequency domain,

$$L(\xi,\eta) = \frac{S(\xi,\eta)P^*(\xi,\eta)}{|S(\xi,\eta)|^2 + \gamma|P(\xi,\eta)|^2}$$

where capitol letters indicate the Fourier transform, γ is the Lagrangian multiplier, and P is a smoothing function. The software exists but has not yet been applied to this problem.

3.6 TESTING PROCEDURES

After placing a microlens array on the XYZ translation stages, a quick coarse scan is made to determine the approximate coordinates of the microlens positions. The image is compared to the expected pattern of microlenses. Next, 2D and 3D scans are made in the vicinity of a single lens in order to refine the XYZ coordinates for the best focus. The position of best focus can be measured to within 2 μm. A final high-resolution scan is made in the plane of best focus.

A software package has been assembled for controlling the experiment and collecting the data. A variety of routines were programmed to allow control of the translation stages, reading of the lock-in-amplifier, and storing the data. These routines were then included within a program to perform 1D, 2D, and 3D scans of the PSF. The number of steps in each direction, the step size, the starting and ending positions, the dwell times at the start of each scan line, and the time constant for the lock-in-amplifier are all adjustable. To take advantage of the wide dynamic range of the detector, the computer program checks the voltage read against the previously set lock-in-amplifier sensitivity, changes scale as needed, and waits for the new reading.

The measured PSF is visualized using commercial software for the analysis of scientific data and custom software for the display of 3D shaded surfaces.

4.0 RESULTS

We now present measured PSF from four different multilevel Fresnel microlenses as indicated in Table 2. Each microlens was designed to concentrate light onto a detector on the back surface of the substrate. The focal lengths indicated are within the material and are the same as the thicknesses of the substrates.

Each microlens is presented with results from a 100- by 100-μm scan with a scan step size of 1 μm. The predicted PSF at the same scale is shown for comparison. No attempt was made to deconvolve the microlens PSF with that of the microscope objective or the detector.

---

4. Gal, G., and W. G. Opyd, "Determination of the Detector Spatial Responsivity by Signal Decorrelation in Spot Scan Measurements," *IEEE 1982 Conference Record of the 16th ASILOMAR Conference on Circuits, Systems, and Computers*, pp. 62-66.

4.1 WIDEBAND SQUARE Si

The square microlens on silicon substrate data represent one of the first microlenses we fabricated. The total thickness of the Fresnel element is given as $\bar{\lambda}/(n - 1)$, where $\bar{\lambda}$ is the design wavelength and n is the index of refraction. Unfortunately, an error was made in the fabrication of the silicon microlenses which were etched to a depth of $\bar{\lambda}/n$. The correct depth is 4.2 μm while the actual depth was 3.1 μm. The effect of this was to change the design wavelength from 10.5 μm to 7.4 μm. This introduced a chromatic error when testing the lens at 10.6 μm due to the Fresnel nature of the element. (The consequence was that energy increased in the side lobes of the PSF.) The reason we show these results is to show our capability to measure the effects of fabrication errors. Consequently, the energy increases in the side lobes of the PSF.

The measured and predicted PSFs for the incorrectly etched lens are shown in Figure 4. The effects of the incorrect etching depth are readily apparent in the four extra side lobes.

4.2 WIDEBAND SQUARE CdTe

The wideband, square CdTe microlenses were correctly fabricated. They are binary, 3-mask (8-level) Fresnel lenses designed for operation at 10.5 μm and tested at 10.6 μm. The width of the central peak in the PSF is 33 μm.

Figure 5 shows a coarse scan covering an area of 250 by 250 μm with a scan step size of 5 μm. The lens array was rotated with respect to the scan axis. The peak intensities are 23 times the mean. The portion of the array shown contains densely packed microlenses. Clearly shown are the repeatability of the microlenses and the concentration of the light into a small area. When fabricated into an integrated focal plane, a 100% effective fill factor can be obtained while allowing room on the back substrate surface for circuitry.

Figure 6 shows a fine scan of a CdTe lens with the scan covering 100 by 100 μm and a scan step size of 1 μm. Predicted and measured performances are shown in Figures 6a and 6b. Figure 6c shows the measured data rendered as a three-dimensional surface.

4.3 WIDEBAND HEXAGONAL CdTe

Figure 7 shows results from a test array that contains both dispersive and non-dispersive microlenses with square, skewed square, and hexagonal shapes. The portion shown contains on-axis hexagonal lenses and first-order dispersive skewed lenses. Some portions of the array are densely packed while some areas are sparsely packed. The sparse areas allow testing away from the peak of the PSF without interference from neighboring lenses. Figure 7 shows the results of a coarse scan used to determine the lens locations. The scan is 10 by 0.5 mm with a scan step size of 20 μm.

Figure 8 shows detailed scans from a single microlens. The scan area is 100 by 100 μm with scan steps of 1 μm. The data are from an on-axis, nondispersive hexagonal lens.

4.4 DISPERSIVE SKEWED CdTe

Figure 9 shows the expected multispectral output of the skewed dispersive microlens. Separate images are shown for 8, 10, 12, and 14 μm. We expect to be testing testing at these wavelengths shortly.

Figure 10 shows detailed scans of single skewed square first-order dispersive microlenses. As can be seen, the shape is distorted from the predicted PSF.

The asymmetric shape of the PSF in Figure 10 is due to the limited acceptance angle of the microscope objective. Figure 11 shows the intersection of the acceptance angle of the 0.5 NA microscope objective with the off-axis cone of light out of a dispersive microlens. The overlap is a thin sliver that causes the severe diffraction effects seen. In an integrated focal plane, this is not a problem because the detector is integrated into the back side of the substrate. Two methods for overcoming this test problem are (1) tilt the microscope objective and (2) micro etch the substrate surface to redirect the output.

5.0 FABRICATION PROCESS CONTROL

5.1 WAVEFRONT QUALITY TESTING

We expect to be creating microlens arrays for use in an ABS unit operating at 1.53 μm. Initial tests will be similar to our current procedure for measuring the PSF from individual microlenses, with the exception of using near-IR sources, optics and detectors. This should be easy compared to working at 10.6 μm.

When a complete ABS unit is available, we will place it in a Michelson interferometer to test its wavefront quality. The interferometer is aligned with a large ($> 100\ \lambda$) amount of tilt between the reference and test beams. This allows analysis of the interferograms using spatial phase shifting interferometry (SPSI). The Optical Metrology Group at Lockheed R&DD has extensive experience using SPSI to obtain high resolution (640 by 480 pixel) and high accuracy ($\lambda/20$ rms per pixel) wavefront maps from various optical systems. This has included transient effects due to shock waves, scan mirror distortion, and testing near IR windows for process-induced aberrations.[5]

The interferometer requires modification to allow easy testing at various scan angles. The modification will consist of placing the mirror in the arm of the interferometer that contains the ABS unit on a lever attached to a rotating stage. As the beam is steered, the mirror rotates to reflect the beam back through the ABS unit.

5.2 TESTING LARGE ARRAYS

For some applications, such as integrated focal planes, each lens in the array must be tested to ensure that manufacturing problems do not cause one or more microlenses to be substandard. Our current apparatus could, in principle, be used to test every lens in a 100 by 100 array of microlens. A moderate resolution (101 by 101 pixels) scan requires around 3 h—the entire array would be tested in 3.5 years! To test the entire array in 1 week, only 1 min per lens is allowed. This amount of time would allow only a very coarse scan.

The testbed is being enhanced with the addition of a pyroelectric vidicon camera to speed up the acquisition of the PSF data. An image is grabbed in 1/30 of a second. We still have the XYZ translation stages to allow us to move from lens to lens. The down side to using the camera is that the dynamic range and signal-to-noise ratio are much worse than our current setup. This makes the camera unsuited to measuring the side lobes in the PSF.

---

5. Shough, D. M., O. Y. Kwon, and D. F. Leary, "Spatial Phase-Shifting Interferometry for Measurement of Aero-Optical Effects," 1992 AIAA Annual Interceptor Conference, Hunstville, AL.

The detector area is a 17-mm-diameter circle with a resolution of 270 TV lines. The diameter corresponds to a circle with a diameter of 106 μm in the plane of the PSF. The damage level is 1 mW/cm^2 at the detector face plate. This corresponds to a point source with a total power of 37 μW being reimaged by our 160X magnification objective. This, in turn, corresponds to an irradiance of 3.7 mW/mm^2 through a 100-μm square lens. The total power through our 0.5-in. aperture should be less than 465 mW. This is a concern with the CO_2 laser but not with the 1 mW lead-salt lasers, unless the entire energy is collected into a beam with a diameter of less than 0.65 mm.

6.0 SUMMARY

The Micro-Optics Technology Group within Lockheed R&DD has designed and fabricated individual microlenses and arrays of microlenses that we have experimentally evaluated. The measurement of properties of microlenses and microlens arrays presents some new challenges. We have listed some of the critical parameters and main features of microlenses that need to be measured in order to characterize their optical performance. The measurement of properties of individual microlenses required some originality and modifications of existing optical testbeds and measurement methods.

We have described our current laboratory testbed and shown results of monochromatic PSF measurements for a variety of fabricated microlenses. This year we will expand our capabilities to include testing at various IR wavelengths for dispersive microlenses. Our future plans are to provide testing for large microlens arrays and to do interferometric testing of micro-optic windows.

TABLE I. MICRO-OPTICS TESTBED CAPABILITIES MATRIX

Capabilities	Single Microlenses	Arrays	Systems
PSF	✓	✓	✓
Wavefront	✓		✓
Shape	✓	✓	

TABLE 2. RESULTS ARE PRESENTED FOR FOUR DIFFERENT MULTILEVEL FRESNEL MICROLENSES WITH THE INDICATED PROPERTIES

Type	Shape	Material	Width (μm)	Focal Length (μm)	Design Wavelength (μm)
Wideband	Square	Si	100	525	7.4
Wideband	Square	CdTe	100	417	10.5
Wideband	Hexagonal	CdTe	115	417	10.0
Dispersive	Skewed	CdTe	100	417	10.0

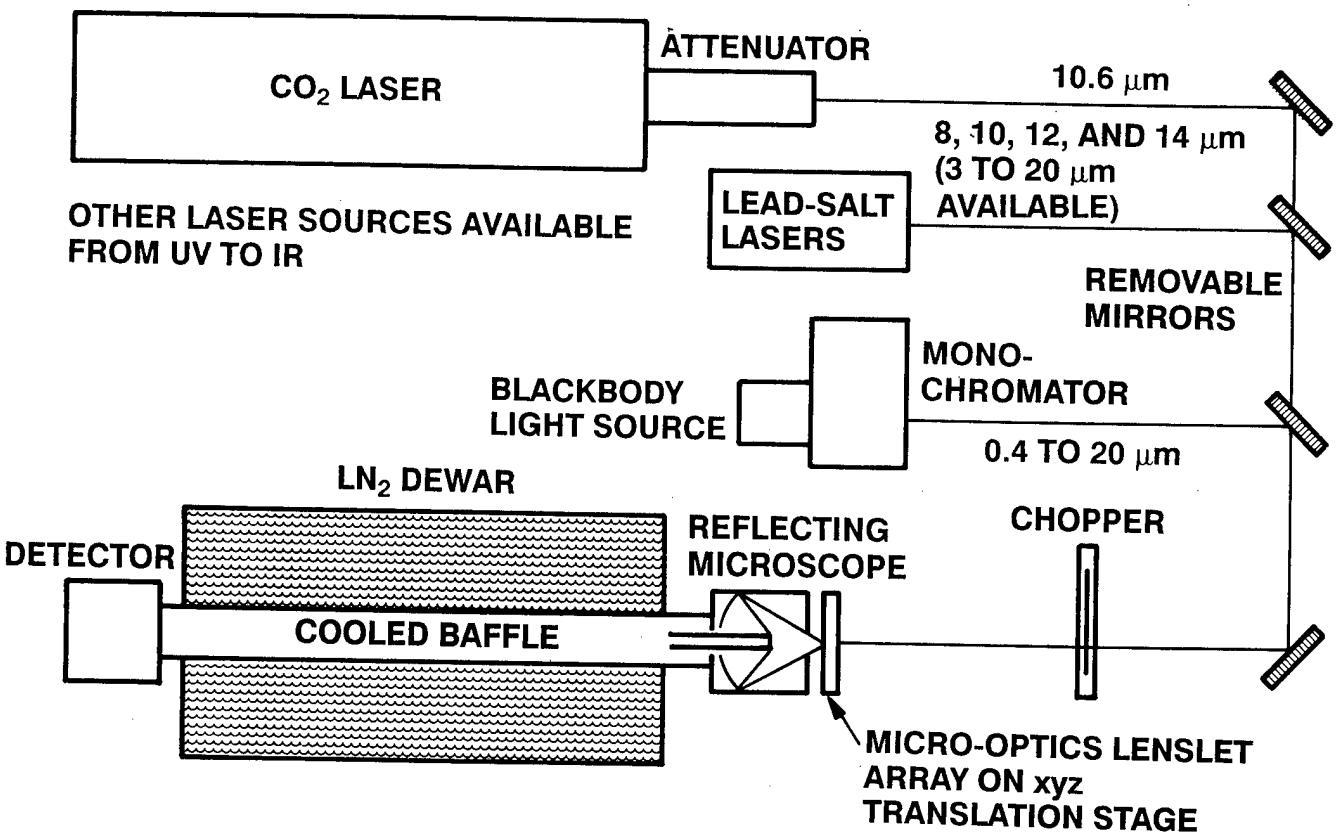

FIGURE 1. CONCEPTUAL DRAWING SHOWING KEY COMPONENTS FOR MEASUREMENT OF PSF.

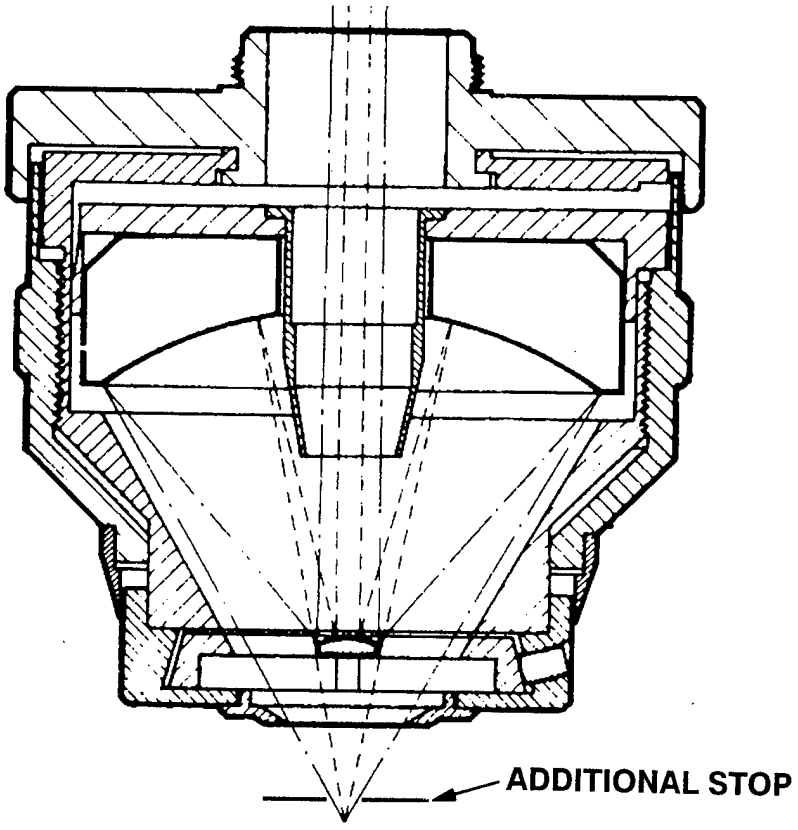

FIGURE 2. EALING MICROSCOPE OBJECTIVE WITH ADDITIONAL STOP.

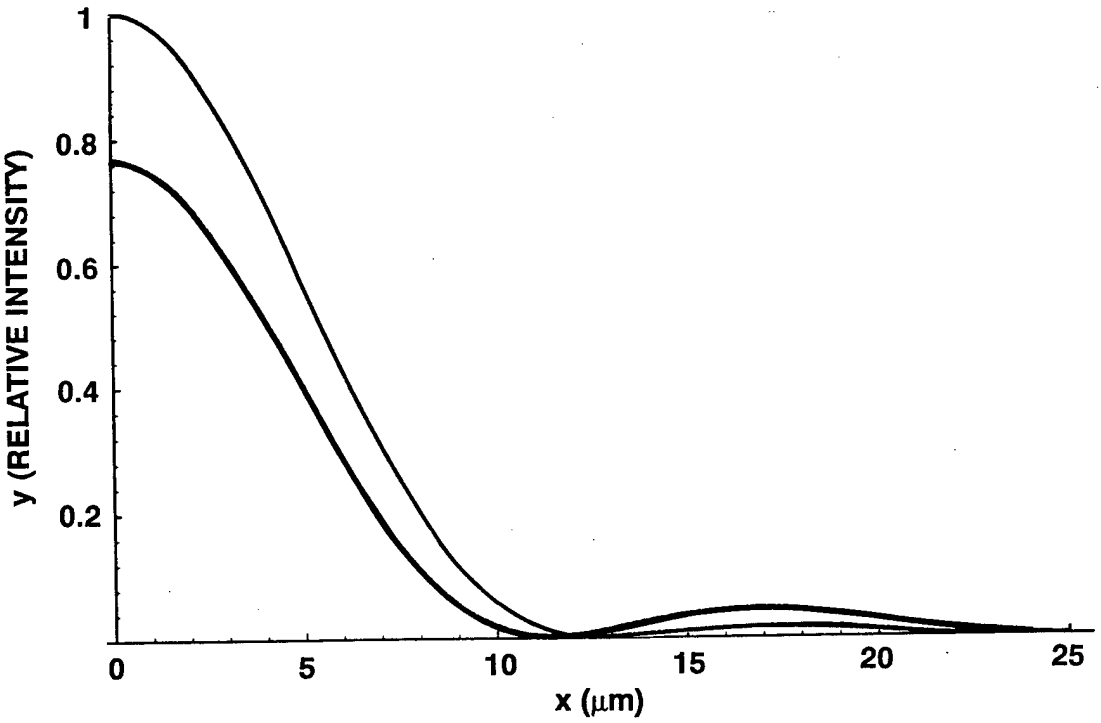

FIGURE 3. PSF WITH (BLACK) AND WITHOUT (GRAY) CENTRAL OBSCURATION.

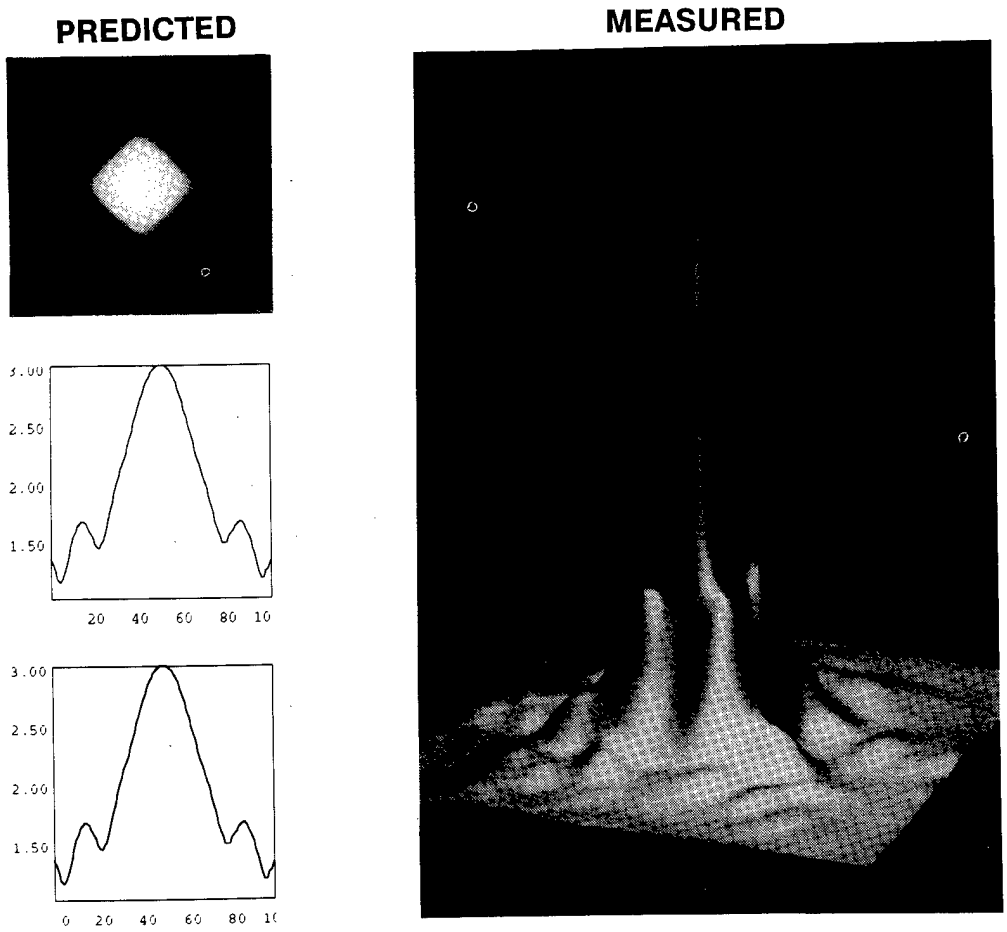

FIGURE 4. PREDICTED AND MEASURED PSFs FOR WIDEBAND, SQUARE, Si MICROLENS.

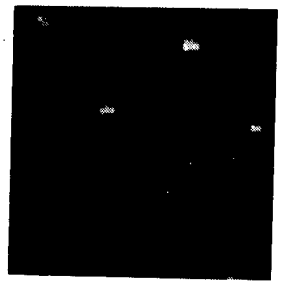

FIGURE 5. COARSE SCAN SHOWS PSFs FROM ARRAY OF MICROLENSES.

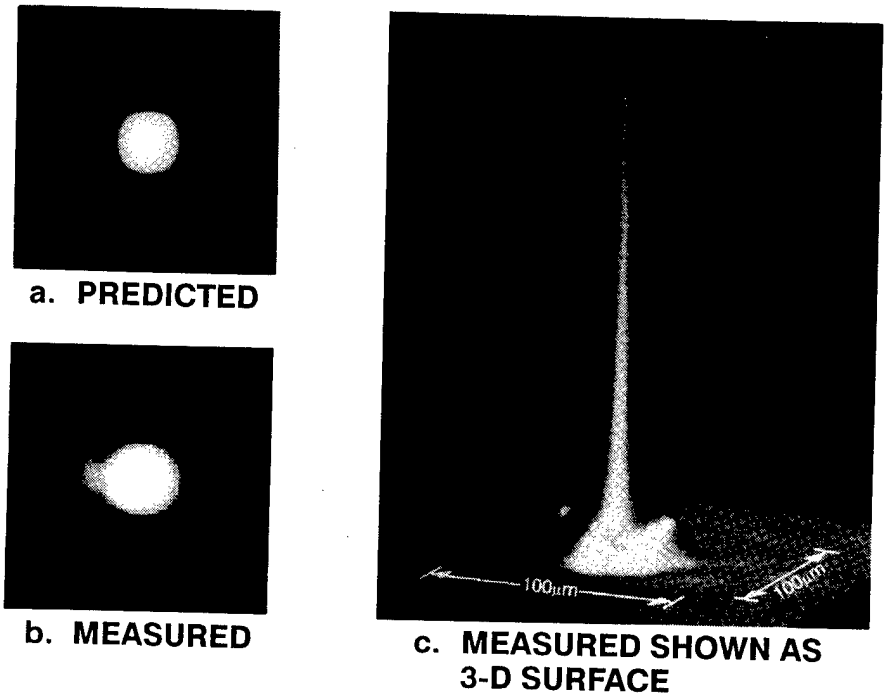

FIGURE 6. PREDICTED AND MEASURED PERFORMANCE OF SQUARE CdTe MICROLENS.

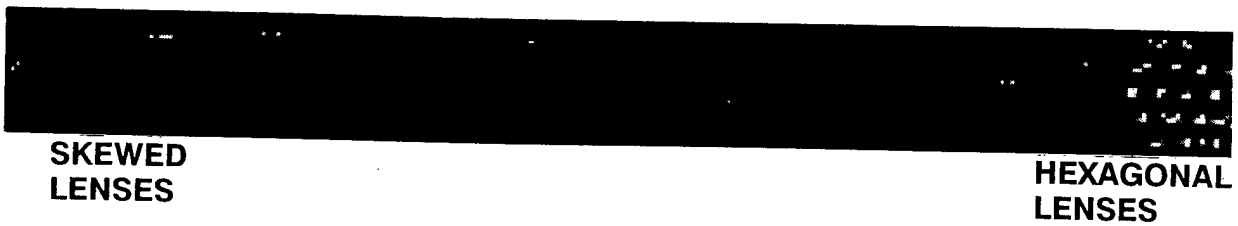

FIGURE 7. COARSE SCAN OF CdTe TEST ARRAY.

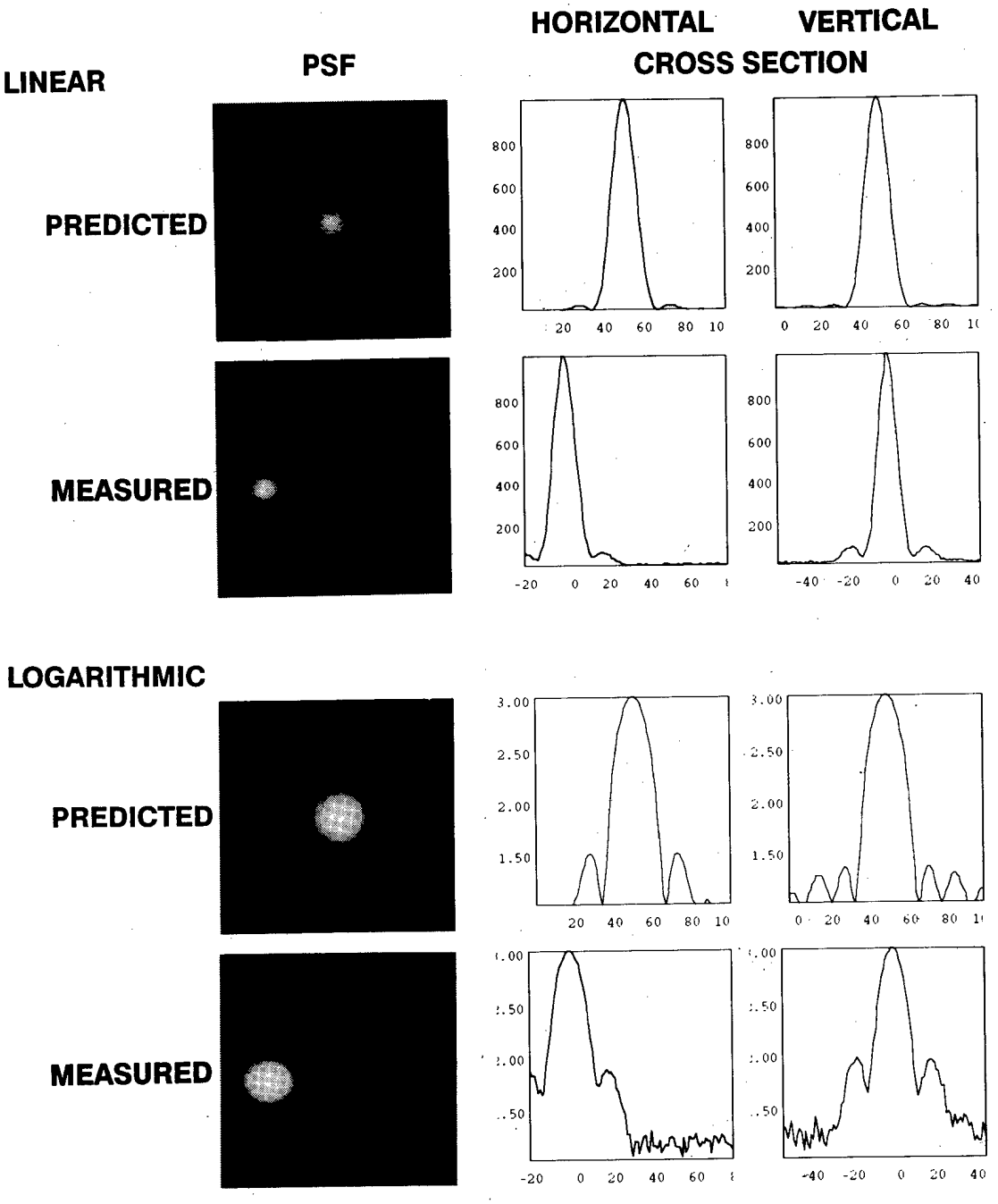

FIGURE 8. DETAILED SCAN OF WIDEBAND HEXAGONAL MICROLENS.

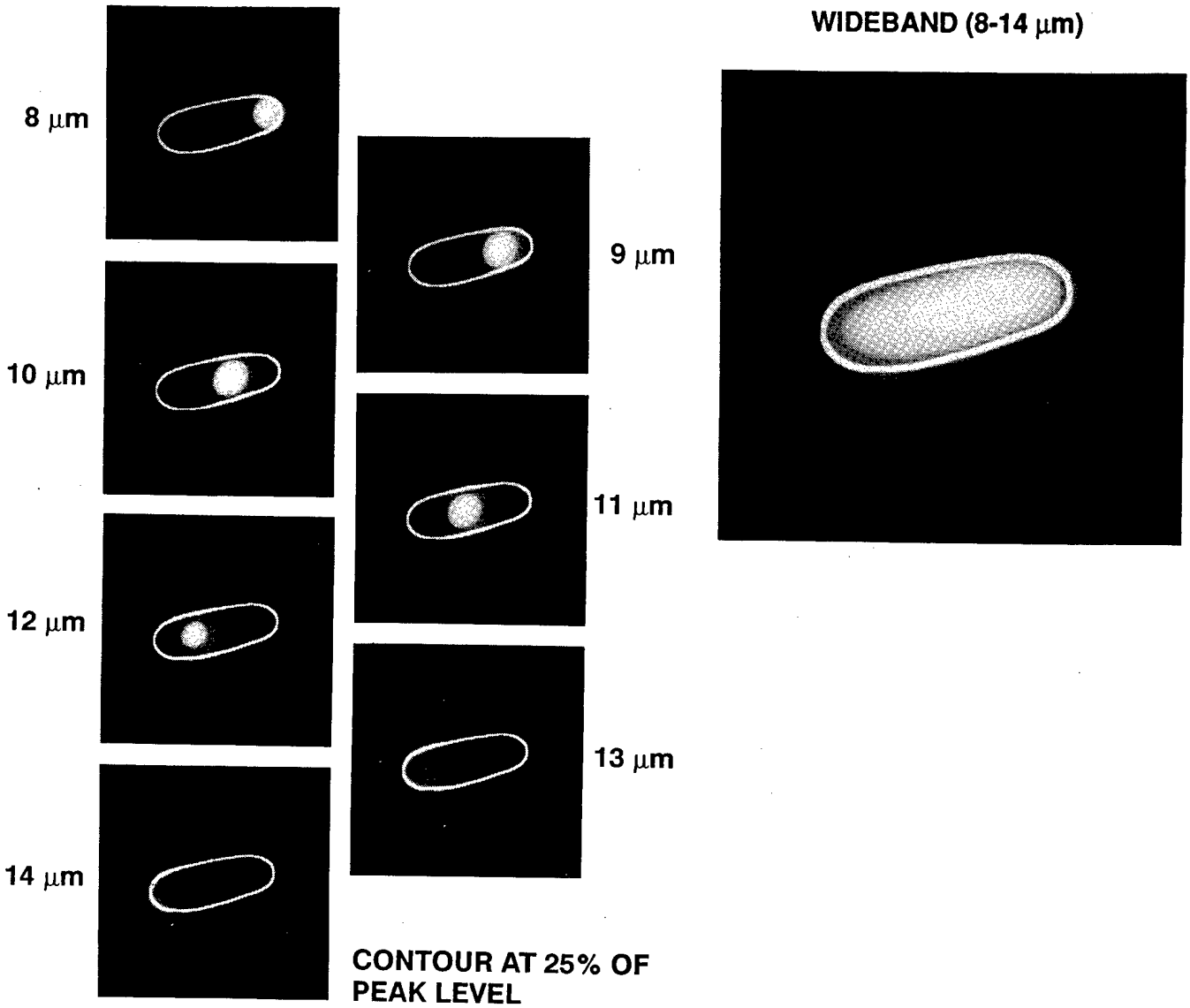

FIGURE 9. PREDICTED MULTISPECTRAL RESPONSE OF SKEWED DISPERSIVE MICROLENS.

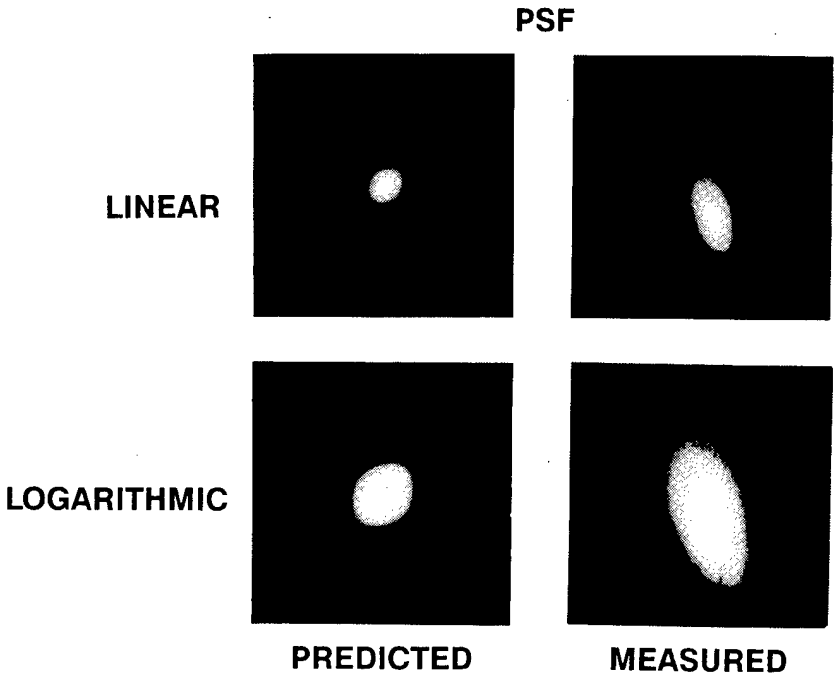

FIGURE 10. DETAILED SCAN OF SKEWED DISPERSIVE CdTe MICROLENS.

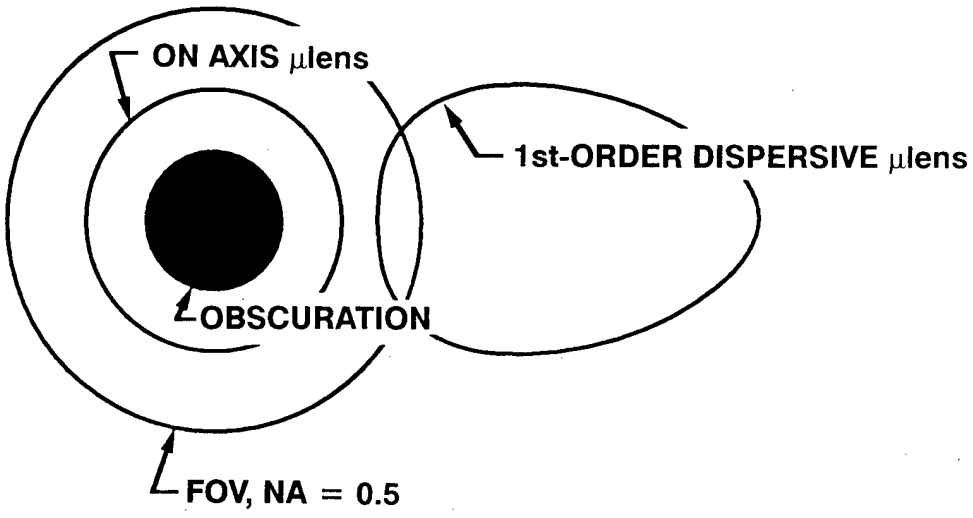

FIGURE 11. OFF-AXIS BEHAVIOR OF MICROSCOPE OBJECTIVE.

Applications of Advanced Diffractive Optical Elements

W. Hudson Welch, James E. Morris and Michael R. Feldman

Digital Optics Corporation
8701 Mallard Creek Rd., Suite 220
Charlotte, NC 28262
(704)549-5556, FAX:(704)548-9050

University of North Carolina at Charlotte
Optical Engineering, Applied Research Center
Charlotte, NC 28223
(704)547-3224, FAX: (704)547-3331

1. Introduction

Digital Optics Corporation is a UNC-Charlotte spin-off company, established to transfer technology developed at UNC-Charlotte for the design and manufacture Computer Generated Holograms (CGH's) and to market products based on CGH technology. DOC acquired core technologies from UNC-Charlotte including: (1) a CGH encoding process that can provide holograms with extremely high diffraction efficiency, (2) a low cost, high precision CGH manufacturing process, and (3) extensive holographic and refractive element design capabilities for design and evaluation of complex optical systems.

These technologies have been used to design and/or manufacture optical components for a variety of applications including:
(1) Generation of Spot arrays
(2) Fiber optic coupling elements
(3) Optical interconnects between VLSI chips within and between Multichip Modules
(4) Imaging systems for Head-Mounted Displays (HMDs).

2. Spot Array Generation

Several holograms for generation of spot arrays have been fabricated. These holograms were designed with the Iterative Discrete On-axis encoding method [1,2]. In Ref. 1 a hologram was designed to generate a 3x3 array of spots. While the theoretical diffraction efficiency for this hologram was 74%, due to fabrication limitations a hologram with only 64% could be fabricated.

Recently improvements have been made in the fabrication process on CGH's as well as in the design methods[2]. This has resulted in higher efficiency holograms for spot array generation. For example, the RSIDO method was used to design a hologram to produce a 32x32 spot array. The experimental diffraction efficiency was 73% with a uniformity of ±5.

3. Fiber-optic Coupling Elements

An F/1 collimating element for a laser diode was designed with the recently developed Radially Symmetric Iterative Discrete On-axis (RSIDO) encoding method. The RSIDO method is similar to the previously reported[1] IDO method. However, the RSIDO method can be used to achieve higher diffraction efficiencies for design of Holographic Optical Elements (HOE's)[3]. During the design process fabrication constraints such as minimum feature size limitations are employed.

The principal advantage of the RSIDO method is that the resulting hologram has extremely high performance for a given set of fabrication constraints. For example, for a 0.5 μm minimum feature size, the RSIDO method can be used to design an F/1 hologram with a diffraction efficiency of 85%. For the same minimum feature size, a comparable hologram designed with previous methods can only achieve a diffraction efficiency of 60%.

Several prototype designs for binary optic lenses for laser diode collimating and focussing were developed and subsequently employed for fabrication. One design had a diffraction efficiency of 87-94% over a 30 nm optical bandwidth. The spot size of this hologram varied between 1 and 1.5 mm over this bandwidth and a distance of 0.7 m from the hologram (hologram diameter was 1.5 mm). For comparison an analytically designed diffraction limited CGH would have a spot size that varied from 0.75 mm to 3.9 mm over the optical bandwidth range.

Over 1,000 fiber optic coupling elements have been fabricated to date by Digital Optics Corporation. These holograms are being tested for insertion into actual systems. Specific manufacturing, packaging and alignment issues have been addressed for each application.

4. Optical interconnects between VLSI chips within and between Multichip Modules

Several holograms have been fabricated for optical interconnection of VLSI chips within and between multichip modules. We have shown that conventional encoding methods for this application yield very low results. For example, for a CGH with a 27 degree deflection angle, the high spatial frequencies at the edges of the CGH, limit the number of phase levels that can be employed to 2. With conventional encoding methods this will limit the diffraction efficiency to 40%. Since, in order to form a link the beam must pass through 2 such holograms, the net link efficiency is limited to 16%.

The efficiency can be improved by using a lensless version of the IDO method[4], termed Fresnel IDO. Both simulation and experimental results indicate that with Fresnel IDO the link efficiency can be increase to approximately 30% for a 27 degree deflection angle.

To further increase the diffraction efficiency the RSIDO method was modified to allow for non-radially symmetric transmittance patterns. The hologram is divided into several regions. Each region is encoded separately with RSIDO and is therefore radially symmetric. This method has been termed the Segmented Radial Partitions (SRP) method. Experimental results indicate that for

a 27 degree deflection angle, the link efficiency is approximately 65%.

The holograms for optical interconnects have been incorporated onto a quartz substrate. Silicon IC and GaAs laser array chips have been attached to the substrate by flip-chip technology. Micro-mirrors, also attached by flip-chip technology, are used to redirect the output of edge-emitting lasers[5, 6].

References

1. M. R. Feldman and C. C. Guest, "Iterative Encoding of High Efficiency Holograms for Generation of Spot Arrays", Optics Letters, **14**, pp. 479-481,1989.

2. J. D. Stack and M. R. Feldman, "Recursive Mean-Squared-Error Algorithm for Iterative Discrete On-axis Encoded Holograms," Appl. Opt., **31**, pp. 4839-4846 , 1992.

3. W. H. Welch, J. E. Morris and M. R. Feldman, "Iterative Discrete On-axis Encoding of radially symmetric computer generated holograms," to be published in JOSA-A , 1993.

4. M. R. Feldman and C. C. Guest, "Design of Computer Generated Holograms for a Shared Memory Network," Proc. of SPIE, **1052**, Jan. 1989.

5. M. R. Feldman, I. Turlik, G. Adema, J. E. Morris, N. Hangzo and W. H. Welch, "Holographic Optical Interconnects for VLSI Multichip Modules," in 42nd Electronic Components & Technology Conference 1992, **1**,pp. 513 - 518 (1992).

6. M. R. Feldman, "Holographic Optical Interconnects for VLSI Multichip Modules," invited paper for IEEE/SPIE International Symposium on Advances in Interconnects and Packaging, Proc. SPIE, **1390-27**, pp. 427-433, 1990.

LASER BEAM STEERING DEVICE

February 1993

M.E. Motamedi, A.P. Andrews, and W.J. Gunning

Rockwell International Science Center
1049 Camino Dos Rios
Thousand Oaks, CA 91360

ABSTRACT

Agile beam steering is a critical requirement for airborne and space based LIDAR and optical communication systems. Design and test results are presented for a compact beam steering device with low inertia which functions by dithering two complementary (positive and negative) binary optic microlens arrays relative to each other in directions orthogonal to the direction of light propagation. The miniaturized system has been demonstrated at scan frequencies as high as 300 Hz, generating a 13 x 13 spot array with a total field of view of 2.4°. The design is readily extendable to a 9.5° field of view and a 52 x 52 scan pattern. The system is compact—less than 2 in. on a side. Further size reductions are anticipated.

1.0 INTRODUCTION

High speed optical beam steering is a major challenge for space based LIDAR systems. If this function is performed mechanically using bulk optical components, the resulting systems are too heavy for the more demanding applications that require rapid optical beam steering. These applications require lower rotational and translational inertia and smaller component displacements. Binary optics beam steering systems fulfill these requirements, achieving a field of view of more than 10 degrees with only a fraction of a millimeter component translation.[1]

We report here test results of a miniature laser beam steering device designed to demonstrate the feasibility of the binary optic approach. The steering mechanism is based on dithering two complementary (positive and negative) binary optic microlens arrays. The first demonstration of this steering concept was reported by Lincoln Laboratory.[1] In this paper, we

[1] W. Goltsos and M. Holz, "Agile beam steering using binary optic microlens arrays", *Optical Engineering*, vol. 29, pp. 1392–1397, (1990).

present a miniaturized version using a pair of 6 mm-aperture, F/6, 8-level binary optic microlens arrays designed to operate at 0.632 μm wavelength. The current actuator design can scan the laser beam at rates of 200 Hz or greater. Beam steering is accomplished by translating the microlens arrays relative to each other in directions orthogonal to the direction of light propagation. The multiple coherent apertures result in a far field spot pattern of fixed points. The current system has demonstrated rapid scanning of a 13 x 13 spot array with a total field of view of 2.4°, and is readily extendable to a 9.5° field of view and a 52 x 52 spot pattern. The microlens arrays are individually driven in orthogonal directions by piezoelectric actuators. The current beam steering system is quite compact—less than 2 in. on a side—and careful redesign with custom designed actuators can lead to a further reduction in size.

We have evaluated the performance of this device and are now studying its suitability for various beam steering applications such as laser radar, laser communication, and optical scanning.

2.0 BEAM STEERING PRINCIPLE

Optical beam steering is based on the principle of the Galilean telescope. The configuration of the system is shown in Figure 1, where a positive lens is followed by a confocal negative lens. The focal length of the negative lens (F_n) is slightly smaller than the focal length of the positive lens (F_p) by an amount equal to the spacing between the two lenses. If the lenses are displaced laterally relative to each other, a plane wave incident along the optic axis will emerge collimated but tilted away from the optic axis. If the negative lens is displaced perpendicular to the optic axis by the amount of x_s, then the tilt angle θ is given by

$$\theta = \arctan \frac{x_s}{F_n} . \tag{1}$$

Let z_{sp} be the separation between the two lenses and F/# be the focal ratio F_p/d of the positive lens, where d is the diameter of the smaller lens. Then Eq. (1) can be rearranged to

$$\theta = \arctan \frac{x_s}{d(F/\#)-z_{sp}} . \tag{2}$$

In practice, ideally the spacing between the two lenses is decreased to minimize vignetting. To determine the maximum steering angle θ_{max}, z_{sp} in Eq. (2) can be neglected and both lenses can be assumed to have the same diameter and focal length (and consequently the same F/#). Therefore, Eq. (2) can be reduced to

$$\theta \approx \arctan \frac{x_s}{d(F/\#)} . \tag{3}$$

The optical system shown in Figure 1 has maximum efficiency at zero scan ($x_s = 0$). As the scan angle increases, the vignetting increases, and the maximum useful scan occurs at $x_s \approx d/2$, where θ_{max} from Eq. (3) becomes

$$\theta_{max} \approx \arctan \frac{1}{2(F/\#)} . \tag{4}$$

Equation (4) suggests that faster lenses (smaller F/#) increase the scan angle. For example, a pair of F/2 lenses (one inch in diameter) in the system shown in Figure 1 has a field of view (FOV) equal to ± 14°.

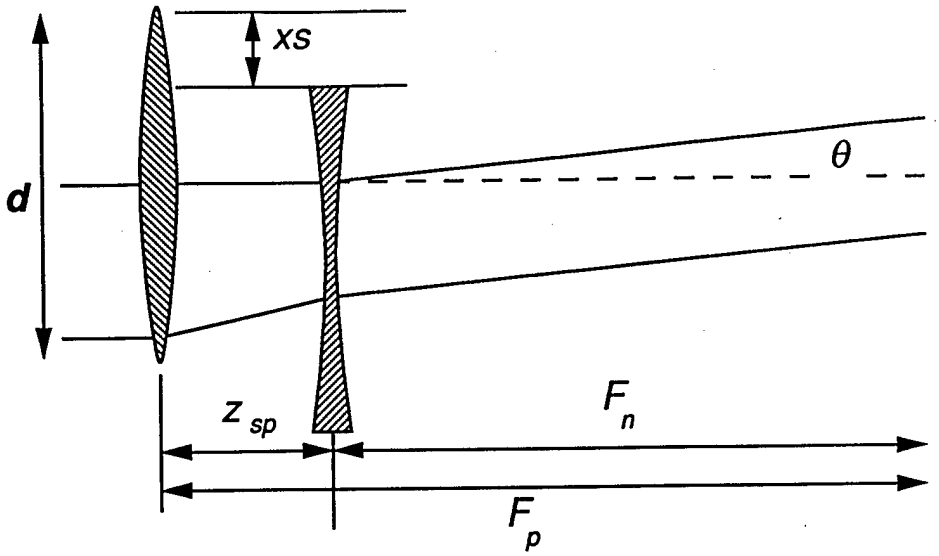

FIGURE 1. CONFIGURATION OF OPTICAL BEAM STEERING CONCEPT USING A PAIR OF GALILEAN CONFOCAL LENSES.

The system in Figure 1 has two drawbacks for optical beam steering: 1) the lenses are refractive, which limits the lens separation; and 2) the large lens diameter requires large translation (on the order of the lens diameter), which makes the system impractical for agile beam steering.

More agility is achieved by replacing the lenses of Figure 1 with a pair of complementary binary optic microlens arrays as shown in Figure 2. The microlens arrays are optically flat with surface relief on the order of one optical wavelength, permitting separation distances of several microns. Individual lenslet sizes can be in the range of 100–200 microns, resulting in maximum translation of similar magnitude. Reducing both the inertia and the travel of the lens system makes the device suitable for agile beam steering. Since Eq. (4) still holds for binary optics, the steering angle of the scanner can be very high. The multiple aperture design of the scanner results in a discrete spot scan pattern. The far field angular spot separation, $\Delta\theta$, is given by

$$\Delta\theta \sim \lambda/d \tag{5}$$

where d is the lenslet size, and the beam divergence, $\delta\theta$, is given by

$$\delta\theta \sim 2\lambda/D \tag{6}$$

where D is the beam diameter.

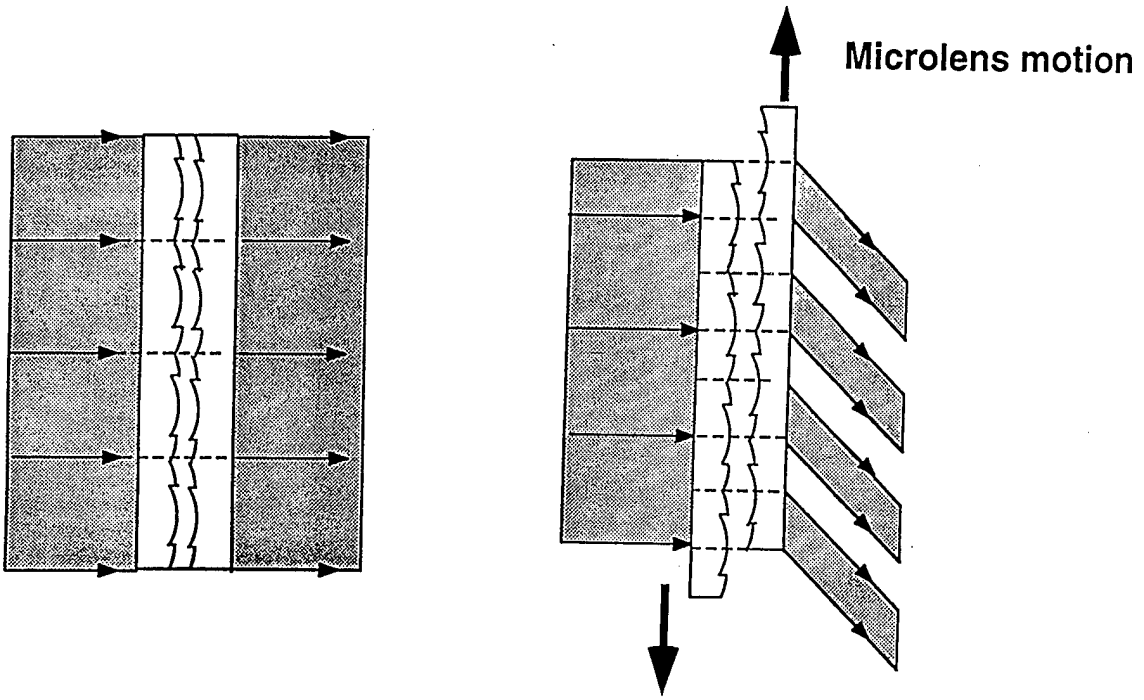

FIGURE 2. COMPLEMENTARY BINARY OPTIC MICROLENS ARRAYS FOR BEAM STEERING DEMONSTRATION.

3.0 BEAM STEERING THEORY

A binary optic[2] beam steering system based on the approach shown in Figure 2 has two parallel complementary microlens arrays spaced several microns apart. Input plane waves pass first through the positive microlens array and then through the negative microlens array. Since the spacing relative to the focal length is small, we can assume the two microlens arrays have the same focal length, f. From this assumption, both microlens arrays have the same F/# and the same microlens size.

Using the model of Sweatt,[3] the one-dimensional optical path function, g(x), can be written as

$$g(x) = \frac{cx^2}{1+\sqrt{1+(\hat{k}+1)c^2x^2}} \qquad (7)$$

[2]G. J. Swanson, "Binary Optics Technology: The Theory and Design of Multi-Level Diffraction Optical Elements", Tech. Report 854, Lincoln Laboratory, MIT, 14 August 1989.

[3]W.C. Sweatt, "Design holographic optical elements as lenses", *J. Opt. Soc. Am.*, Vol. 67 pp. 803-808, 1977.

where c is the surface curvature and $\hat{k}$ is a geometrical constant.

For a pure parabolic function, the value of $\hat{k} = -1$, and Eq. (7) reduces to

$$g(x) = \frac{cx^2}{2} . \tag{8}$$

For practical purposes when F/# is larger than F/4 in Eq. (8), the microlens phase function at the center wavelength, λ_o, can be reduced to

$$\phi_o = \frac{\pi x^2}{\lambda_o f} . \tag{9}$$

From Eq. (9), the microlens transmittance function at a wavelength λ can be shown to be

$$t(x) = \exp\left[\frac{j\pi}{\lambda f} x^2 \right] . \tag{10}$$

Equation (10) is the basic transmittance function for both binary optic microlenses. To formulate the field distribution of the binary optic beam steering system at the far field, we include an artificial imaging lens after the microlenses and evaluate the image at the focal plane. Figure 3 shows the schematic of this optical configuration.

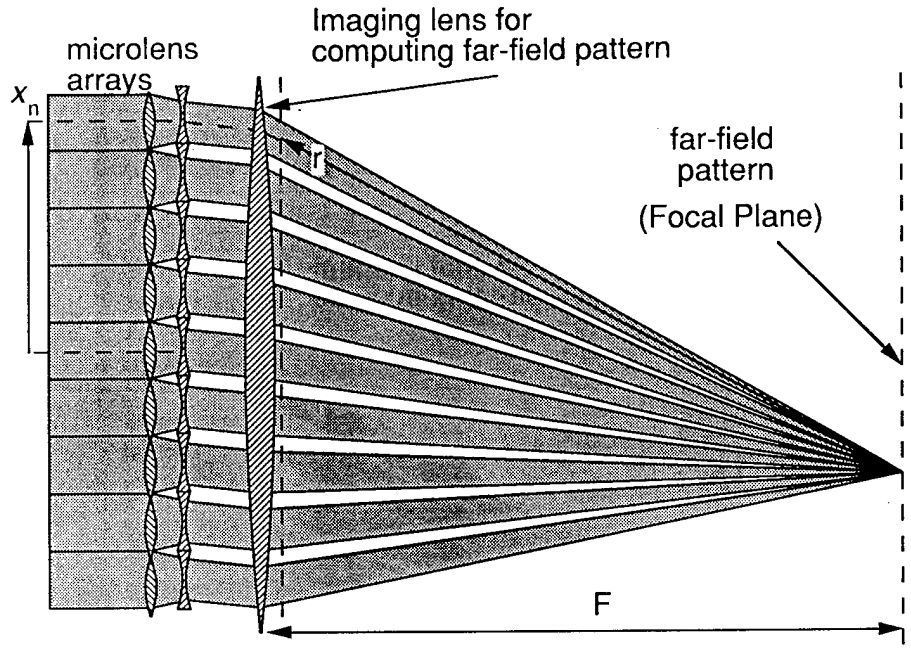

FIGURE 3. SCHEMATIC OF THE OPTICAL ARRANGEMENT FOR MICROOPTIC BEAM STEERING.

Applying Fourier optics[4] and considering the optical arrangement of Figure 3, the one-dimensional far-field pattern of the beam steering device can be shown to be

$$u(x)=u_o \sum_{-N}^{N} \int_{x_n-d/2}^{x_n+d/2} \exp\left[\frac{jk(x'-x_n)^2}{2f}\right]\exp\left[-\frac{jk(x'-(x_n+x_s))^2}{2f}\right]$$

$$\exp\left[\frac{jk\ x'^2}{2F}\right]\exp\left[-jk\sqrt{(x'-x)^2+F^2}\right]dx' . \qquad (11)$$

The first and second exponential factors in Eq. (11) represent the positive and negative microlens arrays, respectively. The variable x_s is the translation of the negative microlens relative to the positive microlens. The third exponential term represents the imaging lens, and the last exponential term is the propagation term. Note that f and F are the focal lengths of the binary optics microlens and imaging lens respectively, and the image plane is at the focal plane. N defines the size of the input beam and x' is the integration variable.

In evaluating u(x) at the far field, the focal length F is introduced for a mathematical model. Equation (11) can be reduced to the far-field intensity profile,

$$I(x) = u(x)\ u(x)^*$$

$$I(x)=I_o \sum_{-N}^{N} \exp\left[-\frac{jk\ x_n x_s}{f}\right] \int_{x_n-d/2}^{x_n+d/2} \exp[jk\ (x_s/f+x/F)x']dx' . \qquad (12)$$

For $x_r=x/F$, the formula (12) reduces to

$$I(x_r)=I_o \sum_{-N}^{N} \exp\left[-\frac{jk\ x_n x_s}{f}\right] \int_{x_n-d/2}^{x_n+d/2} \exp[jk\ (x_s/f+x_r)x']dx' . \qquad (13)$$

The angular scan due to x_r is generally on the order of a few milliradians. To view the behavior of Eq. (13), we plot $I(x_r)$ for $\pm$ 6 mrad, which covers at least two addressable points. Figure 4 shows the variation of $I(x_r)$ at the far field during a complete scan of one addressable point. Figure 4(a) is a plot of $I(x_r)$ at $x_s = 0$ (zero scan).

From Eq. (3), $x_s=(F/\#)\ \lambda$ at the first addressable point. For $\lambda = 0.632\ \mu m$ and F/# = F/6, the value of x_s is 3.79 μm. Figure 4(b) shows the $I(x_r)$ when the scanner has moved one addressable point; during the complete scan of 3.79 μm, the beam energy has been transferred to the next addressable point. During this transfer no portion of the total energy falls between the addressable points, as shown in Figure 4(b). Figure 4(c) is the superimposition of six plots of $I(x_r)$'s for x_s varying from 0 to 3.79 μm.

---

[4]J.W. Goodman, *Introduction to Fourier Optics*, McGraw Hill, New York (1968).

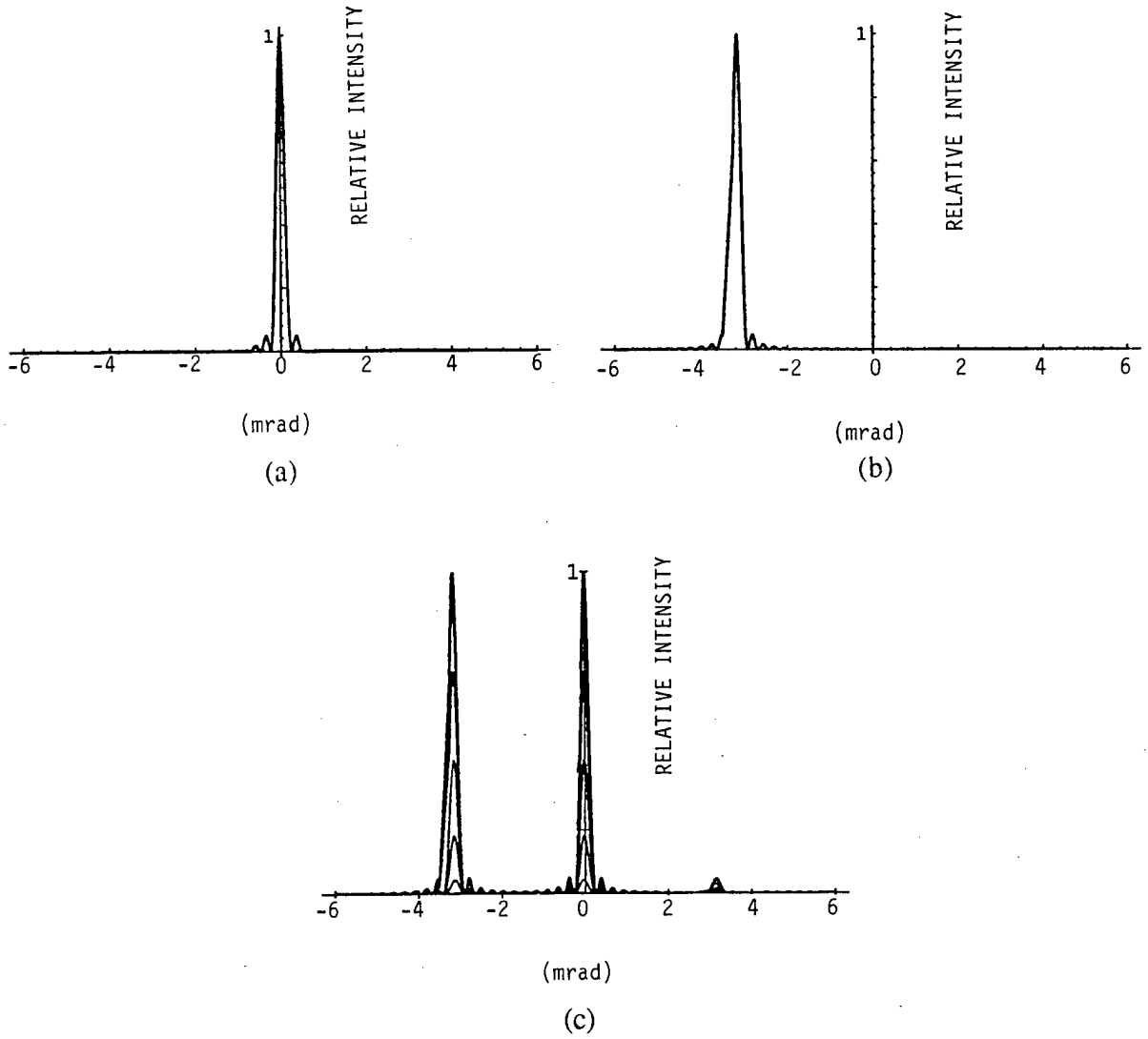

FIGURE 4. VARIATION OF $I(x_r)$ AT THE FAR FIELD DURING A COMPLETE SCAN OF ONE ADDRESSABLE POINT. (a) $I(x)$ AT $x_s=0$; (b) $I(x_r)$ AT $x_s= - 3.79$ μm; (c) SIX SUPERIMPOSED PLOTS OF THE TRANSITION BETWEEN ADDRESSABLE POINTS.

Equation (13) is an integral solution to the behavior of the binary optic beam steering module shown in Figure 2. The relation (13) can be used to calculate the absolute intensity profile of the steering system at any far-field distance z where $z >> Nd$. This approach is more powerful than the approximation model used previously,[1] and it clearly demonstrates the effects of rotation errors, divergence and the near-field behavior of the binary optic beam steering system. More detailed theoretical results will be reported in a later paper.

4.0 BEAM STEERER DESIGN

The miniaturized beam steerer design uses simple parallelogram structures with orthogonal directions of translation for each microlens array. The basic design of this structure for one of the microlens arrays is illustrated in Figure 5. The structure is stiff in rotation and translation, except for rotations about the hinge lines. (The "hinges" of the parallelogram are actually flexible sections.) Each microlens array is mounted in a structure of this type, with their translation directions orthogonal to the optical axis and orthogonal to each other. By making the horizontal legs of the parallelogram sufficiently long, the variation in the spacing between the lenses over a complete scan could be held to tolerable levels during operation.

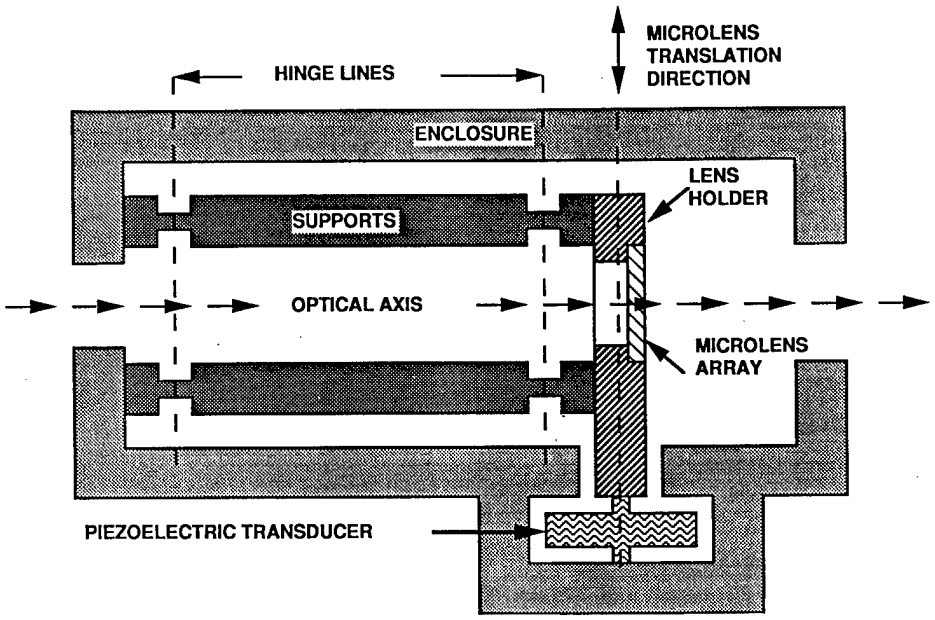

FIGURE 5. PARALLELOGRAM STRUCTURE FOR TRANSLATING MICROLENS ARRAYS.

Each microlens array is translated using a piezoelectric transducer mounted between the frame and the lens holder. Off-the-shelf transducers manufactured by Physik Instrumente (PI model P-288) were used for this demonstration. Smaller and faster devices can be designed using specialized transducers.

The microlenses were designed for a HeNe laser ($\lambda = 0.632$ μm). A low F/# is desirable. For an eight-phase-level binary optic microlens the minimum feature size is $2\lambda(F/\#)/8$.[5] For our 1 μm process, this places a lower limit of F/6 on the microlens F/#. The 32 x 32 arrays of 200 μm square microlenses have 100% fill factor. Flat quartz (better than $\lambda/8$) was used for the substrates. This design is predicted to produce a 52 x 52 spot scan pattern over a total square field of view of 9.5° x 9.5°. Spot separation and beam divergence are predicted to be, using Eqs. (5) and (6), 3.6 mrad and 506 μrad respectively.

---

[5]M.E. Motamedi, W.H. Southwell, R.J. Anderson, W.J. Gunning, M. Holz, " High Speed Binary Microlens in GaAs", *Proceedings* of SPIE, Vol. 1544, pp. 33–44, July 1991.

Binary Optic microlenses were designed as an approximation to a kinoform structure.[6] The binary lens profiles are generated by a stepwise multilevel etch process. As the number of phase levels is increased, the approximation of the kinoform structure is improved. A process consisting of m mask levels produces a structure having $M = 2^m$ phase levels. The etch depth of each mask level, d_i, is given by

$$d_i = \frac{\lambda}{(n-1)2^i} \tag{14}$$

where λ is the optical wavelength, n is the refracture index of the lens material, and i is the number of the individual mask level.

The theoretical diffraction efficiency of a kinoform lens is 100%, if reflection and obscuration losses are ignored. For a binary optic lens, the equivalent diffraction efficiency depends on the number of phase levels, M. This binary optic diffraction efficiency, η, is given by[2]

$$\eta = \left[\frac{\mathrm{Sin}\left(\frac{\pi}{M}\right)}{\left(\frac{\pi}{M}\right)}\right]^2 \tag{15}$$

where M is the total number of phase levels. Efficiency values for practical lenses are $\eta(M = 4) = 0.81$, $\eta(M = 8) = 0.95$, and $\eta(M = 16) = 0.99$.

The lenses operate over a small range in incident angle, so a simple planar holographic lens design was acceptable. The optical path difference (OPD) as a function of lens radius, r, is:

$$OPD(r) = \sqrt{r^2 + f^2} - f, \tag{16}$$

where f is the focal length and the OPD is arbitrarily set to 0 for $r = 0$. Because this is a monotonic function in r, the quantization of the OPD for wavelength λ and parabolic phase function gives mask zones with radii

$$r(p, m) = \sqrt{2f\left(\frac{p\lambda}{2^m}\right)} \tag{17}$$

where $p = 0,1,2,3...$, and r(p, m) are the successive zone radii for the patterns in mask number m. These radii describe the edges of clear and opaque rings on the mask; for a positive lens, and with a positive photoresist as used here, the odd numbered zones give the outside of opaque rings. (The central zone of each mask, defined by $p = 0$ and $p = 1$, is an opaque disk.)[6]

The microlens profiles were designed to be parabolic to reduce aberrations. The focal lengths of the two lenses were adjusted to accommodate a nominal 5 μm separation, and the

---

[6]M.E. Motamedi, W.J. Gunning, M.P. Griswold, R.E. Knowlden, "Silicon Microlenses for Enhanced Optical Coupling to Silicon Focal Planes", *Proceedings* of SPIE, Vol. 1544, pp. 22–32, July 1991.

scanner was designed to maintain 5 ± 0.5 μm spacing between the microlens arrays. For this spacing, the focal length of the negative array is 1195 μm, and the positive array focal length is 1200 μm.

Each microlens was designed using 8 phase levels, which can be generated using three masks. An extra mask was used to fabricate three 10 x 10 x 3 μm platforms which are designed to prevent physical contact of the arrays and for adjusting array separation using interferometry.

5.0 EXPERIMENTAL RESULTS

The binary optic microlens arrays were fabricated out of fused quartz at MIT Lincoln Laboratory using photoresist masking and reactive ion etching (RIE). A mixture of CHF_3 and oxygen was used as the reactive working gas, producing a 200Å/min etch rate. Resist thickness was 5000Å. Thickness and alignment accuracy were measured after each photoresist development step. Etch depths for the three level process were 7020Å, 3510Å, and 1750Å respectively. The layer-to-layer misalignment was less than 0.2 μm and 0.3 μm for the positive and negative microlens arrays, respectively. The first measurement was determined by on-device micrometers located outside the boundaries of the arrays. The etch depth was controlled within 3%. Average step-to-step etch uniformity was better than 5%. Figure 6 shows a photomicrograph of the portion of the positive microlens array. The feature size at the corners of the lens is in the range of the 0.5 μm.

The microlens chips were sawed from the wafer in squares 10 mm on a side and 0.4 mm thick. The total mass of the microlens chip is 140 mg. Each microlens array is aligned to the sides of an opening into a lens holder. During this alignment procedure, the lens is held down by soft vacuum under elevated temperature to bring the bonding epoxy to the liquid phase. After the alignment cycle the temperature is reduced slowly to room temperature while the vacuum level increased. Figure 7 shows the assembled module. Figure 8 shows a close-up of the module aperture exposing the binary optic microlens arrays.

Each array is driven by a piezoelectric actuator, the two arrays being driven in orthogonal directions. The ultimate module field of view of 9.5° is achieved by translating the array by one-half of a lenslet diameter, which is ±100 μm. However, the compact actuators (PI model P-288) chosen for this demonstration have a maximum translation range of ± 25 μm. This allows the scanner to achieve a 13 x 13 spot pattern. A smaller laser scanner device (less than one cubic centimeter) can be designed using a custom actuator.

The beam steering module was tested using the optical setup shown in Figure 9. Light from a HeNe laser is passed through a collimator. Figure 10 shows a photograph of scanner output when both microlenses are aligned and they are parallel to each other with a negligible separation error. The center lobe contains most of the beam energy. The rest of the energy is distributed among the neighboring addressable points.

A desktop computer with a customized D/A converter board was used to generate drive signals for the scan actuators. Programmable patterns of test signals were output to the piezoelectric transducers to control the beam angle in two dimensions.

SCP-0152-A

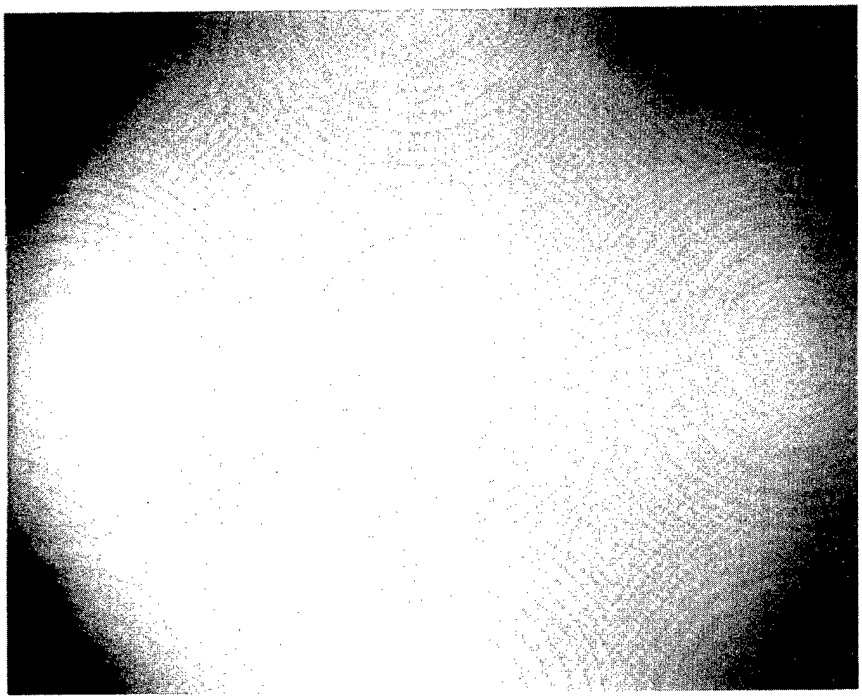

FIGURE 6. PHOTOMICROGRAPH OF MICROLENS ARRAY SEGMENT WITH 200 x 200 μm SQUARE MICROLENSES.

The result of a linear scan is shown in Figure 11. The resulting patterns showed, as predicted, very uniform and well-aligned spots where the majority of the energy is diffracted into a single peak with lesser amounts into neighboring peaks. In Figure 11, the first neighboring addressable points are also slightly illuminated. This is caused by higher diffraction orders, microlens separation error, and process nonuniformity.

The scanner was demonstrated up to a rate of 300 Hz. Operation at higher than 1 KHz is possible with appropriate damping of mechanical resonances.

The results of a spot scan of the energy distribution in the near field at 124 cm from the beam steerer, including a photograph at the same distance, are shown in Figure 11. The measurement showed that 50% of the transmitted energy appears in the principal diffraction lobe. A spot scan in the far field (7 m) resulted in measurements of angular spot separation of 3.6 mrad and beam divergence of 400 μrad, in good agreement with predicted values of 3.6 mrad and 506 μrad respectively.

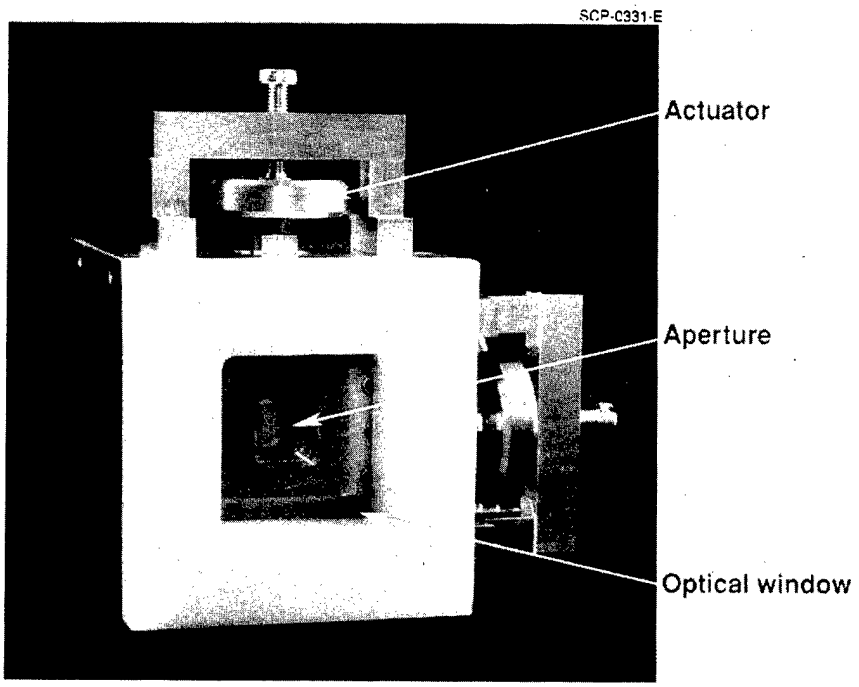

2-dimension steering with piezo actuators

FIGURE 7. MINIATURIZED STEERING MODULE SHOWING PIEZOELECTRIC ACTUATORS.

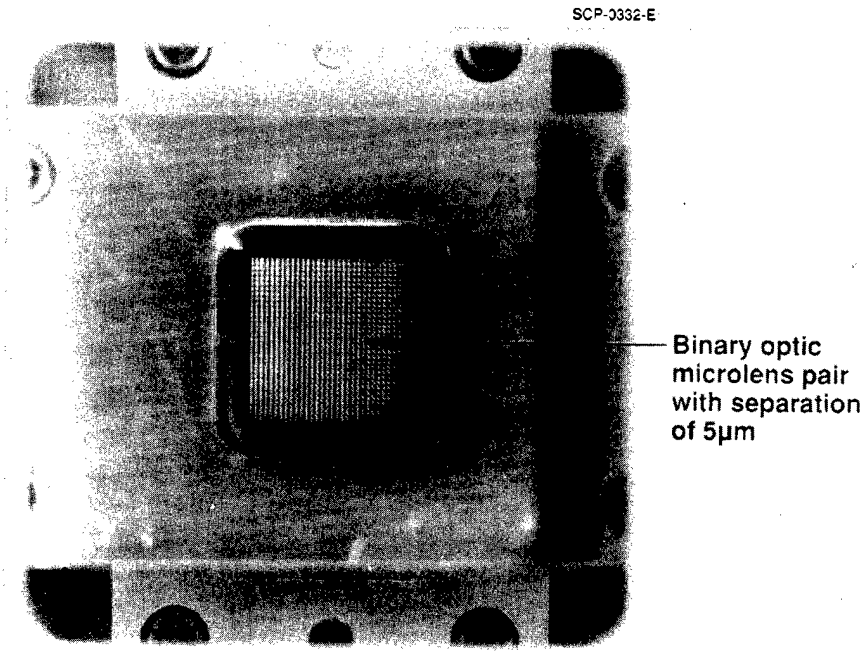

A close up of the aperture

FIGURE 8. CLOSE-UP OF STEERING MODULE APERTURE, SHOWING MICROLENS ARRAYS.

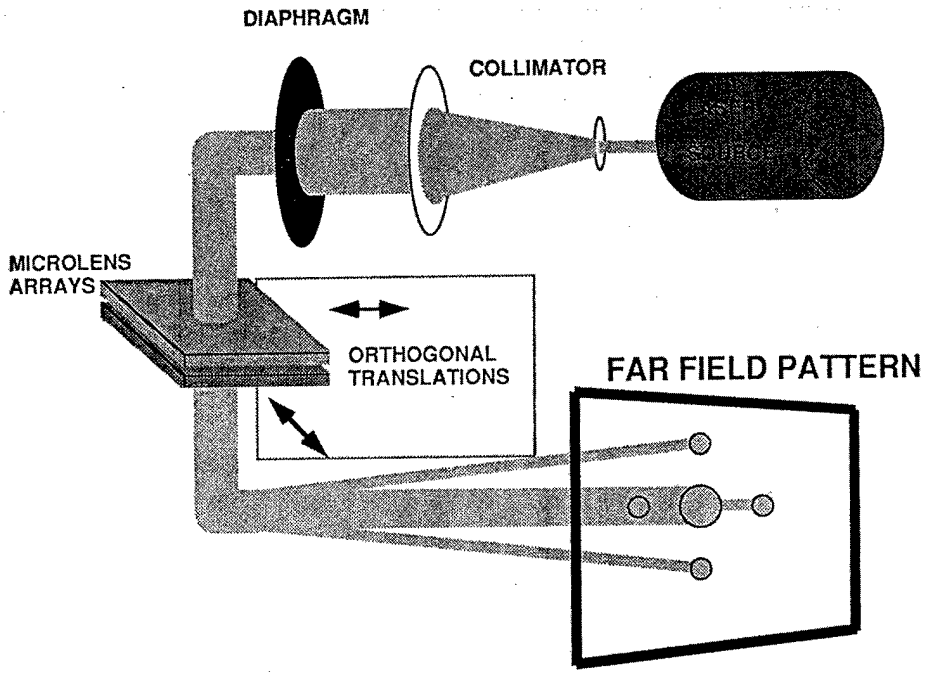

FIGURE 9. SCHEMATIC OF APPARATUS FOR MEASURING FIELD PATTERNS.

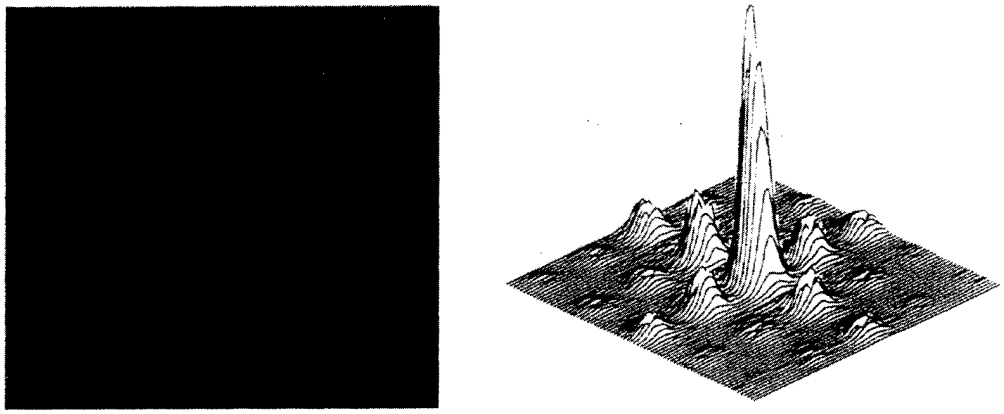

FIGURE 10. PHOTOGRAPH AND SPOT SCAN DATA OF FIELD PATTERN AT 124 cm FROM BEAM STEERER.

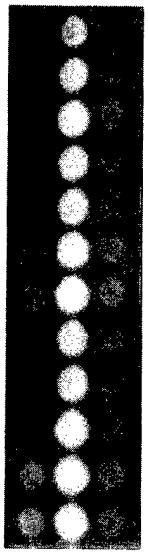

Linear Scan Demonstrated

SCP-0227-C

Rockwell Beam Steering Module Characteristics

- **300 Hz scan rate demonstrated**
  - **Linear, X only, Y only**
  - **Diagonal X + Y**
  - **Random**
- **16 x 16 array demonstrated**

FIGURE 11. MULTICYCLE EXPOSURE OF LINEAR SCAN AT 200 Hz.

CONCLUSION

We have demonstrated that binary optics can be used to design a laser beam steerer that is small, lightweight, and agile. A demonstration device was fabricated and its optical and mechanical properties were verified. The resulting far-field pattern of the scanner showed a single intense spot that agreed well with the theoretical distribution. The scan rate is far superior to any demonstrated to date for this technology and illustrates its potential for laser beam steering applications.

ACKNOWLEDGMENT

The authors gratefully acknowledge the consistent support of Dr. Monte Khoshnevisan in making this research successful. Thanks are due Bill Southwell, Leonard Hale, and Eric Schonning at Rockwell Science Center; Pete Avizonis at Rockwell Strategic Defense Center; and Wilfred Veldkamp at Lincoln Laboratory. We also thank Margaret Stern and Bill Delaney at Lincoln Laboratory for their contribution to processing the microlenses; and Bob Knowlden, William Goltsos and Garret Nenninger from Lincoln Lab for their support in optical modeling and mask design. Thanks are also due to Rockwell Science Center co-workers Don Deakin for development of the microlens optical packaging and Bart Vanderlip for precision machining and assembly of the lens/actuator system.

*SURPHEX™: New Dry Photopolymers for Replication of Surface Relief Diffractive Optics**

Felix P. Shvartsman

DU PONT COMPANY
Imaging Systems, R&D
SURPHEX™ Enterprise
Experimental Station, Box 80352
Wilmington, DE 19880-0352, USA

ABSTRACT

High efficiency, deep groove, surface relief Diffractive Optical Elements (DOE) with various optical functions can be recorded in a photoresist using conventional interferometric holographic and computer generated photolithographic recording techniques. While photoresist recording media are satisfactory for recording individual surface relief DOE, a reliable and precise method is needed to replicate these diffractive microstructures to maintain the high aspect ratio in each replicated DOE. The term "high aspect ratio" means that the depth of a groove is substantially greater, i.e. 2, 3 or more times greater, then the width of the groove. A new family of dry photopolymers SURPHEX™ was developed recently at Du Pont to replicate such highly efficient, deep groove DOE's. SURPHEX™ photopolymers are being utilized in Du Pont's proprietary Dry Photopolymer Embossing (DPE) technology to replicate with very high degree of precision almost any type of surface relief DOE. Surfaces relief microstructures with width/depth aspect ratio of 1:20 (0.1 μm / 2.0 μm) were faithfully replicated by DPE technology. Several types of plastic and glass/quartz optical substrates can be used for economical replication of DOE.

INTRODUCTION

Surface relief Diffractive Optical Elements (DOE) are a specialized class of embossed optical elements which are used to replace conventional optical components in laser scanning devices[1] such as rotating polygon mirrors, galvanometers, and other beam-deflecting devices and their associated optics, such as, for example, integrated holographic optical pickup heads for compact disc players.[2] Recent progress in electron-beam lithography and ion-beam etching micro-fabrication techniques[3-5] demonstrated feasibility of blazed relief microstructures, which improves micro-Fresnel lens focusing efficiency. The high efficiency, deep groove, original surface relief microstructures are obtained by using a photoresist as the recording medium. While photoresist recording media are satisfactory for making individual deep groove, phase DOE, a practical method is needed to replicate faithfully such DOE to maintain the high aspect ratio needed for each replicated element. The term "high aspect ratio" means that the depth of the groove is substantially greater, i.e., 2, 3 or more times greater, than the width of the groove. Although the conventional methods of replicating of embossed holograms meet many of the needs of the graphic arts industry, they have been unsatisfactory for replicating the high efficiency, deep groove DOE required for laser scanning systems and other specific applications. In the case of thermal embossing, the deep groove, high aspect ratio relief hologram is not faithfully reproduced and in the case of molded UV-curable liquid resins, a residue of UV-cured resin remains entrapped in the deep grooves of the mold.

Numerous applications of high performance surface relief DOE has been developed for military and space applications. In the commercial equiepment market a new type of surface relief diffractive scanning elements for the next generation of laser printing/scanning devices and FAX machines is being developed now by several electronic companies. Embossed holograms for security printing and graphic

* *Proceedings of EOS/SPIE International Conference - "Holographics International '92," 26-29 July 1992, Imperial College of Science, London, United Kingdom. Volume **1732, 1992, In press.***

arts recently shifted from monochromatic rainbow holograms into full color 2D/3D images and full color 3D images are under development. Practically in every mentioned above application reliable mass replication of such opto-electronic devices and production cost are the two major factors for successful introduction of this new generation of diffractive optics into the market place.

Du Pont has a long history and experience in extensive research and development, and also in production, of dry photopolymer films for various electronic and imaging applications. First practical dry photopolymer was invented at the Experimental Station of Du Pont in 1948 by Dr. Louis Plambeck. Variety of dry photopolymer films for different applications were commercialized since then, and such Du Pont's products as Dycryl®, Lydel®, Riston®, Cromalin®, and Cyrel®, are worldwide known trade marks. Recently novel Dry Photopolymer Embossing (DPE) technology was developed at Du Pont to replicate faithfully highly efficient, deep groove surface relief DOE.[6] To make DPE technology practical and commercially available new type of optical grade quality proprietary dry photopolymer films SURPHEX™ were specifically developed to be used in this process.

DRY PHOTOPOLYMER EMBOSSING TECHNOLOGY

Since 1948 when first practical dry photopolymer was developed, Du Pont built a powerful technological base in films, photopolymers, and also in related coating and imaging techniques. Development of the DPE technology and SURPHEX™ photopolymers started in 1987, and in 1988 it was successfully applied to replicate different types of diffractive optical elements, including binary optical elements and new generation of deep groove surface relief diffractive scanning elements. The term of "dry photopolymer" film or layer refers to a substantially solvent-free polymeric layer having a creep viscosity between 100 and 200 Megapoises, as measured with a parallel plate rheometer. Such dry photopolymer are contrasted with conventional liquid photopolymerizable layers which typically have viscosities of about several hundred Poises or less. Amounts of ingredients in the dry photopolymerizable compositions will generally be within the following percentage ranges based on total weight of the photopolymer layer:

- **polymeric binders** **35 - 50%**
- **monomeric system** **15 - 25%**
- **plasticizers** **5 - 15%**
- **initiating system** **1 - 5%**
- **other ingredients** **1 - 5%**

In general dry photopolymeric compositions contain an unsaturated monomeric system, a free radical-generating initiating system, and polymeric binders. Other components, which provide new dry photopolymer films SURPHEX™ with specific and unique functional capabilities needed in the DPE technology, can be present in the photopolymerizable compositions in varying amounts. Such components include: plasticizers, antioxidants. optical brighteners, ultraviolet radiation absorbing materials, thermal stabilizers, hydrogen donors and release agents.

The photosensitivity of the photopolymerizable composition is enhanced by a photoinitiating system which may contain a component which sensitizes the composition to practical radiation sources, e.g., visible light. Conventionally a binder is the most significant component of a substantially dry photopolymerizable film or layer in terms of what physical properties the film or laminate will have while being used in the DPE process. The binder serves as a containing medium for the monomer and photoinitiator prior to exposure, and after exposure contributes to the optical and other physical characteristics needed for the optical element. Cohesion, adhesion, flexibility, miscibility, tensile strength, and index of refraction are some of the many properties which determine if a binder is suitable for use in a diffractive optical element.

Several types of optical grade quality dry photopolymer films SURPHEX™ having uniform thickness across the film are being produced in the brand new state-of-the-art commercial clean room facility recently built at one of the Du Pont plants. Descriptions of SURPHEX™ photopolymers and some of potential applications are given in **Table 1**:

Table 1. SURPHEX™ products and potential applications

PRODUCT	DESCRIPTION	APPLICATION
SURPHEX™ - P SURPHEX™ - G	Family of UV curable photopolymer films for DPE on **Plastic** and **Glass** substrates	Diffractive optical components, diffractive scanning elements, diffusion screens for projection and active matrix TV displays
SURPHEX™ - H	Family of UV curable photopolymer films for continuous DPE of embossed **Holograms**	Security printing applications: credit cards, driver licenses, bonds and currency; sales advertisements, gift packaging

Productional thickness of the SURPHEX™ films can be adjusted and optimized in the range of **2-50 μm** to achieve the best replication quality of the high width/depth aspect ratio recorded in the original DOE. Refractive index of the cured, free standing SURPHEX™ films is **1.50±0.01**. Uncured photopolymer layer is a self-adhesive film which bonds firmly to the substrate surface by a simple lamination process without additional adhesive layer or primer. SURPHEX™ films have optical characteristics comparable to those of the substrates and match sufficiently the refractive index of the substrate materials. The photopolymer layer is a thermoplastic composition which upon exposure to actinic radiation, forms a blend of compatible and miscible polymers of higher molecular weight by crosslinking and/or by polymerization. This changes the rheological character of the composition and decreases its solubility in common solvents. Shelf life of the unprocessed SURPHEX™ films is **>2 years**. Precisely controlled physical and chemical properties of the developed photopolymeric formulations allow to produce high quality DOE, which in most cases can not be achieved by utilizing conventional replication technologies and materials.

In the dry photopolymer film manufacturing process specially pre-filterd (0.2 μm filtration station) solution of the SURPHEX™ photopolymer, is being machine web-coated onto the temporary support polyethylene terephthalate film. The primary criteria for the support film is that it possess dimensional stability and the surface smoothness and release characteristics needed to laminate a uniform dry photopolymer layer to the substrate surface without distortion of the layer when the support film is removed. To meet this criteria the cohesive force of the photopolymer layer and its adhesive force to the substrate must be greater than its adhesive force to the temporary support film. A second temporary cover sheet or interleaf may be placed on the second surface of the photopolymerizable layer to protect it from contaminants during storage in roll or stacked cut sheet form and to prevent blocking of the stored element. If used, the protective cover sheet or interleaf is removed from the surface of the photopolymerizable layer before the layer is laminated to the substrate. Different polymer films can be used as the cover film provided the film has a suitable surface smoothness and has less adhesion to the photopolymerizable layer than the layer has to the support film. Suitable protective cover sheets or interleafs include polyethylene, polypropylene, etc.

In the laminating step the protective cover sheet or interleaf, if present, is first removed from the photopolymer layer and the layer is applied to the surface of the substrate under pressure and typically with heat so that interfacial air is removed and void free adhesion between the substrate and the layer is

achieved. Preferably a hot roll laminator is used to achieve such void free adhesion. The embossable photopolymer layer can be laminated to the surface of the substrate in a form of a dry film using any conventional laminating system. Particularly useful are commercial hot roll laminators, e.g., Du Pont Cromalin® Laminator and Du Pont Riston® Hot Roll Laminator. To support the substrate during lamination, it is placed on a temporary carrier sheet of commercial color proofing receptor, e.g., Cromalin® MasterProof Commercial Receptor. The SURPHEX™ film is laminated to the substrate using hot roll laminator operating at a roll surface temperature of 115-124°C. Lamination covers the substrate surface uniformly and seals it around the edges to the carrier sheet. Subsequently laminated substrate is cut out from the temporary carrier sheet with a razor blade.

Typical example of the DPE process is shown schematically in **Figure 1.** All processing steps are being performed in ambient conditions under yellow light. Surface relief microstructure is transferred to the laminated substrate by embossing the dry photopolymer layer with a stamper carrying a surface relief corresponding to the diffractive optical element.

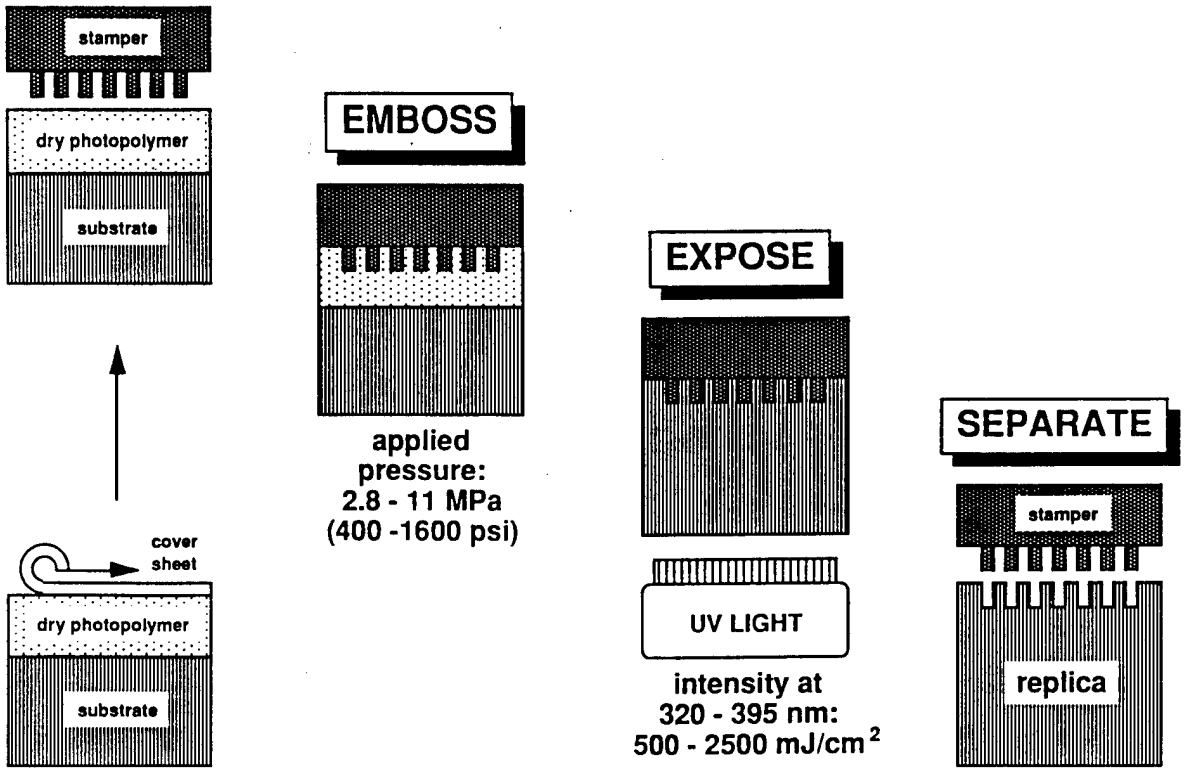

Figure 1. Dry Photopolymer Embossing concept

In the first step of the DPE process the cover sheet is removed from the laminated substrate. The stamper is then laminated to the substrate using a photographic roller or other pressure rolls laminating equipment. The tackiness of the photopolymer layer holds the stamper in place and such sandwich is then placed between two flat plastic (polycarbonate or polymethyl methacrylate) shims to protect the sandwich from the press platens. The sandwich is loaded at room temperature into a 30 ton capacity hydraulic platen press equiped with a manual lever action . The load is quickly increased to a pressure of 2.8 - 11 MPa (400 - 1600 psi). Pressure applied to the sandwich should be optimized depending on the width/depth aspect ratio of the grooves recorded in the stamper. The load is released after 5 - 15 seconds dwell time and the shimmed sandwich is removed from the press. The shims are then removed from the

sandwich. The embossed information layer is then firmly bonded to the substrate and the embossing made permanent by ultraviolet radiation exposure. The stamper/substrate sandwich is placed, with the transparent substrate facing the light source, into a high intensity ultraviolet exposure unit, and after a 5 - 15 second exposure with a UV light intensity at 320 - 395 nm of 500 - 2500 mJ/cm^2, the stamper is removed by flexing the sandwich assembly slightly.

PROPERTIES OF THE DRY PHOTOPOLYMER FILM SURPHEX™

The term of "dry photopolymer" film or layer refers to a substantially solvent-free polymeric layer having a creep viscosity between 100 and 200 Megapoises, as measured with a parallel plate rheometer. Such dry photopolymer are contrasted with conventional liquid photopolymer layers which typically have viscosities of about several hundred Poises or less. Viscosity is measured as creep viscosity with a parallel plate rheometer using a Du Pont Model 1090 Thermal Mechanical Analyzer. In this procedure, a 0.915 mm thick sample is placed in contact between two flat discs (about 6 mm in diameter). A quartz probe which is capable of accepting additional weights is positioned atop the upper disc and the same/disc assembly is maintained at constant temperature of 40°C and RH of 44% throughout the measurement. Creep viscosity is calculated from the rate of decrease of sample thickness under equilibrated conditions. The 0.915 mm sample is prepared by laminating together sufficient layers of the test film to obtain the desired thickness. The laminate is then cut to provide a circular sample slightly larger in diameter than that of the rheometer plates.

As shown in **Figure 2,** a free standing, 25 μm thick cured SURPHEX™ film has 98 - 99% of transmittance in the long UV, Visible, and up to 2000 nm in the near IR region of the spectrum.

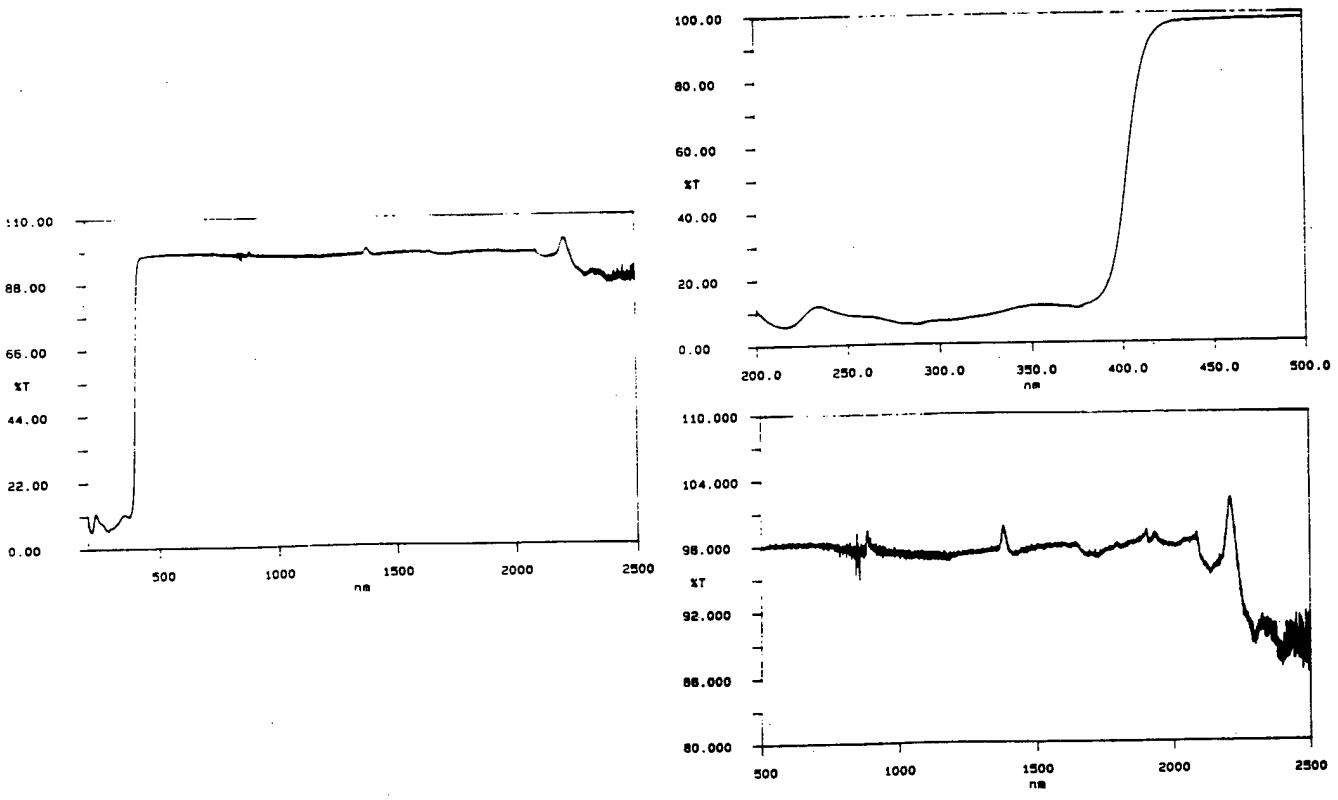

Figure 2. SURPHEX™, 25 μm cured film: UV, Visible and near IR transmittance spectra

In the IR region of the spectrum, shown in **Figure 3,** between 2500 - 5000 nm transmittance of the SURPHEX™ films decreases to ~80%, comparing to the previously reported[7] results of ~ 50%, when a prototype of a dry photopolymer film OPTIMER*-89 was tested in DPE technology. At the longer wavelengths transmittance of the SURPHEX™ films drops to 40 - 60%, reaching only ~30% at 10.6 μm wavelength used for CO_2 laser applications.

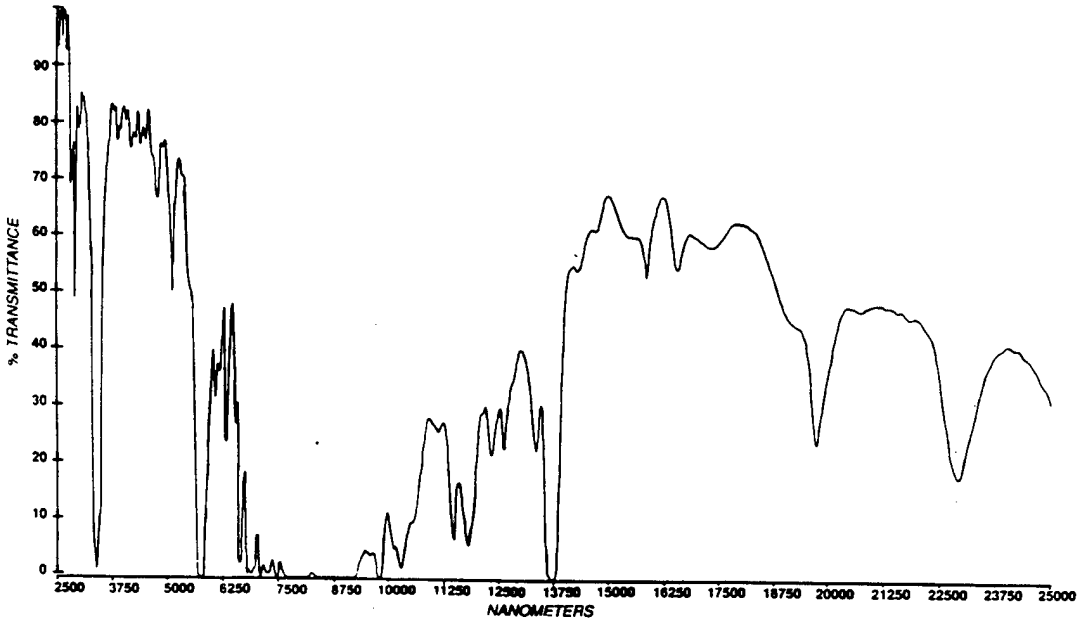

Figure 3. SURPHEX™, 25 μm cured film: IR transmittance spectrum

Differential scanning calorimetry revealed good thermal stability of the SURPHEX™ films. As one can see in **Figure 4**, SURPHEX™ film has one minor γ-transition at **+26.18°C**, which is related apparently to some relaxations in the polymer bulk of one of the binders. Glass transition temperature $\mathbf{T_g}$ was not detected by DSC since cured SURPHEX™ films represent highly miscible blends of several chemically compatible polymers. Between **-40°C** and **+105°C** cured SURPHEX™ film is thermally stable. Above **+110°C** DSC film sample begins to soften and at **+145°C** it becomes slightly brownish, which can be attributed to the decomposition of the film at **+153.57°C**.

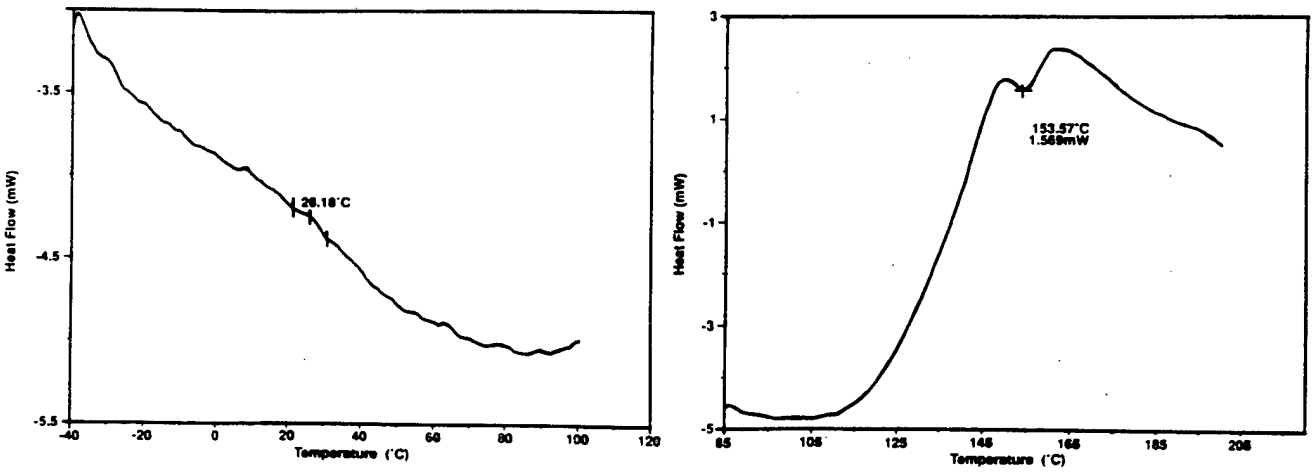

Figure 4. SURPHEX™, cured film: differential scanning calorimetry curve

PERFORMANCE OF SURPHEX™ REPLICAS

Several qualification tests have been performed on the SURPHEX™ replicas made by DPE technology. Results from these accelerated life tests are summarized in **Table 2.** Dimensional stability test was performed during spinning test in which DPE replica was optically aligned on a high-speed motor by viewing cross-scan dot placement (200 times magnified) on a TV monitor. The replica was spun at **10.000 rpm** in enclosed box at constant temperature of **35°C** for **200 hours** and following data was measured at **24-hour** intervals while keeping laser current and diode laser temperature constant:

- physical changes to the DPE replica at visual inspection
- dot size (micrometers) in three meridians -
  - 1 - zero degrees or cross-scan
  - 2 - forty-five degrees (clockwise)
  - 3 - ninety degrees or in-scan
- diffraction efficiency
- dot movement

A number of environmental tests were run on open and sealed surface reief micro structures of the SURPHEX™ replicas and main results from these tests are shown in **Table 2.** As a general comment to the presented performance parameters data it can be said, that DPE technology produces replicas which have optical performance comparable to performance of the original Master-DOE, and environmental properties similar or better then other known polymeric materials used in conventional DOE replication processes.

Table 2. Accelerated life tests of SURPHEX™ replicas

• dimensional stability (SURPHEX™-P)	no visual physical changes and no losses in optical performance after 200 hours of a spinning test at 10.000 rpm and 35°C
• UV exposure stability (SURPHEX™-P)	no physical or spectral changes after >1 year of the accelerated sun test in the exposure unit SUNTEST CPS
• high power resistance, qualitative test (SURPHEX™-G)	replicas made on quartz substrate sustained diffraction limited focal spot sizes under illumination 5x5 mm laser beam with 10 W CO_2 laser with power density of ~ 200 W/cm^2
• environmental stability	
- open gratings (SURPHEX™-P)	no physical or spectral changes and no losses in optical performance after >1 year of normal storage at ambient conditions
- sealed gratings (SURPHEX™-P)	no physical or spectral changes and no losses in optical performance after storage at -20°C in 85% RH for 100 hours and at +60°C in 85% RH for 100 hours

Optical and scanning electron microscope inspections confirm that original DOE surface relief profiles are being transferred to the SURPHEX™ photopolymer layer with a very high fidelity. Several examples of the replicated surface relief microstructures with different width/depth aspect ratios are shown in **Figures 5, 6,** and **7**. Broad range of the width/depth aspect ratios recorded in original HOE have been faithfully reproduced in the DPE replicas and features from 0.1 μm to 3.5 μm were precisely replicated. DPE technology covers full range of the grooves width/depth aspect ratios to produce different types of high quality surface relief or embossed holograms. All presented SEM photographs have the same size code to scale properly dimensions of the original and replicated microstructures. This code can be followed by observing the scaling white dashed line located under magnification number in the lower left corner on every SEM photograph. One can scale replicated microstructures referring to the following size code and by measuring the length of the **last** bigger dash shown in the scaling line under magnification index '**kx**':

|_ _ _ ___|	= **100 μm**
|_ _ ___|	= **10 μm**
|_ ___|	= **1 μm**

Detailed optical microscope scanning profilometry of the DOE shown in **Figure 5** demonstrated that the average difference in the top surface profiles between the original DOE (a) and replicated microstructures of the SURPHEX™ replica (**b, c, and d**) constitutes only several hundred angstroms.

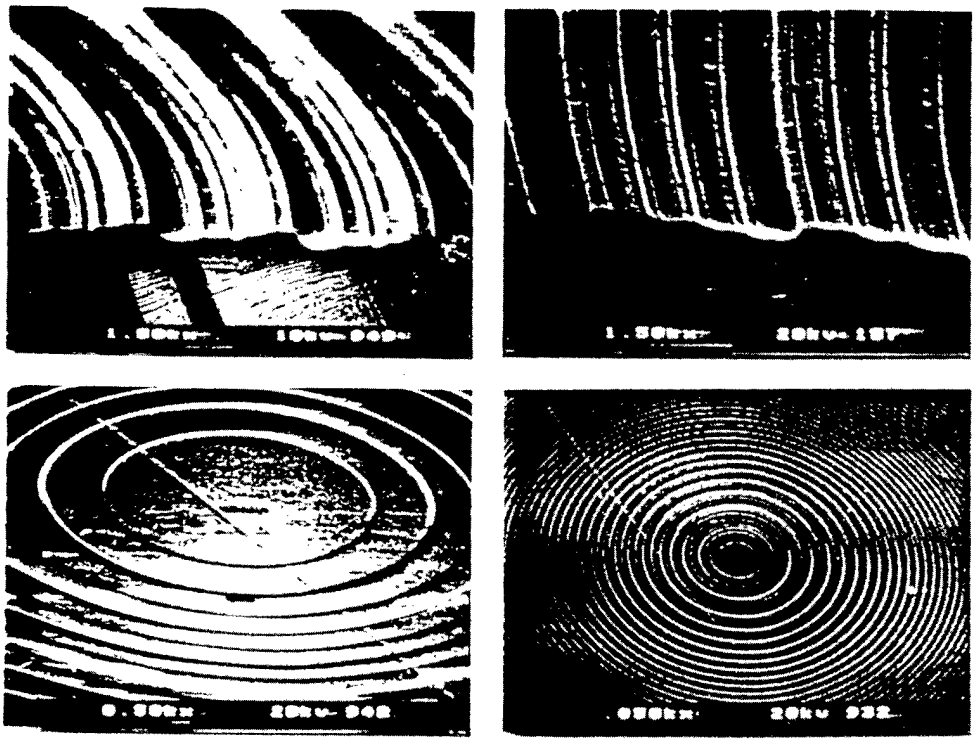

Figure 5. SEM of original DOE (a) and DPE replica (**b, c, and d**): width/depth aspect ratio - 1:10

Figure 6 shows SEM of the DPE replica with the width/depth aspect ratio in the groove of **1:20**, were width at the bottom of the groove is **~0.1 μm** and depth of the same groove is **~2 μm**. Also, as one can see, quite sophisticated curved microstructures of this DOE were faithfully replicated.

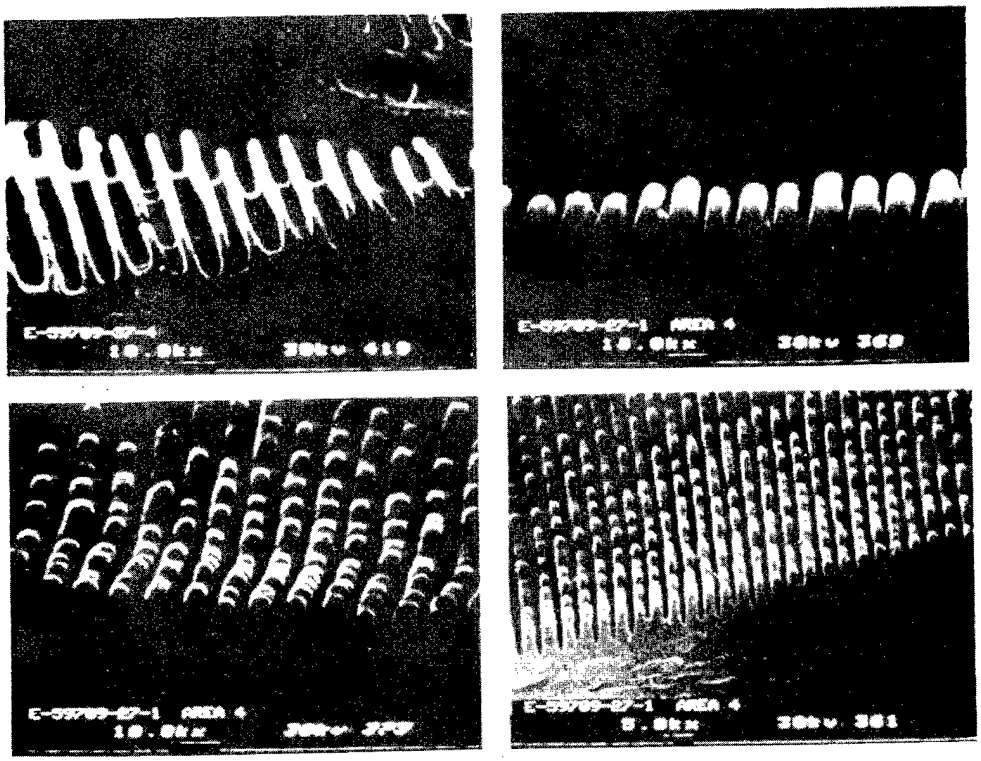

Figure 6. SEM of DOE stamper (**a**) and DPE replica (**b**, **c**, and **d**): width/depth aspect ratio - 1:20

Figure 7 demonstrates SEM of a cross-section of the SURPHEX™ replica from a DOE with a saw-tooth type surface relief profile. This microstructure, which has repeatable small negative curvatures (side pockets of ~50 nm), was precisely replicated by DPE technology into the SURPHEX™-P25 (25 μm thickness) film laminated to a polycarbonate (PC) sheet substrate.

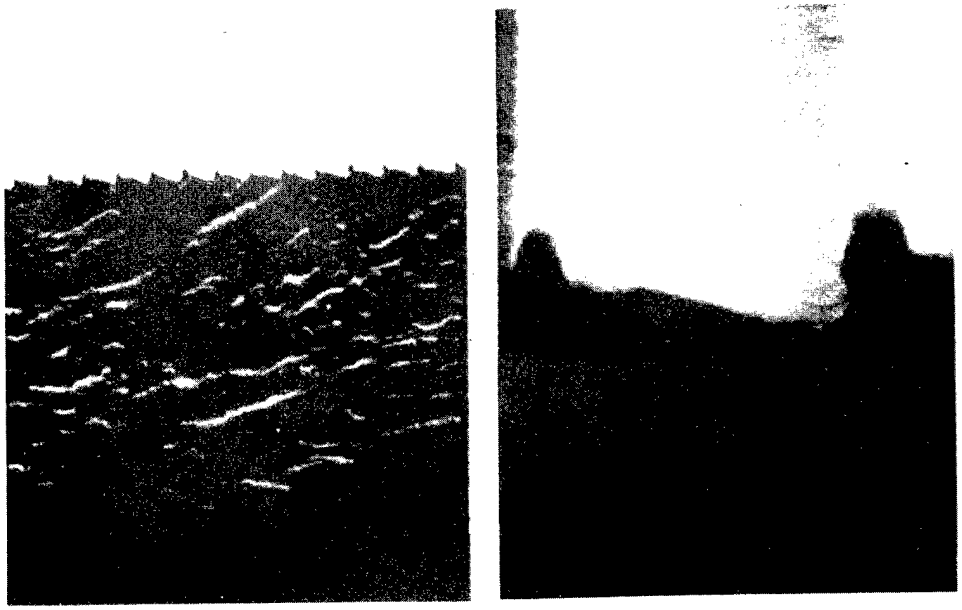

Figure 7. SEM of SURPHEX™ replica of a saw-tooth microstructure: depth - 0.7 μm, pitch - 2μm

CONCLUSIONS

Novel Dry Photopolymer Embossing technology and SURPHEX™ dry photopolymer films can be successfully utilized to replicate different types of surface relief microstructures with a definite advantage in replication of the deep grove surface relief DOE. For each specific DOE application properties of the SURPHEX™ type formulations can be optimized and processing parameters for the DPE replication process can be adjusted to meet required performance specifications. Comparing DPE technology with existing conventional replication processes, such as thermo-embossing, injection molding, wet photo-polymerization (2P-process), and injection-reaction molding, the following advantages should be emphasized:

- ***dry*** UV curable materials improve handling and processing
- very precise replication of the deep groove DOE
- no need for an adhesive layer to mount DOE on a substrate
- wide range of polymeric and inorganic substrate materials
- no size or shape limitations for the SURPHEX™ replica
- potential economical advantage for a ***continuous*** DPE process

ACKNOWLEDGMENTS

Formulations improvements, coating, imaging and processing techniques were developed in collaboration with Dr. A. L. Shobert, Mr. D. G. Gray, and Mr. W. J. Morgan. Continuous and dedicated assistance in the laboratory by Mr. J. M. Brawders is greatly appreciated.

REFERENCES

1. S. Hasegawa, F. Yamagishi, H. Ikeda, and T. Inagaki, "High Resolution Line Scanner for Use in Diode Laser Printers," *Proceedings of SPIE on Practical Holography II,* Vol. **747**, 8-16 (1987).

2. Y. Komma, S. Kadowaki, Y. Hori, and M. Kato, "Holographic optical element for an optical disk head with spot-size detection servo optics," *Applied Optics,* Vol. **29(34)**, 5127-5130, 1990.

3. G. L. Swanson and W. B. Veldkamp, "Diffractive optical elements for use in infrared systems," *Optical Engineering,* Vol. **28(6)**, 605-608 (1989).

4. N. F. Borrelli and D. L. Morse, "Microlens arrays produced by photolytic technique," *Applied Optics,* Vol. **27(3)**, 476-479, 1988.

5. T. Shiono, M. Kitagawa, K. Setsune, and T. Mitsuyu, "Reflection micro-Fresnel lenses and their use in integrated focus sensor," *Applied Optics,* Vol. **27(15)**, 3434-3442, 1989.

6. F. P. Shvartsman, "Holographic optical elements by dry photopolymer embossing," *SPIE-'91 Proceedings,* Vol. **1461**: Practical Holography V, 313-320, 1991.

7. F. P. Shvartsman, "Dry Photopolymer Embossing: Novel Photoreplication Technology for Surface Relief Holographic Optical Elements," *Proceedings of ECO4-'91,* Vol. **1507**: Holographic Optics III: Principles and Applications, 383 - 391, 1991.

Predesign of Diamond Turned Refractive/Diffractive Elements for IR Objectives

Max J. Riedl

OFC Diamond Turning Division
69 Island Street, Keene, NH 03431

ABSTRACT

Diffractive lenses have arrived. Literally hundreds of papers have been published[1-25] and technology impact reports have been written about the exciting addition of a new tool for the lens designer.[1] Sophisticated computer programs have been developed to aid in the optimization of these diffractive phase profiles for a wide variety of applications. Now, several fabrication methods are being pursued to produce these diffractive elements economically. The best known process is the etching of a multi-level relief grating, known as binary optics.[2] This process uses sets of computer generated lithographic masks. Another, more recently developed method is Dry Photopolymer Embossing (DPE).[3] This replication process uses master holograms. And now, diamond turning is being applied for the machining of these elements.[4,5] Diamond turning is especially well suited for infrared optics. As any process has advantages and limitations, so has diamond turning. These advantages and limitations are discussed and general guidelines are presented to aid the designer and systems engineer in the project predesign stage.

1. INTRODUCTION

Diamond turning is a well established fabrication process for shaping high quality optical surfaces on metals, polymers and crystals. It is therefore a natural extension to apply this proven process to generating surface relief phase profiles of diffractive lenses. The ability to guide a single point cutting tool along a predetermined path to an accuracy of a fraction of one wavelength of light makes this process very suitable for this task. The surface finish achieved with diamond turning is of a quality generally acceptable for optical components for the mid- and long wavelength regions of the infrared spectrum.

2. GENERAL REMARKS TO DIAMOND TURNING DIFFRACTIVE SURFACES

Besides material limitations, an important factor that determines the practicality of diamond turning diffractive surfaces is the number of annular zones (modulo 2π) required for a given application. A single point cutting tool has a relatively large radius which is optimized for achieving an acceptable surface finish in a reasonable time. For machining a diffractive surface, this radius should be small to reduce the "shadowing" effect at the transition step from one zone to the next. Much of this paper will address this effect since it is central to the practicality of diamond turning diffractive surfaces.

3. THE PHASE PROFILE FUNCTION

$$\varphi(r) = \frac{2\pi}{\lambda_0} [Ar^2 + Br^4 + Cr^6 + \ldots] \quad (1)$$

This is the well known function for a rotationally symmetric lens surface with r being the radial coordinate of the profile, λ_0 the wavelength of interest, and A,B,C etc. the phase profile coefficients. Their optimum values are determined with computer programs such as CODE V, OSLO and ACCOS. For preliminary evaluation it is worthwhile to truncate this expression and examine the resulting approximations. This is being done in the following sections with the assumption that the object is located at infinity.

4. THE MONOCHROMATIC SINGLET

A spherical wave front exiting a lens can be expressed by

$$\varphi(r) = \frac{2\pi}{\lambda_0} [- \frac{r^2}{2F} + \frac{r^4}{8F^2} - \ldots] \quad (2)$$

By comparison with equation (1) it can be seen that

$$A = - \frac{1}{2F} \quad (3)$$

where F is the focal length of the lens. The negative sign indicates the direction of the phase profile.

The first zone radius, where the 2π transition (one wavelength) occurs is therefore at

$$r_1 = \sqrt{2\lambda_0 F} \quad (4)$$

Others occur at

$$r_n = r_1 \sqrt{n} \quad (5)$$

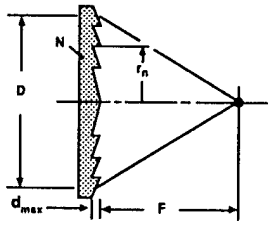

Where n is the zone number. At the limit $r_n = D/2$, with D being the lens diameter.

The total required zones can now be determined from

$$n_{TOT} = \frac{D^2}{8\lambda_0 F} = \frac{F}{8\lambda_0 (F/\#)^2} \quad (6)$$

Example 1 :

For a lens with F = 25 mm, F/# = 2, and λ_0 = 0.6328 μm, we find that approximately 1,235 zones are required to achieve the focusing effect.

A more accurate number, which could be obtained from

$$n_{TOT} = \frac{F}{2\lambda_0 (F/\#)} \left[\sqrt{1 + 4 (F/\#)^2} - 2 (F/\#) \right] \qquad (7)$$

is 1,216. Notice that the first approximation is within 1.6 % which indicates the value of simplicity.

From the expression

$$d_{MAX} = \frac{\lambda_0}{(N - 1)} \qquad (8)$$

we find the maximum depth of a zone at the transition, with N being the index of refraction of the substrate material.

If the material used in the example is plastic, with an index of 1.527, the depth would be approximately 1.2 μm.

5. THE MONOCHROMATIC HYBRID SINGLET

Hybrid is defined here as the combination of refractive and diffractive powers within one element. An interesting case is a convex plano lens for which the basic power is provided by the spherical shape of the first surface and the correction of the spherical aberration is achieved with a diffractive phase profile on the second surface.

Considering third order aberration only, one can express the longitudinal spherical aberration for a thin convex plano lens by [6]

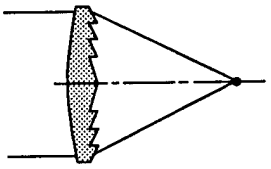

$$W_{SPH} = \frac{[N^2 (N - 2) + 2] F}{128 \lambda_0 N (N - 1)^2 (F/\#)^4} \quad \text{(wavelengths)} \qquad (9)$$

Example 2 : For the same basic lens from example 1, now shaped as a convex plano, we find from equation (9) that W_{SPH} = 41 waves. This means that 41 zones are required to correct 3rd order spherical aberration, since one wavelength is the OPD (optical path difference) for each zone. That is why these lenses are sometimes referred to as "one wavelength Fresnel lenses".

These two examples indicate the difference between having the job done with a diffractive surface on a plane-parallel substrate and a combination of refractive and diffractive powers. To be able to reduce the numbers of zones from 1215 to 41 speaks for itself. Furthermore, it is clear from the results that diamond turning is not an economical method for producing lenses of the first kind in any volume. It is, however, a good way to make prototypes to demonstrate a principle in a timely fashion; because no lithographic masks, no molds or masters are required. Of course, there is not much room for any cutting tool radius. At the edge of the 12.5 mm diameter lens, the spacing of the zones is about 2.6 μm. Therefore, the machining may have to be done by plunge cutting.

6. BROADBAND LENSES[2,5,7]

In addition to spherical aberration, a lens needs to be corrected for chromatic aberration if it is being considered for any broadband application.

To correct color, one takes advantage of the fact that the chromatic aberration of a diffractive element is opposite in sign when compared to the chromatic aberration of a refractive element as indicated in figure 1.

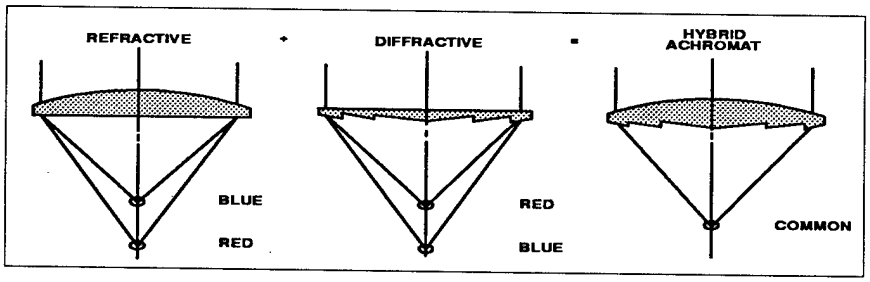

Figure 1. Principle of color correction with diffractive optics

$$\text{Power} \quad \phi_R + \phi_D = \phi_{TOTAL}$$

$$\text{or} \quad F = \frac{F_R F_D}{F_R + F_D} \tag{10}$$

To correct chromatic aberration, the following conditions must exist

$$F_D = (1 - \nu_R/\nu_D) F \tag{11}$$

and

$$F_R = (1 - \nu_D/\nu_R) F \tag{12}$$

with

$$\nu_R = \frac{N_0 - 1}{N_S - N_L} \quad \text{and} \quad \frac{\lambda_0}{\lambda_S - \lambda_L}$$

ν_R is called the Abbe number of refraction and ν_D is the Abbe number of diffraction.
ν_D indicates that for the diffraction effects, the lens material is immaterial.
λ_0 is the center wavelength for which the index of refraction is N_0.
λ_S, λ_L are the short and long limiting wavelengths of the spectral band.

6.1. THE ACHROMATIC SINGLET

An excellent summary of what can be achieved by combining refractive and diffractive powers in a single element to correct spherical and chromatic aberration is shown in figure 2.

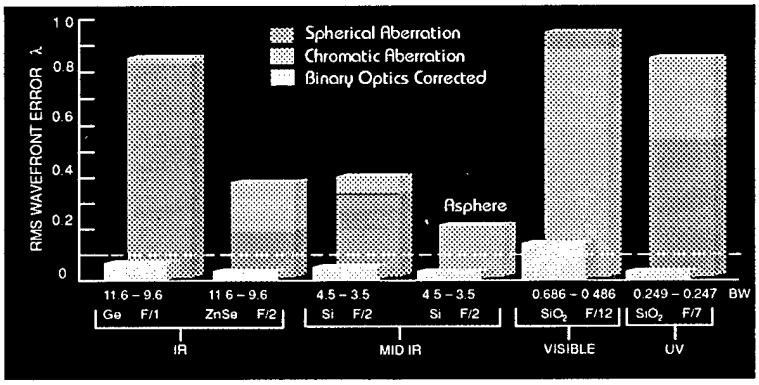

Figure 2. Examples of the chromatic and spherical aberration reduction possible by using a refractive/diffractive lens [With permission from Lincoln Laboratory[2]].

It can be seen clearly how the degree of correction is dependent on the lens material, the spectral region, and the relative aperture. For example, the F/1 germanium lens is overwhelmingly afflicted with spherical aberration and mildly affected by chromatic aberration over the 2 μm band width. On the other hand, the quartz lens applied in the visible spectrum over a band width of 0.2 μm, shows much chromatic and little spherical aberration. To achieve a reasonable correction, the relative aperture had to be increased to F/12.

It can also be seen how advantageous it is to use an aspheric surface for the elimination of spherical aberration. By superimposing the phase profile onto the asphere allows the other surface of the lens to be spherical. The preferred arrangement is to place the aspheric phase profile on the second surface for better environmental protection. The spherical front surface can be produced by conventional manufacturing processes if desired.

To find the first zone radius for such an achromatic singlet, the diffractive focal length is substituted into equation (4) to form

$$r_1 = \sqrt{2\lambda_0 (1 - \nu_R/\nu_D) F} \tag{13}$$

The total number of zones required is then

$$n_{TOT} = \frac{F}{8\lambda_0 (1 - \nu_R/\nu_D) (F/\#)^2} \tag{14}$$

Considering that the center wavelength for the 3 to 5 μm region is 4 μm and the diffractive Abbe number is -2 leads to very simple approximations.

$$r_{1\ 3\text{-}5} \cong \frac{\sqrt{\nu_R F}}{15.8} \quad [r_1 \text{ and F in mm}] \tag{15}$$

and

$$n_{TOT\ 3\text{-}5} \cong \frac{62\,F}{\nu_R\,(F/\#)^2} \quad [\text{F in mm}] \tag{16}$$

Summary for the 3 to 5 μm region

Material	ν_R	r_1	n_{TOT}
Silicon	235.5	1 $[\sqrt{F}]$	0.263 $[F/(F/\#)^2]$
Zinc Selenide	176.7	0.84	0.351
Zinc Sulfide	133.8	0.73	0.463
Germanium	104.8	0.65	0.592

(r_1 and F in mm)

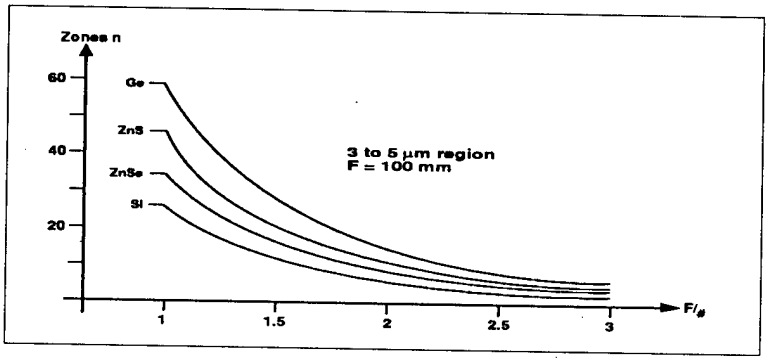

Figure 3. Number of zones as a function of F/# for different materials

Example 3: A ZnSe lens with a relative aperture of F/1.5 requires 16 zones. This is a reasonable low number for a 67 mm diameter diamond turned grating.

Figure 4 shows a 50 mm diameter diamond turned ZnS diffractive lens for the 3 to 5 μm region. The narrowing of the zones towards the edge of the lens can clearly be seen.

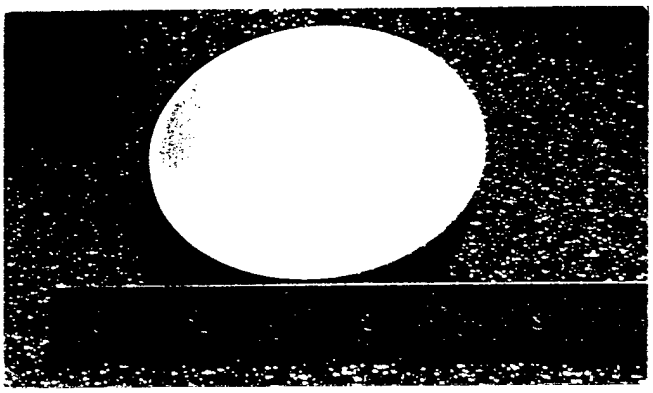

Figure 4. Diamond turned achromatic singlet

Similarly as for the mid IR region, one can summarize for the 8 to 12 μm window, where $\lambda_0 = 10$ μm and $\nu, = -2.5$:

$$r_1 \cong \frac{\sqrt{\nu_R F}}{11.2} \tag{17}$$

and

$$n_{TOT} \cong \frac{31 F}{\nu_R (F/\#)^2} \tag{18}$$

Summary for the 8 to 12 μm region

Material	ν_R	r_1	n_{TOT}
Germanium	863.0	2.62 $[\sqrt{F}]$	0.036 $[F/(F/\#)^2]$
Amtir 3	109.8	0.94	0.282
Zinc Selenide	57.5	0.68	0.539

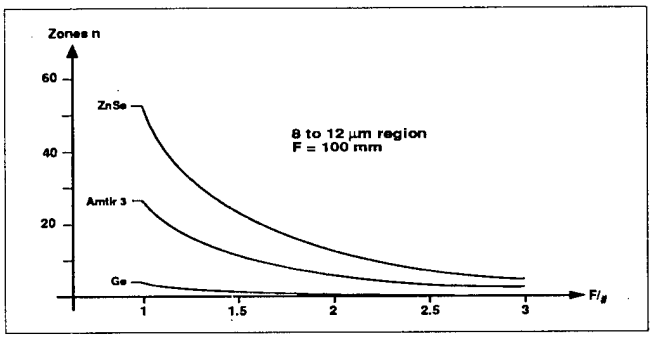

Figure 5. Number of zones as a function of F/# for different materials

One can see how effective germanium is in this region.

6.2. DIFFRACTION EFFICIENCY

It has been stated that the scalar theory used to predict diffraction efficiencies is overly optimistic. An extension to this theory was developed in early 1991 at the Lincoln Laboratory.[8] This extended scalar theory takes into account the ratio of the wavelength and the grating period. The equations developed show that when that ratio is very small -or in other words- if the period is much larger than the wavelength, the impact on the efficiency is negligible. This is the case for all the diamond turned optics discussed here. Therefore, only expressions based on the pure scalar theory will be applied for these predesign considerations.

The grating efficiency referred to the first diffraction order is

$$\varepsilon_1 = \left[\frac{\sin\left[\pi\left(\frac{\lambda_0}{\lambda}-1\right)\right]}{\pi\left(\frac{\lambda_0}{\lambda}-1\right)}\right]^2 \tag{19}$$

This yields, when integrated over a band width of $\Delta\lambda = \lambda_L - \lambda_S$, an approximated average efficiency of

$$\bar{\varepsilon}_1 \cong 1 - \frac{\pi^2}{36}\left(\frac{\Delta\lambda}{\lambda_0}\right)^2 \tag{20}$$

It is very important to be aware of the efficiencies at the band width limits. Looking at the average value can be deceiving and can cause serious systems problems. This is best demonstrated by looking at the limits of the two spectral windows.

The average efficiency for the first order over the 3 to 5 μm window is approximately 0.931, a relative large number. The efficiency at 5 μm is only 0.875 and drops even further down to 0.684 at 3 μm. For the 8 to 12 μm window, the situation is somewhat better, but still of great concern for any given application. The average efficiency over this window is 0.956 with 0.912 at the long wavelength and 0.811 at the short one.

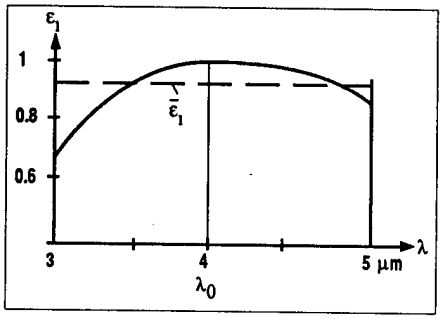

Figure 6

Diffraction efficiency over the 3 - 5 μm region

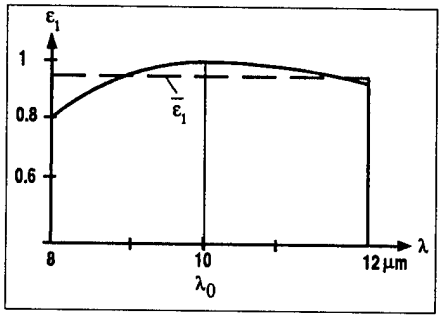

Figure 7

Diffraction efficiency over the 8 - 12 μm region

It is worthwhile to mention that for some specific applications it may be desired to take advantage of this roll-off effect. An example may be a radiometric application which favors that the peak efficiency occurs at say 4.5 μm (detect) with a lower transmission (diffraction efficiency) at say 3.2 μm (guard). Figure 8 shows the efficiency distribution for this case.

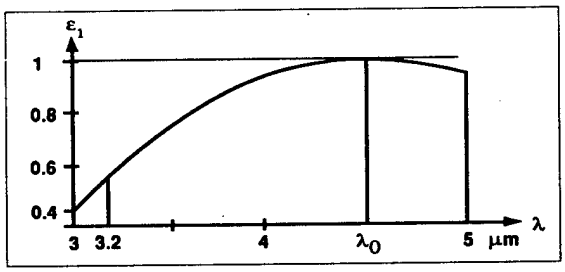

Figure 8. Blazed phase profile, for peaked efficiency at 4.5 μm

Another possibility for the efficiency distribution over the spectral band is to shift the center wavelength λ_0 so that the efficiencies at both limiting wavelengths are equal. From equation (19) one can find by inspection that this occurs for the 3 to 5 μm window when $\lambda_0 = 3.75$ μm and at $\lambda_0 = 9.6$ μm for the 8 to 12 μm window.

As a general comment, one has to keep in mind that the energy not transmitted into the first diffraction order goes into other orders and must be treated as stray or scattered radiation.

6.3. SURFACE ROUGHNESS AND SCATTERING

The surface finish achievable with diamond turning is related to the radius of the cutting tool, the cutting feed rate, the stiffness of the machine and the material being machined.[9,10] Additional factors, such as coolant and others, apply as well. Surprisingly, the surface quality is quite insensitive to surface speed. That is confirmed by the fact that most of the diamond turning machines in use today do not have a continuously variable spindle speed which would be required to maintain a constant surface speed.

From the above parameters one can make some prediction about the expected surface finish.

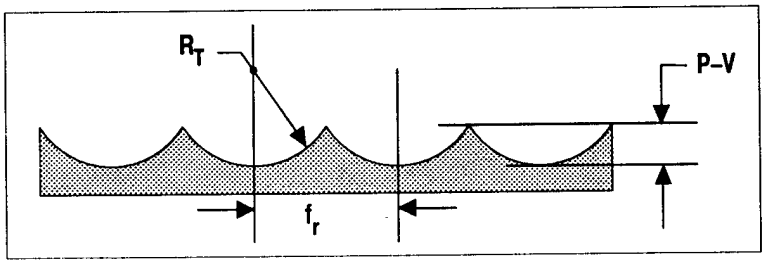

Figure 9. Theoretical Surface Finish

R_T = cutting tool radius
f_r = feed per revolution
P-V = peak to valley surface roughness

From the figure it can easily be seen that

$$P\text{-}V = \frac{f_r^2}{8R_T} \qquad \text{(theoretical)} \tag{21}$$

Typical values are $R_T = 0.030$ inch and $f_r = 0.0003$ inch per revolution. This yields a P-V finish of 0.375 μinch or 95 Å. Surface roughness is usually stated in RMS and a reasonable factor between P-V and RMS is 6. This is also a good factor to be considered for the influence on the finish caused by the limited machine stiffness and other factors mentioned earlier. Therefore, since these two factors cancel each other, a more realistic surface roughness prediction is

$$RMS \cong \frac{f_r^2}{8R_T} \qquad \text{(more realistic)} \tag{22}$$

A surface roughness of 80 to 120 Å is typical. It varies, depending on the material being machined. The roughness profile of an exceptionally smooth diamond turned surface is shown in figure 10. It also confirms the P-V to RMS ratio of approximately 6.

RMS: 6.33 nm
RA: 5.07 nm
P-V: 38.4 nm

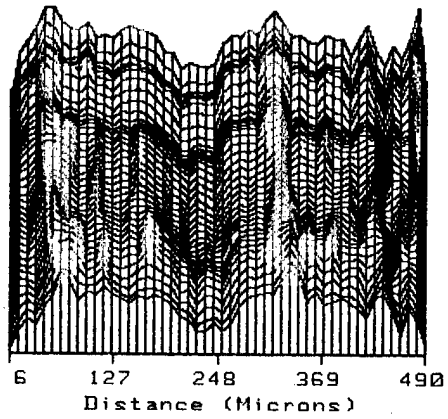

Figure 10. Roughness profile of a diamond turned surface

The roughness of a surface is another source for energy through-put reduction. This is due to scattering. To assess the magnitude of this loss, the relation for TIS (total integrated scatter) developed by the Naval Weapons Center[11] is being applied:

$$TIS = \left[\frac{4\pi\,\delta}{\lambda_0}\right]^2 \tag{23}$$

where δ is the RMS surface roughness and λ_0 is the wavelength of interest. For a roughness of 95 Å and a wavelength of 4 μm, TIS is approximately 0.1%, which is negligible for these predesign considerations.

6.4. BLOCKAGE OF RADIATION CAUSED BY DIAMOND TOOL RADIUS

The radius of the cutting tool forms an annulus at the transition from one zone to another. This causes an energy blockage which is illustrated in figure 11.

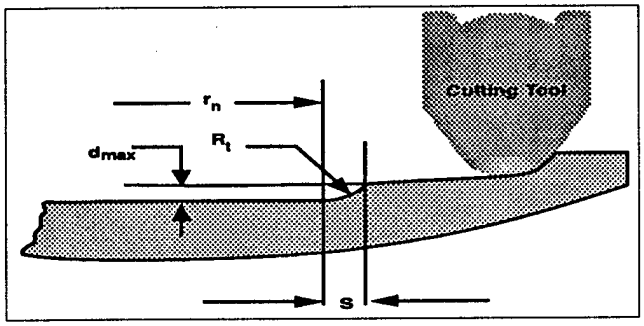

Figure 11. Zone transition geometry, showing the cutting tool radius effect

The area of the blockage or shadow formed by one ring is

$$A_{sr} \cong 2\pi r_n s \tag{24}$$

The total shadow is therefore

$$A_s \cong 2\pi s \sum_{1}^{n_{TOT}-1} r_n \tag{25}$$

With $s = \sqrt{2R_T d_{max}}$ and some additional substitution one can determine that

$$A_s = D\pi \sqrt{\frac{2R_T \lambda_0}{(N-1)\, n_{TOT}}} \sum_{1}^{n_{TOT}-1} \sqrt{n} \tag{26}$$

Over the total lens area $\frac{D^2\pi}{4}$, the loss due to this shadowing effect becomes

$$L = \frac{4\,(F/\#)}{F} \sqrt{\frac{2R_T \lambda_0}{(N-1)\, n_{TOT}}} \sum_{1}^{n_{TOT}-1} \sqrt{n} \tag{27}$$

with N being the index of refraction of the lens material.

Example 4:

The ZnSe lens from example 3, with N = 2.433, F = 100 mm, F/# = 1.5, λ_0 = 4 µm, has 16 zones. With a tool radius of 0.030 inch, the transmission loss due to the tool caused shadowing is approximately 4%. This could be reduced to 2% if the tool radius would be decreased to .010 inch. The surface roughness would go up to 286 Å. To maintain the 95 Å surface roughness, the tool feed would have to be slowed down to 0.00017 inch per revolution. This in turn would approximately double the machining time and therefore increase the cost of the lens. Again, these are all considerations to be taken into account at the preliminary project stages.

Judging from all this, it becomes clear that the optical performance limitation of broad band lenses is not so much dependent on the method of manufacturing but on the roll-off effects in the diffraction efficiency at the upper and lower wavelength limits.

6.5. COMMENTS TO USABLE BAND WIDTH

Looking at equation (20) differently provides a better picture of the relationship between the usable band width for a desired efficiency. It also shows clearly the advantage of using diffractive lenses at longer wavelengths.

$$\Delta\lambda \cong \frac{6\lambda_0}{\pi}\sqrt{1-\bar{\varepsilon}_1} \tag{28}$$

One can see that for an average efficiency of 99% the band width in the visible can only be 0.1 µm. For the mid IR this increases to 0.76 µm and broadens to 1.91 µm for the long wavelengths region. This has been already demonstrated in principle in figure 2.

7. THE AIR SPACED ACHROMATIC DOUBLET

A Petzval type lens has been chosen for these predesign considerations for an air spaced doublet. The uniqueness of such a lens simplifies the discussion and provides a good starting point for a well performing IR objective.

The assumptions for this Petzval objective are:[12]

$F_A = 2F$, $F_B = F$, $d = F$. With this, the BFL = F/2. The stop is at the front element which is the hybrid lens. Both lens elements are from the same material. The symbols and relations are identified in figure 12.

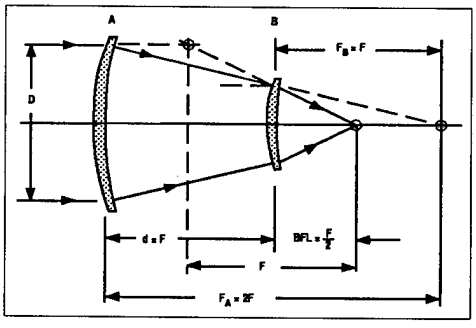

Figure 12. Relations for the basic Petzval objective

Using the same basic approach as for the singlet and applying the general 3rd order expressions for separated thin lenses, the following approximations can be developed.

$$r_1 = \sqrt{\frac{8}{3}\,\lambda_0\,(1 - \nu_R/\nu_D)\,F} \tag{29}$$

and

$$n_{TOT} = \frac{3F}{32\,\lambda_0\,(1 - \nu_R/\nu_D)\,(F/\#)^2} \tag{30}$$

These expressions, simplified for the two spectral windows, are

3 to 5 μm window

First zone radius

$$r_{1\,3\text{-}5} \cong \frac{1}{13.7}\,\sqrt{\nu_R\,F} \tag{31}$$

Total number of zones required

$$n_{TOT\,3\text{-}5} \cong \frac{47\,F}{\nu_R\,(F/\#)^2} \tag{32}$$

8 to 12 μm window

First zone radius

$$r_{1\,8\text{-}12} \cong \frac{1}{9.7}\,\sqrt{\nu_R\,F} \tag{33}$$

Total number of zones required

$$n_{TOT\,8\text{-}12} \cong \frac{23.5\,F}{\nu_R\,(F/\#)^2} \tag{34}$$

Looking at the same materials as before we can summarize for the two regions

Petzval for the 3 to 5 μm region

Material	r_1	n_{TOT}
Silicon	1.1 [$\sqrt{F}$]	0.200 [$F/(F/\#)^2$]
Zinc Selenide	1	0.266
Zinc Sulfide	0.84	0.351
Germanium	0.75	0.448

For Zn Se, F/1.5, F = 100 mm: r_1 = 10 mm and n_{TOT} = 12 zones.

Petzval for the 8 to 12 μm region

Material	r_1	n_{TOT}
Germanium	3 [$\sqrt{F}$]	0.027 [$F/(F/\#)^2$]
Amtir 3	1.1	0.213
Zinc Selenide	0.78	0.407

The remarks made earlier about diffraction efficiency, surface roughness and the shadowing effects remain of course valid for any diamond turned diffractive element in an optical train.

Figure 13 shows such a Petzval objective which replaced a triplet.[5,13] Its focal length is 84 mm and its relative aperture is 1. The elements are made from germanium. It is being used in the 8 to 12 μm band with a staring detector array in the focal plane.

From the table above it can be seen that only 3 zones are required to correct the chromatic aberration. Spherical aberration was eliminated by aspherizing the first surface. The objective has an excellent performance over a total field of view of 8°. The 80% blur spot was calculated to be close to the diffraction limit. The measured one was somewhat larger.

A similar Petzval objective for 3 to 5 μm has been designed and manufactured with silicon elements. It is being tested now. Because Silicon is difficult to diamond turn, another objective with the same focal length of 50 mm has been designed, using ZnSe for the diffractive hybrid front element and a Si lens in the rear. The expected 80% blur spot size is 32 μm over a total flat field of 11.5°. These lenses have been optimized with CODE V and OSLO. The resulting phase profiles obtained with these computer programs confirm the validity of the presented predesign approximations.

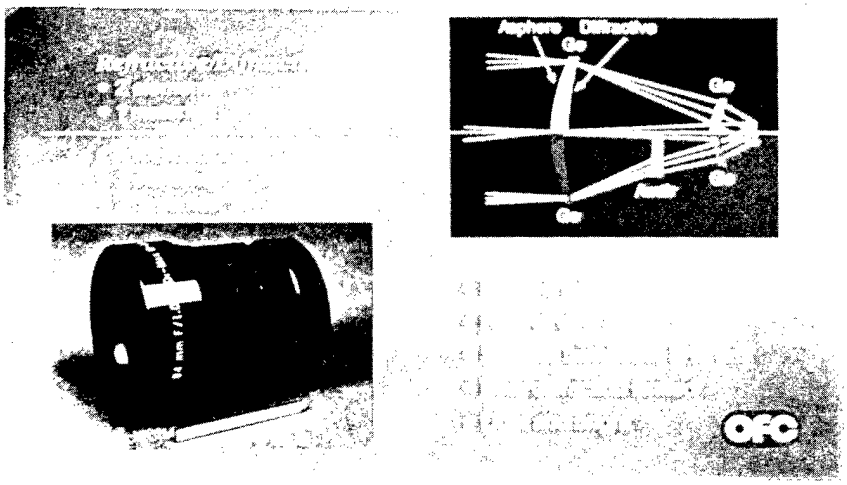

Figure 13. Comparison of a diffractive doublet which replaced a conventional triplet.

8. CONCLUSIONS

From the presented material one can conclude that for reasonable focal lengths the number of diffraction zones required to correct chromatic aberration is relatively small for hybrid lenses applied in the two most common IR windows. This makes it possible and very practical to use the process of diamond turning. Beyond the singlet and the doublet there exists a wide range of opportunities, limited only by ones imagination, for the application of these hybrid components. These diffractive elements are an additional tool for the lens designer. They are of particular value for a system when reduction in weight, cost and size is of interest.

9. ACKNOWLEDGEMENT

We thank the team from the Lincoln Laboratory, Wilfrid Veldkamp, Gary Swanson, and Robert Knowlden, for their continued support and stimulation. We also thank the personnel from Optical Research Associates and Sinclair Optics for their efforts in upgrading and fine tuning their computer programs for HOEs.

10. REFERENCES
(a limited list)

1. Frost & Sullivan, Inc., "Binary Optics, A Technology Impact Report," Summer 1991.
2. G. J. Swanson, "Binary Optics Technology: The Theory and Design of Multilevel Diffractive Optical Elements," Technical Report 854, Lincoln Laboratory 14 August 1989.
3. F. P. Shvartsman, "Dry Photopolymer Embossing: Novel Photoreplication Technology for Surface Relief Holographic Optical Elements," Proc. SPIE Vol.1507, 1991.
4. P. P. Clark and C. Londono, "Production of Kinoforms by Single Point Diamond Machining," Optics News, December 1989.
5. M. J. Riedl and J. T. McCann, "Analysis and Performance Limits of Diamond Turned Diffractive Lenses for the 3-5 and 8-12 Micrometer Regions," SPIE Critical Review, Vol. CR 38, April 1991.
6. M. J. Riedl, "The Single Thin Lens as an Objective for IR Imaging Systems," Electro-optical Systems Design, Nov. 1974.
7. D. Faklis and G. M. Morris, "Optical Design with Diffractive Lenses" Photonics Spectra, Nov. and Dec. 1991.
8. G. J. Swanson, "Binary Optics Technology: Theoretical Limits on the Diffraction Efficiency of Multilevel Diffractive Optical Elements," Technical Report 914, Lincoln Laboratory, 1 March 1991.
9. G. M. Sanger, "The Precision Machining of Optics," in "Applied Optics and Optical Engineering, Volume X," Academic Press, 1987.
10. R. A. Clark, "Design and Specification of Diamond Turned Optics," SPIE Critical Review, Vol. CR 38, April 1991.
11. J. M. Bennett and L. Mattsson," Introduction to Surface Roughness and Scattering," Optical Society of America, Washington D.C. 1989.
12. W. J. Smith, " Modern Optical Engineering, " second edition, page 427, McGraw-Hill 1990
13. T. A. Fritz and J. A. Cox, "Diffractive Optics for Broad Band Infrared Imagers: Design Examples" in Holographic Optics: Optically and Computer Generated, Proc. SPIE Vol. 1052, 1989.
14. D. C. Sinclair, "Designing Diffractive Optics using the Sweatt Model," Sinclair Optics Design notes Vol. 1, No. 1, Winter 1990.
15. I. Cindrich, "Holographic Optics: Design and Applications, Proc. SPIE, Vol. 883, Jan. 1988.
16. G. N. Lawrence, "International Lens Design Conference," Proc. SPIE, Vol. 1354, June 1990.
17. D. A. Buralli and G. M. Morris, "Design of Wide Field Diffractive Landscape Lens," Applied Optics, Vol. 28, No. 18, 15 Sept. 1989.
18. D. A. Buralli, G. M. Morris, and J.R. Rogers, "Optical Performance of Holographic Kinoforms," Applied Optics, Vol. 28, No. 5, 1 March 1989.
19. G. J. Swanson and Veldkamp "Diffractive Optical Elements for use in Infrared Systems," Optical Engineering, Vol. 28, No. 6, 1989.
20. J. Jahns and S. J. Walker, "Two-dimensional Array of Diffractive Microlenses fabricated by Thin Film Deposition" Applied Optics, Vol. 29, No. 7, 1 March.

21. T. Stone and N. George, "Hybrid Diffractive-Refractive Lenses and Achromates," Applied Optics, Vol. 27, No. 14, 1 July 1988.
22. T. J. McHughes and D. A. Zweig, "Recent Advances in Binary Optics" in Holographic Optics: Optically and Computer Generated, Proc. SPIE, Vol. 105, 1989.
23. S. H. Lee, "Recent Advances in Computer Generated Holographic Applications," Optics & Photonic News, July 1990.
24. W. C. Sweatt, "Describing Holographic Optical Elements as Lenses," JOSA 67 (6) 803-808 (1977).
25. W. C. Sweatt, "Mathematical Equivalence between a Holographic Optical Element and an Ultra-high Index Lens," JOSA 69 (3) 486-387 (1979).

OPTICAL SYSTEM STORAGE DESIGN with DIFFRACTIVE OPTICAL ELEMENTS

Raymond K. Kostuk
Electrical and Computer Engineering Dept. and
the Optical Sciences Center
University of Arizona
Tucson, AZ 85721

Charles W. Haggans
3M Data Storage Diskette and Optical Technology Division
1185 Wolters Boulevard
Vadnais Heights, MN 55110-5128

Optical data storage systems are gaining widespread acceptance due to their high areal density and the ability to remove the high capacity hard disk from the system. In magneto-optical read-write systems a small rotation of the polarization state in the return signal from the MO media (~0.5°) is the signal which must be sensed. A typical arrangement used for detecting these signals and correcting for errors in tracking and focusing on the disk is illustrated in Figure 1. Table 1 lists the components required to achieve these functions. The assembly and alignment of this complex system has a direct impact on cost, and also affects the size, weight, and corresponding data access rates. As a result, integrating these optical components and improving packaging techniques is an active area of research and development.

Most designs of binary optic elements have been concerned with optimizing grating efficiency. However, rigorous coupled wave models for vector field diffraction from grating surfaces[1] can be extended to determine the phase and polarization state of the diffracted field, and the design of polarization components. Figure 2 shows a typical grating geometry and the phase (δ) and polarization (α) angles associated with the incident and diffracted fields. A number of grating parameters can be used to modify the polarization

properties and are listed in Table 2.

As indicated, in addition to geometrical factors, the type of interface can also be used to affect the field properties of the diffracted beam. In order to accentuate different polarization effects induced in a beam after interacting with a grating, large angles of incidence (i.e. the angle θ in Figure 2) are required. These angles can be achieved using a beam incident from the substrate of the grating. In addition, fabrication tolerances can be improved if the grating operates on the zero order rather than a higher diffraction order. The grating then serves as a controlled birefringence surface rather than a diffraction grating. This concept is illustrated in Figure 3. At the grating surface a higher effective index exists parallel to the grooves relative to the orthogonal direction. Several aspects of these components were verified experimentally using high spatial frequency lamellar type gratings formed holographically in photoresist. Figure 4 shows a comparison between theory and experiment for the phase (δ) and polarization angle (α) as a function of azimuth angle (Φ). As indicated the comparison is quite good for the dielectric interface case, indicating the utility of coupled wave theory for design.

In the current stage of our work we are examining system configurations which cascade several polarization functions on a single substrate (Figure 5). In this design the beam returning from the MO disk illuminates a cascaded grating element which first couples light into the substrate, then introduces a quarter wave retardation, then a polarization rotation, and finally separates s- and p- polarized fields through a polarization beam splitter. The input coupler and polarization beam splitter are formed in volume gratings, and the two intermediate elements are zero-order elements[2].

Reference

1. Moharam, M. G. and Gaylord, T. K. J. Opt. Soc. Am. 73, 1105-1112 (1983).

2. Haggans, C.W.,``Polarization Properties of Zeroth Order Surface-Relief Gratings with Application to Optical Storage Heads," PhD Thesis, Univ. Ariz., 1992.

FIGURE 1 CONVENTIONAL M-O HEAD

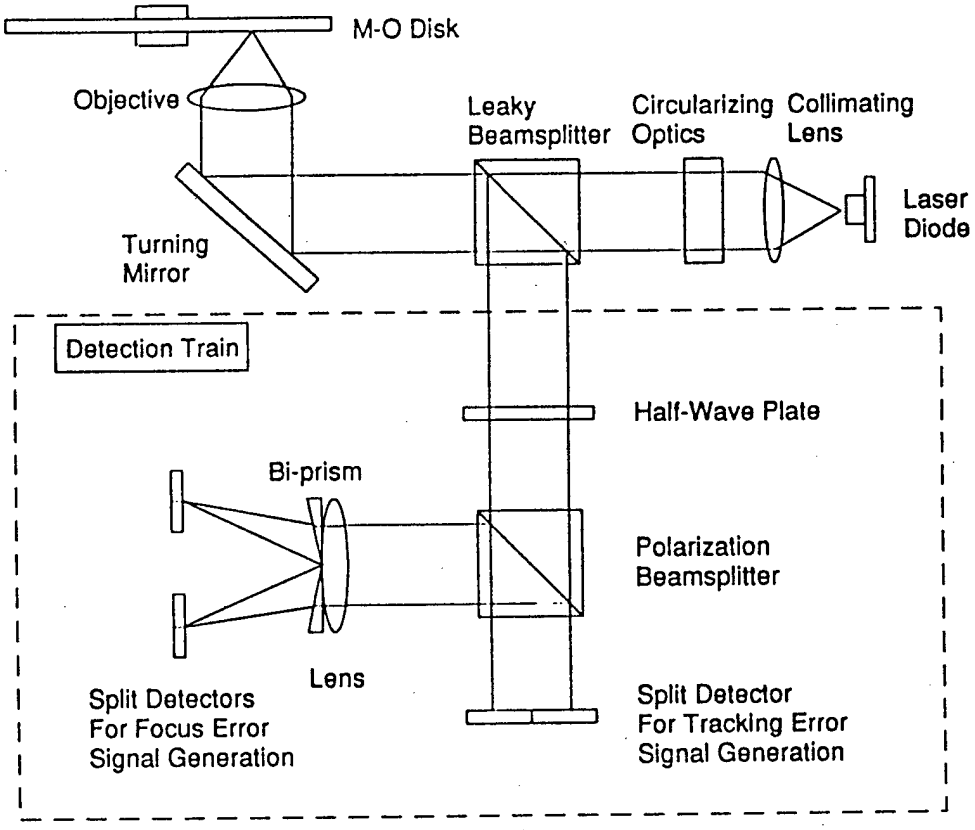

FIGURE 2 GRATING GEOMETRY

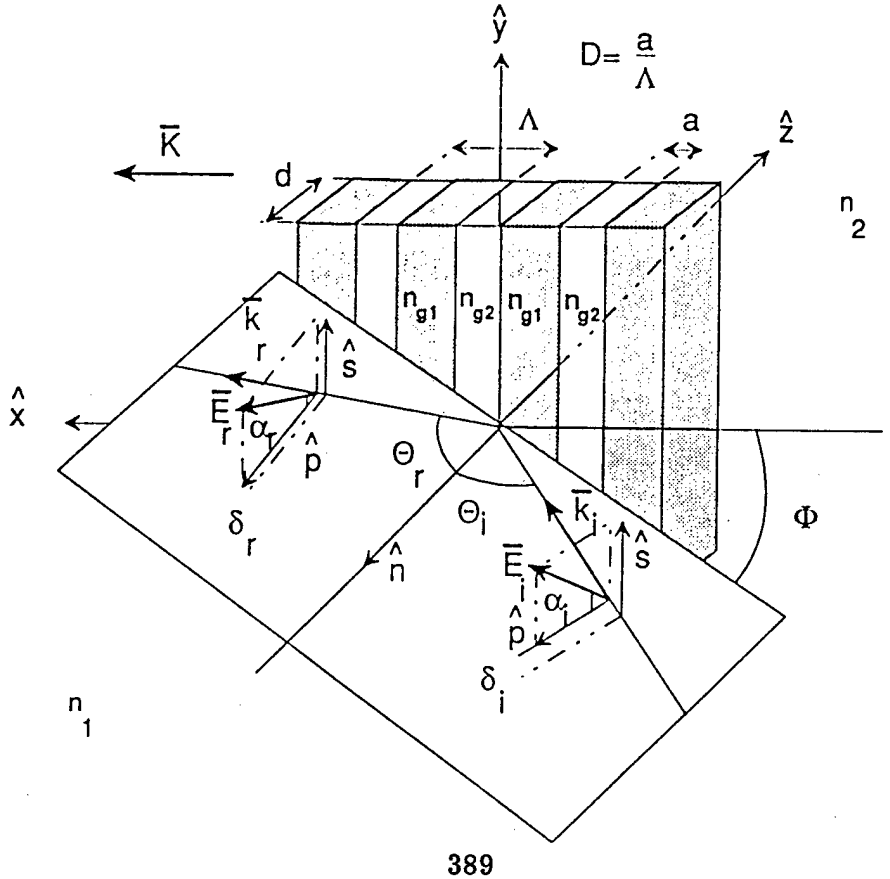

FIGURE 3 ENGINEERED FORM BIREFRINGENCE

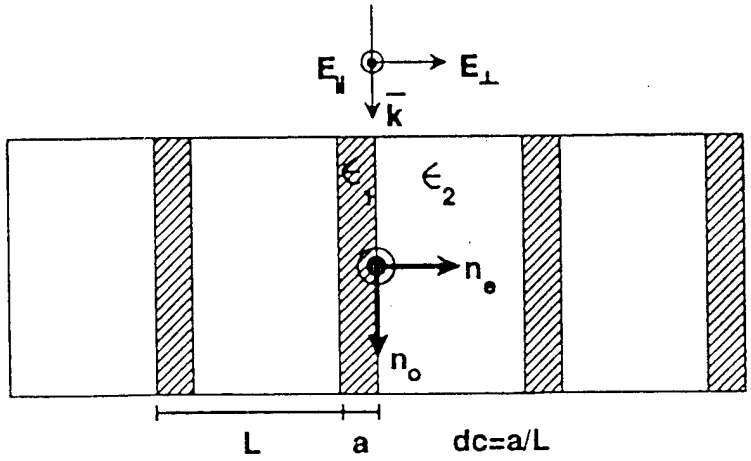

$$\epsilon_{\perp} = \frac{D}{E_{avg}} = \frac{\epsilon_1 \epsilon_2}{dc\epsilon_2 + (1-dc)\epsilon_1} = n_e^2$$

$$\epsilon_{\parallel} = \frac{D_{avg}}{E} = dc\epsilon_1 + (1-dc)\epsilon_2 = n_o^2$$

FIGURE 4 MODEL - EXPERIMENT COMPARISONS of GRATING POLARIZATION PROPERTIES

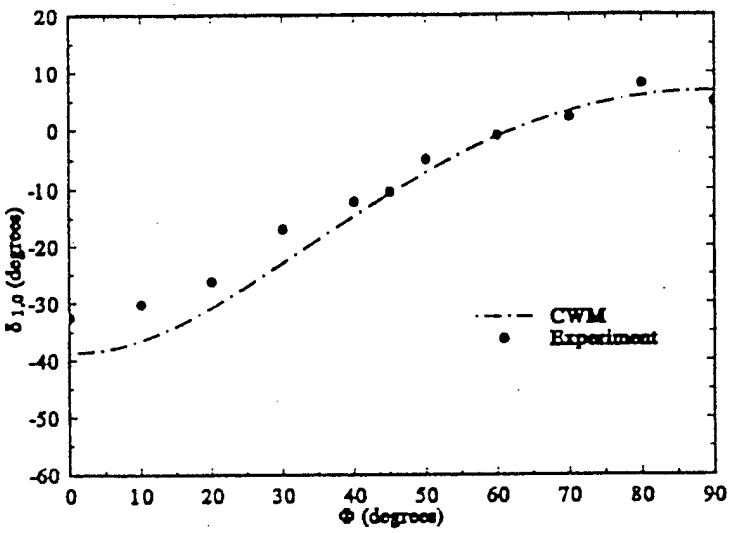

s-p phase difference versus the azimuthal angle of incidence for the zeroth order reflected from the grating of Fig. 5-11. CWM results are for L=1 and N=35.

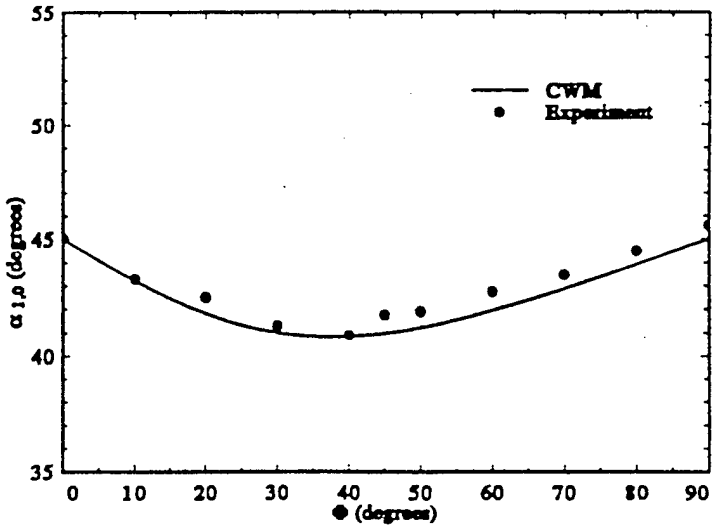

Amplitude ratio angle versus azimuthal angle of incidence for the zeroth order reflected from the grating of Fig. 5-11. CWM results are for L=1 and N=35.

PROPOSED M-O HEAD

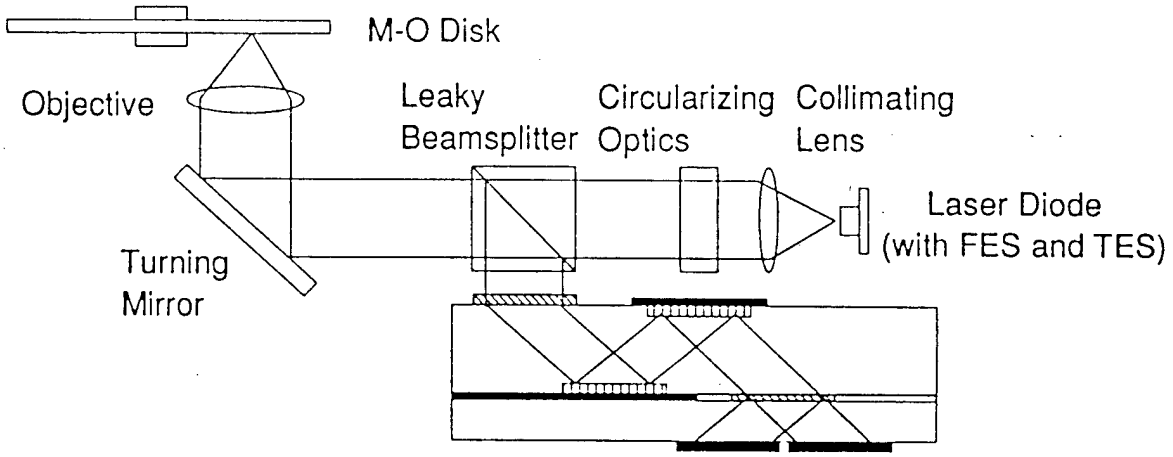

FIGURE 5. Proposed head for using diffractive elements for polarization sensing. The beam returning from the disk is coupled into a substrate, then a quarter wave retarder, a polarization rotator, and a polarization beam splitter before leaving the substrate.

TABLE 1

COMPONENTS REQUIRED for OPTICAL STORAGE SYSTEMS

* HIGH NA OBJECTIVE - PICK UP ELEMENT
* CYLINDRICAL LENSES - QUADRANT DETECTION METHODS
* POLARIZATION COMPONENTS
  - $\lambda/4$ RETARDERS
  - $\lambda/2$ RETARDERS
* POLARIZATION SELECTIVE/NON SELECTIVE BEAM SPLITTERS
* PARTIALLY POLARIZING BEAM SPLITTERS
* BEAM TURNING MIRROR
* CIRCULARIZING PRISM
* ANTI REFLECTION COATINGS
* COST/MANUFACTURING CONSTRAINTS

TABLE 2

GRATING DESIGN PARAMETERS

- CONTROLLABLE INPUT VARIABLES
  - * GRATING DEPTH - d
  - * GRATING PERIOD - Λ
  - * DUTY CYCLE - D
  - * OPERATING WAVELENGTH - λ
  - * AZIMUTH ANGLE - Φ
  - * GRATING INTERFACE - DIELECTRIC/DIELECTRIC; DIELECTRIC/METAL; METAL/DIELECTRIC

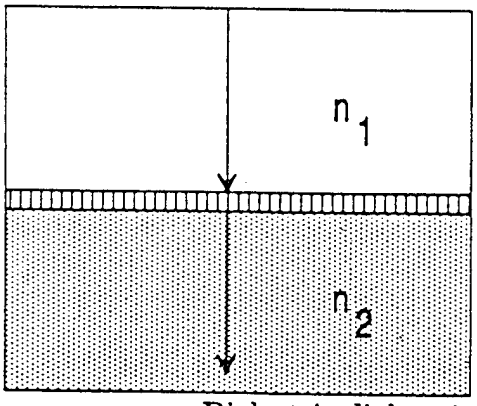

Dielectric-dielectric grating ($n_1<n_2$).

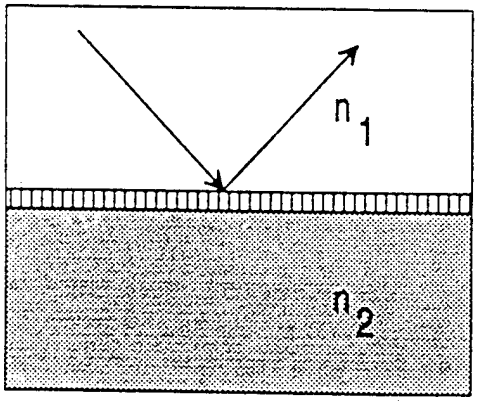

Dielectric-metallic grating.

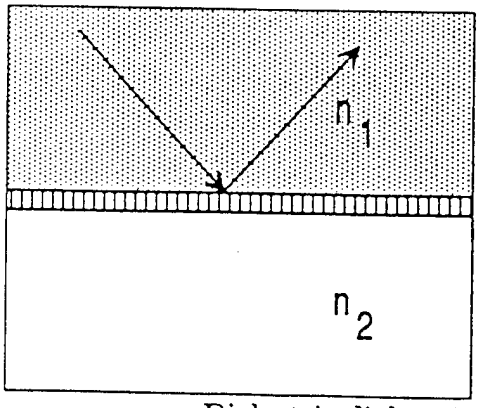

Dielectric-dielectric grating ($n_1>n_2$ and $\Theta>\Theta_c$).

THEORY OF DISPERSIVE MICROLENSES

B. Herman and G. Gal
Lockheed Palo Alto Research Laboratory
3251 Hanover Street, Palo Alto, CA 94304

ABSTRACT

A dispersive microlens is a miniature optical element which simultaneously focuses and disperses light. Arrays of dispersive microlenses have potential applications in multicolor focal planes. They have a 100 percent optical fill factor and can focus light down to detectors of diffraction spot size, freeing up areas on the focal plane for on-chip analog signal processing. Use of dispersive microlenses allows inband color separation within a pixel and perfect scene registration. A dual-color separation has the potential for temperature discrimination. We discuss the design of dispersive microlenses and present sample results for efficient designs.

1.0 INTRODUCTION

For many applications it is desirable to determine the spectral characteristics of a light source. In certain applications it is necessary to do this over very small physical areas, for which miniature optical elements are required. The technology for manufacturing such devices has been available for a long time.[1] Our interest is in describing a miniature optical element that simultaneously disperses and focuses light. We refer to such a device as a dispersive microlens.

Arrays of dispersive microlenses have potential applications in multicolor focal planes. They have a 100% optical fill factor and can focus light down to detectors of diffraction spot size, freeing up area on a focal plane for on-chip analog signal processing. Use of dispersive microlenses allows inband color separation within a pixel and perfect scene registration. A dual-color separation has the potential for use as a temperature discriminator.

We begin with our concept of the dispersive microlens and then give an analysis of its performance. This is followed by discussions of variations of the basic concept (Fresnel, multilevel analog, and multilevel Fresnel elements). We conclude with some examples of efficient designs.

---

1. d'Auaria, L., J. P. Huignard, A. M. Roy, and E. Spitz "Photolithographic Fabrication of Thin Film Lenses," *Opt. Commun.*, Vol. 5, 1972, pp. 232-235.

2.0 DISPERSIVE MICROLENS CONCEPT

Dispersion of light can be caused either by material dispersion, where the material index of refraction is strongly wavelength dependent, or by coherent interference of light passing through (or reflecting from) a diffractive structure. The latter type of dispersion is seen in the familiar diffraction grating and is the type that we are interested in. For dispersive analysis, light is typically passed through (or reflected from) a diffraction grating and then focused by a lens. If an amplitude grating is used, half of the incident light energy does not get through the grating and leads to an inefficient setup. It is therefore desirable to use a phase grating to allow most of the incident light to be focused. Our objective is to combine the dispersion and focusing into a single optical element.[2]

The efficiency of a diffraction grating depends upon its periodic structure. It is theoretically possible to obtain 100% efficiency (at a chosen wavelength) by using a periodic blazed structure. We therefore desire to construct an element which consists of a blazed diffraction grating combined with a focusing element. This concept is illustrated in Figure 1.

In our analysis we will derive the diffraction pattern due to a dispersive microlens and discuss how the different parameters affect the performance of the element.

3.0 ANALYSIS OF THE DISPERSIVE MICROLENS

For ease of exposition, we will assume the element to be illuminated by a normally incident plane wave. The analysis given below can be generalized to non-normal incidence or to light covering the full field of view of the lens. The analysis we give here can be applied to dispersive microlenses that are part of a telecentric system.

We will take the element to be optically thin so that the phase change of the plane wave travelling though it is proportional to the thickness of the element. The element sits upon a substrate (possibly air) through which the focusing and dispersion take place. We assume a scalar description of the field to be accurate enough for our purposes and employ the Fresnel approximation to the Rayleigh-Sommerfeld diffraction integral. This gives

$$E(x,y,z) = \frac{n'}{i\lambda z}\int_{-\infty}^{\infty} dx' \int_{-\infty}^{\infty} dy' \exp\left\{\frac{i\pi n'}{\lambda z}\left[(x-x')^2 + (y-y')^2\right]\right\} E(x',y',0) \qquad (1)$$

where E(x,y,z) is the electric field at point (x, y, z). The field propagates in the z direction with the origin of the coordinate system lying on the substrate surface. The radiation has wavelength λ and the substrate has index of refraction n'.

For the choice of a rectangular dispersive microlens of size w_x by w_y, the evaluation of Eq. (1) at the focal plane of the lens yields

2. Gal, G., "Dispersive Microlens," under patent application, 1992.

$$E(x,y,f) = \frac{n'Gw_y}{i\lambda f} E_0 \exp\left[\frac{i\pi n'}{\lambda f}(x^2 + y^2)\right] \exp\left[\frac{i\pi}{\lambda}\left((n-1)D - \frac{n'xG}{f}\right)\right]$$

$$\frac{\sin\left[\frac{\pi n'Gx}{\lambda f}N\right]}{\sin\left[\frac{\pi n'Gx}{\lambda f}\right]} \operatorname{sinc}\left[\frac{1}{\lambda}\left((n-1)D - \frac{n'xG}{f}\right)\right] \operatorname{sinc}\left[\frac{w_y n'y}{\lambda f}\right] \tag{2}$$

Here, n is the refractive index of the element, f is the focal length of the lens, D is the modulation depth of the grating, G is the grating period, $N = w_x/G$ is the number of grating periods across the element, and the sinc function is defined by $\operatorname{sinc}(u) = \sin(\pi u)/(\pi u)$. The incident plane wave is taken to have an amplitude E_0.

The result Eq. (2) is essentially the Fraunhofer diffraction pattern of a blazed grating. The only difference is that we have replaced the usual frequency variables of Fourier space with explicit parameters involving the element and the radiation. It is important to do this since we will be interested in the element performance at different wavelengths and the wavelength is not a separate parameter in Fourier space.

Because of the nature of the result, we can use our knowledge of blazed gratings to interpret the diffraction pattern. The ratio of sine functions (due to interference effects from the grating) describes the size and position of the grating orders. Diffraction orders appear in the focal plane at positions where the argument of the sine function in the denominator is an integral multiple of π, i.e., at

$$x_j = \frac{\lambda f}{n'G} j$$

The product of sinc functions is the Fraunhofer diffraction pattern of a slit of dimensions G by w_y, displaced in the focal plane because of the tilt of the blaze. The full diffraction pattern is proportional to the product of these two components, as shown in Figure 2.

The most efficient results for the dispersive microlens are obtained when the peak of the sinc functions is centered at a diffraction order. For a given material, this position is controlled by the radiation wavelength and the modulation depth of the grating. If we want the peak to fall at the m^{th} order, then we must have $D = m\lambda/(n-1)$. For the special case of the first diffraction order ($m = 1$), this defines a wavelength $\lambda_b = (n-1)D$, which is called the blaze wavelength.

We now need to calculate efficiencies and dispersion to quantify the performance of the element. The efficiency of the j^{th} order is the energy in the j^{th} order divided by the incident energy on the element:

$$\eta_j = \frac{\int_{j^{th}\text{order}} |E(x',y',f)|^2 dx'dy'}{\int_{\text{aperture}} |E(x',y',0)|^2 dx'dy'} \tag{3}$$

For the case where there are a large number of periods across the element, this expression can be evaluated to give

$$\eta_j = \mathrm{sinc}^2(\lambda_b/\lambda - j),\ N >> 1$$

Note that the maximum efficiency is obtained when $\lambda = \lambda_b/m$ and $j = m$, as expected. This maximum can be obtained only for a single selected wavelength. Since we are interested in a band of wavelengths, we cannot achieve unit efficiency for all wavelengths in the band. This equation tells us the wavelength spread, $\Delta\lambda/\lambda$, for which we can achieve a desired efficiency.

Perhaps a more useful performance measurement is the fraction of energy that gets into the main spot in the diffraction order. (This is important, for example, for determining the amount of energy falling on a detector placed under the element.) This is given by Eq. (3) except that the upper integral is evaluated over the main diffraction spot:

$$\theta_j = \frac{\int_{j^{th}\text{diffraction spot}} |E(x', y', f)|^2 dx'dy'}{\int_{\text{aperture}} |E(x', y', 0)|^2 dx'dy'} \tag{4}$$

Again, for a large number of grating periods, this can be evaluated to give

$$\theta_j = 0.903\left\{\frac{2}{N}\left[1 + 2\sum_{k=1}^{N-1}\mathrm{sinc}\left(\frac{2k}{N}\right)\right]\right\}\mathrm{sinc}^2[\lambda_b/\lambda - j],\ N >> 1$$

In the limit $N \to \infty$, the factor in braces evaluates to 0.903 so that a maximum of 81.5% of the incident energy can be focused into the main diffraction spot.

We now examine the dispersion properties. Let us look at two wavelengths, λ_0 and λ_1, in the j^{th} order. We have $x_j^{(\lambda_0)} = \lambda_0 fj/n'G$ and $x_j^{(\lambda_1)} = \lambda_1 fj/n'G$. Thus the wavelength separation in a particular order is given by

$$x_j^{(\lambda_1)} - x_j^{(\lambda_0)} = \frac{(\lambda_1 - \lambda_0)f}{n'G}j$$

Consequently, higher orders give increased dispersion.

Since the wavelength separation increases with order, eventually the orders for different wavelengths will overlap. This will first occur in adjacent orders. We can avoid overlap of orders by requiring $x_{j-1}^{(\lambda_{max})} + \lambda_{max} f/n'w_x < x_j^{(\lambda_{min})} - \lambda_{min} f/n'w_x$, which reduces to

$$j < \frac{\lambda_{max}}{\lambda_{max} - \lambda_{min}}\frac{\lambda_{max} + \lambda_{min}}{\lambda_{max} - \lambda_{min}}\frac{G}{w_x} \tag{5}$$

3063_BHCK

Thus, we can get the maximum wavelength separation without spectral overlap of orders if we choose the the optimal value of j from Eq. (5). The characteristics of the diffraction patterns which depend on the order are shown in Figure 3. Spectral overlap is clearly seen as the order number increases.

4.0 DISPERSIVE MICROLENS DESIGN OPTIONS

So far, we have not addressed issues related to the fabrication of micro-optical elements. Although we have consistently referred to a dispersive *micro*lens, there is, in fact, nothing in the theory that specifically addresses the size of the element (except, of course, the assumption of the validity of scalar wave theory). When one tries to fabricate miniature optical elements, a number of obstacles appear.[3] We treat two of them here: the element thickness, which we address through the Fresnel element, and the surface smoothness, which we address through the multilevel analog element and the multilevel Fresnel element.

4.1 THE FRESNEL ELEMENT

A common methodology for fabricating micro-optical elements is through photolithographic techniques. The surface structure of the desired element is etched into a substrate to produce the desired result. Fast lenses or elements with deep surface reliefs present fabrication problems because of their large etching depth. One way to sidestep this problem is to convert the element into a Fresnel element whose maximum thickness corresponds to a 2π phase change at a given wavelength. This results in an element that has an overall thickness which is less than the type we have been discussing so far (the "analog" element). There is a tradeoff with using such a type of element, however. The 2π phase change can occur exactly only for a specific wavelength. Thus the element must be designed for a specific wavelength while all other wavelengths will suffer some degree of chromatic aberration. For the blazed grating, this wavelength is best taken to be an integral multiple of the blaze wavelength. We call this wavelength the design wavelength and denote it by $\bar{\lambda}$. An example of the Fresnel element is shown in Figure 4.

In a first approximation, the Fresnel element introduces a focusing phase error (chromatic aberration) given by

$$\frac{\pi n'}{f} x^2 \left(\frac{1}{\lambda} - \frac{1}{\bar{\lambda}} \right)$$

with a maximum error of

$$\frac{n'}{8f} w^2 \left(\frac{1}{\lambda} - \frac{1}{\bar{\lambda}} \right)$$

waves, where w is the larger of w_x and w_y.

---

3. Anderson, W. et al., "Fabrication of Micro-Optical Devices," Conference on Binary Optics, Huntsville, AL, Feb 1993.

A more detailed and quantitative measure of the performance of Fresnel dispersive microlenses can be obtained by introducing a figure of merit that is the ratio of the energies reaching the main diffraction spot from the Fresnel and non-Fresnel elements. In other words, we define

$$r_m^{Fresnel} = \frac{\theta_m^{Fresnel}}{\theta_m^{analog}}$$

where the element is designed to send light mainly to the m^{th} order and the different θs refer to Eq. (4) evaluated for the different elements. Although other figures of merit are possible (e.g., a "chromatic" Strehl ratio), we choose this one since it provides a measure of the dispersive properties of the element along with how well the dispersed light is focused down to the theoretical spot size.

For a square element it can be shown that $r_m^{Fresnel}$ depends on the following set of parameters: the order, m, the number of grating periods across the dispersive microlens, N, the ratio of the blaze and design wavelengths, $\lambda_b / \bar{\lambda}$, the ratio of the radiation and design wavelengths, $\lambda / \bar{\lambda}$, and a parameter which we identify as a Fresnel number, $\mathcal{F} = n'w^2/\lambda f$. For the most common case of first-order diffraction where the blaze and design wavelengths are the same, this reduces to a set of only three parameters.

For most applications, only a few periods across the dispersive microlens are needed to give the desired dispersion; five is a typical number. In Figure 5 we plot $r_m^{Fresnel}$ for dispersive microlenses with five grating periods in the case of first-order diffraction and $\lambda_b = \bar{\lambda}$. Note that the Fresnel dispersive microlens performs well only about a very narrow band about the design wavelength. This band gets smaller as the Fresnel number increases.

Similar plots for cases with up to nine grating periods show almost identical results. For cases of practical interest, then, we can ignore the effect of the number of grating periods and the results can be parameterized by using only the wavelength ratio and the Fresnel number.

Although not shown in Figure 5, it should also be noted that as the wavelength ratio approaches 1/2, the figure of merit begins to increase. This is because the Fresnel element operates efficiently at all the harmonics of the design wavelength, as does the dispersive microlens. The dispersive microlens is not used over a very large band, however, since the efficiencies decrease as the band gets large. Therefore, the behavior exhibited at the harmonics is usually out of the range of a given element design.

Although it may seem that the region of useful operation would be too small to be practical because of its narrowness, we can easily find cases where the Fresnel dispersive microlens is practicable. For example, an f/5, 100-μm square element operating in the infrared in silicon with a design wavelength of 10 μm has a Fresnel number ranging from 8.5 to 5.7 over a wavelength band from 8 to 12 μm. In this band, the figure of merit is at least 80%.

4.2 FABRICATION ISSUES

If the element is fabricated using standard photolithographic techniques, the surface relief of the element is approximated by etching a multilevel structure onto a substrate. The type of elements produced in this way have acquired the name binary optical elements. The etching of the

material is performed using a series of masks, each with an associated etching depth. The maximum number of levels that can be etched using k masks is 2^k. The multilevel approximation changes the performance of the element. Both analog and Fresnel elements can be fabricated with multilevel approximations.

4.2.1 The Multilevel Analog Element

We will assume the multilevel approximation to the analog element to have 2^k levels. The number of levels determines the smoothness to which the depth of the element can be approximated. In Figure 6 we show the approximations to the element for two through eight levels.

We can get an estimate of the effect of the multistep structure on the diffraction pattern by using a multistep approximation to the grating (although not the focusing) part of the element. If we take 2^k levels and 2^k steps across a grating period, then a straightforward calculation shows that the diffraction pattern is given by Eq. (2) with the amplitude of the x-dependent sinc function modified by[4]

$$\frac{\sin[\pi(\lambda_b/\lambda + j)]}{2^k \sin\left[\frac{\pi}{2^k}(\lambda_b/\lambda + j)\right]} \operatorname{sinc}\left(\frac{j}{2^k}\right) \tag{6}$$

and a slight modification of the overall phase factor. If we optimize the grating for wavelength λ, Eq. (6) reduces to $\operatorname{sinc}(j/2^k)$. The efficiencies and spot energies are affected in a similar manner.

Again, a more quantitative measure of performance can be constructed as was the case with the Fresnel element. We take the same figure of merit defined for the multilevel element:

$$r_m^{ML} = \frac{\theta_m^{ML}}{\theta_m^{analog}}$$

This figure of merit is parameterized in the same way as $r_m^{Fresnel}$ with the addition of another parameter, the number of levels, 2^k. In most cases of practical interest, three binary masks are used in the fabrication process. We present in Figure 7 a plot of r_m^{ML} for the same case as in Figure 5 with the additional parameter of $k = 3$ masks (8 levels).

This figure shows that the performance of the multilevel element is good at small Fresnel numbers but drops off rapidly at the Fresnel number increases. This behavior is expected because, in general, as the Fresnel number increases, either (a) the lens becomes faster so the stepped structure does not approximate the increased curvature of the surface as well, or (b) the wavelength gets smaller so the stepped structure looks less and less like a focusing element to the radiation.

If the same plot is made with an increasing number of levels, the same general result is found except that the fall-off behavior becomes more gradual and the oscillatory nature seen becomes shallower. For an infinite number of levels, one expects that there is no fall off and the oscillations disappear.

---

4. Dammann, H., "Spectral Characteristic of Stepped-Phase Gratings," *Optik*, Vol. 53, 1979, pp. 409-417.

4.2.2 The Multilevel Fresnel Element

The final type of element is that which combines the Fresnel element with the multilevel approximation.[5] Because the Fresnel element is usually much thinner than its corresponding analog element, it is better approximated by a smaller number of levels than is the analog element. This means that in the case where a Fresnel element can be used, it is a better choice for fabrication since it will require fewer masks in the photolithographic process.

We can again define a figure of merit based upon the ratio of spot energies for the Fresnel and analog elements:

$$\Gamma_m^{\text{ML Fresnel}} = \frac{\theta_m^{\text{ML Fresnel}}}{\theta_m^{\text{analog}}}$$

A plot of the figure of merit for the case of five grating periods and eight levels is shown in Figure 8. Note that this figure is very similar to Figure 5, except that the amplitude is smaller. The peak value at $\lambda = \bar{\lambda}$ is 0.95 = $\text{sinc}^2(1/8)$, as might be expected from Eq. (6).

5.0 SAMPLE DESIGNS

To show more concrete examples of the performance of the dispersive microlens, we now present two sample designs, one operating in the infrared and one operating in the visible. We will examine how the elements perform under the different design options.

We first take the example mentioned at the end of section 4.1: an f/5, 100-μm square element operating in silicon over the wavelength band 8 μm $< \lambda <$ 12 μm. In this band, silicon has a near-constant index of refraction with a value $n' = 3.4$. We will take first-order diffraction and let $\lambda_b = \bar{\lambda} = 10$ μm. We will take four grating periods across the element, so G = 25 μm. Although the period is not much larger than twice the largest wavelength in the band (thus making the assumption of the validity of scalar theory debatable), it will be sufficient for our purposes. (We are currently investigating the effects of the vector nature of the electromagnetic field on this type of element, although we will not address that here.)

In Figure 9 we see a cross-cut through the center of the diffraction pattern at the element focus for three wavelengths: 8 μm, 10 μm, and 12 μm. These three wavelengths are distinguished by different shades of gray. The different element types are distinguished by different line patterns.

There are several things to note in this figure. First, the analog and Fresnel element operate identically at the design wavelength, as expected. The multilevel element gives the worst performance among all the element types. This is because the approximation to the analog surface by only eight levels is still somewhat coarse. The Fresnel element operates very well at all wavelengths, mostly due to the relatively small Fresnel numbers ($5.7 < \mathcal{F} < 8.5$). Finally, the multilevel Fresnel element gives nearly as good performance as the Fresnel element. If the peak values of the multilevel Fresnel to the Fresnel values are compared, we find the ratios to be 0.95 at all the wavelengths, showing that using only three binary masks gives excellent performance for this design.

---

5. Swanson, G. J., "Binary Optics Technology: Theory and Design of Multilevel Diffractive Optical Elements," *Lincoln Lab. Tech. Rep. 854*, Aug 1989.

We next consider the case of a dispersive microlens operating in the visible region, 0.4 μm $< \lambda <$ 0.7 μm. We take an f/10, 50-μm-square element, this time fabricated in a glass with $n' = 1.5$. The design and blaze wavelengths are taken as $\lambda_b = \bar{\lambda} = 0.55$ μm. This gives a Fresnel number range of 18.8 at 0.4 μm to 10.7 at 12 μm. For increased dispersion, we now take $N = 5$ periods across the element. The results for this element are shown in Figure 10.

Because of the higher dispersion, we now see some spillover into the second order at 0.4 μm. The effect of this can be ameliorated either by a proper placement of detectors under the element or by reducing the wavelength band.

The analog and Fresnel elements again operate identically at the design wavelength; however, the performance at the edges of the band is very poor for the Fresnel element. The performance is worse at 0.4 μm because of the higher Fresnel number. This result shows that, even with a slow lens (f/10), performance of the Fresnel element will be unacceptable if the wavelength is too small and the waveband too wide. To use dispersive microlenses in the visible, therefore, it will be necessary to use analog elements.

We have not displayed the results for multilevel elements in Figure 10 because current photolithographic technology does not allow fabrication at the very small feature sizes required by the masks for these elements. The visible dispersive microlenses will therefore need to be fabricated using an analog technology (e.g., grayscale photolithography[3]).

6.0 SUMMARY

We have presented an analytic theory for describing a micro-optical element which will simultaneously focus and disperse light, the dispersive microlens. Our theory describes how the diffraction pattern from the dispersive microlens is built up and the important parameters needed to quantify the results. The theory can be used to develop efficient designs for a given application.

There are four distinct design options available for the dispersive microlens (and, indeed, for any micro-optical element). These are the analog, multilevel analog, Fresnel, and multilevel Fresnel options. We have defined figures of merit for each of these options which can be used to determine when one type of design is acceptable as a replacement for another type of design. This is useful when fabrication issues become important. Our analysis has shown that Fresnel elements are only useful over a small waveband, except at very low Fresnel numbers. For the common case of eight levels used in photolithographic fabrication, multilevel elements are only useful for very small Fresnel numbers. We have been able to quantify how their performance improves as the number of masks used in the fabrication process increases. For cases where Fresnel elements can be used, the corresponding eight-level Fresnel element gives acceptable results.

In our analysis we have assumed a rectangular element. Other topologies, such as circular or hexagonal elements are possible. The analytical analysis of these elements is more difficult, although the principle remains the same.

For a discussion of the use of dispersive microlenses in systems applications of current interest, the reader is referred to Reference 6.

---

6. Gal, G. et al., "Micro-Optics Technology and Sensor Systems Applications," Conference on Binary Optics, Huntsville, AL, Feb 1993.

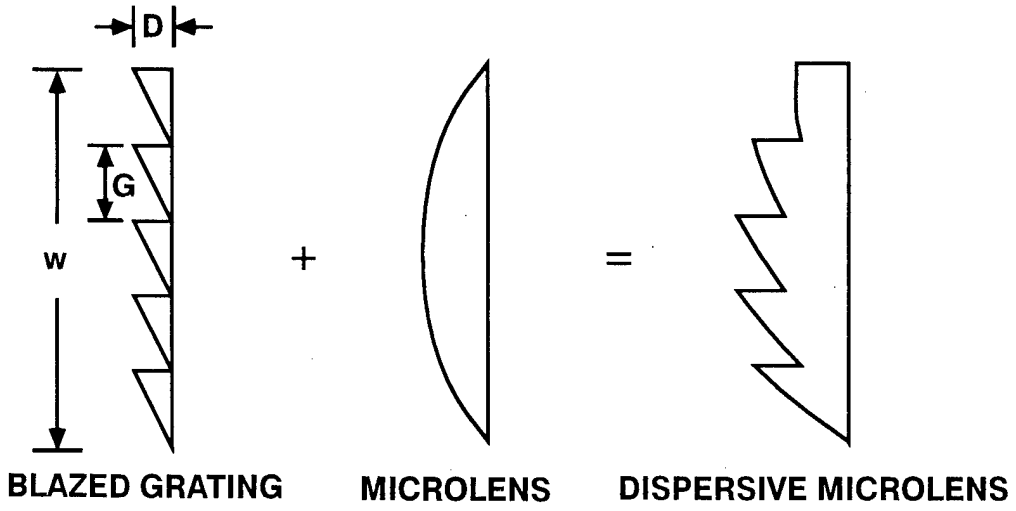

FIGURE 1. DISPERSIVE MICROLENS CONCEPT. The dispersive element is a combination of a blazed grating and a microlens. The grating has a width w, period G, and a modulation depth D.

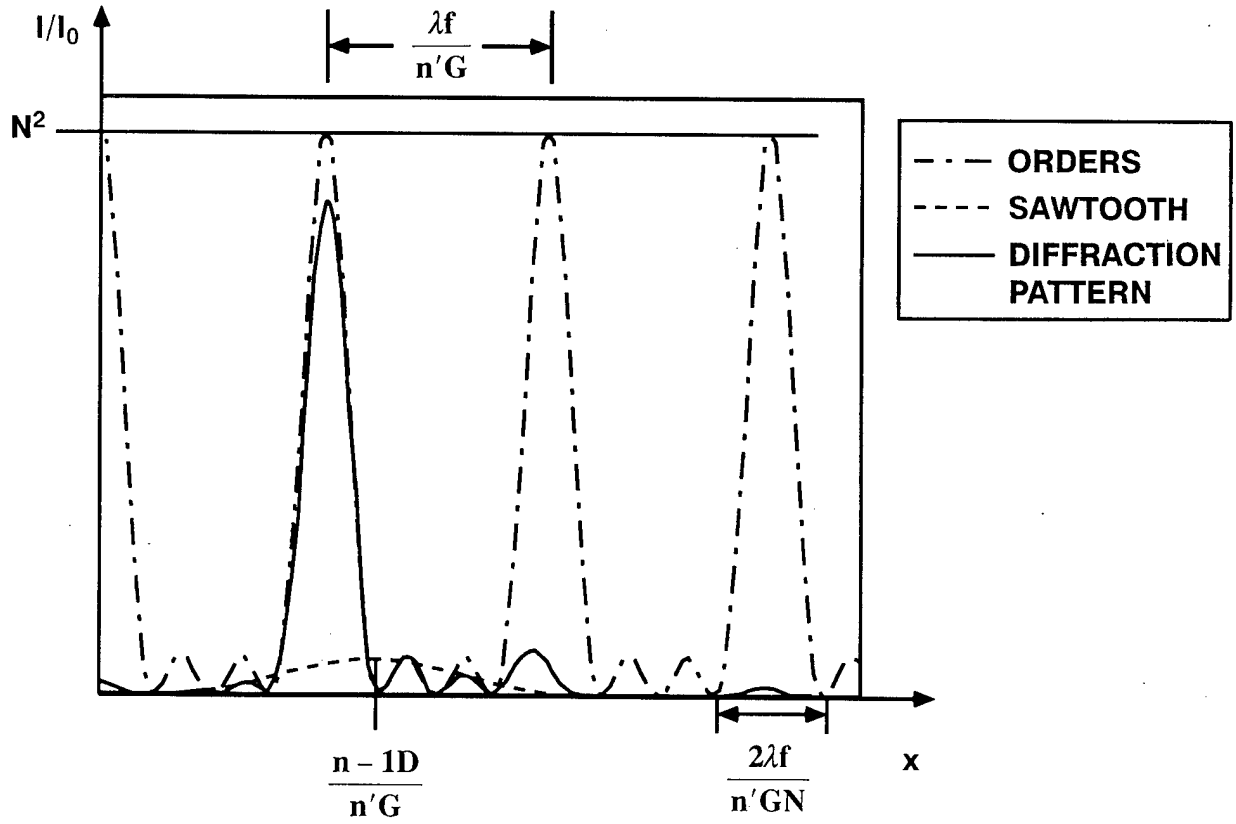

FIGURE 2. DIFFRACTION PATTERN (IN THE *x* DIRECTION) OF THE DISPERSIVE MICROLENS IN THE FOCAL PLANE. The full diffraction pattern is the product of the diffraction patterns due to the periodic structure of the grating and a single sawtooth of the grating. The normalized intensity $I/I_0 = |E/E_0|^2$ is shown.

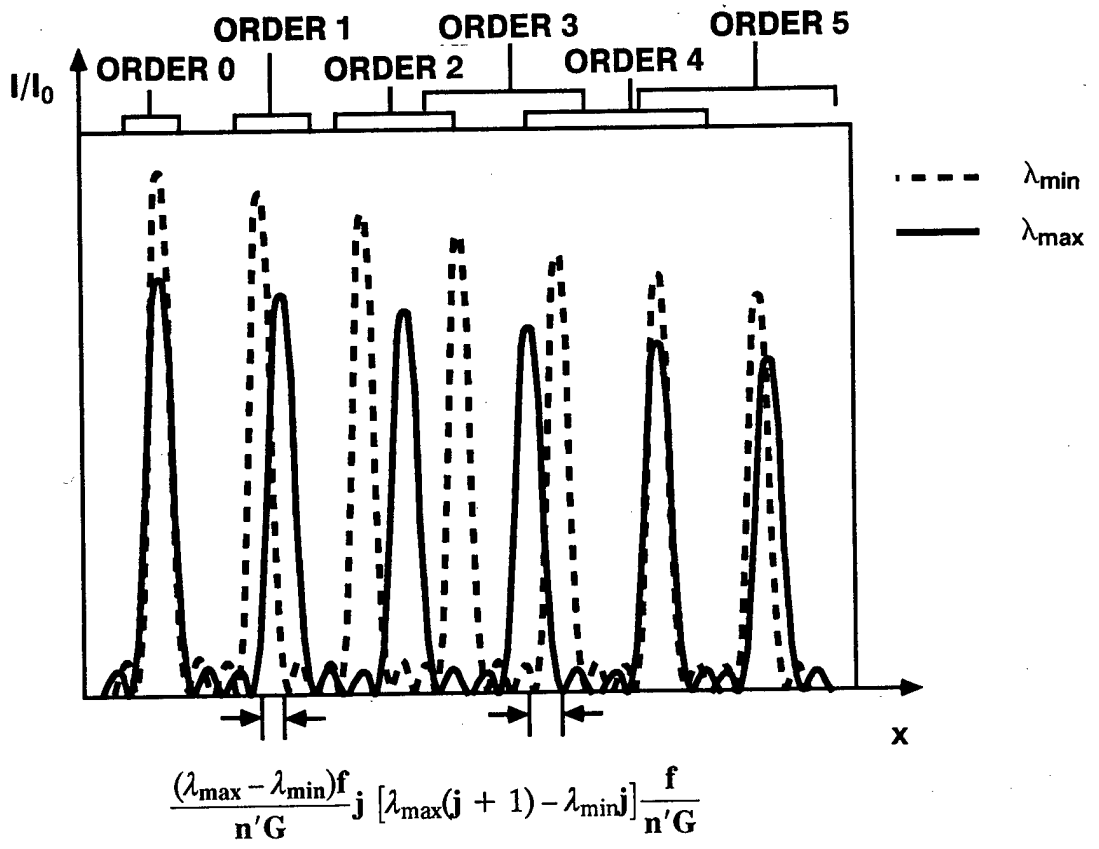

FIGURE 3. DIFFRACTION PATTERN (IN THE x-DIRECTION) OF THE DISPERSIVE MICROLENS IN THE FOCAL PLANE FOR MULTIPLE WAVELENGTHS. Dispersion of wavelengths is shown..

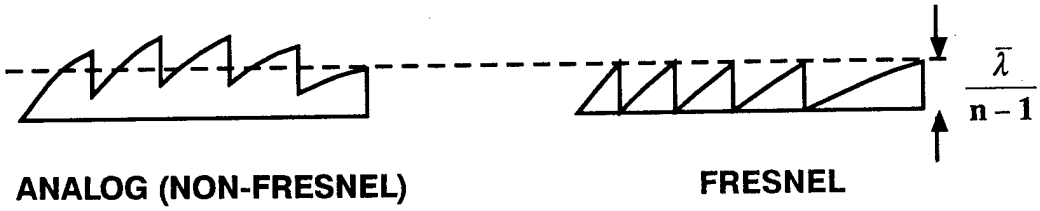

FIGURE 4. AN ANALOG (NON-FRESNEL) ELEMENT AND ITS CORRESPONDING FRESNEL COUNTERPART. The Fresnel element has a maximum thickness of $\bar{\lambda}/(n-1)$ which introduces a 2π phase change at wavelength $\bar{\lambda}$.

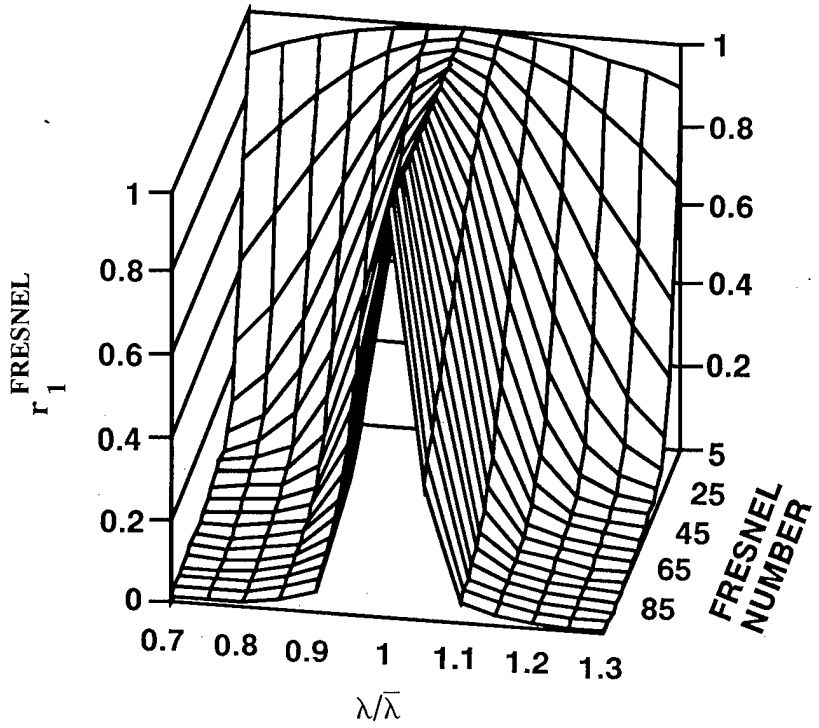

FIGURE 5. FIGURE OF MERIT FOR FRESNEL DISPERSIVE MICROLENS FOR THE CASE OF FIRST-ORDER DIFFRACTION, EQUAL BLAZE AND DESIGN WAVELENGTHS, AND FIVE GRATING PERIODS.

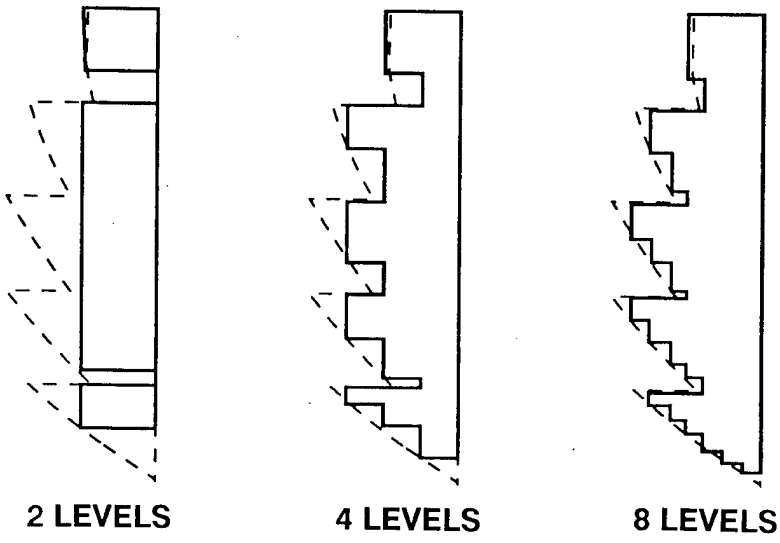

FIGURE 6. SUCCESSIVE MULTILEVEL APPROXIMATIONS TO A DISPERSIVE MICROLENS.

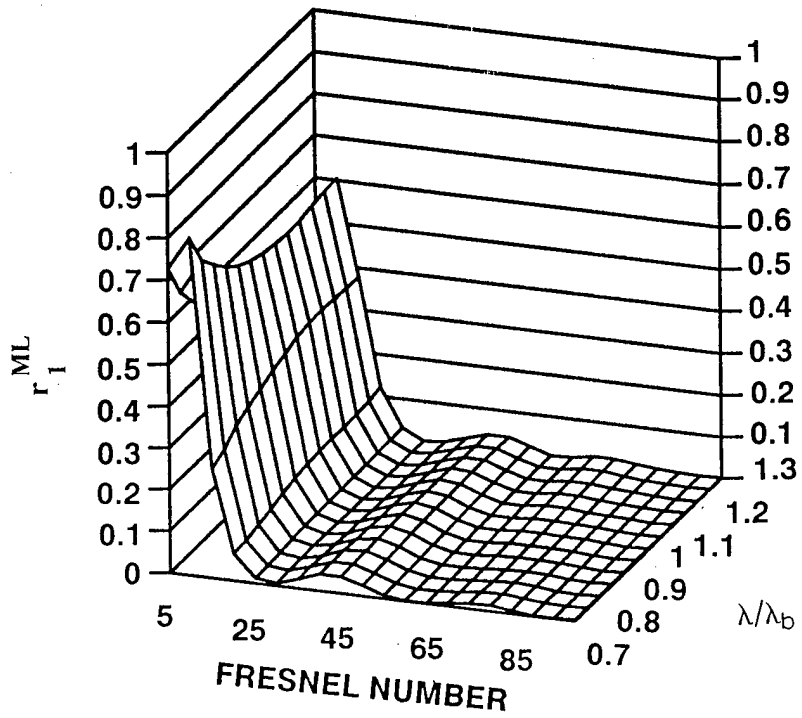

FIGURE 7. FIGURE OF MERIT FOR MULTILEVEL DISPERSIVE MICROLENS FOR THE CASE OF FIRST-ORDER DIFFRACTION, EQUAL BLAZE AND DESIGN WAVELENGTHS, FIVE GRATING PERIODS, AND EIGHT LEVELS.

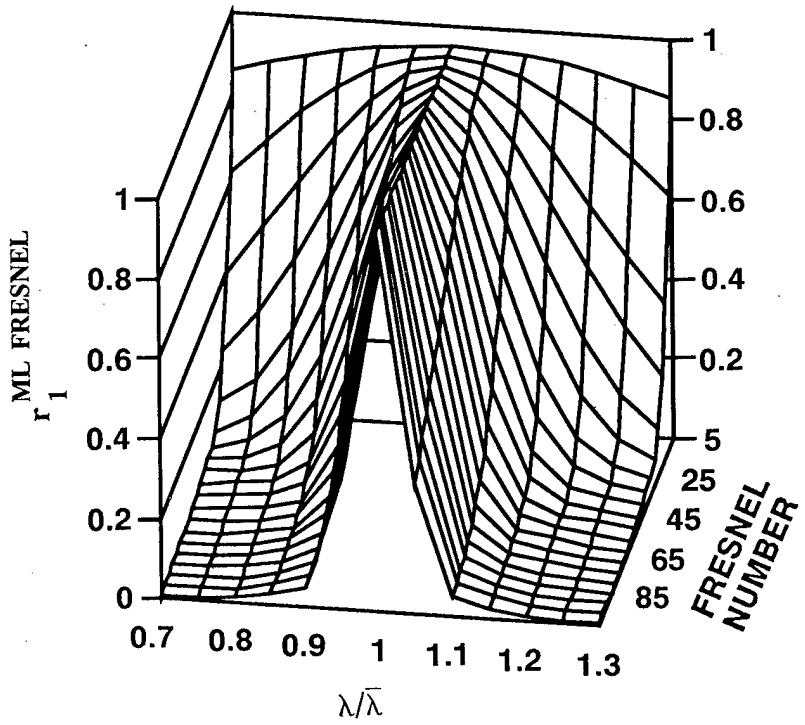

FIGURE 8. FIGURE OF MERIT FOR MULTILEVEL FRESNEL DISPERSIVE MICROLENS FOR THE CASE OF FIRST-ORDER DIFFRACTION, EQUAL BLAZE AND DESIGN WAVELENGTHS, FIVE GRATING PERIODS, AND EIGHT LEVELS.

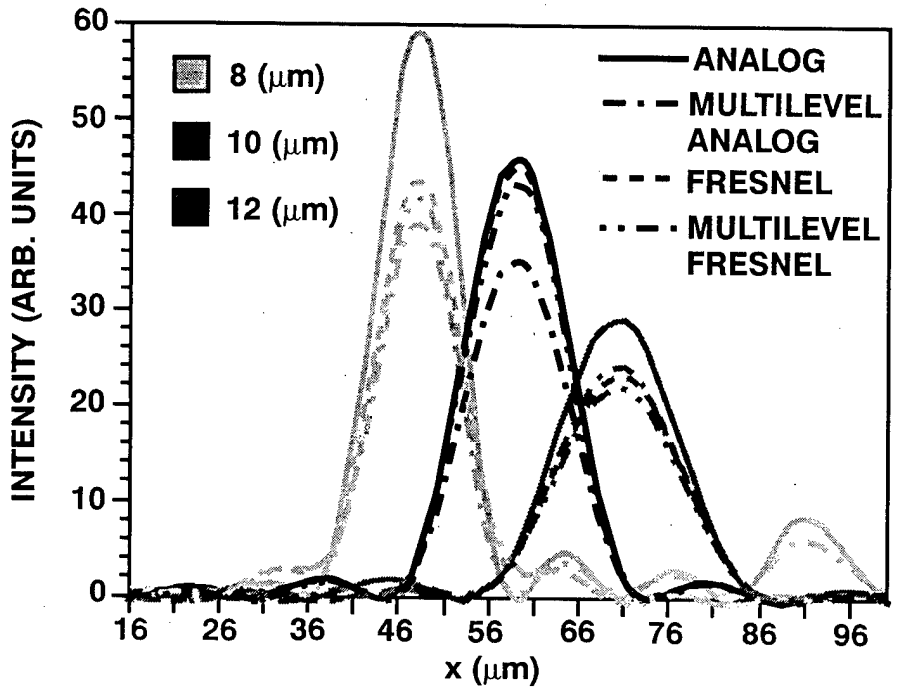

FIGURE 9. DIFFRACTION PATTERNS OBTAINED FROM DIFFERENT DISPERSIVE ELEMENT TYPES FOR A DESIGN OPERATING IN THE LWIR.

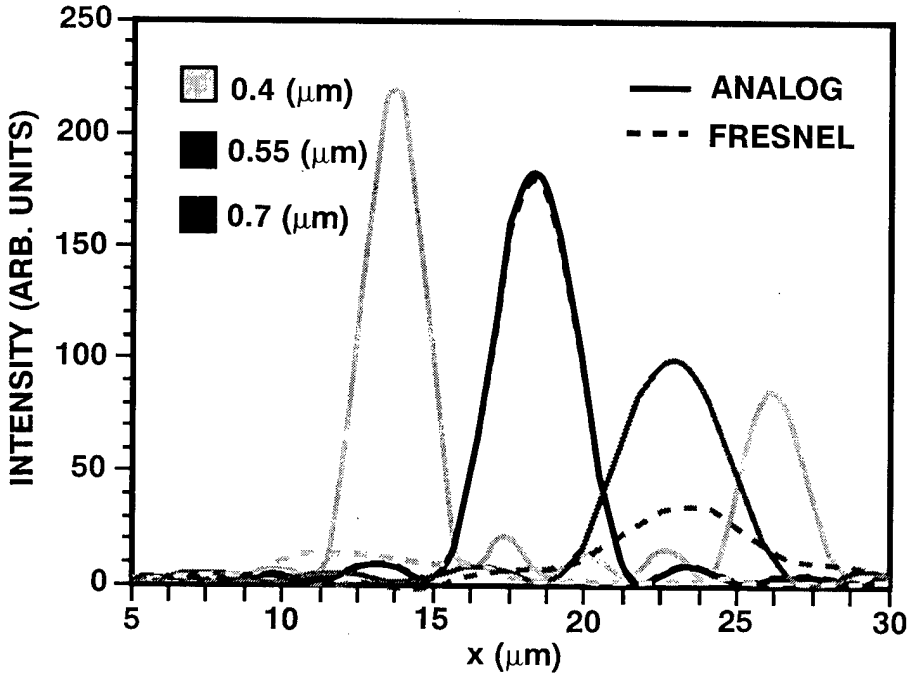

FIGURE 10. DIFFRACTION PATTERNS OBTAINED FROM DIFFERENT DISPERSIVE ELEMENT TYPES FOR A DESIGN OPERATING IN THE VISIBLE.

Color Separation Gratings

Michael W. Farn, Robert E. Knowlden,
Margaret B. Stern and Wilfrid B. Veldkamp
MIT/Lincoln Laboratory, HW45-108
244 Wood St., Lexington, MA 02173-9108

1. ABSTRACT

In this paper, we describe the theory, fabrication and test of a binary optics "echelon." The echelon is a grating structure which separates electromagnetic radiation of different wavelengths, but it does so according to diffraction order rather than by dispersion within one diffractin order, as is the case with conventional gratings. A prototype echelon, designed for the visible spectrum, is fabricated using the binary optics process. Tests of the prototype show good agreement with theoretical predictions.

2. INTRODUCTION

Color discrimination, or the separation of electromagnetic radiation by wavelength, is a basic building block for many applications, both military and commercial. In general, the task of discriminating between objects based on their spectrum can be broadly divided into two classes, based on the fineness of the discrimination. In one class, the unknown spectrum is sampled at very fine intervals, essentially reconstructing the spectrum. Discrimination techniques based on spectroscopy fall in this class. Although this class is quite important, it is not the topic of this paper and will not be discussed further.

In the other class of color discrimination, the unknown spectrum is divided into a small number of bands (typically three or four), which are used to characterize the unknown spectrum. For strategic defense, the majority of applications are in the infrared portion of the spectrum. Separation of the infrared band into several sub-bands can be used to better discriminate between objects (e.g., space debris, decoys and re-entry vehicles) and to more accurately estimate temperatures of objects.

In the visible portion of the spectrum, the earliest example is the human visual system, which perceives color based upon a separation of the spectrum into three bands (the three types of cones in the retina). Partly because the human visual system operates in this fashion, there are a large number of applications which also use this type of color discrimination. Common examples are color printing (separation into cyan, magenta, yellow and black dyes), color photography and motion pictures (separation into red, green and blue-sensitive emulsions), and color television and monitors (separation into red, green and blue sources).

The echelon described in this paper is one device which can be used to achieve the separation of a spectrum into bands. Other devices which can also achieve this separation without loss of energy are gratings, prisms and dichroic beam-splitters [1]. If significant loss of energy is tolerable, then color filters are another device which can be used.

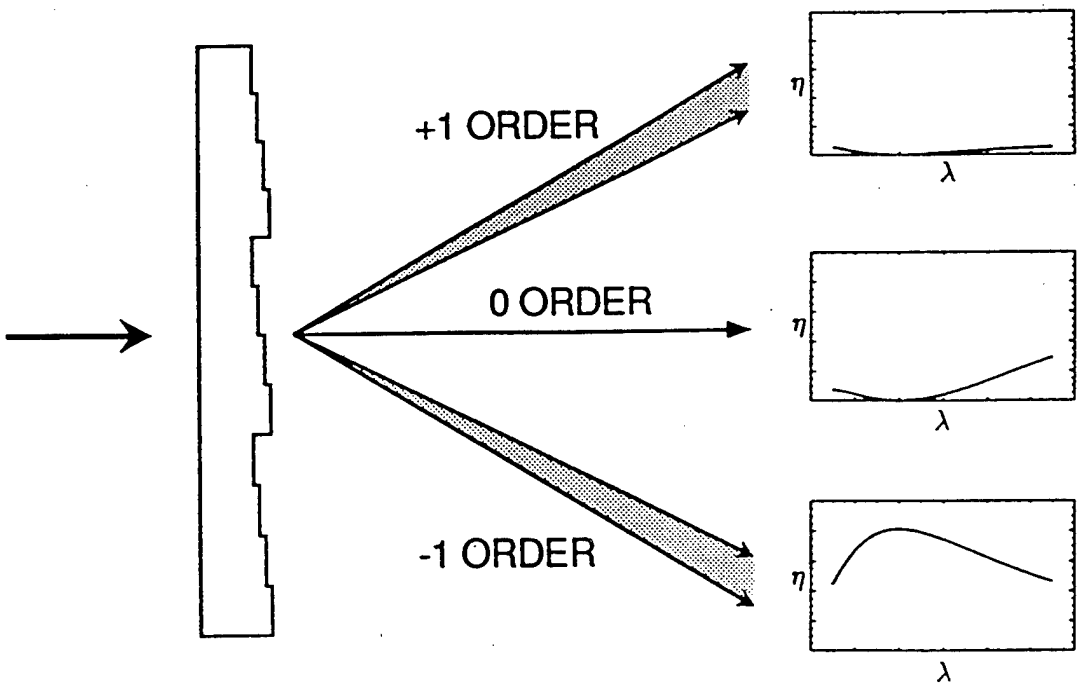

Figure 1: Conventional Binary Optics Grating.

The remainder of this paper describes the echelon in more detail. Section 3 describes the principle of operation of the echelon and the types of color separation it is capable of. Section 4 describes the fabrication of a prototype echelon using the binary optics process and section 5 describes the test of the prototype. Section 6 summarizes the paper.

3. THEORY

3.1. Conventional Grating

In order to better understand the operation of the echelon, it is instructive to examine the conventional method of separating colors via a grating. In binary optics, we approximate a blazed grating by a staircase profile with N steps [2], as shown in figure 1. In the figure, the η vs λ curves depict the spectral content of each order. Each step has a physical depth of

$$d = \lambda_0/[N(n_0 - 1)] \tag{1}$$

where n_0 is the index of the material at the design wavelength λ_0. Each step introduces a $2\pi/N$ phase shift for a total phase shift of 2π across one grating period. Therefore, at λ_0, the grating is blazed for the -1 order. For different wavelengths, the total phase shift introduced across one grating period (neglecting material dispersion) is $2\pi\lambda_0/\lambda$. For wavelengths close to λ_0 (e.g., $0.8 < \lambda/\lambda_0 < 1.3$), the total phase shift is still approximately 2π and the -1 order will contain the majority of energy at that wavelength, as shown by the efficiency curves in figure 1. Specifically, the efficiency of the ith order of an N-step conventional grating is [3]

$$\eta(i,\lambda) \;=\; \mathrm{sinc}^2(i/N)\,\mathrm{sinm}^2[\lambda_0/(N\lambda) + i/N, N] \tag{2}$$

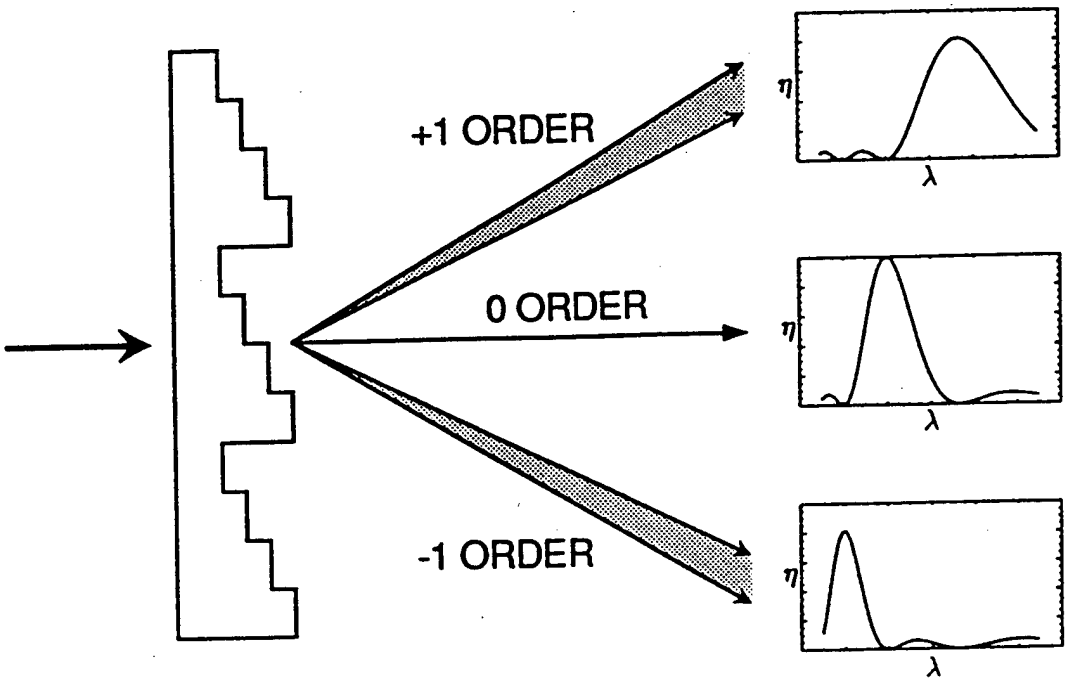

Figure 2: Binary Optics Echelon.

$$\text{where } \mathrm{sinc}(x) = \frac{\sin(\pi x)}{\pi x}$$

$$\text{and } \mathrm{sinm}(x, N) = \frac{\sin(N\pi x)}{N \sin(\pi x)}$$

The sinc term is the efficiency due to the stepped nature of the structure; while the sinm term is a result of the interference between the N phased steps.

In the conventional scheme, all wavelengths are diffracted primarily into the -1 order. However, the dispersion of the grating separates the wavelengths within the -1 order. As depicted by the shaded area in figure 1, the grating diffracts different wavelengths in different directions. Specifically, light of wavelength λ is diffracted at the angle

$$\sin\theta = i\lambda/T \tag{3}$$

where i is the diffraction order and T is the period of the grating.

3.2. Echelon

Now consider the "echelon" of figure 2. Strictly speaking, the structure is not an echelon [4], but we use the term to distinguish it from the conventional binary optics grating. This element also consists of N steps, but each step has a physical depth of

$$d = \lambda_0/(n_0 - 1) \tag{4}$$

Compared to the conventional grating (see equation 1), each step is N times deeper and therefore introduces N times the phase shift, which is exactly a phase shift of 2π at wavelength λ_0. However,

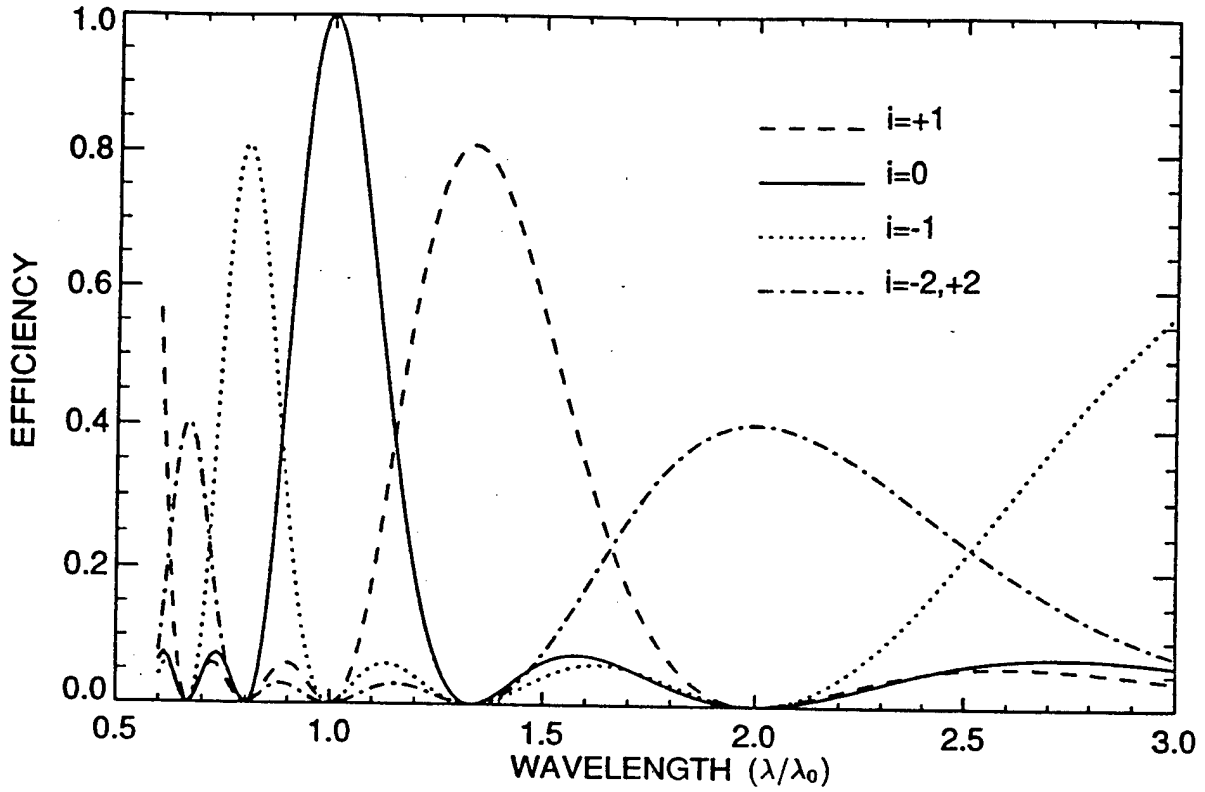

Figure 3: Diffraction Efficiency for 4-step Echelon.

for thin gratings, a phase shift of 2π is equivalent to a phase shift of 0. Therefore, at wavelength λ_0, the echelon behaves like a flat plate and is most efficient in the 0 order, as depicted by the peak in the 0 order efficiency curve in figure 2. Now consider the wavelength $\lambda_{-1} = \lambda_0 N/(N+1)$. At this wavelength, each step introduces a phase shift of $2\pi\lambda_0/\lambda_{-1} = 2\pi + 2\pi/N$, which is equivalent to a phase shift of $2\pi/N$. Therefore, at the wavelength λ_{-1}, the echelon is effectively blazed for the -1 order, as shown by the -1 order efficiency curve. For wavelengths between λ_{-1} and λ_0, the echelon will primarily split energy between the -1 and 0 orders. In a similar fashion, the echelon will be most efficient in the +1 order for wavelength $\lambda_{+1} = \lambda_0 N/(N-1)$. Since the spectrum around λ_{-1} is diffracted mainly into the -1 order, the spectrum around λ_0 mainly into the 0 order, and the spectrum around λ_{+1} mainly into the +1 order, the echelon can be used to separate colors into wavelength bands, as originally proposed by Dammann [5].

In a previous paper [6], Dammann has analyzed stepped-phase structures using scalar diffraction theory. Based on these results and neglecting material dispersion, the efficiency of the ith diffracted order of the N-step echelon is given by

$$\eta(i,\lambda) = \mathrm{sinc}^2(i/N)\,\mathrm{sinm}^2(\lambda_0/\lambda + i/N, N) \tag{5}$$

Figure 3 plots the efficiencies for different orders of a 4-step echelon. As with all the previous expressions, the efficiency $\eta(i,\lambda)$ is the fraction of light at wavelength λ which is diffracted into order i. Accordingly, $\sum_i \eta(i,\lambda) = 1$ for all wavelengths and $\int_\lambda E(\lambda)\eta(i,\lambda)d\lambda$, where $E(\lambda)$ is the incident spectrum, is the total power in order i. For the echelon shown in the figure, we can use

the +1, 0 and -1 orders to separate colors in the $.7\lambda_0$ to $2.0\lambda_0$ region. Also note that the -2 and +2 orders have the same efficiency curves. If we include material dispersion, then equation 5 becomes

$$\eta(i,\lambda) = \mathrm{sinc}^2(i/N)\,\mathrm{sinm}^2(\phi_0 + i/N, N) \quad (6)$$

$$\text{where } \phi_0 = \frac{\lambda_0[n(\lambda)-1]}{\lambda[n(\lambda_0)-1]}$$

and $n(\lambda)$ is the index of the grating material.

Examination of equation 5 reveals that the efficiency of order i will reach a peak when the sinm term is maximized. It can be shown that $\mathrm{sinm}(x, N)$ reaches its maximum value of 1 at integer values of x. Therefore, the efficiency peaks of order i can be calculated by setting the argument of the sinm term equal to an integer and then solving for λ. The resulting peaks occur at

$$\lambda = N\lambda_0/(mN - i), \text{ where } m \text{ is an integer} \quad (7)$$

The width of each diffracted order (as defined by its half power points) can also be calculated (although requiring numerical methods) by use of equation 5. Table 1 tabulates these peak wavelengths and half power points and their corresponding efficiencies for designs with up to 8 steps. As an example, consider the +1 order of a 4-step echelon ($i = +1, N = 4$). From the table, the diffraction efficiency has a peak of 81% at a wavelength of $1.33\lambda_0$. The efficiency falls to half of this, or 40%, at $1.16\lambda_0$ on the short wavelength side and at $1.57\lambda_0$ on the long wavelength side. Note that the response is not symmetric with respect to λ. Instead, it is symmetric with respect to $1/\lambda$.

In table 1, we have set $m = 1$ in order to keep the grating thin. Also, we only consider orders $i < N/2$ for two reasons. First, orders higher than this have efficiencies below 50% as a result of the sinc term. Second, inclusion of these higher orders may result in spectral overlap. That is, two different orders may have relative peaks at the same wavelength (e.g., orders +2 and -2 in figure 3).

The following points summarize the design process for the echelon:

1. Choose the central wavelength λ_0 to determine the wavelength peak of the zero order.
2. Choose the number of steps N to determine the peak wavelengths, peak efficiencies and widths of the other diffracted orders (see table 1).
3. Choose the period T to determine the direction of the diffracted orders (θ in the following section).
4. The grating material determines the step depth d (equation 4).

3.3. Separation of Wavelengths

The purpose of the echelon is to separate wavelengths. As an example, consider the following case. Suppose that we require the wavelengths λ_0 and λ_{-1} to be laterally separated by Δx over a distance z (see figure 4). Then, by trigonometry and the grating equation:

Table 1: Wavelength Bands for an N-Step Echelon

i	N = 3	4	5	6	7	8
+3					1.97 1.75 52% 1.58	1.76 1.60 61% 1.47
+2			1.96 1.67 57% 1.45	1.69 1.50 68% 1.35	1.54 1.40 76% 1.29	1.44 1.33 81% 1.24
+1	1.96 1.50 68% 1.22	1.57 1.33 81% 1.16	1.41 1.25 87% 1.12	1.32 1.20 91% 1.10	1.26 1.17 93% 1.09	1.22 1.14 95% 1.08
0	1.18 1.00 100% .87	1.13 1.00 100% .90	1.10 1.00 100% .92	1.08 1.00 100% .93	1.06 1.00 100% .94	1.06 1.00 100% .95
-1	.85 .75 68% .67	.88 .80 81% .73	.90 .83 87% .78	.92 .86 91% .81	.93 .88 93% .83	.94 .89 95% .85
-2			.76 .71 57% .67	.79 .75 68% .71	.82 .78 76% .74	.84 .80 81 % .77
-3					.73 .70 52% .67	.76 .73 61% .70

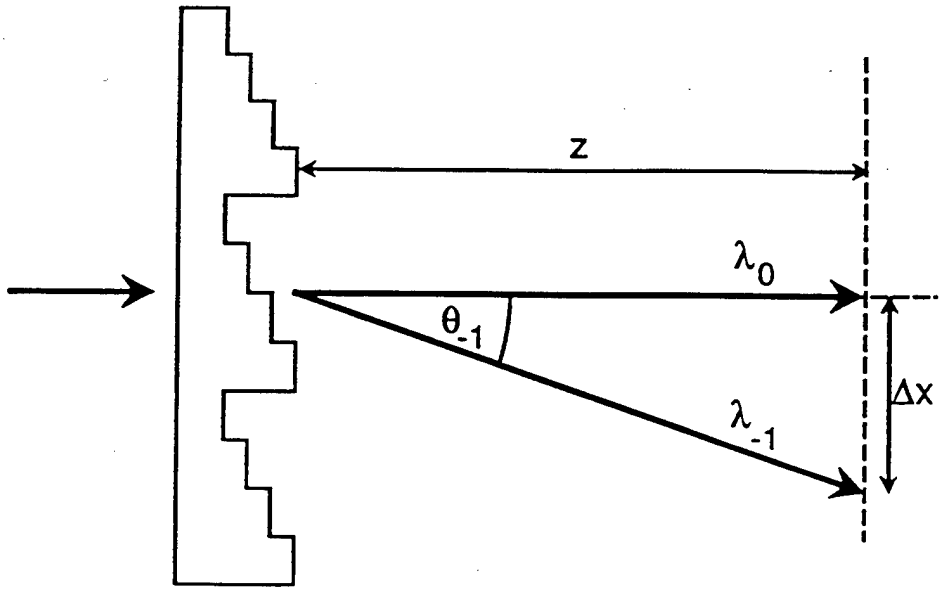

Figure 4: Separation of Wavelengths in an Echelon.

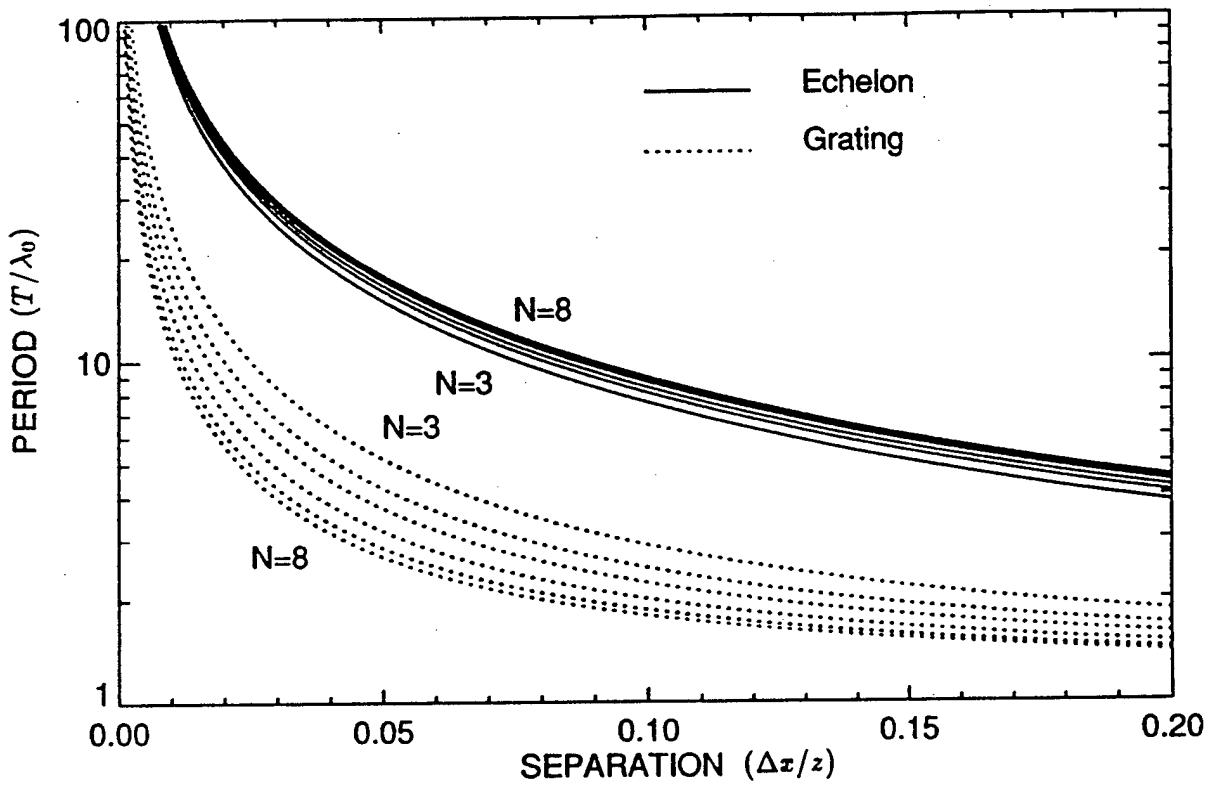

Figure 5: Period Required to Separate Wavelengths.

$$\tan\theta_{-1} = \Delta x/z \tag{8}$$
$$\sin\theta_{-1} = \lambda_{-1}/T \tag{9}$$

For an echelon, λ_{-1} varies with N (see table 1). If we fix N, then λ_{-1} is also fixed (relative to λ_0) and the above equations give the period T required to produce a given offset $\Delta x/z$. The solid curves of figure 5 plot this relationship for different numbers of steps.

Now compare this to the situation in a conventional grating (see figure 6). Again, by trigonometry and the grating equation, we have

$$\tan\theta_0 - \tan\theta_{-1} = \Delta x/z \tag{10}$$
$$\sin\theta_{-1} = \lambda_{-1}/T \tag{11}$$
$$\sin\theta_0 = \lambda_0/T \tag{12}$$

Again, we can plot T vs $\Delta x/z$ (dashed lines in figure 5). The figure shows that a much smaller grating period is required for a conventional grating to achieve the same lateral separation as the echelon. In addition, the conventional grating also laterally offsets the central wavelength by

$$x_0/z = \tan\theta_0 \tag{13}$$

as shown in figure 7. The dashed lines are used to show the correspondance with the dashed curves of figure 5.

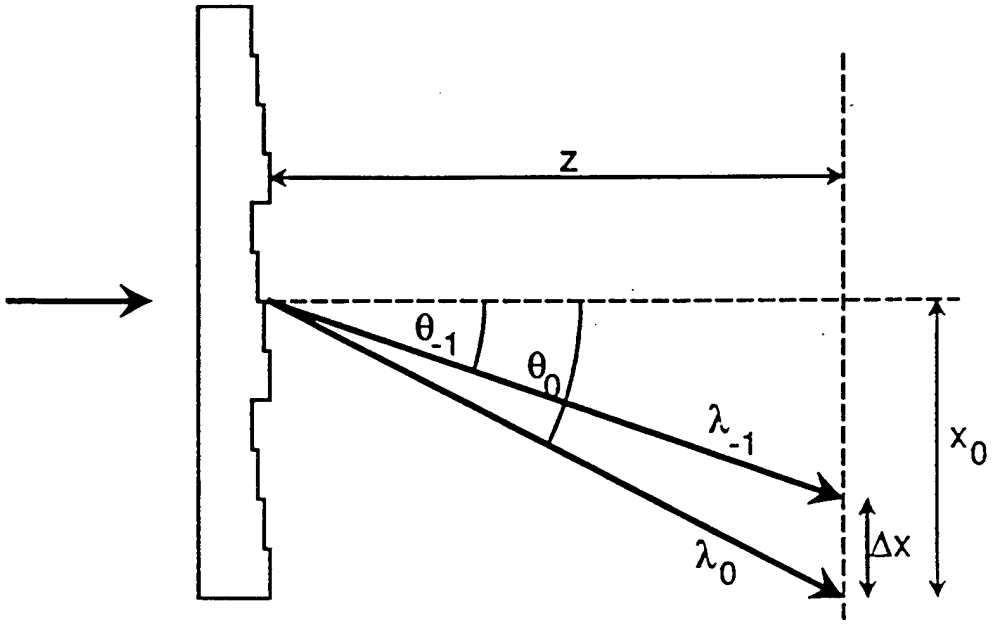

Figure 6: Separation of Wavelengths in a Conventional Grating.

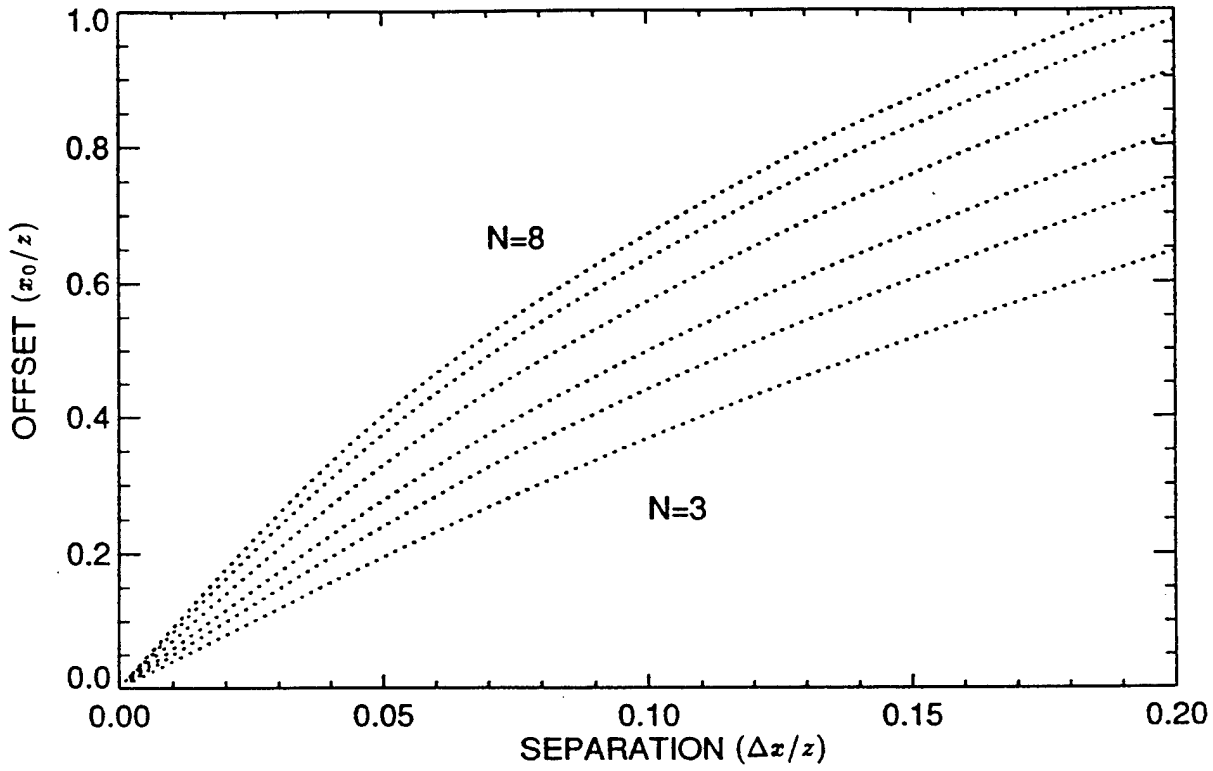

Figure 7: Offset Produced by Conventional Grating.

Table 2: Measured Etch Depths (μm).

Location	First etch	Second etch
Center	1.06	2.23
Edge	1.11	2.36
Corner	1.17	2.44
Target	1.14	2.28

4. FABRICATION

Using binary optics technology [2], we fabricated a 4-step echelon for use in the visible ($N = 4, \lambda_0 = 525nm, T = 16\mu m$). The process begins by transforming the optical design of the echelon into a set of amplitude photomasks; in this case, we use two Cr-photomasks with 50% duty cycle gratings of periods 8 and 16 μm, respectively, to produce the final 16 μm period echelon. These patterns are first replicated into a thin photoresist film (Shipley 1800 positive photoresist) by vacuum-contact photolithography, using a Karl Suss MA6 contact mask aligner operating at 365 nm. The resultant photoresist mask is then transferred into the substrate material to a precise depth by RIE. For substrates, we use 2" diameter, 6 mm thick Suprasil fused silica discs ($n_0 = 1.46$) polished on both sides, with a top surface flatness of $\lambda/10$. The step depth for this echelon is 1.14 μm, as given by equation 4, and the total depth of the echelon is 3.42 μm, three times the step depth.

The mask with the smaller features (the 8 μm period mask) is printed first to maintain linewidth fidelity. The substrate is loaded onto a 6" diameter quartz plate covering the RF powered cathode and then etched in a Perkin Elmer sputter-etch system operated in the RIE mode to the target depth of 1.14 μm. CHF_3 is introduced into the system via a feedback-controlled mass flow controller to a pressure of 10 mTorr. Typical quartz etching rates are 16.5 nm/min at 180 watts RF power and 220 volts bias voltage. Etch depths are controlled by etch time. Selectivity between the photoresist mask and the quartz substrate is approximately two to one.

Next, the coarser mask is aligned to the pattern previously etched into the substrate surface. A Cr film evaporated through a stencil mask onto the pattern edges enhances visibility during alignment. The second application of photoresist must be sufficiently thick to maintain photoresist linewidth across the previously etched 1 μm feature. That is, the photoresist must somewhat planarize the existing topography. Here, we are aided by the large and regular features of the grating. By using a single layer of 2.3 μm thick photoresist, we could preserve the pattern integrity without resorting to more complex multilayer resist techniques. The second mask is then etched to a target depth of 2.28 μm. The use of two masks results in a 4-step echelon, due to the binary coding scheme used to define the masks. The completed echelon covers an area of approximately 25 cm x 35 cm.

The actual etch depths are measured at different locations with a Tencor alpha-step 200 stylus profilometer and the results are tabulated in table 2. A sample measurement is shown in figure 8. The etch depth variation of approximately $\pm 5\%$ is mainly due to a radially non-uniform etch rate across the substrate.

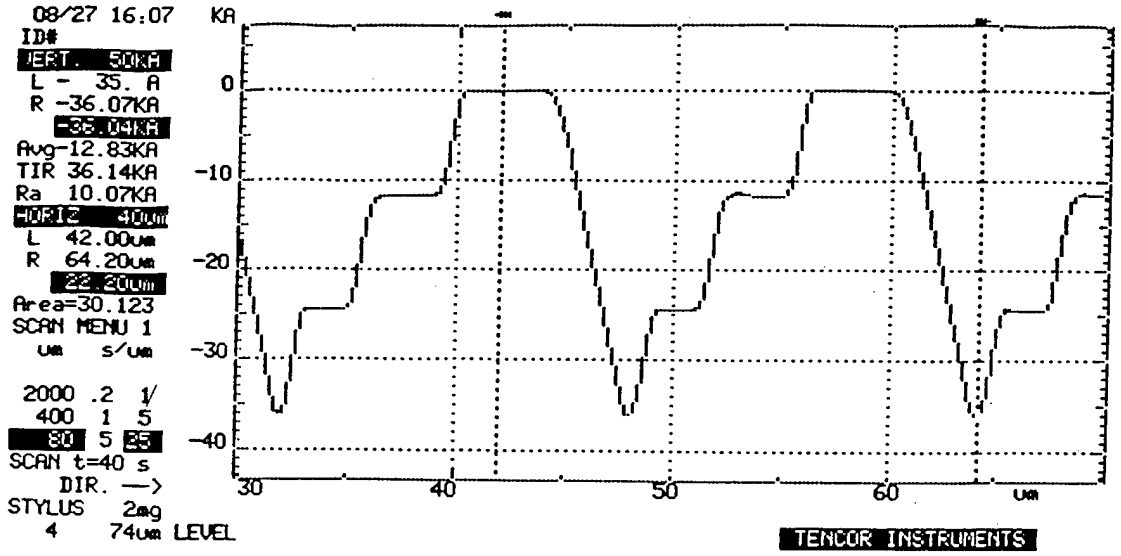

Figure 8: Stylus Profilometer Trace.

5. TEST

The fabricated echelon is tested using the experimental set-up of figure 9. We use a 12 W tungsten-halogen bulb with a diffuser as the source, with the aperture used to control the size of the source. The lens images the source onto the entrance slit of the spectrometer and the echelon splits the single image of the source into multiple images as shown by the dashed lines, each image corresponding to a diffracted order of the echelon. For the 4-step echelon, we are interested only in the -1,0 and +1 orders. The multiple images still fall on the entrance slit of the spectrometer. The aperture in the echelon plane is used to block off stray light and the spatial filter is used to block unwanted orders from entering the spectrometer. The photomultiplier produces a current proportional to the incident light. The load resistor converts this current to an output voltage, which is measured by the lock-in analyzer. The chopper is used in conjunction with the lock-in to increase the SNR of the system.

Initially, all orders are allowed to enter the spectrometer and this measurement is used as the reference. This reference measurement is shown in figure 10. Note that the spectrum is very weak at the shorter wavelengths ($\lambda < 400nm$).

Next, all orders except one are blocked and the spectral content of the unblocked order is measured. This is repeated for orders -1, 0 and +1. The results are shown in figure 11. The solid curves are the theoretical predictions based on equation 6, including the effects of the material dispersion. The connected crosses are the experimental measurements. The theory and experiment agree quite well, except at the shorter wavelengths. We believe this discrepancy is due to the weak reference at these wavelengths and the difficulty of making accurate measurements with respect to this reference.

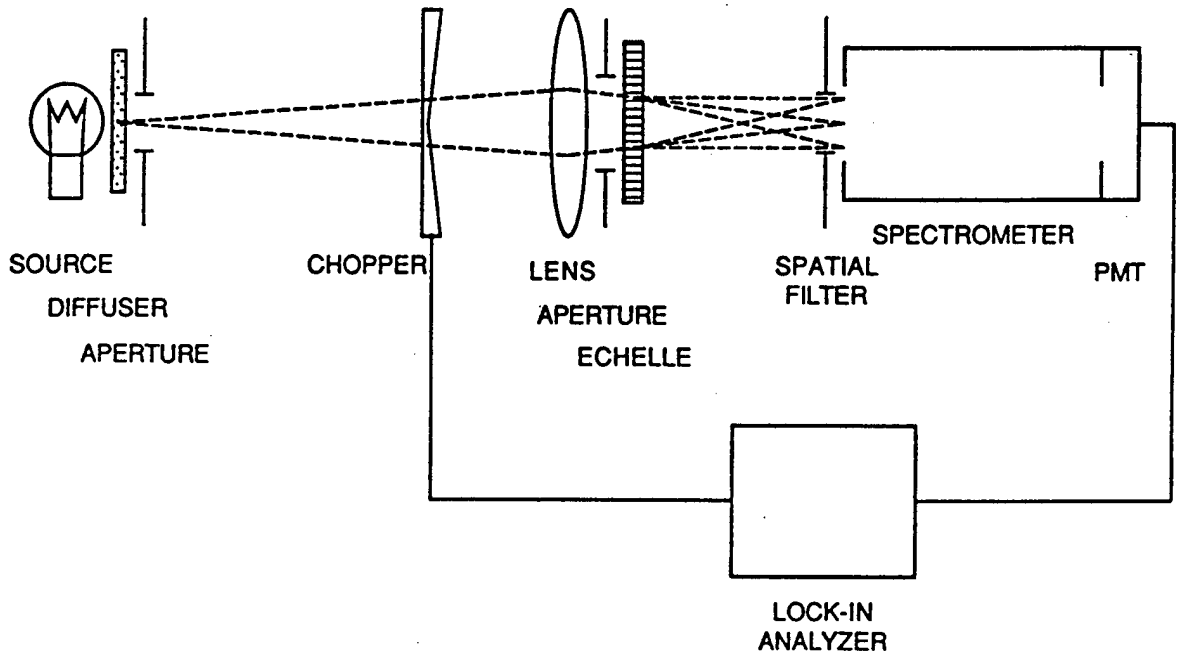

Figure 9: Experimental Set-up.

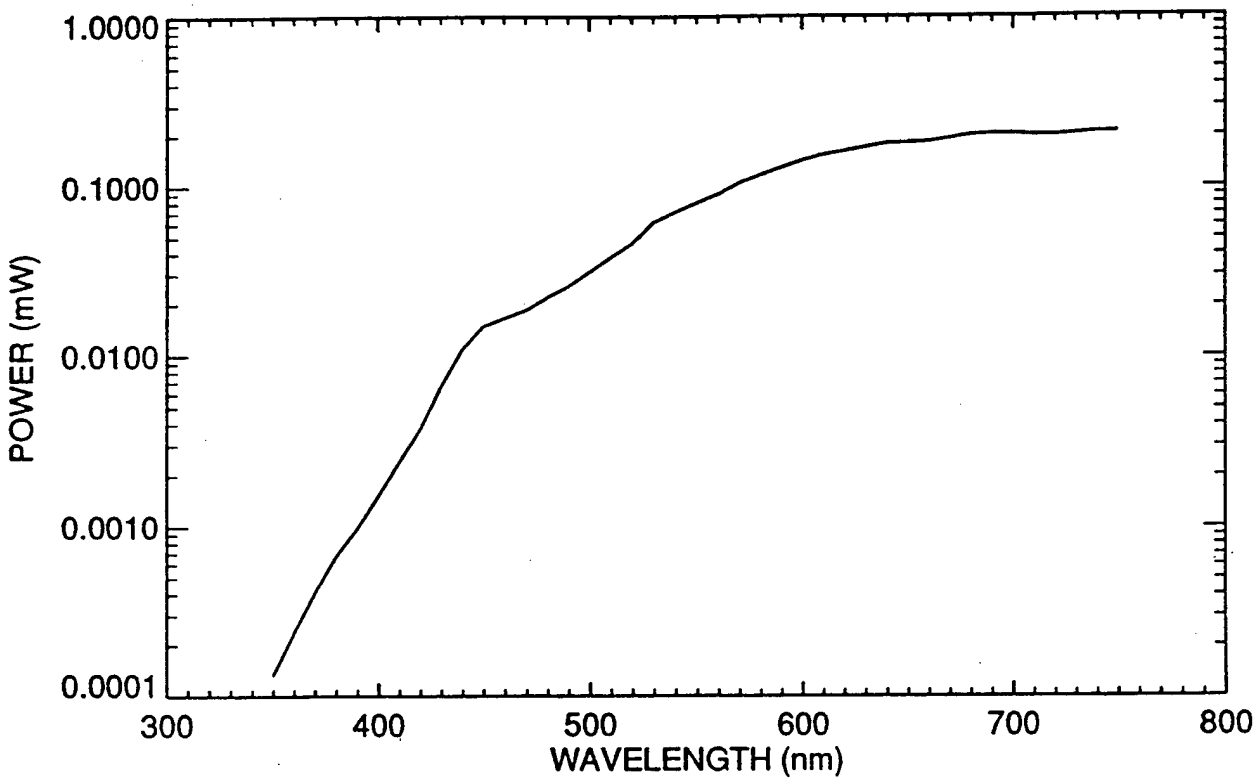

Figure 10: Reference Power.

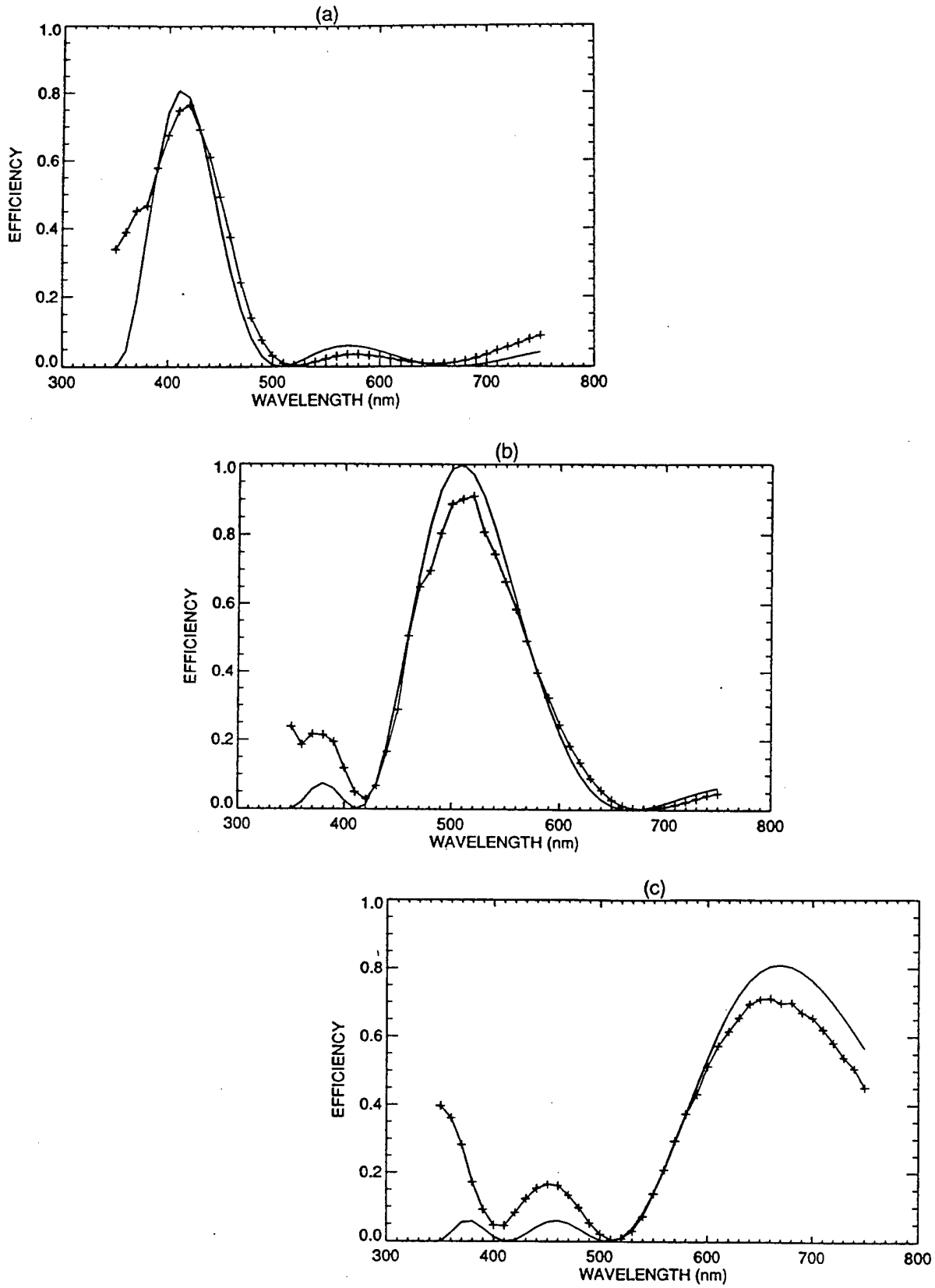

Figure 11: Spectral Composition of Orders (a) -1 Order (b) 0 Order (c) +1 Order

6. SUMMARY

The "echelon" is one device capable of separating a spectrum into several bands. We have analyzed the performance of the echelon, calculating the possible bands and the corresponding efficiencies for echelons of different numbers of steps (see table 1). We have also experimentally demonstrated the feasibility of using the "echelon" design for color discrimination. Using the binary optics process, we fabricated a 4-step echelon with center wavelength of $\lambda_0 = 525nm$. Measurements show that the echelon's spectral response agrees with the theoretical predictions.

7. REFERENCES

1. R. E. Knowlden, private communication.

2. G. J. Swanson, "Binary Optics Technology: The Theory and Design of Multi-level Diffractive Optical Elements," Technical Report 854, MIT/Lincoln Laboratory (1989), DTIC #AD-A213404.

3. G. J. Swanson, "Binary Optics Technology: Theoretical Limits on the Diffraction Efficiency of Multilevel Diffractive Optical Elements," Technical Report 914, MIT/Lincoln Laboratory (1991), DTIC/NTIS #AD-A235404.

4. M. Born and E. Wolf, *Principles of Optics* (Pergamon Press, New York, 1980), 409.

5. H. Dammann, "Color Separation Gratings," *Applied Optics* 17, 2273-2279 (1978).

6. H. Dammann, "Spectral Characteristics of Stepped-phase Gratings," *Optik* 53, 409-417 (1979).

ATTENDEES LIST

MUSTAFA ABUSHAGWR
UNIV.OF ALABAMA/HUNTSVILLE
ELECT.& COMP.ENGR.DEPT.
HUNTSVILLE AL 35899

MAX AMON
MARTIN MARIETTA
P.O.BOX 555837, MS 1040
ORLANDO FL 32819-5837

PARTHA BANERJEE
UNIV.OF ALABAMA/HUNTSVILLE
DEPT.OF ECE
HUNTSVILLE AL 35899

ASHOK BATRA
ALABAMA A&M UNIV.
1304 E.WINNER AVE.
HUNTSVILLE AL 35805

JAMES BILBRO
NASA OPTICS & RF DIV.
EB51
MSFC AL 35812

JOHN BRETNEY
LORAL AEROSPACE
FORD RD.
NEWPORT BEACH CA 92658-9983

JAMES CARTER
UNIV.OF ALABAMA/HUNTSVILLE
700 ERSKINE STREET
HUNTSVILLE AL 35899

RAYMOND CHUVALA
ARMY MISSILE COMMAND
AMCPM-CF-E
REDSTONE ARSENAL AL 35898-5640

HELEN COLE
NASA OPTICS & RF DIV.
EB52
MSFC AL 35812

LESLEY CONDIFF
NIGHT VISION&ELECTR.SENSOR DIR
AMSEL-RD-NV-LPD, MS 677
FT. BELVOIR VA 22060-5677

PRASAD AKKAPEDDI
HUGHES DANBURY OPT.SYS.
100 WOOSTER HEIGHTS RD.
DANBURY CT 06810

STEVE ANDERSON
HUGHES AIRCRAFT CO.
P.O.BOX 902, EO-E1-A176
EL SEGUNDO CA 90245

MICHELE BANISH
SY TECHNOLOGY, INC
4900 UNIVERSITY SQUARE, STE 8
HUNTSVILLE AL 35816

BRENT BEABOUT
NASA/MFSC
MFSC EB34
HUNTSVILLE AL 35812

PETER BLACK
ARMY MISSILE COMMAND
AMSMI-RD-SE-MT
REDSTONE ARSENAL AL 35898

DAN BROWN
SY TECHNOLOGY, INC
4900 UNIVERSITY SQUARE, STE 8
HUNTSVILLE AL 35816

WILLIAM CASE
LORAL VOUGHT SYS.CORP.
P.O.BOX 650003, MS PT-88
DALLAS TX 75265-0003

JEFFREY CITES
ARMY MISSILE COMMAND
AMSMI-RD-WS-CM
REDSTONE ARSENAL AL 35898-5248

TIMOTHY COLE
PHOTRONICS CORP.
270 MOTOR PARKWAY
HAUPPAUGE NY 11788

MICHAEL CONNOLLY
ARMY MISSILE COMMAND
AMSMI-RD-WS-CM
REDSTONE ARSENAL AL 35898-5248

AHMED AL-MANASREH
UNIV.OF ALABAMA/HUNTSVILLE
ECE DEPT.
HUNTSVILLE AL 35899

AHMAD ANEES
UNIV.OF ALABAMA/HUNTSVILLE
CENTER FOR APPL.OPTICS
HUNTSVILLE AL 35899

JOHN BARNUM
SYSTEMS ENGINEER
125 CATHERINE DR.
OXR AL 35763

GREGORY BEHRMANN
ARMY RESEARCH LABORATORY
AMSRL-SS-SF, 2800 POWDER MILL
ADELPHI MD 20783

RONALD BOHLANDER
GEORGIA TECH.RES.INST.
MANUF.RES.CTR.
ATLANTA GA 30332-0800

DAVID BROWN
TELEDYNE BROWN ENGINEERING
300 SPARKMAN
HUNTSVILLE AL 35807

RUSSELL CHIPMAN
UNIV.OF ALABAMA/HUNTSVILLE
PHYSICS DEPT.
HUNTSVILLE AL 35899

JAMES CLARK
NASA-MSFC
MAIL STOP ER21
MSFC AL 35812

ROSE COLEMAN
ERIM
PO BOX 134001
ANN ARBOR MI 48113

DOUG CONRAD
SANTA BARBARA APPLIED OPTICS
4820 MCGRATH ST.
VENTURA CA 93003

MICHAEL ALTMAN
LORAL IRIS
2 FORBES RD., MS 391
LEXINGTON MA 02173

PAUL ASHLEY
ARMY MISSILE COMMAND
AMSMI-RD-WS-CM
REDSTONE ARSENAL AL 35898

LORRAINE BARNUM
UNIVERSITIES SPACE RES.ASSOC
MSFC, ES43
HUNTSVILLE AL 35801

JEFFERSON BENNETT
ARMY MISSILE COMMAND
AMSMI-RD-WS
REDSTONE ARSENAL AL 35898-52

BRYAN BRAMES
THE AEROSPACE CORP.
P.O.BOX 92957, M4/978
LOS ANGELES CA 90009

GEORGE BURRUSS
INDEPENDENT CONSULTANT
142 RALEIGH WAY
HUNTSVILLE AL 35811

MICHAEL CHRISP
JET PROPULSION LAB.
4800 OAK GROVE DR., MS169-21
PASADENA CA 91109

ROD CLARK
SY TECHNOLOGY, INC
4900 UNIVERISTY SQUARE, STE
HUNTSVILLE AL 35816

SYLVIE COLENTIER
SAGEM
72.74 RUE DE LA TOUR BILLY,
95101 ARGENTEUIL FRANCE

ALAN COX
HONEYWELL SYS.& RES.CTR.
10701 LYNDALE AVE.,S
BLOOMINGTON MN 55420

HAROLD CRAIGHEAD
CORNELL UNIVERSITY
CLARK HALL, MS AEP
ITHACA NY 14853

DANTE D'AMATO
UNITED TECHNOLOGIES
54 CAMBRIDGE PARK DR.
CAMBRIDGE MA 02140

JOHN DAVIS
ARMY MISSILE COMMAND
AMSMI-RD-SE-MT
REDSTONE ARSENAL AL 35898

JAMES DAWSON
DYNETICS, INC.
P.O.DRAWER B
HUNTSVILLE AL 34814-5050

WILLIAM DELANEY
TELEDYNE BROWN ENGR.
300 SPARKMAN DR., MS/60
HUNTSVILLE AL 35807

CHARLES DELUISE
AF WRIGHT LABORATORY
WL/DOL-M,BLDG.45
WPAFB OH 45433-7552

KEVIN DENNEN
NICHOLS RES.CORP.
4040 S.MEMORIAL PKWY.
HUNTSVILLE AL 35815-1502

RUSS DEWITT
TELEDYNE BROWN ENGINEERING
300 SPARKMAN DR., MS/60
HUNTSVILLE AL 35807

KATHRYN DIETZ
SVERDRUP TECHNOLOGY/AEDC
9013 AVENUE C, MS9013
ARNOLD AFB TN 37389-9013

STEVEN DONLEY
HUGHES AIRCRAFT CO.
700 BOULEVARD SOUTH, SUITE 302
HUNTSVILLE AL 35802

JAMES DUFFEY
S-CUBED
2501 YALE S.E., STE.300
ALBUQUERQUE NM 87106

ANDREW DULL
LOCKHEED MISL. & SPACE CO.
P.O.BOX 070017
HUNTSVILLE AL 35807-7017

DONALD DUNSTONE
ARMY MISSILE COMMAND
AMSMI-ORD-SE-MT
REDSTONE ARSENAL AL 35898-5270

UWE DUVENECK
ATLAS ELEKTRONIK GMBH
2800 BREMEN 44,P.O.44.85.45
BREMEN, GERMANY

GILL DUYKERS
ARMY MISSILE COMMAND
AMSMI-RD-AS-IR
REDSTONE ARSENAL AL 35898

RON ENG
NASA/MSFC
EB52
HUNTSVILLE AL 35812

CLINTON EVANS
HUGHES-LEITZ OPT.TECH.
328 ELLEN ST., MIDLAND
ONTARIO,CANADA L4R 2H2

DEAN FAKLIS
ROCHESTER PHOTONICS CORP.
330 CLAY RD.
ROCHESTER NY 14623

MICHAEL FARN
MIT LINCOLN LABORATORY
244 WOOD ST., MS HW45-108
LEXINGTON MA 02173

STEVE FAWCETT
NASA OPTICS & RF DIV.
EB53
MSFC AL 35812

RICHARD FEINLEIB
ESSEX CORPORATION
9170 RUMSEY RD.
COLUMBIA MD 21045

MICHAEL FELDMAN
DIGITAL OPTICS CORPORATION
8701 MATLAND CREED RD, STE 220
CHARLOTTE NC 28262

CHEN FENG
UNIV.OF ALABAMA/HUNTSVILLE
CENTER FOR APPLIED OPTICS
HUNTSVILLE AL 35899

JOSEPH FIKES
DYNETICS, INC.
P.O.DRAWER B
HUNTSVILLE AL 35814-5050

PAUL FILEGER
TELEDYNE BROWN ENGR.
300 SPARKMAN DR.
HUNTSVILLE AL 35807

TOM FLOURNOY
ARMY TMDE ACTIVITY
AMXTM-SR
REDSTONE ARSENAL AL 35898-5400

J. WILLIAM FOREMAN
TELEDYNE BROWN ENGR.
300 SPARKMAN DR, MS19
HUNTSVILLE AL 35807

MIKE FREEMAN
OPTICS& VISION LTD.
70 VALE ST., DENBIGH,CLWYD
WALES UK L46 3BW

RUSSELL FREEMAN
ARMY SPACE&STRATEGIC DEF.CMD.
105 WYNN, CSSD-SL-S
HUNTSVILLE AL 35807

GEORGE GAL
LOCKHEED PALO ALTO RES.LAB.
3251 HANOVER ST.
PALO ALTO CA 94304-1191

PATRICK GARDNER
USAF
ASC/YHR
EGLIN AFB FL 32542

THOMAS GAYLORD
GEORGIA TECH
777 ATLANTIC DR., SCHOOL OF
ATLANTA GA 30332-0250

STEPHEN GENTRY
SANDIA NATIONAL LABORATORY
PO BOX 5800, D 9222
ALBUQUERQUE NM 87185

JEFFREY GIERLOFF
LOCKHEED
4800 BRADFORD BLVD.
HUNTSVILLE AL 35807

ELIAS GLYTSIS
GEORGIA TECH.
777 ATLANTIC DR., SCHOOL OF EE
ATLANTA GA 30332-0250

JACQUES GOVIGNON
C.S. DRAPER LABORATORY
555 TECHNOLOGY SQUARE, MS53
CAMBRIDGE MA 02175

EDWARD GRATRIX
HUGHES DANBURY OPT.SYS.
100 WOOSTER HEIGHTS RD.
DANBURY CT 06810

B. D. GUENTHER
ARMY RESEARCH OFFICE
P.O.BOX 12211
RESERACH TRIANGLE NC 27709

WILLIAM GUNNING
ROCKWELL INT'L SCIENCE CENTER
1049 CAMINO DOS RIOS, A20
THOUSAND OAKS CA 91320

JERRY HAGOOD
ARMY MISSILE COMMAND
AMSMI-RD-WS-DP
REDSTONE ARSENAL AL 35898-52

DENNIS HALL
UNIVERSITY OF ROCHESTER
THE INSTITUTE OF OPTICS
ROCHESTER NY 14627

JOHN HARCHANKO
SAIC
6725 ODYSSEY
HUNTSVILLE AL 35806

RICHARD HARTMAN
UNIV.OF ALABAMA/HUNTSVILLE
OB-400, CTR.FOR APPL.OPTICS
HUNTSVILLE AL 35899

FRANK HAYES
ARMY MISSILE COMMAND
AMSMI-RD-AS-IR
REDSTONE ARSENAL AL 35898

BART HENSON
BIONETICS CORPORATION
7608 TEAL DRIVE SW
HUNTSVILLE AL 35802

JOHN HIRS
LORAL INFRARED & IMAGING SYSTEMS
2 FORBES RD.
LEXINGTON MA 02173-7393

DAMIAN HOCHMUTH
UNIV. OF ALABAMA/HUNTSVILLE
3014 KIRKLAND DR.
ALABAMA AL 35810

DIANE HOCHMUTH
TELEDYNE BROWN ENGR.
300 SPARKMAN DR, MS200
HUNTSVILLE AL 35807

FORNEY HOKE
NICHOLS RESEARCH CORP.
4040 S.MEMORIAL PKWY.
HUNTSVILLE AL 35815-1502

DAVE HOLDER
ELECTRONICS & SPACE CORP.
8100 W. FLORISSANT AVE.
ST. LOUIS MO 63136

DALE HOLTER
NICHOLS RESEARCH CORP.
4040 S. MEMORIAL PKWY.
HUNTSVILLE AL 35815-1502

GARY HOUGH
UNIV.OF ALABAMA/HUNTSVILLE
P.O.BOX 999, AEROPHYS.RES.CT
HUNTSVILLE AL 35899

JEFF HOWARD
TELEDYNE BROWN ENGR.
300 SPARKMAN DR.
HUNTSVILLE AL 35807

ROBERT HOWLE
DYNETICS, INC.
P.O.DRAWER B
HUNTSVILLE AL 35814

QIANG HUANG
UNIV.OF ALABAMA/HUNTSVILLE
PHYS.DEPT.
HUNTSVILLE AL 35899

DAVID HULAN
OCA APPLIED OPTICS, INC.
7421 ORANGEWOOD AVE.
GARDEN GROVE CA 92642

JURGEN JAHNS
AT&T BELL LABORATORY
101 CRAWFORDS CORNER RD 4G-524
HOLMDEL NJ 07733

JOHN JAREM
UNIV.OF ALABAMA/HUNTSVILLE
ECE DEPT.
HUNTSVILLE AL 35899

TZONG-SHINN JIANG
UNIV.OF ALABAMA/HUNTSVILLE
702-A SOUTH LOOP ROAD
HUNTSVILLE AL 35805

ERIC JOHNSON
TELEDYNE BROWN ENGINEERING
300 SPARKMAN
HUNTSVILLE AL 35807

GORDON JOHNSTON
NASA HQ, OACT
CODE RSS
WASHINGTON DC 20546

MICHAEL JONES
UNIV.OF ALABAMA/HUNTSVILLE
PHYS. DEPT.
HUNTSVILLE AL 85758

MIKE JONES
GENERAL DYNAMICS
P.O.BOX 748
FT. WORTH TX 76101

REBECCA JORDAN
UNIVERSITY OF ROCHESTER
INST. OF OPTICS., WILMOT BLD
ROCHESTER NY 14620

FRANCIS KAISLER
WESTINGHOUSE ELECTRIC CORP.
P.O.BOX 1693
BALTIMORE MD 21203

KEIICHIRO KANEKO
UNIV.OF ARIZONA
901 N.1ST AVE., #21
TUCSON AZ 85719

RAKESH KAPOOR
ALABAMA A&M UNIVERSITY
DEPT OF PHYSICS
NORMAL AL 35762

ALAN KATHMAN
TELEDYNE BROWN ENGR.
300 SPARKMAN DR.
HUNTSVILLE AL 35807

MICHAEL KAVAYA
NASA/MARSHALL SPACE FLIGHT CRT.
MAIL CODE EB23
HUNTSVILLE AL 35812

BOBBY KENNEDY
NASA MSFC
EB-15
HUNTSVILLE AL 35812

DENNIS KENT
NAVAL AIR WARFARE CENT4ER
P.O.BOX 5152
WARMINSTER PA 18974

JEFF KINZER
TEXAS INSTRUMENTS INC.
P.O.BOX 655012, MS 37
DALLAS TX 75265

PAMELA KNIGHT
ARMY STRATEGIC DEFENSE CMD.
CSSD-SD-S., PO BOX 1500
HUNTSVILLE AL 35807

RAYMOND KOSTUK
UNIV.OF ARIZONA
ELECT.&COMPUTER ENGR.DEPT.
TUCSON AZ 85721

AMY KRANSTEUBER
ARMY MISSILE COMMAND
AMSMI-RD-WS-PO
REDSTONE ARSENAL AL 35898

ROGER KROES
NASA/MSFC
ES74
HUNTSVILLE AL 35812

DONALD LACEY
AF WRIGHT LAB.
WL/MNGS, 101 W. EGLIN BLVD.
EGLIN AFB FL 32542-6810

PIERRE LANGLOIS
NATIONAL OPTICS INSTITUTE
369 FRANQUET ST., SAINTE-FOY
QUEBEC, CANADA G1P 4N8

DAVID LANTEIGNE
ARMY MISSILE COMMAND
AMSMI-RD-WS-PO
REDSTONE ARSENAL AL 35898-5248

PINCHUS LAUFER
INST.FOR DEFENSE ANALYSES
1801 N. BEAUREGARD ST.
ALEXANDRIA VA 22311-1772

MATTHEW LAWRENCE
ARMY MICOM
AMSMI-RD-AS-IR
REDSTONE ARSENAL AL 35898

SHELAH LAWSON
SY TECHNOLOGY,INC.
4900 UNIVERSITY SQ., SUITE 8
HUNTSVILLE AL 35816

SING LEE
UNIV OF CALIFORNIA-SAN DIEGO
ELECT.& COMPUTER ENGR.DEPT.
LA JOLLA CA 92093-0407

RONALD LEGOWIK
ARMY MISSILE COMMAND
AMSMI-RD-SE-MT
REDSTONE ARSENAL AL 35898-52

TOM LI
MARTIN MARIETTA
P.O.BOX 628007, MS/1189
ORLANDO FL 32862

YE LI
UNIV.OF ALABAMA/HUNTSVILLE
CENTER FOR APPLIED OPTICS
HUNTSVILLE AL 35899

TILL LIEPMANN
PACIFIC SIERRA RESEARCH
2901 28TH ST., STE. 385
SANTA MONICA CA 90405

WILLIAM LINDBERG
ARMY MISSILE COMMAND
AMSMI-RD-SE-MT
REDSTONE ARSENAL AL 35898-52

JAW-JUEH LIU
UNIV.OF ALABAMA/HUNTSVILLE
704-H S LOOP R
HUNTSVILLE AL 35805

DAVID LOCKER
ARMY MISSILE COMMAND
AMSMI-RD-QA-QT-RT
REDSTONE ARSENAL AL 35898

DONALD LOCKER
LOGICON R&D ASSOC.
2600 YALE BLVD., SE
ALBUQUERQUE NM 87119

JAMES LOGUE
HUGHES DANBURY OPTICAL SYS.
100 WOOSTER HGT RD., MS/804
DANBURY CT 06810

SHIH-YAU LU
UNIV.OF ALABAMA/HUNTSVILLE
PHYS. DEPT., OPTICS BLDG.
HUNTSVILLE AL 35899

CLIFFORD LUTY
WESTINGHOUSE
9820 SATELLITE BLVD.
ORLANDO FL 32819

JOSEPH MACKOVJAK
US ARMY MISSILE COMMAND
SFAE-MSL-AT-EA
REDSTONE ARSENAL AL 35898

J. MICHAEL MADEWELL
ARMY SPACE & STRATEGIC DEF.C
106 WYNN DR.
HUNTSVILLE AL 35807

HARUO MAEDA
OLYMPUS CORP.
23456 HAWTHORNE BLVD., STE.120
TORRANCE CA 90505

JOSEPH MAIT
ARMY RESEARCH LABORATORY
2800 POWDER MILL AMSRL-SS-SF
ADELPHI MD 20783

PAUL MAKER
JET PROPULSION LAB.
4800 OAK GROVE DR.
PASADENA CA 91109

GREG MARTIN
UNIV.OF ALABAMA/HUNTSVILLE
CAO 322
HUNTSVILLE AL 35899

KEVIN MASCHHOFF
LORAL INFRARED & IMAG.SYS.
2 FORBES RD., MS/146
LEXINGTON MA 02173-7393

MICHAEL MASSIMI
DCS CORP.
1330 BRADDOCK PLACE
ALEXANDRIA VA 22314

KENT MCCORMACK
TEXAS INSTRUMENTS INC.
P.O.BOX 655012
DALLAS TX 75265

J. MICHAEL MCGARY
ARMY SPACE & STRATEGIC DEF.
CSSD-DE-C., PO BOX 1500
HUNTSVILLE AL 35807-3801

PATRICK MCMANUS
NASA MSFC
EB-15, BLDG.4487
MSFC AL 35812

WALTER MENDES
NICHOLS RESEARCH CORP.
4040 S. MEMORIAL PKWY.
HUNTSVILLE AL 35802

GREGORY MILLER
ARMY ACAC
ATZL-CDE-B
FT.LEAVENWORTH KS 66027-5300

WALTER MILLER
ARMY MISSILE COMMAND
AMSMI-RD-AS-OG
REDSTONE ARSENAL AL 35898

RAJ MISRA
UNIV.OF ALABAMA/HUNTSVILLE
1010 HENDERSON ROAD, #10E
HUNTSVILLE AL 35816

RONALD MITCHELL
UWOHALI, INC.
3317 TRIANA BLVD.
HUNTSVILLE AL 35805

NEIL MOHON
DYNETICS
PO DRAWER B
HUNTSVILLE AL 35814

WILLARD MONTGOMERY
LOCKHEED MISL.& SPACE CO.
P.O.BOX 070017
HUNTSVILLE AL 35807-7017

JAMES MORRIS
SAIC
6725 ODYSSEY DR.
HUNTSVILLE AL 35670

MIKE MORRIS
UNIVERSITY OF ROCHESTER
ENGR.& APPL.SCI.,INST.OF OPTIC
ROCHESTER NY 14627

EDWARD MOTAMEDI
ROCKWELL INT'L SCI.CTR.
1049 CAMINO DOS RIOS
THOUSAND OAKS CA 91360

PATRICK NASIATKA
UNIV.OF ALABAMA/HUNTSVILLE
1500 SPARKMAN DR.
HUNTSVILLE AL 35816

ARTHUR NELSON
FOSTER-MILLER INC.
195 BEAR HALL RD.
WALTHAM MA 02154

RICHARD NELSON
SUMMA TECHNOLOGY INC.
500 DISCOVERY DR.
HUNTSVILLE AL 35806

BRUCE NICHOLS
WESTINGHOUSE
P.O.BOX 1521, MS 3K28
BALTIMORE MD 21228

DAVID NICOLAS
NASA MSFC
EB-13
HUNTSVILLE AL 35812

JON NISPER
DONNELLY CORP.
414 E. 40TH ST.
HOLLAND MI 49424

CHRISTOPHER PARRY
AEROJET ELECTRONIC SYS.DIV.
P.O.BOX 296, MS 53/5801
AZUSA CA 91702

ABE POGODA
OSAF
4C1052, THE PENTAGON
WASHINGTON DC 20330-1000

WILLIAM PRESTWOOD
ARMY SPACE&STRATEGIC DEF.CMD.
CSSD-SD-O, 106 WYNN DR.
HUNTSVILLE AL 35807

JANINE REARDON
UNIV.OF ALABAMA/HUNTSVILLE
DEPT.OF PHYS.
HUNTSVILLE AL 35899

PHILIPPE REGNAULT
CSEM
MALADIERE 71, NEUCHATEL CH2000
SWITZERLAND

MAX RIEDL
OFC CORP.
2 MERCER RD.
NATICK MA 01760

CARL ROURK
NICHOLS RESEARCH CORP.
4515 BONNELL DR., #5A
HUNTSVILLE AL 35816

DANNY SAYLOR
AUTOMATED SCIENCES GRP.,INC.
1555 THE BOARDWALK
HUNTSVILLE AL 35816-1825

GREGORY SHARP
TELEDYNE BROWN ENGINEERING
300 SPARKMAN DR, MS19
HUNTSVILLE AL 35807

GREGORY NORDIN
UNIV.OF ALABAMA/HUNTSVILLE
EDE DEPT., EB267
HUNTSVILLE AL 35899

PIERO PERLO
FIAT RESEARCH CENTER
STRADA TORINO 50
ORBASSANO ITALY

GEORGE POLLOCK
ARMY SPACE&STRATEGIC DEF.CMD.
PO BOX 1500, CSSD-SA-EV
HUNTSVILLE AL 35807

DON PURDY
PHILIPS IR DEF.COMPONENTS
MILLBROOK IND.EST.,P.O.BOX 217
SOUTHAMPTON,HAMPS UK SO9 7QG

PATRICK REARDON
UNIV.OF ALABAMA/HUNTSVILLE
OPTICS. BLDG.
HUNTSVILLE AL 35899

DANIEL REILEY
UNIV.OF ALABAMA/HUNTSVILLE
PHYS.DEPT.
HUNTSVILLE AL 35899

APRIL ROBERTSON
TELEDYNE BROWN ENGR.
300 SPARKMAN DR.
HUNTSVILLE AL 35807

MICHELE RUBIN
ESSEX CORPORATION
9170 RUMSEY RD.
COLUMBIA MD 21045

ALLEN SCALES
NICHOLS RESEARCH CORP.
4040 S. MEMORIAL PKWY.
HUNTSVILLE AL 35802

ROSHAN SHETTY
UNIV.OF ARIZONA
OPTICAL SCIENCES CENTER
TUCSON AZ 85721

DANIEL NORTHEM
UNIV.OF ALABAMA/HUNTSVILLE
P.O.BOX 5525
HUNTSVILLE AL 35814-5525

BRUCE PETERS
TELEDYNE BROWN ENGR.
300 SPARKMAN DR.
HUNTSVILLE AL 35807

MICHAEL POWER
HUGHES DANBURY OPTICAL SYS.
100 WOOSTER HEIGHTS RD.
DANBURY CT 06810

DANIEL RAGUIN
UNIVERSITY OF ROCHESTER
INSTITUTE OF OPTICS
ROCHESTER SY 14627

B. R. REDDY
ALABAMA A&M UNIV.
DEPT.OF PHYSICS
NORMAL AL 35762

COLLEEN RICHMOND
ERIM
PO BOX 134001
ANN ARBOR MI 48113

RODNEY ROBERTSON
ARMY SPACE&STRATEGIC DEF.CMD.
CSSD-SD-AL
HUNTSVILLE AL 35807-3801

STEPHEN SAGAN
OPTICAL RESEARCH ASSOC.
550 N. ROSEMEAD BLVD.
PASADENA CA 91107

HARRY SCHLEMMER
CARL ZEISS
DW7022 OBERKOCHEN,CARL-ZEISS
GERMANY

CURTIS SHOEMAKER
3M ELECTRONIC PROD.DIV.
3M CENTER, MS 208-1-01
ST. PAUL MN 55144

KINAM PARK
UNIV.OF ALABAMA/HUNTSVILLE
DEPT.OF ECE
HUNTSVILLE AL 35816

WILLIAM PITTMAN
ARMY MISSILE COMMAND
AMSMI-RD-AS-PM
REDSTONE ARSENAL AL 35898-52

DENNIS PRATHER
ARMY RESEARCH LABORATORY
2800 POWDER MILL RD
ADELPHI MD 20783

JOSEPH RANDALL
NASA/MSFC
HUNTSVILLE AL 35812

ROBERT REDIKER
CYNOSURE, INC.
35 WIGGINS AVE.
BEDFORD MA 01730

DOUGLAS RICKS
NAVAL AIR WARFARE CENTER
CODE C2151
CHINA LAKE CA 93555

RICHARD ROBLE
ELECTRONICS & SPACE CORP.
8100 W. FLORISSANT AVE.
ST. LOUIS MO 63136

DEANNA SALERNO
ARMY MISSILE COMMAND
AMSMI-RD-WS-PO
REDSTONE ARSENAL AL 35898

MILES SCOTT
TELEDYNE BROWN ENGR.
300 SPARKMAN DR., MS/200
HUNTSVILLE AL 35807

D. MICHAEL SHOWALTER
ARMY MISSILE COMMAND
AMSMI-RD-JE-MT
REDSTONE ARSENAL AL 35898-52

LOY SHREVE
TAI, INC.
7500 MEMORIAL PKWY,SW, STE.119
HUNTSVILLE AL 35802

GEORGE SLOAN
ARMY SSDC
CSSD-SD-OS, 106 WYNN DR.
HUNTSVILLE AL 35807-3801

BETH SORNSIN
UNIV.OF ALABAMA/HUNTSVILLE
DEPT.OF PHYSICS
HUNTSVILLE AL 35899

RICHARD STEENBLIK
VIRTUAL IMAGE GROUP
1050 NORTHFIELD CT., STE.300
ROSWELL GA 30076

JULIA TEASLEY
TELEDYNE BROWN ENGR.
300 SPARKMAN DR.
HUNTSVILLE AL 35807

KOSTA VARNAVAS
NASA/MSFC
EB34
MSFC AL 35812

PAUL WANKO
ARMY MISSILE COMMAND
AMSMI-RD-SE-MT
HUNTSVILLE AL 35898-5270

RICHARD WILLIAMS
ARMY MISSILE COMMAND
AMSMI-RD-SE-MT
REDSTONE ARSENAL AL 35898

WILLIAM WITHEROW
NASA/MSFC
ES74, SSL BLDG. 4481
HUNTSVILLE AL 35812

HSUEH-LING YU
UNIV.OF ALABAMA/HUNTSVILLE
4912-B COTTON ROW
HUNTSVILLE AL 35816

FELIX SHVARTSMAN
DUPONT CO.
P.O.BOX 80352
WILMINGTON DE 19880-0352

JERRY SMITH
ARMY MISSILE COMMAND
AMSMI-RD-AC-FS, BLDG.5400
REDSTONE ARSENAL AL 35898

ROBERT SPANDE
NIGHT VISION&ELECTR.SENSOR DIR.
AMSEL-RD-NV-LPD
FT. BELVOIR VA 22060-5677

MARGARET STERN
MIT LINCOLN LAB.
244 WOOD ST., L-237A
LEXINGTON MA 02173-9108

RICHARD TRISSEL
KAISER ELECTRO-OPTICS
2752 LOKER AVE., W.
CARLSBAD CA 92008

PUTCHA VENKATESWARLU
ALABAMA A&M UNIVERSITY
DEPART OF PHYSICS
NORMAL AL 35762

JAMES WELLS
TELEDYNE BROWN ENGR.
300 SPARKMAN DR., MS 19
HUNTSVILLE AL 35807

TIMOTHY WILLIAMS
THE BOEING CO.
P.O.BOX 3707, MS 4C-01
SEATTLE WA 98124

ELEONORA WITTELES
SUMMA TECHNOLOGY, INC.
500 DISCOVERY DR.
HUNTSVILLE AL 35806

BRENT SISNEY
TEXAS INSTRUMENTS INC.
P.O.BOX 660246
DALLAS TX 75266

RONALD SNOW
AERO-THERMO TECHNOLOGY
6703 ODYSSEY DR., STE.303
HUNTSVILLE AL 35806

GARY SPIERS
UNIV.OF ALABAMA/HUNTSVILLE
CENTER FOR APPLIED OPTICS
HUNTSVILLE AL 35899

TONY TAI
ERIM
P.O.BOX 134001
ANN ARBOR MI 48113-4001

THOMAS TUMOLILLO
ARMY MISSILE COMMAND
AMSMI-RD-WS-CM
REDSTONE ARSENAL AL 35898

CHANDRA VIKRAM
UNIV.OF ALABAMA/HUNTSVILLE
CENTER FOR APPL.OPTICS
HUNTSVILLE AL 35899

THOMAS WERNER
HONEYWELL, INC.
10701 LYNDALE AVE.,S.
BLOOMINGTON MN 55420

DAVID WILSON
LOCKHEED
8707 CHURCHILL DR.
HUNTSVILLE AL 35801

JOHN WOOTTON
ELECTRONICS & SPACE CORP.
8100 W. FLORISSANT AVE.
ST. LOUIS MO 63136

CHRIS SLINGER
RSRE
DRA MALVERN,ST.ANDREWS RD.
WORESTSHIRE UK WR14 3PS

MARTIN SOKOLOSKI
SCIENCE & TECHNOLOGY CORP.
409 THIRD ST., SW, STE.203
WASHINGTON DC 20024

SHERMAN STEADMAN
NICHOLS RESEARCH CORP.
C-1 SHALIMAR CTR., 1 11TH AV
SHALIMAR FL 32579

CHEN-WEN TARN
UNIV.OF ALABAMA/HUNTSVILLE
ELECTR.& COMPUTER ENGR.
HUNTSVILLE AL 35899

DOUGLAS TURNURE
NICHOLS RES.CORP.
2537 PIONEER DR.
HUNTSVILLE AL 35803

ROBERT WALKER
UNITED INTERNATL.ENGR.INC.
1500 PERIMETER PKWY., #123
HUNTSVILLE AL 35806

STEPHEN WHICKER
TEXAS INSTRUMENTS INC.
P.O.BOX 655012, MS 39
DALLAS TX 75265

ROBERT WILSON
NASA
LANGLEY RES.CENTER, MS 473
HAMPTON VA 23681-0001

CHARLES WYMAN
MEVATEC
1525 PERIMETER PKWY, STE 500
HUNTSVILLE AL 35806

FINAL PROGRAM

Topics and schedule subject to change due to cancellations or other circumstances beyond our control at the time of the meeting.

TUESDAY MORNING, 23 FEBRUARY 1993

0730 REGISTRATION

0830 CALL TO ORDER AND OPENING REMARKS
Program Co-Chairperson Helen Cole, NASA, Marshall Space Flight Center, Huntsville, AL

0835 WELCOME TO CONFERENCE
Dr. Joe Randall, Director, Astrionics Laboratory, NASA, Marshall Space Flight Center, Huntsville, AL
Mr. Buford Jennings, Associate Director for Technology, RD&EC, MICOM, Redstone Arsenal, AL

0850 KEYNOTE ADDRESS*
Dr. B.D. Guenther, Army Research Office, Research Triangle Park, NC

0930 Perspectives on Binary Optics Programs*†
Dr. Jasper Lupo, ODDR&E(RLM)/DARPA, The Pentagon, Washington, DC

0945 MORNING BREAK

1005 Binary Optics, Trends, and Limitations*
Michael Farn, MIT Lincoln Laboratory, Lexington, MA

1035 TUTORIAL: Design and Fabrication of Binary Optics*
Dr. Michael Morris, University of Rochester, College of Engineering and Applied Science, Institute of Optics, Rochester, NY

1135 LUNCH BREAK

*Indicates Invited Paper
†Withdrawn

TUESDAY AFTERNOON, 23 FEBRUARY 1993

SESSION A: MODELING AND DESIGN

Chairpeople: Dave Lanteigne, Weapons Sciences Directorate, U.S. Army Missile Command, Redstone Arsenal, AL
Steve Anderson, Hughes Aircraft Company, El Segundo, CA

1300 A–1 Review of Rigorous Coupled-Wave Analysis and of Homogeneous Effective Medium Approximations for High Spatial-Frequency Surface-Relief Gratings*
Elias N. Glytsis, David L. Brundrett, and Thomas K. Gaylord, Georgia Institute of Technology, Atlanta, GA

1345 A–2 Scalar Limitations of Diffractive Optical Elements
E.G. Johnson, M.G. Moharam, and D. Pommet, Teledyne Brown Engineering, Huntsville, AL, and University of Central Florida, Orlando, FL

1410 A–3 Sub-Wavelength Structured Surfaces and Their Applications
Daniel H. Raguin and G. Michael Morris, University of Rochester, Institute of Optics, Rochester, NY

1435 AFTERNOON BREAK

1455 A–4 Diffractive Optical Elements for Generating Arbitrary Line Foci
D.W. Prather, J.N. Mait, and J. Van der Gracht, Harry Diamond Laboratories, Adelphi, MD

1520 A–5 Finite Difference Time Domain Analysis of Chirped Dielectric Gratings
D.H. Hochmuth and E.G. Johnson, Teledyne Brown Engineering, Huntsville, AL

1545 A–6 Asymmetric Three Beam Binary Optic Grating
A.D. Kathman, E.G. Johnson, and M.L. Scott, Teledyne Brown Engineering, Huntsville, AL

1610 A–7 Scattering From Binary Optics
Douglas W. Ricks, Naval Air Warfare Center, Weapons Division, China Lake, CA

1635 A–8 Mathematical Modeling for Diffractive Optics
David Dobson, University of Minnesota, School of Mathematics, Minneapolis, MN; and J. Allen Cox, Honeywell Systems & Research Center, Minneapolis, MN

1700 END OF DAY

*Indicates Invited Paper

WEDNESDAY MORNING, 24 FEBRUARY 1993

0730 REGISTRATION

0800 CALL TO ORDER
Program Co-Chairperson William Pittman, U.S. Army Missile Command, Redstone Arsenal, AL

0805 TUTORIAL: Fabrication of Binary Optics*
Dr. Margaret Stern, MIT Lincoln Laboratory, Lexington, MA

SESSION B: FABRICATION
Chairpeople: John Davis, System Engineering and Production Directorate, U.S. Army Missile Command, Redstone Arsenal, AL
Steve Fawcett, NASA, MSFC, Huntsville, AL

0905 Binary Optics Fabrication Capabilities at HDOS
B–1 Mike Power and James Logue, Hughes Danbury Optical Systems, Inc., Danbury, CT

0930 MORNING BREAK

0950 Fabrication Techniques for Very Fast Diffractive Lenses
B–2 Anthony M. Tai and Joseph C. Marron, Environmental Research Institute of Michigan, Ann Arbor, MI

1015 Laser Figuring for the Generation of Analog Micro-Optics and Kineform Surfaces
B–3 Edward J. Gratrix, Hughes Danbury Optical Systems, Inc., Danbury, CT

1040 Diffractive Optics Fabricated by Direct Write Methods With an Electron Beam
B–4 Bernard Kress, David Zaleta, Walter Daschner, Kris Urquhart, Robert Stein, and Sing H. Lee, University of California at San Diego, Dept. of ECE, LaJolla, CA

1105 Phase Holograms in PMMA With Proximity Effect Correction
B–5 P.D. Maker and R.E. Muller, Jet Propulsion Laboratory, Pasadena, CA

1130 Circularly Symmetric, Surface-Emitting Semiconductor Laser
B–6 Rebecca H. Jordan, Oliver King, Gary W. Wick, and Dennis G. Hall, University of Rochester, Institute of Optics, Rochester, NY

1155 LUNCH BREAK

*Indicates Invited Paper

WEDNESDAY AFTERNOON, 24 FEBRUARY 1993

SESSION B (Continued)

1315 B–7 Micro-Optics Technology and Sensor Systems Applications Overview
G. Gal, B. Herman, W. Anderson, R. Whimey, and H. Morrow, Lockheed Missiles and Space Co., Palo Alto, CA

1340 B–8 Fabrication of Micro-Optical Devices
W. Anderson, J. Marley, D. Purdy, and G. Gal, Lockheed Missiles and Space Co., Palo Alto, CA

1405 B–9 Diffractive Optics in Adverse Environments
G.P. Behrmann, Harry Diamond Laboratories, Adelphi, MD

1430 B–10 Low Costs Paths to Binary Optics
Lawrence Domash and Art Nelson, Foster-Miller, Inc., Watham, MA

1455 AFTERNOON BREAK

SESSION C: APPLICATIONS I
Chairpeople: Paul Ashley, Weapons Sciences Directorate, MICOM, Redstone Arsenal, AL
Alan Kathman, Teledyne Brown Engineering, Huntsville, AL

1515 C–1 Diffractive Optics Design for Producibility
J. Steven Anderson, Hughes Aircraft Co., El Segundo, CA; and Robert Spande, Army Night Vision and Electro-Optics Directorate, Ft. Belvoir, VA

1540 C–2 Measurements of Microlens Performance
D. Shough, B. Herman, and G. Gal, Lockheed Missiles and Space Company, Palo Alto, CA

1605 C–3 Applications of Advanced Diffractive Optical Elements
W. Hudson Welch and Michael B. Feldman, Digital Optics Corporation, Charlotte, NC

1630 C–4 Laser Beam Steering Device
M.E. Motamedi, A.P. Andrews, and W.J. Gunning, Rockwell International Science Center, Thousand Oaks, CA

1655 C–5 SURPHEX: New Dry Photopolymers for Replication of Surface Relief Diffractive Optics (U) *
Felix P. Shvartsmen, Dupont Company, Wilmington, DE

1720 END OF DAY

*Indicates Invited Paper

THURSDAY MORNING, 25 FEBRUARY 1993

0800 REGISTRATION

0830 CALL TO ORDER
Program Co-Chairperson Helen Cole, NASA, Marshall Space Flight Center, Huntsville, AL

0835 Predesign of Diamond Turned Refractive/Diffractive Elements for IR Objectives*
Max Riedl, Optical Filter Corporation, Natick, MA

0905 Optical Storage System Design With Diffractive Optical Elements*
Prof. Ray Kostuk and Charles W. Haggans, University of Arizona, Tucson, AZ

SESSION D: APPLICATIONS II
Chairpeople: James Bilbro, Deputy Chief, Optical and RF Systems Division, NASA, MSFC, Huntsville, AL
Paul Maker, Jet Propulsion Laboratory, Pasadena, CA

0935 Theory of Dispersive Microlenses
D–1 B. Herman and G. Gal, Lockheed Missiles and Space Co., Palo Alto, CA

1000 BREAK

1020 Color Separation Gratings*
D–2 Dr. Michael W. Farn, Robert E. Knowlden, Dr. Margaret B. Stern, and Dr. Wilfrid B. Veldkamp, MIT Lincoln Laboratory, Lexington, MA

1045 Fiber Continuity Test Using Multi-Level Diffractive Elements†
D–3 Roshan Shetty and Tom Milster, University of Arizona, Optical Sciences Center, Tucson, AZ

1110 END OF CONFERENCE

*Indicates Invited Paper
†Withdrawn

☆ U.S. GOVERNMENT PRINTING OFFICE 1993—733-050/80108

REPORT DOCUMENTATION PAGE

Form Approved
OMB No. 0704-0188

Public reporting burden for this collection of information is estimated to average 1 hour per response, including the time for reviewing instructions, searching existing data sources, gathering and maintaining the data needed, and completing and reviewing the collection of information. Send comments regarding this burden estimate or any other aspect of this collection of information, including suggestions for reducing this burden, to Washington Headquarters Services, Directorate for Information Operations and Reports, 1215 Jefferson Davis Highway, Suite 1204, Arlington, VA 22202-4302, and to the Office of Management and Budget, Paperwork Reduction Project (0704-0188), Washington, DC 20503.

1. AGENCY USE ONLY *(Leave blank)*	2. REPORT DATE	3. REPORT TYPE AND DATES COVERED
	August 1993	Conference Publication

4. TITLE AND SUBTITLE
Conference on Binary Optics -
An Opportunity for Technical Exchange

5. FUNDING NUMBERS

6. AUTHOR(S)
Helen J. Cole and William C. Pittman, Editors

7. PERFORMING ORGANIZATION NAME(S) AND ADDRESS(ES)
George C. Marshall Space Flight Center
Marshall Space Flight Center, Alabama

8. PERFORMING ORGANIZATION REPORT NUMBER
M-728

9. SPONSORING / MONITORING AGENCY NAME(S) AND ADDRESS(ES)
National Aeronautics and Space Administration
Washington, DC 20546

10. SPONSORING / MONITORING AGENCY REPORT NUMBER
NASA CP-3227

11. SUPPLEMENTARY NOTES
Other sponsors of this conference are shown on the cover of the document.

12a. DISTRIBUTION / AVAILABILITY STATEMENT
Unclassified-Unlimited
Subject Category: 74

12b. DISTRIBUTION CODE

13. ABSTRACT *(Maximum 200 words)*

The papers herein were presented at the Conference on Binary Optics held in Huntsville, AL, February 23-25, 1993. The papers were presented according to subject as follows: Modeling and Design, Fabrication, and Applications. Invited papers and tutorial viewgraphs presented on these subjects are included.

14. SUBJECT TERMS
Holographic Optical Elements, Diffractive Optics, Computer Generated Holography, Binary Optics, Diffraction Gratings

15. NUMBER OF PAGES
443

16. PRICE CODE
A19

17. SECURITY CLASSIFICATION OF REPORT	18. SECURITY CLASSIFICATION OF THIS PAGE	19. SECURITY CLASSIFICATION OF ABSTRACT	20. LIMITATION OF ABSTRACT
Unclassified	Unclassified	Unclassified	Unlimited